UNIVERSITÀ
DEGLI STUDI
FIRENZE

DOTTORATO DI RICERCA IN SCIENZE CHIMICHE

CICLO XXXIII

COORDINATORE Prof. BAGLIONI PIERO

COMBINING INORGANIC NANOPARTICLES WITH LAMELLAR AND NON-LAMELLAR LIPID BILAYERS: FROM INTERACTION TO DESIGN OF SMART HYBRID NANODEVICES

Settore Scientifico Disciplinare CHIM/02

Dottorando
Dott. Caselli Lucrezia

Tutore
Prof. Berti Debora

Coordinatore
Prof. Baglioni Piero

Anni 2017/2020

Abstract

Lipid bilayers are the structural building blocks of cell membranes and represent fundamental motifs in engineered soft matter. Understanding their interaction with nanomaterials, and in particular with nanoparticles (NPs), is one of the central challenges of nanomedicine and materials science, pursuing a twofold goal: i) to respond to the urgent quest for the mechanistic understanding of nano–bio interactions, which determine NPs cytotoxicity in living organisms; ii) to enable the rational design of smart NPs/lipid nanodevices of biocompatible nature for multiple technological purposes. In this work, we combine inorganic NPs with synthetic lipid bilayers, either in lamellar or non-lamellar arrangement, with two main purposes. Lipid bilayers are primarily employed as simplified and highly controllable models of cell membranes, enabling the identification of key determinants at stake in the interaction of engineered NPs with biological interfaces. Secondly, we exploit the conjugation of NPs with lipid bilayered-systems to develop hybrid nanostructures with technological relevance. The work presented here is organized in three parts. Part I focuses on the physicochemical investigation of the interaction of Turkevich-Frens citrated gold NPs (AuNPs@CT) with synthetic model bilayers of different physicochemical features: our results shed light on the peculiar clustering process of AuNPs@CT observed onto natural membranes, which, although well-known and biologically relevant, has remained largely unaddressed. In addition, we show that these results find application in the development of a new plasmon-based assay, for the determination of the mechanical properties of natural membranes. In Part II, we extend the investigation to curved-bilayered structures, ubiquitous in cells under certain conditions. Employing a library of gold nanoparticles (AuNPs) with different physicochemical features, we directly compare the interaction of AuNPs with model membranes of different symmetry, i.e. from lamellar to cubic architectures, encountered in diseased cells: these results constitute the first attempt to systematically investigate the impact of membrane curvature in the interaction with nanomaterials. Finally, in Part III, we address the interaction of cubic lipid assemblies with Superparamagnetic Iron Oxide NPs (SPIONs), showing that, beside its fundamental interest, it can be exploited for the development of smart nanostructured hybrids with potential application in the biomedical field. In summary, the results presented in this work advance our current understanding of the events occurring at Nano-bio Interfaces and pave the way for the development of new technological devices, exploiting the conjugation of NPs with lipid bilayers.

List of Publications

Contributions included in this thesis

Nanoparticles and organized lipid assemblies: from interaction to design of hybrid soft devices (Paper I)

M. Mendozza, L. Caselli, A. Salvatore, C. Montis and D. Berti, *Soft Matter*, 2019, 15 (44), 8951-8970

Shedding light on membrane-templated clustering of gold nanoparticles (Paper II)

C. Montis*, L. Caselli*, F. Valle, A. Zendrini, F. Carlà, R. Schweins, M. Maccarini, P.Bergese and D. Berti, *Journal of Colloids and Interface Science*, 2020, 573, 204-214 (* equally contributed)

A plasmon-based nanoruler to probe the mechanical properties of synthetic and biogenic nanosized lipid vesicles (Paper III)

L. Caselli, A. Ridolfi, J.Cardellini, L. Sharpnack, L. Paolini, M. Brucale, F. Valle, C. Montis, P. Bergese and D. Berti, 2020, Preprint. https://doi.org/10.26434/chemrxiv.13488120.v1 published on *ChemRxiv* and submitted to *Nanoscale Horizons* (December 2020)

Gold nanoparticles interacting with synthetic lipid rafts: an AFM investigation (Paper IV)

Ridolfi*, L. Caselli*, C. Montis, G. Mangiapia, D. Berti, M. Brucale and F. Valle, *Journal of Microscopy*, 2020, 00, 1–10 (* equally contributed)

Interaction of nanoparticles with lipid films: Curvature effects (Paper V)

L. Caselli, A. Ridolfi, G. Mangiapia, E. Gustafsson, N. J. Steinke, C. Montis, T. Nylander and D. Berti, in preparation

Inorganic nanoparticles modify the phase behavior and viscoelastic properties of non-lamellar lipid mesophases (Paper VI)

M. Mendozza, L. Caselli, C. Montis, S. Orazzini, E. Carretti, P. Baglioni and D.Berti, *Journal of Colloid and Interface Science*, 2019, 541, 329-33

On the thermotropic and magnetotropic phase behavior of lipid liquid crystals containing magnetic nanoparticles (Paper VII)

M. Mendozza, C. Montis, L. Caselli, M. Wolf, P. Baglioni and D.Berti, *Nanoscale*, 2018, 10 (7), 3480-3488

Other Contributions

AFM-based High-Throughput Nanomechanical Screening of Extracellular Vesicles

A. Ridolfi, M. Brucale, C. Montis, L. Caselli, L. Paolini, A. Borup, A. Toftegaard Boysen, F. Loria, M. van Herwijnen, M. Kleinjan, P.Nejsum, N. Zarovni, M. Wauben, D. Berti, P. Bergese and F. Valle, *Analytical Chemistry*, 2020, 92, 15, 10274–10282

Microfluidic characterization of biomimetic membrane mechanics with an on-chip micropipette

M. Elias, A. Dutoya, A. Laborde, A. Lecestre, C. Montis, L. Caselli, D. Berti, B. Lonetti, C. Roux, P. Joseph, Micro and Nano Engineering, 2020, 8, 100064

Contents

List of Abbreviations

AFM Atomic Force Microscopy

AFM-FS Force Spectroscopy-based Atomic Force Microscopy

AMF Alternating Magnetic Field

AuNPs Gold Nanoparticles

AuNPs@CT Citrated Gold Nanoparticles

AuNPs@MPA 3-Mercaptopropionic Acid capped-Gold Nanoparticles

AuNRs Gold Nanorods

AuNSs Gold Nanospheres

CITAB Cetyltrimethyl ammonium bromide

LSCM Laser Scanning Confocal Microscopy

DLS Dynamic Light Scattering

DOPC 1,2-dioleoyl-*sn*-glycero-3-phosphocholine

DPPC 1,2-dipalmitoyl-*sn*-glycero-3-phosphocholine

DSPC 1,2-distearoyl-*sn*-glycero-3-phosphocholine

EVs Extracellular Vesicles

GISANS Grazing-Incidence Small-Angle Neutron Scattering

GMO Glycerol Monooleate

IPMS Infinite Periodical Minimal Surface

LSPR Localized Surface Plasmon Resonance

MRI Magnetic Resonance Imaging

NPs Nanoparticles

NR Neutron Reflectivity

PC Phosphocholine

Phyt Phytantriol

POPC 1-Palmitoyl-2- oleoyl-*sn*-phosphocholine

QCM-D Quartz Crystal Microbalance with Dissipation monitoring

R.T. Room Temperature

SANS Small Angle Neutron Scattering

SAXS Small Angle X-ray Scattering

SLB Supported Lipid Bilayer

SPIONs Superparamagnetic Iron Oxide Nanoparticles

SPR Surface Plasmon Resonance

TEM Transmission Electron Microscopy

TMA N,N,N-trimethyl(11-mercaptoundecyl)-ammonium bromide

XRR X-Ray Reflectivity

UV-Vis Spectroscopy UV-Visible Spectroscopy

2D Two-dimensional

3D Three-dimensional

I Fundamentals

Lipid bilayers are the molecular building blocks of cell membranes and ubiquitous structural motifs in synthetic soft matter assemblies. Naturally inspired synthetic bilayered-systems can be employed as artificial platforms mimicking more complex biological assemblies and as biocompatible scaffolds to build artificial devices for nanomedical applications. Combining these systems with inorganic nanomaterials, e.g. engineered nanoparticles (NPs), is therefore of interest both for natural and synthetic soft matter assemblies.

In this work, we investigate the interaction of inorganic NPs of different physicochemical features with synthetic lipid bilayers, both arranged in lamellar and non-lamellar assemblies, with a twofold purpose: i) to mimic the interaction of NPs with biological barriers, e.g. plasma membranes, under highly controlled conditions, to gain insights on the main factors at play in NPs cytotoxicity; ii) to guide the rational design of hybrid smart nanomaterials, where NPs are included into the lipid bilayer, which can be exploited in the nanomedicine field, i.e. as drug delivery systems.

This work is organized as follows: **Chapter I** (**Paper I**) provides a general introduction on engineered NPs and synthetic lipid assemblies, together with the fundamental and applicative implications of their mutual interaction. **Chapter II** presents a theoretical description of the main techniques used for this research work. **Chapter III** summarizes the main results of this project, which will be then separately discussed in three different parts: **Part I** (**Papers II, III** and **IV**) will focus on the aggregation mechanism of Turkevich-Frens citrated gold NPs (AuNPs@CT) onto phosphocholine-based bilayer models: the peculiar clustering of AuNPs@CT was observed onto the surface of natural membranes, e.g. Extracellular Vesicles (EVs), and might have relevant implications in NPs internalization pathways and cytotoxicity. Here, the mechanistic details of this phenomenon, hitherto largely unaddressed, will be elucidated. Beside the fundamental relevance, these findings will also provide the basis for development of a new assay for the assessment of the rigidity of natural membranes. **Part II** (**Paper V**) will widen this investigation, exploring more complex lipid-based models, which mimic transient non-lamellar bilayered-structures encountered in cells. The results gathered represent one of the first insights on the role of membrane curvature on the interactions occurring at the nano-bio interface. **Part III** (**Paper VI, VII**) will report an investigation on the restructuring of non-lamellar lipid assemblies of cubic symmetry, induced by gold and Superparamagnetic Iron Oxide NPs: the findings here reported can be exploited for the design of smart hybrid platforms with potential application in the biomedical field. Finally,

Chapter IV will review the most important findings of this work and introduce possible future developments.

The last part of this thesis will consist of papers – published, submitted or in preparation – connected to this research work.

1.1 The self-assembly of lipids

Lipids represent a major class of biomolecules with essential biological functions, ranging from the structural confinements of cells and organelles, to the storage of energy and molecular signalling [1]. Moreover, they represent versatile building blocks for the design of biocompatible platforms for multiple biomedical applications [2–4]. Their spontaneous assembly in aqueous media is of outmost interest for both natural and engineered systems. Lipids of amphiphilic nature, i.e. comprising a hydrophilic headgroup and a hydrophobic chain (Fig.1.1a, top part), spontaneously associate in water to give rise to an extraordinarily rich variety of liquid crystalline phases, as a function of their chemical structure, temperature, pressure and aqueous phase content and/or composition [5].

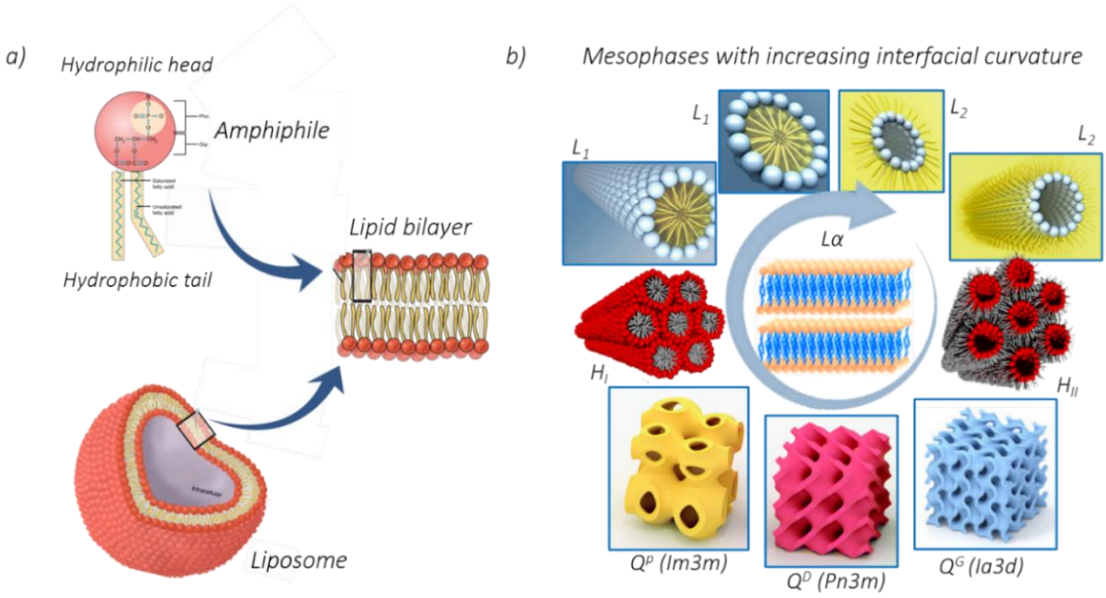

Figure 1.1 *a) Graphical sketch of the basics of lipid self-assembly. From top to bottom: an amphiphilic molecule comprising a hydrophilic head group and a hydrophobic tail, a flat lipid bilayer and a liposome. b) Liquid crystalline lipid phases with increasing interfacial curvature from the extreme left (L_2 inverse spherical and cylindrical micelles) to the extreme right (L_1 direct spherical and cylindrical micelles), passing from the H_{II} the inverse hexagonal phase, the Ia3d, Pn3m and Im3m cubic phases (of inverse and direct nature) and the H_I direct hexagonal phase. The Lα lamellar phase, in the middle, has zero interfacial curvature. Readapted from [6,7].*

The unique polymorphism of lipids originates from the balance of the hydrophobic effect with weak intra- and intermolecular interactions, combined with specific geometric packing constraints [8].

Lipid bilayers (Fig. 1.1a, middle part) are one of the simplest outcomes of lipid self-assembly and represent a fundamental structural unit of almost all living organisms and viruses: indeed, biological membranes are flat sheets, composed of two layers of polar lipid molecules, enclosing the inner environment of cells and confining membrane-bound organelles. From a basic standpoint, the structure of living cells and cell-secreted vesicles can be reproduced at a laboratory level by synthetic "liposomes" of varying sizes [9]: these systems, which we will extensively employ in paragraph **3.1** (**Papers II, III** and **IV**), are characterized by a lamellar lipid bilayer enclosing an inner aqueous pool (Figure 1.1a, bottom part).

However, lipids can also self-assemble into non-lamellar architectures, characterized by different degree of complexity and symmetry in one, two or three dimensions (see some common examples in Figure 1b).

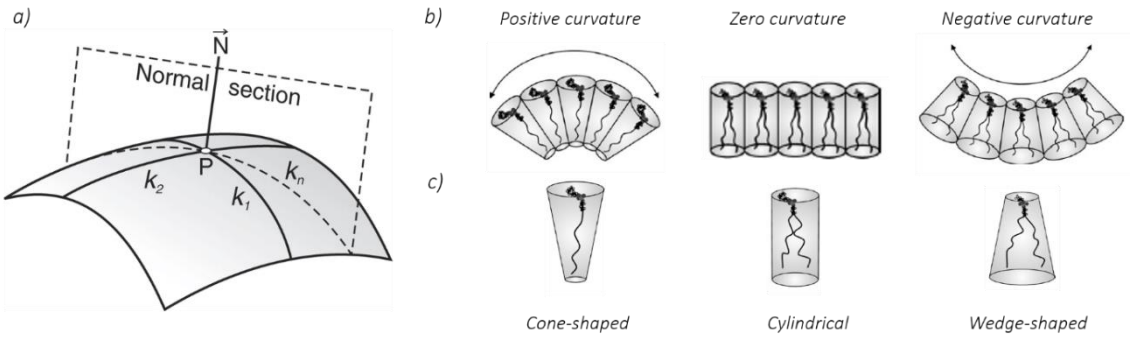

Figure 1.2 *a) Representation of the two principal curvatures k_1 and k_2 e in a point P of a generic surface. Readapted from [10]; b) Lipid monolayer with positive, zero and negative curvature at the lipid/water interface; c) Characteristic cone, cylindrical and wedge shape of amphiphilic lipids, giving rise to direct non-lamellar (positive mean interfacial curvature), lamellar (zero mean interfacial curvature) and inverse non-lamellar (negative mean interfacial curvature) structures. Readapted from [11].*

These different lipid phases can be topologically classified in terms of their lipid/water interface (i.e., the region where lipid polar headgroups are in contact with the aqueous medium), which can be considered as a surface in the 3D space. For any given point (P) of this water/lipid interface, a normal to the surface can be extended and two principal curvatures (k_1 and k_2) can be defined, as the maximum and minimum value of the curvature in the considered point (Fig. 1.2a). k_1 and k_2 can be combined to obtain the Mean (H) and Gaussian (K) curvatures, characterizing the surface in P [11,12]:

$$H = \frac{1}{2}(k_1 + k_2) \quad (1.1)$$

$$K = k_1 k_2 \quad (1.2)$$

The shape of any surface can be univocally determined by defining H and K in all its points [13]. According to the most commonly adopted convention, a positive mean interfacial curvature corresponds to the monolayer bending towards the hydrocarbon chain region, while a negative mean curvature corresponds to the bending in the other way round (Figure 1.2b) [11]. While cylindrical amphiphiles originate lamellar structures, i.e. with zero mean interfacial curvature, positive and negative interfacial H values are favored for the case of cone-shaped and wedge-shaped amphiphiles, respectively (Figure 1.2c) [11]. Liquid crystalline phases with positive interfacial H for all their points are defined "direct" phases, while a negative H throughout the interface is associated with "inverse" phases [12]. As evident from Figure 1b, the interfacial H of common lipid assemblies continuously increases from inverse micelles (L_2) to direct ones (L_1), passing from assemblies with intermediate curvature values.

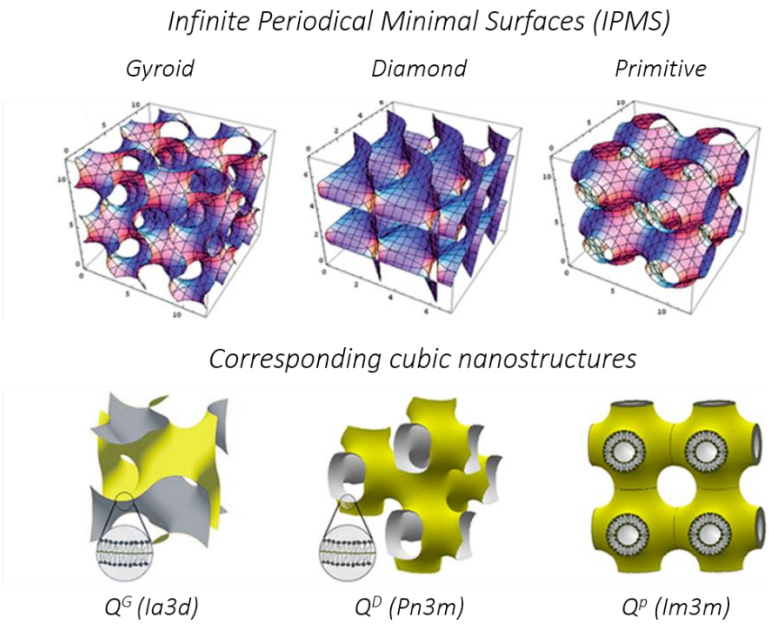

Figure 1.3 *Representation of the infinite periodical minimal surfaces Gyroid, Diamond and Primitive Schwartz, together with the corresponding cubic bicontinuous mesophases Ia3d (Q_G), Pn3m (Q_D) and Im3m (Q_P). Readapted from* [2,14].

Among all these structures, cubic bicontinuous phases (Q-type in Figure 1.1b) have a high biological relevance, spontaneously occurring in natural membranes under selective

conditions (e.g., starvation, infection, oxidative stress and other diseases) [12,15,16]. These so-called "cubic membranes" arise from the folding of the lipid bilayer in the 3D space and represent highly curved membranes arrangements, whose biological function is still poorly understood [17]. Moreover, they have attracted an intense interest from the medical technology field, due to their unique nanostructure [12,18–20]. These phases can occur both as direct and inverse and comprise of a single and continuous lipid bilayer diving the 3D space into two sets of interwoven aqueous nanochannels (Fig. 1.3, bottom part). The three main type of bicontinuous cubic phases encountered in nature are associated to the Pn3m, Im3m and Ia3d crystallographic space groups. For these systems, the bilayer mid-plan sits on mathematical surfaces characterized by zero H and K in all their points, which are called "infinite periodical minimal surfaces" (IPMS) [11]; in particular, Im3m, Pn3m and Ia3d cubic phases are associated with the primitive Schwarz (P), diamond Schwarz (D) and gyroid (G) IPMS (Fig. 1.3, top part), respectively, leading to the alternative names of Q^P, Q^D and Q^G [13].

In this work, we will employ the inverse cubic Pn3m phase of Glycerol monooleate (GMO), a wedge-shaped lipid characterized by high biocompatibility and biodegradability and an extraordinarily variegated polymorphism in water [21]. In paragraph **3.2** (**Paper V**), we will propose this system as innovative biomimetic platform, enabling to investigate the interaction of naturally occurring cubic membranes with inorganic NPs. On the other side, we will show that the structure of the GMO/water Pn3m phase can be finely tuned by the inclusion of nanomaterials and optimized for drug delivery applications (paragraph **3.3**, **Paper VI** and **VII**).

1.2 Inorganic Nanoparticles for Nanomedicine

In the last decades, inorganic NPs have emerged as potentially unique nanomedical tools, offering the possibility to probe and control a multitude of biological processes at a nanoscale level [22]. Their peculiar physicochemical (e.g., optical, magnetic, electronic and catalytic) features, determined by their nanometric size, have been exploited for multiple biomedical applications, including diagnostics, therapeutics and biosensing [23,24]. This thesis will focus on two selected classes of inorganic NPs: i) gold NPs (AuNPs), extensively employed throughout this work (**Chapter 3**, **Papers II**, **III**, **IV**, **V** and **VI**) and ii) SPIONs, which will be the focus of paragraph **3.3** (**Papers VI** and **VII**).

1.2.1 Gold Nanoparticles

AuNPs are one of the most promising nanomaterials for nanomedical applications [25], due to their unique physicochemical properties and ease and versatility of their synthesis [26]. The earliest synthetic route was introduced by Turkevitch et al. in 1951 [27], based on the simple citrate-driven reduction of Au^{3+} to Au^0 in water solution: this method and its more recent modifications [28], extensively employed in this work (paragraph **3.1**, **Papers II**, **III** and **IV**), lead to spherical citrate-stabilized AuNPs, with size control within the 9-120 nm range [26]. Non-spherical AuNPs (e.g., Au nano-cubes, -stars and -rods) are synthetized through more recent protocols: in particular, Au nanorods (AuNRs), which have been found to be the most effective contrast agents for the treatment of cancer though photothermal therapy [29], are synthetized by both top-down (e.g., lithographic and catalytic methods) and bottom-up (e.g., seed-mediated growth and electrochemical methods) approaches [29]. Here (paragraph **3.2**, **Paper V**), we employ a newly developed one-pot seedless synthetic technique [30] to prepare AuNRs with controllable aspect ratio (length/width) and low polydispersity.

AuNPs size, shape and surface functionalization control their physicochemical features, including their optical behavior.

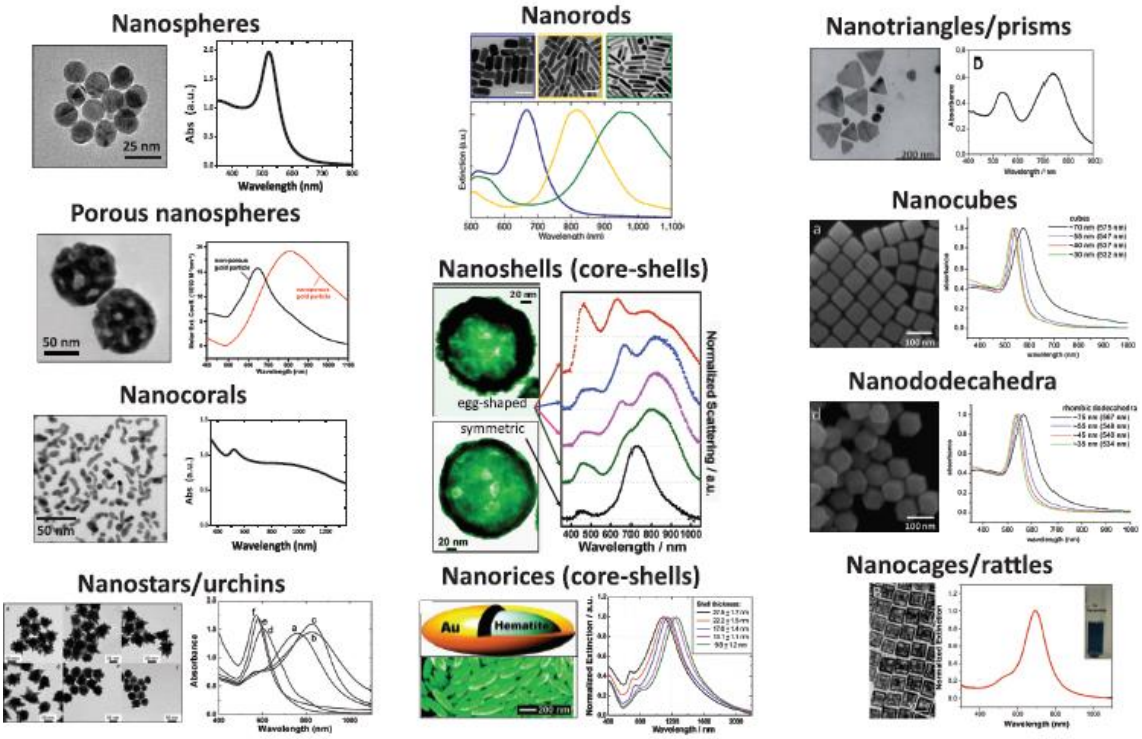

Figure 1.4 *AuNPs with different shapes and corresponding optical extinction (transmission) or scattering (dark-field) spectra. Reprinted from* [31].

Due to their peculiar interaction with light, AuNPs exhibit unique optical properties, underpinning their potential in an impressive number of medical applications (e.g., from photodiagnostics, to photothermal therapy of cancers and other diseases, to cell-imaging) [26]. The so-called "plasmonic" properties of AuNPs have been attributed to the collective coherent oscillation of conduction band electrons of AuNPs, which is induced by the electromagnetic field of light. This oscillation, known as localized surface plasmon resonance (LSPR), resonates with the a characteristic frequency of light and induces a strong absorption in the visible region, which originates the characteristic ruby color of AuNPs dispersions [32]. This phenomenon is strongly dependent on NPs size, shape and inner structure, as evident from Fig. 1.4 [31]. In addition, the LSPR is dependent on the chemical environment of AuNPs: this makes of AuNPs direct nano-probes, able to sense local variations in their proximal environment [31], such as modifications occurring at the AuNPs surface (e.g., ligand-exchange events) or in their surrounding medium, and the assembly of multiple AuNPs in bigger structures (i.e., NPs clustering).

In particular, when single AuNPs come into close proximity (center-to-center distance smaller than five times their radius [32]), new collective oscillation modes emerge, due to the coupling of individual AuNPs LSPR [31]. Being lower in energy with respect to individual AuNPs plasmon modes, these new oscillations lead to a red-shifted LSPR and a darkening of the AuNPs dispersion [32]. This phenomenon is the current focus of a very active research area, aimed at building-up smart materials with tailored optical properties for multiple technological applications [32–34]. Here, we leverage the optical variations of citrated AuNPs' LSPR, induced by coupling, to monitor and characterize their spontaneous aggregation on synthetic and biogenic lipid vesicles (paragraph **3.1**), with relevant implications both from a fundamental (**section 3.1.1** and **3.1.3**, **Papers II** and **IV**) and applicative standpoint (**section 3.1.2**, **Paper III**).

1.2.2 Superparamagnetic Iron Oxide Nanoparticles

Due to their unique magnetic properties, magnetic NPs are expected to play a major role on the medicine of tomorrow [35]. Magnetic NPs are intensively investigated as contrast agents for magnetic resonance imaging (MRI), as carriers enabling magnetic guidance for non-invasive drug and gene delivery and as nanosources of heat, for the treatment of cancer *via* magnetic fluid hyperthermia [36]. Due to their biocompatibility and biodegradability, Superparamagnetic Iron Oxide Nanoparticles (SPIONs) represent the most widely employed magnetic nanomaterials for Nanomedicine, with applications as MRI contrast agents already on the market and underway clinical trials as magnetic targeted vectors [35]. In this work (paragraph **3.3**, **Papers VI** and **VII**), we employ magnetite

(Fe_3O_4)-based SPIONs, synthetized through a well-characterized protocol [37] leading to hydrophobic oleic acid/oleylamine-capped NPs, with 5 nm in size and low polydispersity.

Due to their small size, Iron Oxide NPs exhibit a peculiar magnetic behavior, i.e. superparamagnetism: indeed, at sizes of tens of nanometers and below, ferri- or ferromagnetic materials are a single magnetic domain, endowed with a particularly high magnetic susceptibility. However, differently from the corresponding bulk materials, NPs lose their net magnetization in the absence of an external field, when temperature is higher than the so-called "blocking temperature" (T_B) [36]. Although depending on the material, T_B is usually below room temperature (r.t.): indeed, at r.t. the thermal energy is able to induce thermal fluctuations of the NPs magnetic moment, due to either the movement of NPs within their fluid medium (Brownian fluctuations) or internal fluctuations of the magnetic moment with respect to the crystal lattice (Néel fluctuations), producing the relaxation of the magnetization when the magnetic field is removed [36]. This superparamagnetic property leads the potential of SPIONs in Nanomedicine: their high magnetic susceptibility allows for easily driving SPIONs to specific biological targets (e.g., tumors to be treated or imaged though MRI) through a static magnetic field, while the lack of remnant magnetization after the removal of fields enables preserving NPs colloidal stability in biological fluids [35]. In addition, SPIONs are able to convert the magnetic energy supplied by alternating magnetic fields into thermal one, through Brown and/or Néel relaxation mechanisms, serving as colloidal mediators for heat generation [36]; this property underpins the application of SPIONs in magnetically induced hyperthermia treatment of cancer cells. More importantly for this work (see paragraph **3.3**, **Papers VI** and **VII**), SPIONs can be combined with a thermosensitive lipid matrix, to obtain hybrid devices for controlled drug delivery applications.

1.3 The combination of inorganic NPs with bilayered-lipid assemblies (Paper I)

The combination of inorganic NPs with lipid lamellar and non-lamellar bilayered-assemblies represents a very active research field, meeting some of the urgent needs of Nanomedicine. Indeed, including stimuli-responsive NPs within a nanostructured lipid matrix is one of the most promising strategies for the development of smart nano-hybrids for diagnostic and therapeutic applications. Moreover, this combination can be used to mimic nano-bio interactions in simplified conditions, aimed at predicting the degree of toxicity of nanomaterials. In addition, the unique features of NPs, dictated by their nanometric size, can be used to probe different physicochemical properties of both synthetic and natural soft matter assemblies, which are not easily accessible with more traditional techniques.

In the following, I will introduce the main energetic contributions at stake when NPs are put in contact with lipid bilayers, devoting a particular attention to interactions of non-covalent nature (section 1.3.1). Then, I will review the state of the art on the combination of NPs with synthetic bilayered-assemblies, for both biomimetic studies (section 1.3.2) and nanomedical applications (1.3.3).

1.3.1 The interaction of NPs with lipid bilayers: the role of non-specific forces

When a free-standing lipid bilayer is exposed to a NP, the interaction that follows leads to different outcomes, depending on the energetics of the system. In a simple model of a bioinorganic interface, i.e. a spherical NP of radius R_1 interacting with a lipid membrane of curvature $1/R_2$, the energetic balance between repulsive and attractive forces can be roughly expressed by a classical DLVO (Derjaguin–Landau–Verwey–Overbeek) formalism (eqn. (1.3)), in which the NP-bilayer energy of adhesion (E_{adh}) is described by the electrical double layer (E^{EL}) and the London–van der Waals (E^{LW}) energy contributions:

$$E_{Adh} = E^{EL} + E^{LW} \quad (1.3)$$

where the terms E^{EL} and E^{LW} are described in eqn. (1.4) and (1.5) [38], respectively:

$$E^{EL} = \frac{\varepsilon R_1 R_2 (\psi_1^2 + \psi_2^2)}{4(R_1 + R_2)} \left[\frac{2\psi_1 \psi_2}{(\psi_1^2 + \psi_2^2)} \ln\left(\frac{1 + e^{-kd}}{1 - e^{-kd}}\right) + \ln\left(1 - e^{-2kd}\right) \right] \quad (1.4)$$

$$E^{LW} = A \frac{R_1 R_2}{6(R_1 + R_2)} \left(\frac{1}{d} - \frac{1}{(d + h)}\right) - \frac{A}{6} \ln\left(\frac{d}{d + h}\right) \quad (1.5)$$

with ψ_1 and ψ_2 surface potentials of the NP and the membrane, d NP-bilayer separation, k the Debye length, h membrane thickness and A the Hamaker constant. While the E^{LW} contribution is always of attractive nature, E^{EL} can be positive or negative, depending on both NP and bilayer's surface charges: if NP-bilayer attractive terms overcome the repulsive ones (i.e., $E_{adh} < 0$), the adhesion of the NP to the lipid membrane is thermodynamically favored. Adhesion can be potentially followed by wrapping of the NP by the membrane, depending on the balance between NP-bilayer adhesion (E_{adh}) and membrane elasticity (E_{el}). Indeed, the energetic gain due to the adhesion forces is maximized by increasing the contact area between the NP and the lipid membrane (eqn. (1.6)) [39]:

$$E_{adh} = -w \int_0^{S_{ad}} dS \quad (1.6)$$

with w adhesion energy per unit area and S_{ad} membrane-NP contact area. Concurrently, the increment in NP's wrapping degree is associated with an increasing membrane deformation penalty (E_{el}), expressed through the Cahnam–Helfrich–Evans formalism [39]:

$$E_{el} = \int_0^{S} dS[\gamma + 2k_B(H - c_0)^2 + k_G K] \quad (1.7)$$

with S the entire interfacial area.

From eqn. (1.7), the deformation penalty depends on the membrane topology, i.e. mean H and Gaussian K curvatures (eqn. (1.1) and (1.2)), on its mechanical (surface tension γ and bending rigidity k_B) and intrinsic properties (spontaneous curvature c_0 and Gaussian saddle splay modulus k_G). The interplay between E_{adh} and E_{el} ultimately determines the NP–membrane arrangement which minimizes the energy of the system, from unwrapped NPs (e.g., for small nanoparticles and/or weakly interacting with the lipid phase), to fully engulfed NPs (e.g., for larger and/or strongly adhered nano-objects), as sketched in Fig. 1.5a. In the framework of this theoretical description, in recent years the interaction of NPs with lipid membranes has been explored for different purposes: from fundamental studies aimed at a understanding the possible adverse effects of nanomaterials, to applicative ones, where the interaction of NPs and lipid bilayers is exploited for the design of engineered hybrid assemblies for analytical and material science applications.

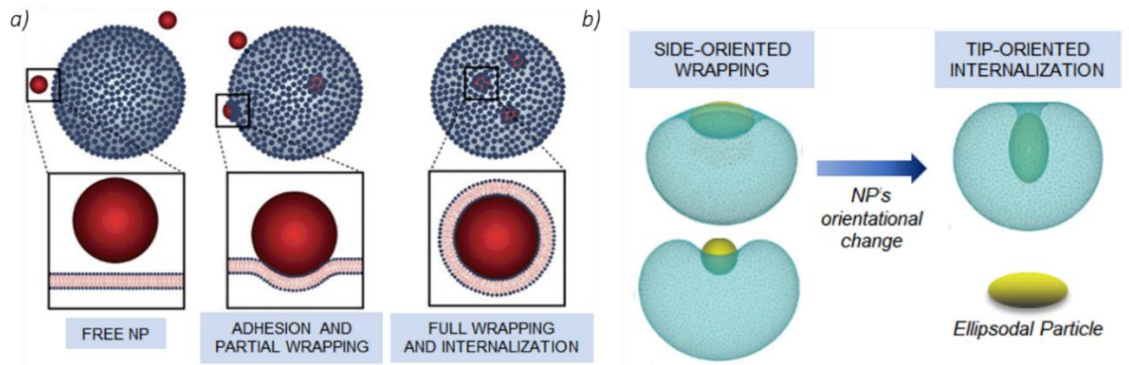

Figure 1.5 *a) Illustration of the three possible configurations for a NP interacting with a lipid membrane: from left to right, (i) NP free in the environment (repulsive contribution to the np–bilayer total interaction overcoming the attractive one); (ii) NP's adhesion to the membrane, causing its partial wrapping and (iii) NP's full engulfment (strong attractive NP–bilayer forces). Readapted from ref [40]; b) representation of ellipsoidal NP's reorganization from a side-oriented configuration, adopted during the wrapping process, to a tip-oriented configuration, minimizing the energy required for full NP's engulfment and internalization. Reproduced from ref. [41]*

1.3.2 Interaction of NPs with lipid bilayers for the study of nano-bio interfaces

Despite the impressive technological advancement of engineered nanomaterials for Nanomedicine, their clinical translation is severely limited by the poor understanding of their behaviour in living organisms. The interaction of nanomaterials with living systems is mediated by biological barriers, such as cell plasma membranes, which primarily determine NPs biological fate and possible cytotoxic effects [42–49] Thus, understanding the interaction of NPs with biological interfaces is the key to fill the gap between the design/development of nanomaterials and their end use application. In this context, synthetic lipid assemblies (paragraph 1.1), taken as simplified models of plasma membrane, represent key tools to investigate nano–bio interactions under highly controlled conditions [44,45,50] and in the absence of any receptor-mediated interaction, present in more complex biological environments [51–53]. In recent years, the combination of experimental observations on model membranes with the theoretical modelling of NP-membrane interaction (section 1.3.1) allowed disentangling the main determinants in NP-membranes non-specific interactions, laying the foundations to predict NPs behaviour in biological systems. In the following, some of these determinants, either related to NP or to the membrane, will be briefly reviewed.

Key NPs features in the interaction with lipid membranes

Depending on NPs size, the NP-membrane interaction can result in different outcomes: NPs with size comparable or smaller than the bilayer thickness can be embedded within the bilayer or translocate across it, by simple diffusion or opening pores; larger particles (>10 nm) can be engulfed by lipid membranes, with multiple experimental observations pointing at the existence of an optimal NP size for wrapping [54,55]. From the theoretical standpoint, the energetic balance between the adhesion forces (eqn. (1.6)) and the membrane elastic deformation penalty (eqn. (1.7)) results in two characteristic NPs limiting radii for a successful engulfment [39]:

$$R_{kw} = \sqrt{\frac{2k_b}{E_{adh}}} \quad (1.8)$$

$$R_{k\gamma} = \sqrt{\frac{2k_b}{E_{adh} - \gamma}} \quad (1.9)$$

For relatively small membrane deformations, i.e. within the "bending-dominated regime", the wrapping process is controlled by the competition between membrane bending rigidity and NP's adhesion strength, leading to a critical radius R_{kw}: for $R<R_{kw}$, NPs remain unwrapped, while for $R>R_{kw}$ NPs are fully engulfed. For membrane deformations

larger than $\sqrt{2k_b/\gamma}$, i.e. in the "tension-dominated regime" [39,40,56], the NP wrapping depends also on γ, which leads to a second crossover NP radius $R_{k\gamma}$ (eqn. (1.9)).

Differently from NPs size, the impact of NPs shape on nano-bio interactions is far less understood: from the theoretical standpoint, the increase of the surface area/volume ratio from spherical to non-spherical NPs maximizes the surface available for adhesion and wrapping by lipid membranes (eqn. (1.6)), enhancing their reactivity and potentially inducing higher *in vivo* cytotoxic effects [57]. On the other side, the high local surface curvature of asymmetric NPs increases the energy barrier associated to membrane deformation [39,56]: this is predicted to lead to preferential wrapping orientations of asymmetric NPs, to minimize the energy cost for membrane deformation [41,58] (Fig. 1.5b).

NPs shape and size often represent minor factors in the interaction of NPs with lipid interfaces, which is primarily mediated by the ligands coating the NP surface; the physicochemical nature of the coating agent determines NPs polarity and interfacial properties, directly involved in the electrostatic and London–van der Waals contributions to NPs adhesion to a lipid bilayer (eqn. (1.4) and (1.5)). Ligand charge plays a major role in the phenomenon: indeed, since most of biologically-inspired model membranes have zwitterionic or slightly anionic nature, cationic NPs promote a stronger interaction with respect to anionic ones, which is often associated with relevant adverse cytotoxic effects *in vivo* [59–64]. In addition, the polarity of the coating agent controls NPs spontaneous localization when challenging a lipid bilayer: while hydrophilic NPs larger than 10 nm can be partially or fully wrapped by the membrane, smaller hydrophobic NPs can either spontaneously cross [65,66] or be entrapped [65] within the lipid membrane depending on their polarity.

Eventually, the binding strength between the NPs surface and its coating agent affects both single NP–membrane interactions and collective NP–NP interactions at the nano–bio interface: physisorbed ligands, which can be easily displaced from the NP surface through ligand-exchange [67], are associated to an enhanced reactivity of NPs, which can be considered as ''naked''. In paragraph **3.1** (**Paper II**), we will show that hydrophilic weakly absorbed ligands on the surface of AuNPs, i.e. citrate anions, can be easily replaced by membrane lipid components, promoting peculiar aggregation phenomena at the nano-bio interface. Moreover, in paragraph **3.3** (**Paper VII**), we will demonstrate that hydrophobic physisorbed ligands, i.e., oleic acid/oleylamine coatings on iron oxide NPs, are associated with NPs pearl-necklace aggregation inside monoolein bilayers.

Key membrane features in the interaction with NPs

The compositional heterogeneity of biological membranes, comprising of thousands of different lipids, carbohydrates and proteins [68], can be reproduced, at different complexity levels, by model membranes. In recent years, it has been shown that the composition of

synthetic bilayers determines specific physicochemical, mechanical and thermodynamic properties affecting the interaction with NPs. As an example, membrane surface potential, determined by the percentage of non-ionic, anionic and cationic lipids [69], strongly affects the interaction with NPs, as predicted by eqn. (1.4). Moreover, the interaction with nanomaterials is deeply affected by the presence of specific membrane components, such as cholesterol: this molecule, which is one of the most abundant sterols in biological membranes, affects the fluidity of lipid bilayers, promoting peculiar NPs-membrane interactions [70–72], which will be the focus of section **3.1.3** (**Paper IV**).

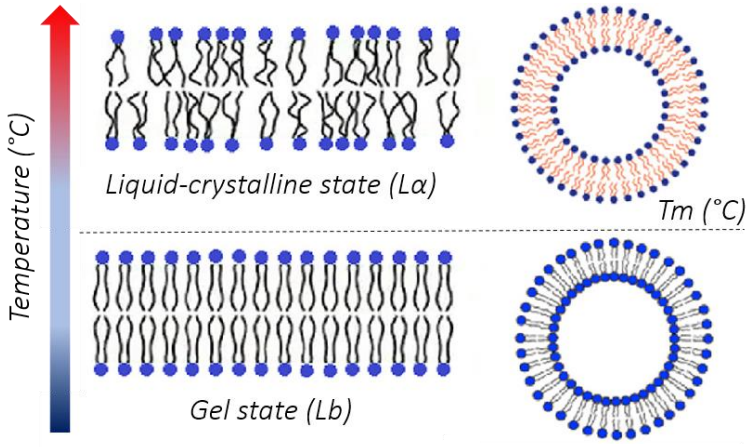

Figure 1.6 *Representation of gel and liquid-crystalline state of a flat lipid bilayer and a bilayer-enclosed liposome.The conversion between the two physical states is triggered by heating above the melting temperature (Tm). Readapted from [21].*

More importantly, the molecular structure of membrane lipid components determines the packing of lipids within the bilayer at a given temperature: this, in turn, affects both the physical state, relevant for the discussion of paragraph **3.1** (**Papers II**, **III** and **IV**), and the overall topological curvature of the membrane, which will represent the main topic of paragraph **3.2** (**Paper V**). These two latter parameters are of prominent relevance in the interactions with nanomaterials and will be separately discussed in the following.

The physical state of a lipid bilayer at a given temperature is dictated by the molecular geometry of lipid components, determining its gel–liquid crystalline phase behavior. By increasing temperature, lipid bilayers undergo a main phase transition from the so-called ‘‘gel state’’ (L_b), where hydrocarbon chains are tightly packed and almost locked in place, to a ‘‘fluid state’’ (L_α), where lipids freely diffuse within the 2D membrane plane (Figure 1.6). The ‘‘melting transition temperature’’ (T_m) is specific for a given lipid composition and determines the mechanical response of the membrane at a given temperature. In particular, the high values of membrane bending rigidity (k_B) of gel phase bilayers with respect to fluid phase ones [56] are responsible for their reduced reactivity towards

nanomaterials, mainly due to the increased energy cost of membrane to bend and wrap around a NP (eqn. (1.7)). This topic will be the focus of **sections 3.1.1** and **3.1.2** (**Papers II** and **III**), dealing with PC bilayers of different bending rigidity interacting with citrated AuNPs.

Beside the physical state, membrane topology is theoretically predicted to play a crucial role in the interaction with NPs. As discussed in paragraph 1.1, natural and synthetic lipid bilayers may fold into flat, as well as more organized non-planar bilayered-structures, whose interaction with NPs represents a highly unexplored research area. From a theoretical standpoint, non-zero values of mean (eqn. (1.2)) and Gaussian (eqn. (1.3)) curvatures lead to a modification of Helfrich energy (eqn. (1.7)) with respect to the case of lamellar membranes, which is connected to variations in the elastic response towards externally induced deformations (e.g., NPs adhesion and wrapping). Moreover, different topologies are associated with a variation in the frustration packing free energy (E_P) of the system [73] (eqn. (1.10)) which might have important implications in the interaction with NPs.

$$E_P = k(l - l_r)^2 \quad (1.10)$$

with k stretching rigidity of lipid chains, l and l_r hydrophobic chain extension in the stretched and relaxed state, respectively.

Paragraph **3.2** (**Paper V**) will deal on the impact of membrane curvature in the interaction with nanomaterials, comparing the effect of prototypical NPs on lamellar and cubic non-lamellar synthetic models. Paragraph **3.3** (**Paper VI** and **VII**) will focus on the structural modifications induced by hydrophobic NPs on lipid assemblies, including biologically relevant phase transitions between lipid mesophases of different curvature. These transitions, which share similar energy barriers and molecular re-arrangements with membrane fusion processes [42], will be rationalized combining the Helfrich theory (eqn. (1.7)) with geometrical packing considerations (eqn. (1.10)).

1.3.3 Interaction of Nanoparticles with synthetic lipid bilayers for the development of hybrid soft devices

Besides the fundamental interest, the interaction of NPs with lipid membranes can be exploited to design and develop hybrid nanostructured materials for applications in different technological fields, ranging from Nanomedicine, to biosensing, to material science.

As highlighted in paragraph 1.1, lipids' self-assembly in water gives rise to a wide variety of structures with different geometry, which can host hydrophilic-coated NPs in the aqueous regions and/or hydrophobic-coated NPs in the hydrophobic domains. Remarkably, NPs can spontaneously insert within the lipid scaffolds due to non-specific forces (section 1.3.1), thus representing a facile approach to obtain relatively complex hybrid materials with controlled structure and defined physicochemical properties.

The combination of NPs with lipid assemblies leads to materials with interesting features: (i) the biocompatibility of the lipid moiety allows envisioning their application in biomedical fields; (ii) the self-assembly of lipids is responsive to temperature, hydration and other experimental conditions, whose variations can be triggered on demand, by external stimuli applied to NPs included within the lipid scaffold: this allows building-up new materials endowed with stimuli-responsiveness for applications in different fields, e.g. controlled drug delivery; (iii) the confinement of NPs in lipid assemblies can locally concentrate and impose them a spatial arrangement: this can lead to an enhancement of NPs-related signals, e.g. optical or MRI readout for diagnostic applications. Moreover, the membrane-templated organization of NPs can induce variations in their physicochemical features (e.g., optical properties), which can be used to probe multiple properties of synthetic and natural host lipid scaffolds.

The inclusion of different kinds of inorganic NPs within lipid assemblies of lamellar nature represents a widely employed strategy for developing hybrid nanomedicines: magnetoliposomes, i.e. lipid vesicles embedded with hydrophobic SPIONs, represent a well-known example of hybrid material endowed with NPs-induced responsivity to static and alternating magnetic fields, which makes them good candidates in remotely controlled drug delivery [74–76]. More recently lamellar lipid vesicles have been also combined with hydrophobic AuNPs, to build-up photoresponsive and thermosensitive hybrid liposomes [77]. In addition, multifunctional hybrid liposomes containing magnetoplasmonic nanoparticles (SPIONs@Au) were recently developed, merging the hypothermic and photothermal abilities of the two inorganic building blocks for image-guided delivery of anti-HIV drugs [78,79].

In **section 3.1.2** (**Paper III**), the combination of citrated AuNPs with phosphocholine vesicles of lamellar nature is exploited to develop a new hybrid assay: here, the peculiar optical properties of AuNPs, arising from their bilayer-templated aggregation at the vesicles surface, is exploited to probe the mechanical properties of the lipid membrane itself, with relevant implications from both a technological and biological standpoint.

Besides lamellar lipid structures, the employment of lipid scaffolds of non-lamellar nature has attracted growing interest in the last two decades [7,12,18,80–85]; this is mainly related to the possibility to host much higher amounts of hydrophobic species (e.g., active principles for targeted delivery applications) with respect to their lamellar analogues [81,86,87].

Moreover, their complex inner architecture has been recognized to promote a strong interaction with biological barriers [88,89], enhancing the uptake and therapeutic efficiency of medicines. The inclusion of NPs within these promising architectures can be exploited not only to introduce stimuli-responsiveness, but also to finely tune their structure, engineering it for its final purpose: this will represent the focus of paragraph **3.3** (**Paper VI** and **VII**), wherein we will exploit the inclusion of inorganic NPs within lipid cubic phases to finely manipulate and optimize their structure for technological applications in the drug delivery field.

II Methods

In this chapter, I will briefly introduce the working principles of the main investigation techniques used in this work. Details on the employed instrumentations, approaches adopted for data analysis and the samples' environment are extensively described in the full text and/or SI of the papers connected to this thesis.

2.1 Atomic Force Microscopy (AFM)

Atomic force microscopy (AFM) is a non-destructive technique, allowing to obtain bi-dimensional surface maps with nanometric resolution and information on several physicochemical properties of the sample [90,91]. The working principle of an AFM experiment consists of measuring the interaction forces between the AFM probe, which comprises of a cantilever with a tip (with a nanometric radius) at its free end, and the sample [92].

To obtain an AFM surface topography image, the AFM tip is brought close to the sample and then raster-scanned over the x-y plane of its surface, mapping the tip-sample interactions at each point. This is accomplished by finely controlling the AFM probe's position through a piezoelectric stage, onto which the probe is mounted.

While scanning the surface, the AFM tip undergo attractive or repulsive interactions with the sample (e.g., Van der Waals, electrostatic, capillary, magnetic interactions, etc.), leading to a negative or positive bending of the cantilever, respectively. The force experienced by the tip while the cantilever is deflected can be described by the Hook law:

$$F = -kx \quad (2.1)$$

with k spring constant of the cantilever and x cantilever deflection. Thus, the extent of the cantilever deflection depends on k (a cantilever-related property) and the strength of forces between the tip and the sample.

The up/down and side deflection of the cantilever as the tip scans along the surface is monitored through a laser beam, reflected from the back of the reflective AFM cantilever. This beam is tracked by a position sensitive photo-detector, recording the vertical and lateral motion of the probe. The deflection sensitivity of the detector is calibrated in

terms of how many nanometers of motion correspond to a unit of voltage measured on the detector.

While detecting the deflection of the lever during scanning, the position-sensitive detector also provides a feedback to maintain the accurate response and a constant setpoint. Different feedback parameters (setpoint values) are alternatively chosen, depending on the AFM operational mode [93].

AFM can operate in different working modes, allowing for imaging the sample and/or probing local physicochemical properties (e.g., magnetic, elastic, electric properties, etc.). "Contact", "non-contact" and "tapping" modes are the most widely employed AFM modes and can be distinguished in terms of the cantilever behaviour.

In the contact mode, the tip is in physical contact with the sample, while scanning its surface.

For the case of topographic imaging, the mapping of the surface can be obtained by fixing the tip-sample force (i.e., F of eqn. (2.1)), by using the feedback loop (i.e., constant-force mode). Alternatively, the height of the probe above the sample (i.e., x of eqn. (2.1)) can be kept fixed, monitoring the cantilever deflection during the scanning of the sample's surface (i.e., constant-height mode).

In the tapping mode the cantilever oscillates in close proximity of the sample surface, at the resonance frequency of the cantilever and at a defined amplitude. This amplitude is kept constant during scanning, constituting the feedback parameter.

In the non-contact mode, the cantilever does not touch the sample surface, as it oscillates above it with a lower amplitude with respect to the tapping mode. The oscillation frequency is slightly higher than the cantilever's resonance frequency. In this case, either the amplitude or the frequency of oscillation can be chosen as feedback parameters.

A less common AFM operating mode is the "PeakForce Tapping" mode, recently developed by Bruker [94]; this mode has been extensively employed in this work (paragraph 3.1, **Paper III**), to record force spectroscopy data.

Within this approach, the cantilever oscillates with a frequency below its resonance frequency in the proximity of the sample's surface, periodically touching it. The tip-sample interaction force at each touch is instantaneously recorded and used by the feedback loop to control and minimize the applied force on the sample [94].

2.2 Laser Scanning Confocal Microscopy (LSCM)

Laser scanning confocal microscopy (LSCM) allows for imaging thin optical sections, with high-resolution and depth selectivity, in specimens of thickness up to 100 micrometers [95]. Images are acquired point-by-point within a selected optical section, while sections of different depths can be subsequently reconstructed, allowing three-dimensional imaging of objects. In LSCM, the specimen is irradiated in a point-wise fashion with a laser beam and the fluorescence, arising from the interaction between the laser light and the sample, is detected point by point. To obtain information about the entire specimen, the laser beam is guided across the specimen (or viceversa), through a scanning process. As can be seen from Figure 2.1 [95], a coherent light beam is emitted by a laser excitation source and passes through a pinhole (aperture pinhole), situated in a conjugate plane with a scanning point on the specimen and a second pinhole positioned in front of the detector (a photomultiplier tube). The laser is reflected by a dichromatic mirror and scanned across the specimen, illuminating points of 0.25-0.8 µm in diameter in a defined focal plane; secondary fluorescence emitted from the specimen (in the same focal plane) passes back through the dichromatic mirror and is focused as a confocal point at the detector pinhole aperture. Only a small fraction of the out-of-focus fluorescence emission is delivered through the pinhole aperture, while most of it does not contribute to the resulting image: this increases the image quality and resolution with respect to conventional fluorescence microscopy. In addition, optical sectioning allows a great number of slices to be cut and recorded at different planes of the specimen, with the specimen being moved along the optical axis (Z) by controlled increments (0.5-1.5 µm).

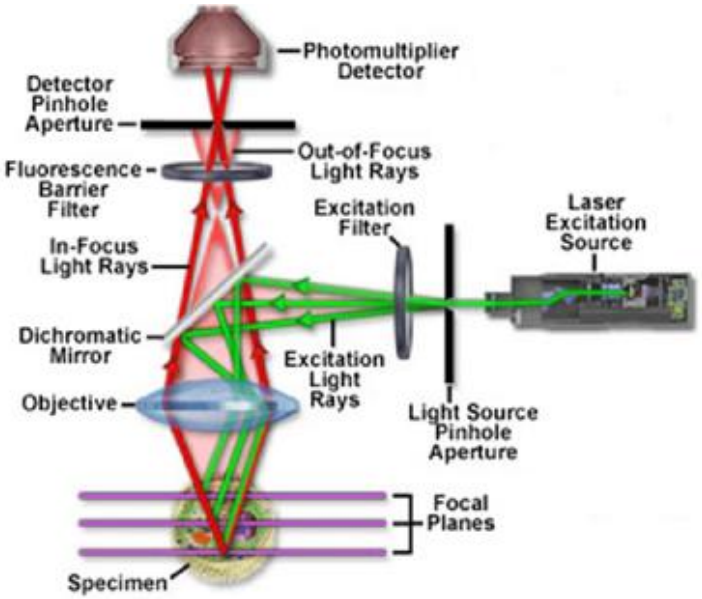

Figure 2.1 *Confocal microscopy geometry from Olympus microscopy resource centre [95].*

The result is a 3D data set, which provides information about the spatial structure of the object. Here, we employ CLSM for the optical imaging investigation described in paragraph **3.2**; details on the used instrument and data analysis are reported in the full text of **Paper V**.

2.3 Small-Angle X-Ray and Neutron Scattering (SAXS and SANS)

In the Small-Angle Scattering (SAS) techniques, the elastic scattering from a sample is recorded at very low angles, which opens the possibility to investigate nanostructured materials, with disomogeneities ranging from few nm to hundreds of nm [96]. In a SAS experiment, a beam of collimated radiation with a defined wavelength (λ), which can be a neutron (SANS) or an X-ray photon (SAXS) beam, is directed at the specimen (Figure 2.2); the light elastically scattered by the sample is collected by a position-sensitive mono- or bi-dimensional detector, which converts the bidimensional intensity pattern into a monodimensional curve, describing the scattering intensity (I(q)) as a function of the so-called scattering vector q [96].

q is the modulus of the resultant between the incident, k_i, and the scattered, k_s, wavevectors, and is given by [96,97]:

$$|q| = |kf - ki| = \frac{4\pi n}{\lambda} sin(\theta) \quad (2.2)$$

with 2θ scattering angle and n refractive index of the sample.

I(q) results from the constructive and destructive interference between the waves scattered from all the illuminated atoms of the specimen and contains a structural information, accounting for the shape, size and interaction between the different scattering centres within the sample [96,97]:

$$I(q) = KN_P V_P^2 (\Delta\rho)^2 P(q) S(q) + B \quad (2.3)$$

with K the amplitude accounting for instrumental factors, N_P numerical density of the scattering particles, V_P the scattering particle volume fraction and B incoherent background. Importantly, P(Q) is the particles "form factor", accounting for their shape, while S(Q) is the interparticle "structure factor", accounting for the spatial correlation between different scatterers within the sample [96,97]. Finally, $\Delta\rho$ is a contrast term, quantifying the difference between the interaction of the probe with the sample and the surrounding medium. This term depends on the type of probe/sample interaction, which is defined by the nature of the probe itself: in a SAXS experiment, it arises from the differences in the electron density between the sample and the continuous medium [96,97].

On the other side, in a SANS experiment, $\Delta\rho$ originates from differences between the interaction of the neutron beam with the nuclei of the specimen and that of the medium [96].

In this work, SAXS is extensively employed for different purposes, spanning from the characterization of the size and shape of inorganic NPs, to the analysis of the inner structure of lipid mesophases, to the investigation of the interaction between NPs and soft matter assemblies.

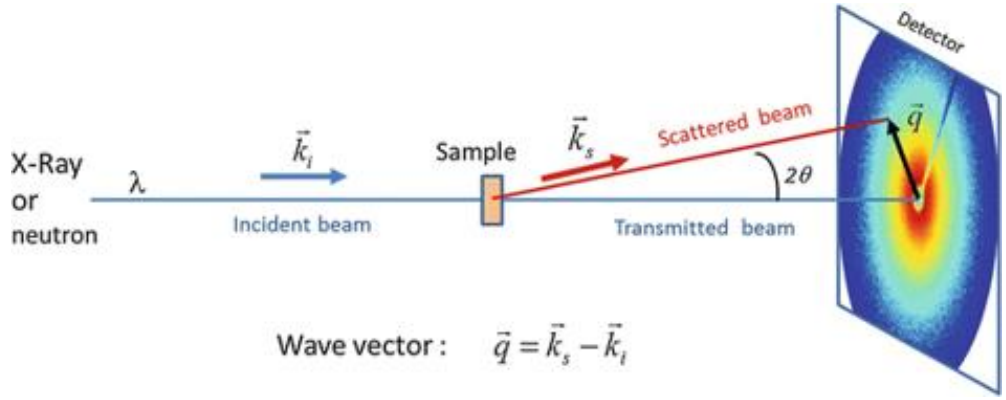

Figure 2.2 *Geometry of a Small-Angle Scattering experiment. The incident beam hits the sample and the pattern of scattered light (assuming elastic scattering) is revealed with a 2D detector. the modulus of the wave vector q is defined as 4πsin(ϑ)/λ) with 2ϑ being the angle between the incident and scattered beams.*

As X-ray source, either a laboratory source or synchrotron light, providing a higher X-ray flux, has been employed, with instrumental details reported in the full text and/or SI of the attached papers. On the other side, SANS has been employed in the work described in paragraph **3.1**, with technical information on the instrument and data analysis being detailed in the full text and SI of **Paper II**.

2.4 Dynamic Light Scattering (DLS)

Dynamic light Scattering (DLS) is one of the most popular methods to determine the size of nanoparticles. When NPs are small compared to the wavelength of light, they scatter the light in all the directions when exposed to it, according to the so-called “Rayleight scattering”. When a sample containing NPs is hit by a coherent and monochromatic light source, a time-dependent fluctuation in the intensity of the scattered light can be observed. These scattering intensity fluctuations are due to NPs undergoing Brownian motion within the dispersion and, thereby, contain information on the hydrodynamic size

of NPs through the Stokes-Einstain relation [98]. This information can be derived from an autocorrelation of the scattering intensity trace recorded during the experiment. The normalized scattered intensity time autocorrelation function (C(t)) of the scattered light intensity (I(t)) may be written as follows [98]:

$$C(t) = \frac{\langle I(t)I(0)\rangle}{\langle I(0)I(0)\rangle} = \left[1 + \beta\left[g^{(1)}(t)\right]^2\right] \quad (2.4)$$

where β is a constant determined by the specific experimental setup and $g^{(1)}(t)$ is the normalized first order (scattered electric field) time autocorrelation function. For a dilute dispersion of monodisperse NPs, $g^{(1)}(t)$ is a single exponential function, with a time decay connected with the translational self-diffusion coefficient of the NP (D) and the scattering length vector (q), as follows:

$$g^{(1)}(t) = \exp(-q^2 Dt) \quad (2.5)$$

For a relatively polydisperse sample, a general approach is to expand the autocorrelation function in terms of the distribution moments of the decay rates through the cumulant analysis [99], stopped at the second order:

$$g^{(1)}(t) = \exp\left(-\Gamma_1 t \frac{1}{2!}\Gamma_2 t\right) \quad (2.6)$$

with $\Gamma_i = q^2 D_i$, reciprocal decay time for each different size population within the sample.

A more powerful method considers a weighted and continuous distribution of the decay rates, leading to the following form of the autocorrelation function [98]:

$$g^{(1)}(t) = \int_0^\infty W(\Gamma)\exp(\Gamma t)\, d\Gamma \quad (2.7)$$

with W(Γ) intensity-weighted size distribution of the scattering objects. In order to determine W(Γ) it from the autocorrelation function, a Laplace inversion is necessary, requiring mathematical techniques, known as regularization techniques. Among them, Provencher has developed an algorithm called 'CONTIN', which has become the method of choice for analyzing polydisperse samples, yielding a distribution of the decay rates weighted for the overall contribution to the scattered intensity [98].

DLS has been extensively employed throughout this work (paragraphs **3.1** and **3.2**), with details on DLS instruments and data analysis being fully reported in the full text and SI of **Papers II, III, IV** and **V**.

2.5 X-Ray and Neutron Reflectometry (XRR and NR)

Reflectivity experiments with neutrons or X-Rays give insight into the structure and composition of thin films at interfaces. The short wavelengths of the probe allow for a sub-nanometer resolution [100].

In a reflectometry experiment, a beam of neutrons or X-rays hits the sample at an incident angle θ_i. Part of this beam will be elastically scattered by the sample, resulting in its reflection in the plane of incidence at the same angle as the incident one (specular reflection) or at a different angle (off-specular reflection) [100].

In the case of specular reflection, momentum transfer vector q (eqn. (2.2)) is perpendicular to the sample surface (i.e., the (x, y) plane) and, therefore, only has a z-component in the direction normal to the surface, i.e. $q_z = 2k_i$ (see Fig. 2.3a).

In its simplest form, a reflectometry experiment measures the intensity of a specularly reflected neutron or X-Ray beam, as the wavelength or the angle of incidence of the probe is varied [101]. Specular reflectivity is usually expressed as a function of q_z, i.e. the only non-null component of the q vector, which can be obtained from the wavelength of the probe and the sample reflection angle (which, for the case of specular reflectivity, is equal to the incident angle θ_i) from the following relation [101]:

$$q_z = \frac{4\pi}{\lambda} sin(\theta_i) \quad (2.8)$$

In a typical NR or XRR experiment, a neutron or X-Ray beam of very low divergence impinges on a thin film surface at a grazing incidence [101]. Up to a critical angle of incidence the neutron beam undergoes total external reflection and, beyond that, the beam penetrates the stratification of the sample and gets reflected at the interfaces.

Due to the absence of q_x and q_y components of the q vector, a specular reflectivity measurement only provides information on the structure of the sample in the direction perpendicular to its surface; for the common case of a layered thin film, this experiment yields information on the thickness of the layers, their densities, interface roughness, etc.

On the contrary, in the case of off-specular reflection, q will also have non-null q_x and q_y components, being not perpendicular to the sample surface (Figure 2.3b). Off-specular reflection is measured by recording the reflectivity of the sample outside the specular condition, i.e. angle of reflection (θ_f) ≠ angle of incidence (θ_i). In this case, the reflected beam, with non-zero q_x and q_y components, provides information on the lateral (x,y) structure of the sample, such as interface roughness and structure of in-plane domains.

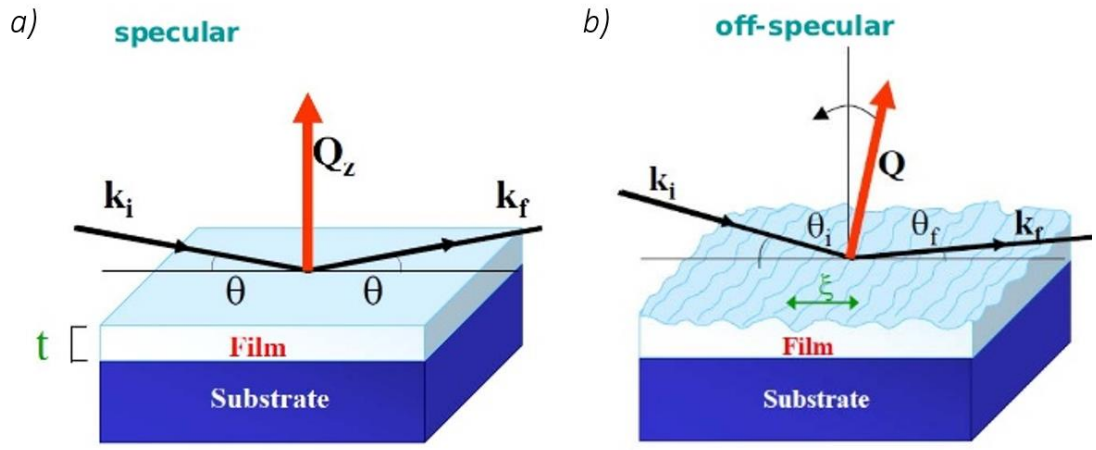

Figure 2.3 *Representative sketch of the specular and off-specular reflections from an ideal interface.*

Here, specular X-Ray Reflectometry is employed for the study reported in **section 3.1.1** (**Paper II**), aimed at investigating the absorption of AuNPs onto a thin supported lipid bilayer. On the other side, specular Neutron Reflectometry is used to characterize rafted supported lipid bilayers (**section 3.1.3**, **Paper IV**), while we employ off-specular NR to investigate the interaction of AuNPs with lipid membranes of high lateral organization, i.e. lipid films with cubic symmetry (paragraph **3.2**, **Paper V**). Detailed information on the instruments employed and data treatment are reported in the full text and SI of the Papers attached to this thesis.

III Summary of Results

Part 1.

3.1 Interaction of citrated gold Nanoparticles with lipid bilayers: from fundamental understanding to applications (Papers II, III, IV)

Turkevich-Frens gold nanoparticles stabilized with citrate anions (AuNPs@CT) are one of the most explored class of inorganic nanoparticles for biomedical applications. Upon incubation with synthetic and natural lipid vesicles, they exhibit an intriguing behavior [61,102–106]: a redshift of the AuNPs@CT localized surface plasmon resonance absorption is observed, due to interparticle coupling resulting from a membrane-templated clustering of AuNPs [61,106–109] (see paragraph 1.1). The clustering of NPs in proximity of cell membranes has been recognized to deeply affect their internalization and cytotoxic pathways [42,63]; moreover, the membrane-induced variations in AuNPs@CT LSPR have been recently exploited to develop surface plasmon-based biosensors [110,111]. Despite its fundamental and applicative relevance, a thorough understanding of the phenomenon is still missing to date.

In the first part of the work (section **3.1.1**), which is the subject of a recently published paper (**Paper II**), we will characterize from a physicochemical standpoint the interaction of AuNPs@CT with zwitterionic 1-palmitoyl-2-oleoyl-sn-glycero-3-phosphocholine (POPC) bilayers, as synthetic models of cell membranes. The gathered results will enable elucidating the main factors at play in AuNPs@CT aggregation onto lipid bilayers, leading to a comprehensive description of the phenomenon. In the second part of the work (section **3.1.2**), we will exploit this acquired knowledge to develop an AuNPs@CT-based nanoplasmonic assay for the determination of the mechanical properties of natural membranes, whose full description can be found in a recently submitted manuscript (**Paper III**). Eventually, section **3.1.3** will summarize the main results of a freshly published work (**Paper IV**), wherein the findings on AuNPs@CT interaction with simple phosphocholine bilayers are used as starting point to head towards more complex model systems, approaching the reality of cell membranes: the impact of introducing nanoscale heterogeneities within the membrane, i.e. lipid rafts, in the interaction with AuNPs@CT will be explored.

3.1.1 Interaction of AuNPs with POPC model bilayers (Paper II)

Here, we employ an ensemble of optical, structural and surface techniques to characterize the interaction of AuNPs@CT (16 nm diameter, zeta potential: 36 ± 2 mV) with model POPC vesicles of 100 nm in size and slightly negative Z-potential (-4.9 ± 0.4 mV, see SI of **Paper II** for AuNPs@CT and liposomes characterization). The main physicochemical and structural features of this interaction are separately summarized in the following (see **Paper II** full text for details) and ultimately merged into a final mechanistic hypothesis of interaction.

Optical features of AuNPs/vesicles: Irreversible aggregation driven by ligand exchange

As described in section 1.2.1, UV-Vis Spectroscopy can be used to monitor AuNPs surface plasmon resonance absorption, whose variations can be directly related to AuNPs aggregation. Here, we employed UV-Vis spectroscopy to study the clustering of AuNPs@CT induced upon mixing with POPC liposomes (see SI of **Paper II** for the preparation of samples). Fig. 3.1a shows that the addition of decreasing amounts of liposomes causes a progressive broadening of the LSPR peak of AuNPs@CT and, eventually, the appearance of a redshifted shoulder for the lowest amounts of added liposomes; this phenomenon, also visible by naked-eyes (Fig. 3.1b), is a clear indication that the clustering of AuNPs is a membrane-dependent phenomenon, which strictly occurs on the liposomal surface, so that the lower the liposomal surface extension available, the higher the aggregation extent of AuNPs@CT.

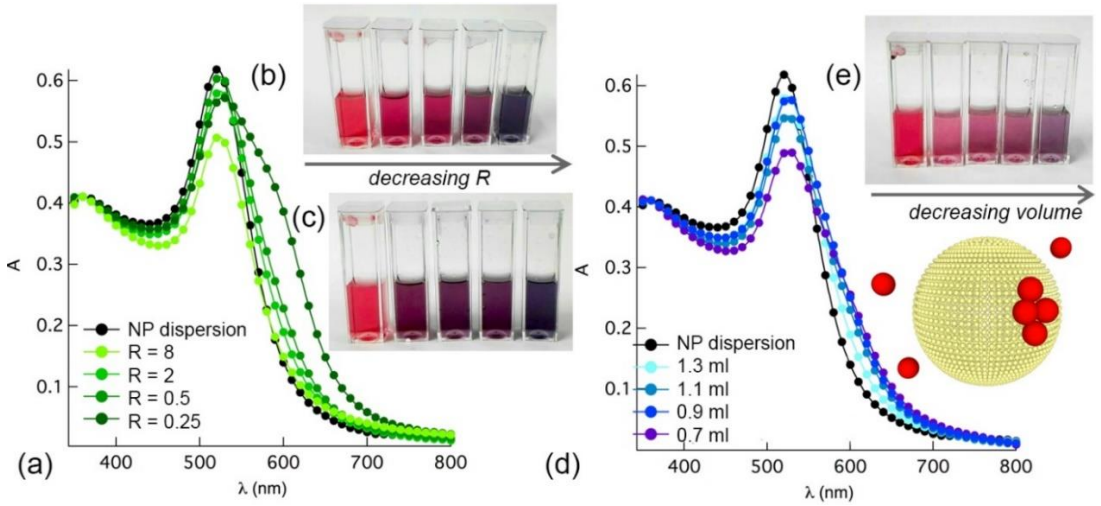

Figure 3.1 *UV-Vis spectra of AuNPs@CT (1.3 nM) in the presence of different amounts of POPC liposomes (R (Liposomes/AuNPs@CT number ratio) = 8; 2; 0.5, and 0.25) and visual appearance of the corresponding samples (b, c); (d) UV-Vis spectra R = 2 complexes, initially mixed in different volumes, and then diluted to the same final volume and visual appearance of the corresponding samples (e).*

Importantly, Fig. 3.1c-e highlight that kinetic effects are of prominent relevance: in particular, both the mixing order of the species (i.e., liposomes added to the AuNPs@CT (Fig. 3.1c) vs. AuNPs@CT added to liposomes (Fig. 3.1b)) and the volume at which AuNPs@CT and liposomes are initially mixed (Fig. 3.1d-e) determine meaningful differences in the extent of NPs clustering; this suggests that the membrane-induced aggregation of AuNPs@CT proceeds under kinetic control and it is of irreversible nature. This feature implies the presence of an irreversible step in the process, which constitutes the driving force of the whole phenomenon. A set tailored experiments, reported below, allowed identifying this crucial step with a ligand exchange between the POPC lipid composing the membrane and the AuNPs@CT capping agent, i.e. citrate.

As discussed in section 1.3.2, the nature of NPs surface ligands mediates their interaction with lipid interfaces, primarily determining the nano-bio interaction pathway and its outcome. Differently from most of AuNPs capping agents, citrate anions are only physisorbed on the NPs surface and can be easily displaced by other covalent or noncovalent ligands [67,112], leaving the gold surface "naked" and highly reactive.

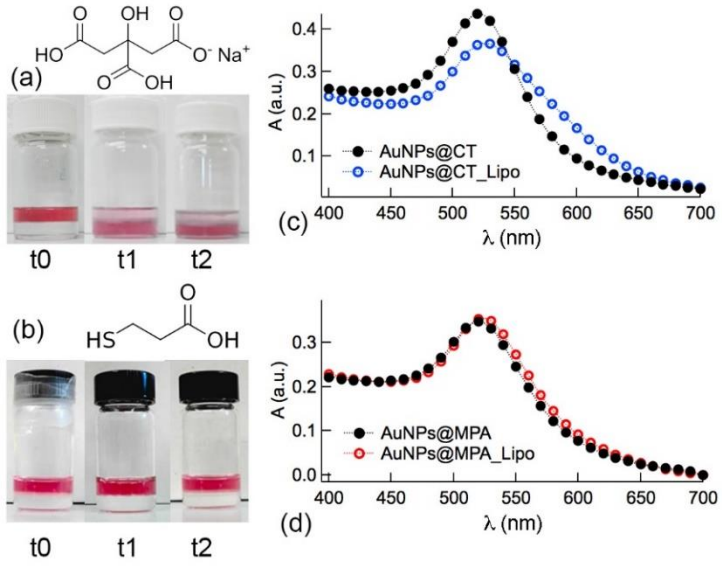

Figure 3.2 *(a, b) Photos of the two-phase system (NPs + water)/(chloroform + POPC) of (a) AuNPs@CT and (b) AuNPs@MPA, captured: soon after chloroform addition (t0), after 20 min (t1) and 24 h (t2). (c, d) Representative UV-Vis spectra of R = 1 (c) AuNPs@CT and (d) AuNPs@MPA before and after incubation with POPC liposomes.*

To explore the implications of citrate exchangeable nature, we compared the behavior of AuNPs@CT with the one of equal-sized AuNPs, capped with a covalently bounded thiolated ligand of similar size and charge as citrate (3-mercaptopropionic acid, MPA): in a 1:1 (v:v) $CHCl_3$/water biphasic system, where POPC molecules are present in the organic

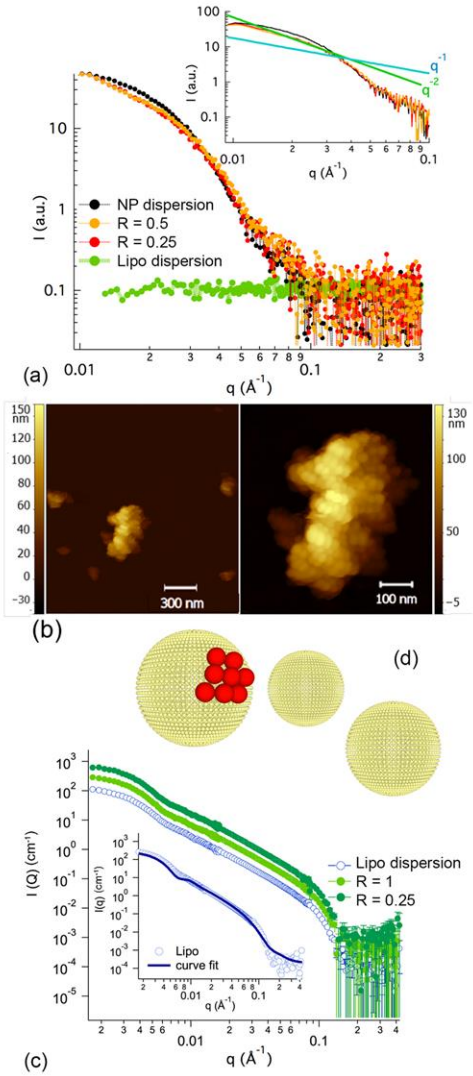

Figure 3.3 *(a) SAXS of POPC liposomes in the presence of different amounts of AuNPs (R = 0.5 and 0.25); comparison of the experimental curves with the power laws $I(q)=q^{-1}$ and $I(q)=q^{-2}$ (inset). (b) Representative AFM images of POPC liposomes after interaction with AuNPs (R = 0.25); magnification of the AFM image which highlights AuNP aggregates. (c) SANS profiles of POPC liposomes in the presence of different amounts of AuNsP (R = 1 and 0.25); the curve fit for liposomes according to a polydisperse core-shell model is consistent with vesicles of a 45 nm radius and 0.3 PDI (inset). SANS measurements performed at D11, ILL.*

phase, AuNPs are either blocked in the aqueous phase (i.e., AuNPs@MPA in Fig. 3.2b) or completely transferred to the organic phase (i.e., citrated AuNP in Fig. 3.2a), depending on the nature of the ligand. This opposite behaviour is due to the fact that, while MPA is not exchanged with POPC due to the strength of the Au-S bound, citrate is easily displaced by the lipid at the chloroform-water interface, where a monolayer of POPC is present, leading to the extraction of AuNPs to the organic phase. This correlates well with the optical behaviour of AuNPs when incubated with POPC liposomes in water: differently from AuNPs@CT (Fig. 3.2c), AuNPs@MPA do not aggregate upon mixing with vesicles (Fig. 3.2d), highlighting a major role of citrate-POPC exchange in driving the clustering of AuNPs.

We can conclude that the kinetic nature of the AuNPs@CT clustering onto lipid bilayers finds an explanation at a molecular level in the irreversible nature of citrate-POPC ligand exchange at the nano-bio interface, which, involving a partial substitution of the citrate shell with POPC and citrate release, would represent an irreversible binding step.

Structural features of AuNPs/vesicles: the asymmetric shape and distribution of clusters

We characterized the structure of AuNPs@CT-POPC liposomes complexes combining solution ensemble techniques (SAXS and SANS) with atomic force microscopy (liquid AFM). SAXS and SANS provide complementary structural information at the nanoscale: the high AuNPs/H_2O contrast in SAXS emphasizes the structural features of AuNPs@CT and of their aggregates, whereas the high lipid/D_2O contrast in SANS provides access to structural details of

NPs' effects on the lipid bilayer. Fig. 3.3a displays SAXS profiles of AuNPs/liposomes complexes at 2 and 4 AuNPs per liposome on average. Due to the low concentration, the scattering of liposomes is not distinguishable from the water background, thereby the signal is exclusively due to AuNPs@CT. When liposomes are present, the scattered intensity shows a clear q^{-2} trend in the low-q range (Fig. 3.3a, inset) (see SI of **Paper II** for quantitative analysis of SAXS profiles), hinting at a fractal arrangement of the primary particles [113], not observed in the absence of liposomes. AFM in liquid on the same samples (Fig. 3.3b) showed compact assemblies of AuNPs on lipid vesicles or vesicle aggregates; even if AFM doesn't allow to establish whether the aggregates are of 2D or 3D nature, a SAXS power law with a decay exponent higher than 2 is expected from a 3D compact cluster of AuNPs@CT [113–115]. Therefore, the combination of AFM and SAXS results is consistent with the formation of 2D clusters of tightly packed AuNPs on the liposomes surface. Importantly, since AuNPs@CT and liposomes share comparable concentrations, the presence of membrane-confined extended AuNPs@CT aggregates on a single liposome implies a strongly uneven distribution of AuNPs@CT: some liposomes will be extensively coated by AuNPs, while others will be devoid of NPs. This conclusion is supported at the ensemble level by SANS analysis (Figure 3.3c), showing no significant variations induced on liposomes scattering profiles upon interaction with AuNPs@CT, in line with the hypothesis that the vast majority of the liposomes remain ''undressed".

To summarize, the combination of SANS, AFM and SAXS highlights two key features of AuNPs@CT aggregation onto lipid membranes: i) AuNPs@CT clusters are of asymmetric, i.e. 2D, nature; ii) AuNPs@CT aggregation extensively occurs on a limited number of liposomes, leading to a strongly uneven distribution of AuNPs@CT among the vesicles ensemble.

Thermodynamic insights on AuNPs aggregation: the role of membrane bending rigidity

As described in section 1.3.2, the physicochemical properties of lipid bilayers are recognized to strongly affect the interaction with NPs. Recent studies address the interaction of AuNPs@CT with lipid vesicles of similar composition as the system here considered: specifically, it was found that, depending on the membrane physical state, the aggregation of AuNPs@CT was either inhibited (e.g., on gel phase DPPC bilayers) or promoted (e.g., on liquid-crystalline phase DOPC bilayers), according to an on-off mechanism [102,106]. This has been generally interpreted in terms of membrane fluidity's differences between gel and fluid phase membranes. Here, we show that membrane bending rigidity, more than fluidity, plays a key role in AuNPs@CT membrane-templated aggregation. Membrane bending rigidity, which is increasingly recognized as a key-factor affecting the reactivity of synthetic and natural bilayers towards nanomaterials [38,56],

controls the extent of NPS wrapping (eqn. (1.7)), ultimately determining the NP-membrane contact area and the strength of interactions at the nano-bio interface.

Here, we investigated the impact of membrane bending rigidity by introducing high bending costs on the AuNPs@CT-bilayer interaction and monitoring the subsequent effect on AuNPs clustering. AuNPs@CT were incubated with POPC supported lipid bilayers (SLBs) obtained on a silicon wafer (see **Paper II** for preparation), where the close interaction with the support hinders membrane bending and wrapping around NPs, while the membrane lateral fluidity is scarcely modified [116]. The XRR profiles (Fig. 3.4a) of POPC SLBs in the absence and in the presence of AuNPs@CT only differs for a slight shift in the XRR oscillations of the bilayer form factor to lower q values, consistent with the adhesion of only few AuNPs@CT on the lipid membrane [117] (see SI of **Paper II** for details).

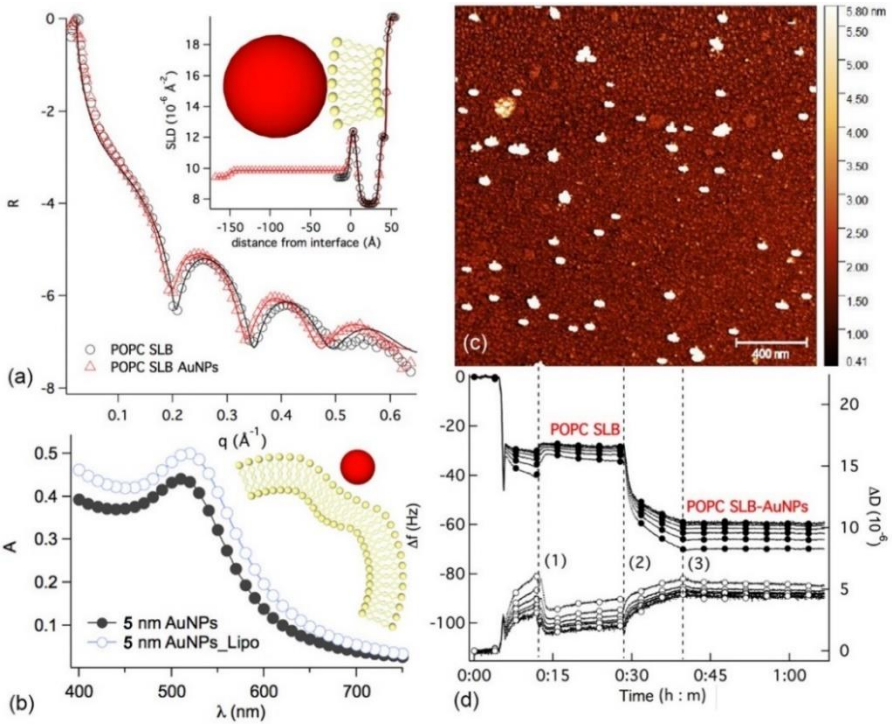

Figure 3.4 *a) XRR profiles of a POPC SLB before and after incubation with AuNPs; the curve fitting of the experimental curve and derived scattering length density (SLD) profile (inset). XRR measurements performed at ID03, ESRF. (b) UV-vis plasmon resonance spectra of small-diameter (5 nm) citrated AuNPs in the absence and in the presence of POPC liposomes (R = 0.1); (c) Liquid AFM of AuNPs on a POPC SLB. (d) QCM-D experiment on the adsorption of AuNPs on a POPC SLB: lines and filled circles represent the frequency shifts, while lines and empty circles the dissipation factors; the curves are normalized for the overtone numbers. The graph highlights that, after the formation of a stable POPC SLB (1), the AuNP injection (2) results in the stable adsorption of some NPs on the target membrane, with an overall coverage of approximately 3.5% of the SLB surface (see SI of* ***Paper II*** *for details).*

AFM images confirm this finding, showing AuNPs@CT embedded in the SLB as single objects or dimers (Fig. 3.4c), while QCM-D data (Fig. 3.4d) highlight that AuNPs@CT only cover the 3.5% of the SLB surface. Taken all together, these results show that AuNPs@CT adhere to the rigid SLB membrane, while their clustering is significantly limited, which points out a key role of membrane rigidity.

To corroborate this result, we investigated the effect of AuNPs@CT size in the interaction with POPC liposomes: indeed, as explained in section 1.3.1 (eqn. (1.7)), decreasing NP size involves an higher energy penalty for the membrane to deform around the NP surface, due to the higher imposed local curvature.

Challenging POPC liposomes with significantly smaller AuNPs@CT (5 nm instead of 16 nm in diameter, see SI of **Paper II** for synthesis), we observed no trace of plasmon coupling from AuNP UV–Vis absorbance (Fig. 3.4b): this indicates that 5 nm AuNPs@CT, which are expected to be wrapped by the membrane to a lower extent, do not cluster, which confirms a major role of membrane bending rigidity in the AuNPs@CT /POPC liposome interaction.

We interpreted this result considering that the bending capacity of the bilayer determines the extent of wrapping around a NP (eqn. (1.7)), i.e. the NP-membrane contact area where the citrate-POPC exchange takes place. The removal of citrate reduces the interparticle electrostatic repulsion on the membrane, enabling short-range NP-NP Van der Waals interactions, which leads to the formation of AuNPs clusters on the lipid surface. If wrapping is inhibited by high bending costs, AuNPs@CT clustering is not observed for the same NP coating and lipid membrane, which can be attributed the lower POPC-citrate substitution on the NP surface, preventing short-range interactions.

AuNPs@CT-lipid bilayers interaction: a mechanistic hypothesis

The ensemble of experimental results can be framed in a mechanistic hypothesis, which would account for: i) the irreversible adsorption of AuNPs@CT; ii) the 2D-clustering of AuNPs@CT on selected liposomes; iii) the role of membrane bending rigidity in the AuNPs@CT aggregation.

Considering the strong imbalance in the distribution of AuNPs@CT clusters, we hypothesized the presence of a specific driving force directing the targeting of selected liposomes: this was identified with the release of citrate (and Stern counterions) at the wrapped area of an AuNPs@CT, which follows POPC ligand exchange. When multivalent citrate anions are released, the ionic strength at the ligand-exchange site will locally increase to a significant extent, lowering the kinetic barrier for NPs aggregation and establishing preferential trails for AuNPs@CT recruitment towards the liposome

concerned. This hypothesis would fit into a multistep model (Fig. 3.5), where the following steps can be outlined:

(i) Adhesion. The negative charge of AuNPs@CT, imparted by the citrate coating, prevents NP-NP aggregation in water solution; however, the electrostatic barrier for the adhesion of AuNPs@CT to the bilayer is significantly lower, due to the low surface charge of liposomes. Thermal fluctuations can easily bring AuNPs@CT close to the bilayer, where adhesion, driven by short-range Van der Waals attraction, occurs.

(ii) Wrapping. AuNPs@CT adhesion locally imposes a high curvature to the membrane. Provided that NPs size is large enough and that membrane bending rigidity is sufficiently low, the partial wrapping of AuNPs@CT takes place, leading to the irreversible POPC-citrate ligand exchange. The extent of citrate displacement depends on the NP wrapped area and, thereby, on the balance between the NP-membrane adhesion forces and the energy penalty due to membrane bending.

(iii) "Citrate-trail." The release of citrate and associated counterions determines a localized increase in the ionic strength: this in turn increases the probability of the adhesion of another NP to the same liposome, followed by a synergistic cascade effect, where each adhered NP partially releases its coating to mark the pathway for the following NP.

(iv) 2D-membrane-templated aggregation. Once more than one AuNP@CT is present on the same liposome, the decreased NP-NP electrostatic repulsion due to partial citrate release, together with the tendency of the membrane to decrease the locally imposed curvature due to NP's adhesion, leads to the formation of 2D membrane-confined AuNPs@CT supracrystals on the lipid bilayer.

Combining the DLVO formalism with the Helfrich elastic theory (section 1.3.1), this mechanistic hypothesis discloses how thermodynamic (i.e., electrostatic and Van der Waals interactions, lipid membrane elastic properties) and kinetic effects (citrate-lipid exchange at the nano-bio interface) are intertwined.

It is worth to notice that this whole phenomenon is intimately connected to- and mainly driven by AuNPs@CT surface features, rather than their chemical composition; indeed, it does not occur when Au-covalently bounded ligands are involved [67]. Under this perspective, we can easily hypothesize that this behaviour will be shared by different nanomaterials (e.g., inorganic NPs with a different core) with similar surface properties, with broad impacts for colloid science and technology. As an example, the understanding of this phenomenon might have relevant implications for the use of different NPs' kinds in Nanomedicine, since NPs' internalization in cells as clusters, rather than as primary NPs, has dramatic effects on their bioactivity. Moreover, the acquired fundamental knowledge

on AuNPs@CT interaction with synthetic bilayers can be also exploited for technological purposes, e.g. the rational design of engineered hybrid materials for applicative purposes. In particular, the following section, which summarizes the main results of **Paper III**, will illustrates how the newly discovered dependence of AuNPs@CT aggregation on membrane bending rigidity can be used for determining the mechanical properties of natural membranes.

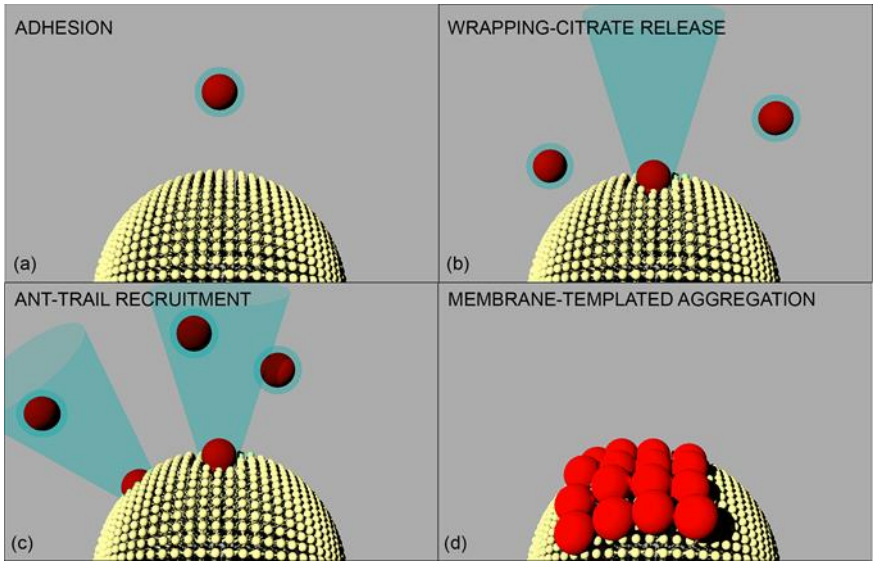

Figure 3.5 *Mechanism of interaction between AuNPs and the lipid membrane. (a) Adhesion-docking; (b) wrapping-ligand exchange; (c) citrate-trail recruitment; (d) 2D-membrane-templated aggregation.*

3.1.2 AuNPs as nanoprobes of the nanomechanical properties of biological membranes: a “stiffness ruler” based on nanoplasmonics (Paper III)

The mechanical properties of membrane-enclosed compartments (e.g., cells, organelles, enveloped viruses, biogenic and synthetic vesicles) regulate their response to external deformations and are relevant in several physical, chemical and biological processes [42,51,52,118]. Depending on their deformability, synthetic vesicles engineered for drug delivery display different pharmacokinetics and internalization mechanism [119]. The mechanical properties of cells and bound-organellae are involved in numerous biological processes (e.g., cell fusion, growth and differentiation, internalization of NPs or viruses [120–123], etc.) and are recognized as biomarkers of pathological cell conditions [124–126].

Although central for a number of research areas (from nanomedicine, to biophysics and pharmaceutical technology), the accurate assessment of the mechanical properties of both synthetic and natural soft matter objects remains a major challenge [52,127]. Traditional methodologies (shape fluctuation optical analysis [128], micropipette aspiration [129], X-ray scattering [130,131] and neutron spin-echo [132]) are cost- and/or time-consuming, with results often affected by a non-negligible discrepancy [127,133–136].

Recently, techniques that enable an active probing of the mechanical response of the entire membranous compartment to an applied deformation (i.e., its "stiffness") emerged as unique tools to provide a comprehensive description of the mechanical properties of the system [137]. Unfortunately, such methods (e.g., Atomic Force Microscopy based Force Spectroscopy (AFM-FS), optical tweezers, etc.), probing a single object at a time, are labour-intensive and low-throughput. Moreover, they are often affected by statistical inaccuracy and neglect the intrinsic variability across populations in biogenic samples. Equally importantly, experienced users are often required for both performing measurements and analysing data.

Here, we propose AuNPs@CT as effective nanoprobes of the stiffness of soft objects, with typical submicron size; this approach overcomes the limitations of the current methods. The "stiffness nanoruler" consists in a simple colorimetric assay, which exploits the unique plasmonic properties of AuNPs@CT, absorbed onto lipid membranes, to assess the rigidity of synthetic and natural vesicles according to a fast, inexpensive and facile approach (see **Paper III** full text for details).

In section **3.1.1** (**Paper II**), we put forward a mechanistic hypothesis where the wrapping extent of AuNPs@CT by the lipid membrane of POPC vesicles, regulated by their mechanical properties, is one of the main drivers for their aggregation onto the vesicles' surface. Leveraging this finding, here we employ a set of synthetic PC vesicles of different rigidity to highlight a clear functional correlation between the membrane mechanical properties and the aggregation extent of AuNPs@CT, monitored through UV-Vis spectroscopy. This newly discovered functional dependence is then applied to estimate the stiffness of synthetic and natural lipid vesicles of unknown composition and properties, e.g. the one of biogenic Extracellular Vesicles (EVs).

Starting from four different phospholipids (characterized by the same polar headgroup, but different hydrophobic chains, see the inset in Figure 3.6b), we prepared six batches of 100 nm vesicles dispersions in water (see SI of **Paper III** for preparation and characterization) composed of pure or mixed lipids, hereafter referred as DSPC, DSPC/DPPC (50/50 %mol); DPPC; DPPC/POPC (50/50 %mol); POPC and DOPC.

As widely reported in the literature on lipid bilayers, this set of vesicles will display different T_m of the bilayers (section 1.3.2); therefore, while some membranes will be in

the gel phase at r.t., other will be in the liquid-crystalline state [138,139]. This different phase state of the membranes affects the mechanical properties of vesicles (see section 1.3.2 for details) [140–143].

We exploit AFM-FS to determine the stiffness of liposomes at r.t.: Fig. 3.6a reports the force-distance curves for each dispersion, where the force experienced by the AFM tip while indenting the sample is plotted against the tip-sample separation.

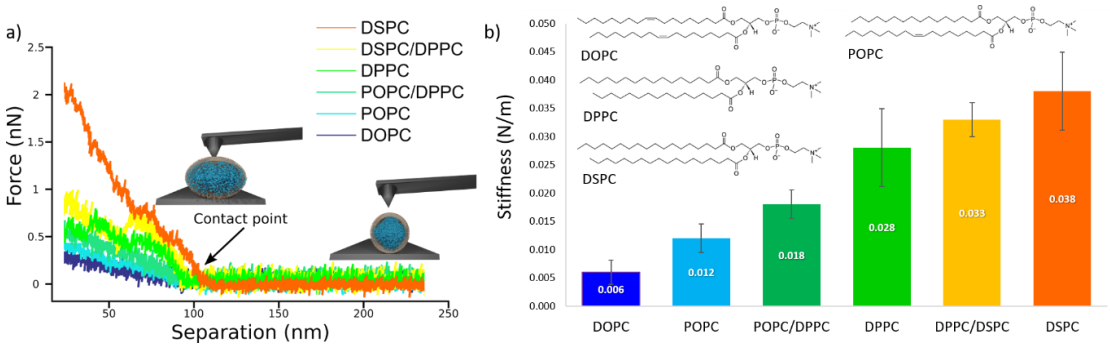

Figure 3.6 *a) AFM force-distances curves for the different vesicles batches, together with graphical representation of vesicles deformation induced by the AFM tip at two different separation distances; b) Stiffness values (N/m) of DOPC; POPC, POPC/DPPC, DPPC and DSPC vesicles, determined through force-distance based AFM; All error bars represent the uncertainties obtained by bootstrapping (1000 repetitions of 5 draws, with replacement). The inset show the chemical formulas of 1,2-distearoyl-sn-glycero-3-phosphocholine (DSPC), 1,2-dipalmitoyl-sn-glycero-3-phosphocholine (DPPC), 1-palmitoyl-2-oleoyl-glycero-3-phosphocholine (POPC) and 1,2-dioleoyl-sn-glycero-3-phosphocholine (DOPC).*

The slope observed in the linear regime (i.e., at distances shorter than the contact point) represents the stiffness of the vesicles (Fig. 3.6b) (see **Paper III** full text and SI for details). This stiffnesses' set, was then used to validate our new optical method for the assessment of stiffness.

To this purpose, we challenged the same set of vesicles with a water dispersion of citrated AuNPs@CT (see **Paper III** for the preparation of hybrid samples) and monitored the spectral variations in the region of the plasmon absorbance of AuNPs@CT through UV-Vis spectroscopy (Figure 3.7a).

While the spectrum of AuNPs@CT in the absence of lipid vesicles is marked by a well-defined surface plasmon resonance band at 522 nm, the mixing with liposomes determines a variation in the AuNPs@CT plasmon absorbance, which is maximized by decreasing membrane stiffness in a continuous trend: going from DSPC to DOPC the colour of AuNPs@CT dispersion shifts from red to increasingly dark shades of violet and blue (bottom inset in Figure 3.7a), which is associated to the progressive emergence of a high-wavelength shoulder in their absorbance spectrum, eventually resulting in a

secondary plasmon peak at about 625 nm (Figure 3.6a). This new spectral feature is the hallmark of the AuNPs@CT aggregation, whose spatial proximity produces the coupling of primary AuNPs@CT plasmons (section 1.2.1).

These experimental observations can be framed within our model of membrane-templated AuNPs@CT aggregation, illustrated in section 3.1.1.

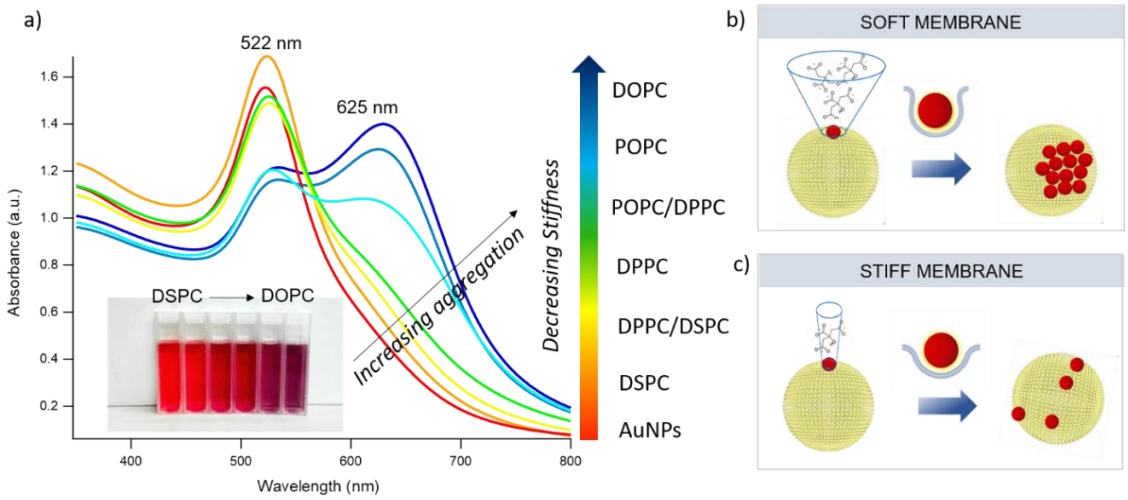

Figure 3.7 *a) UV-Vis spectra of AuNPs@CT (1.3 nM) in the presence of different synthetic vesicles (0.2 Nm,) at a liposomes/AuNPs number ratio of 1/100. The visual appearance of the corresponding samples is shown in the bottom inset; b) Mechanism of interaction between AuNPs@CT and lipid vesicles characterized by different stiffness. The image on the top sketches the adhesion of an AuNP onto a soft membrane, provoking the partial release of citrate and counterions, as a consequence of the AuNP's wrapping by the membrane (section 3.1.1). This results in the formation of AuNPs aggregates onto the vesicle's surface. The image on the bottom represents the docking of an AuNP onto a stiffer lipid membrane, resulting in a lower AuNP's wrapping extent and citrate release, leading to a decrease of AuNP-AuNP distance with respect to the bulk solution, without AuNPs clustering.*

AuNPs@CT aggregation is initiated by the wrapping of AuNPs@CT by the membrane, where the citrate/POPC exchange promotes the release of citrate and counterions. As sketched in Figure 3.7b, the wrapped area per particle, which depends on the energetic cost required to bend the membrane, ultimately regulates the extent of citrate release and, thereby, the aggregation AuNPs@CT.

This gradual dependence AuNPs@CT aggregation on the stiffness of synthetic vesicles, which was further confirmed by Synchrotron SAXS analysis (see **Paper III** for details), can be exploited to set-up a UV-Vis spectroscopic assay to probe the mechanical properties of unknown lipid vesicles. To this purpose, we defined an empirical descriptor of

AuNPs@CT aggregation, i.e. the "stiffness index" (S.I.), which accounts for the main AuNPs@CT spectral variations induced by liposomes (see **Paper III** for the evaluation of S.I. from UV-Vis spectra). This allowed building-up an empirical 'AuNPs@CT spectral response' vs. 'membrane stiffness' scale, reported in Figure 3.8a, where the S.I. values of the different PC vesicles are plotted against their membrane stiffness, measured through AFM-FS.

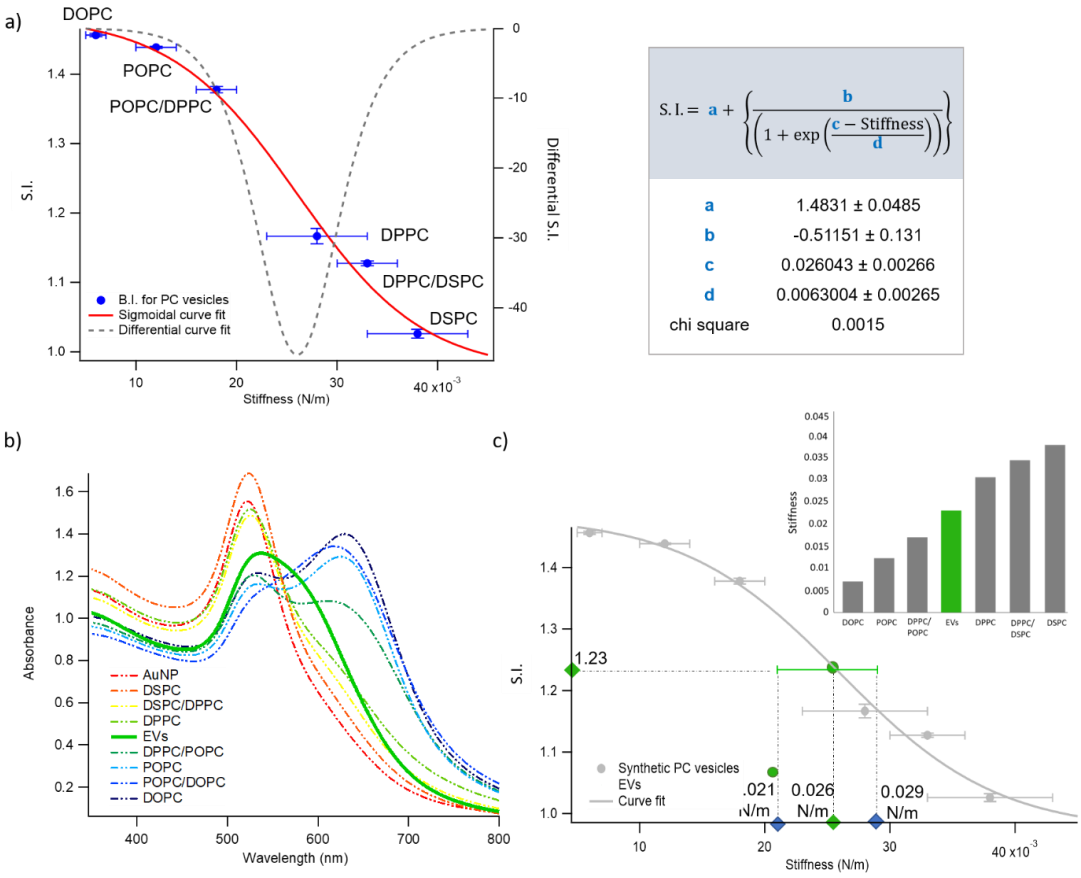

Figure 3.8 *a) S.I. values (blue spots) with relative errors bars plotted as a function of membrane stiffness. The red curve represents the sigmoidal curve fit, while the grey dashed curve represents the first derivative of the sigmoidal curve fit with respect to stiffness. The coefficient values ± standard deviation and chi square obtained from the fitting, together with the mathematical expression characterizing the sigmoidal curve fit, are reported in the right inset; b) UV-Vis absorbance of AuNPs@CT (1.3 nM) the presence of synthetic PC vesicles (dashed curves) and natural extracellular vesicles (solid green curve) at a lipid concentration of 0.04 mg/ml; d) Sigmoidal fit curve representing the sigmoidal trend of S.I. as a function of membrane stiffness. The EVs S.I. (1.23), evaluated through UV-Vis spectroscopy, and stiffness, predicted by the sigmoidal law (0.026 N/m), are reported as grey points in the graph. The grey error bar represents the stiffness interval obtained through AFM-FS for EVs. The right inset represents the stiffness values of PC vesicles (grey bars) and EVs (green bar) determined through AFM-FS.*

Each S.I. point represents the average value obtained from measurements on five independent samples, highlighting a particularly high reproducibility (see y-error bars in the figure and SI of **Paper III** for detailed information).

The relationship between AuNPs@CT plasmon properties and membrane stiffness can be quantitatively described by a sigmoidal law, having the following expression:

$$S.I. = a + \left\{ \frac{b}{\left(1 + exp\left(\frac{c - Stiffness}{d}\right)\right)} \right\} \quad (3.1)$$

with a, b, c and d parameters obtained by fitting the experimental values of S.I. vs. stiffness (see red curve fit and right inset of Figure 3.8a) with eqn. (3.1).

This calibration equation sets a functional connection between the spectral variations of AuNPs@CT , as described by the S.I., and the vesicles' stiffness, and can be exploited to quantitatively estimate the mechanical properties of lipid membranes of unknown composition and properties, with high sensitivity and reproducibility. We notice that with this method we are able to easily discriminate systems with very close stiffnesses, as POPC and DOPC membranes, whose mechanical properties are usually not distinguishable with many other techniques [144,145], while -to the best of our knowledge- the error associated is the lowest among all the other available methods to measure membrane stiffness. In addition, the presence of a sigmoidal law, which exhibits the highest variation of S.I. in the central region of the selected set of membrane stiffness (see grey dashed curve of Figure 3.8a, representing the first derivative of the sigmoidal fit) provides maximum sensitivity in the region where the rigidities of natural membranes usually fall (i.e., between 0.02-0.025 N/m [146]).

This method requires minimal sample amounts and can be applied to complex biogenic systems. As a proof-of-principle, we tested the assay on a sample of extracellular vesicles, EVs (see SI of **Paper III** for details on cell line and characterization of EVs), which are membrane-bound vesicles secreted by eukaryotic cells, acting as essential mediators of cell signalling and potential biomarkers of pathological conditions [147–149].

The stiffness of EVs, determined through AFM-FS, falls in the middle of the stiffness interval defined by the synthetic standards used for calibration (right inset of Figure 3.8c); accordingly, the optical modification induced by EVs on AuNPs@CT, monitored through UV-Vis (Figure 3.8b), is intermediate between the ones of DPPC and DPPC/POPC synthetic standards. This striking agreement demonstrates that the correlation between

AuNPs@CT aggregation and membrane stiffness, observed in synthetic vesicles, still holds for far more complex systems of biological origin. More importantly, the value of stiffness estimated from the S.I. of the AuNPs@CT/EVs hybrid, according to the calibration trend (0.026 N/m), falls right in the middle of the EVs rigidity range determined through AFM (see Figure 3.8c), demonstrating the predictive ability of this optical method.

In summary, the nanoplasmonic properties of AuNPs@CT can be effectively used to assess the stiffness of soft matter objects with a higher sensitivity with respect to the current methods. In addition, the method here proposed can be applied on sample quantities as small as 15 µl (with a concentration of EVs in the 10^{-8} M range), which represents a game-changer for precious biological samples, otherwise untraceable. Moreover, differently from other methods (e.g., AFM-FS, micropipette etc..) which probe the elasticity of single objects [137], it allows for the determination of the ensemble-averaged membrane stiffness, where possible variability across the population is considered. To conclude, this new approach would overcome most of the limitations of the current methods, employing a time and cost effective colorimetric and/or spectrophotometric determination of membrane nanomechanics.

3.1.3 Towards more reliable membrane models: the role of lipid rafts in AuNPs aggregation on lipid bilayers (Paper IV)

In this last part of this work, we extend the knowledge acquired on AuNPs@CT interaction with simple PC bilayers (sections 3.1.1-2) to more sophisticated biomimetic systems, moving closer to the complexity of biological membranes. This is the subject of a recent publication (**Paper IV**), addressing the role of nanoscale heterogeneities within the membrane, i.e. “lipid rafts”, in the interaction with NPs.

Biological membranes feature the presence of discrete micro and/or nanodomains, where lipids, such as cholesterol, sphingomyelin, saturated glycerophospholipids and glycosphingolipids, self-segregate in the liquid-ordered phase (L_b), which is immiscible with the surrounding liquid-crystalline disordered phase (L_α) [150] (section 1.3.2). These lipid rafts are involved in various biological functions and act as sites for the assembly of signalling molecules and the selective adsorption of nanosized materials [151–154]. Importantly, multiple evidence shows that membrane lateral heterogeneities play a role in NPs internalisation and cytotoxicity [71,72,155]; however, the physicochemical details of NPs/lipid rafts interaction remain largely unknown to date.

To address this issue, we exploited AFM to directly visualise the interaction of prototypical inorganic nanoparticles, i.e. AuNPs@CT, with model multicomponent SLBs (DOPC/DSPC/cholesterol (39/39/22 mol%)), reproducing the nanometric lateral heterogeneity of cell membranes.

SLBs were formed through vesicle fusion and primarily characterized by Neutron Reflectivity (see **Paper IV** full text and SI for details), highlighting the presence of a continuous planar bilayer onto the silicon substrate of 5 nm in thickness (see right inset of Figure 3.9a for a graphical representation).

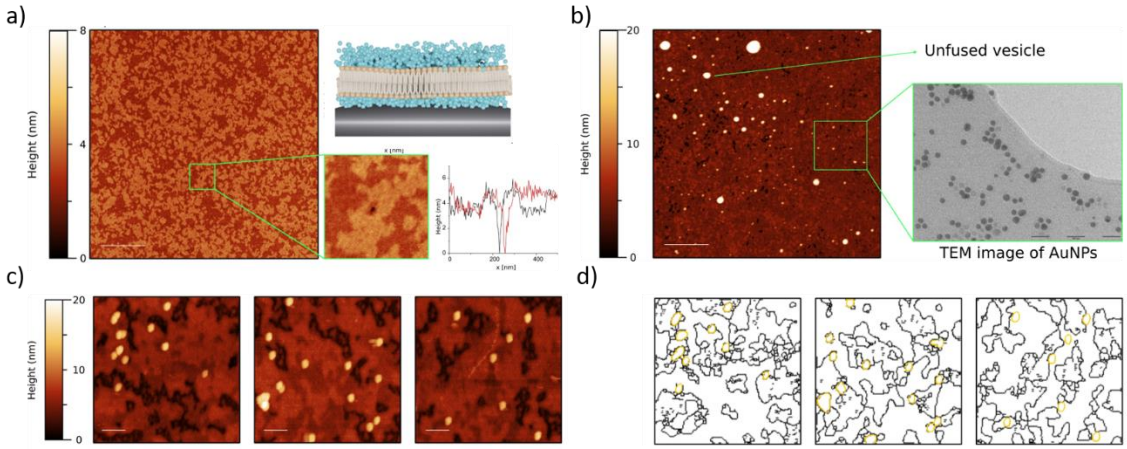

Figure 3.9 *a) Representative AFM topography of the SLB. The bilayer uniformly covers the surface, displaying both the L_b (brighter thicker regions) and L_α phases (darker thinner regions) as segregated domains. The reported scalebar is 1 µm. The 500x500 nm micrograph (bottom inset) displays the small hole in the bilayer that allowed flattening the image with respect to the SiO_2 surface. Two perpendicular height profiles were traced, horizontally and vertically, across the whole image (top inset); the profiles confirm the presence of the two distinct lipid phases covering the surface; b) Representative AFM topography of the SLB following the injection of AuNPs. Lipid rafts are still visible as differently shaded areas. The larger and heterogeneous spherical objects represent unfused vesicles while the smaller ones are the AuNPs that have been homogeneously adsorbed on the lipid bilayer. Scalebar is 1 µm. The inset reports a Transmission Electron Microscopy (TEM) image of the AuNPs that were used in the experiments, scalebar is 100 nm (refer to the SI of **Paper IV** for details regarding TEM characterization); c) Representative AFM micrographs that clearly display the selective adsorption of AuNPs along the boundaries of the lipid rafts (brighter regions of the SLB that correspond to the L_b lipid phase). From the images it is also possible to distinguish between isolated and clustered NPs. All scalebars are 100 nm; d) Contour images obtained from the micrographs. Black lines represent the rafts edges while gold circles define the contours of the AuNPs. The gold NPs edges are always in contact with at least one of the lines describing the lipid segregated phase boundaries.*

AFM was then used to resolve in detail the in-plane rafts morphology, spotting the presence of nanometric domains of different heights, i.e. 3.7 vs. 4.7 nm (Figure 3.9a and **Paper IV** for details): the thicker domains were associated with a cholesterol- and DSPC-

enriched L_b phase, while thinner regions to the L_α lipid phase, mainly composed of DOPC [156].

Figure 3.9b shows a representative AFM topography of the SLB following the AuNPs@CT injection within the AFM cell: the bigger spherical objects represent vesicles that still have to fuse with the bilayer, while the smaller ones are the AuNPs@CT, which seem to be homogeneously distributed above the SLB (See **Paper IV** for the details on the method used to discriminate unfused vesicles from AuNPs@CT).

To precisely determine whether the AuNPs@CT target specific locations on the lipid matrix, we reduced the size of the scanned region to $\sim 600 \times 600$ nm (Figure 3.8c) and used the software Gwyddion 2.53.16 to precisely localize AuNPs@CT adsorbed on the SLB. The contour images of AuNPs@CT and rafts, highlighted in Figure 3.8d in different colours (see **Paper IV** for details on the analysis of images), reveal that the 91% of NPs absorb along the edges of lipid phase boundaries. To the best of our knowledge, this finding constitutes the first direct proof that NPs preferentially target and accumulate at the boundaries of lipid rafts.

This phenomenon can be explained considering that phase boundaries represent energetically favourable niches for lipid–NPs interactions: the thickness mismatch along the boundaries of neighbouring domains increases the exposure of lipid hydrocarbon regions to water, which involves high interfacial energy costs.

When absorbing onto the lipid bilayer, AuNPs induce the bending of the membrane, which entails an energy penalty increasing the free energy of the overall process (eqn. (1.7)), section 1.3.1). This bending cost is minimized along the phase boundaries, due the local negative curvature of the membrane induced by the thickness mismatch: this generates energetically favourable conditions for the selective adsorption of AuNPs@CT at the edges of lipid rafts, where the free energy of NP/lipid interaction is reduced.

In addition, through the application of an AFM-based morphometric nanomechanical characterisation, we further investigated the reorganisation of the lipid bilayer, as a consequence of the AuNPs@CT adsorption: combining the AFM evaluation of AuNPs@CT average contact angle on the SLB with simple geometrical considerations (Fig. 3.10), we found that AuNPs penetrate the lipid bilayer at the rafts boundaries and reach the underlying substrate (see full text of **Paper IV** for details).

This result further extends the characterisation of the NPs–lipid interaction, showing that rafts boundaries represent not only preferential absorption sites, but also regions of enhanced permeability: here, the mechanical stress induced by the thickness mismatch between different domains facilitates the membrane wrapping around the adsorbed NPs, allowing their full penetration within the bilayer.

To summarize, here we showed that AuNPs@CT preferentially target lipid phase boundaries both as adsorption and penetration sites, hence providing the first direct proof of this selective NPs/lipid rafts interaction pathway.

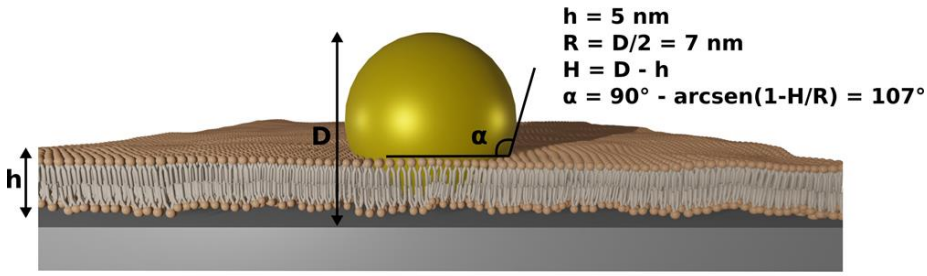

Figure 3.10 *Schematic representation of the configuration used to evaluate, from a conceptual point of view, the contact angle that would characterize an AuNPs with a diameter of 14 nm, adsorbed on a rigid flat surface and surrounded by a ~ 5 nm lipid bilayer.*

Part 2.

3.2 Interaction of inorganic Nanoparticles with lamellar and non-lamellar model membranes: curvature effects in nano-bio interactions (Paper V)

This chapter extends our investigation to synthetic lipid membranes of non-lamellar nature (paragraph 1.1), to explore the effects of surface curvature (eqn. (1.1) and (1.2)) on nano-bio interactions.

For NPs, the curvature is crucial for the interaction with biological interfaces [157]. NPs curvature, defined by NPs size and shape, strongly affects their reactivity and interaction with lipid membranes. Indeed, it determines the area available for NPs adsorption on lipid surfaces [57], modulating the strength of NPs-membrane adhesion forces (paragraph 1.3); moreover, a high surface curvature, either uniformly distributed on the surface of NPs (e.g., small NPs with sizes of a few nm) or localized at the sharp edges of asymmetric NPs (e.g., nanorods), is associated with higher energetic costs in terms of wrapping and internalization by membranes (section 1.3) [41,58,158,159]. Finally, curvature plays a significant role in the surface functionalization of NPs (e.g., ligand surface density), affecting their chemical identity [157]. For these reasons, NPs curvature is intensively investigated as a critical determinant in their interaction with natural and synthetic membranes.

On the contrary, the role of membrane interfacial curvature, connected with membrane geometry (section 1.1), represents a less explored research field, which could potentially be of similar impact at the nano-bio interface. As introduced in section 1.1, a flat configuration of the lipid bilayer is the most commonly encountered geometry in membranes of healthy cells; however, curved membrane configurations, as cubic bicontinuous arrangements, are known to occur in cells under pathological conditions (e.g., drug detoxification, starving, infection, oxidative stress, and cancer disease) [12,15,17] and during cell membrane fusion [160–162]. Up to now, investigations related to cubic membranes has been limited to a descriptive level, while the biological function of membrane arrangements with non-zero interfacial curvature remains unexplored [12,17].

This chapter will summarize the main results of a paper in preparation (**Paper V**), where we report one of the first systematic studies on the role of curvature in nano-bio interactions.

Here, the impact of curvature is investigated by focusing either on the lipid membrane and on NPs. On the “membrane side”, we compared model lipid films of different geometry, i.e. flat lamellar (Lα) phases, with zero mean (H, eqn.(1.1)) and Gaussian (K, eqn.(1.2)) interfacial curvatures, and curved cubic (Pn3m) phases, with negative

interfacial H and K. On the "NPs side", we employed AuNPs of similar size and surface coating, but different shapes, namely: i) gold spheres (AuNSs), with uniform positive H and K, and ii) gold nanorods (AuNRs), with two highly-curved surfaces (the poles) of similar H and K as AuNSs, separated by a cylindrical body with zero K and reduced H, i.e. one half of that of AuNSs.

Figure 3.11 highlights the main physicochemical features of these four building blocks.

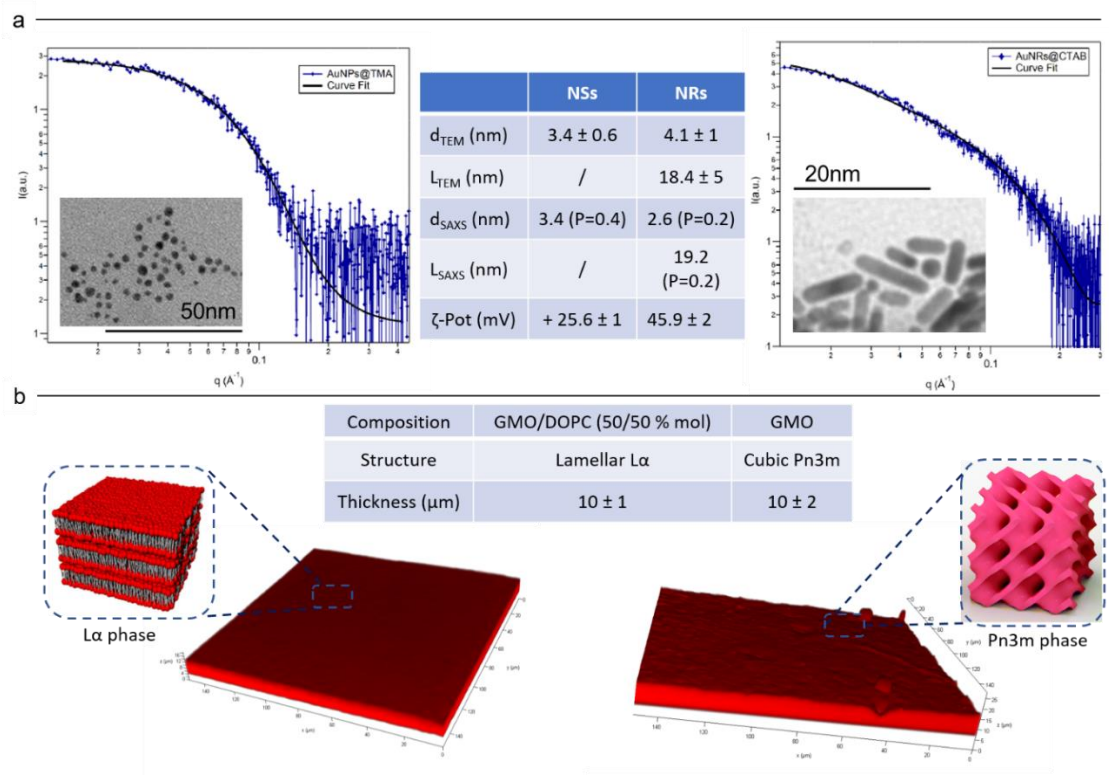

	NSs	NRs
d_{TEM} (nm)	3.4 ± 0.6	4.1 ± 1
L_{TEM} (nm)	/	18.4 ± 5
d_{SAXS} (nm)	3.4 (P=0.4)	2.6 (P=0.2)
L_{SAXS} (nm)	/	19.2 (P=0.2)
ζ-Pot (mV)	+ 25.6 ± 1	45.9 ± 2

Composition	GMO/DOPC (50/50 % mol)	GMO
Structure	Lamellar Lα	Cubic Pn3m
Thickness (μm)	10 ± 1	10 ± 2

Figure 3.11 Panel a) Physicochemical characterization of NPs. *Left and right parts: SAXS profile of AuNSs and AuNRs in water and corresponding curve fits according to a Schultz spheres model for AuNSs and a Cylinder poly radius model for AuNRs, from the NIST package SANS Utilities. Left insets report TEM images of AuNSs and AuNRs; Middle part: Table reporting values of Z-potential, diameter and/or diameter and length of AuNSs and AuNRs, determined by TEM and SAXS analyses. SAXS results are obtained from proper fitting procedures (see SI of* ***Paper V****), providing polydispersity values (i.e., "P" in the table).* ***Panel b) Physicochemical characterization of lipid films.*** *Left and right parts: Three-dimensional reconstruction of a confocal fluorescence z-stack of images of the lamellar and cubic films (tilted surface area of 150 x 150 μm). The insets reports the inner Lα and Pn3m structures; Middle part: Table reporting composition, internal structure, and average thickness of lipid films.*

AuNSs and AuNRs (Panel A) capped with the cationic ligand mercaptoundecyl-N,N,N-trimethyl ammonium bromide (TMA) and Cetyltrimethyl ammonium bromide (CTAB), respectively, present a net positive surface charge in water (see Z-potential values in Figure 3.11, Panel A and refer to the full text and SI of **Paper V** for NPs synthesis and

characterization). SAXS and TEM analyses highlight AuNSs and AuNRs of similar core diameter and AuNRs with average aspect ratio of 4.5 (evaluated from SAXS).

Lipid films with different internal structure (Panel B) were formed by spin-coating of lipid/n-hexane solutions with different compositions (i.e., GMO for the cubic phase and GMO/DOPC (50/50 mol %) for the lamellar phase) onto a solid substrate and subsequent hydration (see **Paper V** for details). The 3D reconstruction of the films labelled with Nile Red, performed with CLSM (see section 2.2 and **Paper V** for more information), reveals homogeneous thickness at the micron scale.

Sections **3.2.1** and **3.2.2** report the investigation on the interaction of these lamellar and cubic films with AuNSs and AuNRs.

We were interested in structural features at two length scales, which were investigated combining structural techniques with nanoscale resolution (i.e., Neutron Reflectivity (NR) and Grazing-Incidence Small-Angle Neutron Scattering (GISANS)) with CSLM, that gives insight on micron-scale structural details. This combination directly connects NPs-induced modifications in lipid films' internal nanostructure (section **3.2.1**) with morphological alterations of the whole membrane (section **3.2.2**), occurring at the micro-scale level. In the last part of this work (section **3.2.3**), we interpret our findings and propose a NPs-membrane interaction mechanism, which accounts for the observed curvature effects.

3.2.1 NPs/lipid films interaction: structural modifications at the nanoscale

We investigated the internal nanostructure of lipid films with or w/o AuNSs and AuNRs through Neutron Reflectivity (OFFSPEC reflectometer [163], Isis Neutron and Muon Source, Rutherford Appleton Laboratory, UK). GMO and GMO/DOPC films on silicon blocks were mounted inside the measuring cell; after 12 h of equilibration, the reflectivity in D_2O was recorded (see **Paper V** for details). Subsequently, AuNPs in D_2O (0.12 mg/ml in Au) were pumped in the cell, and the reflectivity was acquired after 8 h of additional incubation.

The reflectivity profiles of mixed GMO/DOPC (Fig. 3.12a) and pure GMO (Fig. 3.12b) films without AuNPs are consistent with the formation of highly ordered Lα and Pn3m mesophases, respectively, with prominent Bragg peaks corresponding to the typical reflexes of these two arrangements (see **Paper V** for details).

The addition of AuNSs to the lamellar film (Fig. 3.12a) produces a significant reduction in the Bragg peaks' intensity (see green curve as compared to red one), connected with a partial disruption of the Lα arrangement. Conversely, the impact of AuNSs on the cubic film seems negligible, suggesting that the Pn3m nanostructure is completely preserved,

even after 13 hours of interaction (8 h of incubation + 5 h of measurement). This result was further confirmed by NR measurements performed at REFSANS [164] (Heinz Maier-Leibnitz Zentrum in Garching), on the same system and under the same experimental conditions, highlighting a Pn3m structure which is unmodified by AuNSs (see Fig. S3 of SI of **Paper V** for details).

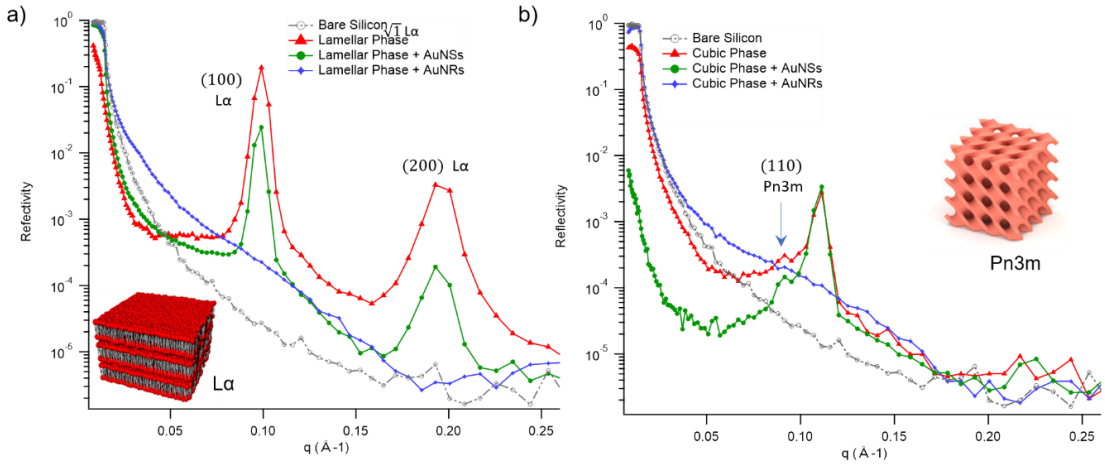

Figure 3.12 *a) Reflectivity vs. q profiles of GMO/DOPC lamellar phase film in the absence (red curve) and the presence of AuNSs (green curve) and AuNRs (blue curve). The reflectivity of the bare silica surface is also reported (gray curve). The inset sketches the inner Lα structure of the lipid film; b) Reflectivity vs. q profiles of GMO cubic phase film in the absence (red curve), and the presence of AuNSs (green curve) and AuNRs (blue curve). The reflectivity of the bare silica surface is also reported (gray curve). The inset sketches the inner cubic Pn3m structure of the lipid film.*

Thus, differences in membrane curvature seem to produce a significant variation in the films' structural response.

To get more insight on this phenomenon, we further investigated the impact of AuNSs on cubic phases in a longer time frame, by means of GISANS (REFSANS [164], Heinz Maier-Leibnitz Zentrum, Garching, Germany): our results, reported in **Paper V**, highlight a partial disruption of the Pn3m structure, observed after 32 h of incubation with AuNSs. This suggests that AuNSs do impact the structure of cubic membranes; however, the effect occurs for longer exposure times than for lamellar phases, pointing out an essential role of curvature in the structural stability of the model membranes.

The impact of AuNRs on both lamellar and cubic films is dramatically stronger: indeed, they destroy both the lamellar (blue curve of Figure 3.12a) and cubic (blue curve in Figure 3.12b) arrangements, as evident from the absence of Bragg reflexes in the corresponding reflectivity profiles. At variance with the case of AuNSs, this robust interaction with AuNRs does not allow discriminating between the structural response of lamellar and cubic phases in the time frame of our experimental observations; to gain insight on this faster

disruption process, we performed Neutron Reflectivity kinetics studies (REFSANS [164], Heinz Maier-Leibnitz Zentrum, Garching, Germany), allowing for monitoring the structural alteration produced by AuNRs on a shorter time scale. To the purpose, we measured the reflectivity of lipid films in H_2O, right before and after the injection of AuNRs within the measuring cell, at time intervals of 2.5 minutes over 5 hours (see **Paper V** for further details).

In Fig. 3.13, we report the (Q_z, Q_x) representations of NR data, along with the corresponding NR detector screens (right insets), for the lamellar (Panel A) and cubic film (Panel B), before and at different times from the addition of AuNRs.

(Q_z, Q_x) representations enable the analysis both of the specular and the off-specular reflectivity of the samples [165]: indeed, the integrated intensity along the specular reflectivity line (see blue line in the left (Qz, Qx) plot of Panel B) gives the specular reflectivity profile of lamellar and cubic films, which are analogous to the ones of Fig. 3.12a-b (reported in the SI of **Paper V**).

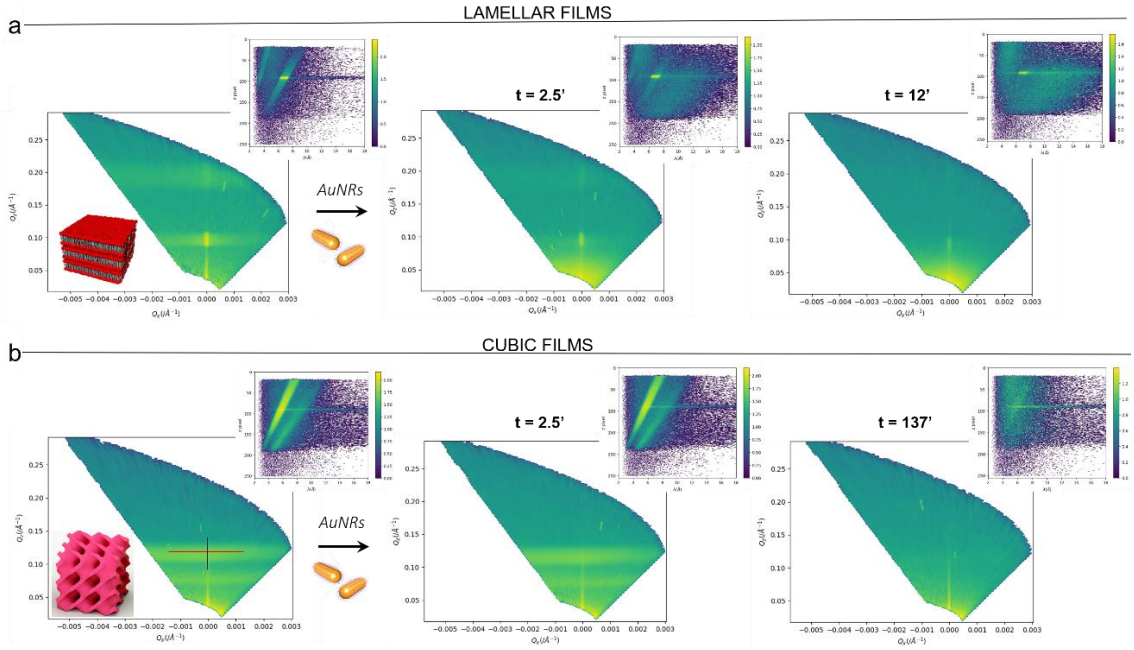

Fig.3.13 Panel a: *(Qz, Qx) representations of the off-specular scattering of a lamellar film in the absence of AuNRs and for different elapsed times from the injection of AuNRs. The insets represent the NR detector;* ***Panel b:*** *(Qz, Qx) representations of the off-specular scattering of a cubic film in the absence of AuNRs and for different elapsed times from the injection. The insets represent the corresponding images of the NR detector.*

Also, the (Q_z, Q_x) maps of both lamellar and cubic films in the absence of AuNPs show pronounced off-specular patterns, i.e. out of the specular reflectivity line, consisting in

marked “Bragg sheets” [165] (see the red line in the left (Qz, Qx) plot of Panel B, as an example). These off-specular features are also visible in the corresponding detector screens, as higher intensity stripes. Bragg sheets are characteristic of highly ordered samples and coincide with the Bragg peaks from the specular reflectivity [165], distinguishing the Lα and Pn3m structures of lamellar and cubic films, respectively (see **Paper V** for further details).

Due to their high intensity, off-specular Bragg sheets allow monitoring the impact of AuNRs on lipid films' structure over time. Panels A and B highlight a strong effect of AuNRs on both lamellar and cubic arrangements, which can be identified in the smearing out of their characteristic Bragg sheets; this effect advances with time and ultimately leads to the complete loss of the off-specular feature, hinting to the disruption of the films’ inner architecture. However, lamellar films completely lose their organization significantly faster than cubic ones, with Braggs sheets completely vanishing within 12 minutes. On the contrary, cubic phase-related off-specular is still detectable after more than two h of incubation with AuNRs. Thus, cubic phases show an enhanced structural resilience towards the action of rods with respect to lamellar ones, which is entirely in line with the findings on spherical particles. In addition, this slower disruption process allowed us to appreciate a subtler detail of the restructuring action of AuNRs on cubic phases; in particular, we highlighted a non-negligible shrinkage of the cubic phase lattice parameter (i.e., 2 Å), after only 2.5’ of incubation with AuNRs (see specular reflectivity profiles of Fig. S4 of SI of **Paper V**). This effect, which is observed when the cubic arrangement is still intact (Figure 3.13, middle (Qz, Qx) plot of Panel B), might be the driving force for the progressive collapse of the mesophase.

In summary, the NR analysis, performed both as static and kinetic investigation, allowed characterizing NPs-lipid films interactions at a nanoscale level: giving access to the alterations induced by NPs on the nanostructure of model films, it highlighted a crucial role of curvature, of either the membrane or the NPs, in nano-bio interactions.

To connect this nanoscale structural information with the impact of AuNPs on the membrane as a whole, we further observed the NPs-films interaction on a larger length scale (i.e., micron-scale): through CSLM, we monitored real-time the morphological modification induced by AuNPs on lipid films, for a comprehensive view of the phenomenon.

3.2.2 NPs/lipid films interaction: real-time morphological effects at the micron-scale

CLSM measurements were performed over the same time frame of NR kinetics, with fluorescently labelled lamellar and cubic films imaged before and after the injection of AuNPs (see **Paper V** for details on sample preparation and imaging). Figure 3.14 gathers representative side-view confocal microscopy images of a lamellar film absorbed onto a glass substrate, challenged by AuNSs (Panel a) and AuNRs (Panel b).

AuNSs produces an initial swelling of the film (20'), increasing the distance between the different lamellae composing this structure; this leads to the progressive peeling-off of the lamellar film (60'), with a gradual detachment of the outer surface layers. Once removed from the original matrix, these lipid layers start to bend and roll-up in closed onion-like vesicles (180'), which get partially adsorbed onto the film surface. After 180' of incubation, only a thin layer of the original lamellar film is preserved on the glass surface, partially covered by micron-sized multilamellar vesicles. AuNRs produce a similar morphological modification, which, however, occurs in a faster time frame: indeed, an massive swelling of the lamellar film is observed after just 1' from the AuNRs addition, while the peeling-off already starts after 5', leading to the complete disruption of the film within 10'.

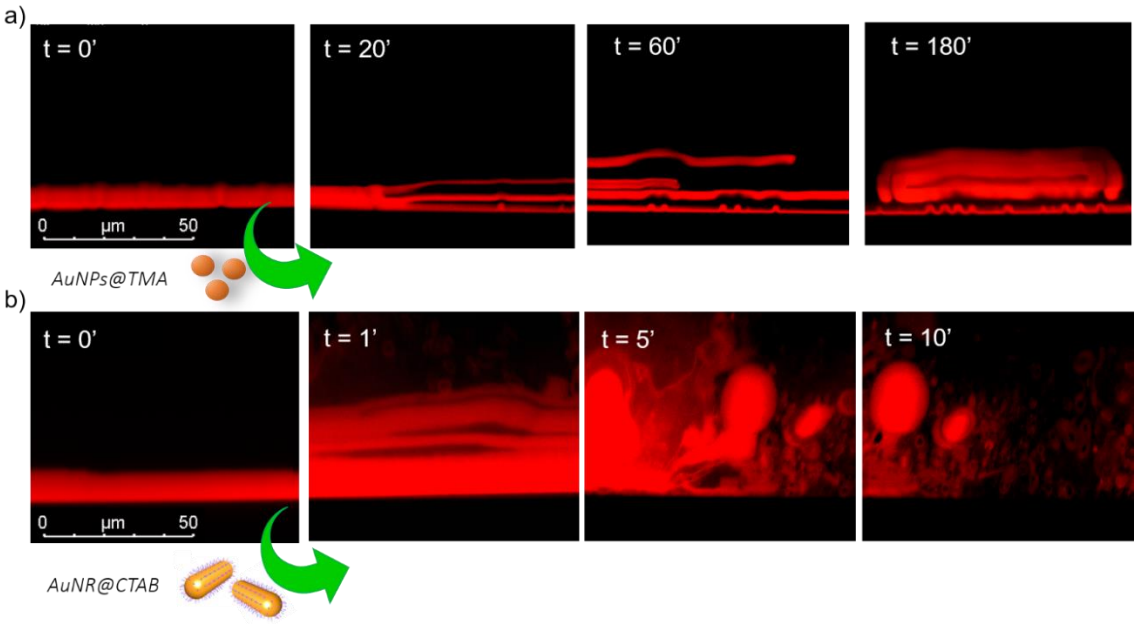

Figure 3.14 Panel a) *Representative confocal microscopy images (side view) of a lamellar film right before and after 20', 60', 180' from the addition of AuNSs;* ***Panel b)*** *Representative confocal microscopy images (side view) of a lamellar film right before and after 1', 5', 10' from the addition of AuNRs.*

A completely different behaviour is observed when AuNPs challenge cubic films (Fig. 3.15). Specifically, AuNSs (Panel A) seem to "excavate" the cubic membrane (30'), producing cavities of increasing depth over time, which ultimately reach the glass surface. After 180' of incubation, the lipid film, although mostly intact, presents micron-sized holes (top-view inset in Panel A).

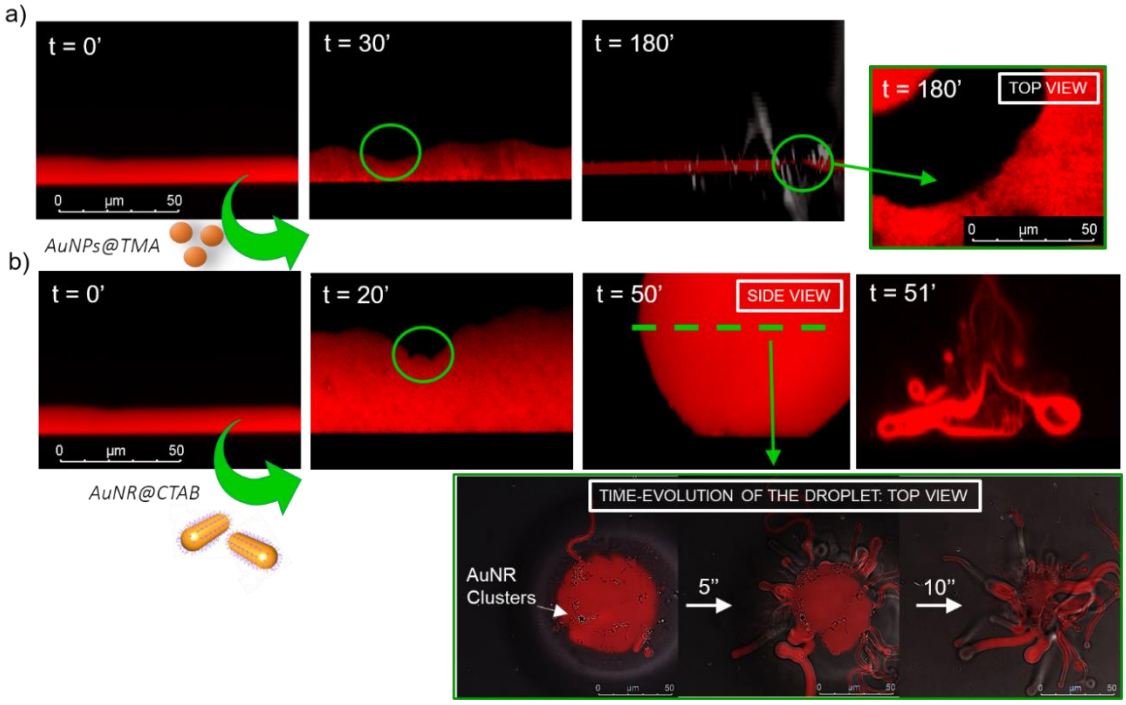

Figure 3.15 Panel a): *Representative confocal microscopy images (side view) of a cubic film right before and after 30', 180' from the addition of AuNSs The right inset represents the top view of cubic film after 180' incubation with AuNSs;* ***Panel b):*** *Representative confocal microscopy images (side view) of a cubic film right before and after 20', 50', 51' from the addition of AuNRs. The bottom right inset collects three top view images of a lipid droplet acquired at 0", 5" and 10" from its formation. The final pictures were obtained from the overlay between the absorption of AuNRs (gryscale) and the fluorescence of Nile Red, labelling the lipid hydrophobic matrix (red color).*

As already observed for the case of lamellar membranes, AuNRs are associated with a similar disruptive mechanism as AuNSs, which is, however, faster and of more profound nature (Panel B): AuNRs initially increase the film's roughness (20'), with the formation of micron-scale "hills and hollows" across the membrane. Then, the lipid film gets progressively eroded, with the depth of the hollows increasing with time: within 50', this leads to the complete retraction of the film in localized areas of the glass, i.e. its de-wetting, giving rise to isolated thick lipid droplets. These droplets get destroyed by the action of AuNRs within a few seconds from their formation. This process's temporal evolution can be followed by imaging a horizontal section of a droplet (top-view bottom

inset, Panel B) at different times from its formation, in both fluorescence and transmission mode. The overlay between the transmission (gray scale) and the fluorescence (red scale) contributions allows us to simultaneously capture the morphological evolution of the lipid matrix (fluorescently labelled) and the AuNPs (low-transmission black spots in the image). At t=0', AuNRs are mostly located as micron-sized clusters at the lipid droplet edges, encircling it. Then (5" image), they start to excavate and unroll the droplet advancing from the edges, i.e. their accumulation points, leading to its complete collapse within 10".

Overall, we can conclude that: i) perfectly in line with the structural analysis (section 3.2.1), the impact of AuNRs on both lamellar and cubic films is stronger and leads to faster morphological modifications than AuNSs; ii) AuNPs interact with lamellar and cubic phases according to two different and well-defined mechanisms, i.e. the peeling-off of the lamellar assembly and the excavation of the cubic one. As these two phenomena were observed for both spherical and cylindrical AuNPs, i.e. independently from their shape, membrane curvature seems to be the main factor determining the NPs-membrane interaction pathway.

3.2.3 NPs/lipid films interaction: curvature effects

The ensemble of gathered results, offering a view on different length scales, highlights that NPs-model membrane interaction is deeply affected by both membrane interfacial curvature (connected to the geometry of the lipid phase) and NPs surface curvature (associated to NPs shape).

Both NR and CLSM results point out a major role of AuNPs asymmetric shape in this interaction; in particular, NR measurements show that AuNRs induce a complete loss of Lα and Pn3m nanostructures within less than 15' and 2 h, respectively. On the contrary, the combination of NR and GISANS analyses highlights that AuNSs act on a completely different time frame, with a partial disruption of lamellar and cubic structures after 13 h and 32 h, respectively. These observations are perfectly in line with CLSM findings, showing a direct connection between the micron scale morphological alteration and the nanoscale restructuring of lipid films, induced by AuNPs. Thus, we can conclude that NPs curvature is a major player, with asymmetric geometries being associated with highly destructive effects. Importantly, this behaviour holds for both lamellar and non-lamellar models, highlighting a universal effect of NPs asymmetry in nano-bio interactions.

Beside NPs surface curvature, we found that the interfacial curvature of the lipid membrane is a key factor at stake in NPs-films interactions. Specifically, NR and CLSM

analyses highlight that, for a given NPs' type, membrane geometry determines both the strength and the pathway of interaction with NPs: indeed, independently from their shape, NPs induce a faster disruption of the inner nanostructure of lamellar membranes with respect to cubic ones, which results into more rapid morphological modifications at the micron-scale. This hints to a universal role of membrane curvature in in nano-bio interactions, with highly curved membranes showing an enhanced structural stability towards nanomaterials.

Combining the NR and CSLM data, it is possible to define two different mechanisms describing the interaction of lamellar and cubic phases with NPs, responsible for their different stability.

The faster structural modification of Lα films induced by both AuNSs and AuNRs (section 3.2.1) is associated with an initial swelling, followed by the progressive exfoliation of the multilamellar arrangement (section 3.2.2), proceeding from the outer lamellar layers. We can hypothesize that, right after their injection, AuNPs start to penetrate the outer part of the lamellar film, i.e. the one exposed to the water external medium. This penetration would primarily occur via electrostatic and dipolar interactions between the cationic coating of AuNPs and the polar headgroup of the lipids composing the membrane, directly exposed to the water phase; this interaction would enable the insertion of AuNPs, together with their hydration shell, within the hydrophilic domains of the phase, i.e. the water layers separating the different lamellae. Then, the mismatch between the thickness of the water layers (between 2 and 3 nm, see **Paper V** for details) and NPs hydrodynamic size (see DLS measurement in the SI of **Paper V**) would be responsible for the initial swelling of the lamellar film (Fig. 3.14). Then, the increasing inter-lamellar distance would reduce the interactions between different lamellae, producing the detachment of the outer lamellar layers, i.e. the ones in direct contact with NPs. Indeed, lipid bilayers of equal composition are held together only by weak Van Der Waals forces, in equilibrium with repulsive electrostatic and entropic contributions [8]. Thus, inter-bilayer interactions can be easily overwhelmed by attractive single bilayer-NPs forces of electrostatic nature. The thinning of the film would favour the penetration of NPs within its deeper part, i.e. the one closer to the solid support, provoking its progressive peeling-off. The loss of the lamellar periodicity as the layers are being detached the one from the other can be connected to the progressive smearing out of the Lα-structural features, observed through NR (Fig. 3.12 and 3.13).

A completely different interaction mechanism can be outlined for the case of cubic membranes, related with their higher structural stability. NR data highlight a progressive disruption of the cubic Pn3m nanostructure by NPs, which starts from the shrinkage of its lattice parameter (section 3.2.1). This nanoscale phenomenon parallels a progressive excavation of the film observed at the micron-scale (section 3.2.2), leading to its de-

wetting; interestingly, this phenomenon proceeds from NPs clusters, which, acting like micron-sized "diggers", progressively erode and unroll the lipid matrix. We can hypothesize that, in this case, NPs are not able to fully penetrate the inner aqueous region of the film, i.e. the aqueous nanochannels of 4.4 nm in diameter (see **Paper V** for details), due to its peculiar nanostructure. Indeed, cubic phases represent a highly interconnected 3D network, where a single lipid bilayer folds in the space originating bicontinuous aqueous and lipid domains (paragraph 1.1); this robust 3D architecture would impede a full insertion of NPs within the aqueous channels of smaller size (which would lead to its disruption due to size mismatch), preventing a fast unfolding. Instead, the attractive NPs-lipid headgroups forces would result in the absorption of NPs, residing onto the film surface as clusters. As highlighted by NR analysis, their presence induces an immediate shrinking of the phase, leading to local water expulsion and subsequent dehydration: we can speculate that this phenomenon drives the progressive collapse of the cubic arrangement, which would proceed from the different NPs accumulation points across the membrane, leading to the formation of multiple isolated droplets.

To summarize, we found that NPs-lipid membrane interaction depends on both the internal nanostructure of the membrane and the shape of NPs. These two variables represent two sides of the same coin, as a single parameter, i.e. curvature, can describe their variations. In these terms, we can state that a non-uniform NPs surface curvature promotes a more robust interaction with the lipid matrix. On the other hand, when referring to the membrane interfacial curvature, we observe that flat membranes experience more substantial disruptive effects than curved ones when exposed to NPs. We hypothesize that this is due to the different inner structure of lamellar and cubic membranes: the bilayers composing the lamellar films are only held together by weak Van der Waals interactions and, thereby, can be easily detached the one from the other by the action of NPs. On the other hand, cubic phase films consist of a single 3D architecture, which offers a broader resistance against NPs' disruptive effects.

These findings represent one of the first insight into membrane curvature's role in the interactions with nanomaterials. Notably, the newly discovered enhanced resilience of cubic membranes might have important implications at a biological level.

As already introduced, the biological function of curved membranes is poorly understood: in particular, whether their formation is solely a result of aberrant processes within diseased cells or represent a functional response to these pathologies remains unclear [164].

Engineered NPs share their size with biologically relevant entities (i.e. DNA, surface proteins, biogenic extracellular vesicles, and viruses), which often results in similar interaction pathways with cells (paragraph 1.3). Thus, we might connect the higher structural stability exhibited by cubic membranes towards NPs with a similar behaviour

towards natural nano-objects, such as viral pathogens. In this perspective, our findings suggest a possible “protective role” of the cubic architecture, which occurs in infected, stressed, or starved cells. This arrangement would represent a biological barrier with enhanced structural resilience, occurring in extreme cell conditions to minimize the membrane response towards harmful external perturbations.

Part 3.

3.3. Inclusion of inorganic NPs in cubic membranes: from understanding to the development of hybrid smart materials (Papers VI, VII)

As detailed in paragraph 1.3, the inclusion of inorganic NPs within nanostructured lipid assemblies combines the rich polymorphism of lipid phases with the advanced functional properties provided by NPs, expanding the applicative spectrum of these two building blocks.

Among the possible lipid scaffolds, cubic phases (paragraph 1.1) have recently emerged in the biomedical research field: their internal cubic structure enables the encapsulation of larger amounts of hydrophobic molecular additives with respect to dispersed lamellar lipid phases (e.g., liposomes), featuring their application as highly efficient vehicles for drug, gene and food ingredients delivery [19,86]. Moreover, their particularly high interfacial surface is connected to an enhanced interaction with biological barriers [88,166], enabling to reach the desired target inside the cell, with relevant implications in therapeutic and diagnostic fields.

Some recent studies report on the insertion of different kinds of inorganic NPs within cubic lipid systems for applicative purposes [84,167]; however, fundamental knowledge on the effects of NPs on the structure of lipid mesophases, enabling the rational design and optimization of hybrid materials for the desired biomedical purpose, is still limited.

In the first part of this work (section **3.3.1**), which summarizes **Paper VI** and part of **Paper VII**, we will report a thorough characterization of the structural impact of two different kinds of hydrophobic NPs, i.e. AuNPs and SPIONs, on the self-assembly of Phytantriol (Phyt) (Fig.3.16a), i.e. a polymorphic amphiphile able to form Pn3m cubic phases in water excess and room temperature.

On the basis of our results, we will propose a general model to interpret and predict the effects of NPs on the lipid phase behaviour, where the structural modifications induced by NPs on the cubic phase only depend on their size and volume fraction, but not on their chemical identity. The last part of the work (section **3.3.2**) will be the subject of **Paper VII**: here, the knowledge gathered on NPs/lipid self-assembly will be applied to the rational design of hybrid cubic phases, composed of SPIONs and glycerol monooleate (GMO), i.e. a "*generally recognized as safe*" lipid from FDA and commonly used in the food industry [168]. We will show that the inclusion of SPIONs within this biocompatible matrix has the twofold advantage of i) enabling a fine control of the lipid structure and ii) introducing

responsiveness to magnetic fields. These two possibilities will lead to the design of a new smart hybrid platform, optimized for applications in the drug delivery field.

3.3.1 Phase behaviour of lipid mesophases containing hydrophobic NPs (Papers VI and VII)

Here, we report a detailed structural investigation of Phyt/water cubic phases doped with two different types of hydrophobic NPs of similar size (3-4 nm in diameter), namely dodecanethiol-capped AuNPs and oleic acid/oleylamine-capped SPIONs (see **Paper VI** full text and SI for the synthesis and characterization of NPs and the preparation of hybrid samples). Thanks to their hydrophobic coating, NPs are expected to localize within the hydrophobic domains of the mesophase, while their small size is predicted to not destroy the Phyt lipid bilayer [169].

Figure 3.16 reports the structural effect of increasing amounts of AuNPs (Fig. 3.16b) and SPIONs (Fig. 3.16c) on the Phyt/water system (at 25°C and in water excess), monitored through SAXS. While the Bragg peaks of a neat cubic Pn3m arrangement are clearly recognizable in the absence of NPs, in line with literature [170], the addition of NPs deeply impacts the structure and phase behavior. Remarkably, at relatively low NPs concentrations we observe a shrinking of the Pn3m cubic phase (see SI of **Paper VI** for details), while a phase transition from cubic (Pn3m) to hexagonal (H_{II}) phase occurs upon increasing the amount of both AuNPs or SPIONs. This effect is evident from the appearance of the typical Bragg reflexes of the H_{II} phase, which replace the ones of the Pn3m arrangement at the highest NPs amounts. In the absence of NPs, the Pn3m-H_{II} transition is triggered by heating the Phyt/water system above 50°C. The ability of NPs to shift the boundaries between different mesophases has been observed for similar hybrid systems, e.g. silica NPs embedded within phospholipid assemblies [171], and might be implied in possible cytotoxic effects of small NPs.

To interpret this behavior, we consider the total free energy per unit area of a lipid bilayer (g_T) as a balance between g_C and g_P, i.e. the elastic curvature (eqn. (1.7)) and the frustration packing (eqn. (1.10)) free energies per unit area of the bilayer [11]:

$$g_T = g_C + g_P \quad (3.2)$$

The variation of the total free energy (Δg_T), involved in the transition from the cubic (initial) to the hexagonal (final), phase is:

$$\Delta g_T = g_{H_{II}} - g_{Pn3m} = \Delta g_C + \Delta g_P \quad (3.3)$$

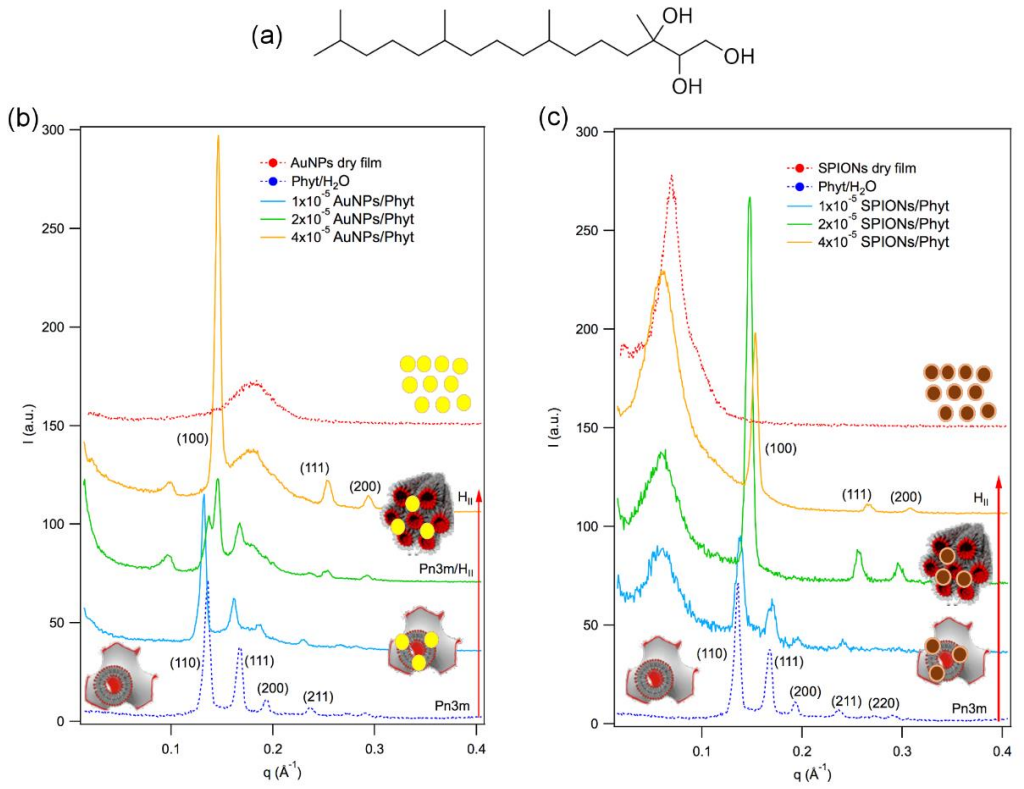

Figure 3.16 *(a) Chemical structure of Phyt; (b, c) SAXS profiles of Phyt/H2O system in the absence (blue dashed line) and in the presence of (b) AuNPs and (c) SPIONs at the concentrations of 1×10^{-5}, 2×10^{-5}, 4×10^{-5} per Phyt molecule. The dashed red lines represent the scattering profile of a dry film of AuNPs and SPIONs. The Miller indexes assignments (hkl) of the Pn3m and hexagonal phase are reported in the graphs.*

In the absence of NPs, the hexagonal phase is characterized by a higher g_P than the cubic one ($\Delta g_P > 0$) [11], and by a lower energy of elastic curvature ($\Delta g_C < 0$) [172]: thus, the Pn3m phase dominates at r.t., due to $|\Delta g_P|$ being larger than $|\Delta g_C|$ (Fig. 3.17, left part). Since the Pn3m-H_{II} transition in neat Phyt/water systems is already favoured by the elastic contribution (Δg_C), we hypothesize that the major effect of NPs is to lower $|\Delta g_P|$ (Fig. 3.17, right part): this effect would be dependent on NPs amount and provoke a full replacement of the Pn3m phase with the H_{II} one for a defined NPs concentration threshold. In eqn. (1.10), g_P is defined by a harmonic oscillator-like law, describing the stretching or compression of lipid chains with respect to their relaxed state. Within the Pn3m structure, the lipids close to a NP experience an increase in their frustration packing, as their hydrocarbon chains stretch to fill the hydrophobic cavities created by the insertion of the NP (Fig. 3.17). On the contrary, NPs can fill the voids of the hexagonal

arrangement (Fig. 3.17), without any stretching penalty for the lipid hydrocarbon chains: these two concomitant effects would lead to a decrease in $|\Delta g_P|$, which represents a possible driving force for the cubic to hexagonal phase transition.

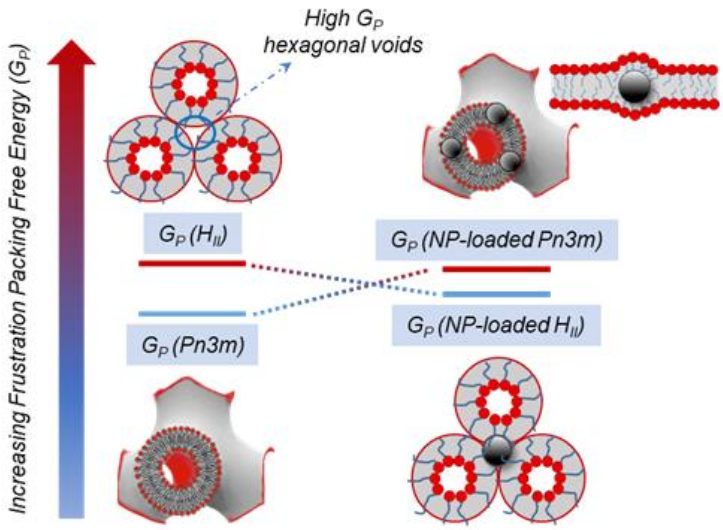

Fig. 3.17 *Effects of NPs on lipid mesophases architectures. Illustrative scheme of the NPs-induced modification of the Frustration Packing Energy (G_P) of both cubic and hexagonal mesophases.*

To obtain a full characterization of the NPs/Phyt system phase behaviour, we further explored the temperature dependence in the range 25-50°C, at fixed NPs/Phyt ratio of 1×10^{-5}. While the SAXS profiles of the binary Phyt/H2O system show the characteristic Pn3m-H_{II} transition at 50 °C [170] (Fig. 3.18a), the behaviour of hybrid systems is substantially different: in the presence of SPIONs (Fig. 3.18b) or AuNPs (Fig. 3.18c), the Pn3m phase persists at room temperature, but a temperature increase to 35°C is sufficient to promote the transition to the hexagonal phase.

We can conclude that the presence of NPs enables to finely control the structure of the Phyt/water system, in two different ways: depending on NPs' concentration, either a shrinking of the cubic phase (lower NPs amounts) or a transition to the hexagonal one (higher NPs amounts) is induced. The same result can be achieved by heating at a fixed NPs amounts, which triggers the Pn3m-H_{II} at temperatures which can be considerably lower than those observed for the binary system. The transition temperatures are controlled by the NPs' concentration (see full text and SI of **Papers VI** and **VII** for details).

Remarkably, the core of NPs does not show to affect the restructuring of the hybrid system. This description has therefore a general validity, holding for hydrophobic NPs with sizes comparable with the thickness of the lipid bilayer, irrespectively of composition.

This structural fine-tuning, enabled by NPs, and specifically the possibility to control the Pn3m-H_{II} transition temperature to near-physiological values, can be exploited to design temperature-responsive drug delivery systems. The transition to hexagonal phases implies a significant lowering of water content [170,173], with abrupt water expulsion and possible release of hydrophilic active principles, originally confined in the water channels of the cubic phase.

In order to exploit this opportunity for controlled drug delivery, we focused on GMO/water assemblies, which are characterized by a similar phase behaviour as Phyt/water systems, but superior biocompatibility and biodegradability[168]. The next paragraph, which summarizes the results of **Paper VII**, will report the combination of this lipid matrix with the same hydrophobic SPIONs employed for Phyt/water systems, with a more specific focus on the rational design of hybrid drug delivery vehicles.

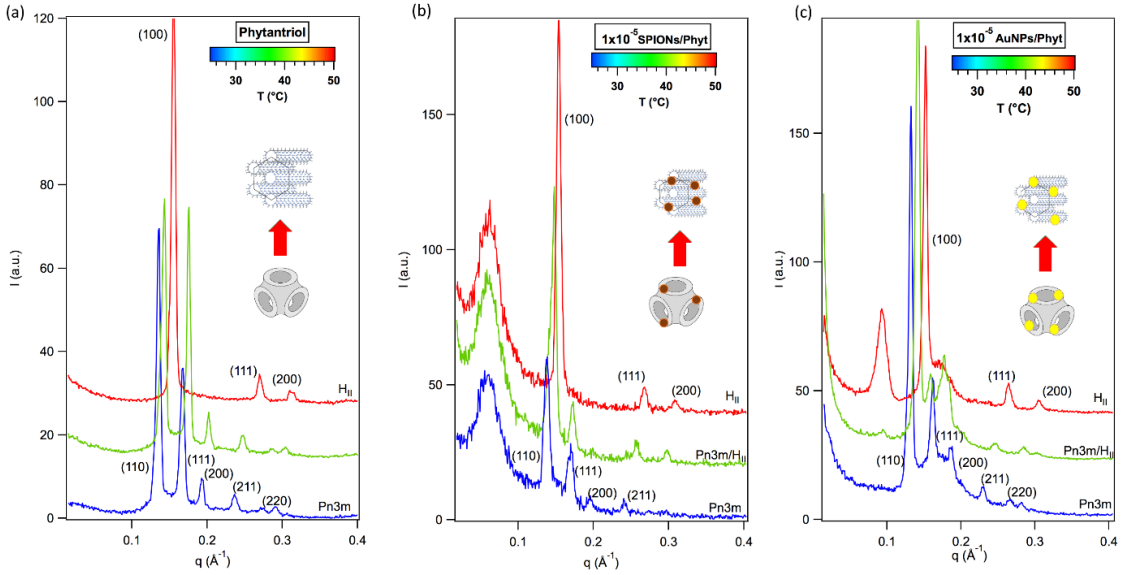

Fig. 3.18 *SAXS profiles of Phyt/H_2O mesophases in the absence (a) and in the presence of (b, c) 1 × 10^{-5} NPs ((b) SPIONs and (c) AuNPs) per Phyt molecule at 25 °C (blue), 35 °C (green curves) and 50 °C (red curves); the Miller indexes assignments (hkl) of the Pn3m and hexagonal phase are reported in the graphs.*

3.3.2 Design and characterization of GMO/SPIONs cubic phases for controlled drug delivery (Paper VII)

Here, we report the design and optimization of GMO/water cubic phases embedded with oleic acid/oleylamine-capped SPIONs (see **Paper VII** full text and SI for synthesis and

characterization of NPs and the preparation of hybrid samples) for controlled drug delivery purposes.

Through SAXS, we characterized the structure of these bulk assemblies (in water excess), as a function of SPIONs concentration and temperature. Then, we explored the phase behaviour of dispersed cubic GMO/SPIONs particles (i.e., "magnetocubosomes"), which, due to their low viscosity, represent more easily injectable drug delivery formulations with respect to bulk materials [174]. Finally, we addressed the magnetotropic behaviour of these hybrids, highlighting the promising possibility to control their structure and release properties through the magnetic responsiveness provided by SPIONs.

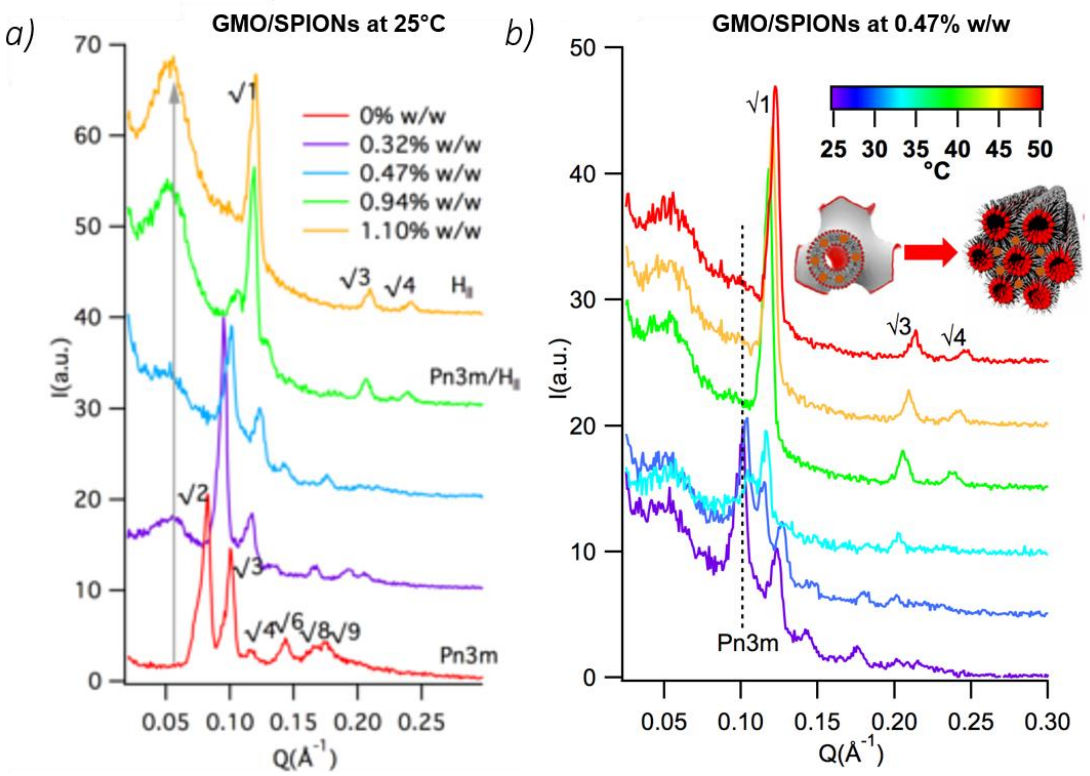

Figure 3.19 *a) SAXS profiles of GMO 50% w/w water liquid crystalline phases in the presence of different SPIONs amounts: from bottom to top, SAXS profiles of the samples with increasing SPIONs percentages (0; 0.32; 0.47; 0.94; 1.1% w/w with respect to GMO amount) are displayed with suitable offsets; b) SAXS profiles of the GMO/water system assembled with 0.47% w/w SPIONs and 50% w/w water at 25–30–35–40–45–50 °C. Cubic to hexagonal phase transition is observed above 35 °C.*

SAXS profiles in Figure 3.19 highlight that SPIONs induce a structural modification which is very similar to the one observed for Phyt/water system (section 3.3.1): at r.t. (Fig. 3.19a), increasing amounts of SPIONs induce a progressive shrinkage of the GMO/water cubic phase, ultimately leading to the transition to the hexagonal arrangement. In

addition, increasing concentrations of SPIONs progressively lower the Pn3m-H_{II} transition temperature of neat GMO/water assemblies, which is around 80°C [175]. While the full structural analysis of the systems can be found in the SI of **Paper VII**, Figure 3.19b reports a very interesting example of this behaviour: specifically, the inclusion of 0.47% w/w of SPIONs is able to trigger the Pn3m-H_{II} transition in the 30–40 °C range, i.e. close to physiological temperatures, envisioning the possibility to control the release of active principles in biological fluids (section 3.3.1).

To explore the applicative potential of this hybrid, we adopted a twofold approach: i) we investigated the thermotropic behavior of the system at a dispersed level, i.e. in the form of an aqueous dispersion of GMO/water/SPIONs nanostructured particles (magnetocubosomes), representing a more suitable solution for drug delivery applications; ii) we performed an on-line investigation of the structural responsiveness of bulk GMO/water/SPIONs assemblies to alternating magnetic fields (AMFs): this allowed monitoring the magnetotropic response of the system, for potential application in magnetically modulated drug delivery. These two different investigations are separately reported in the following.

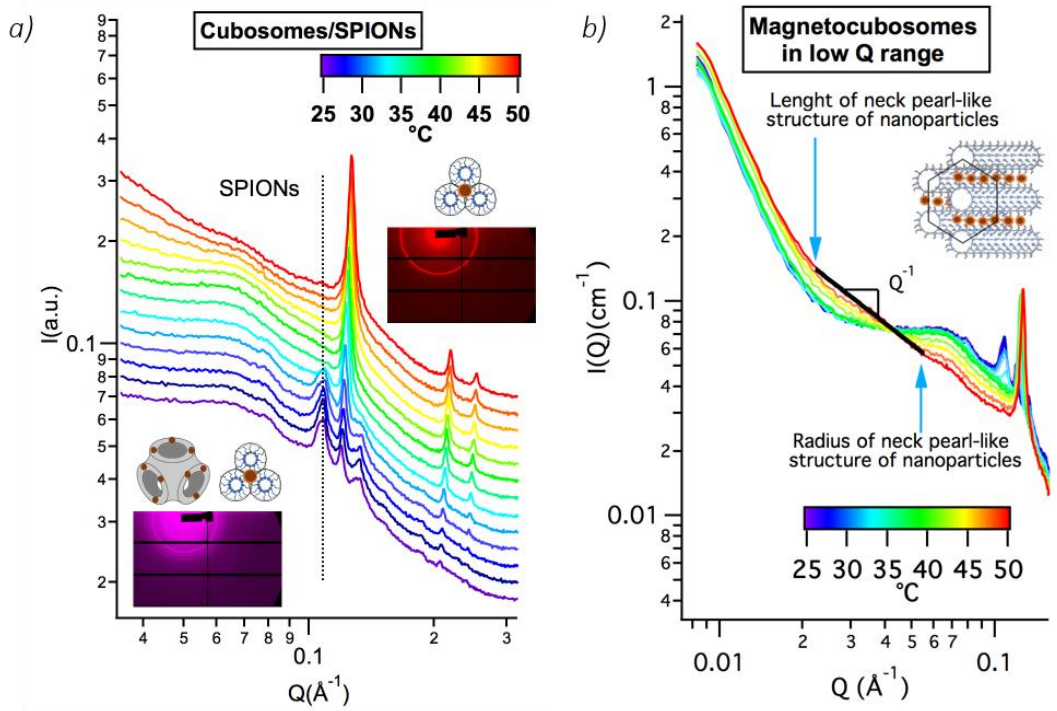

Figure 3.20 *a) SAXS curves of magnetocubosomes monitored in the 25 °C–49 °C temperature range with 2 °C temperature steps; b) Detail on low-q range of SAXS curves of magnetocubosomes acquired in the 25–49 °C temperature range. A variation of the scattering intensity for magnetic nanoparticles was detected during the increase of temperature. At 49 °C, the self-organization of SPIONs into the lipid architecture shows a pearl-necklace like structure (q^{-1}).*

By dispersing the GMO/SPIONs bulk system though a steric stabilizer (Pluronic F-127)[176], we obtained stable magnetocubosomes (200-250 nm of diameter) in water (see full text and SI of **Paper VII** for details on the preparation), preserving the inner cubic organization of the former bulk phases.

Through Synchrotron SAXS (see **Paper VII** for details), we investigated the structure of magnetocubosomes within a temperature range of 25–49 °C: at 0.47% w/w SPIONs percentage (Figure 3.20a), we observed a Pn3m-H_{II} phase coexistence even at 25 °C, while the cubic phase signature disappears above 35 °C, indicating a complete transition to the hexagonal arrangement. The larger stability range of the H_{II} phase is thus preserved at a dispersed level, enabling a possible use of magnetocubosomes as drug carriers with a temperature-controlled release ability.

In addition, a very interesting feature emerges in the low-q region of magnetocubosomes SAXS profiles, as temperature increases (Fig. 3.20b): starting from 42°C, a distinct and relatively extended q^{-1} scalar law appears beyond the Guinier region of single NPs (see **Paper VII** for details), consistent with a reorganization of SPIONs in pearl-necklace aggregates.

This is probably due to a temperature-induced decrease in the viscosity of the lipid phase, enabling particle diffusion into the lipid hydrophobic domains and aggregation, driven by NP-NP magnetic dipolar interactions. The clustering of SPIONs can profoundly modify their magnetic properties and has been recently proposed as an effective way to enhance their heating power for magnetic fluid hyperthermia applications [177]. With our results, we demonstrate that a fine control on the SPIONs arrangement can be achieved exploiting the polymorphic behaviour of a lipid scaffold, paving the way for a facile and inexpensive tailoring of the magnetic response for multiple technological purposes.

As a last characterization, we explored the magnetic response of GMO/water/SPIONs assemblies for applicative purposes. As introduced in section 1.2.2, SPIONs relax their magnetization under the exposure to AMFs through the release of heat: this effect has been used in drug delivery to trigger the release of model hydrophilic drugs confined within liposomes [178,179] or magnetocubosomes [174,180].

Here, for the first time, we report the structural effects of the AMF on the structure of the GMO/water/SPIONs cubic phase, monitored “live” through SAXS (see full text and SI of **Paper VII** for details on the experimental set-up and applied AMF).

While the AMF does not induce structural changes in the neat GMO/water cubic phase (Fig. 3.21a), the appearance of an extra peak is observed when SPIONs are present (Fig. 3.21b), whose intensity enhances increasing the AMF application time.

The position of this peak perfectly matches the first reflection of the H_{II} phase (see Fig. 3.19b), highlighting that the heat released by SPIONs effectively promotes a locally confined Pn3m-H_{II} phase transition. Thus, this transition, occurring with expulsion of water and confined hydrophilic molecules, can be remotely triggered by an AMF, enabling a non-invasive approach for spatially and temporarily controlling the release of payloads from cubic hybrid assemblies.

To summarize, here we investigated the thermotropic and magnetotropic behaviour of GMO/water/SPIONs assemblies, both in their bulk and dispersed form. SPIONs deeply affect the lipid phase behaviour, shifting the boundaries between mesophases. This effect can be harnessed to tune the structural response of the lipid scaffold to AMFs and drive the release of host molecules, envisioning the application of GMO/SPIONs mesophases as magnetoresponsive drug-delivery systems. In addition, lipid mesophases steer the organization of single NPs into magnetic supraparticles with preserved colloidal stability. This approach opens the way to control the spontaneous supraorganization of SPIONs in a lipid scaffold, with the possibility to tune and enhance the heating power of SPIONs for magnetic hyperthermia treatments.

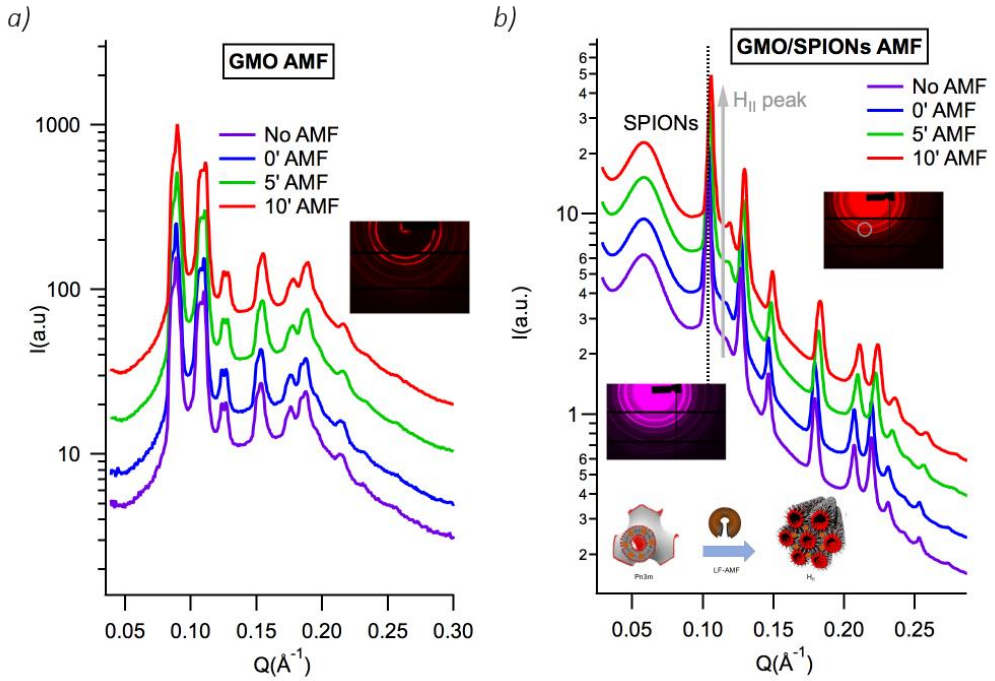

Fig. 3.21 *SAXS curves of (a) GMO bulk cubic phase and (b) GMO bulk cubic phase with 0.47% SPIONs monitored during 10 minutes of AMF application at r.t. (a) A very mild shift of cubic phase Bragg peaks is present upon 10 minutes of AMF application, corresponding to an temperature increase of 0.6 °C; (b) An extra-peak at low-q occurs, attributable to the H_{II} phase, proving the occurrence of a Pn3m/H_{II} phase transition.*

IV Conclusions

The interaction of engineered nanomaterials with bio-inspired soft matter assemblies is gaining prominent relevance for fundamental and applied purposes. Nanoparticles, either intentionally administered or accidentally released into the environment, face biological barriers within living organisms. This interaction ultimately determines their biological fate and cytotoxicity: a physicochemical understanding of the nano-bio interface, essential to fully exploit NPs biomedical potential and limit adverse effects, can be achieved by combining NPs with organized synthetic lipid assemblies, enabling the investigation in highly controlled conditions. Besides, nanosized particles' peculiar features elicit their use as nanoscale probes of biologically relevant properties of synthetic and natural soft matter materials. Finally, the combination of NPs with organized lipid architectures represents a leading strategy towards the development of smart engineered nanomedicines for multiple biomedical purposes.

We combined inorganic NPs of different physicochemical properties with soft matter lipid assemblies, either based on lamellar or non-lamellar bilayers, to achieve these goals.

With phosphocholine liposomes, we explored the aggregation of AuNPs@CT occurring on natural membranes (e.g., the ones of EVs), which might have relevant implications on NPs' internalization and cytotoxicity. Combining an ensemble of optical (UV-Vis Spectroscopy), structural (SAXS, SANS, and AFM), and surface (XRR and QCM-D) techniques, we disentangled kinetic and thermodynamic factors underpinning this interaction, building-up a comprehensive mechanistic model. These results are not only relevant for a fundamental understanding of nano-bio interactions, but they also opened the door to the development of a simple optical assay to determine the mechanical properties of synthetic and natural membrane-enclosed compartments, e.g. biogenic nanovesicles. This "stiffness nanoruler" exploits the plasmonic shift of AuNPs@CT absorbed on the membrane of vesicles, monitored through UV-Vis spectroscopy, to directly probe their rigidity in a fast, low-cost and high-throughput way.

In a second part of the work, we broadened the investigation on nano-bio interfaces by focusing on non-lamellar membranes encountered in cells under pathological conditions, whose biological function is largely unknown.

Here for the first time, we systematically investigated the role of membrane curvature in nano-bio interactions: to this purpose, we directly compared lamellar with cubic membrane mimics in their interaction with a library of model AuNPs, endowed with different physicochemical properties. We combined Confocal Microscopy, allowing for

direct visualization of NP-membrane interactions at the micron scale level, with Neutron Reflectivity, providing information on the restructuring of the lipid membrane at the nanoscale. We highlighted that lamellar and cubic membranes interact with NPs according to well-distinct mechanisms. Importantly, we also pointed out an enhanced structural resilience of cubic phases towards NPs, suggesting a possible protective function of cubic arrangements arising in diseased cells.

Finally, we addressed the structural modifications induced by SPIONs on GMO cubic mesophases as a function of NPs concentration, temperature, and the application of an alternating magnetic field. We then exploited our findings to design smart hybrid platforms, which elicit possible applications in controlled drug delivery.

In conclusion, the investigation presented in this work advances our current understanding of nano-bio interfaces, relevant for the optimization of NPs therapeutic potential and important to limit unwanted side effects. In addition, these results can pave the way for developing new technological devices, arising from the combination of smart NPs with biocompatible lamellar and non-lamellar assemblies.

V Bibliography

1 H. Khandelia and I. Vattulainen, *Lipid Organization, Aggregation, and Self-assembly.*, Roberts G.C.K. (eds) Encyclopedia of Biophysics, Springer, Berlin, Heidelberg, 2013.

2 R. Koynova, B. Tenchov and R. C. Macdonald, *ACS Biomater. Sci. Eng.*, 2015, **1**, 130–138.

3 H. Shrestha, R. Bala and S. Arora, *J. Pharm. 2014*.

4 A. Yaghmur and O. Glatter, *Adv. Colloid Interface Sci.*, 2009, **147**–**148**, 333–342.

5 J. M. Seddon and R. H. Templer, *Chapter 3 - Polymorphism of Lipid-Water Systems.*, Elsevier Science B.V., 1995, vol. 1.

6 G. Tresset, *PMC Biophys.*, 2009, **2**, 1–25.

7 T. G. Meikle, S. Yao, A. Zabara, C. E. Conn, C. J. Drummond and F. Separovic, *Nanoscale*, 2017, **9**, 2471–2478.

8 J. N. Israelachvili, *Intermolecular and Surface Forces*, 2011, vol. 53.

9 A. Attama, M. A. Momoh and P. F. Builders, *Recent Adv. Nov. Drug Carr. Syst.*, 2012, 107–140.

10 J. Gielis, *Natural Curvature Conditions. In: The Geometrical Beauty of Plants.*, Atlantis Press, Paris, 2017.

11 G. C. Shearman, O. Ces, R. H. Templer and J. M. Seddon, *J. Phys. Condens. Matter*, 2006, **18**, S1105–S1124.

12 R. Mezzenga, J. M. Seddon, C. J. Drummond, B. J. Boyd, G. E. Schröder-Turk and L. Sagalowicz, *Adv. Mater.*, 2019, **31**, 1–19.

13 S. Hyde, S. Andersson, K. Z. Larsson, T. Blum, S. L. Landh and B. W. Lidin, *The Language of Shape: The Role of Curvature in Condensed Matter: Physics, Chemistry and Biology*, 1997.

14 C. V. Kulkarni, O. Ces, R. H. Templer and J. M. Seddon, *Soft Matter*, 2013, **9**, 6525–6531.

15 Z. A. Almsherqi, T. Landh and S. D. Kohlwein, *Cubic Membranes : The Missing Dimension of Cell Membrane Organization*, Elsevier Inc., 1st edn., 2009, vol. 274.

16 Q. Xiao and E. Al., *ACS Cent. Sci.*, 2016, **2**, 943–953.

17 Z. A. Almsherqi, S. D. Kohlwein and Y. Deng, 2006, **173**, 839–844.

18 C. J. Drummond and C. Fong, 2000, **4**, 449–456.

19 C. Guo, J. Wang, F. Cao, R. J. Lee and G. Zhai, *Drug Discov. Today*, 2010, **15**, 1032–1040.

20 J. Barauskas, *Lyotropic liquid crystals as delivery vehicles for food ingredients*, Woodhead Publishing Limited, 2006.

21 N. Wang, M. Chen and T. Wang, *J. Control. Release*, 2019, **303**, 130–150.

22 J. Conde, J. T. Dias, V. Grazú, M. Moros, P. V. Baptista and J. M. de la Fuente, *Front. Chem.*, 2014, **2**, 1–27.

23 J. J. Giner-Casares, M. Henriksen-Lacey, M. Coronado-Puchau and L. M. Liz-Marzán, *Mater. Today*, 2016, **19**, 19–28.

24 S. Bayda, M. Hadla, S. Palazzolo, P. Riello, G. Corona, G. Toffoli and F. Rizzolio, *Curr. Med. Chem.*, 2017, **25**, 4269–4303.

25 X. Huang and M. A. El-Sayed, *J. Adv. Res.*, 2010, **1**, 13–28.

26 E. Boisselier and D. Astruc, *Chem. Soc. Rev.*, 2009, **38**, 1759–1782.

27 J. Turkevitch, P. C. Stevenson and J. Hillier, *Discuss. Faraday Soc.*, 1951, **11**, 55–75.

28 J. Kimling, M. Maier, B. Okenve, V. Kotaidis, H. Ballot and A. Plech, *J. Phys. Chem. B*, 2006, **110**, 5700–5707.

29 X. Huang, S. Neretina and M. A. El-Sayed, *Adv. Mater.*, 2009, **21**, 4880–4910.

30 M. R. K. Ali, B. Snyder and M. A. El-Sayed, *Langmuir*, 2012, **28**, 9807–9815.

31 V. Amendola, R. Pilot and M. Frasconi, *J. Phys. Condens. Matter*, 2017, **29**, 203002.

32 S. K. Ghosh and T. Pal, *Chem. Rev.*, 2007, **107**, 4797–4862.

33 R. T. Hill, J. J. Mock, A. Hucknall, S. D. Wolter, N. M. Jokerst, D. R. Smith and H. E. T. Al, *ACS Nano*, 2012, **6**, 9237–9246.

34 P. K. Jain, W. Huang and M. A. El-sayed, *Nano Lett.*, 2007, **7**, 2080–2088.

35 C. Sun, J. S. H. Lee and M. Zhang, *Adv. Drug Deliv. Rev.*, 2008, **60**, 1252–1265.

36 J. P. Fortin, C. Wilhelm, J. Servais, C. Ménager, J. C. Bacri and F. Gazeau, *J. Am. Chem. Soc.*, 2007, **129**, 2628–2635.

37 and G. L. Shouheng Sun, Hao Zeng, David B. Robinson, Simone Raoux, Philip M. Rice, Shan X. Wang, *J.Am.Chem.Soc.*, 2004, **126**, 273–279.

38 R. Michel and M. Gradzielski, *Int. J. Mol. Sci.*, 2012, **13**, 11610–11642.

39 S. Dasgupta, T. Auth and G. Gompper, *J. Phys. Condens. Matter*, 2017, **29**, aa7933.

40 C. Contini, M. Schneemilch, S. Gaisford and N. Quirke, *J. Exp. Nanosci.*, 2018, **13**, 62–81.

41 A. H. Bahrami, *Soft Matter*, 2013, **9**, 8642.

42 C. M. Beddoes, C. P. Case and W. H. Briscoe, *Adv. Colloid Interface Sci.*, 2015, **218**, 48–68.

43 A. M. Farnoud and S. Nazemidashtarjandi, *Environ. Sci. Nano*, 2019, **6**, 13–40.

44 M. Henriksen-Lacey, S. Carregal-Romero and L. M. Liz-Marzán, *Bioconjug. Chem.*, 2017, **28**, 212–221.

45 E. Rascol, J. M. Devoisselle and J. Chopineau, *Nanoscale*, 2016, **8**, 4780–4798.

46 E. Blanco, H. Shen and M. Ferrari, *Nat. Biotechnol.*, 2015, **33**, 941–951.

47 P. Falagan-Lotsch, E. M. Grzincic and C. J. Murphy, *Proc. Natl. Acad. Sci. U. S. A.*, 2016, **113**, 13318–13323.

48 C. J. Murphy, A. M. Vartanian, F. M. Geiger, R. J. Hamers, J. Pedersen, Q. Cui, C. L. Haynes, E. E. Carlson, R. Hernandez, R. D. Klaper, G. Orr and Z. Rosenzweig, *ACS Cent. Sci.*, 2015, **1**, 117–123.

49 L. J. Fox, R. M. Richardson and W. H. Briscoe, *Adv. Colloid Interface Sci.*, 2018, **257**, 1–18.

50 G. Rossi and L. Monticelli, *Biochim. Biophys. Acta - Biomembr.*, 2016, **1858**, 2380–2389.

51 K. L. Chen and G. D. Bothun, *Environ. Sci. Technol.*, 2014, **48**, 873–880.

52 A. E. Nel, L. Mädler, D. Velegol, T. Xia, E. M. V Hoek, P. Somasundaran, F. Klaessig, V. Castranova and M. Thompson, *Nat. Mater.*, 2009, **8**, 543–57.

53 S. Zhang, H. Gao and G. Bao, *ACS Nano*, 2015, **9**, 8655–8671.

54 X. Chen, F. Tian, X. Zhang and W. Wang, *Soft Matter*, 2013, **9**, 7592–7600.

55 Y. Roiter, M. Ornatska, A. R. Rammohan, J. Balakrishnan, D. R. Heine and S. Minko, *Nano Lett.*, 2008, **8**, 941–944.

56 A. H. Bahrami, M. Raatz, J. Agudo-Canalejo, R. Michel, E. M. Curtis, C. K. Hall, M. Gradzielski, R. Lipowsky and T. R. Weikl, *Adv. Colloid Interface Sci.*, 2014, **208**, 214–224.

57 Q. Mu, G. Jiang, L. Chen, H. Zhou, D. Fourches, A. Tropsha and B. Yan, *Chem. Rev.*, 2014, **114**, 7740–7781.

58 S. Dasgupta, T. Auth and G. Gompper, *Nano Lett.*, 2014, **14**, 687–693.

59 T. Pfeiffer, A. De Nicola, C. Montis, F. Carlà, N. F. A. Van Der Vegt, D. Berti and G. Milano, *J. Phys. Chem. Lett.*, 2019, **10**, 129–137.

60 S. Tatur, M. Maccarini, R. Barker, A. Nelson and G. Fragneto, *Langmuir*, 2013, **29**, 6606–6614.

61 C. Montis, V. Generini, G. Boccalini, P. Bergese, D. Bani and D. Berti, *J. Colloid Interface Sci.*, 2018, **516**, 284–294.

62 K. Murugan, Y. E. Choonara, P. Kumar, D. Bijukumar, L. C. du Toit and V. Pillay, *Int. J. Nanomedicine*, 2015, **10**, 2191–2206.

63 I. Canton and G. Battaglia, *Chem. Soc. Rev.*, 2012, **41**, 2718–2739.

64 M. Calero, M. Chiappi, A. Lazaro-Carrillo, M. J. Rodríguez, F. J. Chichón, K. Crosbie-Staunton, A. Prina-Mello, Y. Volkov, A. Villanueva and J. L. Carrascosa, *J. Nanobiotechnology*, 2015, **13**, 1–15.

65 C. F. Su, H. Merlitz, H. Rabbel and J. U. Sommer, *J. Phys. Chem. Lett.*, 2017, **8**, 4069–4076.

66 R. C. Van Lehn and A. Alexander-Katz, *Soft Matter*, 2014, **10**, 648–658.

67 X. Wang, X. Wang, X. Bai, L. Yan, T. Liu, M. Wang, Y. Song, G. Hu, Z. Gu, Q. Miao and C. Chen, *Nano Lett.*, 2019, **19**, 8–18.

68 H. I. Ingolfsson, M. N. Melo, F. J. Van Eerden, C. A. Lopez, T. A. Wassenaar, X. Periole, A. H. De Vries, D. P. Tieleman and S. J. Marrink, *J. Am. Chem. Soc.*, 2014, **136**, 14554−14559.

69 A. M. Farnoud and S. Nazemidashtarjandi, *Environ. Sci. Nano*, 2019, **6**, 13–40.

70 T. Róg, M. Pasenkiewicz-gierula, I. Vattulainen and M. Karttunen, *BBA - Biomembr.*, 2009, **1788**, 97–121.

71 E. S. Melby, A. C. Mensch, S. E. Lohse, D. Hu, G. Orr, C. J. Murphy, R. J. Hamers and J. A. Pedersen, *Environ. Sci. Nano*, 2016, **3**, 45.

72 D. Hartono, K. Yang and L. L. Yung, *Biomaterials*, 2010, **31**, 3008–3015.

73 S. J. M. Shearman G C, Ces O, Templer R H, *J. Phys. Condens. Matter*, 2006, **18**, S1105–S1124.

74 R. Martínez-González, J. Estelrich and M. A. Busquets, *Int. J. Mol. Sci.*, 2016, **17**, 1–14.

75 P. B. Santhosh, B. Drašler, D. Drobne, M. E. Kreft, S. Kralj, D. Makovec and N. P. Ulrih, *Int. J. Nanomedicine*, 2015, **10**, 6089–6104.

76 S. Saesoo, S. Sathornsumetee, P. Anekwiang, C. Treetidnipa, P. Thuwajit, S. Bunthot, W. Maneeprakorn, L. Maurizi, H. Hofmann, R. U. Rungsardthong and N. Saengkrit, *Colloids Surfaces B Biointerfaces*, 2018, **161**, 497–507.

77 A. K. Rengan, A. B. Bukhari, A. Pradhan, R. Malhotra, R. Banerjee, R. Srivastava and A. De, *Nano Lett.*, 2015, **15**, 842–848.

78 A. Tomitaka, H. Arami, Z. Huang, A. Raymond, E. Rodriguez, Y. Cai, M. Febo, Y. Takemura and M. Nair, *Nanoscale*, 2018, **10**, 184–194.

79 M. E. Khosroshahi, *J. Nanomed. Nanotechnol.*, , DOI:10.4172/2157-7439.1000298.

80 A. A. Attama, M. A. Momoh and P. F. Builders, in *Recent advances in novel drug carrier systems*, 2012, vol. 5, pp. 107–140.

81 C. Guo, J. Wang, F. Cao, R. J. Lee and G. Zhai, *Drug Discov. Today*, 2010, **15**, 1032–1040.

82 Y. Chen, P. Ma and S. Gui, *Biomed Res. Int.*, , DOI:10.1155/2014/815981.

83 R. Negrini and R. Mezzenga, *Langmuir*, 2012, **28**, 16455–16462.

84 M. Szlezak, D. Nieciecka, A. Joniec, M. Pękała, E. Gorecka, M. Emo, M. J. Stébé, P. Krysiński and R. Bilewicz, *ACS Appl. Mater. Interfaces*, 2017, **9**, 2796–2805.

85 L. Van'T Hag, L. De Campo, C. J. Garvey, G. C. Feast, A. E. Leung, N. R. Yepuri, R. Knott, T. L. Greaves, N. Tran, S. L. Gras, C. J. Drummond and C. E. Conn, *J. Phys. Chem. Lett.*, 2016, **7**, 2862–2866.

86 C. Montis, B. Castroflorio, M. Mendozza, A. Salvatore, D. Berti and P. Baglioni, *J. Colloid Interface Sci.*, 2015, **449**, 317–326.

87 C. Fong, T. Le and C. J. Drummond, *Chem. Soc. Rev.*, 2012, **41**, 1297–1322.

88 B. P. Dyett, H. Yu, J. Strachan, C. J. Drummond and C. E. Conn, *Nat. Commun.*, , DOI:10.1038/s41467-019-12508-8.

89 H. M. G. Barriga, M. N. Holme and M. M. Stevens, *Angew. Chemie Int. Ed.*, 2019, **58**, 2958–2978.

90 M.-P. Mingeot-Leclercq, M. Deleu, R. Brasseur and Y. F. Dufrêne, *Nat. Protoc.*, 2008, **3**, 1654–1659.

91 S. W. Chen, J. Teulon, C. Godon and J. Pellequer, *Journl Mol. Recognit.*, 2015, **29**, 51–55.

92 G. Binning and C. F. Quate, *Phys. Rev. Lett.*

93 N. Jalili and K. Laxminarayana, *Mechatronics*, 2004, **14**, 907–945.

94 Https://www.bruker.com/., Accessed: 2019-09-01.

95 B. Matsumoto, *Cell Biological Applications of Confocal Microscopy*, 2nd Editio., 2002.

96 Terence Cosgrove, *Colloid Science: Principles, Methods and Applications, 2nd Edition*, 2010.

97 A. Guinier, G. Fournet and C. B. Walker, *Small-Angle Scattering of X-Rays*, 1955.

98 R. Pecora, *J. Nanoparticle Res.*, 2000, **2**, 123–131.

99 P. N. Pusey, *Introduction to Scattering Experiment. In "Neutron,X-rays and Light.Scattering Methods Applied to Soft Condensed Matter"*, Elsevier Science, 2002.

100 G. Fragneto-Cusani, *J. Phys. Condens. Matter*, 2001, **13**, 4973–4989.

101 J. Penfold, *Neutron reflectometry- a probe Mater. Surfaces*, 2004, 45–58.

102 K. Sugikawa, T. Kadota, K. Yasuhara and A. Ikeda, *Angew. Chemie - Int. Ed.*, 2016, **55**, 4059–4063.

103 J. Liu, *Langmuir*, 2016, **32**, 4393–4404.

104 F. Wang and J. Liu, *Nanoscale*, 2015, **7**, 15599–15604.

105 C. Montis, D. Maiolo and I. Alessandri, , DOI:10.1039/c4nr00838c.

106 F. Wang, D. E. Curry and J. Liu, *Langmuir*, 2015, **31**, 13271–13274.

107 F. Wang and J. Liu, *Nanoscale*, 2015, **7**, 15599–15604.

108 C. Montis, D. Maiolo, I. Alessandri, P. Bergese and D. Berti, *Nanoscale*, 2014, **6**, 6452–6457.

109 K. Sugikawa, T. Kadota, K. Matsuo, K. Yasuhara and A. Ikeda, *Materials (Basel).*, 2017, **10**, 1–10.

110 D. Maiolo, L. Paolini, G. Di Noto, A. Zendrini, D. Berti, P. Bergese and D. Ricotta, *Anal. Chem.*, 2015, **87**, 4168–4176.

111 A. Zendrini, L. Paolini, S. Busatto, A. Radeghieri, M. Romano, M. H. M. Wauben, M. J. C. van Herwijnen, P. Nejsum, A. Borup, A. Ridolfi, C. Montis and P. Bergese, *Front. Bioeng. Biotechnol.*, 2020, **7**, 1–10.

112 K. Rana, J. R. Bhamore, J. V. Rohit, T. J. Park and S. K. Kailasa, *New J. Chem.*, 2018, **42**, 9080–9090.

113 S. Lazzari, L. Nicoud, B. Jaquet, M. Lattuada and M. Morbidelli, *Adv. Colloid Interface Sci.*, 2016, **235**, 1–13.

114 J. Sui, P. Zhao, B. Bin-Mohsin, L. Zheng, X. Zhang, Z. Cheng, Y. Chen and G. Chen, *Sci. Rep.*, 2016, **6**, 1–11.

115 R. Thouy and R. Jullien, *J. Phys. I*, 1996, **6**, 1365–1376.

116 L. Guo, J. Y. Har, J. Sankaran, Y. Hong, B. Kannan and T. Wohland, *ChemPhysChem*, 2008, **9**, 721–728.

117 A. Nelson, *J. Appl. Crystallogr.*, 2006, **39**, 273–276.

118 P. K. K. Nagayama, *Particles at Fluid Interfaces and Membranes: Attachment of Colloid Particles*, Elsevier Science, 1st Editio., 2001.

119 P. Guo, D. Liu, K. Subramanyam, B. Wang, D. T. Auguste and M. A. Moses, *Nat. Commun.*, , DOI:10.1038/s41467-017-02588-9.

120 M. Simunovic, C. Prévost, P. Bassereau and P. Bassereau, *Phil. Trans. R. Soc. A*, 2016,

374, 20160034.

121 P. B. Canham, *J. Theor. Biol.*, 1970, **26**, 61–81.

122 E. A. Evans, *Biophys. J.*, 1974, **14**, 923–931.

123 D. Vorselen, S. M. van Dommelen, R. Sorkin, M. C. Piontek, J. Schiller, S. T. Döpp, S. A. A. Kooijmans, B. A. van Oirschot, B. A. Versluijs, M. B. Bierings, R. van Wijk, R. M. Schiffelers, G. J. L. Wuite and W. H. Roos, *Nat. Commun.*, 2018, **9**, 1–9.

124 A. C. Dumitru, M. Poncin, L. Conrard, Y. F. Dufrêne, D. Tyteca and D. Alsteens, *Nanoscale Horizons*, 2018, **3**, 293–304.

125 I. Safeukui, P. A. Buffet, G. Deplaine, S. Perrot, V. Brousse, A. Sauvanet, B. Aussilhou, P. H. David, S. Dokmak, A. Couvelard, D. Cazals-hatem, O. Mercereau-puijalon and N. Mohandas, *Blood Adv.*, 2018, **2**, 1–4.

126 C. Alibert, B. Goud and J. Manneville, *Biol. Cell*, 2017, **109**, 167–189.

127 D. Bochicchio and L. Monticelli, *The Membrane Bending Modulus in Experiments and Simulations : A Puzzling Picture*, Elsevier Inc., 1st edn., 2016, vol. 23.

128 N. Bezlyepkina, R. L. Knorr, R. Lipowsky and R. Dimova, *Soft Matter*, 2010, **6**, 1472–1482.

129 J. R. Henriksen and J. H. Ipsen, *Eur. Phys. J. E*, 2004, **167**, 149–167.

130 C. Length, G. Fragneto, T. Charitat, E. Bellet-amalric and R. Cubitt, *Langmuir*, 2003, **19**, 7695–7702.

131 J. Pan, S. Tristram-nagle and J. F. Nagle, *Phys. Rev. E*, 2009, **80**, 021931.

132 M. Mell, L. H. Moleiro, Y. Hertle, P. Fouquet, R. Schweins, T. Hellweg and F. Monroy, *Eur. Phys. J. E*, 2013, **36**, 75.

133 J. F. Nagle, M. S. Jablin, S. Tristram-nagle and K. Akabori, *Chem. Phys. Lipids*, 2015, **185**, 3–10.

134 D. Marsh, *Chem. Phys. Lipids*, 2006, **144**, 146–159.

135 J. F. Nagle, *Faraday Discuss.*, 2013, **161**, 11–29.

136 R. Dimova, *Adv. Colloid Interface Sci.*, 2014, 208, 225–234.

137 M. C. Piontek, R. B. Lira and W. H. Roos, *Biochim. Biophys. Acta - Gen. Subj.*, 2019, 129486.

138 R. L. Biltonen and D. Lichtenberg, *Chem. Phys. Lipids*, 1993, **64**, 129–142.

139 S. Mabrey and J. M. Sturtevant, *Proc. Natl. Acad. Sci. USA*, 1976, **73**, 3862–3866.

140 J. F. Nagle, J. Pan, S. Tristram-nagle and N. Kuc, *Biophys J.*, 2008, **94**, 117–124.

141 R. Dimova, B. Pouligny and C. Dietrich, *Biophys. J.*, 2000, **79**, 340–356.

142 C. Lee, W. Lin and J. Wang, *Phys. Rev. E*, 2001, **64**, 020901.

143 K. R. Mecke and T. Charitat, *Langmuir*, 2003, **19**, 2080–2087.

144 G. Niggemann, M. Kummrow, W. Helfrich, G. Niggemann, M. Kummrow, W. H. The and B. Rigidity, *J. Phys. II Fr.*, 1995, **5**, 413–425.

145 J. F. Nagle, *Chem. Phys. Lipids*, 2017, **205**, 18–24.

146 A. Ridolfi, M. Brucale, C. Montis, L. Caselli, L. Paolini, A. Borup, A. T. Boysen, F. Loria, M. J. C. Van Herwijnen, M. Kleinjan, P. Nejsum, N. Zarovni, M. H. M. Wauben, D. Berti, P. Bergese and F. Valle, *Anal. Chem.*, 2020, **92**, 10274–10282.

147 G. Raposo and P. D. Stahl, *Nat. Rev. Mol. Cell Biol.*, 2019, **20**, 509–510.

148 G. Van Niel, G. D. Angelo and G. Raposo, *Nat Rev Mol Cell Biol.*, 2018, **19**, 213–228.

149 M. Yáñez-mó and E. Al., *J Extracell Vesicles*, 2015, **14**, 27066.

150 R. Koynova and B. Tenchov, *OA Biochem.*, 2013, **1**, 1–9.

151 C. E. Erdinc Sezgin, Ilya Levental, Satyajit Mayor, *Nat Rev Mol Cell Biol*, 2017, **18**, 361–374.

152 S. Busatto, A. Zendrini, A. Radeghieri, L. Paolini, M. Romano, M. Presta and P. Bergese, *Biomater. Sci.*, 2020, **8**, 39–63.

153 S. K and I. E., *Nature*, 1997, **387**, 569–572.

154 D. Lingwood and K. Simons, *Science (80-.).*, 2010, **327**, 46–50.

155 J. K. Sheavly, J. A. Pedersen and R. C. Van Lehn, *Nanoscale*, 2019, **11**, 2767–2778.

156 F. A. Heberle, R. S. Petruzielo, J. Pan, P. Drazba, N. Kučerka, R. F. Standaert, G. W. Feigenson and J. Katsaras, *J. Am. Chem. Soc.*, 2013, **135**, 6853–6859.

157 E. Gonzalez Solveyra and I. Szleifer, *Wiley Interdiscip Rev Nanomed Nanobiotechnol.*, 2016, **8**, 334–354.

158 S. Dasgupta, T. Auth and G. Gompper, *Soft Matter*, 2013, **9**, 5473–5482.

159 R. Vácha, F. J. Martinez-Veracoechea and D. Frenkel, *Nano Lett.*, 2011, **11**, 5391–5395.

160 K. Larsson, *J. Phys. Chem.*, 1989, **93**, 7304–7314.

161 H. H. Shen, J. G. Crowston, F. Huber, S. Saubern, K. M. McLean and P. G. Hartley, *Biomaterials*, 2010, **31**, 9473–9481.

162 J. M. Seddon, *Acta Pharm*, 1992, **42**, 255–62.

163 R. M. Dalgliesh, S. Langridge, J. Plomp, V. O. De Haan and A. A. Van Well, *Phys. B Condens. Matter*, 2011, **406**, 2346–2349.

164 R. Kampmann, M. Haese-Seiller, V. Kudryashov, B. Nickel, C. Daniel, W. Fenzl, A. Schreyer, E. Sackmann and J. Rädler, *Phys. B Condens. Matter*, 2006, **385**–**386**, 1161–1163.

165 F. Ott and S. Kozhevnikov, *J. Appl. Crystallogr.*, 2011, **44**, 359–369.

166 P. Vandoolaeghe, A. R. Rennie, R. A. Campbell, R. K. Thomas, F. Höök, G. Fragneto, F. Tiberg and T. Nylander, *Soft Matter*, 2008, **4**, 2267–2277.

167 E. Venugopal, S. K. Bhat, J. J. Vallooran and R. Mezzenga, *Langmuir*, 2011, **27**, 9792–9800.

168 C. V. Kulkarni, W. Wachter, G. Iglesias-Salto, S. Engelskirchen and S. Ahualli, *Phys. Chem. Chem. Phys.*, 2011, **13**, 3004–3021.

169 H. S. Wi, K. Lee and H. K. Pak, *J. Phys. Condens. Matter*, , DOI:10.1088/0953-8984/20/49/494211.

170 J. Barauskas and T. Landh, *Langmuir*, 2003, **19**, 9562–9565.

171 J. M. Bulpett, T. Snow, B. Quignon, C. M. Beddoes, T. Y. D. Tang, S. Mann, O. Shebanova, C. L. Pizzey, N. J. Terrill, S. A. Davis and W. H. Briscoe, *Soft Matter*, 2015, **11**, 8789–8800.

172 R. H. Templer, J. M. Seddon, P. M. Duesing, R. Winter and J. Erbes, *J. Phys. Chem. B*, 1998, **102**, 7262–7271.

173 P. Wadsten-Hindrichsen, J. Bender, J. Unga and S. Engström, *J. Colloid Interface Sci.*, 2007, **315**, 701–713.

174 C. Montis, B. Castroflorio, M. Mendozza, A. Salvatore, D. Berti and P. Baglioni, *J. Colloid Interface Sci.*, , DOI:10.1016/j.jcis.2014.11.056.

175 B. Angelov, A. Angelova, V. M. Garamus, S. Lesieur, M. Ollivon, S. Funari, R. Willumeit, P. Couvreur, F.- France, V. Uni and P. Sud, *J. AM. CHEM. SOC.*, 2007, **129**, 13474–13479.

176 J. Y. T. Chong, X. Mulet and B. J. Boyd, *Steric Stabilizers for Cubic Phase Lyotropic Liquid Crystal Nanodispersions (Cubosomes)*, Elsevier Inc., 1st edn., 2015.

177 P. Guardia, R. Di Corato, L. Lartigue, C. Wilhelm, A. Espinosa, M. Garcia-Hernandez, F. Gazeau, L. Manna and T. Pellegrino, *ACS Nano*, 2012, **6**, 3080–3091.

178 Y. Chen, A. Bose and G. D. Bothun, *ACS Nano*, 2010, **4**, 3215–3221.

179 M. S. Martina, J. P. Fortin, C. Ménager, O. Clément, G. Barratt, C. Grabielle-Madelmont, F. Gazeau, V. Cabuil and S. Lesieur, *J. Am. Chem. Soc.*, 2005, **127**, 10676–10685.

180 M. Szlezak, D. Nieciecka, A. Joniec, M. Pękała, E. Gorecka, M. Emo, M. J. Stébé, P. Krysiński and R. Bilewicz, *ACS Appl. Mater. Interfaces*, 2017, **9**, 2796–2805.

VI List of Papers

Paper I

Nanoparticles and organized lipid assemblies: from interaction to design of hybrid soft devices

M. Mendozza, L. Caselli, A. Salvatore, C. Montis and D. Berti, *Soft Matter*, 2019, 15 (44), 8951-8970

Soft Matter

PERSPECTIVE

View Article Online
View Journal | View Issue

Cite this: *Soft Matter*, 2019, **15**, 8951

Nanoparticles and organized lipid assemblies: from interaction to design of hybrid soft devices

Marco Mendozza, Lucrezia Caselli, Annalisa Salvatore, Costanza Montis * and Debora Berti *

Received 8th August 2019,
Accepted 25th October 2019

DOI: 10.1039/c9sm01601e

rsc.li/soft-matter-journal

This contribution reviews the state of art on hybrid soft matter assemblies composed of inorganic nanoparticles (NP) and lamellar or non-lamellar lipid bilayers. After a short outline of the relevant energetic contributions, we address the interaction of NPs with synthetic lamellar bilayers, meant as cell membrane mimics. We then review the design of hybrid nanostructured materials composed of lipid bilayers and some classes of inorganic NPs, with particular emphasis on the effects on the amphiphilic phase diagram and on the additional properties contributed by the NPs. Then, we present the latest developments on the use of lipid bilayers as coating agents for inorganic NPs. Finally, we remark on the main achievements of the last years and our vision for the development of the field.

1. Introduction

Lipid bilayers are ubiquitous structural motifs in natural and synthetic soft matter assemblies. Their interaction with nanostructured matter, and in particular with nanoparticles (NPs), is therefore of interest both for natural and engineered systems. In addition, the shared length and energy scales, combined with the peculiar properties of inorganic matter at the nanoscale, can be harnessed to use NPs to probe selected physical properties of membranes or to modify the amphiphilic phase diagram under external stimuli.

In this contribution we will review the state of the art concerning research on hybrid soft matter assemblies composed of inorganic NPs and synthetic lipid bilayers, either in lamellar or non-lamellar arrangement.

This topic is currently a very active area of research, with implications ranging from the design of smart nanostructured hybrid devices, where nanoparticles are included or functionalized with lipid bilayers, to the quest for mechanistic understanding of events taking place at the nano–bio-interface, relevant for nanomedicine and toxicity of nanomaterials.

Department of Chemistry "Ugo Schiff", University of Florence, and CSGI (Italian Center for Colloid and Surface Science, Via della Lastruccia 3, Sesto Fiorentino, 50019 Firenze, Italy. E-mail: montis@csgi.unifi.it, debora.berti@unifi.it

Marco Mendozza

Marco Mendozza received his MSc in Chemical Sciences-Physical Chemistry from University of Florence in 2016. Currently he is pursuing his PhD in Physical Chemistry under the supervision of Prof. Debora Berti at the University of Florence. His research focuses on the investigation of the phase behavior and viscoelastic properties of non-lamellar lipid membranes assembled with hydrophobic inorganic stimuli responsive nanoparticles (iron oxide and gold nanoparticles) in order to design new functional materials, with envisaged applications the biomedical field.

Lucrezia Caselli

Lucrezia Caselli obtained her MSc degree in Chemical Sciences from the University of Florence in Italy in 2017. She is now a PhD student in Chemical Sciences at the University of Florence. Her main research interest concerns Physical Chemistry of Soft Matter, with particular focus on self-assemblies with biological relevance. Her research topics include the interaction of inorganic nanomaterials with synthetic model cellular membranes, engineering of hybrid nanoparticle/lipid assemblies for responsive drug delivery, microfluidic design and application of innovative model systems for the study of the nano-bio interfaces.

This review will focus on some selected classes of inorganic nanomaterials, namely metals (Au and Ag), metal oxides (like iron and zinc oxide) and silica NPs. The interaction of several other kinds of nanomaterials with lipid bilayers has been described in the literature and we refer the readers to some excellent recent reports on these topics.[1–8]

In this contribution, particular attention will be devoted to non-covalent interactions that take place when NPs and lipid bilayers are put into contact. Understanding the nature and the key determinants of these interactions is instrumental both for fundamental and applied soft matter research.

This review is organized as follows: a short theoretical section will introduce the main energetic contributions at stake when NPs interact with lipid bilayers (Section 2). Then, we will provide an overview of the most relevant studies which have recently addressed the interaction of NPs with synthetic phospholipid bilayers, meant as simplified and highly controllable mimics of cell membranes (Section 3). In this section, we will emphasize some examples where the investigation on model systems contributed disclosing non-covalent interactions at play in living systems. Then, we will review (Section 4) the design of hybrid nanostructured materials composed of lipid bilayers and inorganic nanoparticles, with particular emphasis on the effects on the amphiphilic phase diagram and on the additional properties contributed by the NPs. Then, we will present the latest developments on the use of lipid bilayers as coating agents for inorganic NPs (Section 5), whose aim is the improvement of dispersibility, biocompatibility and pharmacokinetic properties. Finally, a conclusive Section will remark the main achievements of the last years and our vision for the development of the field.

2. Interaction of nanoparticles with lipid membranes: the role of non-covalent forces

In this section we will consider the events following the exposure of a free-standing synthetic lipid bilayer to NPs, by outlining the different contributions to the total interaction energy.

2.1 Theoretical description of NPs–lipid membrane interaction

The interaction between a NP and a lipid bilayer might lead to NP's adhesion on the bilayer, which can be followed by partial or total engulfment by the membrane. In a well-defined medium and at a given temperature, the NP docking to lipid membranes is thermodynamically favoured if the adhesion energy $E_{adh} < 0$, *i.e.*, if the attractive terms overcome the repulsive ones. Considering a prototypical model of a bioinorganic interface, with a spherical NP of radius R_1 interacting with a liposomal membrane with curvature $1/R_2$, the energetic balance between repulsive and attractive forces can be approximately described

Annalisa Salvatore

Annalisa Salvatore obtained her MSc degree in Chemical Sciences-Physical Chemistry at University of Florence in 2013 and started her PhD research under the supervision of Prof. Debora Berti, in the same year. Her doctoral research focused on the interaction of natural and synthetic lipid assemblies with inorganic nanoparticles. During her postdoctoral fellowship, she extended her interests to the synthesis of inorganic nanoparticles as consolidants for bone remains of archeological interest, as well as in the preparation and stabilization of graphene derivatives.

Costanza Montis

Costanza Montis obtained her PhD in Chemical Sciences from the University of Florence (Italy) in 2013. She is now a researcher in the Department of Chemistry of the University of Florence and member of the Italian Consortium for Colloid and Surface Science (CSGI). Her scientific background is Physical Chemistry of Soft Matter. Her main research topics include the biophysical understanding of nano–bio interfaces; the design of lipid–nanoparticles hybrid materials for biomedical applications; the study of nanostructured materials for applications in restoration of works of art.

Debora Berti

Debora is Full Professor of Physical Chemistry at the Department of Chemistry of the University of Florence and member of the Italian Consortium for Colloid and Surface Science (CSGI). Debora's scientific background is Physical Chemistry of Soft Matter. Her research topics include hybrid nano and micro particle/lipid assemblies for responsive drug delivery, interaction of nanostructured assemblies with model membranes, design and application of nanostructured fluids for the conservation of cultural heritage. Debora has a well-established track record of her work, with more than 130 authored or co-authored research papers and several chapters contributed in specialized books.

by a classical DLVO (Derjaguin–Landau–Verwey–Overbeek) formalism, as in eqn (1), including only the electrical double layer (E^{EL}) and the London–van der Waals (E^{LW}) contributions to the total energy of adhesion:

$$E_{adh} = E^{EL} + E^{LW} \quad (1)$$

where the terms E^{EL}, derived as a combination between the linear Debye–Huckel and the Derjaguin approximations and valid for surface potentials <25 mV, and E^{LW} are described in eqn (2) and (3), respectively:[9]

$$E^{EL} = \frac{\varepsilon R_1 R_2(\psi_1^2+\psi_2^2)}{4(R_1+R_2)}\left[\frac{2\psi_1\psi_2}{(\psi_1^2+\psi_2^2)}\ln\left(\frac{1+e^{-kd}}{1-e^{-kd}}\right) + \ln\left(1-e^{-2kd}\right)\right] \quad (2)$$

$$E^{LW} = -A\frac{R_1R_2}{6(R_1+R_2)}\left(\frac{1}{d}-\frac{1}{(d+h)}\right)-\frac{A}{6}\ln\left(\frac{d}{d+h}\right) \quad (3)$$

where ψ_1^2 and ψ_2^2 are the surface potentials of the NP and the membrane, d the NP–membrane distance, k the Debye length, h the membrane's thickness, and A is the Hamaker constant. Although the DLVO theory generally succeeds in predicting the colloidal stability of hard colloids (*e.g.*, inorganic NPs) suspended in a liquid medium, it often fails in describing the interaction of NPs with free-standing bilayers; a more comprehensive description for E_{adh} includes additional repulsive hydration forces establishing at short NPs–membrane distances, as well as hydrophobic NP–lipid chain attraction (the interested reader is referred to a recent report for the analytical expression of the these two supplementary energetic contributions[9]).

Once the NP is adsorbed onto the lipid surface (*i.e.*, $E_{adh}<0$), the elastic properties of the membrane comes into play, and their balance with the adhesion forces determines the degree of membrane deformation and NP's wrapping. Specifically, the energetic gain due to the adhesion forces is maximized by increasing the contact area between the NP and the lipid membrane, according to eqn (4):[10]

$$E_{adh} = -w\int_0^{S_{ad}} dS \quad (4)$$

with w adhesion energy per unit area and S_{ad} the contact area between the membrane and the NP. On the other side, the NP's wrapping is associated with a free energy cost of imposing membrane deformation (E_{el}), which is expressed through the Cahnam–Helfrich–Evans formalism:[10]

$$E_{el} = \int_0^S dS\left[\gamma + 2k_B(H-c_0)^2+\bar{k}K\right] \quad (5)$$

with S the entire interfacial area.

As we can see from eqn (5), the deformation penalty depends both on the membrane's topology, through the mean H and Gaussian K curvatures, and on the interface's mechanical and elastic properties, expressed by the surface tension γ, bending rigidity k_B, spontaneous curvature c_0 and Gaussian saddle splay modulus $\bar{k}$. It is the fine interplay between E_{adh} and E_{el} that ultimately defines the NP–membrane arrangement which minimizes the system's energy, ranging from completely unwrapped NPs (*e.g.*, for small nanoparticles and/or weakly interacting with the lipid phase), to larger and/or strongly adhered nano-objects, eventually fully engulfed by the lipid membrane (see Fig. 1A).

Based on the above treatment, we will now discuss the several NPs- and membrane-related factors implicated in this interaction, with particular attention on size, shape, surface coating of NPs and NP–NP correlations; on the "membrane" side, we will take into account some selected physicochemical properties and the zero or non-zero curvature.

Depending on their size, the adhesion of NPs on a target planar membrane can result in different effects: small NPs can either remain embedded in the lipid membrane or directly diffuse through it; relatively larger particles (>10 nm) can be wrapped by the membrane.[11] This process is finely controlled by the energetic balance between the adhesion forces (eqn (4)) and the membrane's elastic deformation penalty (eqn (5)), leading to an optimal size for wrapping, as first observed by Roiter *et al.*[12] In particular, two characteristic NPs' limiting radii for a successful engulfment by lipid membranes can be theoretically predicted:[10]

$$R_{kw} = \sqrt{\frac{2k_b}{E_{adh}}} \quad (6)$$

$$R_{k\gamma} = \sqrt{\frac{2k_b}{E_{adh}-\gamma}} \quad (7)$$

within the bending-dominated regime (*i.e.*, for relatively small membrane's deformation), the membrane tension can be neglected, and the wrapping process is mainly controlled by the competition between membrane's bending and NP's adhesion strength, defining a critical radius R_{kw}. NPs with $R<R_{kw}$ remain unwrapped, while larger NPs ($R>R_{kw}$) are fully engulfed inside the lipid scaffold. For larger membrane's deformation (*e.g.*, induced by micron-sized particles), a characteristic length scale $\lambda = (2k_b/\gamma)^{1/2}$, which depends solely on membrane's properties, marks the crossover from the bending-dominated to the stretching-dominated regime[9,13] (Fig. 1B), where the γ-dependent wrapping extent gradually increases with NP's size. The full engulfment is reached for a second crossover NP's radius $R_{k\gamma}$ (eqn (7)), representing a larger NP's limiting size, which is required for the internalization in the case of finite tension-membranes.

2.2 Key NPs features in the interaction with lipid membranes

Concerning NPs shape, the increase of the surface area/volume ratio from spherical to asymmetrical NPs (*e.g.*, nanorods, nanoprisms and nanocubes), maximizes the surface available for absorption onto lipid membranes (eqn (4)), enhancing their reactivity;[14] on the other side, the local particle's surface curvature is predicted to increase the energy barrier associated to membrane's deformation, stabilizing partial-wrapping states also for tensionless membranes.[9,10] Moreover, the interaction of asymmetric NPs with target lipid membranes can lead to

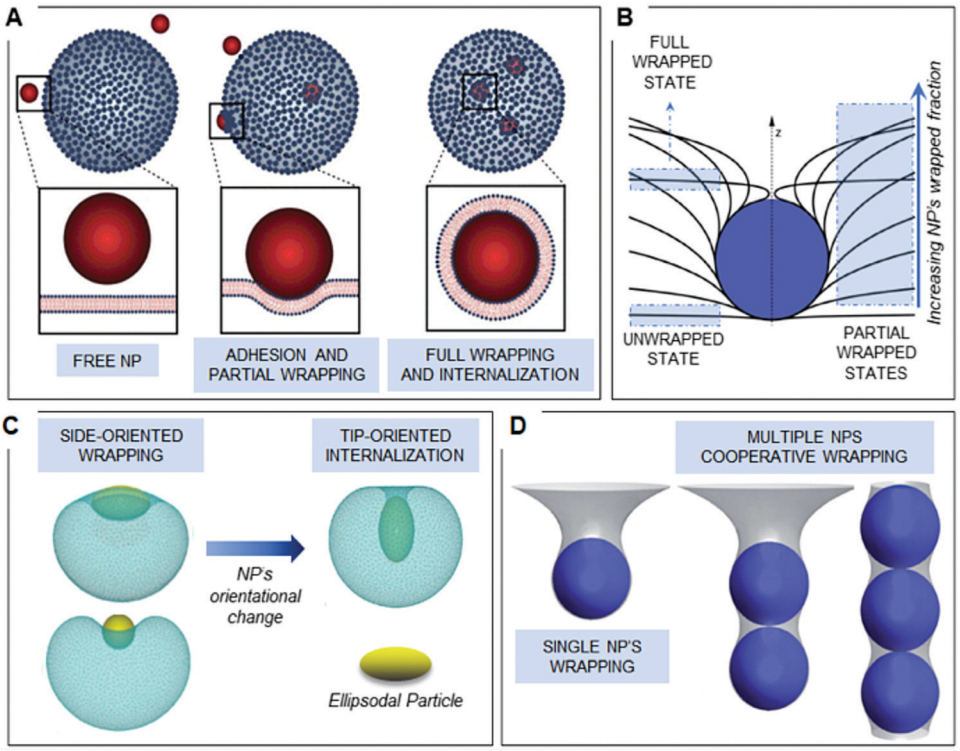

Fig. 1 Theory of NPs–lipid membranes interactions. Panel A: illustration of the three possible configurations for a NP interacting with a lipid membrane: from left to right, (i) NP free in the environment (repulsive contribution to the NP–bilayer total interaction overcoming the attractive one), (ii) NP's adhesion to the membrane, causing NP's partial wrapping and (iii) NP's full engulfment (strong attractive NP–bilayer forces). Readapted from open access ref. 13. Panel B: illustrative picture representing unwrapped, fully wrapped and different wrapping degree-intermediate configurations for a NP interacting with a fluid interface. Reproduced from ref. 101 with permission from The Royal Society of Chemistry. Panel C: ellipsoidal NP's reorganization from a side-oriented configuration, adopted during the wrapping process, to a tip-oriented configuration, minimizing the energy required for full NP's engulfment and internalization. Reproduced from ref. 16 with permission from The Royal Society of Chemistry. Panel D: illustrative picture of (from left to right) a single NP wrapped by a fluid interface, two and three NPs wrapped in a membrane tube. Reproduced from ref. 101 with permission from The Royal Society of Chemistry.

preferential wrapping orientations, to minimize the energy cost for wrapping[15,16] (see Fig. 1C). Eventually, the asymmetric shape of NPs can drive peculiar self-assembly phenomena at the nano–bio interface, some examples of which are given in Section 3.

The NPs surface functionalization represents another important factor affecting the interaction with membranes; in particular, NPs surface charge has a major impact on adhesion both onto charged and zwitterionic interfaces, setting the sign and magnitude of the electrostatic long-range contribution of (eqn (1)).[3,17–21] Furthermore, the adhesion of charged NPs to a target membrane is also associated to an entropic gain, deriving from the release of small counterions from the NP surface[22] (see Fig. 1D). On the other side, the presence of polymeric steric stabilizers on the NPs surface, like for PEGylated particles, often decreases the adhesion energy; this effect can be understood considering the mobility loss experienced by the polymer chains approaching the lipid surface, which entails a considerable entropic penalty for membrane adhesion. Moreover, NPs' surface functionalization determines their polarity, which is key in controlling their spontaneous localization when challenging a free-standing lipid membrane: generally, hydrophilic nanomaterials with size larger than 10 nm reside at the membrane surface, with the possibility to be partially or fully wrapped by the membrane. Conversely, depending on their hydrophobicity,[23] small particles can either spontaneously cross[24,25] or be entrapped[24] within the lipid membrane, provoking an alteration of the bilayer's frustration packing energy.[26–31]

Eventually, interparticle forces between different membrane-bound NPs may originate cooperative phenomena, ultimately leading to the simultaneous wrapping and engulfment of multiple NPs (see Fig. 1D), which will be discussed in detail in Section 3.

2.3 Key membrane features in the interaction with NPs

Membrane-related characteristics have a crucial role in the interaction with NPs. In particular, the composition of lipid bilayers determines specific physico-chemical, viscoelastic and thermodynamic properties of relevance in the interaction with NPs. Membrane's surface potential, determined by the percentage of non-ionic, anionic and cationic lipids, strongly affects the electrostatic contribution to NPs adhesion (eqn (1)), while the presence of specific components (*e.g.*, cholesterol) and their relative abundance, give rise to characteristic behaviours, which will be extensively discussed in Section 3.

Equally important, the molecular geometry of the membrane's components determines the equilibrium arrangement of lipids within the bilayer. The molecular packing represents the main

factor affecting both the physical state and the overall topological curvature of membranes, which are two prominent determinants in the interactions with nanomaterials.

In particular, the interactions at the nano-lipid interface is extremely affected by the gel–liquid crystalline phase behaviour of lipid membranes: by increasing temperature, lipid bilayers undergo a main phase transition from the so-called "gel state" (L_β), where hydrocarbon chains are tightly packed and almost locked in place, to a "fluid state" (L_α), where lipids freely diffuse within the 2D membrane's plane. The "melting transition temperature" (T_m) is specific for a given lipid composition and determines the elastic response of membranes at a given temperature. In particular, gel phase bilayers show a reduced reactivity with nanomaterials, mostly due to the high value of their bending rigidity (k_B) with respect to the fluid phase,[9] which strongly hampers the membrane's bending and wrapping around NPs (see eqn (5)–(7)). On the other side, the interaction with NPs, which can proceed through polar headgroups (hydrophilic NPs) or hydrophobic chains (hydrophobic NPs), might affect the lipid molecular packing, leading to micro and macroscopic modifications in the membrane structure and thermotropic behaviour (specific examples will be provided in the following Section).

As predicted from eqn (5), the membrane's topology plays a crucial role in its elastic response to NP's induced deformations. Although lipid membranes are generally visualized as flat bilayers (H and G in eqn (5) equal to zero), both biomembranes and synthetic lipid assemblies may fold into more organized non-lamellar bilayered structures.[32] The interaction of nanomaterials with such non-lamellar structures may have a noteworthy relevance both for biomimetic and technological applications,[33,34] (as discussed in details in the following Section) while it remains, to date, a highly unexplored research area.

Differently from planar membranes, curved membranes are defined by positive (direct phases) or negative (inverse phases) mean curvature (H) and non-zero Gaussian curvature (K)[35] in each point of their surface, with H and G described by eqn (8) and (9), respectively:

$$H = \frac{1}{2}(c_1 + c_2) \quad (8)$$

$$K = c_1 c_2 \quad (9)$$

with c_1 and c_2 minimum and maximum values of curvature at a specific point of membrane surface.

The non-zero values of H and K lead, as predicted from eqn (5), to a modification of their Helfrich energy and elastic response towards externally induced deformations (*e.g.*, NPs' wrapping) with respect to the case of lamellar membranes. Moreover, different topologies are associated with a frustration packing free energy (E_P), which varies according to eqn (10):[36]

$$E_P = k(l - l_r)^2 \quad (10)$$

with k stretching rigidity of lipid chains, l and l_r hydrophobic chain extension in the stretched and relaxed state, respectively. Phase transitions between different geometries, including changes in both elastic and frustration packing energies, have high biological relevance, sharing similar energy barriers and molecular re-arrangements with membrane fusion processes.[37] Several recent studies, which will be addressed in Section 4, demonstrated that both hydrophilic and hydrophobic NPs can promote phase transitions between model mesophases with different geometry,[26,27,34,37–41] lowering the energy barrier required to switch from low to high curvature phases. One of the first attempts to elucidate this effect is represented by recent works,[26,42] where the transition temperature from cubic to hexagonal phases in monoolein liquid crystals is demonstrated to be finely controlled by inclusion of hydrophobic iron oxide NPs (see Section 4). This behaviour was explained by combining the Helfrich theory in eqn (5) with geometrical considerations: NPs increase the frustration packing energy of the cubic phase (eqn (10)), while they have a milder effect on the hexagonal arrangement, by inserting into its hydrophobic voids (see Fig. 2).

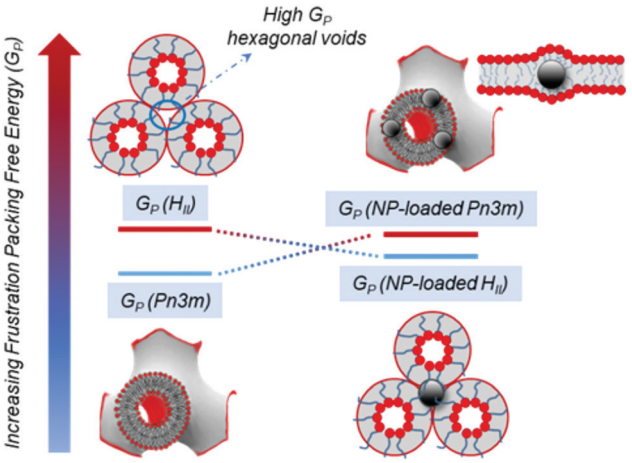

Fig. 2 Effects of NPs on lipid mesophases architectures. Illustrative scheme of the NP-induced modification of the Frustration Packing Energy of both cubic and hexagonal mesophases.

In the framework of this theoretical description, in recent years the interaction of NPs with lipid membranes has been explored with different approaches and for different purposes: from fundamental studies employing lipid bilayers as biomimetic platforms of tuneable physicochemical feature for investigating the interaction with prototypical nanoparticles, aimed at a better understanding of the efficiency and possible adverse effects of nanomaterials designed for biomedical applications, to applicative studies, where the interaction of NPs and lipid membranes is exploited for analytical purposes; from the engineering of lipid assemblies with NPs inclusion, in order to form smart hybrid materials for applications in materials science, to the functionalization of NPs with a lipid coating, to improve their biocompatibility and pharmacokinetic properties.

In Section 3 we will review the interaction of NPs with synthetic lipid bilayers, taken as simplified models of real plasma membranes: in line with Section 2, we will consider the main physicochemical factors, either related to NPs or to the lipid membrane, affecting the interaction under simplified conditions. We will provide relevant examples from the recent

literature, highlighting the connections, whenever they are relevant, between the findings on cell models and the *in vitro*/*in vivo* observations.

3. NPs/biomembrane interactions: from biophysical studies of nano–bio interfaces to applications

One of the main issues limiting the development of nanomedicine and the translation of engineered nanomaterials into medical practice, is the poor understanding of their fate in biological fluids, and their short-term and long-term possible adverse cytotoxic effects.[37,43–49] Recent reports have also highlighted how nanodevices designed for nanomedicine applications, whose functionality/efficiency has been proved at the lab-scale, completely fail reaching their biological targets once in a living organism.[50] As a matter of fact, to date, nano-therapeutics available on the market are mainly limited to polymeric- and liposomal-based formulations,[51,52] while, apart from some iron oxide NPs-based formulations, inorganic and metallic particles are at research stage or in clinical trials.[53] With the ultimate aim to fill the gap between the design/synthesis/development of nanomaterials for nanomedicine and their end use application, it is necessary to improve our fundamental knowledge on the interaction of nanomaterials with biologically relevant interfaces, particularly, cell membranes.

Plasma membrane, primarily composed by a mixed phospholipid bilayer with embedded proteins, protects the cell interior and ensures its communication with the external environment. The mechanisms of cell signalling processes are extremely complex and length scale-dependent, with smaller molecules spontaneously crossing the lipid barrier and larger and/or polar molecules harnessing protein-mediated transportations across the membrane.[13] The nanoscale, shared by engineered particles and biologically relevant macromolecules (*i.e.*, DNA, viruses, surface proteins), is mostly associated with endocytic pathways, where the internalisation of nano-objects is generally controlled by the membrane through specific receptor–protein binding for the case of biological species.[54,55] However, it has been demonstrated that synthetic NPs can be wrapped and internalized by both model and real cell membranes in the absence of any receptor-mediated interaction,[43,55,56] under exclusive control of non-specific interactions taking place at the nano–bio interface, and membrane's elasticity.

In this context, synthetic lipid membranes (together with more complex systems, as organ-on-a-chip and 3D cells arrays, mimicking an entire tissue[57]), are interesting biomimetic systems, which, by mimicking the main structural unit of plasma membranes, allow investigating phenomena at the nano–bio interface in simplified and highly controlled conditions.[44,45,58]

In recent years, both experimental and theoretical studies have addressed the interaction of NPs with synthetic lipid membranes, aimed at establishing clear connections between the results in simplified model systems and what observed in real cells, in order to enabling predictive strategies for the design of evermore efficient and non-toxic nanomaterials for nanomedicine.

In the following sections recent relevant studies on NPs–synthetic lipid membranes interactions, together with their implications for the understanding of real nano–bio interfaces, will be revised, particularly focusing on: the effect of NPs coating (surface charge, exchangeability of the ligand, steric hindrance of the coating, impact of the protein corona) (Section 3.1); the effect of NPs size and shape (with particular interest on the relevance of NPs clusterization in cell uptake) (Section 3.2); the effect of NPs adhesion on the composition, integrity and viscoelastic properties of the target membrane (Section 3.3). In addition, the interaction of inorganic NPs and lipid membranes has been exploited for analytical purposes, in order to label/signal/probe selected properties of cells or lipid assemblies in complex biological media, both exploiting specific and non-specific interactions of NPs with the target membranes. This latter research field will be reviewed in Section 3.4.

3.1 Biophysics of nano–bio interfaces: NPs coating

3.1.1 NPs surface charge. The intrinsic characteristics of NPs (*i.e.*, core composition, size, shape) often have a secondary impact on the interaction with a target lipid membrane, which is primarily mediated by the ligands coating the NP's surface: the surface characteristics of NPs determine polarity and interfacial properties, directly involved in the electrostatic and London–van der Waals contributions to NPs' adhesion to a lipid interface (see Section 2.1 for the theoretical background). The interaction of NPs with target membranes is primarily affect by the charge of both components (see eqn (2)). In order to closely resemble real plasma membranes, most of the employed model bilayers in biomimetics are characterized by a zwitterionic or slightly anionic nature. Therefore, negatively charged NPs tend to be electrostatically repelled from the membrane, undergoing to weaker interactions with respect to cationic ones: remarkably, this is also observed for real cell membranes, where the uptake is generally much lower for anionic NPs than for cationic ones.[59–61] However, the situation of real cells is complicated by the presence of other interaction pathways of specific nature, representing an alternative with respect to non-specific forces. Several studies have highlighted that nonionic, anionic and cationic NPs of similar sizes undergo different internalization routes, from clathrin- or caveolae-mediated endocytosis to non-endocytic pathways, like passive diffusion.[62,63] Even if characterized by limited interaction capability, yet anionic NPs are attractive for biomedical applications, due to limited adverse cytotoxic effects. In addition, despite the dominantly repulsive electrostatic forces, several reports have shown successful internalization of anionic NPs, as silica or Gold NPs (AuNPs).[63–65] Conversely, cationic NPs have a strong tendency to interact with negatively charged membranes: it has been shown that cationic NPs adhere and clusterize onto synthetic target membranes, extract lipids from the membrane, ultimately provoking localized membrane disruption or integrity loss.[22,66,67] In line with this findings, they are often characterized by limited stability in biological media and,

above all, relevant toxic effects on real cells.[13,68,69] Recently, Lee *et al.*[70] hypothesized, by means of a systematic study using a charge library of modified AuNPs, that the magnitude of the positive charge is not the sole factor determining the extent of interaction with target membranes and, thereby cytotoxicity. They conclude that spatial proximity of positively charged functional groups within a hydrophobic moiety is a common characteristic of toxic gold colloids.

3.1.2 NPs coated with steric stabilizers. A common strategy to increase the colloidal stability of NPs in biological media consists in the passivation of NPs with bulky ligands, to endow them with steric stabilization. This kind of coating also improves the pharmacokinetic properties of NPs: for instance, it is well known that PEGylation prevents opsonisation, improving the circulation time of the nanomaterial. This stealth effect of PEG in preventing opsonisation depends on its steric hindrance: it has been shown that both NPs uptake and circulation time depend on the molecular weight of PEG coating the NPs.[71] Moreover, thanks to molecular dynamic simulations, Lin *et al.*[72] elucidated the effect of both the grafting density and polymer's chain length on the shielding ability of PEG layers bounded to gold NPs of varying size. Similar examples of steric stabilization of NPs have recently been proposed by Jiang and co-workers, who have employed poly(zwitterionic)protein functionalization (for instance poly(carboxybetaine)) to improve pharmacokinetic properties of NPs,[73,74] while other examples of polyzwitterionic coatings are poly(acrylic acid) derivatives, poly(maleic anhydride-*alt*-1-alkene) derivatives or poly(sulfobetaine) derivatives, which offer several advantages over PEGylation (see as a reference the Review from Garcia *et al.*[73]).

PEGylation or steric stabilization affects the interaction of NPs with synthetic target membranes, with possible implications also at the real membranes' level. Indeed, the use of steric stabilizers, like PEG, is theoretically predicted to decrease the adhesion of NPs to lipid membranes, due to the high entropic loss associated to the adsorption process (see Section 2).

In a recent study,[75] through large scale molecular dynamic simulations, Gal and coworkers extensively characterized the interaction of PEGylated SPIONs of different size with both synthetic membranes of different composition and real cancer and kidney cells. In the frame of classic DLVO theory (Section 2), they presented a direct comparison of NP–synthetic and real membrane interactions, linking weak NP adsorption to anionic lipid membranes, due to NP–bilayer electrostatic interactions, with eukaryote cell uptake, without membrane penetration. Moreover, they showed that the NP–membrane electrostatic attraction is suppressed by increasing PEG molecular weight and NP size, which they correlated with low cell uptake and no cytotoxicity in two cell lines.

A common strategy to circumvent the poor ability of steric-stabilized NPs to interact with cells *via* non-specific interactions, limiting their cell uptake and therapeutic/diagnostic efficiency, is to exploit the NP–membrane specific interactions, which are available for the case of real plasma membranes: endowing NPs surface with targeting moieties, might result in promoting the effective docking of NPs on cell membranes and improving the successful achievement of their biological target. For instance, in a proof-of-concept study it was shown that adding biotin or streptavidin moieties allows specific binding of polymer-coated NPs to beads carrying the complementary unit;[76] Kaaki *et al.*[77] highlighted the efficient targeting of human breast carcinoma cells by folic acid-conjugated iron oxide NPs with a PEG coating. However, partially contradictory results were obtained by Krais *et al.* on similar system, where no folate-dependent targeting was highlighted.[78]

3.1.3 NPs coating with exchangeable ligands. The binding mode and strength between the NPs and the coating agent determine both single NP–membrane interactions and collective NP–NP interactions at the nano–bio interface: physisorbed ligands, which can be easily displaced from the NP's surface through ligand-exchange, are associated to enhanced reactivity of NPs, which can be considered as ''naked''. Recently, hydrophobic physisorbed ligands, *i.e.*, oleic acid/oleylamine coatings on iron oxide NPs, have been associated to small NPs' pearl-necklace aggregation inside monoolein bilayers.[26] Moreover it has been shown that hydrophilic weakly absorbed ligands on the surface of AuNPs can promote peculiar aggregation phenomena occurring on the lipid membrane,[18,19] which are particularly significative also for the case of repulsive NPs/membrane electrostatic interactions (*e.g.*, between negatively charged gold NPs and slightly anionic synthetic free-standing bilayers). Moreover, weakly bound physisorbed ligand onto the NPs surface can be easily replaced with other molecules establishing covalent or stronger non-specific interaction with the bare NPs surface: remarkably, it has been recently demonstrated by Wang *et al.*,[79] that weak ligands, as citrate and short DNA fragments onto the gold surface, can be effectively replaced with lipid components of cell membranes, resulting in unique interfacial phenomena. Indeed, when ligand exchange processes occur at the interface, NPs might aggregate into ordered monolayers on the lipid membrane, which might affect membrane integrity and cell internalization efficiency and pathway.

3.1.4 Protein corona coating of NPs. An interesting aspect is the functionalization of NPs surface with the so-called protein corona.[14,55,80,81] From the pioneering studies of K. Dawson[82–84] and coauthors, it has been progressively established that NPs in biological fluids are spontaneously covered by a self-assembled layer of proteins (an inner non-exchangeable layer and an external exchangeable one), which determines a ''biological identity'' of the NPs and, ultimately, their ability to interact with cells.[44,80,85,86] The composition of the protein corona depends on the nature of NPs core, on their shape and on their surface coating. In particular, the surface charge of NPs also affects the adhesion of biomolecules present in biological media, modifying the protein corona, in terms of composition and orientation.[62,87,88] It has also been highlighted that during NPs internalization, the tendency of corona proteins is, at least partially, to remain attached to NPs surface.[83,89,90] Since proteins are generally characterized by significant steric hindrance and amphiphilic nature, they specifically mediate the interaction of the NPs with plasma membranes. In this context, it has been highlighted that slight physicochemical

modifications of the proteins modify their binding and orientation on NPs, strongly affecting the biological uptake of NPs.[91] Recently, the controlled formation of the protein corona has been exploited both for application purposes (*e.g.*, for applications in cancer vaccines[92]) and also to control in a predictable way the protein-corona-mediated interaction of NPs with cell membranes. For instance, pre-incubation of NPs with serum has been exploited to prevent NPs aggregation in biological media, improve their cell uptake and decrease their cytotoxic effects.[69] The comprehension, control and exploitation of protein corona formation is therefore a key milestone in determining and predicting NPs fate in living organisms.

3.2 Biophysics of nano–bio interfaces: NPs size and shape

As discussed in Section 2, when a NP adheres to a planar lipid membrane, it locally imposes a curvature modification, which depends on the size of NPs and on the viscoelastic properties of the membrane (eqn (5)), which eventually controls the occurrence and extent of NPs wrapping by the membrane; therefore, NPs size also determines the response of the bilayer to its adhesion and, ultimately, the effects on the target membrane and the internalization pathway. NPs with size comparable or smaller than the lipid bilayer thickness can either be entrapped within the membrane[30] or translocate across the lipid bilayer by diffusing through[25,93,94] or by opening pores in the membrane,[95] which is normally associated to a high cytotoxicity *in vivo*.[56,96] On the contrary, wrapping represents the dominant mechanism for larger particles (>10 nm) interacting with bilayers, which is associated to their entrance into cells in living organisms.[11] Often, depending on NPs size, adhesion to a target membrane might result in the NPs clusterization: indeed, under specific conditions, membranes actively drive the self-assembly of adsorbed NPs, as a result of the tendency of the membrane to minimize the NP-induced deformation and its associated elastic cost (eqn (5)).[97] As a result, small-sized NPs have been observed to preferentially interact with membranes as clusters,[67,98] while fluid membranes have been theoretically predicted to mediate the asymmetric aggregation of spherical nanoparticles onto lipid surface.[99] This aspect is particularly significant for medical application of nanomaterials, since NPs uptake in model and real membranes is often preceded by aggregation at the nano–bio interface.[11] In addition, mathematical models and molecular dynamic simulations have revealed that membrane-induced interactions between bound particles can lead to collective NPs wrapping and internalization: in particular, Zhang *et al.*[100] revealed that NPs translocation proceeds in a cooperative way, with a key role played by NPs quantity, while Lipowsky *et al.*[101,102] showed that spherical NPs can be cooperatively wrapped in tubular membrane invaginations.

While the effect of NP's size has been extensively investigated, much less is known on the impact of NP's geometry. Asymmetrically shaped NPs, like nanorods, nanodisks and nanostars, are particularly attractive materials, due to the peculiar properties (optical, magnetic, electronic and so on) arising from anisotropy.[103] Depending on their shape, anisotropic NPs can efficiently interact with a target membrane and translocate across it. MD studies on the interaction of NPs of different non-spherical shapes highlighted reorientation of NPs in proximity to the target membrane, to maximize the interaction, leading to strong shape and orientational dependence on the translocation[104] (see Fig. 3A). In addition, it has to be considered that, from a theoretical standpoint, it is thermodynamically more favourable for a lipid membrane to wrap a spherocylinder than a sphere of the same radius.[105] Consistently with the theoretical predictions, non-spherical NPs, from nanostars to nanorods, are efficiently internalized by cells, in a shape and, for nanorods, aspect-ratio dependent manner.[106,107] Experimental studies on biomimetic membranes have shown that the asymmetric shape of NPs can drive peculiar self-assembly phenomena at the nano–bio

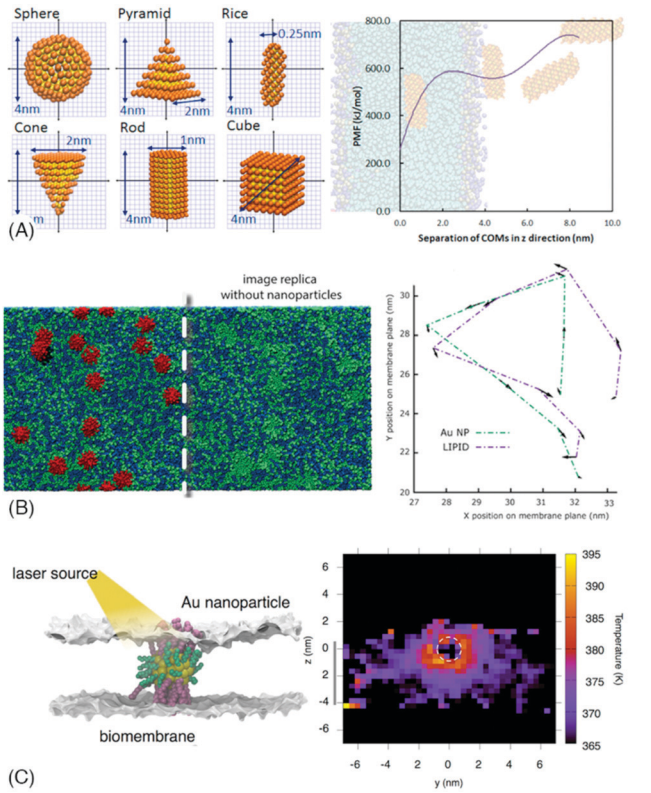

Fig. 3 Theoretical studies on nano–bio interfaces. Panel A: molecular dynamics study to compute translocation rate constants of NPs of different shapes through lipid membranes; (left) coarse-grained gold nanoparticles setup; (right) analysis of rice NP translocation: potential of mean force, PMF (kJ mol^{-1}) profile as a function of distance of the NP from the lipid bilayer. Adapted with permission from ref. 104. Copyright (2012) American Chemical Society. Panel B: lipid membrane modifications upon interaction with cationic gold NPs: (left) lateral phase separation of 1 : 1 anionic (green) and zwitterionic (blue) lipids in the presence of gold NPs (red); (right) trajectories of NP (green) and anionic lipid (blue) highlighting the slaved diffusion of anionic lipids upon interaction with NPs. Adapted with permission from ref. 22. Copyright (2019) American Chemical Society. Panel C: nonequilibrium molecular dynamics simulations to investigate photoporation of lipid membranes through the irradiation of AuNPs: the NPs, stably bound to cell membranes, convert the radiation into heat; a quantitative prediction of the temperature gradient around the NP upon irradiation is evaluated. Adapted with permission from ref. 197 Copyright (2017) American Chemical Society.

interface:[10,37] as an example, we recently demonstrated that gold nanorods (Au NRs) are wrapped by model and real cell membranes as end-to-end NPs' clusters,[67] reducing the energy penalty required for the membrane to bend around highly curved edges. The induced tension due to the adhesion of asymmetric NPs determines effects of lipid extraction, observed both on model membranes and macrophage cells, eventually provoking extensive disruption of the membrane, related to a significant *in vitro* cytotoxicity.[67]

3.3 Biophysics of nano–bio interfaces: membrane composition

Cell membranes are characterized by a high degree of compositional heterogeneity, typically comprising of thousands of different lipids, carbohydrates and proteins,[108] which is reproduced, at different complexity levels, by model membranes. The chemical composition of both synthetic and natural bilayers strongly affects their elasticity, physical state and structure, thereby determining their response towards external stimuli. A clear example is the recent work of Lunnoo *et al.*,[109] in which model bilayers with different compositional complexity levels correspond, as predicted by their proposed MD simulations, to diverse cellular uptake pathways of neutral 10 nm gold NPs. Going more into details, the presence of charges on the lipid membrane emphasizes the interaction with oppositely charged particles, as expected from eqn (2)[96] in Section 2; however, it has been demonstrated that electrostatic interactions play a major role also for neutral zwitterionic lipids facing anionic and cationic NPs.[110,111] In addition, it has been observed that the molecular structure of membrane's lipid components (*e.g.*, saturation degree of hydrophobic chains) represents another factor to take into account, affecting the penetration level of NPs inside the lipid region.[112] Furthermore, cholesterol, one of the most abundant sterols in real lipid membranes, deeply affects the structure and fluidity of lipid bilayers; moreover, it is involved in the formation of lipid rafts,[113] which, for reasons not yet fully understood, increase the extent of NPs–membrane interactions: as an example, Melby *et al.*[114] showed that positively charged AuNPs bind significantly more to phase-segregated bilayers with respect to single phase ones, while Hartono *et al.*[115] associated higher cholesterol concentrations in lipid monolayers to stronger interactions with protein-coated AuNPs, leading to monolayer disruption.

3.4 Biophysics of nano–bio interfaces: NPs-induced membrane modifications

The self-assembled nature and lateral fluidity of plasma membranes determine a capability of the membrane to reorganize and locally and transiently restructure itself in response to biological stimuli. This is the case considering for instance the transient formation of lipid rafts, in relationship with cell trafficking phenomena, or considering ligand (drug)–receptor interactions at cell surface, triggering complex biological responses. In this respect, several studies have addressed the effects on NPs on a target lipid membrane upon adhesion. A first effect is the induced lateral phase separation within the target membrane: theoretical studies on cationic NPs have highlighted their tendency to recruit anionic lipids in the adhesion area, determining the formation of phase separated patches within the membrane (see Fig. 3B).[22,116] The alteration of membrane's phase behaviour induced by NPs is a growing research topic, with several studies contributing building-up a complex picture, which is far from being understood. As an example, the group of Granick[111] reported a different effect of silica anionic[117] and cationic particles on phospholipid membranes, with negative NPs inducing gelation and positive ones provoking fluidification. Considering anionic silica NPs with different size, the group of Zhang *et al.*[118] reports that the gelation, or ''freeze effect'' on DOPC giant unilamellar vesicles (GUV) is promoted by small NPs (18 nm), while large particles (>78 nm) promote membrane wrapping. By significantly decreasing the phospholipid lateral mobility, the release of tension through stress-induced fracture mechanics results in a microsize hole in the GUVs after interaction. On the other hand, membrane wrapping leads to increased lipid lateral mobility and the eventual collapse of the vesicles.

Von White *et al.*[30] registered an increase in the gel-to-liquid crystalline transition temperature of synthetic lipid vesicles induced by the embedding of hydrophobic AuNPs, while Chakraborty *et al.*[119] reported the opposite effect, *i.e.*, phospholipid bilayer softening, due to hydrophobic AuNPs inclusions; on the other side, recent studies demonstrated that hydrophilic (negatively and positively charged) AuNPs induce the same effect at the nanoscale, promoting the formation of rigidified lipid domains around the NPs' surface, characterized by a reduced lipid motion with respect to the surrounding fluid phase.[21,22,120,121] Both the induced lateral phase separation on a target membrane and the induced modification of the viscoelastic properties might represent, at the biological level, both biologically relevant signals, activating cell entry pathways, or else might be of relevance in inducing cytotoxic effects (Fig. 3C).

3.5 Analytical applications of NP–lipid membrane interactions

An interesting research topic related to the interaction of NPs with lipid membranes is its exploitation for analytical purposes. Inorganic NPs are characterized by peculiar properties, making them suitable to provide a readout, generally an optical (fluorescence, scattering) or magnetic signal, which can provide qualitative or quantitative information of different nature. Knowles and coworkers have shown how the spontaneous formation of a supported lipid bilayer on a polystyrene NPs patterned support can be exploited to form membrane regions of high curvature, due to NPs partial wrapping: these areas spontaneously accumulate specific, single-tailed lipids, of higher spontaneous curvature, and can be exploited to monitor the interaction of biomolecules with membrane areas of high curvature;[122] Liu *et al.*[123] have formed AuNPs patterned surfaces (see Fig. 4B), for mechanical tension measurements in living cells. Cho and coworkers[124] have designed a nanoplasmonic biosensor made of an array of gold, silicon oxide or titanium oxide nanodisks coated with different lipid architectures

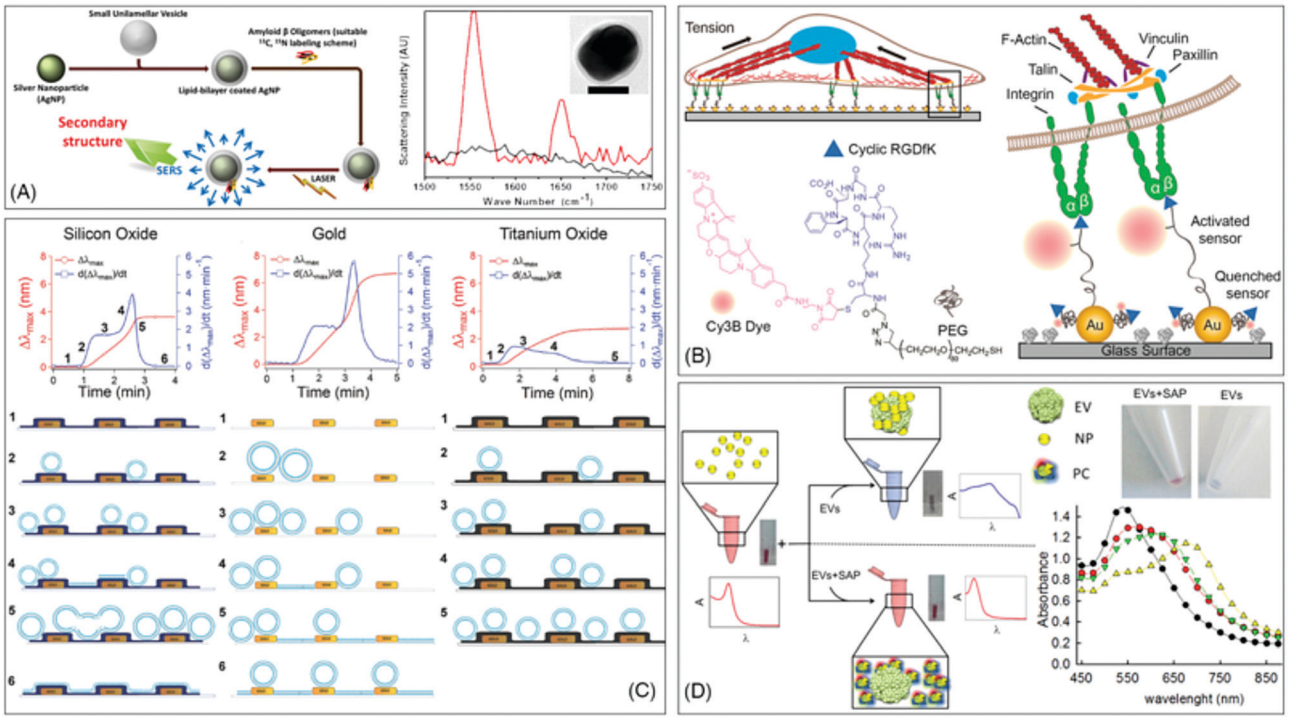

Fig. 4 Analytical applications of NP–lipid membrane interactions. Panel A: SERS technique exploiting the spontaneous binding of proteins to lipid bilayer-encapsulated AgNPs to probe lipid membrane-attached oligomers; (left) set-up of the technique (right) TEM micrograph of lipid-coated AgNPs; SERS spectrum of melittin in the presence of AgNPs (black) and lipid-coated AgNPs (red). Adapted with permission from ref. 127. Copyright (2015) American Chemical Society. Panel B: molecular tension fluorescence microscopy applied to the investigation of fibroblast cells layered on a substrate with an array of precisely spaced functionalized AuNPs: cartoon summarizing the experimental set-up. Adapted with permission from ref. 123. Copyright (2014) American Chemical Society. Panel C: self-assembly formation of lipid membranes on nanoplasmonic sensor platforms. Time-resolved extinction maximum wavelength shift measurements (red) and corresponding time derivative (blue) for vesicle adsorption onto (left) silicon oxide-coated nanodisk surface, (center) bare gold nanodisks on glass surface, and (right) titanium oxide-coated nanodisk surface. Adapted with permission from ref. 124. Copyright (2014) WileyVCH Verlag GmbH & Co. KGaA, Weinheim. Panel D: (left) set-up of the nanoplasmonic assay for probing by eye protein contaminants (single and aggregated exogenous proteins, SAP) in EV preparations; (right) Eppendorf tubes containing AuNPs in the presence of EVs (blue) or EVs + SAP (red), highlighting the sensitivity of the assay to EVs protein contaminants; UV-visible absorbance spectra of AuNPs, in the presence of increasing amounts of EVs, highlighting the sensitivity of the assay to EVs concentration. Adapted with permission from ref. 130. Copyright (2015) American Chemical Society.

(see Fig. 4C), vesicles arrays, supported lipid bilayers or a coexistence of the two systems, spontaneously formed due to different pathways of interaction between lipid vesicles and the nanodisks of different material: localized surface plasmon resonance experiments detecting a membrane-active peptide highlighted a strong dependence of the interaction between the peptide and the lipid bilayer, depending on the architecture of the lipid scaffold. Limaj *et al.*[125] designed an infrared biosensor to monitor the molecular behaviour and dynamics of lipid membranes, based on the adsorption of lipid vesicles on an engineered substrate functionalized with gold nanoantennas for surface enhanced infrared absorption (SEIRA) experiments. Suga *et al.*[126] exploited the interaction of hydrophobic (dodecanthiol-modified) AuNPs with phospholipids and phospholipid assemblies, to investigate the behavior of lipid membranes at a molecular length-scale through Surface-Enhanced Raman Spectroscopy (SERS). The same technique is employed by Bhowmik *et al.*,[127] who exploited the formation of a lipid coating wrapping Silver NPs (AgNPs) to probe through SERS the molecular behavior of protein oligomers spontaneously binding to the lipid coating of AgNPs (this example will be also discussed in Section 5) (see Fig. 4A). Recently, we have shown that synthetic Giant Unilamellar Vesicles of POPC promote the clusterization of Turkevich–Frens citrated AuNPs on the lipid membrane itself.[121] This phenomenon, which has been investigated by other groups, provokes a modification of the plasmon resonance peak of AuNPs, which is visible also by naked eyes as a colour change of AuNPs dispersion from red to blue.[17,128] Interestingly, this effect is similarly observed when the same AuNPs challenge biogenic natural vesicles (extracellular vesicles, EVs)[120,129] and it has been found as strongly dependent on the concentration of EVs and on the presence of protein contaminant. Therefore, an analytical method for EVs has been developed, offering an easy and fast assay for purity and concentration of EVs, based on nonspecific interactions between NPs and lipid membranes[130–132] (see Fig. 4D).

4. Engineering lipid assemblies: inclusion of NPs in lipid scaffolds

Depending on their molecular structure and on the environmental conditions, lipids in water self-assemble into very

diverse structures, from simple planar lamellar phases, as vesicles, to non-lamellar curved bilayered structures (as cubic mesophases),[133–135] to inverse monolayered tubular arrangements (as inverse hexagonal mesophases). These different structural arrangements, formed by spontaneous self-assembly, can host hydrophilic-coated NPs in the aqueous regions and/or hydrophobic-coated NPs in the hydrophobic domains.

NPs can spontaneously insert in the lipid scaffolds, due to non-specific forces, such as hydrophobic, electrostatic and van der Waals interactions (see Section 2), thus representing a facile approach to obtain a complex hybrid material with controlled structure and defined properties arising from the combination of lipid and NP building blocks.

In particular, the inclusion of NPs in lipid scaffolds allows obtaining materials with specific interesting features: (i) the biocompatibility of the lipid scaffold (dependent on its composition) allows envisioning the employment of these hybrid materials for biomedical applications; (ii) the self-organization and phase behavior of lipid mesophases is generally responsive to the inclusion of external species, to temperature, hydration and other experimental conditions, which variations can be triggered, in a space and time controlled manner, by external stimuli applied to the NPs included in the lipid scaffold (*e.g.*, magnetoliposomes). This is a very interesting opportunity for several applications, for instance the development of drug delivery systems (DDS) with controlled release abilities; (iii) the inclusion and confinement of NPs in lipid scaffolds has the effect to locally concentrate them and to impose them a spatial arrangement. This localized NPs concentration increase might be of relevance to enhance NPs-related signals (for instance optical or MRI readout for diagnostic applications); in addition, the increased concentration, together with a defined structural architecture, might induce peculiar collective properties of NPs, arising from the lipid scaffold-imposed arrangement.

In the following sections we will revise this topic, in particular focusing on the effect of NPs inclusion on the overall features of lipid/NP hybrid materials (Section 4.1), and, subsequently, on applicative examples of NP/lipid hybrids made of NPs included in lamellar (Section 4.2) and non-lamellar (Section 4.3) lipid mesophases.

4.1 NPs inclusion in lipid scaffolds: structural and physicochemical effects

The hydrophobic or hydrophilic nature of NPs, which depends on the coating agent, is the key factor in determining the localization in a lipid assembly. Both lamellar (*i.e.*, liposomes, Giant Unilamellar Vesicles) and non-lamellar (*i.e.*, cubic or hexagonal structures) lipid assemblies are characterized by the coexistence of hydrophobic and hydrophilic domains, capable to host NPs of different nature. In all NPs–lipid hybrids, the inclusion of NPs in the lipid architecture affects the physico-chemical and structural properties of the lipid scaffold, modifying for instance the fluidity and bending properties of the membrane, its local thickness, the phase behavior and the viscoelastic properties. For instance, it has been shown that the inclusion of hydrophobic superparamagnetic iron oxide NPs (SPIONs) in the lipid membrane of DPPC liposomes increases the average thickness of the membrane and modifies the orientation of the phospholipid chains, affecting the lipid melting temperature.[136,137] In addition, depending on the chemical nature of hydrophobic NPs embedded in a lipid bilayer, they can either stabilize or destabilize the lipid ordering, causing opposite effects on the phase behavior of the lipid scaffold; it has been shown that 4 and 5.7 nm AgNPs[31] increase the fluidity of the membrane, reducing the degree of ordering of the lipid tails, while 5 nm maghemite NPs[29] increase membrane rigidity. Finally, the inclusion of nanoparticles can also modify the final structure of the bilayer: for instance, a Cryo-TEM investigation of Chen *et al.* on liposomes containing hydrophobic SPIONs has highlighted the formation of liposomes' aggregates with SPIONs clusters acting as bridging agents (see Fig. 5A and B). These local perturbations highlight that some structural rearrangement of a planar lipid membrane can be possible preserving the overall lipid mesophase architecture; however, as reported by Briscoe *et al.*,[40] significant amounts of NPs inclusion might promote, for defined lipid compositions and specific temperature/pressure conditions, a phase transition from lamellar to hexagonal mesophases. In general, as already pointed out in Section 2, the inclusion of NPs in a planar bilayer increases the frustration packing energy of the lipid molecules eventually promoting the re-organization in a different mesophase, characterized by a more negative curvature; the mismatch between the equilibrium curvature and the perturbed arrangement due to NP inclusion, favors the transition to a more thermodynamically stable structure.

These examples highlight how the effect of NPs on lipid membranes is variable, but possibly predictable, on the basis of minimum energy considerations; therefore, the physico-chemical properties of the target lipid membrane and of the NPs to be inserted in the lipid scaffold can be tuned in order to modify the behavior of the membrane in a desired manner, engineering the system for its final purpose.

4.2 Applications of NPs/lamellar lipid assemblies hybrids

Among hybrid nanostructures where NPs are included in lamellar assemblies, particularly relevant are magnetoliposomes (MLs), where hydrophobic SPIONs are included in the lipid bilayers of lipid vesicles.[138–140] Their responsivity to static (SMF) and alternating magnetic fields (AMF) makes MLs good candidates in nanomedicine as DDS,[141] able to release drugs confined in the lumen of liposomes in a time and space controlled manner, upon application of external stimuli.[142,143] Despite their potentiality, the inclusion of small NPs in the bilayer can be exploited only for drug delivery purposes, while generally, no bulk heating effect can be induced by small NPs subjected to AMFs, as shown in several studies:[144] therefore, they cannot be applied in hyperthermia therapies, for the thermal ablation of cells; however, as reported by Di Corato *et al.*,[145] using hydrophilic SPIONs loaded in the vesicles' lumen combined with a photosensitizer, results in a synergistic effect, observed both *in vitro* and *in vivo*, making this strategy, which exploits a multifunctional

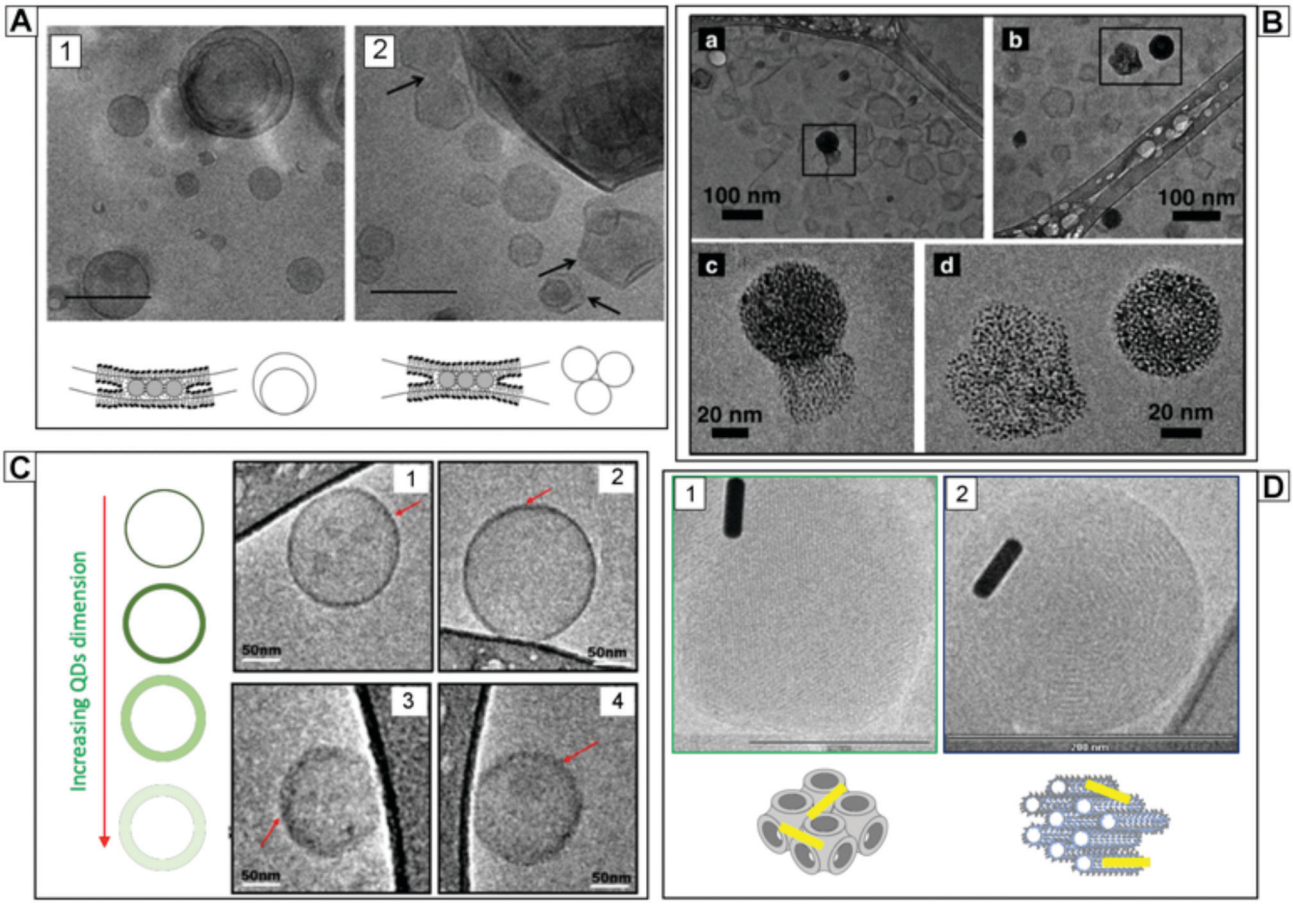

Fig. 5 Cryo-microscopies of lamellar and non-lamellar lipid membranes assembled with hydrophobic NPs. Panel A: cryo-TEM images highlighting the structural changes induced by hydrophobic SPIONs interacting with liposomes: on the left, TEM image showing liposomes arranged in a multiwalled configuration with SPIONs bridging; on the right, TEM image of liposomes' aggregates bridged by SPIONs clusters embedded in the bilayer. Adapted with permission from ref. 29. Copyright (2010) American Chemical Society. Panel B: DPPC liposomes decorated with dodecanethiol-capped AuNPs shown at different magnifications. Adapted with permission from ref. 28. Copyright (2017) American Chemical Society. Panel C: TEM images of POPC/POPE liposomes assembled with quantum dots (QDs) of different sizes embedded in the bilayer. The size increase of QDs (from 1 to 4 progressively) increases the perturbation of the lipid membrane: lipid membrane appears sharp when small QDs are included (1 and 2), while with the larger ones the membrane becomes fuzzier (3 and 4). Reproduced from ref. 150 with permission from The Royal Society of Chemistry. Panel D: cryo-SEM of non-lamellar mesophases interacting with Au NRs. On the left Phytantriol cubic mesophase, on the right Phytantriol hexagonal mesophase, both assembled with Au NRs. Adapted with permission from ref. 156. Copyright (2012) American Chemical Society.

nanomaterial, very promising for therapeutic applications. Recently, MLs decorated both with hydrophobic and hydrophilic SPIONs have been shown to release on-demand hydrophilic or hydrophobic payloads, depending on the frequency and application time of an AMF.[127]

Besides SPIONs, hydrophobic AuNPs were recently used[146] to build-up photoresponsive and thermosensitive hybrid liposomes. In addition, multifunctional hybrid liposomes containing magneto-plasmonic nanoparticles (SPIONs@Au), merging the possibility to combine hypothermic and photothermal treatments were recently shown[147,148] for image-guided delivery of anti-HIV drugs to the brain: generally, the successful delivery of antiretroviral drugs to the brain is limited due to the presence of the blood–brain barrier (BBB); in this case the authors reported an enhanced BBB transmigration efficiency under AMF without its disruption; moreover, the treatment of HIV virus with multifunctional liposomes successfully reduced the viral replication.

Several studies have addressed the inclusion of quantum dots in lipid assemblies: despite their unique optical properties, they are characterized by significant acute cytotoxic effects. With the aim to realize a contrast agent for imaging applications,[138,149,150] several studies have shown that the confinement of CdSe dots in lipid bilayers increases their biocompatibility, while preserving their fluorescence features, making the system more suitable for biomedical applications (see Fig. 5C).

4.3 Applications of NPs/non-lamellar lipid assemblies hybrids

As anticipated in Section 2, the inclusion of NPs into non-lamellar lipid assemblies mostly affects the structure of the mesophase, in terms of the lattice parameter and, consequently, of the diameter of the nanochannels and amount of water contained in the lipid architecture. If the size of NPs is similar or smaller than the lattice parameter, NPs can be easily encapsulated in the architectures. Venugopaal *et al.*[38] investigated

the encapsulation of hydrophilic Silica NPs of 8 nm diameter in monolinolein mesophase: in this case, the NPs were too large to be encapsulated in the nanochannels (of 3–3.8 nm diameter); nevertheless, the addition of NPs determined the overall dehydration of the lipid scaffold, eventually causing, for high concentrations, the transition of the assembly geometry to a gyroid cubic structure (*Ia3d*). The authors interpret this behavior considering that, since the energy cost to include the NPs in the nanochannels is extremely high (above $100k_BT$), the NPs tend to minimize their interfacial energy, aggregating along the grain boundaries of the mesophase, similarly to what reported concerning lamellar structures.[151] The same authors investigated also the structural features of monolinolein mesophases loaded with hydrophilic SPIONs. Upon application of a static magnetic field, a reorganization of the lipid domains along the direction of the field[152,153] was found, highlighting how the responsiveness of SPIONs to magnetic fields can be exploited to induce structural modifications in the whole lipid mesophase. This effect has been applied for instance to control the release of drugs confined in the lipid mesophases[152] or, as the same authors reported,[154] for the application in optical memory storage.

The inclusion of hydrophobic NPs in non-lamellar mesophases can be easily achieved exploiting the hydrophobic interactions that spontaneously drive the NPs localization in the hydrophobic regions of the self-assembly. However, also in this case, the size of NPs is of paramount importance, to avoid the disruption of the lipid scaffold. Recently, the inclusion of hydrophobic SPIONs into 1-monoolein diamond cubic phase was reported, highlighting that the amount of included NPs, together with temperature, controls the phase transition from cubic to hexagonal phase. Since this transition is accompanied by a significant dehydration of the mesophase, the structural rearrangement is accompanied by the release of most of the water content of the nanochannels. This thermoresponsive hybrid material was also found to be responsive to AMFs, representing, therefore, a promising system for the delivery of hydrophilic drugs in a time and space-controlled manner.[33] Recently, it was shown that this thermotropic effect of liquid crystalline phases loaded with hydrophobic NPs is a general phenomenon, highlighted also for cubic mesophases formed of phytantriol and hydrophobic AuNPs.[20]

Very few examples in the literature address the inclusion of non-spherical NPs in non-lamellar lipid assemblies: Boyd *et al.*[155] reported on hydrophobic NRs included in phytantriol, selachyl alcohol and monoolein lipid mesophases, with the aim to build-up photo-responsive hybrid materials (see Fig. 5D). The authors investigated the effect of NRs on the cubic mesophases, highlighting a slight reduction in the phase transition temperature and in the lattice parameter. Interestingly, similarly to spherical hydrophobic NPs, gold NRs shift the cubic-to-hexagonal boundaries to lower temperatures.[156] For hexosomes of selachyl alcohol, it was shown that the lattice parameter or water volume fraction[26,27] are not affected by the presence of AuNRs; the authors suggested that NRs are positioned along the direction of hexosomes, but, due to their large sizes (55.5 nm in length and 16 nm in width) they are in close proximity of the lipid bilayer, without being efficiently included inside it. Nevertheless, the application of a NIR laser on the hybrid structure promoted the phase transition from cubic to hexagonal phase, similarly to what observed with the application of AMF on monoolein-SPIONs hybrids.

5. Surface engineering of inorganic NPs: functionalization of NPs with a lipid coating

Recently, several research groups have addressed the functionalization of inorganic NPs or clusters of NPs with lipids to form lipid-coated NPs with a supported lipid bilayer (SLB and liposomes[3]). The validity of this approach is twofold: first, a lipid coating of appropriate composition might strongly improve the biocompatibility of inorganic NPs: this is particularly critical for the very toxic quantum dots. The second advantage is the increased dispersibility in body fluids and improved pharmacokinetic properties. As a matter of fact, without a proper coating, bare NPs introduced by parenteral administration, are rapidly opsonized and removed by phagocytes from the blood stream[54] and accumulated in liver and spleen,[157,158] often causing oxidative stress.[159,160]

Although this could be even convenient for those treatments where the desired aim is to modulate local immune responses,[161] it is worth considering the use of a capping agent that prevents leakage of the drug, protects the carriers from degrading enzymes, and shields them from the immune system avoiding side effects.[162,163] Among several potential capping systems, lipid bilayers are especially advantageous[164] for several reasons: (i) the escape from endosomal vesicles of the nanomaterial and successful reaching of its biological target, upon endocytic uptake, is strongly favoured in the presence of a lipid coating, improving the ability of NPs to passively permeate to the inner core of the cell;[165,166] (ii) the presence of a lipid coating is helpful in preventing NPs aggregation in biological environment; (iii) lipid coating is highly tuneable in composition (for instance PEGylated lipids, to further improve nanoparticle pharmacokinetic properties,[167] can be easily incorporated, as well as cholesterol, added as a controlling fluidity agent) and can be easily functionalized and designed to match the specific requirements of the desired application.[168–170] As introduced in Section 2, the achievement of such a coating depends on the size of the NP to be coated and on the viscoelastic properties of the membrane. Generally, relatively large NPs, imposing a low curvature to the target membrane, can be successfully completely wrapped and coated by a lipid membrane, while small particles need to be wrapped and coated as clusters. In the following sections we will review the most relevant examples and applications of lipid-coated inorganic nanoparticles, considering one by one the different types of nanoparticles, silica NPs (Section 5.1), gold and silver NPs (Section 5.2) and iron oxide NPs (Section 5.3).

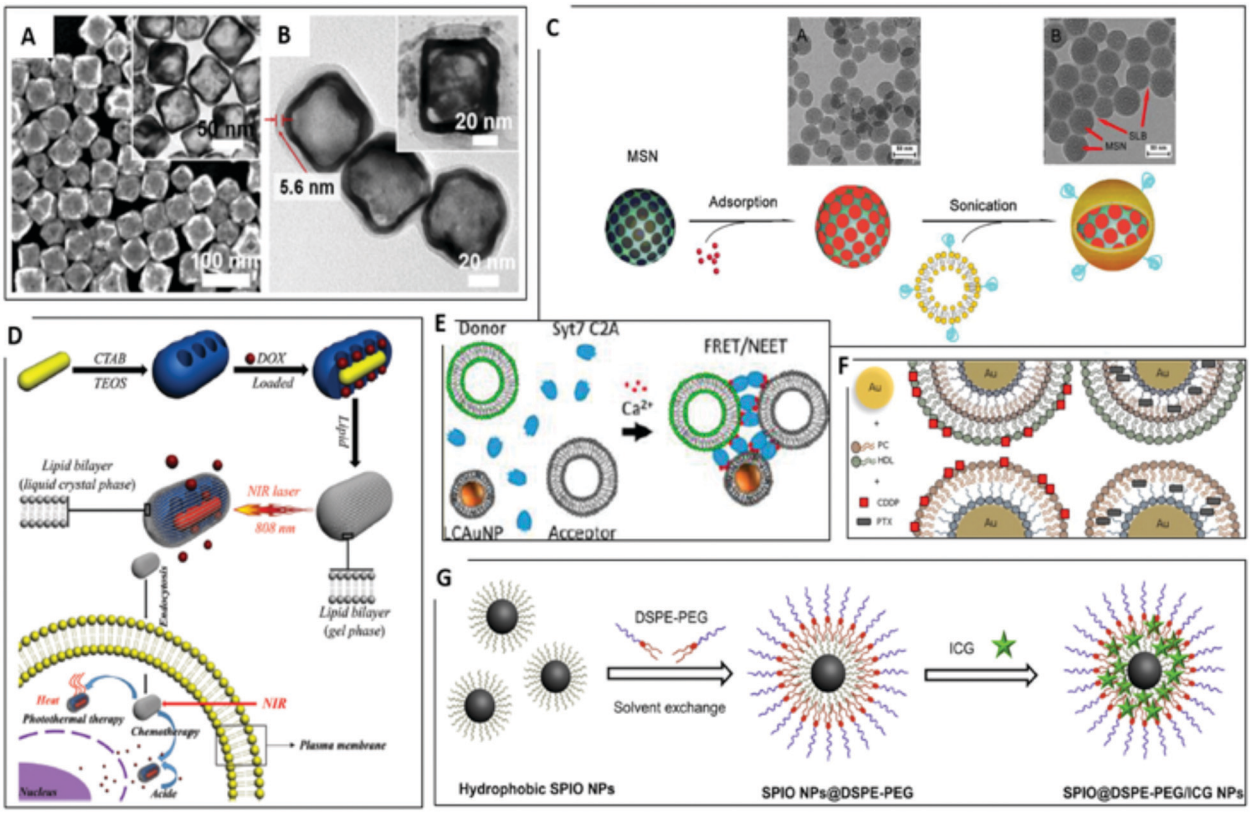

Fig. 6 Lipid-coated NPs. Panel A and B: TEM images of bare Au nanocages (A) and the same nanocages covered by a lipid bilayer (B) used as nanovaccine for cancer immunotherapy. Reprinted with permission from ref. 187 © Elsevier; panel C: schematic overview of the procedure for the fabrication of doxorubicin (DOX)-loaded SLB-mesoporous silica NPs. The thermal responsiveness of the lipids circumvents the premature leakage of the payload. The insets show the related TEM images. Adapted and reprinted with permission from ref. 178 © Elsevier; panel D: schematic illustration of the fabrication process of DOX-AuNR@mSiO_2 covered by a lipid bilayer and the corresponding NIR laser-controlled intracellular DOX release. Reprinted with permission from ref. 192 © RSC; panel E: model of the Ca^{2+}-dependent liposome and lipid-coated AuNPs clustering in presence of synaptotagmin (Syt). Reprinted with permission from ref. 185 © ACS; panel F: conceptual scheme of lipid-coated gold carriers for the release of paclitaxel and cisplatin. Reprinted with permission from ref. 183 © Elsevier; panel G: schematic illustration of the preparation protocol of SPION@DSPE-PEG loaded with indocyanine green. Reprinted with permission from ref. 193 © Elsevier.

5.1 Lipid-coated silica NPs

Leveraging the pioneering works of Rapuano's group,[171,172] over the last years several research groups have addressed the decoration of silica nanoparticles with SLBs.[173] Recently, Mousseau *et al.* showed an example of fluorescent silica NPs covered by a pulmonary surfactant Curosurf®. They found that a complete SLB coverage of silica nanoparticles is obtained only through sonication, which disrupts lipid vesicles and promotes full wrapping of the NPs. *In vitro* assays confirmed that the presence of the SLB mitigated the particle toxicity and improved internalization rates.[174]

Tada and co-workers tested the impact of a lipid coating (using different types of lipid bilayers) on the cytolocalization of silica NPs prepared with methylene blue, for applications in Photodynamic Therapy (PDT).[175,176]

Mackowiak *et al.*[177] showed an example of mesoporous silica NPs surrounded by a cationic DOPC/DOTAP SLB with targeting ligands on the surface of the nanoconstruct and a photosensitizer molecule covalently attached to the surface of mesoporous silica NPs, for controlled and targeted drug delivery applications. In this case, the presence of the SLB coating was also aimed at improving the capability of the system to retain a drug inside the mesoporous structure of NPs before photoactivation to induce the release of the cargo.

An alternative route to obtain controlled release of drugs from lipid-coated mesoporous silica NPs, based on the use of thermo-responsive lipids, was recently presented by Zhang *et al.*: they combined the high drug loading capacity of mesoporous silica NPs with the thermal responsiveness of a mixture of lipids, DPPC/DSPC/Chol/DSPE-PEG2000, allowing the possibility to release on-demand the payload at hyperthermia temperature, circumventing the premature leakage at physiological temperature[178] (see Fig. 6C).

5.2 Lipid-coated gold and silver NPs

Taking advantage of their antimicrobial properties, AgNPs have been widely used in the last decades both in industrial and in biomedical applications.[179–181] Furthermore, due the localized surface plasmon resonance (LSPR) of AgNPs, they can be exploited for the development of biosensors. For this purpose, Bhowmik and co-workers[127] developed a method to determine the conformation of membrane-bound proteins: unlike conventional

SERS, that requires immobilization of molecules, they exploited the spontaneous binding of proteins to lipid bilayer-coated AgNPs. In this way, they probed the behavior of membrane-attached oligomers of Amyloid-β40 (Aβ40), whose conformation is of relevance in Alzheimer's disease. AuNPs are the most widely studied inorganic NPs, thanks to their facile synthetic and functionalization routes, and their plasmonic properties that can be harnessed in a plethora of applications, ranging from optical imaging, spectroscopy and photothermal therapy. Du *et al.* formed a liposomes–AuNPs hybrid system as a vector for nucleic acids, for applications in gene therapy.[182]

England and co-workers[183,184] (see Fig. 6F) prepared AuNPs functionalized with multiple layers (two or three) of phosphatidylcholine, alkanethiol, high density lipoprotein and phosphatidylcholine/alkanethiol for the delivery of hydrophobic and hydrophilic drugs for the treatment of solid tumours. By exploiting the optical properties of AuNPs, Reed *et al.* developed a novel hybrid for sensitive detection of proteins based on apposition and aggregation of liposomes induced by Ca^{2+} ions using Förster resonance energy transfer (FRET) assays[185] (see Fig. 6E). Wang *et al.* recently proposed a novel approach to overcome the low delivery efficiency of plasmids by condensing them on peptide-modified AuNPs, successively covered with a mixture of phospholipids.[186]

In addition to spherical NPs, liposomes-coated gold nanocages[187] (see Fig. 6A and B) have been reported as possible nanovaccines for cancer immunotherapy: the authors demonstrated that the hybrid carrier exhibited enhanced antitumor effects, inhibiting tumour growth in lung metastasis models. In addition, lipid-coated hollow gold nanoshells have been recently developed for synergistic chemotherapy and photothermal therapy for the treatment of pancreatic cancer.[188] By taking advantage of the unique structure of hollow gold nanoshells, the authors successfully demonstrated the co-delivery of two drugs, one loaded in the lipid bilayer and the other one loaded in the hydrophilic interior of the nanoshell.

Furthermore, the possibility to extend lipid coverage to Au NRs has been recently explored. Recent studies have addressed the functionalization of Au NRs with a phospholipid bilayer, composed of POPC[189] and, more recently, DMPC,[190] to increase biocompatibility and bioavailability of NRs. In addition, lipid capped Au NRs (obtained with DPPC vesicles containing lipids with a thiol headgroup) have been demonstrated to be suitable label-free biosensors[191] for the detection of lipophilic drugs in aqueous solutions or lipopeptides in serum. Finally, moving to a more complex architecture, Han *et al.*[192] (see Fig. 6D) demonstrated the possibility to use silica and phospholipids to cover AuNRs, coupling the photothermal and thermo-responsive properties in the same nanoplatform.

5.3 Lipid-coated iron oxide NPs

SPIONs are among the most attractive NPs for biomedical applications, ranging from applications in MRI to responsive nanocarriers for drug delivery to therapeutic applications in hyperthermia (see Fig. 6G). Bao *et al.*[193] synthesized DSPE-PEG coated SPIONs loaded with indocyanine green molecules as superparamagnetic carriers capable to easily accumulate in tumours sites and act as biodegradable nanotheranostic agents. In the emerging field of nanovaccines, the group of Ruiz-de-Angulo[194] presented a biocompatible multifunctional system designed to both act as delivery vehicle and radiotracer for PET/SPECT imaging: using lipid-coated magnetite nanoparticles, they efficiently included in the construct $^{67}Ga^{3+}$ as radiotracer, plus an antigen and an adjuvant. *In vivo* imaging highlighted the efficient targeting capability of the system and cell uptake. Recently, the same authors presented bacteria-mimicking NPs, that is a similar construct (*i.e.*, lipid coated magnetite nanoparticles), coated with lipooligosaccharides, which efficiently acts as adjuvants[195] for application in cancer vaccine field.

Enveloping a magnetic iron oxide core with a lipid shell facilitates bioconjugation, biocompatibility, and delivery, as well reported by Wang *et al.*[19]: in their work they provide a general solution for coating iron oxide and other metal oxides with a simple mixing in water, facilitating applications in biosensing, separation, and nanomedicine.

A multifunctional system for dual imaging (fluorescence and MRI) of hepatocellular carcinoma was reported by Liang *et al.*:[196] through the thin film hydration method, they covered magnetite NPs previously conjugated with a NIR fluorescent dye; the lipid bilayer was decorated with a polymer targeting tumour hepatocytes, able to steer the carrier to the specific site. By flow cytometry and confocal laser scanning microscopy they assessed the specific cellular uptake, followed by *in vivo* tests on tumor-bearing mice.

6. Conclusions

In this contribution we have reviewed the latest developments concerning the interaction of NPs with amphiphilic bilayers arranged in lamellar and non-lamellar mesophases.

This area is a very lively research field, where efforts are motivated by several scientific purposes. First of all, the application of nanostructured materials in the biomedical field requires a precise knowledge of the nano–bio-interface: bilayered synthetic assemblies are a very convenient and simple platform to elucidate the interactions with cell membranes and internalization of nanomedical devices. In addition, the design of smart nanostructured hybrid devices, where NPs are included in soft matter assemblies to contribute new properties and modulate their phase diagram is a very relevant and active research field. Related to this latter area is the use of lipid bilayers as coating shells for inorganic nanoparticles, to improve their biocompatibility and interaction with cell membranes.

In all cases, the mechanistic understanding of the main thermodynamic parameters involved in this interaction and their dependence on the physico-chemical features both of NPs and of the bilayers, are a necessary prerequisite to engineer soft matter hybrids and formulate NPs with potential applications in the biomedical field. Soft Matter science represents therefore the central discipline, whose scientific and methodological approaches will be more and more pivotal to contribute

meaningful progresses in this field. If the promises held by this approach will be fulfilled in the next decades, many of the current hurdles that nowadays hamper the full development of nanomedicine can be overcome.

Finally, a precise knowledge of the above-mentioned features allows engineering NPs to probe the properties of complex bilayer assemblies, both of natural and synthetic origin. This is a very exciting and promising area, where fundamental and applied efforts should be directed in the next decade.

Conflicts of interest

There are no conflicts to declare.

Acknowledgements

Costanza Montis acknowledges the European Union's Horizon 2020 programme (evFOUNDRY grant agreement 801367). All the authors thank CSGI for financial support.

References

1 C. Lu, Y. Liu, Y. Ying and J. Liu, *Langmuir*, 2017, **33**, 630–637.
2 P.-J. J. Huang, F. Wang and J. Liu, *Langmuir*, 2016, **32**, 2458–2463.
3 X. Wang, X. Li, H. Wang, X. Zhang, L. Zhang, F. Wang and J. Liu, *Langmuir*, 2019, **35**, 1672–1681.
4 F. Wang and J. Liu, *J. Am. Chem. Soc.*, 2015, **137**, 11736–11742.
5 F. Wang and J. Liu, *Nanoscale*, 2013, **5**, 12375.
6 Y. Liu and J. Liu, *Nanoscale*, 2017, **9**, 13187–13194.
7 V. C. Sanchez, A. Jachak, R. H. Hurt and A. B. Kane, *Chem. Res. Toxicol.*, 2012, **25**, 15–34.
8 R. Koole, M. M. van Schooneveld, J. Hilhorst, K. Castermans, D. P. Cormode, G. J. Strijkers, C. de Mello Donega, D. Vanmaekelbergh, A. W. Griffioen, K. Nicolay, Z. A. Fayad, A. Meijerink and W. J. M. Mulder, *Bioconjugate Chem.*, 2008, **19**, 2471–2479.
9 A. H. Bahrami, M. Raatz, J. Agudo-Canalejo, R. Michel, E. M. Curtis, C. K. Hall, M. Gradzielski, R. Lipowsky and T. R. Weikl, *Adv. Colloid Interface Sci.*, 2014, **208**, 214–224.
10 S. Dasgupta, T. Auth and G. Gompper, *J. Phys.: Condens. Matter*, 2017, **29**, 373003.
11 X. Chen, F. Tian, X. Zhang and W. Wang, *Soft Matter*, 2013, **9**, 7592.
12 Y. Roiter, M. Ornatska, A. R. Rammohan, J. Balakrishnan, D. R. Heine and S. Minko, *Nano Lett.*, 2008, **8**, 941–944.
13 C. Contini, M. Schneemilch, S. Gaisford and N. Quirke, *J. Exp. Nanosci.*, 2018, **13**, 62–81.
14 Q. Mu, G. Jiang, L. Chen, H. Zhou, D. Fourches, A. Tropsha and B. Yan, *Chem. Rev.*, 2014, **114**, 7740–7781.
15 S. Dasgupta, T. Auth and G. Gompper, *Nano Lett.*, 2014, **14**, 687–693.
16 A. H. Bahrami, *Soft Matter*, 2013, **9**, 8642.
17 F. Wang and J. Liu, *Nanoscale*, 2015, **7**, 15599–15604.
18 F. Wang, D. E. Curry and J. Liu, *Langmuir*, 2015, **31**, 13271–13274.
19 F. Wang, X. Zhang, Y. Liu, Z. Y. W. Lin, B. Liu and J. Liu, *Angew. Chem., Int. Ed.*, 2016, **55**, 12063–12067.
20 X. Liu, X. Li, W. Xu, X. Zhang, Z. Huang, F. Wang and J. Liu, *Langmuir*, 2018, **34**, 6628–6635.
21 J. Liu, *Langmuir*, 2016, **32**, 4393–4404.
22 T. Pfeiffer, A. De Nicola, C. Montis, F. Carlà, N. F. A. van der Vegt, D. Berti and G. Milano, *J. Phys. Chem. Lett.*, 2019, **10**, 129–137.
23 M. Schulz, A. Olubummo and W. H. Binder, *Soft Matter*, 2012, **8**, 4849.
24 C. F. Su, H. Merlitz, H. Rabbel and J. U. Sommer, *J. Phys. Chem. Lett.*, 2017, **8**, 4069–4076.
25 R. C. Van Lehn and A. Alexander-Katz, *Soft Matter*, 2014, **10**, 648–658.
26 M. Mendozza, C. Montis, L. Caselli, M. Wolf, P. Baglioni and D. Berti, *Nanoscale*, 2018, **10**, 3480–3488.
27 M. Mendozza, L. Caselli, C. Montis, S. Orazzini, E. Carretti, P. Baglioni and D. Berti, *J. Colloid Interface Sci.*, 2019, **541**, 329–338.
28 M. R. Preiss, A. Hart, C. Kitchens and G. D. Bothun, *J. Phys. Chem. B*, 2017, **121**, 5040–5047.
29 Y. Chen, A. Bose and G. D. Bothun, *ACS Nano*, 2010, **4**, 3215–3221.
30 G. Von White, Y. Chen, J. Roder-Hanna, G. D. Bothun and C. L. Kitchens, *ACS Nano*, 2012, **6**, 4678–4685.
31 G. D. Bothun, *J. Nanobiotechnol.*, 2008, **6**, 1–10.
32 Z. A. Almsherqi, T. Landh, S. D. Kohlwein and Y. Deng, in *International Review of Cell and Molecular Biology*, Elsevier Inc., 1st edn, 2009, vol. 274, pp. 275–342.
33 D. P. Chang, J. Barauskas, A. P. Dabkowska, M. Wadsäter, F. Tiberg and T. Nylander, *Adv. Colloid Interface Sci.*, 2015, **222**, 135–147.
34 W. K. Fong, R. Negrini, J. J. Vallooran, R. Mezzenga and B. J. Boyd, *J. Colloid Interface Sci.*, 2016, **484**, 320–339.
35 I. W. Hamley, *Angew. Chem.*, 2003, **115**, 1730–1752.
36 G. C. Shearman, O. Ces, R. H. Templer and J. M. Seddon, *J. Phys. Condens. Matter*, 2006, **18**, S1105–S1124.
37 C. M. Beddoes, C. P. Case and W. H. Briscoe, *Adv. Colloid Interface Sci.*, 2015, **218**, 48–68.
38 E. Venugopal, S. K. Bhat, J. J. Vallooran and R. Mezzenga, *Langmuir*, 2011, **27**, 9792–9800.
39 M. Szlezak, D. Nieciecka, A. Joniec, M. Pękała, E. Gorecka, M. Emo, M. J. Stébé, P. Krysiński and R. Bilewicz, *ACS Appl. Mater. Interfaces*, 2017, **9**, 2796–2805.
40 J. M. Bulpett, T. Snow, B. Quignon, C. M. Beddoes, T.-Y. D. Tang, S. Mann, O. Shebanova, C. L. Pizzey, N. J. Terrill, S. A. Davis and W. H. Briscoe, *Soft Matter*, 2015, **11**, 8789–8800.
41 C. M. Beddoes, J. Berge, J. E. Bartenstein, K. Lange, A. J. Smith, R. K. Heenan and W. H. Briscoe, *Soft Matter*, 2016, **12**, 6049–6057.
42 C. Montis, B. Castroflorio, M. Mendozza, A. Salvatore, D. Berti and P. Baglioni, *J. Colloid Interface Sci.*, 2015, **449**, 317–326.
43 K. L. Chen and G. D. Bothun, *Environ. Sci. Technol.*, 2014, **48**, 873–880.

44 M. Henriksen-Lacey, S. Carregal-Romero and L. M. Liz-Marzán, *Bioconjugate Chem.*, 2017, **28**, 212–221.
45 E. Rascol, J.-M. Devoisselle and J. Chopineau, *Nanoscale*, 2016, **8**, 4780–4798.
46 E. Blanco, H. Shen and M. Ferrari, *Nat. Biotechnol.*, 2015, **33**, 941–951.
47 P. Falagan-Lotsch, E. M. Grzincic and C. J. Murphy, *Proc. Natl. Acad. Sci. U. S. A.*, 2016, **113**, 13318–13323.
48 C. J. Murphy, A. M. Vartanian, F. M. Geiger, R. J. Hamers, J. Pedersen, Q. Cui, C. L. Haynes, E. E. Carlson, R. Hernandez, R. D. Klaper, G. Orr and Z. Rosenzweig, *ACS Cent. Sci.*, 2015, **1**, 117–123.
49 L. J. Fox, R. M. Richardson and W. H. Briscoe, *Adv. Colloid Interface Sci.*, 2018, **257**, 1–18.
50 S. Wilhelm, A. J. Tavares, Q. Dai, S. Ohta, J. Audet, H. F. Dvorak and W. C. W. Chan, *Nat. Rev. Mater.*, 2016, **1**, 16014.
51 D. Bobo, K. J. Robinson, J. Islam, K. J. Thurecht and S. R. Corrie, *Pharm. Res.*, 2016, **33**, 2373–2387.
52 Y. H. Choi and H. K. Han, *J. Pharm. Investig.*, 2018, **48**, 43–60.
53 J. M. Caster, A. N. Patel, T. Zhang and A. Wang, *Wiley Interdiscip. Rev.: Nanomed. Nanobiotechnol.*, 2017, **9**, e1416.
54 C. D. Walkey and W. C. W. Chan, *Chem. Soc. Rev.*, 2012, **41**, 2780–2799.
55 A. E. Nel, L. Mädler, D. Velegol, T. Xia, E. M. V. Hoek, P. Somasundaran, F. Klaessig, V. Castranova and M. Thompson, *Nat. Mater.*, 2009, **8**, 543–557.
56 S. Zhang, H. Gao and G. Bao, *ACS Nano*, 2015, **9**, 8655–8671.
57 N. S. Bhise, J. Ribas, V. Manoharan, Y. S. Zhang, A. Polini, S. Massa, M. R. Dokmeci and A. Khademhosseini, *J. Controlled Release*, 2014, **190**, 82–93.
58 G. Rossi and L. Monticelli, *Biochim. Biophys. Acta, Biomembr.*, 2016, **1858**, 2380–2389.
59 V. Pillay, K. Murugan, Y. E. Choonara, P. Kumar, D. Bijukumar and L. C. du Toit, *Int. J. Nanomed.*, 2015, **10**, 2191.
60 I. Canton and G. Battaglia, *Chem. Soc. Rev.*, 2012, **41**, 2718.
61 M. Calero, L. Gutiérrez, G. Salas, Y. Luengo, A. Lázaro, P. Acedo, M. P. Morales, R. Miranda and A. Villanueva, *Nanomedicine*, 2014, **10**, 733–743.
62 S. Behzadi, V. Serpooshan, W. Tao, M. A. Hamaly, M. Y. Alkawareek, E. C. Dreaden, D. Brown, A. M. Alkilany, O. C. Farokhzad and M. Mahmoudi, *Chem. Soc. Rev.*, 2017, **46**, 4218–4244.
63 Y. Jiang, S. Huo, T. Mizuhara, R. Das, Y. W. Lee, S. Hou, D. F. Moyano, B. Duncan, X. J. Liang and V. M. Rotello, *ACS Nano*, 2015, **9**, 9986–9993.
64 K. A. Dawson, A. Lesniak, F. Fenaroli, M. P. Monopoli, A. Christoffer and A. Salvati, *ACS Nano*, 2012, 5845–5857.
65 J. Blechinger, A. T. Bauer, A. A. Torrano, C. Gorzelanny, C. Bräuchle and S. W. Schneider, *Small*, 2013, **9**, 3970–3980.
66 S. Tatur, M. MacCarini, R. Barker, A. Nelson and G. Fragneto, *Langmuir*, 2013, **29**, 6606–6614.
67 C. Montis, V. Generini, G. Boccalini, P. Bergese, D. Bani and D. Berti, *J. Colloid Interface Sci.*, 2018, **516**, 284–294.
68 E. Fröhlich, *Int. J. Nanomed.*, 2012, **7**, 5577–5591.
69 J. A. Yang, S. E. Lohse and C. J. Murphy, *Small*, 2014, **10**, 1642–1651.
70 E. Lee, H. Jeon, M. Lee, J. Ryu, C. Kang, S. Kim, J. Jung and Y. Kwon, *Sci. Rep.*, 2019, **9**, 2494.
71 Y. C. Park, J. B. Smith, T. Pham, R. D. Whitaker, C. A. Sucato, J. A. Hamilton, E. Bartolak-Suki and J. Y. Wong, *Colloids Surf., B*, 2014, **119**, 106–114.
72 J. Lin, H. Zhang, V. Morovati and R. Dargazany, *J. Colloid Interface Sci.*, 2017, **504**, 325–333.
73 K. P. García, K. Zarschler, L. Barbaro, J. A. Barreto, W. O'Malley, L. Spiccia, H. Stephan and B. Graham, *Small*, 2014, **10**, 2516–2529.
74 L. Zhang, H. Xue, C. Gao, L. Carr, J. Wang, B. Chu and S. Jiang, *Biomaterials*, 2010, **31**, 6582–6588.
75 N. Gal, A. Lassenberger, L. Herrero-Nogareda, A. Scheberl, V. Charwat, C. Kasper and E. Reimhult, *ACS Biomater. Sci. Eng.*, 2017, **3**, 249–259.
76 E. Giovanelli, E. Muro, G. Sitbon, M. Hanafi, T. Pons, B. Dubertret and N. Lequeux, *Langmuir*, 2012, **28**, 15177–15184.
77 K. Kaaki, K. Hervé-Aubert, M. Chiper, A. Shkilnyy, M. Soucé, R. Benoit, A. Paillard, P. Dubois, M. L. Saboungi and I. Chourpa, *Langmuir*, 2012, **28**, 1496–1505.
78 A. Krais, L. Wortmann, L. Hermanns, N. Feliu, M. Vahter, S. Stucky, S. Mathur and B. Fadeel, *Nanomedicine*, 2014, **10**, 1421–1431.
79 X. Wang, X. Wang, X. Bai, L. Yan, T. Liu, M. Wang, Y. Song, G. Hu, Z. Gu, Q. Miao and C. Chen, *Nano Lett.*, 2019, **19**, 8–18.
80 P. Vedantam, G. Huang and T. R. J. Tzeng, *Cancer Nanotechnol.*, 2013, **4**, 13–20.
81 B. Pelaz, G. Charron, C. Pfeiffer, Y. Zhao, J. M. De La Fuente, X. J. Liang, W. J. Parak and P. Del Pino, *Small*, 2013, **9**, 1573–1584.
82 M. P. Monopoli, D. Walczyk, A. Campbell, G. Elia, I. Lynch, F. Baldelli Bombelli and K. A. Dawson, *J. Am. Chem. Soc.*, 2011, **133**, 2525–2534.
83 F. Bertoli, D. Garry, M. P. Monopoli, A. Salvati and K. A. Dawson, *ACS Nano*, 2016, **10**, 10471–10479.
84 S. Milani, F. Baldelli Bombelli, A. S. Pitek, K. A. Dawson and J. Rädler, *ACS Nano*, 2012, **6**, 2532–2541.
85 G. Caracciolo, O. C. Farokhzad and M. Mahmoudi, *Trends Biotechnol.*, 2017, **35**, 257–264.
86 A. Lesniak, A. Salvati, M. J. Santos-Martinez, M. W. Radomski, K. A. Dawson and C. Åberg, *J. Am. Chem. Soc.*, 2013, **135**, 1438–1444.
87 D. Hühn, K. Kantner, C. Geidel, S. Brandholt, I. De Cock, S. J. H. Soenen, P. Riveragil, J. M. Montenegro, K. Braeckmans, K. Müllen, G. U. Nienhaus, M. Klapper and W. J. Parak, *ACS Nano*, 2013, **7**, 3253–3263.
88 W. Lin, T. Insley, M. D. Tuttle, L. Zhu, D. A. Berthold, P. Král, C. M. Rienstra and C. J. Murphy, *J. Phys. Chem. C*, 2015, **119**, 21035–21043.
89 C. C. Fleischer and C. K. Payne, *Acc. Chem. Res.*, 2014, **47**, 2651–2659.
90 F. Wang, L. Yu, M. P. Monopoli, P. Sandin, E. Mahon, A. Salvati and K. A. Dawson, *Nanomedicine*, 2013, **9**, 1159–1168.

91 L. Treuel, S. Brandholt, P. Maffre, S. Wiegele, L. Shang and G. U. Nienhaus, *ACS Nano*, 2014, **8**, 503–513.
92 S. Fogli, C. Montis, S. Paccosi, A. Silvano, E. Michelucci, D. Berti, A. Bosi, A. Parenti and P. Romagnoli, *Nanomedicine*, 2017, **12**, 1647–1660.
93 R. P. Carney, T. M. Carney, M. Mueller and F. Stellacci, *Biointerphases*, 2012, **7**, 17.
94 F. Simonelli, D. Bochicchio, R. Ferrando and G. Rossi, *J. Phys. Chem. Lett.*, 2015, **6**, 3175–3179.
95 S. Li and N. Malmstadt, *Soft Matter*, 2013, **9**, 4969.
96 A. M. Farnoud and S. Nazemidashtarjandi, *Environ. Sci.: Nano*, 2019, **6**, 13–40.
97 A. Šarić and A. Cacciuto, *Soft Matter*, 2013, **9**, 6677–6695.
98 K. Jaskiewicz, A. Larsen, D. Schaeffel, K. Koynov, I. Lieberwirth, G. Fytas, K. Landfester and A. Kroeger, *ACS Nano*, 2012, **6**, 7254–7262.
99 A. Šarić and A. Cacciuto, *Phys. Rev. Lett.*, 2012, **108**, 118101.
100 H. Zhang, Q. Ji, C. Huang, S. Zhang, B. Yuan, K. Yang and Y. Q. Ma, *Sci. Rep.*, 2015, **5**, 10525.
101 M. Raatz, R. Lipowsky and T. R. Weikl, *Soft Matter*, 2014, **10**, 3570–3577.
102 A. H. Bahrami, R. Lipowsky and T. R. Weikl, *Phys. Rev. Lett.*, 2012, **109**, 188102.
103 N. D. Burrows, A. M. Vartanian, N. S. Abadeer, E. M. Grzincic, L. M. Jacob, W. Lin, J. Li, J. M. Dennison, J. G. Hinman and C. J. Murphy, *J. Phys. Chem. Lett.*, 2016, **7**, 632–641.
104 S. Nangia and R. Sureshkumar, *Langmuir*, 2012, **28**, 17666–17671.
105 R. Vácha, F. J. Martinez-Veracoechea and D. Frenkel, *Nano Lett.*, 2011, **11**, 5391–5395.
106 Y. Qiu, Y. Liu, L. Wang, L. Xu, R. Bai, Y. Ji, X. Wu, Y. Zhao, Y. Li and C. Chen, *Biomaterials*, 2010, **31**, 7606–7619.
107 A. Espinosa, A. K. A. Silva, A. Sánchez-Iglesias, M. Grzelczak, C. Péchoux, K. Desboeufs, L. M. Liz-Marzán and C. Wilhelm, *Adv. Healthcare Mater.*, 2016, **5**, 1040–1048.
108 H. I. Ingólfsson, M. N. Melo, F. J. Van Eerden, C. Arnarez, C. A. Lopez, T. A. Wassenaar, X. Periole, A. H. De Vries, D. P. Tieleman and S. J. Marrink, *J. Am. Chem. Soc.*, 2014, **136**, 14554–14559.
109 T. Lunnoo, J. Assawakhajornsak and T. Puangmali, *J. Phys. Chem. C*, 2019, **123**, 3801–3810.
110 M. Laurencin, T. Georgelin, B. Malezieux, J. M. Siaugue and C. Ménager, *Langmuir*, 2010, **26**, 16025–16030.
111 B. Wang, L. Zhang, S. C. Bae and S. Granick, *Proc. Natl. Acad. Sci. U. S. A.*, 2008, **105**, 18171–18175.
112 G. D. Bothun, N. Ganji, I. A. Khan, A. Xi and C. Bobba, *Langmuir*, 2017, **33**, 353–360.
113 T. Róg, M. Pasenkiewicz-Gierula, I. Vattulainen and M. Karttunen, *Biochim. Biophys. Acta, Biomembr.*, 2009, **1788**, 97–121.
114 E. S. Melby, A. C. Mensch, S. E. Lohse, D. Hu, G. Orr, C. J. Murphy, R. J. Hamers and J. A. Pedersen, *Environ. Sci. Nano*, 2016, **3**, 45–55.
115 D. Hartono, Hody, K.-L. Yang and L.-Y. Lanry Yung, *Biomaterials*, 2010, **31**, 3008–3015.
116 F. Lolicato, L. Joly, H. Martinez-Seara, G. Fragneto, E. Scoppola, F. Baldelli Bombelli, I. Vattulainen, J. Akola and M. Maccarini, *Small*, 2019, **15**, 1805046.
117 R. Michel, E. Kesselman, T. Plostica, D. Danino and M. Gradzielski, *Angew. Chem., Int. Ed.*, 2014, **53**, 12266.
118 S. Zhang, A. Nelson and P. A. Beales, *Langmuir*, 2012, **28**, 12831–12837.
119 S. Chakraborty, A. Abbasi, G. D. Bothun, M. Nagao and C. L. Kitchens, *Langmuir*, 2018, **34**, 13416–13425.
120 C. Montis, A. Zendrini, F. Valle, S. Busatto, L. Paolini, A. Radeghieri, A. Salvatore, D. Berti and P. Bergese, *Colloids Surfaces B Biointerfaces*, 2017, **158**, 331–338.
121 C. Montis, D. Maiolo, I. Alessandri, P. Bergese and D. Berti, *Nanoscale*, 2014, **6**, 6452–6457.
122 J. C. Black, P. P. Cheney, T. Campbell and M. K. Knowles, *Soft Matter*, 2014, **10**, 2016–2023.
123 Y. Liu, R. Medda, Z. Liu, K. Galior, K. Yehl, J. P. Spatz, E. A. Cavalcanti-Adam and K. Salaita, *Nano Lett.*, 2014, **14**, 5539–5546.
124 G. H. Zan, J. A. Jackman, S.-O. Kim and N.-J. Cho, *Small*, 2014, **10**, 4828–4832.
125 O. Limaj, D. Etezadi, N. J. Wittenberg, D. Rodrigo, D. Yoo, S. H. Oh and H. Altug, *Nano Lett.*, 2016, **16**, 1502–1508.
126 K. Suga, T. Yoshida, H. Ishii, Y. Okamoto, D. Nagao, M. Konno and H. Umakoshi, *Anal. Chem.*, 2015, **87**, 4772–4780.
127 D. Bhowmik, K. R. Mote, C. M. MacLaughlin, N. Biswas, B. Chandra, J. K. Basu, G. C. Walker, P. K. Madhu and S. Maiti, *ACS Nano*, 2015, **9**, 9070–9077.
128 K. Sugikawa, T. Kadota, K. Yasuhara and A. Ikeda, *Angew. Chem., Int. Ed.*, 2016, **55**, 4059–4063.
129 C. Montis, S. Busatto, F. Valle, A. Zendrini, A. Salvatore, Y. Gerelli, D. Berti and P. Bergese, *Adv. Biosyst.*, 2018, **2**, 1700200.
130 D. Maiolo, L. Paolini, G. Di Noto, A. Zendrini, D. Berti, P. Bergese and D. Ricotta, *Anal. Chem.*, 2015, **87**, 4168–4176.
131 S. Busatto, A. Giacomini, C. Montis, R. Ronca and P. Bergese, *Anal. Chem.*, 2018, **90**, 7855–7861.
132 A. Mallardi, N. Nuzziello, M. Liguori, C. Avolio and G. Palazzo, *Colloids Surf., B*, 2018, **168**, 134–142.
133 J. Zhai, C. Fong, N. Tran and C. J. Drummond, *ACS Nano*, 2019, **13**, 6178–6206.
134 R. Mezzenga, J. M. Seddon, C. J. Drummond, B. J. Boyd, G. E. Schröder-Turk and L. Sagalowicz, *Adv. Mater.*, 2019, 1900818.
135 H. M. G. Barriga, M. N. Holme and M. M. Stevens, *Angew. Chem., Int. Ed.*, 2019, **58**, 2958–2978.
136 A. Salvatore, C. Montis, D. Berti and P. Baglioni, *ACS Nano*, 2016, **10**, 7749–7760.
137 O. Bixner and E. Reimhult, *J. Colloid Interface Sci.*, 2016, **466**, 62–71.
138 R. Martínez-González, J. Estelrich and M. A. Busquets, *Int. J. Mol. Sci.*, 2016, **17**, 1–14.
139 B. Drasler, P. Budime Santhosh, D. Drobne, M. Erdani Kreft, S. Kralj, D. Makovec and N. Poklar Ulrih, *Int. J. Nanomed.*, 2015, **10**, 6089.

140 S. Saesoo, S. Sathornsumetee, P. Anekwiang, C. Treetidnipa, P. Thuwajit, S. Bunthot, W. Maneeprakorn, L. Maurizi, H. Hofmann, R. U. Rungsardthong and N. Saengkrit, *Colloids Surf., B*, 2018, **161**, 497–507.
141 E. Amstad, J. Kohlbrecher, E. Müller, T. Schweizer, M. Textor and E. Reimhult, *Nano Lett.*, 2011, **11**, 1664–1670.
142 S. Nappini, S. Fogli, B. Castroflorio, M. Bonini, F. Baldelli Bombelli and P. Baglioni, *J. Mater. Chem. B*, 2016, **4**, 716–725.
143 J. Haša, J. Hanuš and F. Štěpánek, *ACS Appl. Mater. Interfaces*, 2018, **10**, 20306–20314.
144 P. Pradhan, J. Giri, F. Rieken, C. Koch, O. Mykhaylyk, M. Döblinger, R. Banerjee, D. Bahadur and C. Plank, *J. Controlled Release*, 2010, **142**, 108–121.
145 R. Di Corato, G. Béalle, J. Kolosnjaj-Tabi, A. Espinosa, O. Clément, A. K. A. Silva, C. Ménager and C. Wilhelm, *ACS Nano*, 2015, **9**, 2904–2916.
146 A. K. Rengan, A. B. Bukhari, A. Pradhan, R. Malhotra, R. Banerjee, R. Srivastava and A. De, *Nano Lett.*, 2015, **15**, 842–848.
147 A. Tomitaka, H. Arami, Z. Huang, A. Raymond, E. Rodriguez, Y. Cai, M. Febo, Y. Takemura and M. Nair, *Nanoscale*, 2018, **10**, 184–194.
148 M. E. Khosroshahi, L. Ghazanfari, Z. Hassannejad and S. Lenhert, *J. Nanomed. Nanotechnol.*, 2015, **6**, 298.
149 R. B. Lira, M. A. B. L. Seabra, A. L. L. Matos, J. V. Vasconcelos, D. P. Bezerra, E. De Paula, B. S. Santos and A. Fontes, *J. Mater. Chem. B*, 2013, **1**, 4297–4305.
150 M. Wlodek, M. Kolasinska-Sojka, M. Szuwarzynski, S. Kereïche, L. Kovacik, L. Zhou, L. Islas, P. Warszynski and W. H. Briscoe, *Nanoscale*, 2018, **10**, 17965–17974.
151 J. B. Marlow, M. J. Pottage, T. M. McCoy, L. De Campo, A. Sokolova, T. D. M. Bell and R. F. Tabor, *Phys. Chem. Chem. Phys.*, 2018, **20**, 16592–16603.
152 J. J. Vallooran, R. Negrini and R. Mezzenga, *Langmuir*, 2013, **29**, 999–1004.
153 J. J. Vallooran, S. Handschin, S. Bolisetty and R. Mezzenga, *Langmuir*, 2012, **28**, 5589–5595.
154 J. J. Vallooran, S. Bolisetty and R. Mezzenga, *Adv. Mater.*, 2011, **23**, 3932–3937.
155 W. K. Fong, T. L. Hanley, B. Thierry, A. Tilley, N. Kirby, L. J. Waddington and B. J. Boyd, *Phys. Chem. Chem. Phys.*, 2014, **16**, 24936–24953.
156 W. K. Fong, T. L. Hanley, B. Thierry, N. Kirby, L. J. Waddington and B. J. Boyd, *Langmuir*, 2012, **28**, 14450–14460.
157 S. M. Moghimi, A. C. Hunter and T. L. Andresen, *Annu. Rev. Pharmacol. Toxicol.*, 2011, **52**, 481–503.
158 S. Mitragotri and J. Lahann, *Adv. Mater.*, 2012, **24**, 3717–3723.
159 W. H. De Jong, W. I. Hagens, P. Krystek, M. C. Burger, A. J. A. M. Sips and R. E. Geertsma, *Biomaterials*, 2008, **29**, 1912–1919.
160 P. Aggarwal, J. B. Hall, C. B. McLeland, M. A. Dobrovolskaia and S. E. McNeil, *Adv. Drug Delivery Rev.*, 2009, **61**, 428–437.
161 T. A. Wynn, A. Chawla and J. W. Pollard, *Nature*, 2013, **496**, 445–455.
162 B. Illes, P. Hirschle, S. Barnert, V. Cauda, S. Wuttke and H. Engelke, *Chem. Mater.*, 2017, **29**, 8042–8046.
163 K. Raemdonck, K. Braeckmans, J. Demeester and S. C. De Smedt, *Chem. Soc. Rev.*, 2014, **43**, 444–472.
164 A. Luchini and G. Vitiello, *Front. Chem.*, 2019, **7**, 1–16.
165 M. E. Davis, Z. Chen and D. M. Shin, *Nat. Rev. Drug Discovery*, 2008, **7**, 771–782.
166 N. Kamaly, Z. Xiao, P. M. Valencia, A. F. Radovic-Moreno and O. C. Farokhzad, *Chem. Soc. Rev.*, 2012, **41**, 2971.
167 Z. Shen, H. Ye, M. Kröger and Y. Li, *Phys. Chem. Chem. Phys.*, 2017, **19**, 13294–13306.
168 A. Luchini, R. K. Heenan, L. Paduano and G. Vitiello, *Phys. Chem. Chem. Phys.*, 2016, **18**, 18441–18449.
169 T. M. Allen and P. R. Cullis, *Adv. Drug Delivery Rev.*, 2013, **65**, 36–48.
170 E. Terreno, F. Uggeri and S. Aime, *J. Controlled Release*, 2012, **161**, 328–337.
171 R. Rapuano and A. M. Carmona-Ribeiro, *J. Colloid Interface Sci.*, 1997, **193**, 104–111.
172 R. Rapuano and A. M. Carmona-Ribeiro, *J. Colloid Interface Sci.*, 2000, **226**, 299–307.
173 A. L. Troutier and C. Ladavière, *Adv. Colloid Interface Sci.*, 2007, **133**, 1–21.
174 F. Mousseau, C. Puisney, S. Mornet, R. Le Borgne, A. Vacher, M. Airiau, A. Baeza-Squiban and J. F. Berret, *Nanoscale*, 2017, **9**, 14967–14978.
175 L. M. Rossi, P. R. Silva, L. L. R. Vono, A. U. Fernandes, D. B. Tada and M. S. Baptista, *Langmuir*, 2008, **24**, 12534–12538.
176 D. B. Tada, E. Suraniti, L. M. Rossi, C. A. P. Leite, C. S. Oliveira, T. C. Tumolo, R. Calemczuk, T. Livache and M. S. Baptista, *J. Biomed. Nanotechnol.*, 2014, **10**, 519–528.
177 S. A. Mackowiak, A. Schmidt, V. Weiss, C. Argyo, C. Von Schirnding, T. Bein and C. Bräuchle, *Nano Lett.*, 2013, **13**, 2576–2583.
178 Q. Zhang, X. Chen, H. Shi, G. Dong, M. Zhou, T. Wang and H. Xin, *Colloids Surf., B*, 2017, **160**, 527–534.
179 S. Chernousova and M. Epple, *Angew. Chem., Int. Ed.*, 2013, **52**, 1636–1653.
180 R. R. Arvizo, S. Bhattacharyya, R. A. Kudgus, K. Giri, R. Bhattacharya and P. Mukherjee, *Chem. Soc. Rev.*, 2012, **41**, 2943.
181 L. Cheng, M. D. Weir, H. H. K. Xu, J. M. Antonucci, N. J. Lin, S. Lin-Gibson, S. M. Xu and X. Zhou, *J. Biomed. Mater. Res., Part B*, 2012, **100**, 1378–1386.
182 B. Du, L. Tian, X. Gu, D. Li, E. Wang and J. Wang, *Small*, 2015, **11**, 2333–2340.
183 C. G. England, A. M. Gobin and H. B. Frieboes, *Eur. Phys. J. Plus*, 2015, **130**, 231.
184 H. Frieboes, C. England, T. Priest, G. Zhang, X. Sun, D. Patel, L. McNally, V. van Berkel and A. Gobin, *Int. J. Nanomed.*, 2013, 3603.
185 D. J. Hamilton, M. D. Coffman, J. D. Knight and S. M. Reed, *Langmuir*, 2017, **33**, 9222–9230.
186 P. Wang, L. Zhang, W. Zheng, L. Cong, Z. Guo, Y. Xie, L. Wang, R. Tang, Q. Feng, Y. Hamada, K. Gonda, Z. Hu,

X. Wu and X. Jiang, *Angew. Chem., Int. Ed.*, 2018, **57**, 1491–1496.
187 R. Liang, J. Xie, J. Li, K. Wang, L. Liu, Y. Gao, M. Hussain, G. Shen, J. Zhu and J. Tao, *Biomaterials*, 2017, **149**, 41–50.
188 B. K. Poudel, B. Gupta, T. Ramasamy, R. K. Thapa, S. Pathak, K. T. Oh, J. H. Jeong, H. G. Choi, C. S. Yong and J. O. Kim, *Colloids Surf., B*, 2017, **160**, 73–83.
189 C. J. Orendorff, T. M. Alam, D. Y. Sasaki, B. C. Bunker and J. A. Voigt, *ACS Nano*, 2009, **3**, 971–983.
190 P. B. Santhosh, N. Thomas, S. Sudhakar, A. Chadha and E. Mani, *Phys. Chem. Chem. Phys.*, 2017, **19**, 18494–18504.
191 E. T. Castellana, R. C. Gamez and D. H. Russell, *J. Am. Chem. Soc.*, 2011, **133**, 4182–4185.
192 X. Cui, W. Cheng and X. Han, *J. Mater. Chem. B*, 2018, **6**, 8078–8084.
193 Y. Ma, S. Tong, G. Bao, C. Gao and Z. Dai, *Biomaterials*, 2013, **34**, 7706–7714.
194 A. Ruiz-De-Angulo, A. Zabaleta, V. Gómez-Vallejo, J. Llop and J. C. Mareque-Rivas, *ACS Nano*, 2016, **10**, 1602–1618.
195 G. Traini, A. Ruiz-de-Angulo, J. B. Blanco-Canosa, K. Zamacola Bascarán, A. Molinaro, A. Silipo, D. Escors and J. C. Mareque-Rivas, *Small*, 2019, **15**, 1803993.
196 J. Liang, X. Zhang, Y. Miao, J. Li and Y. Gan, *Int. J. Nanomed.*, 2017, **12**, 2033–2044.
197 A. Torchi, F. Simonelli, R. Ferrando and G. Rossi, *ACS Nano*, 2017, **11**, 12553–12561.

Paper II

Shedding light on membrane-templated clustering of gold nanoparticles

C. Montis*, L. Caselli*, F. Valle, A. Zendrini, F. Carlà, R. Schweins, M. Maccarini, P.Bergese and D. Berti, *Journal of Colloids and Interface Science*, 2020, 573, 204-214 (* equally contributed)

Journal of Colloid and Interface Science 573 (2020) 204–214

Contents lists available at ScienceDirect

Journal of Colloid and Interface Science

journal homepage: www.elsevier.com/locate/jcis

Shedding light on membrane-templated clustering of gold nanoparticles ☆

Costanza Montis [a,1], Lucrezia Caselli [a,1], Francesco Valle [b], Andrea Zendrini [c], Francesco Carlà [d], Ralf Schweins [e], Marco Maccarini [f], Paolo Bergese [c,*], Debora Berti [a,*]

[a] Department of Chemistry and CSGI, University of Florence via della Lastruccia3, 50019 Florence Italy
[b] ISMN-CNR and CSGI via Gobetti 101 40129 Bologna Italy
[c] Department of Molecular and Translational Medicine, University of Brescia, Viale Europa 11, 25123 Brescia, Italy
[d] ESRF, The European Synchrotron, Grenoble France
[e] Institut Laue-Langevin, DS/LSS, 71 Avenue des Martyrs, CS 20156, F-38042 Grenoble CEDEX 9, France
[f] Univ. Grenoble Alpes, CNRS, TIMC-IMAG-SyNaBi (UMR 5525), 38000 Grenoble, France

GRAPHICAL ABSTRACT

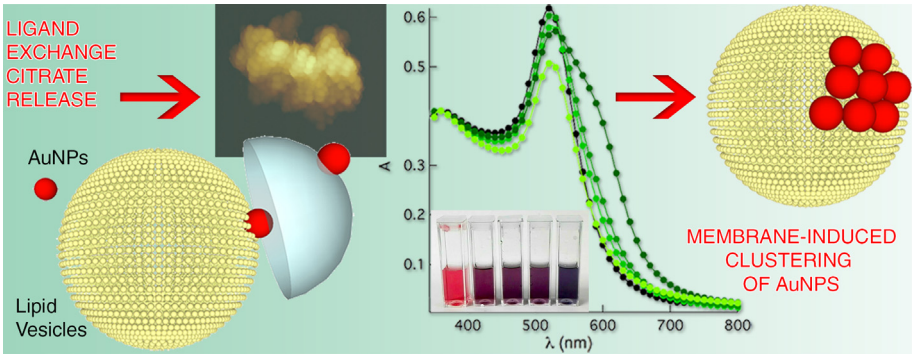

ARTICLE INFO

Article history:
Received 19 December 2019
Revised 30 March 2020
Accepted 31 March 2020
Available online 1 April 2020

Keywords:
Gold nanoparticles
Lipid bilayers
Surface plasmon resonance
Membranes
Nano-Bio interface

ABSTRACT

The use of inorganic nanoparticles in biomedical and biotechnological applications requires a molecular-level understanding of interactions at nano-bio interfaces, such as cell membranes. Several recent reports have shown that gold nanoparticles (AuNP), in the presence of fluid lipid bilayers, aggregate at the lipid/aqueous interface, but the precise origin of this phenomenon is still not fully understood. Here, by challenging synthetic lipid membranes with one of the most typical classes of nanomaterials, citrate-coated AuNP, we addressed the cooperative nature of their interaction at the interface, which leads to AuNP clustering. The ensemble of optical (UV–Vis absorbance), structural (small-angle neutron and X-ray scattering) and surface (X-ray reflectivity, quartz crystal microbalance, atomic force microscopy) results, is consistent with a mechanistic hypothesis, where the citrate-lipid ligand exchange at the interface is the molecular origin of a multiscale cooperative behavior, which ultimately leads to the formation of clusters of AuNP on the bilayer. This mechanism, fully consistent with the data reported so far in the literature for synthetic bilayers, would shed new light on the interaction of engineered nanomaterials with biological membranes. The cooperative nature of ligand exchange at the AuNP-liposome interface, pivotal

☆ All authors have given approval to the final version of the manuscript.
* Corresponding authors.
E-mail addresses: paolo.bergese@unibs.it (P. Bergese), debora.berti@unifi.it (D. Berti).
[1] CM and LC contributed equally to this work.

https://doi.org/10.1016/j.jcis.2020.03.123

in determining clustering of AuNP, will have relevant implications for NP use in Nanomedicine, since NP will be internalized in cells as clusters, rather than as primary NP, with dramatic effects on their bioactivity.

1. Introduction

Understanding the behavior of nanomaterials in biological environments is a longstanding research challenge, necessary to fully harness the medical potential of nanomaterials and rationally assess their cytotoxicity [1–3]. In particular, interactions at the nano-bio interface are recognized as pivotal steps to determine the fate of nanostructured materials in living systems [4–7]. In this respect, the study of interactions of nanomaterials with synthetic lipid membranes can contribute robust fundamental knowledge and help identifying some of the main factors implied in the behavior in biological systems [6–9].

Turkevich-Frens gold nanoparticles coated with a layer of citrate anions (AuNP) are one of the most studied and explored class of inorganic nanoparticles for biomedical applications. Upon incubation with lipid membranes, they can exhibit an intriguing behavior: the presence of lipid vesicles affects the optical properties of the AuNP, displayed as a shift of the surface plasmon resonance, with a marked color variation of the dispersion [10–14]. This effect, a clear signature of membrane-templated clustering of AuNP [13,15], is relevant both from a fundamental and from an applicative perspective. The clustering of NP is a relevant feature that determines their cell internalization pathway [4,16]; moreover, some technological applications of this membrane-induced aggregation are already in use, like in a recently developed analytical assay to estimate the purity and concentration of extracellular vesicles [17].

Despite the number of studies on citrated AuNP and the fundamental and applicative implications of their clustering, occurring in the presence of natural and synthetic lipid membranes, this phenomenon has started to be addressed only recently [12,13,18]. These investigations have provided evidence that AuNP aggregation on lipid membranes eventually leads to the formation of an AuNP crust on the target membrane [13] and that the clustering extent depends on membrane fluidity [10,14] and nature of the coating agent [12]. However, a thorough mechanistic understanding of the phenomenon, which reconciles the experimental observations reported so far, is still lacking.

In this study we present a comprehensive investigation of the interaction of AuNP with synthetic free-standing and supported bilayers composed of POPC (1-palmitoyl-2-oleoyl-*glycero*-3-phosphocholine), which results in AuNP clustering. Combining optical (UV–Vis absorbance), structural (small-angle neutron and X-ray scattering) and surface (X-ray reflectivity, quartz crystal microbalance, atomic force microscopy) techniques, we disentangle the main probabilistic, kinetic and thermodynamic contributions. In addition, based on the ensemble of experimental results here presented, we propose an original hypothesis on the molecular mechanism of the bilayer-driven clustering, whose key step is identified as the POPC-citrate ligand exchange.

2. Materials and methods

2.1. Materials

Tetrachloroauric (III) acid (≥99.9%), trisodium citrate dihydrate (≥99.9%), MeOH (99.8%), $CHCl_3$ (≥99.9%), NaCl (≥99.5%), $CaCl_2$ (99.999%) and D_2O (99 atom % D) were provided by Sigma-Aldrich (St. Louis, MO). The same for 1-palmitoyl-2-oleoyl-*sn-glycero*-3-phosphocholine (POPC) (≥98.0%), tannic acid (99.8%) and 3-mercaptopropionic acid (MPA) (99.0%). All chemicals were used as received. Milli-Q grade water was used in all preparations.

2.2. Synthesis of AuNP

Citrated gold nanospheres of 16 nm diameter were synthesized according to the classical Turkevich-Frens protocol [19,20], whose details are reported in the SI (page S2 of Supplementary Materials and Methods section). To obtain 16 nm MPA-capped AuNP the following method was adopted: 500 μL of an aqueous solution of 3-mercaptopropionic acid (5×10^{-3} M) were added to 5 mL of freshly prepared 16 nm-citrated AuNP ($7.8 \cdot 10^{-9}$ M). The mixture was stirred for 30 s and left at 4 °C overnight. To obtain smaller citrated NP (5 nm diameter), a slightly different procedure was adopted, with addition of tannic acid traces to the inverse Turkevich method [21]. Briefly, 1 mL of $HAuCl_4$ aqueous solution (25 mM) was injected into 150 mL of sodium citrate aqueous solution (2.2 mM), mixed with 0.1 mL of tannic acid (2.5 mM). The addition was carried out at 70 °C under vigorous magnetic stirring and led to the instantaneous color change of the solution from transparent to dark grey. After few minutes, the solution turned orange, indicative of the formation of sub-10 nm gold nanoparticles. The nanoparticles solution was then slowly cooled down to room temperature.

2.3. Preparation of POPC vesicles and supported lipid bilayers (SLB)

For POPC liposomes preparation, a standard method of dry film rehydration was adopted, followed by freeze–thaw cycles and extrusion (see page S3 of SI for details). For SLBs formation a similar procedure was adopted: briefly, a dry lipid film of POPC was suspended in warm (50 °C) aqueous solution containing 100 mM NaCl by vigorous vortex mixing and then tip-sonicated for 30 min. SLBs were prepared by adding 10 mM $CaCl_2$ to the vesicles' dispersion and subsequently depositing a droplet of the vesicles' dispersion on a silicon wafer previously polished and activated in a plasma cleaner. A stable SLB layered on the support was obtained by rinsing the vesicles' dispersion with pure milliQ water, after incubation of the vesicles with the support for twenty minutes at room temperature. Further details are reported in the SI (page S3).

2.4. Small angle X-ray scattering

SAXS measurements were carried out on a S3-MICRO SAXS/WAXS instrument (HECUS GmbH, Graz, Austria) which consists of a GeniX microfocus X-ray sealed Cu Kα source (Xenocs, Grenoble, France) of 50 W power which provides a detector focused X-ray beam with λ = 0.1542 nm Cu Kα line. The instrument is equipped with two one-dimensional (1D) position sensitive detectors (HECUS 1D-PSD-50 M system): each detector is 50 mm long (spatial resolution 54 μm/channel, 1024 channels) and cover the SAXS q-range $0.003 < q < 0.6$ Å $^{-1}$. The temperature was controlled by means of a Peltier TCCS-3 Hecus. The analysis of SAXS curves was carried out using Igor Pro [22]. Details on the measurements and data analysis are reported in the SI (see page S10 of Supplementary Characterization of Gold Nanoparticles).

2.5. Small angle neutron scattering

SANS experiments were performed on D11 at the Institut Laue – Langevin (Grenoble, France). All measurements have been done at 25 °C in cylindrical quartz cuvettes of 1 mm path length. A neutron beam size of 13 mm in diameter has been employed. Three instrument settings were used, all with a neutron wavelength of 6 Å, having a FWHM of 9%. The sample to detector distances were 1.5 m, 8 m and 39 m with corresponding collimation distances of 5.5 m, 8 m and 40.5 m respectively. Scattered intensities were collected with a MWPC ^{3}He detector with 128 · 128 pixels of 7.5 · 7.5 mm^2 size. Data were normalized with respect to the measurement of a 1 mm path length MilliQ H_2O cuvette, for which the differential scattering cross section for 6 Å on D11 has been determined to 0.983 cm^{-1} via a cross calibration against h/d polymer blends. Data reduction was done using the LAMP software package available at the Institut Laue – Langevin. All data were corrected for the scattering of a dark current, as a background the scattering of an empty cell has been subtracted. In a second step the data were radially averaged and the scattering from the background (D_2O) has been subtracted. Transmissions were measured at a sample to detector distance of 8 m with a collimation distance of 8 m.

2.6. X-ray reflectivity

XRR experiments were performed at the ID03 surface diffraction beamline of the ESRF. The experiments were conducted using the six-circle diffractometer with vertical scattering geometry of experimental hutch 1. During the experiment, a drop of buffer solution was maintained on the sample surface. In order to minimize the beam damage, a 24 keV x-ray beam de-focused in the horizontal plane has been used, with a resulting beam size of 45 × 600 μm^2 at the sample position. These conditions have been already successfully used to characterize similar samples in analogue conditions [23,24]. The images were collected using a Maxipix camera (ESRF) (2 × 2 chips, 516 × 516 pixels) at a distance of 772 mm from the sample. The software MOTOFIT was employed for the analysis of the XRR curves. Details on data analysis are reported in the SI (page S19 of Supplementary Data Analysis).

2.7. Atomic force microscopy liquid imaging

AFM experiments in liquid were performed at the SPM@ISMN facility in Bologna using a Multimode VIII (Bruker, Santa Barbara, CA, US) and at the Partnership for Soft Condensed Matter (PSCM) in Grenoble using a Cypher S (Asylum Research, Santa Barbara, CA, US). In the first case images were collected in peakforce tapping using SNL Bruker cantilevers with nominal spring constant of 0.24 N/m and 2–10 nm curvature radius, in the second one Olympus BL-AC40TS cantilevers were chosen to perform tapping mode imaging. Details on samples preparation and image analysis are reported in the SI (page S8 of Supplementary Materials and Methods).

2.8. Quartz crystal microbalance with dissipation monitoring (QCM-D)

QCM-D experiments were performed on a Q-Sense E4 instrument (Q-Sense, Gothenburg, Sweden) in the Partnership for Soft Condensed Matter Laboratory (PSCM) Grenoble (France) [25–27]. The instrument was equipped with four flow liquid cells (0.5 mL internal volume), each containing a coated quartz sensor with 4.95 MHz fundamental resonance frequency, mounted horizontally. The active surface of the sensors (~1 cm^2) was coated with a thin SiO_2 layer (~100 nm thick). The sensors were cleaned prior to use by ozone cleaning, bath sonication in chloroform, acetone and ethanol and extensively rinsed with MilliQ water and ethanol. The experiments were performed at 18 °C and solvent exchange in the measurement chamber was achieved with a peristaltic pump. First, the sensors were placed in the chambers and water was injected at a low flow rate (0.07 mL/min), the frequencies (f) and corresponding energy dissipation factors (D) were measured for the odd harmonics (1st–13th). A stable baseline for both f and D of the different harmonics was ensured before the injection of the vesicles. The QCM-D curves reported are normalized by the overtone number. Details on data analysis are reported in the SI (page S9 of Supplementary Materials and Methods).

3. RESULTS AND discussion

3.1. UV–Vis characterization of liposomes-induced clustering of AuNP

After mixing a 1.3 nM dispersion of negatively charged citrated AuNP (16 nm diameter, zeta potential: −36 ± 2 mV,) with 100 nm-sized zwitterionic POPC liposomes (zeta potential: −4.9 ± 0.4), we monitored the spectral variations in the region of the plasmon resonance band of AuNP. Fig. 1 shows the observed changes, as several factors and/or experimental conditions were varied, in particular: (i) POPC liposomes/AuNP ratio (*R*) (Fig. 1a, 1b), (ii) mixing sequence (Fig. 1c), (iii) volume of the solution (Fig. 1d, 1e) (see pages S3-S6 of SI for details on the preparation of samples).

The reference sample is a 1.3 nM dispersion of AuNP in water, where the negative charge of citrate coating provides electrostatic stabilization (black curves, Fig. 1a, d) which prevents NP aggregation. In this sample, the absorbance is characterized by an intense and defined surface plasmon band at 521 nm, typical of colloidally stable gold particles of nanometric size. The addition of decreasing amounts of liposomes causes a progressive broadening of the plasmon resonance peak and, eventually, the appearance of a red-shifted shoulder (Fig. 1a). The observed shift, due to plasmon-plasmon coupling, originates from the spatial proximity of NP and is the hallmark of NP aggregation. This effect has been already observed in several reports [10–12,14] showing that, for defined experimental conditions, AuNP will cluster on the liposomal surface. Here, in line with a recent study [12], we show that the extent of clustering, also detectable by the naked eye as a red-to-blue color change of the dispersion (Fig. 1b), strictly depends on the relative amounts of liposomes and AuNP (Fig. 1a). In contrast to salt-induced aggregation of AuNP, which is maximized increasing the ionic strength, this shift is maximum for the lowest amounts of added liposomes. This is a clear indication that the clustering of AuNP is a membrane-dependent phenomenon, which strictly occurs on the liposomal surface, so that the lower the liposomal surface extension available, the higher the aggregation extent of AuNP.

Up to now, reports on membrane-induced clustering of citrated AuNP have focused mainly on energetics. For instance, it has been shown that the interaction is inhibited if the lipid membrane is negatively charged, accounting for an electrostatic repulsive contribution [10,15]; that the clustering depends on the phase properties of the target, i.e., the melting temperature of the composing lipid bilayer [14,18]; that the chemical nature of the coating agent affects the affinity of AuNP with the target membrane [11,15]; that the adhesion of NP might affect the phase behavior of the target membrane [13,28,29].

With respect to these previous contributions, the experimental results shown here provide additional details: in particular, kinetic effects are of prominent relevance. In fact, the mixing order of the species (i.e., liposomes added to the AuNP dispersion (Fig. 1c) vs AuNP added to the liposome dispersion (Fig. 1b)) determines meaningful differences in the extent of NP clustering, which do

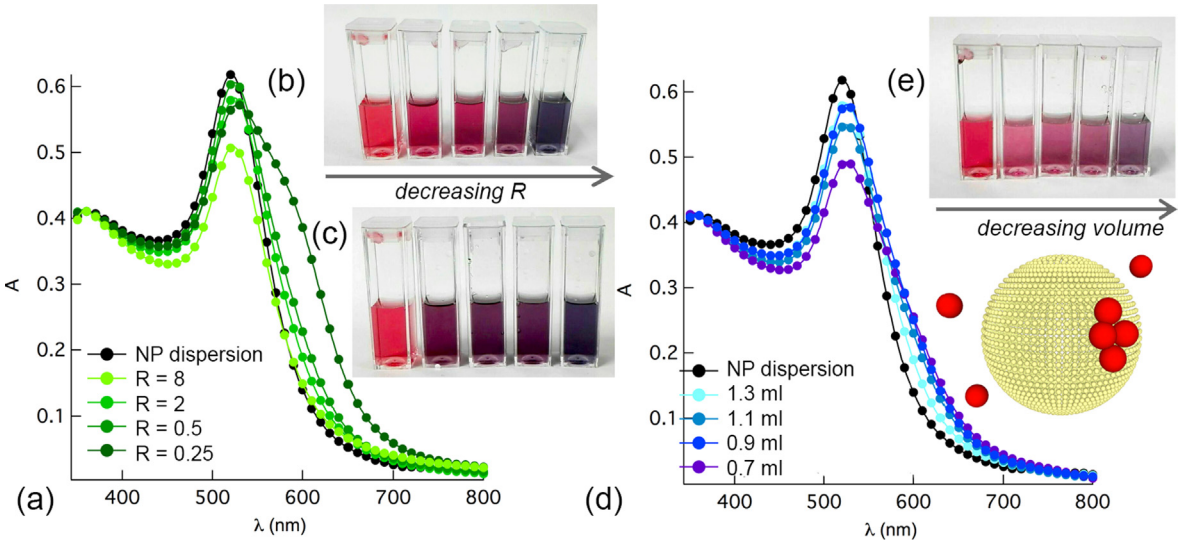

Fig. 1. UV–Vis characterization of AuNP-POPC vesicles interaction. UV–Vis spectra of AuNP (1.3 nM) in the presence of different amounts of POPC liposomes (R = 8; 2; 0.5, and 0.25) and visual appearance of the corresponding samples (b, c). (d) UV–Vis spectra of Liposomes/AuNP R = 2 complexes, initially mixed in different volumes, and then diluted to the same final volume and visual appearance of the corresponding samples (e).

not disappear even after one week incubation (data not shown), suggesting that the membrane-induced aggregation of AuNP is irreversible and does not evolve to a more thermodynamically stable state, in the time frame of our experimental observations. To strengthen this conclusion, we observed that a variation of the volume at which AuNP and liposomes are initially mixed (see page S3 of SI for the detailed preparation of samples) strongly affects the extent of NP clustering in a similarly irreversible fashion. Specifically, liposomes/AuNP hybrids of Fig. 1d-e were incubated at different volumes, modifying liposomes and AuNP concentrations during mixing, but not their relative numerical ratio, and then diluted to the same final volume: the reduction of the interaction volume is associated to larger variations of the spectral properties which are not leveled after one week, providing further evidence of the irreversible nature of the AuNP aggregation process.

While it is clear from the recent literature that thermodynamic contributions, as NP-membrane and NP-NP Van der Waals attractive forces, are involved in AuNP docking to the membrane and AuNP-AuNP aggregation on the liposomal surface, both the kinetic control and the irreversible nature of the process have been so far unaddressed, to the best of our knowledge.

3.2. Structural characterization of AuNP-liposome aggregates

SAXS, SANS and AFM were used to investigate the structure of AuNP-POPC liposome dispersions (Fig. 2). In recent studies, Cryo-EM was also used to visualize AuNP clusters on liposomes [12,14,18]. Here we provide an ensemble-averaged description, combining solution ensemble techniques (SAXS and SANS) with atomic force microscopy (liquid AFM). SAXS and SANS provide complementary structural information at the nanoscale: the high AuNP/H_2O contrast in SAXS emphasizes the structural features of the NP and of their aggregates, if present, whereas the high lipid/D_2O contrast in SANS provides access to structural details of the NP effects on the lipid bilayer.

Fig. 2a displays the SAXS spectra obtained for R = 0.5 and R = 0.25, i.e. with 2 and 4 AuNP per liposome on average. For both samples the scattering due to liposomes is not distinguishable from the water background at these concentrations (green curve), and the signal is exclusively due to AuNP, either single or aggregated. When liposomes are present, the scattered intensity shows a clear q^{-2} trend in the low-q range, (Fig. 2a, inset), superimposed to the form factor of primary AuNP, measured as a control sample. A quantitative estimation of the low-q slope, obtained by fitting the experimental AuNP-liposomes curves in Fig. 2 to a multiple level Guinier-Porod model [30], can be found at Page S14 of SI. The occurrence of this power-law behavior hints at a fractal arrangement of the primary particles [31], not observed in the absence of liposomes.

We also imaged the R = 0.25 sample with AFM in liquid [32]. Fig. 2b shows a representative example of a compact assembly of AuNP on lipid vesicles (or vesicle aggregates), whose 2D or 3D nature is not clear. In agreement with the literature [33–35], we would expect a SAXS power law with a decay exponent higher than 2 from a 3D compact aggregate of AuNPs. Therefore, the combination of AFM and SAXS results could be consistent with the formation of 2D clusters of AuNPs tightly packed on the liposomes surface.

Since in these dispersions AuNP and liposomes have comparable concentrations, the formation of membrane-confined extended aggregates of AuNP on a single liposome implies a strongly uneven distribution of AuNP: some liposomes will be extensively coated by AuNP, while others will be devoid of particles.

This conclusion is supported at the ensemble level by SANS, performed on the same AuNP-POPC liposome complexes (Fig. 2c). No significant variations are observed in the scattering profiles upon interaction with AuNP, in line with the hypothesis that the vast majority of the liposomes remain "undressed". On the other hand, AFM provides proof of consistent aggregation at the level of single complexes (Fig. 2b).

This phenomenon, i.e., a spontaneous aggregation of AuNP only on a limited number of liposomes, is a key feature of membrane-templated aggregation of AuNP, whose peculiar aspects will be addressed in the next paragraph.

3.3. Distribution of AuNP among liposomes

We evaluated the distribution of AuNP among liposomes by determining the relative abundancy of single and aggregated AuNP from the UV–Vis spectra (Fig. 1); the analysis was performed considering the spectral profiles as the convolution of the original

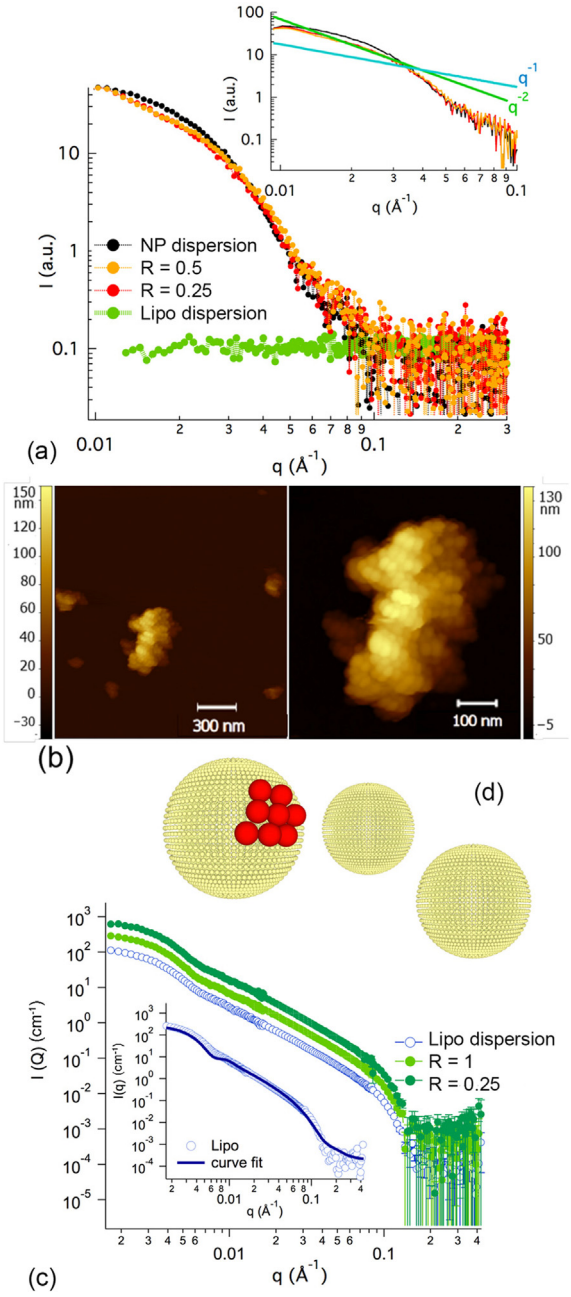

Fig. 2. Structural characterization of AuNP-POPC liposome complexes. (a) SAXS of POPC liposomes in the presence of different amounts of AuNP (R = 0.5 and 0.25); comparison of the experimental curves with the power laws $I(q) \propto q^{-1}$ and $I(q) \propto q^{-2}$ (inset). (b) Representative AFM images of POPC liposomes after interaction with AuNP (R = 0.25); magnification of the AFM image which highlights the AuNP aggregates. (c) SANS profiles of POPC liposomes in the presence of different amounts of AuNP (R = 1 and 0.25); the curve fit for liposomes according to a polydisperse core–shell model is consistent with vesicles of a 45 nm radius and polydispersity 0.3 according to a Schulz distribution (inset)". SANS measurements were performed at D11, ILL.

plasmon resonance peak (centered at 521 nm) and an additional red-shifted peak due to aggregated AuNP (see page S19 of Supplementary Data Analysis for details) [36]. The relative area of each peak can be considered as a rough estimate of the percentage of single and aggregated AuNP. Interestingly, even for $R > 1$, with liposomes in excess with respect to AuNP, this evaluation yields a high percentage of aggregated AuNP: as an example, for R = 2, with a number density of liposomes double with respect to AuNP (see Fig. 1), we found a percentage of aggregated AuNP of 44% (see pages S19-S22 of SI for details).

To frame this result from a statistical perspective, we tried to estimate the probability of finding multiple AuNP on the same liposome as a function of R. For simplicity, we considered AuNP and liposomes as dimensionless objects that undergo irreversible and complete association. This description, yet very simple, is of general applicability and allows making no assumption on the nature of the interaction forces at stake.

In this scenario, the distribution probability of AuNP per liposome (Pj, with j > 0 number of NP on the same liposome) is described through a Poisson distribution, employed in the past to describe the distribution of molecular probes in micellar dispersions [37] (see pages S15-S19 of SI for details):

$$Pj = \frac{R^{(1-j)} \times e^{-(1/R)} \times j}{j!} \quad (1)$$

where R is the liposomes/AuNP number ratio, as previously defined. As described in Eq. (1), Pj represents the probability to find an AuNP sharing the same liposomal surface with other j-1 gold nanoparticles. Therefore, for each R experimentally investigated there is a finite probability for multiple AuNP occupancy on the same vesicle, whose relative weight strongly depends on the stoichiometry: according to Eq. (1), the probability of finding two or more AuNP on the same liposome increases with decreasing R, in line with the UV–Vis results (Fig. 1a-c). Therefore, the qualitative dependence of AuNP aggregation on R can be understood in terms of enhanced probability of multiple occupancy.

However, the Poisson model definitively fails when a quantitative analysis is attempted: specifically, the AuNP aggregation extent, evaluated with Eq. (1), is systematically underestimated for each R investigated.

For example, for R = 2 this model predicts that the majority of liposomes (about 60%) will be unoccupied and that AuNP will distribute among the remaining 40% liposomes (See equation S1 and Fig. S5 a) for details) either associating as a 1:1 or multiple:1 AuNP/liposome complex.

More specifically, the majority of AuNP (61%) should associate with liposomes in a 1:1 fashion, while 30% should occur as "pairs", and only 9% will exhibit j > 2 (see Eq. (1) and Fig. S5 b) for details).

This description is clearly not consistent with SAXS and UV–Vis results, which point at marked multiple occupancy. In addition, the Poisson-based model does not consider the finite sizes of liposomes and AuNP, which would further drastically reduce the expected percentage of aggregated AuNP (comprising of both dimers and oligomers) to 1.6% for R = 2 (see pages S15-S19 of SI for details).

To summarize the results so far, besides energetic contributions for adhesion and clustering, two distinctive features emerge: (i) the kinetic control of binding and aggregation, which results in irreversible clustering; (ii) the strongly uneven distribution of AuNP aggregates on selected liposomes.

In order to better disentangle these aspects, we address more in detail two "chemical" factors which might have a major impact and, specifically, the nature of the AuNP coating (3.4) and the viscoelastic properties of the lipid membrane (3.5).

3.4. Role of ligand on AuNP-liposomes interaction

The nature of surface ligands mediates the interaction between NP surface and lipid interfaces, both for synthetic and natural membranes. It is well-established that a positively charged coating agent will promote a dramatic interaction of NP with biological or biomimetic interfaces [15,38–40]; likewise, it is known that surface coatings with large steric hindrance (as PEG) will inhibit

interactions with lipid membranes [15,41,42]. For small anionic ligands, the nano-bio interaction pathway strongly depends on the chemical nature of the ligand itself. For instance, the phenomenon here investigated has been observed specifically for the citrate-coated AuNP. This suggests a possibly overlooked role of the ligand in AuNP-membrane interactions, which should be related to specific molecular features of citrate that discriminate its behavior with respect to other small anionic ligands.

This capping agent is physisorbed on NP surface and can be easily displaced through "ligand-exchange" reactions. The behavior of citrate as an exchangeable capping agent is well-known: citrate is often used as intermediate ligand to functionalize NP [43,44], it is easily exchanged to thiolated ligands and, recently, it has been also shown that it can be displaced by other non-covalent capping agents [45], such, for instance, adenine [46].

To better address this point and its implications for the case under study, we compared the behavior of citrate-capped AuNP and AuNP capped with a thiolated ligand of similar size and charge as citrate but poorly exchangeable (3-mercaptopropionic acid, MPA).

To this purpose, we evaluated in a qualitative way the chemical affinity of citrated and MPA-coated AuNP towards POPC, i.e. the lipid component of vesicles, in a 1:1 (v:v) $CHCl_3$/water biphasic system. As a control experiment, we put in contact aqueous dispersions of MPA-capped AuNP or citrated AuNP with chloroform: even after 24 h the organic phase is transparent, while the aqueous phase maintains its vivid color (see Fig. S10 of SI for details). As expected, AuNP will be localized in water, due to their high surface charge density, imparted by the anionic ligands. If POPC is present in the organic phase (dissolved as a monomer at 1 mg/ml concentration), depending on the nature of ligands, we observe a dramatically different behavior.

While no significant variation is observed for MPA-AuNP with respect to the control experiment (Fig. 3b), for citrate-capped AuNP the transfer of NP to the organic phase starts immediately and is complete after 24 h (Fig. 3a). The spectral properties of the organic phase indicate the presence of single primary AuNP (see Fig. S9 of SI for details). The dispersion of NP in the organic phase is consistent with stabilization provided by a monolayer of POPC, with the hydrophilic zwitterionic headgroup on the particle surface and hydrophobic tails pointing towards the solvent.

This opposite behavior is clearly due to the fact that MPA is not exchanged with POPC, due to the strength of the Au-S bonds at the Au surface, while citrate is easily displaced by the lipid at the chloroform-water interface, where a monolayer of POPC is present, eventually leading to complete extraction of AuNP to the organic phase. This assay, even if qualitative, provides a clear and unambiguous indication that the affinity of AuNP for POPC strongly depends on the chemical nature of the ligand originally present on the NP.

Remarkably, this finding is strongly related to the behavior of AuNP when incubated with POPC liposomes in water: Fig. 3c and 3d show the UV–Vis spectra of AuNP (citrate-capped, 3c and MPA-capped, 3d) added to liposome dispersions at R = 1. While the citrated AuNP exhibit the already discussed spectral redshift, the MPA-capped NP display a negligible variation of the absorption profile, which might be related to the adsorption of the NP on liposomal membrane [12], but definitely not to aggregation, occurring for citrated AuNP.

We put forward the hypothesis that also in this case the citrate-POPC exchange is a major player in the interaction between NP and POPC liposomes and subsequent NP clustering. The ligand exchange at AuNP-liposome interface, with partial substitution of the citrate shell with POPC and release of citrate and counterions in water, would represent an irreversible binding step.

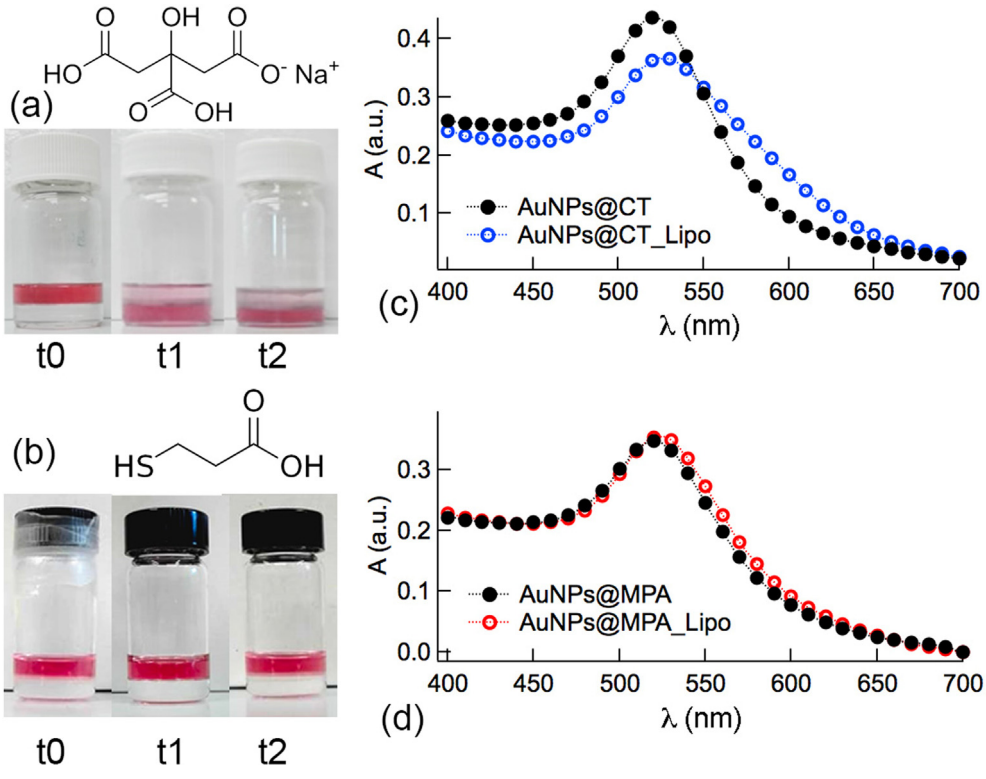

Fig. 3. Role of citrate in the membrane-templated clustering of AuNP. (a, b) Photos of the two-phase system (NP + water)/(chloroform + POPC) of (a) AuNP@Ct and (b) AuNP@MPA captured: soon after chloroform addition (t0), after 20 min (t1) and 24 h (t2). (c, d) Representative UV–Vis spectra of $R = 1$ (c) AuNP@Ct and (d) AuNP@MPA before and after incubation with POPC liposomes.

Therefore, the irreversible and kinetic nature of the lipid membrane binding and induced clustering, which is an unexplored key aspect in the liposomes/AuNP interaction, might find an explanation at a molecular level in the irreversible nature of citrate-POPC ligand exchange at the nano-bio interface.

3.5. Role of membrane elasticity on AuNP-liposomes interaction

Besides surface charge and composition [47,48], the phase state of the bilayer (gel or liquid crystalline) strongly affects the viscoelastic properties of the membrane and its response to NP adhesion. Recent studies addressed the interaction of citrated AuNP with lipid vesicles of similar composition as the system here considered (i.e., phosphatidylcholine phospholipids): the interaction of AuNP with lipid vesicles in gel and liquid crystalline phases was compared, either employing DPPC vesicles below and above the lipid membrane melting temperature (i.e., the gel to liquid crystalline transition temperature) [10], or considering vesicles of different lipid compositions at the same temperature (i.e. DOPC liquid crystalline and DPPC gel phase vesicles) [14]. Depending on the phase state of the membrane, aggregation of citrated AuNP was either inhibited (gel phase) or promoted (liquid crystalline phase). The authors have interpreted this result as due to a hampered lateral diffusion of the adhered AuNP when the target membrane is in the gel phase, which eventually limits aggregation. Therefore, the membrane lateral fluidity is considered the crucial factor to promote clustering of AuNP. Membrane fluidity modifications (particularly the formation of unstable lateral phase boundaries on fluid membranes upon citrated AuNP adhesion) are also considered as a main driving force to AuNP clustering in another recent study [14]. While membrane fluidity can definitely play a role, other membrane viscoelastic properties might have been overlooked. Specifically, membrane bending rigidity is increasingly recognized as a key-factor which affects the reactivity of synthetic and natural bilayers towards nanomaterials [49,50]. The ability of a membrane to elastically deform and wrap around a NP, maximizing the interfacial contact area, is closely related to the balance between NP-bilayer adhesion energy and membrane bending energy (*viz.* elastic energy [49]), representing the energy cost for the bilayer to modify its spontaneous zero curvature. This balance determines the extent of NP wrapping and NP-membrane contact area, controlling the strength of interactions at the nano-bio interface [15,49–51].

Bending rigidity undergoes a dramatic variation passing from gel to liquid crystalline bilayers (for instance the bending moduli of fluid POPC and gel DPPC are $\approx 0.9 \times 10^{-19}$J and $\approx 15.5 \times 10^{-19}$J at 25 °C, respectively [52]), which might have a crucial role in the interaction with AuNP.

To address this point, we determined the impact of membrane bending on membrane-templated clustering by monitoring POPC-AuNP interaction in systems where NP wrapping is hampered, due to high bending costs. We monitored POPC-AuNP hybrids obtained upon incubation of AuNP with POPC supported lipid bilayers (SLBs), obtained through vesicle fusion on a silicon wafer. The close interaction with the support prevents membrane bending, and in turn hinders AuNP wrapping by the membrane. Conversely, the

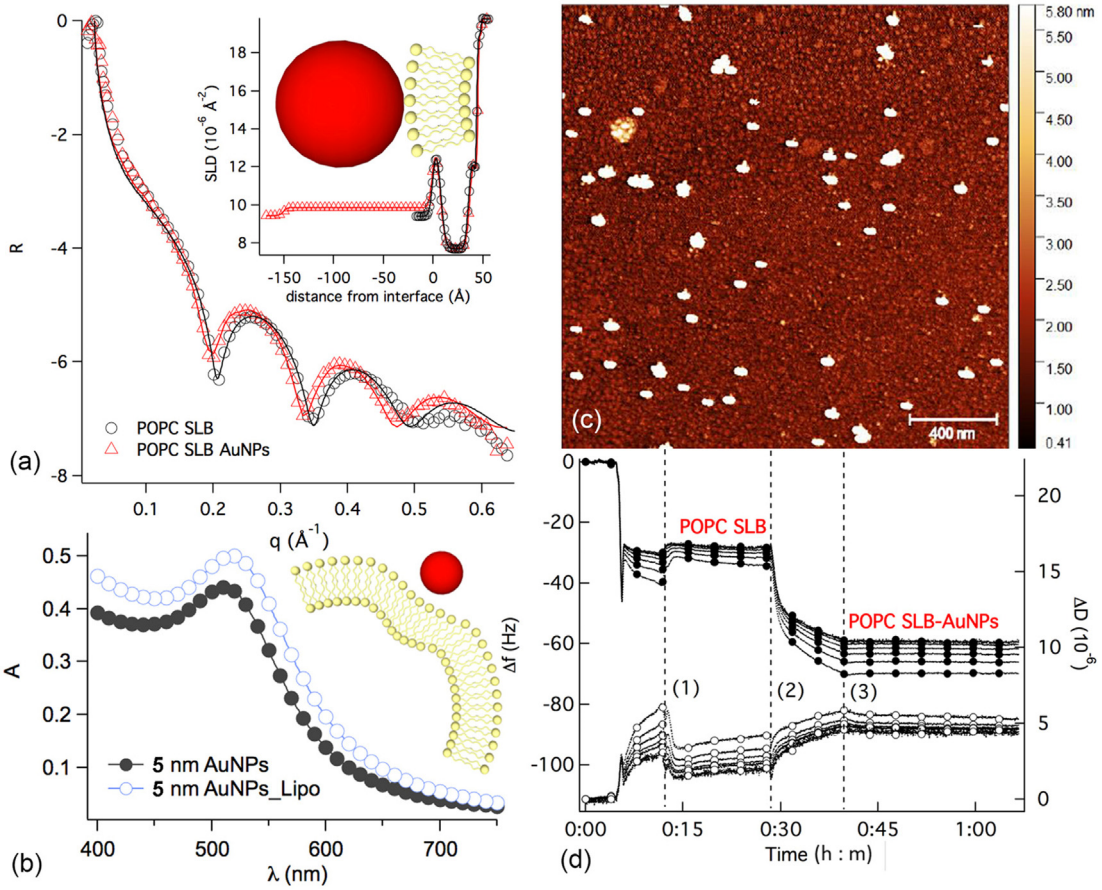

Fig. 4. Wrapping contribution to membrane-templated AuNP clustering. (a) XRR profiles of a POPC SLB before and after incubation with AuNP, the curve fitting of the experimental curve and derived SLD profile (inset). (b) UV–vis plasmon resonance spectra of small-diameter (5 nm) citrated AuNP in the absence and in the presence of POPC liposomes for R = 0.1. (c) Liquid AFM of AuNP on a POPC SLB. (d) QCM-D experiment on the adsorption of AuNP on a POPC SLB: lines and filled circles represent the frequency shifts, while lines and empty circles represent the dissipation factors; the curves are normalized for the overtone numbers. XRR measurements were performed at ID03, ESRF.

lateral fluidity of POPC SLBs is retained or scarcely modified [53], as they are in the same physical state (i.e. liquid crystalline (fluid) state) as POPC vesicles. To rule out NP clusters formation due to the possible presence of residual intact liposomes on the SLB, all the samples were extensively washed after incubation.

Fig. 4a compares the XRR [23] profiles of POPC SLBs in the absence and in the presence of AuNP. AuNP cause only a slight shift in the XRR oscillations of the bilayer form factor to lower q values, consistent with the adhesion of few NP on the lipid membrane (see curve fitting results in Table S2 of SI and the resulting scattering length density (SLD) profile along the bilayer thickness, Fig. 4a inset) [54]. This finding is confirmed in real space with AFM images, where AuNP are embedded in the membrane as single objects or dimers (Fig. 4c); in addition, QCM-D data (Fig. 4d) show that, after the formation of a stable POPC SLB (Fig. 4d, (1)) [27], the AuNP injection (2) results in the stable adsorption of some NP on the target membrane, with an overall coverage of approximately 3.5% of the SLB surface (see pages S9 of SI for details).

From these results, we conclude that AuNP adhere to the target membrane, but membrane-templated clustering of AuNP is significantly or completely limited, which points out a key role of membrane rigidity. We can conclude that the extent of NP wrapping by the membrane is one of the main factors driving the clustering of AuNP coated with citrate.

In order to further corroborate this result, we investigated the effect of AuNP size in the interaction with POPC liposomes.

While the adhesion energy per unit membrane is, to a first approximation, not dependent on the curvature locally imposed by the NP to the wrapping membrane [55], the bending energy per unit surface area of the bilayer (g_{be}) [55,56] depends on the inverse of the NP radius square, as follows:

$$g_{be} = \frac{2}{r^2} k_c \tag{2}$$

with k_c the bending modulus of the bilayer and r the NP radius.

To investigate the effect of reducing NP size we challenged POPC liposomes with significantly smaller citrated AuNP (5 nm instead of 16 nm in diameter, see paragraph 2 and page S2 of SI for details). Small AuNP impose an extremely high local curvature to the lipid membrane, whose deformation involves a higher energetic penalty with respect to 16 nm AuNP. Sharing the same exchangeable ligand, i.e. citrate, as 16 nm AuNP, small AuNP show the same affinity for POPC as bigger ones, as demonstrated by a control experiment in the biphasic water/chloroform system (see Fig. S11 of SI for details); thus, the only difference between the two cases is then bending cost for unit area, which should result in a consistently lower wrapping for small NP (see Eq. (2)).

Fig. 4b displays an UV–Vis experiment similar to the one in Fig. 1a, apart from the particle size: the plasmon coupling is here absent even for R = 0.1, suggesting that membrane adsorption might even occur, but membrane-templated aggregation is prevented. To summarize, 5 nm NP, which are expected to be wrapped by the membrane to a lower extent (Eq. (2)), do not cluster, which confirms a major role of membrane bending elasticity in the citrated AuNP/liposome interaction.

To better interpret these results, we should consider that the bending capacity of the membrane determines its ability to bend and wrap around the NP, as highlighted in several recent studies [49,50]. Therefore, the wrapping extent of the NP determines the contact area between a NP and the membrane, where the citrate-POPC ligand exchange can take place.

Remarkably, increasing the contact area extension maximizes the portion of particle surface that will undergo citrate-POPC exchange. This ligand substitution will reduce the interparticle electrostatic repulsion on the membrane, enabling short-range NP-NP Van der Waals interactions, which can lead to the formation of 2D arrays of AuNP on the liposomal surface.

If wrapping is inhibited or limited by high bending costs, AuNP clustering is not observed, for the same coating and the same membrane: we attribute this effect to the lower POPC-citrate substitution on the NP surface, which prevents short-range interactions.

3.6. AuNP-liposomes interaction: A mechanistic hypothesis

The ensemble of experimental results reported here can be framed in a mechanistic hypothesis, which would account for the irreversible adsorption and 2D-clustering of AuNP on liposomes, and for the main driving energetic contributions.

(i) First adsorption of the AuNP drives bending of the lipid bilayer, which, by wrapping the AuNP, triggers irreversible POPC-citrate ligand exchange and, in turn, citrate and counterions' release in the NP immediate proximity.
(ii) the ligand exchange, decreasing NP-NP electrostatic repulsion, enables NP adhered to the same liposome to approach to distances at which Van der Waals attraction becomes effective, ultimately promoting AuNP ordered arrangement on the lipid membrane.

If this description explains the results presented here and those reported in the literature, one observation remains unclear, namely the strongly uneven distribution of AuNP among liposomes, which is not elucidated by statistical considerations (see paragraph 3.3) or by the mechanistic hypothesis above reported. Such an uneven distribution of AuNP membrane-confined clusters, present only on selected vesicles, implies the presence of a specific driving force, which acts cooperatively.

We put forward the hypothesis that a key contribution to this statistically unbalanced distribution is the release of citrate (and Stern counterions) at the liposome/NP interface, which follows POPC ligand exchange.

If the multivalent citrate ligands are released from the wrapped area of an AuNP (together with strongly-bound counterions), the ionic strength at the interface will locally and transiently increase to a significant extent. This local ionic strength increase will transiently decrease the Debye length, lowering the kinetic barrier for NP aggregation.

We can hypothesize that an iterative process takes place: the first AuNP binds randomly to the membrane, releasing a sufficient quantity of citrate anions to recruit another AuNP, which will adhere to the membrane and undergo the same extent of ligand exchange and citrate release, thereby trapping other AuNP. This will establish a preferential trail for AuNP towards a selected liposome and the distribution of NP will not be ruled by statistical considerations.

Unfortunately, to the best of our knowledge and expertise, it is not possible to perform an experiment which could directly probe a transient and localized increase of ionic strength in proximity of the adhesion point of a 16 nm AuNP on a single 100 nm liposome.

However, this iterative mechanism would be fully consistent with the experimentally observed connection between the extent of NP membrane wrapping and NP aggregation.

As a matter of fact, the increase of wrapping would also imply an increase of citrate release and, therefore, an increase in the efficiency of AuNP recruitment on a selected liposome.

This hypothesis scheme of a "citrate-trail" recruitment of AuNP would fit into a multistep model, such as the one sketched in Fig. 5.

Within the DLVO formalism, accounting for both a long-range repulsive electrostatic potential and a short-range attractive London-Van der Waals potential, we outline the following interaction steps:

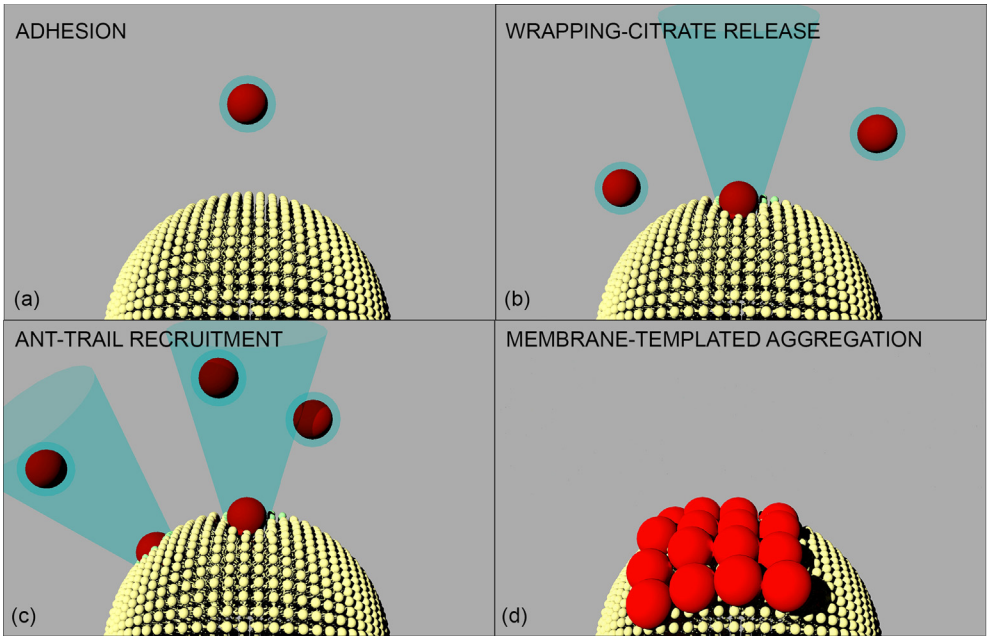

Fig. 5. Mechanism of interaction between AuNP and the lipid membrane. (a) Adhesion-docking; (b) wrapping-ligand exchange; (c) citrate-trail recruitment; (d) membrane-templated aggregation.

(i) Adhesion (i.e., AuNP docking to the liposomal membrane). The negative charge of AuNP, imparted by the citrate coating, provides a strong electrostatic repulsive contribution preventing short-range Van der Waals NP-NP interactions, while the electrostatic barrier for the adhesion of AuNP to the bilayer is significantly lower (POPC is zwitterionic, and liposomes have a slightly negative zeta potential). Thermal fluctuations can easily bring AuNP close to the bilayer, and eventually, adhesion driven by short-range liposome-AuNP attraction occurs.

(ii) Wrapping. Due to docking, a locally high curvature is imposed in the membrane. Depending on the NP size and on the bending modulus of the membrane, the NP is partially wrapped by the liposomal membrane and irreversible ligand exchange between citrate and POPC occurs (which contributes to the kinetic-irreversible nature of citrated AuNP-lipid vesicles interaction). The extent of citrate displacement depends on the area wrapped by the membrane and therefore on the balance between the NP-membrane adhesion energy and the energy penalty due to membrane bending.

(iii) Citrate-trail. Wrapping causes the release of citrate and associated counterions, which determine a transient localized increase in the ionic strength. This action in turn increases the probability of the adhesion of another AuNP to the same liposome followed by a synergistic cascade effect, where each adhered AuNP partially releases its citrate coating to mark the membrane-adhesion pathway for the following AuNP.

(iv) Membrane-templated aggregation. Once a relatively high number of AuNP is present on the same liposome, the decreased AuNP-AuNP electrostatic repulsion due to partial citrate release, together with the tendency of the membrane to decrease the locally imposed curvature due to AuNP adhesion, leads the formation of a curved membrane-confined AuNP aggregate on the lipid membrane.

4. Conclusions

We addressed the mechanistic features of the aggregation of citrate-coated gold nanoparticles on synthetic lipid membranes. This phenomenon, although recently highlighted in some studies on nano-bio interfaces [10,12,13,18] and even exploited for bioanalytical assays [17], has never been fully disentangled and explained. Combining optical spectroscopy (UV–vis absorbance), bulk structural techniques (Small Angle Neutron and X-ray Scattering) and surface analysis (X-ray Reflectivity, Atomic Force Microscopy), we identified the main factors involved in the interaction of AuNP with synthetic lipid vesicles and the subsequent aggregation of NP. This allowed proposing a mechanistic hypothesis which would also explain and reconcile the data reported in the recent literature [10,14]. We disclose how thermodynamic (i.e., electrostatic and Van der Waals interactions, lipid membrane viscoelastic properties) and kinetic effects (citrate-lipid exchange at the nano-bio interface) are intertwined. For the first time, we suggest the key role of citrate and citrate-lipid ligand exchange to drive aggregation. This mechanism would imply that a small coating molecule, i.e., citrate, drives the response of a target lipid membrane to NP adhesion, resembling, in a very simple system, the mechanisms of small-molecule-activated biological responses in cell signaling phenomena. Moreover, the cooperative nature of ligand exchange at the AuNP-liposome interface, pivotal in determining clustering of AuNP, will have relevant implications for NP use in Nanomedicine, since NPs will be internalized in cells as clusters, rather than as primary NP, with dramatic effects on their bioactivity.

CRediT authorship contribution statement

Costanza Montis: Conceptualization, Data curation, Investigation, Methodology, Writing - original draft. **Lucrezia Caselli:** Conceptualization, Data curation, Investigation, Methodology, Writing - original draft. **Francesco Valle:** Data curation, Investigation. **Andrea Zendrini:** Data curation, Investigation. **Francesco Carlà:** Data curation, Investigation. **Ralf Schweins:** Data curation, Investigation. **Marco Maccarini:** Data curation, Investigation. **Paolo Bergese:** Conceptualization, Data curation, Funding acquisition, Methodology, Supervision, Writing - review & editing. **Debora Berti:** Conceptualization, Data curation, Funding acquisition, Methodology, Supervision, Writing - review & editing.

Declaration of Competing Interest

The authors declare that they have no known competing financial interests or personal relationships that could have appeared to influence the work reported in this paper.

Acknowledgements

Funding Sources: ECRF (Ente Cassa di Risparmio di Firenze) and evFOUNDRY (H2020-FETOPEN-2016-2017—Project ID: 801367). AFM experiments were performed at the SPM@ISMN microscopy facility in Bologna and at the Partnership for Soft Condensed Matter (PSCM), Grenoble with the help of Marie Capron and Alain Panzarella. The Partnership for Soft Condensed Matter (PSCM) is also gratefully acknowledged for QCM-D and Dynamic Light Scattering measurements; CM acknowledges ECRF (Ente Cassa di Risparmio di Firenze) and evFOUNDRY (H2020-FETOPEN-2016-2017—Project ID: 801367) for a financial support. The following DOI: 10.5291/ILL-DATA.9-13-597 identifies SANS experimental data acquired at ILL. 2016-2017—Project ID: 801367) for a financial support. The following DOI: 10.5291/ILL-DATA.9-13-597 identifies SANS experimental data acquired at ILL.

Appendix A. Supplementary data

Supplementary data to this article can be found online at https://doi.org/10.1016/j.jcis.2020.03.123.

References

[1] M. Henriksen-Lacey, S. Carregal-Romero, L.M. Liz-Marzán, Current challenges toward in vitro cellular validation of inorganic nanoparticles, Bioconjug. Chem. 28 (1) (2017) 212–221, https://doi.org/10.1021/acs.bioconjchem.6b00514.
[2] A.E. Nel, L. Mädler, D. Velegol, T. Xia, E.M.V. Hoek, P. Somasundaran, F. Klaessig, V. Castranova, M. Thompson, Understanding Biophysicochemical Interactions at the Nano-Bio Interface, Nat. Mater. 8 (7) (2009) 543–557, https://doi.org/10.1038/nmat2442.
[3] L.J. Fox, R.M. Richardson, W.H. Briscoe, Historical Perspective PAMAM Dendrimer - Cell Membrane Interactions, Adv. Colloid Interface Sci. 257 (2018) 1–18, https://doi.org/10.1016/j.cis.2018.06.005.
[4] C.M. Beddoes, C.P. Case, W.H. Briscoe, Understanding Nanoparticle Cellular Entry: A Physicochemical Perspective, Adv. Colloid Interface Sci. 218 (2015) 48–68, https://doi.org/10.1016/j.cis.2015.01.007.
[5] G. Rossi, J. Barnoud, L. Monticelli, Polystyrene Nanoparticles Perturb Lipid Membranes, J. Phys. Chem. Lett. 5 (1) (2014) 241–246, https://doi.org/10.1021/jz402234c.
[6] F. Simonelli, D. Bochicchio, R. Ferrando, G. Rossi, Monolayer-Protected Anionic Au Nanoparticles Walk into Lipid Membranes Step by Step, J. Phys. Chem. Lett. 6 (16) (2015) 3175–3179, https://doi.org/10.1021/acs.jpclett.5b01469.
[7] C.F. Su, H. Merlitz, H. Rabbel, J.U. Sommer, Nanoparticles of Various Degrees of Hydrophobicity Interacting with Lipid Membranes, J. Phys. Chem. Lett. 8 (17) (2017) 4069–4076, https://doi.org/10.1021/acs.jpclett.7b01888.
[8] P. Gkeka, L. Sarkisov, P. Angelikopoulos, Homogeneous Hydrophobic-Hydrophilic Surface Patterns Enhance Permeation of Nanoparticles through Lipid Membranes, J. Phys. Chem. Lett. 4 (11) (2013) 1907–1912, https://doi.org/10.1021/jz400679z.
[9] M. Mendozza, L. Caselli, S. Salvatore, C. Montis, D. Berti, Nanoparticles and Organized Lipid Assemblies: From Interaction to Design of Hybrid Soft Devices, Soft Matter 15 (44) (2019) 8951–8970, https://doi.org/10.1039/c9sm01601e.
[10] K. Sugikawa, T. Kadota, K. Yasuhara, A. Ikeda, Anisotropic Self-Assembly of Citrate-Coated Gold Nanoparticles on Fluidic Liposomes, Angew. Chemie - Int. Ed. 55 (12) (2016) 4059–4063, https://doi.org/10.1002/anie.201511785.
[11] J. Liu, Interfacing Zwitterionic Liposomes with Inorganic Nanomaterials: Surface Forces, Membrane Integrity, and Applications, Langmuir 32 (18) (2016) 4393–4404, https://doi.org/10.1021/acs.langmuir.6b00493.
[12] F. Wang, J. Liu, Self-Healable and Reversible Liposome Leakage by Citrate-Capped Gold Nanoparticles: Probing the Initial Adsorption/Desorption Induced Lipid Phase Transition, Nanoscale 7 (38) (2015) 15599–15604, https://doi.org/10.1039/C5NR04805B.
[13] C. Montis, D. Maiolo, I. Alessandri, P. Bergese, D. Berti, Interaction of Nanoparticles with Lipid Membranes: A Multiscale Perspective, Nanoscale 6 (12) (2014) 6452–6457, https://doi.org/10.1039/C4NR00838C.
[14] F. Wang, D.E. Curry, J. Liu, Driving Adsorbed Gold Nanoparticle Assembly by Merging Lipid Gel/Fluid Interfaces, Langmuir 31 (49) (2015) 13271–13274, https://doi.org/10.1021/acs.langmuir.5b03606.
[15] C. Montis, V. Generini, G. Boccalini, P. Bergese, D. Bani, D. Berti, Model Lipid Bilayers Mimic Non-Specific Interactions of Gold Nanoparticles with Macrophage Plasma Membranes, J. Colloid Interface Sci. 516 (2018) 284–294, https://doi.org/10.1016/j.jcis.2018.01.064.
[16] I. Canton, G. Battaglia, Endocytosis at the Nanoscale, Chem. Soc. Rev. 41 (7) (2012) 2718, https://doi.org/10.1039/c2cs15309b.
[17] D. Maiolo, L. Paolini, G. Di Noto, A. Zendrini, D. Berti, P. Bergese, D. Ricotta, Colorimetric Nanoplasmonic Assay to Determine Purity and Titrate Extracellular Vesicles, Anal. Chem. 87 (8) (2015) 4168–4176, https://doi.org/10.1021/ac504861d.
[18] K. Sugikawa, T. Kadota, K. Matsuo, K. Yasuhara, A. Ikeda, Growth of Anisotropic Gold Nanoparticle Assemblies via Liposome Fusion, Materials (Basel). 10 (11) (2017) 1–10, https://doi.org/10.3390/ma10111317.
[19] J. Turkevich, P.C. Stevenson, J. Hillier, A Study of the Nucleation and Growth Processes in the Synthesis of Colloidal Gold, Discuss. Faraday Soc. 11 (1951) 55–75, https://doi.org/10.1039/DF9511100055.
[20] G. Frens, Controlled Nucleation for the Regulation of the Particle Size in Monodisperse Gold Suspensions, Nat. Phys. Sci. 241 (1973) 20–22, https://doi.org/10.1038/physci241020a0.
[21] J. Piella, N.G. Bastús, V. Puntes, Size-Controlled Synthesis of Sub-10-Nanometer Citrate-Stabilized Gold Nanoparticles and Related Optical Properties, Chem. Mater. 28 (4) (2016) 1066–1075, https://doi.org/10.1021/acs.chemmater.5b04406.
[22] S.R. Kline, Reduction and Analysis of SANS and USANS Data Using IGOR Pro, J. Appl. Crystallogr. 39 (6) (2006) 895–900, https://doi.org/10.1107/S0021889806035059.
[23] B. Gumí-Audenis, L. Costa, L. Redondo-Morata, P.E. Milhiet, F. Sanz, R. Felici, M. I. Giannotti, F. Carlà, In-Plane Molecular Organization of Hydrated Single Lipid Bilayers: DPPC: Cholesterol, Nanoscale 10 (1) (2018) 87–92, https://doi.org/10.1039/c7nr07510c.
[24] B. Gumí-Audenis, F. Carlà, M.V. Vitorino, A. Panzarella, L. Porcar, M. Boilot, S. Guerber, P. Bernard, M.S. Rodrigues, F. Sanz, et al., Custom AFM for X-Ray Beamlines. In Situ Biological Investigations under Physiological Conditions, J. Synchrotron Radiat. 22 (6) (2015) 1364–1371, https://doi.org/10.1107/S1600577515016318.
[25] M.L. Ainalem, R.A. Campbell, T. Nylander, Interactions between DNA and Poly (Amido Amine) Dendrimers on Silica Surfaces, Langmuir 26 (2010) 8625–8635, https://doi.org/10.1021/la9047177.
[26] M. Rodahl, F. Höök, C. Fredriksson, C.A. Keller, A. Krozer, P. Brzezinski, M. Voinova, B. Kasemo, Simultaneous Frequency and Dissipation Factor QCM Measurements of Biomolecular Adsorption and Cell Adhesion, Faraday Discuss. 107 (1997) 229–246, https://doi.org/10.1039/a703137h.
[27] C. Montis, Y. Gerelli, G. Fragneto, T. Nylander, P. Baglioni, D. Berti, Nucleolipid Bilayers: A Quartz Crystal Microbalance and Neutron Reflectometry Study, Colloids Surfaces B Biointerfaces 137 (2016) 203–213, https://doi.org/10.1016/j.colsurfb.2015.07.039.
[28] B. Wang, L. Zhang, S. Chul, S. Granick, Nanoparticle-Induced Surface Reconstruction of Phospholipid Membranes, Natl. Acad. Sci. United States Am. 105 (47) (2008) 18171–18175. https://doi.org/https://doi.org/10.1073/pnas.0807296105.
[29] T. Pfeiffer, A. De Nicola, C. Montis, F. Carlà, N.F.A. van der Vegt, D. Berti, G. Milano, Nanoparticles at Biomimetic Interfaces: Combined Experimental and Simulation Study on Charged Gold Nanoparticles/Lipid Bilayer Interfaces, J. Phys. Chem. Lett. (2018) 129–137, https://doi.org/10.1021/acs.jpclett.8b03399.
[30] B. Hammouda, A New Guinier – Porod Model, J. Appl. Crystallogr. 43 (4) (2010) 716–719, https://doi.org/10.1107/S0021889810015773.
[31] Feigin, L. A.; Svergun, D. S. Structure Anaysis by Small Angle X-Ray and Neutron Scattering; Taylor, G. W., Ed.; Plenum Press, New York: Princeton, 1987.
[32] A. Antosova, Z. Gazova, D. Fedunova, E. Valusova, E. Bystrenova, F. Valle, Z. Daxnerova, F. Biscarini, M. Antalik, Anti-Amyloidogenic Activity of Glutathione-Covered Gold Nanoparticles, Mater. Sci. Eng. C 32 (8) (2012) 2529–2535, https://doi.org/10.1016/j.msec.2012.07.036.
[33] S. Lazzari, L. Nicoud, B. Jaquet, M. Lattuada, M. Morbidelli, Fractal-like Structures in Colloid Science, Adv. Colloid Interface Sci. 235 (2016) 1–13, https://doi.org/10.1016/j.cis.2016.05.002.
[34] J. Sui, P. Zhao, B. Bin-Mohsin, L. Zheng, X. Zhang, Z. Cheng, Y. Chen, G. Chen, Fractal Aggregation Kinetics Contributions to Thermal Conductivity of Nano-Suspensions in Unsteady Thermal Convection, Sci. Rep. 6 (2016) 39446, https://doi.org/10.1038/srep39446.
[35] R. Thouy, R. Jullien, Structure Factors for Fractal Aggregates Built Off-Lattice with Tunable Fractal Dimension, J. Phys. I 6 (10) (2003) 1365–1376, https://doi.org/10.1051/jp1:1996141.
[36] V. Sharma, C. Chotia, Tarachand, V. Ganesan, G.S. Okram, Influence of Particle Size and Dielectric Environment on the Dispersion Behaviour and Surface Plasmon in Nickel Nanoparticles, Phys. Chem. Chem. Phys. (2017), https://doi.org/10.1039/c7cp01769c.
[37] R.J. Hunter, Foundations of Colloid Science, Colloids and Surfaces A: Physicochemical and Engineering Aspects (2001), https://doi.org/10.1016/S0927-7757(02)00170-X.
[38] M. Maccarini, R. Barker, A. Nelson, G. Fragneto, et al., Effect of Functionalized Gold Nanoparticles on Floating Lipid Bilayers, Langmuir 29 (22) (2013) 6606–6614, https://doi.org/10.1021/la401074y.
[39] F. Lolicato, L. Joly, H. Martinez-Seara, G. Fragneto, E. Scoppola, F. Baldelli Bombelli, I. Vattulainen, J. Akola, M. Maccarini, The Role of Temperature and

Lipid Charge on Intake/Uptake of Cationic Gold Nanoparticles into Lipid Bilayers, Small 15 (23) (2019) 1805046, https://doi.org/10.1002/smll.201805046.
[40] T. Pfeiffer, A. De Nicola, C. Montis, F. Carlà, N.F.A. Van Der Vegt, D. Berti, G. Milano, Nanoparticles at Biomimetic Interfaces: Combined Experimental and Simulation Study on Charged Gold Nanoparticles/Lipid Bilayer Interfaces, J. Phys. Chem. Lett. 10 (2) (2019) 129–137, https://doi.org/10.1021/acs.jpclett.8b03399.
[41] Y.C. Park, J.B. Smith, T. Pham, R.D. Whitaker, C.A. Sucato, J.A. Hamilton, E. Bartolak-Suki, J.Y. Wong, Effect of PEG Molecular Weight on Stability, T2 Contrast, Cytotoxicity, and Cellular Uptake of Superparamagnetic Iron Oxide Nanoparticles (SPIONs), Colloids Surfaces B Biointerfaces 119 (2014) 106–114, https://doi.org/10.1016/j.colsurfb.2014.04.027.
[42] K.P. García, K. Zarschler, L. Barbaro, J.A. Barreto, W. O'Malley, L. Spiccia, H. Stephan, B. Graham, Zwitterionic-Coated, "Stealth" Nanoparticles for Biomedical Applications: Recent Advances in Countering Biomolecular Corona Formation and Uptake by the Mononuclear Phagocyte System, Small 10 (13) (2014) 2516–2529, https://doi.org/10.1002/smll.201303540.
[43] T. Zhu, K. Vasilev, M. Kreiter, S. Mittler, W. Knoll, Surface Modification of Citrate-Reduced Colloidal Gold Nanoparticles with 2-Mercaptosuccinic Acid, Langmuir 19 (2003) 9518–9525, https://doi.org/10.1021/la035157u.
[44] K. Rana, J.R. Bhamore, J.V. Rohit, T.J. Park, S.K. Kailasa, Ligand Exchange Reactions on Citrate-Gold Nanoparticles for a Parallel Colorimetric Assay of Six Pesticides, New J. Chem. 42 (2018) 9080–9090, https://doi.org/10.1039/c8nj01294f.
[45] X. Wang, X. Wang, X. Bai, L. Yan, T. Liu, M. Wang, Y. Song, G. Hu, Z. Gu, Q. Miao, et al., Nanoparticle Ligand Exchange and Its Effects at the Nanoparticle-Cell Membrane Interface, Nano Lett. 19 (1) (2019) 8–18, https://doi.org/10.1021/acs.nanolett.8b02638.
[46] G.S. Perera, S.A. Athukorale, F. Perez, C.U. Pittman, D. Zhang, Facile Displacement of Citrate Residues from Gold Nanoparticle Surfaces, J. Colloid Interface Sci. 511 (2018) 335–343, https://doi.org/10.1016/j.jcis.2017.10.014.
[47] T. Lunnoo, J. Assawakhajornsak, T. Puangmali, In Silico Study of Gold Nanoparticle Uptake into a Mammalian Cell: Interplay of Size, Shape, Surface Charge, and Aggregation, J. Phys. Chem. C 123 (6) (2019) 3801–3810, https://doi.org/10.1021/acs.jpcc.8b07616.
[48] H.I. Ingo, M.N. Melo, F.J. Eerden, Van, C.A. Lopez, T.A. Wassenaar, X. Periole, A. H. Vries, De, D.P. Tieleman, S.J. Marrink, Lipid Organization of the Plasma Membrane, J. Am. Chem. Soc. 136 (41) (2014) 14554–14559.
[49] A.H. Bahrami, M. Raatz, J. Agudo-Canalejo, R. Michel, E.M. Curtis, C.K. Hall, M. Gradzielski, R. Lipowsky, T.R. Weikl, Wrapping of Nanoparticles by Membranes, Adv. Colloid Interface Sci. 208 (2014) 214–224, https://doi.org/10.1016/j.cis.2014.02.012.
[50] R. Michel, M. Gradzielski, Experimental Aspects of Colloidal Interactions in Mixed Systems of Liposome and Inorganic Nanoparticle and Their Applications, Int. J. Mol. Sci. 13 (9) (2012) 11610–11642, https://doi.org/10.3390/ijms130911610.
[51] J. Agudo-Canalejo, R. Lipowsky, Critical Particle Sizes for the Engulfment of Nanoparticles by Membranes and Vesicles with Bilayer Asymmetry, ACS Nano 9 (4) (2015) 3704–3720, https://doi.org/10.1021/acsnano.5b01285.
[52] O. Et-Thakafy, N. Delorme, C. Gaillard, C. Mériadec, F. Artzner, C. Lopez, F. Guyomarch, Mechanical Properties of Membranes Composed of Gel-Phase or Fluid-Phase Phospholipids Probed on Liposomes by Atomic Force Spectroscopy, Langmuir 33 (21) (2017) 5117–5126, https://doi.org/10.1021/acs.langmuir.7b00363.
[53] L. Guo, J.Y. Har, J. Sankaran, Y. Hong, B. Kannan, T. Wohland, Molecular Diffusion Measurement in Lipid Bilayers over Wide Concentration Ranges: A Comparative Study, ChemPhysChem 9 (5) (2008) 721–728, https://doi.org/10.1002/cphc.200700611.
[54] A. Nelson, Co-Refinement of Multiple-Contrast Neutron/X-Ray Reflectivity Data Using MOTOFIT, J. Appl. Crystallogr. 39 (2) (2006) 273–276, https://doi.org/10.1107/S0021889806005073.
[55] M. Raatz, R. Lipowsky, T.R. Weikl, Cooperative Wrapping of Nanoparticles by Membrane Tubes, Soft Matter 10 (20) (2014) 3570–3577, https://doi.org/10.1039/c3sm52498a.
[56] E. Sackmann, Membrane Bending Energy Concept of Vesicle- and Cell-Shapes and Shape-Transitions, FEBS Lett. 346 (1) (1994) 3–16.

Supporting Information for:

Shedding Light on Membrane-Templated Clustering of Gold Nanoparticles

Costanza Montis, Lucrezia Caselli, Francesco Valle, Andrea Zendrini, Francesco Carlà, Ralf Schweins, Marco Maccarini, Paolo Bergese, Debora Berti

Supplementary Materials and Methods

Synthesis of 16 nm-citrated AuNP

Anionic gold nanospheres of 16 nm in size were synthesized according to the Turkevich-Frens method [1,2]. Briefly, 20 mL of a 1mM $HAuCl_4$ aqueous solution was brought to boiling temperature under constant and vigorous magnetic stirring. 2 mL of 1% citric acid solution were then added and the solution was further boiled for 20 minutes, until it acquired a deep red color. The nanoparticle dispersion was then slowly cooled down to room temperature.

Synthesis of 5 nm-citrated AuNP

Anionic gold nanospheres of 5 nm in size were synthesized by the addition of tannic acid traces to the inverse Turkevich method [3]. Briefly, 1 mL of $HAuCl_4$ aqueous solution (25 mM) was injected into 150 mL of sodium citrate aqueous solution (2.2 mM), mixed with 0.1 mL of tannic acid (2.5 mM). The addition was carried out at 70°C under vigorous magnetic stirring and led to the instantaneous

color change of the solution from transparent to dark grey. After few minutes, the solution acquired an orange color, indicative of the formation of sub-10 nm gold nanoparticles. The nanoparticles dispersion was then slowly cooled down to room temperature.

Synthesis of 16 nm-MPA capped AuNP

500 μL of an aqueous solution of 3-mercaptopropionic Acid ($5 \cdot 10^{-3}$ M) were added to 5 ml of freshly prepared 16 nm-citrated AuNP ($7.8 \cdot 10^{-9}$ M). The mixture was agitated for 30 s and left at 4°C overnight.

Preparation of POPC liposomes

The proper amount of lipid was dissolved in chloroform and a lipid film was obtained by evaporating the solvent under a stream of nitrogen and overnight vacuum drying. The film was then swollen and suspended in warm (50 °C) milliQ-water by vigorous vortex mixing, in order to obtain a final 4 mg/ml lipid concentration. The resultant multilamellar vesicles (MLV) in water were subjected to 10 freeze-thaw cycles and extruded 10 times through two stacked polycarbonate membranes with 100 nm pore size at room temperature, to obtain unilamellar vesicles (ULV) with narrow and reproducible size distribution. The filtration was performed with the Extruder (Lipex Biomembranes, Vancouver (Canada)) through Nuclepore membranes.

Preparation of POPC SLB

For Small Unilamellar Vesicles preparation the proper amount of POPC was dissolved in chloroform/methanol 6:1 (v/v). A lipid film was obtained by evaporating the solvent under a stream of nitrogen and overnight vacuum drying. The film was then swollen and suspended in warm (50°C) 100 mM NaCl aqueous solution by vigorous vortex mixing. To prepare Unilamellar vesicles (ULV) with narrow distribution, the dispersion was then tip-sonicated for 30 minutes. SLB were prepared by adding 10 mM $CaCl_2$ to the dispersion of vesicles and subsequently depositing a droplet of the dispersion of vesicles on a silicon wafer previously polished and activated in a plasma cleaner. A stable SLB layered on the support was obtained by rinsing the dispersion of vesicles with pure milliQ water, after incubation of vesicles with the support for twenty minutes at r.t..

Preparation of POPC/AuNP Hybrids

The hybrid samples preparation procedure for each figure of the main text is reported below:

- Figure 1a): Fixed volumes (787 µL) of dispersion of vesicles with variable liposomes concentrations (0 M for the black curve, while from the darkest to the lightest green curve: $1.3 \cdot 10^{-9}$ M, $2.6 \cdot 10^{-9}$ M, $9.8 \cdot 10^{-9}$ M and $4.1 \cdot 10^{-8}$ M) were placed inside 3 mL UV-Vis plastic cuvette. Then,

500 µL of 16 nm-citrated gold nanoparticles ($7.8 \cdot 10^{-9}$ M, see "Synthesis of 16 nm-citrated Gold Nanoparticles" and "Supplementary Characterization of Gold Nanoparticles" of SI) were added, in order to probe the effect of different liposomes/AuNP@CT molar ratios (from 8:1 for the lightest green curve, to 1:4 for the darkest green curve) on the plasmonic features of hybrid mixtures, at a fixed interaction volume of ~1.3 mL. Water was then added to reach a final volume of 3 mL inside the plastic cuvette and spectra recorded.

- Figure 1b): the same preparation protocol of Figure 1a) was followed. From left to right: cuvette containing neat AuNP dispersion (in the absence of liposomes), 8:1, 2:1, 1:2 and 1:4 liposomes/AuNP@CT molar ratio samples.
- Figure 1c): 787 µL of different concentration liposomes solutions (0 M, $1.3 \cdot 10^{-9}$ M, $2.6 \cdot 10^{-9}$ M, $9.8 \cdot 10^{-9}$ M and $4.1 \cdot 10^{-8}$ M) were added to 500 µL of fixed concentration ($7.8 \cdot 10^{-9}$ M) 16 nm-gold nanoparticle dispersion. Water was added to reach a final volume of 3 mL inside the plastic cuvette and spectra recorded. From left to right: cuvette containing neat AuNP dispersion (in the absence of liposomes),, 8:1, 2:1, 1:2 and 1:4 liposomes/AuNP@CT molar ratio samples.
- Figure 1d): A fixed volume (190 µL) of $4.1 \cdot 10^{-8}$ M liposomes dispersion (see "Preparation of POPC liposomes" in the current section of SI) was

placed in a 3 mL plastic cuvette and added with different water amounts (from 0 to 787 µL), in order to obtain colloidal suspensions with variable dilutions. Then, 500 µL of 16 nm-citrated gold nanoparticles dispersion ($7.8 \cdot 10^{-9}$ M) was added, in order to probe the effect of different interaction volumes (from 1.3 mL for the lightest blue curve, to 0.7 mL for the purple curve) on the plasmonic features of hybrid mixtures, at a fixed liposomes/AuNP@CT ratio of 2:1. Water was added to reach a final volume of 3 mL inside the plastic cuvettes and spectra recorded.

- Figure 1e): the same preparation protocol of Figure 1d) was followed. From left to right: cuvette containing neat AuNP dispersion (in the absence of liposomes),, 1.3, 1.1, 1.9 and 0.7 mL interaction volume-hybrid mixtures.
- Figure 2a): The green curve in figure represents the SAXS profile of the $4.1 \cdot 10^{-8}$ M liposome dispersion (see "Preparation of POPC liposomes" in the current section of SI), while the AuNP@CT and hybrid mixtures SAXS profiles were recorded on samples prepared according to a previously described protocol (see Figure 1a)). All the samples were diluted 1:3 in water, in order to make the structure factor contribute to the total scattering intensity negligible and placed into sealed glass capillaries of 1.5 mm in diameter for the curves acquisition.
- Figure 2b): The 1:8 liposomes/AuNP@CT molar ratio mixture was

prepared as previously described for Figure 1a). 10 µL of hybrid dispersion was then spotted onto freshly cleaved mica substrates and dried at room temperature. After ~ 2 hours, the AFM images were acquired.

- Figure 3a, b): 3 mL of a $1.3 \cdot 10^{-9}$ M aqueous dispersion of AuNP@CT (for Figure 3a)) and AuNP@MPA (for Figure 3b)) were added to 3 mL of POPC lipid solution in chloroform inside a 20 mL glass vial; a chloroform (bottom)/water (top) biphasic system was readily formed. The vial was sealed with parafilm and slightly shaken.
- Figure 3c): The black curve is the absorbance spectrum of a $1.3 \cdot 10^{-9}$ M AuNP@CT aqueous dispersion, while the blue curve was recorded from an hybrid mixture prepared as follows: the 787 µL of a $5 \cdot 10^{-9}$ M liposomes solutions were placed inside a 3 mL UV-Vis plastic cuvette. Then, 500 µL of $7.8 \cdot 10^{-9}$ M 16 nm-citrated gold nanoparticles dispersion was added, in order to obtain a 1:1 liposomes/AuNP@CT molar ratio. Water was then added to reach a final volume of 3 mL inside the plastic cuvette and the spectrum recorded.
- Figure 3d): The black curve is the absorbance spectrum of a $1.3 \cdot 10^{-9}$ M AuNP@MPA aqueous dispersion, while the blue curve represents the absorbance of an hybrid liposomes/AuNP@MPA mixture, prepared according to the same protocol followed for the liposomes/AuNP@CT

mixture in Figure 3c).

- Figure 4a, 4c): Si wafer were cleaned prior to use by plasma cleaning, bath sonication in chloroform, acetone and ethanol and extensively rinsed with MilliQ water and ethanol. A SLB of POPC was obtained according to the previously described protocol. 20 μL of the as-synthesized 16 nm AuNP@CT aqueous dispersion were added as a single droplet on top of the SLB. After 20 minutes incubation the sample was extensively washed with milliQ water and the measurements acquired.
- Figure 4b): The red curve is the absorbance spectrum of a 5 nm-neat AuNP@CT aqueous dispersion ($9.5 \cdot 10^{-8}$ M, see "Synthesis of 5 nm-citrated Gold Nanoparticles" and "Supplementary Characterization of Gold Nanoparticles" of SI), while the blue curve was recorded from an hybrid mixture prepared as follows: 190 μL of a $4.1 \cdot 10^{-8}$ M liposomes dispersion were placed inside a 3 mL UV-Vis plastic cuvette. Then, 2810 μL of $9.5 \cdot 10^{-8}$ M 5 nm-citrated gold nanoparticles dispersion were added, in order to obtain a ~1:36 liposomes/AuNP@CT molar ratio. The spectrum was recorded.

UV-vis spectroscopy

UV-Vis spectra were measured with a JASCO UV-Vis spectrophotometer.

Small Angle X-ray Scattering

SAXS measurements on AuNP aqueous dispersions, liposomes dispersions and AuNP-liposomes hybrid systems were carried out in sealed glass capillaries of 1.5 mm diameter. To analyze gold nanospheres' curves we chose a model function with a spherical form factor and a Schulz size distribution:[4], it calculates the scattering for a polydisperse population of spheres with uniform scattering length density. The distribution of radii is a Schulz distribution given by the following equation:

$$f(R) = (z+1)^{z+1} x^z \frac{exp[-(z+1)x]}{R_{avg}\Gamma(z+1)}$$

where R_{avg} is the mean radius, $x = R/R_{avg}$ and z is related to the polydispersity. The form factor is normalized by the average particle volume, using the 3rd moment of R:

$$\langle V \rangle = \frac{4\pi}{3}\langle R^{+3} \rangle = \frac{4\pi}{3}\langle R \rangle^3 \frac{(z+3)(z+2)}{(z+1)^2}$$

The scattering intensity is:

$$I(q) = \left(\frac{4\pi}{3}\right)^2 N_0 \Delta\rho^2 \int_0^\infty f(R) R^6 F^2(qR) dR$$

where N_0 is the total number of particles per unit volume, $F(R)$ is the scattering amplitude for a sphere and $\Delta\rho$ is the difference in scattering length density between the particle and the solvent. Concerning AuNP- liposomes hybrids, SAXS curves were acquired on samples where the concentration of liposomes

was low enough to consider negligible their contribution to the overall scattered intensity (see the SAXS profile of Figure 2a in the main text, which intensity is in the range of the background in the whole q-range investigated); therefore, the measured SAXS profile could be considered only due to the AuNP contribution. In this respect, AuNP-liposomes hybrids were analyzed taking into account the form factor of AuNP (which can be analyzed as previously described), with an additional contribution (the appearance of a $I(q) \approx q^{-2}$ that can be attributed to the 2D arrangement of AuNP).

X-ray Reflectivity

The images were collected using a Maxipix camera (ESRF) (2x2 chips, 516x516 pixels) at a distance of 772 mm from the sample. The software MOTOFIT was employed for the analysis of the XRR curves. A five-layer model was employed to analyze the reflectivity profiles of neat SLBs, with scattering length density values calculated for each layer: a bulk subphase of Si, a superficial layer of SiO_2; a second layer of hydration water; a third layer composed of the polar headgroups of the SLB of the inner leaflet; a fourth layer composed of the bilayer lipid chains; a fifth layer composed of the polar headgroups of the outer bilayer leaflet; a bulk superphase of solvent. The scattering length density values for the polar headgroups and lipid chains, which were estimated by taking into account the

chemical compositions and the submolecular fragment volumes of phosphatidylcholines as determined by Armen et al. through molecular dynamic simulations [5]. The SLD values of the polar headgroup and the chain of the lipids were then considered as fitting parameters and varied, to take into account of possible SLD variations due to solvent penetration or due to AuNP presence.

Atomic Force Microscopy liquid imaging

AFM Images were processed with Gwyddion [6] (by simply plane-fitting).

SLB were prepared according to the previously described protocol, while the AuNP-vesicles samples were previously incubated in solution, then dropped onto freshly cleaved mica and finally gently rinsed with the chosen imaging buffer.

Transmission Electron Microscopy (TEM)

Trasmission electron microscopy (TEM) images were acquired with a STEM CM12 Philips electron microscope equipped with an OLYMPUS Megaview G2 camera, at CeME (CNR Florence Research Area, Via Madonna del Piano, 10 - 50019 Sesto Fiorentino).

Drops of 16 nm and 5 nm citrated AuNP, diluted ten times, were placed on 200 mesh carbon-coated copper grids with a diameter of 3 mm and a thickness of 50 μm (Agar Scientific) and dried at room temperature. Then, samples were analyzed at an accelerating voltage of 100 keV.

Dynamic Light Scattering (DLS)

DLS measurements were performed using a Malvern Panalytical Zetasizer Nano ZS90 instrument which does DLS measurements at a fixed scattering angle of 90°. A 4 mW laser of 633 nm wavelength is used as light source, the lag times of the correlator start from 25 ns as shortest and go up to 8000 s, using a maximum number of 4000 channels. After checking monomodality with a CONTIN fit, the Autocorrelation Functions were analyzed through the cumulant fitting limited to the second order, allowing an estimate of the hydrodynamic diameter and the polydispersity of POPC liposomes, which were found equal to: 100 ± 2 nm (hydrodynamic diameter) with a 0.11 (PDI).

Quartz Crystal Microbalance with Dissipation Monitoring (QCM-D)

In a QCM-D experiment the piezoelectric quartz crystal is excited at its fundamental resonance frequency and the variations both in resonance frequency, Δf, and energy dissipation factors, ΔD, are measured for several harmonics simultaneously. For a rigid film evenly distributed on the surface of the sensor and thin enough, as compared to the weight of the crystal, a linear relation, the Sauerbrey equation, connects the adsorbed mass (Δm) and the shift in resonant frequency (Δf):[7]

$$\Delta m = -\frac{c}{o_n}\Delta f$$

where C depends on the thickness and intrinsic properties of the crystal; the overtone number is represented by o_n (3, 5, 7, 9, 11 and 13). As discussed elsewhere [8], this model can be generally applied for SLBs and was employed in this work for the analysis of the QCM-D data for SLBs. The frequency shifts of the 3rd overtone were employed for the calculations. The same approach, i.e., Sauerbrey equation, was adopted to roughly evaluate the adsorption extent of AuNP on the SLB. Being c = 17.7 ng/cm^{2}Hz, and the overall frequency shift due to AuNP adsorption on POPC SLB of approximately 40 Hz, the adsorbed AuNP mass per surface area can be estimated as: 708 ng/cm^2. Taking into account a 15 nm diameter for AuNP and a 19320 kg/m^3 density of gold, the mass of a single AuNP is approximately equal to $3.4 \cdot 10^{-8}$ ng. Therefore, the number of adsorbed AuNP on the SLB is approximately $2.08 \cdot 10^{10}$ AuNP/cm^2, which, taking into account the cross section of the single NP ($A = \pi R^2$, with R= 7.5 nm), leads to an overall surface coverage of the SLB of about 3.5%.

Supplementary Characterization of Gold Nanoparticles

Transmission Electron Microscopy

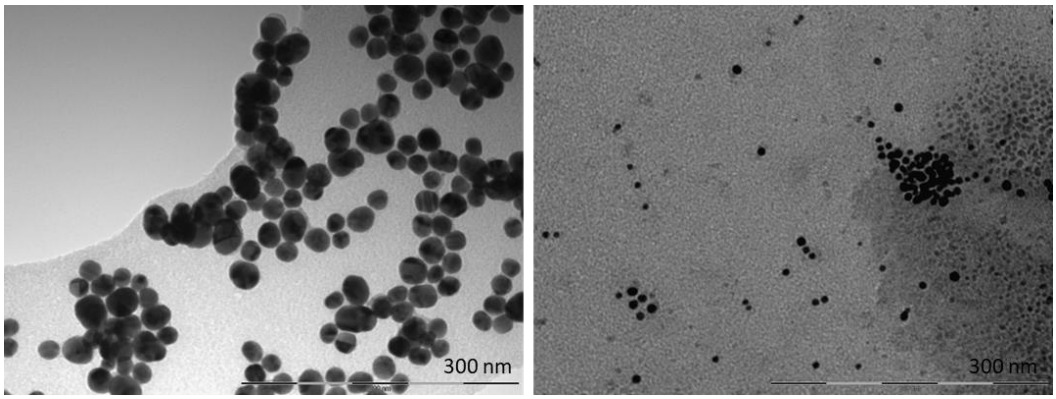

Figure S1 Representative Transmission electron microscopy (TEM) images of 16 nm citrated gold nanoparticles (left) and 5 nm citrated golf nanoparticles (right).

Small Angle X-ray Scattering

The structural parameters (Table S1) of the two different batches of citrate gold nanoparticles were evaluated from SAXS curves (Figure S2) according to the models reported in the Materials and Methods section of SI.

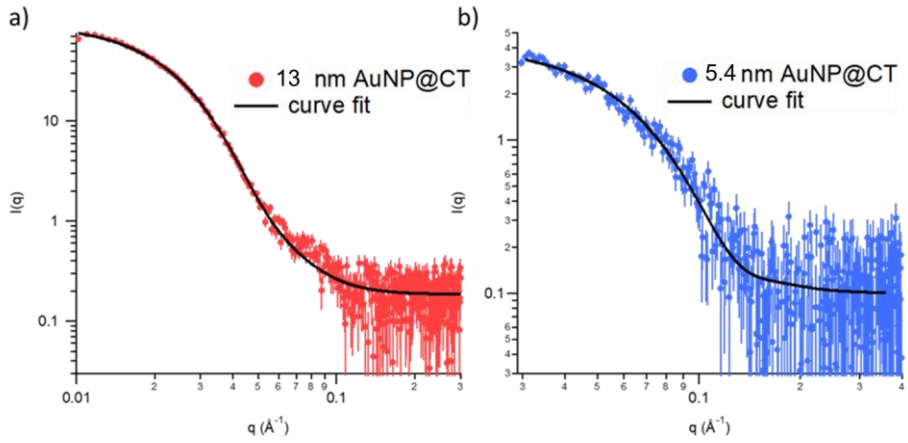

Figure S2 Experimental SAXS curves (markers in each graph) obtained for 13 nm AuNP@CT (left) and 5.4 nm AuNP@CT (right) and curve fit (solid black

line in each graph) according to the Schulz spheres model from the NIST package SANS Utilities. The size and polydispersity obtained from the fitting procedure are summarized in the Table S1 below.

	R_{core} (nm)	poly
13 nm AuNP@CT	6.5	0.3
5.4 nm uNP@CT	2.7	0.2

Table S1 Structural parameters of the nanoparticles obtained from analysis of SAXS curves according to the models described in the Materials and Methods section.

UV-vis Spectroscopy

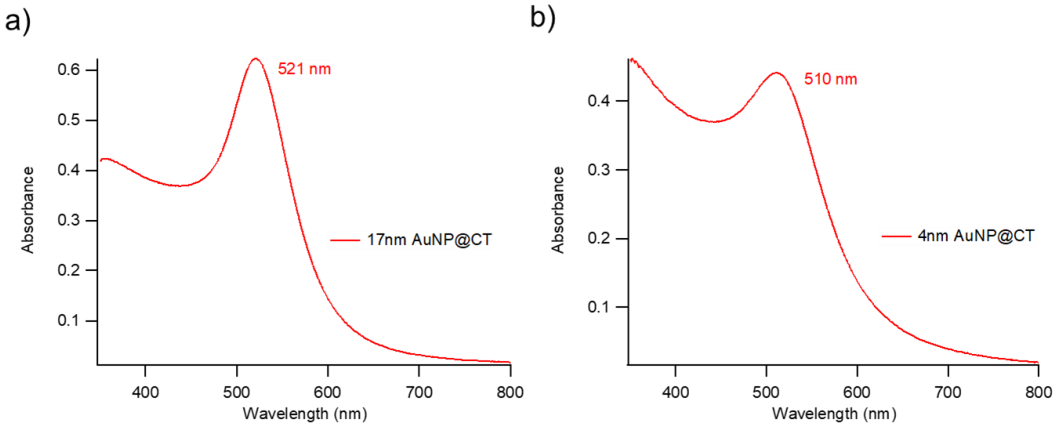

Figure S3 UV-Vis absorption spectra of gold nanospheres: (a) 16 nm AuNP@CT dispersion (after 1:5 dilution in water) and (b) 5 nm AuNP@CT pure dispersion. The plasmon absorption peaks are highlighted in each graph and are around 521 nm for the 16 nm nanospheres and around 510 nm for the 5 nm gold nanoparticles.

The size of the two different batches of citrate gold nanoparticles (16 and 5 nm in diameter) was further evaluated from UV-Vis Spectroscopy by the following equation [9]:

$$d = \exp\left(B_1 \frac{A_{spr}}{A_{450}} - B_2\right)$$

with d diameter of gold nanoparticles, A_{spr} absorbance at the surface plasma resonance peak, A_{450} absorbance at the wavelength of 450 nm and B_1 and B_2 dimensionless parameters, taken as 3 and 2.2, respectively. The diameter values obtained are 17 nm and 4 nm for the bigger and the smaller nanoparticles, respectively.

Evaluation of AuNP concentration

The concentration of citrated gold nanoparticles was determined via UV-Vis spectrometry, using the Lambert-Beer law ($E(\lambda) = \varepsilon(\lambda)lc$) and taking the extinction values $E(\lambda)$ at the LSPR maximum, i.e. λ = 521 nm and λ = 510 for the bigger and the smaller AuNP, respectively. The extinction coefficient $\varepsilon(\lambda)$ for the two different batches of gold nanoparticles was determined by the following equation [10]:

$$\ln(\varepsilon) = k\ln(d) + a$$

with d core diameter of nanoparticles, and k and a dimensionless parameters

($k = 3.32111$ and $a = 10.80505$). The arithmetic mean of the sizes obtained by both the optical and the scattering analyses was selected both for the smaller and for the bigger nanoparticles, leading to $4.8 \cdot 10^8$ $M^{-1}cm^{-1}$ and $4.6 \cdot 10^6$ $M^{-1}cm^{-1}$ for the 16 nm and the 5 nm AuNP, respectively . The final concentrations of citrated AuNP are ~$7.8 \cdot 10^{-9}$ M and ~$9.5 \cdot 10^{-8}$ M for the 16 nm and 5 nm AuNP, respectively.

Supplementary Characterization of POPC Liposomes

Evaluation of liposomes concentration

The lipid concentration in the starting colloidal dispersion was estimated to be 4 mg/mL from the initial lipid and water amounts employed in the formation and swelling of POPC lipid films (see "Preparation of POPC liposomes" in the Materials and Methods section), assuming the absence of lipid loss due to the extrusion procedure. The liposomes concentration (~$4.1 \cdot 10^{-8}$ M) was easily calculated from the lipid concentration, considering that each liposomal vesicle comprises of ~125664 lipids. This latter value was calculated considering a lipid cross section of 0.5 nm^2 and an average diameter of liposomes of 100 nm (from Dynamic Light Scattering measurements in the current section of SI), corresponding to a surface area of ~30000 nm^2 (surface area=$4\pi r^2$); the doubled surface area was divided by the lipid cross section in order to obtain the lipid number per liposome, assuming that approximately one half of the lipids is localized in the external leaflet of a liposome. Eventually, the liposomes concentration was simply obtained dividing the total lipid number, corresponding to the 4 mg/mL lipid concentration, by the lipid number per liposome.

Supplementary Theoretical considerations on AuNP-membrane interaction

Guinier-Porod fit model for AuNP aggregates on liposomes

Experimental scattering profiles for AuNP-liposomes complex of Figure 2 (main text) were fitted to a multilevel Guinier-Porod model, developed by Boualem Hammouda (NIST)[11], which models scattering as system of levels composed of Guinier and Porod (power law) areas. As evident from Figure S4, the experimental scattering profiles can be nicely fitted by considering two Guinier areas and two Porod power slopes, which is routinely done for two-dimensions objects (2D AuNPs aggregates in this case). By fitting the data, we obtained a quantitative estimation of the main parameters describing the system (see the box in Figure S4): Rg1 represents the gyration radius of single AuNP and is estimated as 6.95 ± 0.15 nm, in pretty good agreement with SAXS and UV-Vis characterization of AuNP, reported in previous sections of SI. Moreover, P (Porod exponent of single AuNP) was evaluated as 4.2 ± 0.05, as expected for smooth nanoparticles surfaces. While G is simply a Guinier scaling factor, S2 (1.95 ± 0.01) represent the dimensionality of AuNP aggregates, as obtained from fitting the low-q region of the scattering profile. The background was kept fixed (0.05) during fitting.

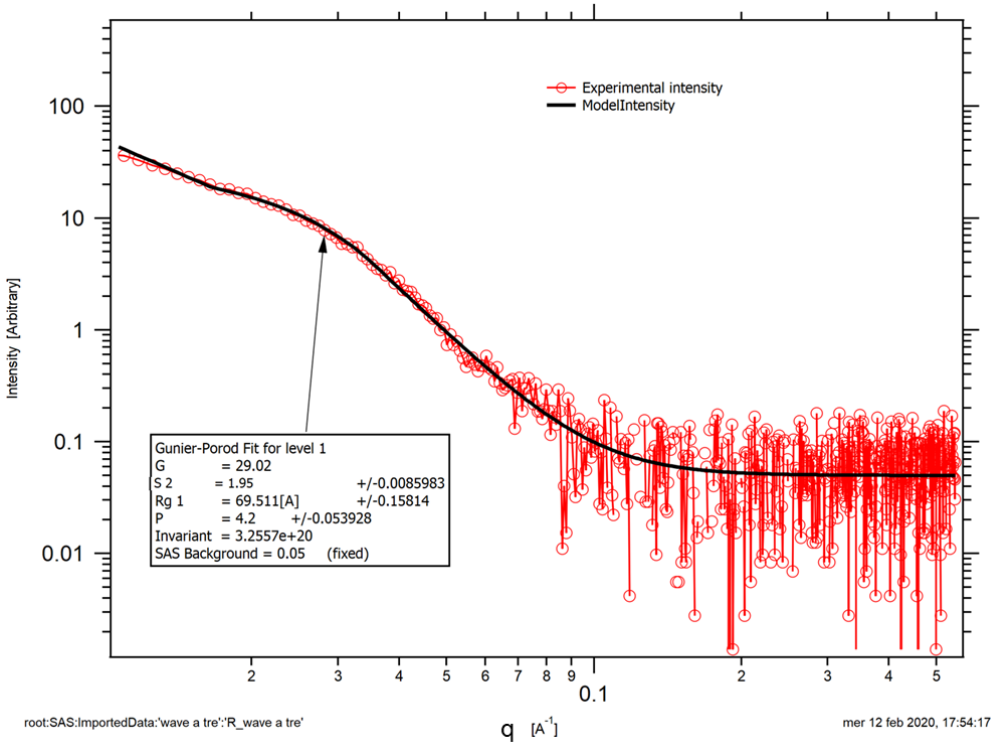

Figure S4 Experimental SAXS profile of AuNP-liposome complexes at R=0.25 (red curve) and Model intensity according to Guinier-Porod fit model (black curve). The parameter in the box represent the quantitative estimation from the fitting for the AuNP gyration radius (Rg1), Porod exponent of AuNP (P) and dimensionality of AuNP aggregates (S2). G is a Guinier scaling factor.

Poisson distribution for the interaction of dimensionless AuNP and liposomes

To rationalize the liposomes-AuNP interaction, we can treat the NP binding event to the liposome surface from a probabilistic point of view, elaborating a statistic

model relying on some assumptions:

i. Dimensionless nature of both nanoparticles and liposomes;
ii. Random binding between AuNP and liposomes (absence of preferential interactions);
iii. Irreversible bond between nanoparticles and liposomes;
iv. Complete association of nanoparticles with liposomes (absence of free AuNP in the dispersion after mixing with liposomes);
v. Each nanoparticle can only bind one liposome;
vi. One liposome can virtually host an infinite number of nanoparticles.

On the basis of these hypotheses, the probability (Π_j) of finding any liposome with a certain number (j) of AuNP attached on its surface can be described by the Poisson distribution [12], which, for specific liposomes' and AuNPs' concentrations in the solution, leads to the following equation:

$$\Pi_j = \frac{R^{-j} e^{(-1/R)}}{j!} \qquad (S1)$$

with R liposomes/AuNP molar ratio. Figure S5 a) reports the graphical representation of Π_j for four different R values.

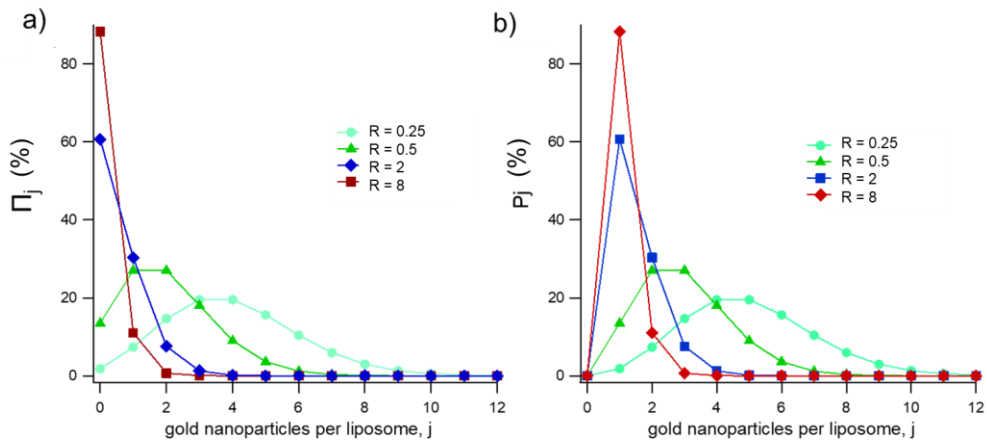

Figure S5 Poisson statistical distributions at different R. (a) Π_j, probability to find a liposome with j gold nanoparticles attached (b) P_j, probability to find a nanoparticle with j as association number.

As can be seen, variable percentages of bare and multiple AuNP covered liposomes must be taken into account for all the R values, with their relative weight exclusively dependent on R (eq.1). Considering $R = 2$ (blue curve in Figure s5a)), more than the 60% of the total ensemble of liposomes is composed of AuNP-free vesicles, ~30% of liposomes is associated with a single AuNP, while the remaining vesicles (less than 10%) are bound with more than one nanoparticle.

Remarkably, the Poisson distribution can also be used to describe the distribution of gold nanoparticles (Pj) among liposomes as a function of the association number j (with $j > 0$), which is linked to Π_j as follows::

$$P_j = \frac{R^{(1-j)} e^{(-1/R)} j}{j!} = \Pi_j^{(j-1)} \qquad (S2)$$

with $j = 1$ representing the single AuNP on a liposome, $j = 2$ the pair-association of AuNP on the same liposome, etc.

Π_j and P_j represent two well-distinct Poisson distributions: in particular, Π_j describes the probability to find a liposome with j gold nanoparticles attached on its surface, while P_j represents the probability to find an AuNP sharing the same liposomal surface with other $j - 1$ gold nanoparticles. P_j as a function of j is graphically represented in Figure S5b): for $R = 2$ about 60% of NP are likely to be found alone onto a liposome's surface, while the ~40% share surface of the same liposome with other AuNP, with the latter percent value dramatically dropping down at higher R (~12% for $R = 8$).

Poisson distribution correction for AuNP and liposomes sizes

The previous considerations are valid for point liposomes, while the (i) assumption has to be relaxed in order to give a better description of the actual situation in the solution. Assuming a 2D nature of the aggregates on lipid membranes, the liposomes' surface area (~30000 nm^2, as evaluated from Dynamic Light Scattering) sets a limit to the number of nanoparticles which can be attached to the lipid surface; considering the AuNP projected area onto a

liposome's surface (201 nm^2 from UV-vis and SAXS analyses), one can easily fix the surface's saturation value of a liposome at ~156 nanoparticles. However, these considerations do not substantially affect the Poisson distribution of eq.S2, since the Pj values are substantially negligible for $j > 10$, for all the experimentally considered *R*.

Taking a step forward to the rationalization of the experimental results, we should bear in mind that each particle absorbed at the lipid-water interface decreases the available area for the potential attachment of other AuNP and, consequently, the Pj values for $j > 1$.

Eventually, relaxing the point liposomes and nanoparticles condition leads to a further crucial consideration: even if the total percentage AuNP sharing the same liposome surface is far from being negligible for all the considered R values, the coexistence of multiple AuNP onto the same lipid membrane does not necessarily imply a coupling of their plasmon resonances; on the contrary, the ~600 nm shoulder insurgence in absorbance spectra (Figure 1 a) and d) of the main text) indicates a strong coupling between near-touching nanoparticles, implying an average interparticle distance less than 1 nm, as determined from previous theoretical studies [13]. Thereby, the probability of developing a strong plasmon coupling at the liposome surface (P_C) depends not only on the previously described Pj, but also on the ratio between the coupling promoting-area (S_C) and the total liposome's surface (S_T). This leads, for the simplest case of two AuNP

sharing the same lipid membrane, to the following equation:

$$P_C = P_2 \cdot P_{N-T} = P_2 \cdot \frac{S_C}{S_T} \qquad (S3)$$

with the "near-touching probability" (P_{N-T}) of the two nanoparticles given by the ratio between S_{C2} and S_{T2}, i.e., the coupling promoting surface (inside which a AuNP plasmon resonances coupling is promoted) and total area available for the binding of one particle, if a first particle is already fixed in any liposome surface's position. To evaluate S_C and S_T a simple geometrical model was chosen, where S_T is calculated subtracting the projected area of the first AuNP onto the lipid surface to the total liposome's area, while S_{C2} corresponds to the blue ring area in Figure S6, determined as follows:

$$S_T = \pi(3r)^2 - \pi r^2 \qquad (S4)$$

with r AuNP radius.

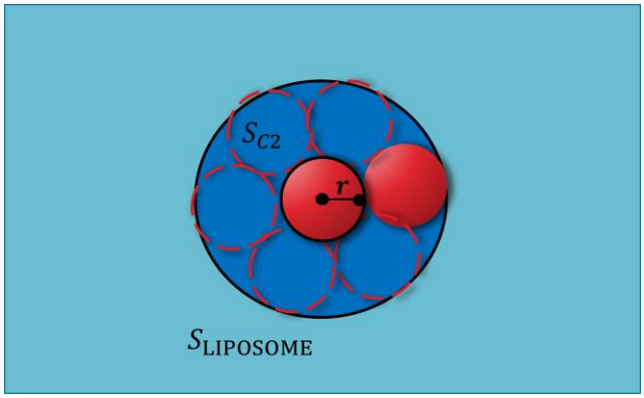

Figure S6 Graphical representation of the liposome's surface (S_T) and the coupling promoting-area (S_C, dark blue ring in the figure) for the case of two gold nanoparticles sharing the same lipid surface (red spheres in the figure).

From the combination of eq. (S3) with (S4), it is possible to evaluate P_C for any R value: this leads, for the case of $R = 2$ (mentioned in the main text), to a probability of developing a strong plasmon coupling at the liposome surface *(Pc)* of 1.6% t for two AuNP sharing the same liposome's surface (*j=2).*

Supplementary Data analysis

UV-Vis spectra analysis and deconvolution

With the aim to compare the aggregated fraction of AuNP predicted by the Poisson model with the one experimentally observed, we performed a deconvolution procedure on the absorption spectra of POPC-AuNP hybrids with Fityk deconvolution software[14], separating the single-nanoparticles contribution to SPR, to the one of the aggregated AuNPs. To this purpose, all the experimental spectra were firstly subtracted by a broad band, accounting for the interband transition of metallic nanoparticles and constituting a constant background signal for all the absorption spectra considered. For the construction of this baseline, we followed the procedure described below.

The absorbance A of an AuNP dispersion is described by the following equation:

$$A = log_{10}\frac{I_0}{I} = \frac{NC_{ext}b}{2.303} \qquad (S6)$$

with b optical path (=1 cm), N number of scattering objects for unit volume and

$Cext$ extinction cross section of a single nanoparticle. The $Cext$ of eq. S6 can be described by a complex dielectric function that depends on the frequency of light and comprises of both a real and an imaginary part, ε' and ε'' respectively:

$$C_{ext} = \frac{24\pi^2 R^3 \varepsilon_m^{\frac{3}{2}}}{\lambda} \times \frac{\varepsilon''(\omega)}{(\varepsilon'(\omega) + 2\varepsilon_m)^2 + \varepsilon''(\omega)} \quad (S7)$$

with R nanoparticles radius, λ wavelength and ε_m medium dielectric function (assumed constant and equal to 1.78 for water in the visible wavelength range). By the consideration of eq. (S7), eq. (S6) can be rewritten as a function of ε' and ε'', as follows:

$$A = \frac{24N\pi^2 R^3 \varepsilon_m^{\frac{3}{2}} b}{2.303\lambda} \times \frac{\varepsilon''(\omega)}{(\varepsilon'(\omega) + 2\varepsilon_m)^2 + \varepsilon''(\omega)} \quad (S8)$$

Both ε' and ε'' comprise of a bound electron contribution, arising from interband transitions, and a free electron contribution, determined by the intraband transitions of the conduction electrons; these two contributions are considered to be independent from each other, so that the real and imaginary parts of the dielectric function are given by [15]:

$$\varepsilon'(\omega) = \varepsilon'_b(\omega) + \varepsilon'_f(\omega) \quad (S9)$$

$$\varepsilon''(\omega) = \varepsilon''_b(\omega) + \varepsilon''_f(\omega) \quad (S10)$$

The contribution of the bound electrons can be considered independent from the

NP structure adopted in dispersion [15] and all the absorbance changes observed should be related to the free electron contribution; therefore, the theoretical evaluation of this contribution allows establishing the nanoparticles background absorbance, against which all the recorded spectra must be compared.

Taking into account eq. (S8), the absorbance due to interband transitions (A_b) is:

$$A_b = \frac{24N\pi^2R^3\varepsilon_m^{\frac{3}{2}}b}{2.303\lambda} \times \frac{\varepsilon''_b(\omega)}{(\varepsilon'_b(\omega) + 2\varepsilon_m)^2 + \varepsilon''_b(\omega)} \qquad \text{(S11)}$$

Being N, ε_m and b known and R determinable from the UV-Vis spectrum and SAXS analysis (see Supplementary Characterization of Gold Nanoparticles of the Supporting Information), A_b theoretical value is unambiguously determined once the bound electrons contribution to the dielectric function as a function of frequency is evaluated. In the present case, the values obtained by Johnson and Christy [16] for $\varepsilon''_b(\omega)$ in the range 280-800 nm were used, while the $\varepsilon'_b(\omega)$ values were obtained by subtracting the free electron value $\varepsilon'_f(\omega)$ from Drude theory, including the core polarizability from the real part of the dielectric function which was experimentally measured by Johnson and Christy. The obtained baseline is shown in Figure S7 and was employed to deconvolve the experimental UV-vis absorbance of the hybrid POPC-AuNP system shown in Figure S8.

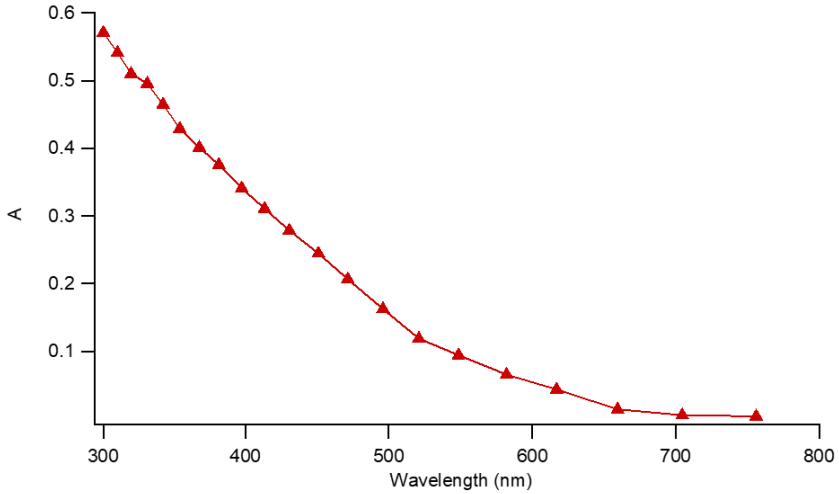

Figure S7 Calculated background absorbance due to the bound electronic contribution to the dielectric function and used as a baseline for the deconvolution of all experimental UV-vis spectra.

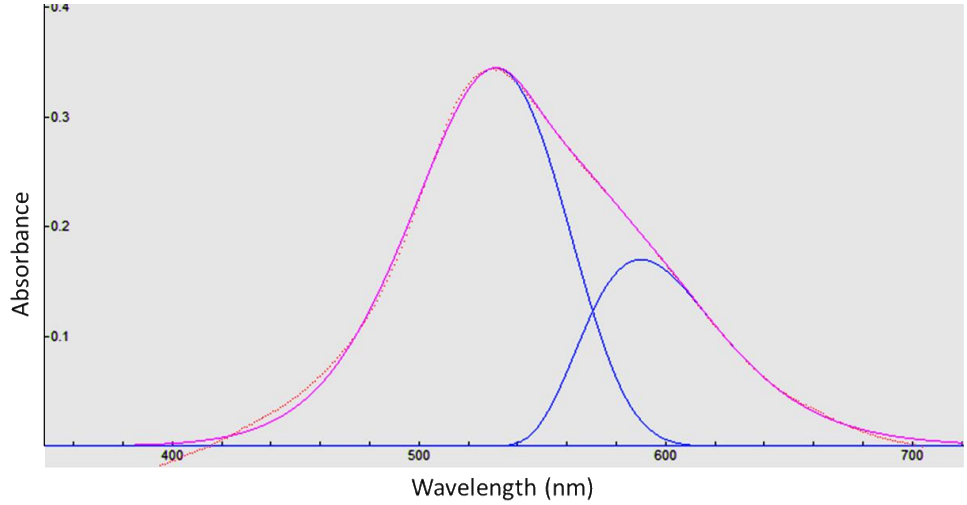

Figure S8 Deconvolution of the experimental spectrum of the 2:1 liposome/AuNP@CT ratio sample, at the minimum interaction volume (violet curve in Figure 1d) of the main text): the violet curve is the baseline-corrected experimental spectrum, the pink-dotted curve is the logNormal fit, while those blue represent the primary (free nanoparticles) and the secondary (aggregated nanoparticles) simulated bands. The area under the two red curves (27.4 and 12.4,

respectively) is correlated to the relative weight of single and coupled AuNP.

X-ray Reflectivity results

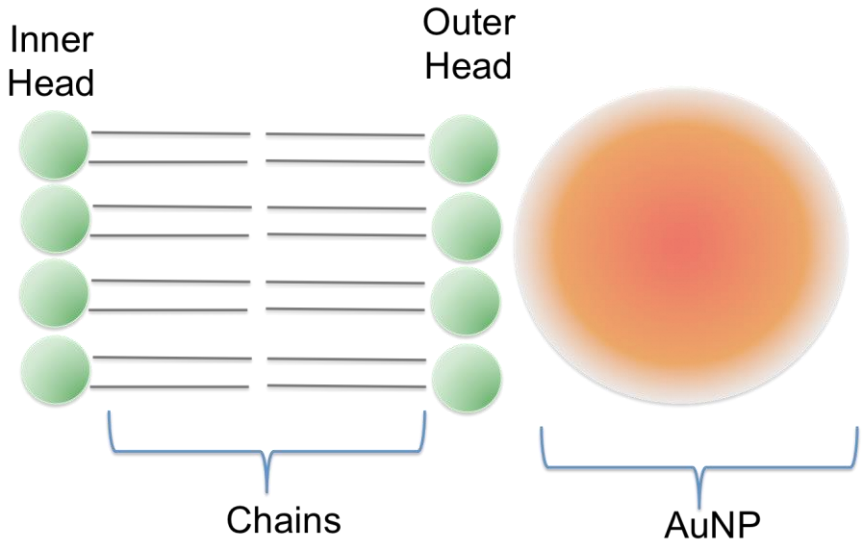

Bilayer Parameters		POPC SLB	POPC SLB AuNP
Inner Head	**d inner head (Å)**	7 ± 1	7± 1
	SLD inner head (10^{-6} Å^{-2})	14.4 ± 0.5	14 .4
Chains	**d chains (Å)**	29 ± 2	30.8 ± 2
	SLD chains (10^{-6} Å^{-2})	7.7 ± 0.2	7.7
Outer Head	**d outer head$_{sup}$ (Å)**	6 ± 1	6 ± 1
	SLD outer head$_{sup}$ (10^{-6} Å^{-2})	14.4 ± 0.5	14 .4
	d AuNP (Å)	-	150

AuNP	SLD AuNP (10^{-6} Å^{-2})	-	10.2 ± 0.5

Table S2: Curve fitting results of XRR data measured for the "naked" POPC SLB and for the same SLB in the presence of AuNP (POPC SLB AuNP), obtained with MOTOFIT. Head parameters obtained for the lipid polar headgroups (inner heads are facing the support, outer heads are facing the solution), Chains parameters obtained for the lipid chains: SLD scattering length density of chains and polar headgroups (SLD were considered as fitting parameters, in order to take into account of solvent penetration effects, however, solvent penetration extent was found negligible both for the heads and for the chains layers). For the samples with AuNP the SLD values for POPC SLD were fixed to the ones in the absence of AuNP, as well as the diameter of AuNP (150 Å), in order to obtain an estimate of the SLD of the AuNP layer and, therefore, evaluate the amount of adsorbed AuNP. Considering a scattering length density of $124 \cdot 10^{-6}$ Å^{-2} for AuNP, the adsorbed layer of AuNP contains around 99% water. A scheme of the bilayer is reported in the figure.

Supplementary Graphs and Images

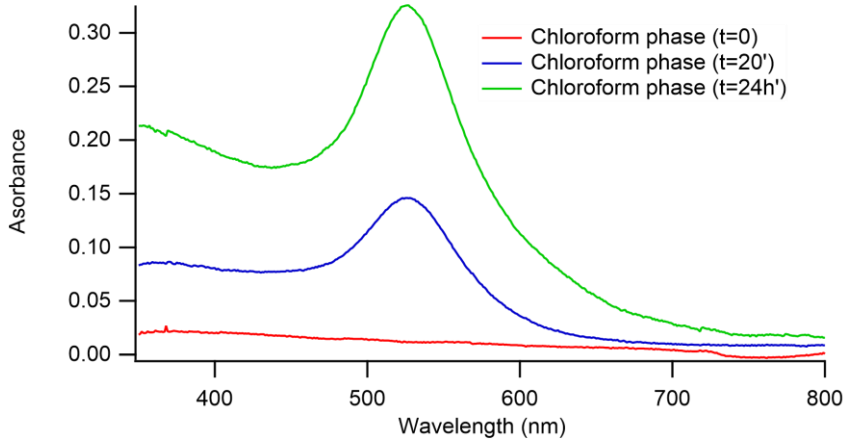

Figure S9 Absorbance of the chloroform phase extracted from the biphasic (citrated AuNP + water)/(chloroform + POPC) system at different times from the preparation: soon after the mixing for the red curve, after 20 minutes for the blue curve and after 24 hours for the green curve.

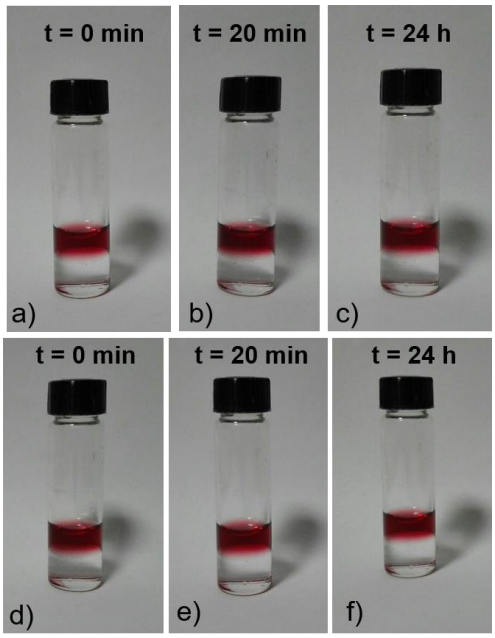

Figure S10 Images of the biphasic (NP + water)/(chloroform in the absence of POPC) system taken at different times from the preparation: (a, b, c) The two-phase system (NP + water)/(chloroform) soon after chloroform addition, after 20 minutes and 24 h for the case of citrated AuNP; (d, e, f) The two-phase system (NP + water)/(chloroform) soon after chloroform addition, after 20 minutes and 24 h for the case of MPA-capped AuNP.

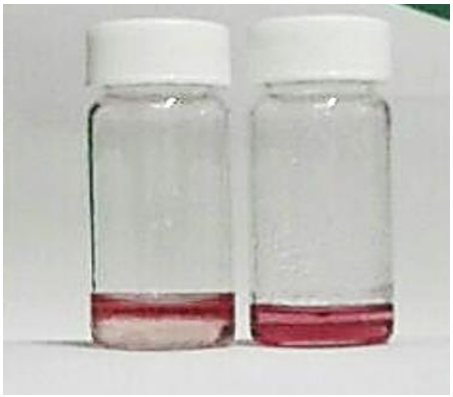

Figure S11 Picture of the two-phase system (5 nm citrated AuNP in water phase)/(chloroform phase) system: the vial on the left represents the (5 nm citrated AuNP in water phase)/(chloroform phase) system after 24 h from the mixing; the vial on the right represents the (5 nm citrated AuNP in water phase)/(chloroform phase + POPC 1 mg/ml) system after 24 h from the mixing

Bibliography

(1) Turkevich, J.; Stevenson, P. C.; Hillier, J. A Study of the Nucleation and Growth Processes in the Synthesis of Colloidal Gold. *Discuss. Faraday Soc.* **1951**, *11* (0), 55–75. https://doi.org/10.1039/DF9511100055.

(2) Frens, G. Controlled Nucleation for the Regulation of the Particle Size in Monodisperse Gold Suspensions. *Nat. Phys. Sci.* **1973**, *241*, 20–22. https://doi.org/10.1038/physci241020a0.

(3) Piella, J.; Bastús, N. G.; Puntes, V. Size-Controlled Synthesis of Sub-10-Nanometer Citrate-Stabilized Gold Nanoparticles and Related Optical Properties. *Chem. Mater.* **2016**, *28* (4), 1066–1075. https://doi.org/10.1021/acs.chemmater.5b04406.

(4) Kotlarchyk, M.; Chen, S.-H. Analysis of Small Angle Neutron Scattering

Spectra from Polydisperse Interacting Colloids. *J. Chem. Phys.* **1983**, *79* (5), 2461. https://doi.org/10.1063/1.446055.

(5) Armen, R. S.; Uitto, O. D.; Feller, S. E. Phospholipid Component Volumes: Determination and Application to Bilayer Structure Calculations. *Biophys. J.* **1998**, *75* (2), 734–744. https://doi.org/10.1016/S0006-3495(98)77563-0.

(6) Nečas, D.; Klapetek, P. Gwyddion : An Open-Source Software for SPM Data Analysis. *Cent. Eur. J. Phys.* **2012**, *10* (1), 181–188. https://doi.org/10.2478/s11534-011-0096-2.

(7) Höök, F.; Kasemo, B.; Nylander, T.; Fant, C.; Sott, K.; Elwing, H. Variations in Coupled Water, Viscoelastic Properties, and Film Thickness of a Mefp-1 Protein Film during Adsorption and Cross-Linking: A Quartz Crystal Microbalance with Dissipation Monitoring, Ellipsometry, and Surface Plasmon Resonance Study. *Anal. Chem.* **2001**, *73* (24), 5796–5804. https://doi.org/10.1021/ac0106501.

(8) Ainalem, M. L.; Kristen, N.; Edler, K. J.; Hook, F.; Sparr, E.; Nylander, T. DNA Binding to Zwitterionic Model Membranes. *Langmuir* **2010**, *26* (7), 4965–4976. https://doi.org/10.1021/la9036327.

(9) Haiss, W.; Thanh, N. T. K.; Aveyard, J.; Fernig, D. G. Determination of Size and Concentration of Gold Nanoparticles from UV-Vis Spectra. *Anal. Chem.* **2007**, *79* (11), 4215–4221. https://doi.org/10.1021/ac0702084.

(10) Liu, X.; Atwater, M.; Wang, J.; Huo, Q. Extinction Coefficient of Gold Nanoparticles with Different Sizes and Different Capping Ligands. *Colloids Surfaces B Biointerfaces* **2007**, *58* (1), 3–7. https://doi.org/10.1016/j.colsurfb.2006.08.005.

(11) Hammouda, B. A New Guinier – Porod Model. *J. Appl. Crystallogr.* **2010**, *43* (4), 716–719. https://doi.org/10.1107/S0021889810015773.

(12) Hunter, R. J. Foundations of Colloid Science. *Oxford Univ. Press Inc., New York*, **2001**, Page 472 (Exercise 9.6.1.). https://doi.org/10.1016/S0927-7757(02)00170-X.

(13) Guo, L.; Xu, Y.; Ferhan, A. R.; Chen, G.; Kim, D. R. Oriented Gold Nanoparticle Aggregation for Colorimetric Sensors with Surprisingly High Analytical Figures of Merit. *J Am Chem Soc.* **2013**, *135* (33), 12338–12345. https://doi.org/10.1021/ja405371g.

(14) Wojdyr, M. Fityk : A General-Purpose Peak Fitting Program. *J. Appl. Crystallogr.* **2010**, *43* (5–1), 1126–1128. https://doi.org/10.1107/S0021889810030499.

(15) Sendroiu, I. E.; Mertens, S. F. L.; Schiffrin, D. J. Plasmon Interactions between Gold Nanoparticles in Aqueous Solution with Controlled Spatial Separation. *Phys. Chem. Chem. Phys.* **2006**, *8* (12), 1430. https://doi.org/10.1039/b518112g.

(16) Johnson, P. B.; Christy, R. W. Optical Constants of the Noble Metals. *Phys. Rev. B* **1972**, *6* (12), 4370–4379. https://doi.org/10.1103/PhysRevB.6.4370.

Paper III

A plasmon-based nanoruler to probe the mechanical properties of synthetic and biogenic nanosized lipid vesicles (Paper III)

L. Caselli, A. Ridolfi, J.Cardellini, L. Sharpnack, L. Paolini, M. Brucale, F. Valle, C. Montis, P. Bergese and D. Berti, 2020, Preprint. https://doi.org/10.26434/chemrxiv.13488120.v1 published on *ChemRxiv* and submitted to *Nanoscale Horizons* (December 2020)

COMMUNICATION

A plasmon-based nanoruler to probe the mechanical properties of synthetic and biogenic nanosized lipid vesicles

Received 00th January 20xx,
Accepted 00th January 20xx

DOI: 10.1039/x0xx00000x

Lucrezia Caselli[a,b], Andrea Ridolfi [a,b,c], Jacopo Cardellini[a,b], Lewis Sharpnack[d], Lucia Paolini[b,e], Marco Brucale[b,c], Francesco Valle[b,c], Costanza Montis*[a,b], Paolo Bergese[b,e,f] and Debora Berti*[a,b]

Membrane-delimited compartments, as lipid vesicles, are ubiquitous in natural and synthetic systems. The mechanical properties of such vesicles are crucial for several physical, chemical, and biological processes. However, their accurate determination is still challenging and requires sophisticated instruments and data analysis. Here we report the first evidence that the surface plasmon resonance (SPR) of citrated gold nanoparticles (AuNPs) adsorbed on synthetic vesicles is finely sensitive to the vesicles' mechanical properties. We leverage this finding to demonstrate that the spectrophotometric tracking of the SPR provides quantitative access to the stiffness of vesicles of synthetic and natural origin, such as extracellular vesicles (EVs). This plasmon-based "stiffness nanoruler" paves the way for developing a facile, cost-effective, and high-throughput method to assay the mechanical properties of vesicles of nanometric size and unknown composition.

Introduction

Membrane-delimited compartments (e.g., cells, organelles, enveloped viruses, biogenic vesicles, etc.) are among the basic units of living organisms and widespread structural motifs in bio-inspired nanomaterials, such as liposomes. Their mechanical properties, which regulate the response to external deformations, are crucial in a host of biologically-relevant interactions at the nanoscale [1–5]. The deformability of liposomes or polymeric vesicles for drug delivery affects their pharmacokinetics in the bloodstream and their internalization mechanisms [6]. The mechanical properties of cells and membrane bound-organelles are key in numerous biological processes (e.g. cell fusion, growth and differentiation, endo- and exocytosis, uptake of nanoparticles or viruses [7–9], etc.) and in the onset of pathological cell conditions [10–13]. Recent reports have highlighted that the mechanical response of extracellular vesicles, (EVs, membrane-delimited nanoparticles secreted by all cell types and essential mediators of cell signalling [14–16]) is a biomarker for malignant conditions of parental cells [17,18]. In addition, the nanomechanics of pathogens, including viruses with a lipid envelope (e.g. Moloney murine leukemia virus and HIV [19]) was recently connected to their infectivity [20].

Although central in several research areas, the accurate assessment of the mechanical properties of synthetic or natural vesicles still poses a challenge [21,22]. Traditional methods provide insights into biologically-relevant descriptors of the mechanical response of the lipid membrane, such as the bilayer's bending rigidity [23–27]. However, these techniques are cost- and time-consuming, and often yield discrepant results, as pointed out in several reports [21,22,28–30]. More recently, techniques that actively probe the mechanical properties at a whole-vesicle level, rather than those of the lipid shell (e.g. Atomic Force Microscopy-based Force Spectroscopy (AFM-FS), optical tweezers, etc.) are gaining the central stage [31]. These methods allow determining the overall mechanical response of the vesicle to applied deformations, i.e., its "stiffness". The measured stiffness includes contributions both from the membrane shell and the enclosed volume, accounting for the mechanical properties of the internal pool, volume variations upon deformation, osmotic imbalance, etc. Unfortunately, the experimental methods proposed so far probe a single particle at a time and require sophisticated instruments or/and highly experienced users [31].

Here, we propose AuNPs as nanoprobes of the stiffness of membranous nano-objects, with typical submicron sizes. This approach overcomes many limitations of the currently available methods, measurements can be performed with an UV-Vis spectrophotometer and limited data analysis is required. In the following, this communication will (i) explore how the stiffness of liposomes modulates the surface plasmon resonance (SPR) of AuNPs adsorbed on their membrane and (ii) propose this previously unnoticed relationship as the working principle of a

[a] *Department of chemistry, University of Florence, Via della Lastruccia 3, Sesto Fiorentino, 50019 Florence, Italy.*
[b] *Consorzio Sistemi a Grande Interfase, Department of Chemistry, University of Florence, Sesto Fiorentino, Italy*
[c] *Consiglio Nazionale delle Ricerche, Istituto per lo Studio dei Materiali Nanostrutturati (CNRISMN), via Gobetti 101, 40129 Bologna (Italy).*
[d] *ESRF - The European Synchrotron, 38043 Grenoble, France*
[e] *Department of Molecular and Translational Medicine, University of Brescia, Brescia, Italy*
[f] *Consorzio Interuniversitario Nazionale per la Scienza e la Tecnologia dei Materiali, Florence, Italy*

† Footnotes relating to the title and/or authors should appear here.
Electronic Supplementary Information (ESI) available: [details of any supplementary information available should be included here]. See DOI: 10.1039/x0xx00000x

new, accessible and robust spectrophotometric method to evaluate the stiffness of both synthetic and natural lipid vesicles of unknown composition.

The SPR of AuNPs is finely sensitive to the chemical environment and the interparticle distance, which underpins their application as nanoscale probes [32]. The coupling between the SPR of proximal AuNPs, which results from AuNPs close approach or aggregation, was exploited for the first time by El-Sayed and co-workers as a plasmon ruler [33] and is nowadays used in a number of bioanalytical assays [34,35]. The CONAN (COlloidal NANoplasmonic) assay is a recent example, where the AuNPs SPR shift upon incubation with EVs is exploited to determine their purity and concentration [36–38]; in this latter case, the SPR shift arises from the spontaneous aggregation of AuNPs on the lipid membrane of vesicles (of both synthetic and natural origin, as EVs). This membrane-induced aggregation has been the focus of several recent investigations [39–44]. Specifically, the membrane-induced aggregation of AuNPs has been interpreted as on-off mechanism to date [45,46], switchable by the physical state of the membrane: fluid-phase bilayers, characterized by free lipid diffusion and low rigidity, would promote aggregation, resulting in a marked change of AuNPs SPR profile. Conversely, the aggregation of AuNPs would be completely inhibited on tightly packed gel-phase membranes, characterized by a higher rigidity. Here we demonstrate instead that the SPR shift of AuNPs shows a functional dependence on the stiffness of synthetic vesicles, which allows defining a "stiffness nanoruler". In analogy with the plasmon nanoruler, introduced as distance-sensor [33], this plasmon-based descriptor leverages the unique sensitivity of AuNPs SPR to determine the mechanical properties of lipid vesicles. As a proof-of-principle of applicability to complex natural systems, we tested the assay on EVs, whose stiffness is of prominent relevance in cellular adhesion and uptake [47] and a characteristic that distinguish EVs deriving from malignant and nonmalignant cells [17,18].

Results and Discussion

We prepared a library of unilamellar liposomes having a similar average diameter (~ 100 nm) and low polidispersity indexes (see Supporting Information for details on preparation and characterization) from a set of synthetic phosphatidylcholines (PC) differing for length and/or degree of unsaturation of the acyl chains (Figure 1a). The free-standing bilayers, either in the gel or fluid phase at room temperature (Figure 1a), display different rigidities [48–51]. Given their very similar size distributions and the absence of any osmotic imbalance between the lumen and the external medium, the rigidity of the

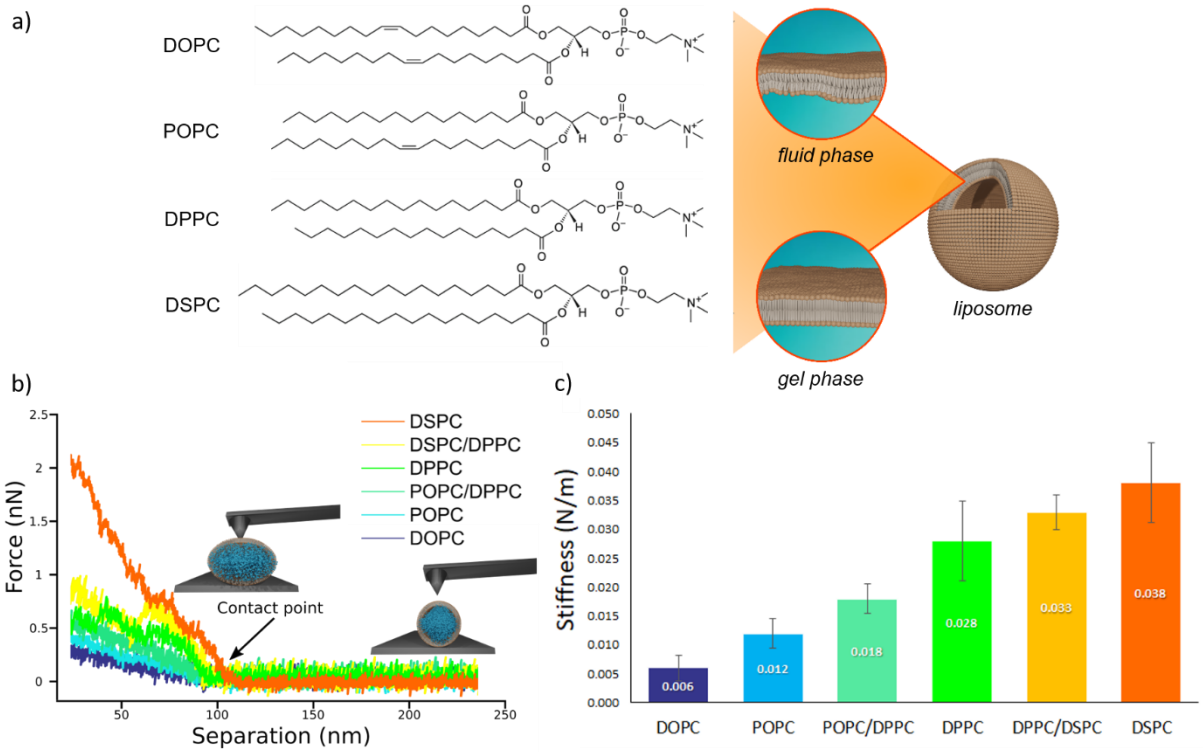

Figure 1. AFM characterization of vesicles stiffnesses. a) Chemical formulas of the four lipids used for the preparation of liposomes (1,2-distearoyl-sn-glycero-3-phosphocholine (DSPC), 1,2-dipalmitoyl-sn-glycero-3-phosphocholine (DPPC), 1-palmitoyl-2-oleoyl-glycero-3-phosphocholine (POPC) and 1,2-dioleoyl-sn-glycero-3-phosphocholine (DOPC)); depending on the molecular composition, the lipid bilayer enclosing a liposome exhibits a different degree of molecular packing at room temperature, which determines the phase (i.e., fluid or gel) of the membrane. b) AFM force-distances curves for the different vesicles batches, together with graphical representation of vesicles deformation induced by the AFM tip at two different separation distances. Liposomes samples are DOPC; POPC, POPC/DPPC (50/50 mol%), DPPC, DPPC/DSPC (50/50 mol%) and DSPC vesicles; c) Stiffness values (N/m) of the different vesicles, determined through AFM-FS; All error bars represent the uncertainties obtained by bootstrapping (1000 repetitions of 5 draws, with replacement).

lipid shells can be considered the sole responsible for the overall stiffnesses of the vesicles.

Figure 1b reports representative AFM-FS force/distance plots of single-vesicle indentation events for each lipid [52,53]. The slope of the linear regime occurring immediately after the contact point represents the stiffness of the vesicles; the stiffnesses in Figure 1c were obtained by averaging the values for multiple vesicles (see Supporting Information for further details). Taken together, the entire series of stiffness values measured on the selected library of synthetic PC standards can be regarded as a stiffness gauge in which the rigidity monotonically increases from DOPC to DSPC vesicles, in line with the literature [21,54]. This set will be used to validate the stiffness plasmon nanoruler.

The vesicles were then challenged with a water dispersion of negatively charged citrated AuNPs (13 ± 0.6 nm diameter, zeta potential: -36 ± 2 mV), and the changes in the SPR profile monitored after 15 minutes (Figure 2a).

The AuNPs dispersion in the absence of lipid vesicles shows a well-defined SPR peak centred at 522 nm (red curve); upon mixing with liposomes, an immediate colour change is visible to the naked eye (inset, Figure 2a), which clearly depends on the composition of the target membrane. Going from DSPC to DOPC, we observe colour shifts from red to increasingly dark shades of violet and blue. The variation in the SPR profile gradually increases as the stiffness of vesicles decreases. Specifically, from the stiffest vesicles (DSPC) to the softest ones (DOPC), the progressive emergence of a high-wavelength shoulder can be observed, eventually resulting in a secondary plasmon peak at about 625 nm (see Figure 2a).

This new spectral feature is the hallmark of the aggregation of AuNPs, whose spatial proximity produces the coupling of the individual AuNPs plasmons.

To get insights into the structure of AuNPs aggregates, we performed Small Angle X-ray Scattering (SAXS) for DOPC, POPC, DPPC and DSPC liposomes challenged with AuNPs (Figure 2b).

The power-law dependence in the low-q region highlights the presence of AuNPs clusters on fluid-phase bilayers, with a fractal dimension which increases as the stiffness of vesicles decreases (Figure 2b, inset, and Supporting Information) [55]. The spatial correlation between AuNPs was determined from the structure factor S(q), inferred from the high-q region of the scattering profiles (Figure 2b, inset, and Supporting Information). The position of the S(q) correlation peaks for fluid-phase liposomes is consistent with NP-NP center-to-center distances comparable with the particle diameter and decreasing with vesicles stiffness (14.5 nm and 14.1 nm for POPC and DOPC, respectively). For liposomes in the gel phase, no low-q upturn of intensity was detected and the positional correlation corresponds to significantly higher NP-NP distances (i.e., 30.5 nm and 30.2 nm for DSPC and DPPC, respectively), hinting at the presence of multiple AuNPs adsorbed on the same liposomal surface, but not aggregated.

According to recent reports, the aggregation of AuNPs on lecithin vesicles is switched on and off by the membrane phase [45,46]: aggregation is inhibited on gel-phase bilayers (e.g. DPPC and DSPC at r.t.) and promoted by fluid-phase membranes (e.g. DOPC and POPC at r.t.), with no dependence on the molecular composition for bilayers in the same phase [45,46]. Conversely, the UV-Vis and SAXS data here shown provide additional insights,

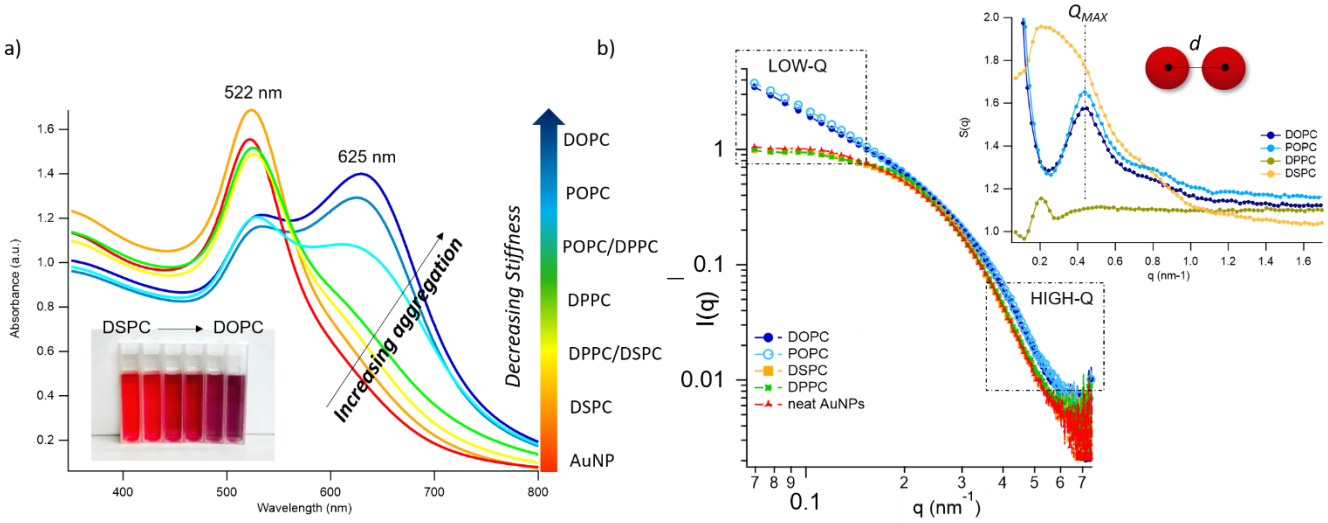

Figure 2. AuNPs interaction with lipid bilayers of different stiffness. a) UV-Vis spectra of AuNPs (1.3 nM) incubated with synthetic vesicles (0.2 nM) (liposomes/AuNPs number ratio 1/100). Inset: visual appearance of the same samples. b) SAXS profiles of NPs with and without vesicles (1:8 vesicles/NPs ratio). Under these conditions, the scattering from vesicles (subtracted from the scattering of AuNPs-vesicles mixtures) is negligible and the observed signal is only due to AuNPs. The power law dependence at low-q is connected to the presence of AuNPs clusters and to their morphology. The power-law exponents for DOPC and POPC, i.e. -1.54 and -1.5 respectively (see Supporting Information), are consistent with an increasing fractal dimension of clusters as the stiffness of vesicles decreases. The absence of such power-law for gel-phase liposomes is related to non-aggregated AuNPs, preserving their original diameter. The right inset is the structure factor (S(q)) vs q, extracted from the high-q range of vesicles/NPs profiles (see Supporting Information).

highlighting that -in these experimental conditions- AuNPs clustering on lipid vesicles is not abruptly switched-on by varying the membrane physical state, but is rather modulated by the membrane stiffness in a "continuous fashion".

This dependence can be exploited to set-up a UV-Vis spectroscopic assay to probe the mechanical properties of lipid vesicles. With this aim, we analysed the optical spectra to extract a quantitative descriptor. The so-called "stiffness index", S.I., (see Figure 3a), accounting for the main variations in the AuNPs SPR profile, was used to build-up an empirical 'AuNPs spectral response' vs 'vesicles' stiffness' scale. The S.I. for each AuNPs/vesicles hybrid is calculated dividing the area subtended by the absorbance spectrum in the 560-800 nm range by the area relative to the total spectral range (350-800 nm). The results are then normalized for the S.I. of neat AuNPs (which is then equal to 1 by definition) to obtain positive integer values of S.I., which gradually increase with increasing AuNPs aggregation extent.

Figure 3b reports the S.I. (blue dots) obtained for the liposome set plotted as a function of vesicles stiffness, obtained from AFM-FS measurements (Figure 1). Each point represents the average value obtained from five independent batches, which highlights a particularly high reproducibility.

The dependence of the S.I. on stiffness can be expressed by a sigmoidal law, with the following expression:

$$S.I. = \frac{b}{1 + exp\left(\frac{c - S}{d}\right)} + a \quad (1)$$

with S the stiffness obtained from AFM-FS and a, b, c and d constant fitting parameters (see red profile in Figure 3b for the best fitting curve and Supporting Information for further details).

For this set of synthetic vesicles, having superimposable size distributions and a luminal content identical to the external medium, the stiffness differences observed in AFM-FS are only due to a membrane contribution, which results from the different composition of the bilayers. As it is well-stablished, the mechanical response of a lipid bilayer is mainly controlled by its bending rigidity [21], quantified by the bilayer bending modulus. Therefore, in these experimental conditions, it is the bilayer bending modulus that determines the overall stiffness of the vesicles and in turn the extent of AuNPs aggregation (i.e. the S.I.).

Interestingly, in a recent simulation Lipowsky and co-authors [56] report a sigmoidal correlation between the wrapping efficiency of spherical NPs interacting with model membranes and the bilayer bending modulus. This relation holds for fixed NPs radius and membrane-NPs adhesion energy, which perfectly matches our experimental conditions (i.e. NPs of defined size and vesicles with fixed PC headgroups).

This finding is fully in line with a recent report [44], where AuNPs wrapping, modulated by the membrane bending modulus, is recognized as the main driver for the membrane-templated aggregation of AuNPs, through the mechanism sketched in Figure 3c.

The dependence of the S.I. on the stiffness of vesicles (eqn. 1) allows a quantitative estimate of the mechanical properties of membrane-enclosed compartments of unknown composition. The method here proposed possess high sensitivity and reproducibility. In fact, it is able to robustly discriminate systems with very close stiffnesses, as POPC and DOPC vesicles, whose mechanical properties are usually not distinguishable with many other techniques [54,57].

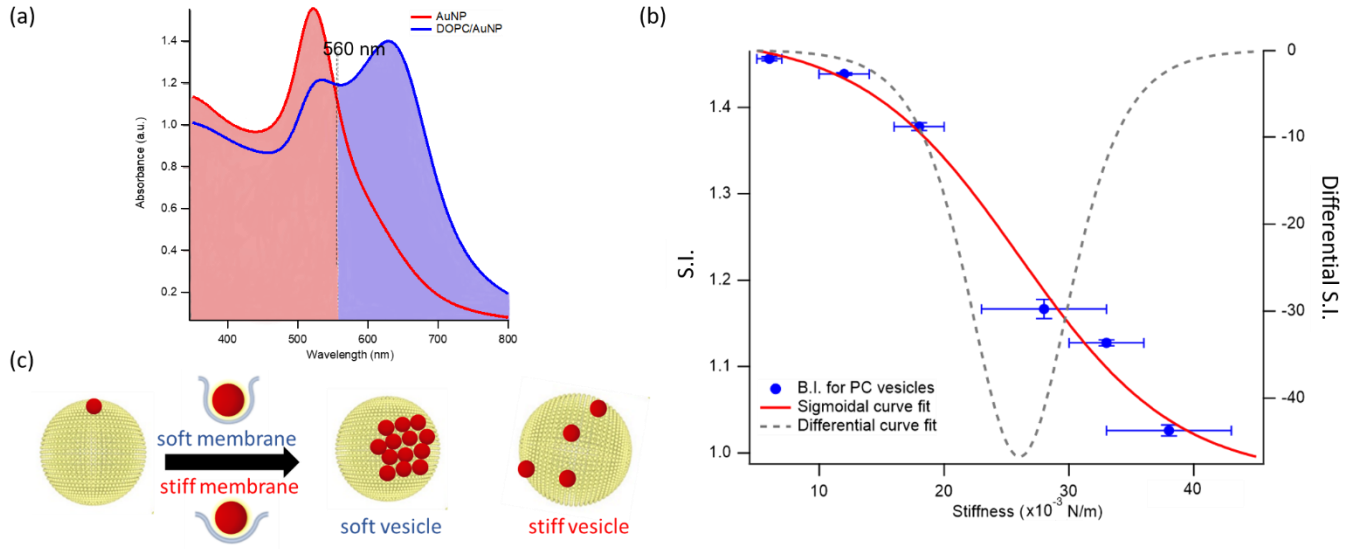

Figure 3. Quantification of Liposomes-induced variation in the AuNPs SPR profile. a) Visual description of the stiffness index (S.I.); b) S.I. values (blue spots) with relative errors bars plotted as a function of membrane stiffness. The red curve is the sigmoidal curve fit, while the grey dashed curve is the first derivative of the sigmoidal curve fit with respect to stiffness (see Supporting Info for details on fitting parameters). c) Mechanism of interaction between AuNPs and vesicles characterized by different stiffness. The adhesion of an AuNP on a soft membrane is followed by a significant AuNP wrapping by the membrane, resulting into AuNPs aggregation on the vesicle surface. The AuNP docking on a stiffer membrane results in a lower wrapping extent, preventing AuNPs clustering.

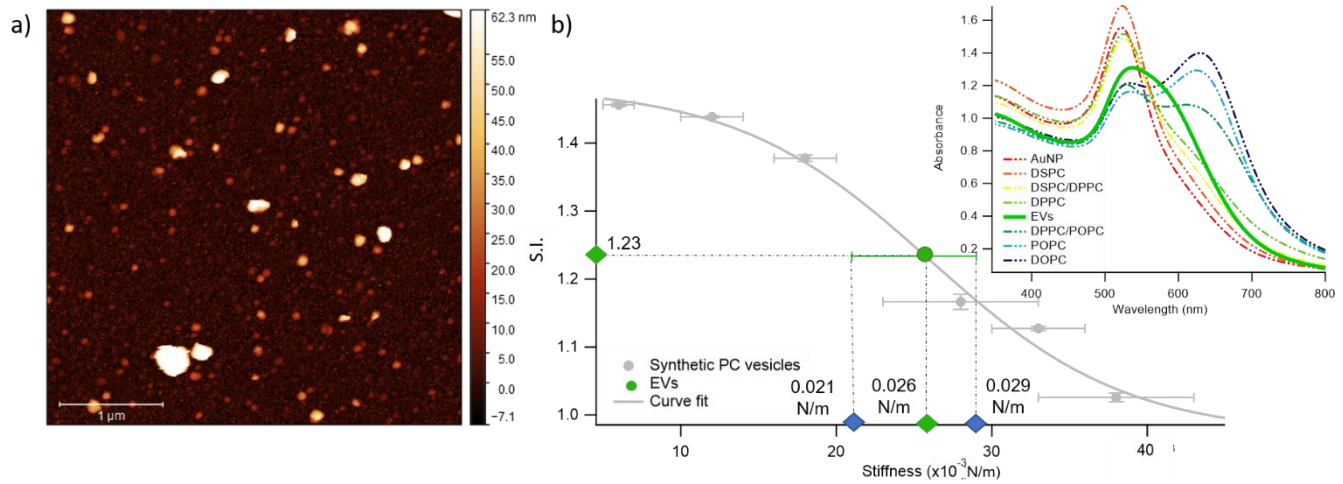

Figure 4. Quantification of Liposomes-induced variation in the SPR profile of AuNPs. a) Representative AFM image of EVs; b) Sigmoidal trend of the S.I. as a function of membrane stiffness. The EVs' S.I. (1.23), evaluated through UV-Vis spectroscopy, and stiffness, predicted by the sigmoidal law (0.026 N/m), are reported as green points in the graph. The green error bar represents the stiffness interval obtained through AFM-FS for EVs. The right inset reports the UV-Vis spectra of AuNPs (1.3 nM) in the presence of synthetic PC vesicles (dashed curves) and natural EVs (solid green curve) at a lipid concentration of 0.04 mg/ml.

In addition, the presence of a sigmoidal law, which exhibits the highest variation of S.I. in the central region of the selected set of stiffnesses (see grey dashed curve of Figure 3b, representing the first derivative of the sigmoidal fit) provides maximum sensitivity in the region where the rigidities of natural membranes usually fall (i.e. 0.02-0.025 N/m [58]).

We chose EVs to further validate the method and to provide evidence of its applicability on membranous nanoparticles which are more challenging both in terms of compositional and structural complexity, as well as in analyte availability. Specifically, we assayed a sample EVs from the murine cell line TRAMP-C2, with size and z-potential similar to the PC synthetic liposomes (see Supporting Information for details). The EVs were separated from the cell culture medium and characterized at the best of the current state of the art [59], by the protocols described in Paolini et al. (medium EVs) [60]. The morphology of EVs was investigated by liquid imaging AFM (see Figure 4a), showing the characteristic spherical cap shape of EVs adhered onto a substrate and an average diameter of 74.3 nm (refer to Supporting Info for further details).

The stiffness of EVs, determined through AFM-FS as previously described for PC liposomes, falls in the middle of the stiffness interval defined by the synthetic standards used for calibration (0.025 ± 0.004 N/m), in between the values obtained for DPPC and DPPC/POPC vesicles (see Figure 1c). EVs were mixed with AuNPs in the same conditions (AuNPs/vesicles number ratio, incubation time and temperature) previously employed for synthetic liposomes and the SPR profile change of AuNPs was recorded through UV-Vis spectroscopy (right inset of Figure 4b). In full agreement with the AFM analysis, this SPR profile variation, S.I. = 1.23 ± 0.01, is intermediate between the ones of DPPC, S.I. = 1.16 ± 0.01, and DPPC/POPC, S.I.= 1.377 ± 0.005. This result demonstrates that the correlation between AuNPs aggregation and vesicles stiffness, observed in liposomes, also holds for the case of far more complex nanosized vesicles of biological origin. More importantly, the value of stiffness estimated from the S.I. of the AuNPs/EVs hybrid according to the calibration trend (i.e., 0.0259 ± 0.0005 N/m) falls right in the middle of the EVs stiffness range determined through AFM (Figure 4b): this striking agreement proves the predictive ability of this new optical method, showing that the nanoplasmonic properties of AuNPs can be effectively harnessed to assess the stiffness of membrane-confined objects with high sensitivity.

Conclusions

The determination of the stiffness of synthetic and natural vesicles is particularly challenging. Here, we show that the SPR of AuNPs can be exploited to quantify this property: combining UV-Vis spectroscopy, Small Angle X-ray Scattering and AFM-based force spectroscopy, we prove that AuNPs aggregation, induced by the interaction with lipid membranes and quantified by an empirical index S.I., exhibits a clear dependence on the mechanical properties of synthetic vesicles. This dependence, expressed by a sigmoidal law, can be used to estimate the stiffness of biological membrane compartments, e.g. EVs, of unknown composition and properties. Similarly to the plasmon ruler developed by El-Sayed *et al.*[33], where the SPR of AuNPs are used to probe their mutual distance, we define a "stiffness nanoruler", where the plasmon resonance is applied to probe the nanomechanics of a target membrane. This method, proposed here for the first time, requires commonly available instrumentation, is very reproducible and sensitive, and permits the analysis on sample quantities as small as 15 µl (with a concentration of EVs in the 10^{-8} M range), which represents a game-changer for precious biological samples, otherwise intractable. Moreover, differently from other methods (e.g., AFM, micropipette) which probe the stiffness of single objects, it allows for the determination of ensemble-averaged stiffness, where possible variability across the population is considered.

Conflicts of interest

There are no conflicts to declare

Acknowledgements

This work has been supported by the European Community through the evFOUNDRY project (H2020-FETopen, ID: 801367). We also acknowledge MIUR-Italy ("Progetto Dipartimenti di Eccellenza 2018-2022, ref B96C1700020008" allocated to Department of Chemistry "Ugo Schiff") for the economic support. We thank the SPM@ISMN research facility for support in the AFM experiments. The European Synchrotron Radiation Facility (ESRF) is acknowledged for provision of beam-time.

References

1 M. Mendozza, L. Caselli, D. Berti and A. Salvatore, *Soft Matter*, 2019, **15**, 8951–8970.
2 A. E. Nel, L. Mädler, D. Velegol, T. Xia, E. M. V Hoek, P. Somasundaran, F. Klaessig, V. Castranova and M. Thompson, *Nat. Mater.*, 2009, **8**, 543–57.
3 C. M. Beddoes, C. P. Case and W. H. Briscoe, *Adv. Colloid Interface Sci.*, 2015, **218**, 48–68.
4 P. K. K. Nagayama, *Particles at Fluid Interfaces and Membranes: Attachment of Colloid Particles*, Elsevier Science, 1st Editio., 2001.
5 K. L. Chen and G. D. Bothun, *Environ. Sci. Technol.*, 2014, **48**, 873–880.
6 P. Guo, D. Liu, K. Subramanyam, B. Wang, D. T. Auguste and M. A. Moses, *Nat. Commun.*, , DOI:10.1038/s41467-017-02588-9.
7 M. Simunovic, C. Prévost, P. Bassereau and P. Bassereau, *Phil. Trans. R. Soc. A*, 2016, **374**, 20160034.
8 P. B. Canham, *J. Theor. Biol.*, 1970, **26**, 61–81.
9 E. A. Evans, *Biophys. J.*, 1974, **14**, 923–931.
10 A. C. Dumitru, M. Poncin, L. Conrard, Y. F. Dufrêne, D. Tyteca and D. Alsteens, *Nanoscale Horizons*, 2018, **3**, 293–304.
11 I. Safeukui, P. A. Buffet, G. Deplaine, S. Perrot, V. Brousse, A. Sauvanet, B. Aussilhou, P. H. David, S. Dokmak, A. Couvelard, D. Cazals-hatem, O. Mercereau-puijalon and N. Mohandas, *Blood Adv.*, 2018, **2**, 1–4.
12 C. Alibert, B. Goud and J. Manneville, *Biol. Cell*, 2017, **109**, 167–189.
13 D. Vorselen, S. M. van Dommelen, R. Sorkin, M. C. Piontek, J. Schiller, S. T. Döpp, S. A. A. Kooijmans, B. A. van Oirschot, B. A. Versluijs, M. B. Bierings, R. van Wijk, R. M. Schiffelers, G. J. L. Wuite and W. H. Roos, *Nat. Commun.*, 2018, **9**, 1–9.
14 G. Raposo and P. D. Stahl, *Nat. Rev. Mol. Cell Biol.*, 2019, **20**, 509–510.
15 G. Van Niel, G. D. Angelo and G. Raposo, *Nat Rev Mol Cell Biol.*, 2018, **19**, 213–228.
16 M. Yáñez-mó and E. Al., *J Extracell Vesicles*, 2015, **14**, 27066.
17 B. Whitehead, L. P. Wu, M. L. Hvam, H. Aslan, M. Dong, L. DyrskjØt, M. S. Ostenfeld, S. M. Moghimi and K. A. Howard, *J. Extracell. Vesicles*, 2015, **4**, 1–11.
18 L. Paolini, A. Zendrini and A. Radeghieri, *Biomark. Med.*, 2018, **12**, 383–391.
19 C. Carrasco, M. Castellanos, P. J. De Pablo and M. G. Mateu, *Proc. Natl. Acad. Sci. U. S. A.*, 2008, **105**, 4150–4155.
20 W. H. Roos, *Semin. Cell Dev. Biol.*, 2018, **73**, 145–152.
21 J. F. Nagle, M. S. Jablin, S. Tristram-nagle and K. Akabori, *Chem. Phys. Lipids*, 2015, **185**, 3–10.
22 D. Bochicchio and L. Monticelli, *The Membrane Bending Modulus in Experiments and Simulations : A Puzzling Picture*, Elsevier Inc., 1st edn., 2016, vol. 23.
23 N. Bezlyepkina, R. L. Knorr, R. Lipowsky and R. Dimova, *Soft Matter*, 2010, **6**, 1472–1482.
24 J. R. Henriksen and J. H. Ipsen, *Eur. Phys. J. E*, 2004, **167**, 149–167.
25 C. Length, G. Fragneto, T. Charitat, E. Bellet-amalric and R. Cubitt, *Langmuir*, 2003, **19**, 7695–7702.
26 J. Pan, S. Tristram-nagle and J. F. Nagle, *Phys. Rev. E*, 2009, **80**, 021931.
27 M. Mell, L. H. Moleiro, Y. Hertle, P. Fouquet, R. Schweins, T. Hellweg and F. Monroy, *Eur. Phys. J. E*, 2013, **36**, 75.
28 D. Marsh, *Chem. Phys. Lipids*, 2006, **144**, 146–159.
29 J. F. Nagle, *Faraday Discuss.*, 2013, **161**, 11–29.
30 R. Dimova, *Adv. Colloid Interface Sci.*, 2014, 208, 225–234.
31 M. C. Piontek, R. B. Lira and W. H. Roos, *Biochim. Biophys. Acta - Gen. Subj.*, 2019, 129486.
32 V. Amendola, R. Pilot and M. Frasconi, *J. Phys. Condens. Matter*, 2017, **29**, 203002.
33 P. K. Jain, W. Huang and M. A. El-sayed, *Nano Lett.*, 2007, **7**, 2080–2088.
34 W. Zhao, M. M. Ali, S. D. Aguirre, M. A. Brook and Y. Li, *Anal. Chem.*, 2008, **80**, 8431–8437.
35 C. C. Chang, C. P. Chen, T. H. Wu, C. H. Yang, C. W. Lin and C. Y. Chen, *Nanomaterials*, 2019, **9**, 1–24.
36 D. Maiolo, L. Paolini, G. Di Noto, A. Zendrini, D. Berti, P. Bergese and D. Ricotta, *Anal. Chem.*, 2015, **87**, 4168–4176.
37 A. Zendrini, L. Paolini, S. Busatto, A. Radeghieri, M. Romano, M. H. M. Wauben, M. J. C. van Herwijnen, P. Nejsum, A. Borup, A. Ridolfi, C. Montis and P. Bergese, *Front. Bioeng. Biotechnol.*, 2020, **7**, 1–10.
38 A. Mallardi, N. Nuzziello, M. Liguori, C. Avolio and G. Palazzo, *Colloids Surfaces B Biointerfaces*, 2018, **168**, 134–142.
39 A. Ridolfi, L. Caselli, C. Montis, G. Mangiapia, D. Berti, M. Brucale and F. Valle, *J. Microsc.*, 2020, **00**, 1–10.
40 C. Montis, D. Maiolo, I. Alessandri, P. Bergese and D. Berti, *Nanoscale*, 2014, **6**, 6452–6457.
41 C. Montis, V. Generini, G. Boccalini, P. Bergese, D. Bani and D. Berti, *J. Colloid Interface Sci.*, 2018, **516**, 284–294.
42 J. Liu, *Langmuir*, 2016, **32**, 4393–4404.
43 F. Wang and J. Liu, *Nanoscale*, 2015, **7**, 15599–15604.
44 C. Montis, L. Caselli, F. Valle, A. Zendrini, F. Carlà, R. Schweins, M. Maccarini, P. Bergese and D. Berti, *J. Colloid Interface Sci.*, 2020, **573**, 204–214.
45 K. Sugikawa, T. Kadota, K. Yasuhara and A. Ikeda, *Angew. Chemie - Int. Ed.*, 2016, **55**, 4059–4063.
46 F. Wang, D. E. Curry and J. Liu, *Langmuir*, 2015, **31**, 13271–13274.

47 R. Sorkin, R. Huisjes, F. Boškovic, D. Vorselen, S. Pignatelli, Y. Ofir-birin, J. K. F. Leal, J. Schiller, D. Mullick, W. H. Roos, G. Bosman, N. Regev-rudzki, R. M. Schiffelers and G. J. L. Wuite, *Small*, 2018, **1801650**, 1–8.

48 J. F. Nagle, J. Pan, S. Tristram-nagle and N. Kuc, *Biophys J.*, 2008, **94**, 117–124.

49 R. Dimova, B. Pouligny and C. Dietrich, *Biophys. J.*, 2000, **79**, 340–356.

50 C. Lee, W. Lin and J. Wang, *Phys. Rev. E*, 2001, **64**, 020901.

51 K. R. Mecke and T. Charitat, *Langmuir*, 2003, **19**, 2080–2087.

52 U. C. Afm, S. Sharma, H. I. Rasool, V. Palanisamy, C. Mathisen, Ḱ. M. Schmidt, D. T. Wong and J. K. Gimzewski, *ACS Nano*, 2010, **4**, 1921–1926.

53 M. Krieg, G. Fl, D. Alsteens, B. M. Gaub, W. H. Roos, G. J. L. Wuite, H. E. Gaub, C. Gerber and Y. F. Dufr, *Nat. Rev. Phys.*, 2019, **1**, 41–57.

54 J. F. Nagle, *Chem. Phys. Lipids*, 2017, **205**, 18–24.

55 L. A. Feigin and D. S. Svergun, *Structure Anaysis by Small Angle X-Ray and Neutron Scattering*, Plenum Press, New York, Princeton, 1987.

56 M. Raatz, R. Lipowsky and T. R. Weikl, *Soft Matter*, 2014, **10**, 3570–3577.

57 G. Niggemann, M. Kummrow, W. Helfrich, G. Niggemann, M. Kummrow, W. H. The and B. Rigidity, *J. Phys. II Fr.*, 1995, **5**, 413–425.

58 A. Ridolfi, M. Brucale, C. Montis, L. Caselli, L. Paolini, A. Borup, A. T. Boysen, F. Loria, M. J. C. Van Herwijnen, M. Kleinjan, P. Nejsum, N. Zarovni, M. H. M. Wauben, D. Berti, P. Bergese and F. Valle, *Anal. Chem.*, 2020, **92**, 10274–10282.

59 C. Théry and E. Al., *J. Extracell. Vesicles*, 2018, **7**, 1535750.

60 L. Paolini, S. Federici, G. Consoli, D. Arceri, A. Radeghieri, I. Alessandri and P. Bergese, *J. Extracell. Vesicles*, 2020, **9**, 1741174.

Supporting Information for:

A plasmon-based nanoruler to probe the mechanical properties of synthetic and biogenic nanosized lipid vesicles

Lucrezia Caselli, Andrea Ridolfi, Jacopo Cardellini, Lewis Sharpnack, Lucia Paolini, Marco Brucale, Francesco Valle, Costanza Montis, Paolo Bergese and Debora Berti

Supplementary Materials and Methods

Materials

Tetrachloroauric (III) acid (≥ 99.9%) and trisodium citrate dihydrate (≥ 99.9%) for the synthesis of AuNPs were provided by Sigma-Aldrich (St. Louis, MO). 1,2-dioleoyl-sn-glycero-3-phosphocholine (DOPC) (>99%), 1-palmitoyl-2-oleoyl-sn-glycero-3-phosphocholine (POPC) (≥ 98.0%), 1,2-dipalmitoyl-sn-glycero-3-phosphocholine (DPPC) (>99%) and 1,2-distearoyl-sn-glycero-3-phosphocholine (DSPC) (>99%) for the liposomes preparation were provided by Sigma-Aldrich (St. Louis, MO). All chemicals were used as received. Milli-Q grade water was used in all preparations.

Synthesis of citrated AuNPs

Anionic gold nanospheres of 16 nm in size were synthesized according to the Turkevich-Frens method [1,2]. Briefly, 20 mL of a 1mM $HAuCl_4$ aqueous solution was brought to boiling temperature under constant and vigorous magnetic

stirring. 2 mL of 1% citric acid solution were then added and the solution was further boiled for 20 minutes, until it acquired a deep red color. The nanoparticles dispersion was then slowly cooled down to room temperature.

Preparation of liposomes

The proper amount of lipid was dissolved in chloroform and a lipid film was obtained by evaporating the solvent under a stream of nitrogen and overnight vacuum drying. The film was then swollen and suspended in warm (50 °C) milliQ-water by vigorous vortex mixing, in order to obtain a final 4 mg/ml lipid concentration. The resultant multilamellar liposomes in water were subjected to 10 freeze-thaw cycles and extruded 10 times through two stacked polycarbonate membranes with 100 nm pore size at room temperature, to obtain unilamellar liposomes with narrow and reproducible size distribution. The filtration was performed with the Extruder (Lipex Biomembranes, Vancouver (Canada)) through Nuclepore membranes.

Preparation of liposomes/AuNPs hybrids

The hybrid samples preparation procedure for Figure 2a of the main text is the following: 20 µL of liposomes (previously diluted to a final lipid concentration of 0.04 mg/ml) or extracellular vesicles were placed inside a 500 µL UV-Vis

plastic cuvette. Then 100 µL of citrated gold nanoparticles ($6.7 \cdot 10^{-9}$ M, see "Synthesis citrated Gold Nanoparticles" and "Supplementary Characterization of Gold Nanoparticles" of SI) were added, in order to have a final concentration (inside the cuvette) of ~$5 \cdot 10^{-11}$ M and of ~$5 \cdot 10^{-9}$ M for liposomes and AuNPs, respectively, and AuNPs/liposomes number ratio of ~100. Samples were incubated for 15 minutes, then the UV-Vis spectra were recorded.

The hybrid samples preparation procedure for Figure 2b of the main text is the following: fixed volumes (768.9 µL) of AuNPs dispersion ($6.7 \cdot 10^{-9}$ M) were added to 20 µL of liposomes (see Table S4 of SI for liposomes concentration), in order to have a final AuNPs/liposomes number ratio of ~8. Samples were incubated for 15 minutes, then placed in glass capillaries of 1 mm diameter and Small-Angle X-Ray profiles acquired.

UV-vis spectroscopy

UV-Vis spectra were measured with a JASCO UV-Vis spectrophotometer.

Small Angle X-ray Scattering

SAXS measurements for the characterization of AuNPs were carried out on a S3-MICRO SAXS/WAXS instrument (HECUS GmbH, Graz, Austria) which consists of a GeniX microfocus X-ray sealed Cu Kα source (Xenocs, Grenoble,

France) of 50 W power which provides a detector focused X-ray beam with λ = 0.1542 nm Cu Kα line. The instrument is equipped with two one-dimensional (1D) position sensitive detectors (HECUS 1D-PSD-50 M system). Each detector is 50 mm long (spatial resolution 54 μm/channel, 1024 channels) and covers the SAXS q-range (0.003< q <0.6 ˚Å −1). The temperature was controlled by means of a Peltier TCCS-3 Hecus. The analysis of SAXS curves was carried out using Igor Pro.[3] SAXS measurement on AuNPs aqueous dispersion was carried out in a sealed glass capillary of 1.5 mm diameter. To analyze gold nanospheres' curves we chose a model function with a spherical form factor and a Schulz size distribution:[4], it calculates the scattering for a polydisperse population of spheres with uniform scattering length density. The distribution of radii is a Schulz distribution given by the following equation:

$$f(R) = (z+1)^{z+1} x^z \frac{exp[-(z+1)x]}{R_{avg}\Gamma(z+1)}$$

where R_{avg} is the mean radius, $x = R/R_{avg}$ and z is related to the polydispersity. The form factor is normalized by the average particle volume, using the 3rd moment of R:

$$\langle V \rangle = \frac{4\pi}{3}\langle R^{+3} \rangle = \frac{4\pi}{3}\langle R \rangle^{+3} \frac{(z+3)(z+2)}{(z+1)^2}$$

The scattering intensity is:

$$I(q) = \left(\frac{4\pi}{3}\right)^2 N_0 \Delta\rho^2 \int_0^\infty f(R) R^6 F^2(qR) dR$$

where N_0 is the total number of particles per unit volume, $F(R)$ is the scattering amplitude for a sphere and $\Delta\rho$ is the difference in scattering length density between the particle and the solvent.

SAXS measurements for the characterization of AuNPs/liposomes hybrids were collected at beamline ID02 at the European Synchrotron Radiation Facility (ESRF, Grenoble, France) [5]. A scattering vector (of magnitude q) range of $0.007 \leq q \leq 0.2$ nm^{-1} was covered with two sample–detector distances (1 and 10 m) and a single-beam setting for an X-ray monochromatic radiation wavelength with a wavelength of $\lambda = 0.10$ nm (12.46 keV). The beam diameter was adjusted to 72.4 μm in the horizontal (x) direction and 42.3 μm in the vertical (y) direction (full width at half-maximum at the sample). Assuming a Gaussian distribution, the portion of the beam that is hitting outside the channel can be estimated. When the channel is centered, this is ~0.3% but closer to the edge and more beam overlaps the edge. The beamstop diameter was 2 mm. As a detector, a 2D Rayonix MX-170HS with a pixel size of 44 × 44 μm2 was used, which was housed in an evacuated flight tube, at a sample-to-detector distance of alternatively 10 m (leading to an available q-range of 0.007-0.02 nm^{-1}) or 1 m (leading to an available q-range of 0.07-0.2 nm^{-1}). The exposure times for the background- and sample measurements were 0.5 s for the case of 1 m sample-to-detector distance and 0.3 s for the case of 10 m sample-to-detector distance. Measured scattering patterns were normalized to an absolute intensity scale after applying standard

detector corrections and then azimuthally averaged to obtain the one-dimensional intensity profiles, denoted by I (q).

Atomic Force Microscopy (AFM)

Surface Preparation and Sample Deposition

All AFM experiments were performed on poly-L-lysine (PLL) coated glass coverslips. All reagents were acquired from Sigma-Aldrich Inc (www.sigmaaldrich.com) unless otherwise stated. Microscopy borosilicate glass slides (15mm diameter round coverslips, Menzel Gläser) were first immersed in a 3:1 mixture of 96% H_2SO_4 and 50% aqueous H_2O_2 ('oxidising piranha') solution for 2 h in order to remove any organic residue present on their surface; after that, they were cleaned in a sonicator bath (Elmasonic Elma S30H) for 30 minutes in acetone, followed by 30 minutes in isopropanol and 30 minutes in ultrapure water (Millipore Simplicity UV). Clean slides were incubated overnight in a 0.0001% (w/v) PLL solution at room temperature, thoroughly rinsed with ultrapure water and dried with nitrogen. A 10 µl-droplet of the vesicle-containing solution under study was deposited on a PLL-functionalized glass slide and left to adsorb for 10 minutes at 4°C, then inserted in the AFM fluid cell (see below) without further rinsing. The concentration of each vesicle-containing solution was adjusted in order to maximize the surface density of isolated, individual vesicles and minimize clusters of adjoining vesicles.

AFM Setup

All AFM experiments were performed in ultrapure water at room temperature on a Bruker Multimode (equipped with Nanoscope V electronics, a sealed fluid cell and a type JV piezoelectric scanner) using Bruker SNL-A probes (triangular cantilever, nominal tip curvature radius 2-12 nm, nominal elastic constant 0.35 N/m, calibrated with the thermal noise method.

AFM Imaging

Imaging was performed in PeakForce mode. In order to minimize vesicle deformation or rupture upon interaction with the probe, the applied force setpoint was kept in the 150-250 pN range. Lateral probe velocity was not allowed to exceed 5μm/s. Feedback gain was set at higher values than those usually employed for optimal image quality in order to ensure minimal probe-induced vesicle deformation upon lateral contact along the fast scan axis (please refer to Ridolfi et al. [6] for further details). The average height value of all bare substrate zones was taken as the baseline zero height reference. Image background subtraction was performed using Gwyddion 2.53.16 [7].

AFM-based Force Spectroscopy (AFM-FS)

The mechanical characterization of vesicles via AFM force spectroscopy was performed by first scanning the sample (see previous paragraph) to locate individual vesicles. The chosen vesicles were then imaged reducing the scan size for achieving higher accuracy. We recorded a series of force/distance curves at

multiple XY positions (typically around 64-100 curves arranged in a square array covering the vesicle initial location) for each individual vesicle. In most cases, only a few curves showed the mechanical fingerprint of an intact vesicle response to indentation: a linear deformation upon applied pressure during probe penetration. Of these, we first discarded those curves with probe-vesicle contact points occurring at probe-surface distances below vesicle height as measured by imaging. Remaining traces (typically 1-3 per vesicle) were analyzed to calculate vesicle stiffness (k_S).

Transmission Electron Microscopy

Trasmission electron microscopy (TEM) images were acquired with a STEM CM12 Philips electron microscope equipped with an OLYMPUS Megaview G2 camera, at CeME (CNR Florence Research Area, Via Madonna del Piano, 10 - 50019 Sesto Fiorentino). A drop of citrated AuNPs, diluted ten times, was placed on 200 mesh carbon-coated copper grids with a diameter of 3 mm and a thickness of 50 μm (Agar Scientific) and dried at room temperature. Then, the sample was analyzed at an accelerating voltage of 100 keV.

Dynamic Light Scattering

DLS measurements at $\theta = 90°$ were performed using a Brookhaven Instrument 90 Plus (Brookhaven, Holtsville, NY). Each measurement was an average of ten

repetitions of one minute each and repeated ten times. The autocorrelation functions were analyzed through the cumulant fitting stopped to the second order or with Laplace inversion according to CONTIN algorithm, allowing an estimate of the hydrodynamic diameter of particles.

Z-Potential Measurements

Zeta potential measurements were performed using a Zeta Potential Analyzer (Zeta Plus, Brookhaven Instruments Corporation, Holtsville, NY). Zeta potentials were obtained from the electrophoretic mobility u, according to Helmholtz-Smoluchowski equation: $\zeta = (\eta/\varepsilon) \times u$ with η being the viscosity of the medium, ε the dielectric permittivity of the dispersing medium. The Zeta Potential values are reported as averages from ten measurements.

Supplementary Characterization of Gold Nanoparticles

Transmission Electron Microscopy

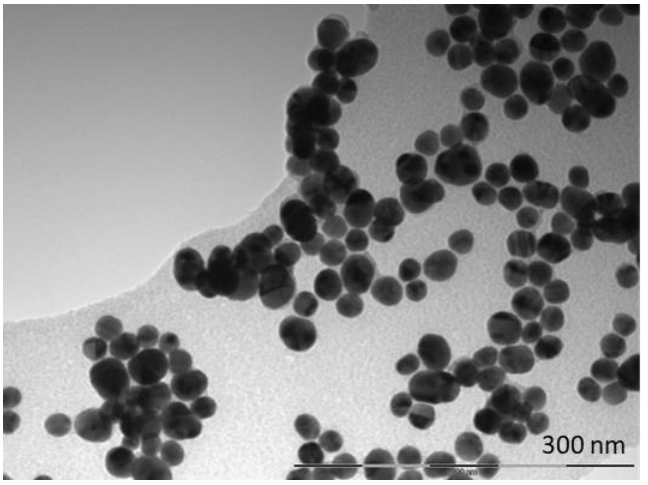

Figure S1 Representative Transmission electron microscopy (TEM) images of citrated gold nanoparticles acquired with a STEM CM12 Philips electron microscope, at CeME (CNR Florence Research Area, Via Madonna del Piano, 10 - 50019 Sesto Fiorentino). The sample was placed on a 200 mesh carbon-coated copper grid.

Small Angle X-ray Scattering

The analysis of SAXS curves was carried out using Igor Pro.[3] SAXS measurements on AuNPs aqueous dispersion were carried out in sealed glass capillaries of 1.5 mm diameter. To analyze gold nanospheres' curves we chose a model function with a spherical form factor and a Schulz size distribution:[4], it calculates the scattering for a polydisperse population of spheres with uniform scattering length density. The distribution of radii is a Schulz distribution given by the following equation:

$$f(R) = (z+1)^{z+1} x^z \frac{exp[-(z+1)x]}{R_{avg}\Gamma(z+1)}$$

where R_{avg} is the mean radius, $x = R/R_{avg}$ and z is related to the polydispersity. The form factor is normalized by the average particle volume, using the 3rd moment of R:

$$\langle V \rangle = \frac{4\pi}{3}\langle R^{+3} \rangle = \frac{4\pi}{3}\langle R \rangle^{+3} \frac{(z+3)(z+2)}{(z+1)^2}$$

The scattering intensity is:

$$I(q) = \left(\frac{4\pi}{3}\right)^2 N_0 \Delta\rho^2 \int_0^\infty f(R) R^6 F^2(qR) dR$$

where N_0 is the total number of particles per unit volume, $F(R)$ is the scattering amplitude for a sphere and $\Delta\rho$ is the difference in scattering length density between the particle and the solvent. The structural parameters (Table S1) of citrated gold nanoparticles were evaluated from the SAXS profile of their water dispersion (Figure S2) according to the models reported in the Materials and Methods section of SI.

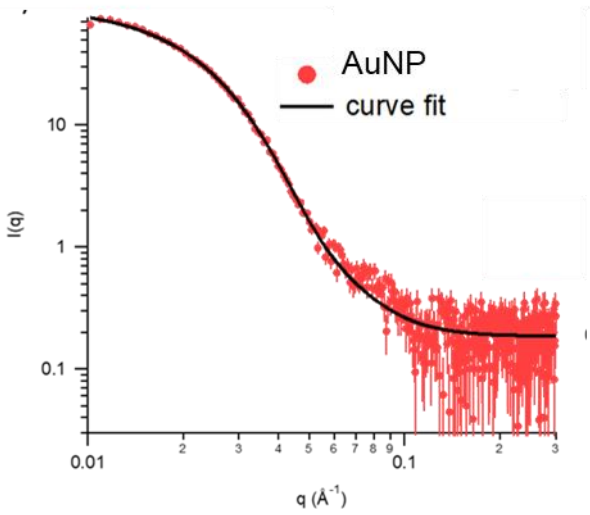

Figure S2 Experimental SAXS curve (red markers) obtained for AuNPs and curve fit (solid black line) according to the Schulz spheres model from the NIST package SANS Utilities. The size and polydispersity obtained from the fitting procedure are summarized in the Table S1 below.

	R_{core} (nm)	poly
AuNP	6.5	0.3

Table S1 Structural parameters of the nanoparticles obtained from the analysis of SAXS curves according to the the Schulz spheres model.

Dynamic Light Scattering and Z-Potential

AuNPs hydrodynamic diameter and surface charge in MilliQ water were evaluated through Dynamic Light Scattering and Zeta-Potential, respectively,

and reported in Table S2.

	D_h (nm)	Z-Potential (mV)
AuNPs	15.8 ± 0.3	-36 ± 2

Table S2 Hydrodynamic diameter obtained from Dynamic Light Scattering and Zeta Potential values of AuNPs.

UV-vis Spectroscopy

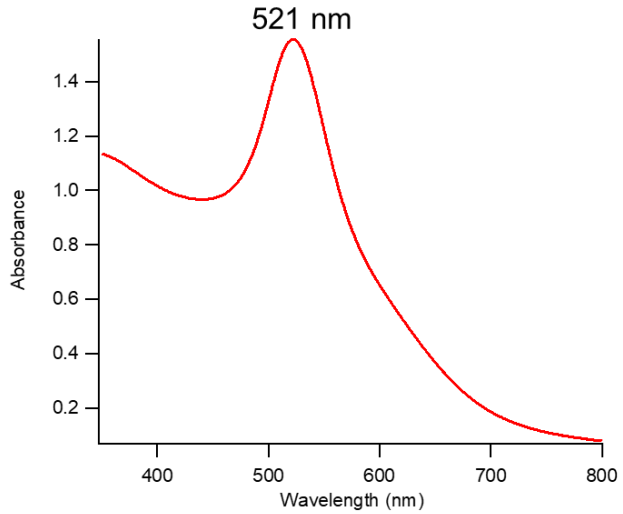

Figure S3 UV-Vis absorption spectra of AuNPs after 1:5 dilution in water. The plasmon absorption peak is at around 521 nm.

The size of AuNPs was further evaluated from UV-Vis Spectroscopy by the following equation [8]:

$$d = \exp\left(B_1 \frac{A_{spr}}{A_{450}} - B_2\right)$$

with d diameter of gold nanoparticles, A_{spr} absorbance at the surface plasma resonance peak, A_{450} absorbance at the wavelength of 450 nm and B_1 and B_2 are dimensionless parameters, taken as 3 and 2.2, respectively. The diameter value obtained is of 13.5 nm.

The concentration of citrated gold nanoparticles was determined via UV-Vis spectrometry, using the Lambert-Beer law ($E(\lambda) = \varepsilon(\lambda)lc$), taking the extinction values $E(\lambda)$ at the LSPR maximum, i.e. λ = 521 nm. The extinction coefficient $\varepsilon(\lambda)$ of gold nanoparticles dispersion was determined by the method reported in literature [9], by the following equation:

$$\ln(\varepsilon) = k\ln(d) + a$$

with d core diameter of nanoparticles, and k and a dimensionless parameters ($k = 3.32111$ and $a = 10.80505$). The arithmetic mean of the sizes obtained by optical and scattering analyses was selected, leading to a $\varepsilon(\lambda)$ of $2.8 \cdot 10^8$ $M^{-1}cm^{-1}$. The final concentration of the citrated AuNPs is therefore ~$5.6 \cdot 10^{-9}$ M.

Supplementary Characterization of Liposomes

Dynamic Light Scattering and Zeta-Potential

	D_h (nm)	Zeta P
DOPC	118.6 ± 0.2	-16 ± 1
POPC	103.8 ± 0.1	-19 ± 3
POPC/DPPC	92.1 ± 0.2	-22 ± 1
DPPC	115.7 ± 0.1	-13 ± 1
DPPC/DSPC	104 ± 0.2	-10 ± 1
DSPC	127.7 ± 0.2	-19 ± 1

Table S3 Hydrodynamic diameter obtained from Dynamic Light Scattering and Zeta Potential values of synthetic liposomes.

Evaluation of Liposomes concentration

The lipid concentration in the starting colloidal dispersion was estimated to be 4 mg/mL from the initial lipid and water amounts employed in the formation and swelling of lipid films (see "Preparation of liposomes" in the Materials and Methods section), assuming the absence of lipid loss due to the extrusion procedure. The liposomes concentration in the final dispersion was subsequently

calculated considering the hydrodynamic diameter of each liposomal batch (Table S3 of SI). In particular, from the liposomes' average diameter, the liposomal surface area (surface area=$4\pi r^2$) can be calculated; the doubled surface can be subsequently divided by the lipid cross section (0.5 nm^2) in order to obtain the lipid number per liposome, assuming that approximately one half of the lipids is localized in the external leaflet of a liposomes, since the bilayer thickness, about 4-5 nm, is negligible with respect to the liposomes' average diameter. Eventually, the total weighted lipid concentration was divided by the total number of lipids per liposome, yielding the real liposome concentration, which is reported in Table S4 for each liposomes' dispersion.

	Concentration (M)
DOPC	$3.2 \cdot 10^{-8}$
POPC	$3.1 \cdot 10^{-8}$
POPC/DPPC	$3.6 \cdot 10^{-8}$
DPPC	$3.1 \cdot 10^{-8}$
DPPC/DSPC	$3.8 \cdot 10^{-8}$
DSPC	$3.5 \cdot 10^{-8}$

Table S4 Final liposomes' concentration in each liposomal batch.

Supplementary Characterization of EVs

Zeta Potential

The Zeta Potential of EVs dispersion in milliQ water was measured as described in the "Material and Methods" section of SI and is equal to -21 ± 3 mV.

AFM characterization of synthetic and natural lipid vesicles

AFM Mechanical Characterization

According to the Canham-Helfrich theory, the mechanical response of a vesicle to an applied force is elastic; this behavior is reflected in the linear relationship between the force and tip penetration, in the AFM force-distance curves, right after the contact point (see Fig.1b in the main text). Calculating the slope of this linear part, gives the value of the vesicle stiffness, a mechanical parameter that accounts for multiple contributions, the most relevant being the intrinsic membrane rigidity (the bending modulus) and the vesicle luminal, i.e. internal, pressure. The latter contribution describes the vesicle pressurization following the deformation applied by the AFM tip. This deformation generates a volume variation that increases the pressure within the vesicle. While the bending modulus is an intrinsic descriptor of the lipid membrane bending rigidity, the internal pressure and hence the stiffness depend on the size of each vesicle. Indeed, the volume variation associated with a given tip penetration varies with

the vesicle size (i.e. the same penetration will result in higher volume variations for smaller vesicles); as a consequence, vesicles that are heterogenous in size will be subjected to different pressurizations following similar indentation events. However, both the measured liposomes and EVs are characterized by low polydispersity, this allows considering the stiffness a size-independent parameter. Moreover, since all the tested liposomes were characterized by similar size distributions and same polar headgroups, they will experience similar pressurizations and electrostatic attractions to the substrate; as a result, we can assume that changes in their stiffness are entirely ascribable to differences in their membrane rigidity, which can be recapitulated by the bending modulus. Membrane rigidity may vary depending on the phase behavior of the lipid bilayer, a temperature dependent parameter. All the measurements were performed at 28°C, where neat DOPC and POPC vesicles are in the fluid phase, while DPPC and DSPC ones are in the gel phase. In fluid-state membranes, lipid molecules can diffuse freely within the bilayer plane, while in gel- state membranes lipids are more tightly packed and their motion is more constrained. As a consequence, gel- phase bilayers are expected to be stiffer than fluid- phase ones. Our results from the Force Spectroscopy FS analysis (Figure 1c, main text) confirms this behavior, with DPPC and DSPC vesicles being substantially stiffer than DOPC and POPC ones. Two other important parameters that can affect the stiffness of a lipid bilayer are the chain length and its degree of saturation; e. g. DSPC

possesses two fully saturated chains, longer than all the other measured ones, resulting in the highest measured stiffness. Overall, the obtained stiffness values for neat DOPC, POPC, DPPC and DSPC vesicles (Figure 1c, main text) are in good agreement with results from recent AFM-FS investigations on similar vesicles [10]. Another interesting aspect to highlight is that the stiffnesses measured for the hybrid lipid vesicles (POPC/DPPC and DPPC/DSPC) have intermediate values with respect to liposomes made of the two pure components.

AFM-based characterization of EVs size distribution and concentration

AFM imaging was employed to obtain the size distribution of the EVs sample. A total of 179 EVs were imaged; from the topography of the AFM images, assuming the vesicle surface area conservation and by applying simple geometric consideration (see Ridolfi et al.[11] for further details) it is possible to obtain the values of the diameter that the vesicles would have had in solution, prior to their adsorption to the surface (we refer to this parameter as "Size"). Figure S4 displays the size distribution for the EVs sample used in this study. The measured EVs have a mean size of 74 nm with a standard deviation of 30 nm.

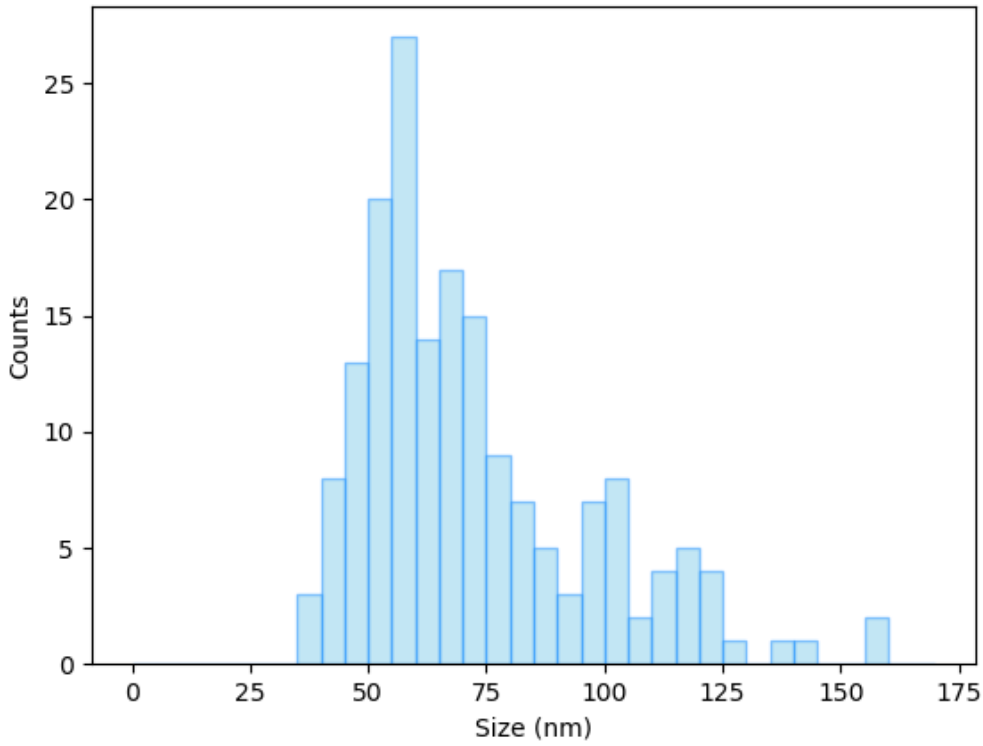

Figure S4: EVs size distribution obtained from the AFM imaging analysis. The size of the EVs (reported in the horizontal axis), indicates the diameter that the vesicles would have had in solution, prior to their adsorption.

AFM imaging was also used to estimate the starting concentration of the EVs sample. To do this, we compared the number of DPPC liposomes (coming from a solution with a known concentration and having a size distribution similar to the EVs) adsorbed on the glass surface with the number of EVs adsorbed on the same glass surface. This represents only a qualitative procedure and it is based on different assumptions: i) the interactions of DPPC liposomes with the glass surface are similar to the EVs ones, ii) the recorded images are representative of

both the vesicles samples, iii) the size distributions of the two samples are similar to each other. The concentration of the DPPC starting solution is 0.02 mg/ml; analysing the AFM images, we recorded a total of 329 vesicles in 4 different images, giving an average of 82.25 vesicles per image. Measuring EVs from TRAMP cells, we sampled 5 images, obtaining a total number of 166 EVs; 33.20 EVs per image. From proportionality considerations, it is possible to estimate the concentration of the EVs, spotted on the glass coverslips, using the following expression:

DPPC concentration (mg/ml):DPPC liposomes per image=EVs concentration (mg/ml) :EVs per image

From the expression we obtained a concentration of 0.008 mg/ml for the EVs sample. Since the EVs starting solution have been diluted six times before being spotted on the glass surface, the starting concentration is~0.048 mg/ml.

Supplementary Characterization of liposomes/AuNPs hybrids

Small-Angle X-Ray Scattering

SAXS measurements on liposomes/AuNPs hybrids were recorded at ID02 beamline, ESRF (Grenoble, France), using a sample-to-detector distance of 10 m. The analysis of SAXS curves was carried out using Igor Pro[3]. SAXS

measurements on liposomes/AuNPs aqueous dispersion were carried out in sealed glass capillaries of 1 mm diameter.

The SAXS profiles of DOPC liposomes/AuNPs and POPC liposomes/AuNPs in Figure 2b were fitted according to a linear fit in the 0.0695-0.1142 nm^{-1}q-range, to obtain the slope values reported in the main text (-1.5404 ± 0.00297 for DOPC and -1.4987 ± 0.00612 for POPC). The fitting yielded a chisquare of 0.000239052 and 0.00106975, for DOPC/AuNPs and POPC/AuNPs respectively.

The SAXS results of inset of Figure 2b were collected at ID02 beamline, ESRF (Grenoble, France), using a sample-to-detector distance of 1 m.

The scattering intensity (I(q)) is defined by the following equation:

$$I(q) = KN_pV_p^2(\Delta\rho)^2P(q)S(q) + B$$

With k instrumental constant, N_p scattering nanoparticles' number per unit volume, V_p nanoparticle's volume, $\Delta\rho$ contrast of the experiment, B background intensity, P(q) e S(q) form and structure factors, respectively.

In order to obtain the structure factor of the liposome/AuNPs complex, we divided the scattering intensity of the liposomes/AuNPs hybrid by the scattering intensity of the neat AuNPs dispersion (at a suitable dilution of 1:10):

$$\frac{I(q)_{Hyb}}{I(q)_{NP}} \sim \frac{S(q)_{Hyb}P(q)_{Hyb}}{S(q)_{NP}P(q)_{NP}}$$

For a diluted AuNPs dispersion the structure factor can be considered equal to 1. In addition, in the high-q region (0.1-1.6 nm^{-1}), the form factor of liposomes/AuNP hybrids can be approximated to the one of neat AuNPs, leading to the following:

$$\frac{I(q)_{Hyb}}{I(q)_{NP}} = S(q)_{Hyb}$$

The mean interparticle distance between the AuNPs within the aggregates (d) can be obtained from the S(q) vs q (nm^{-1}) plot (see inset of Figure 2b of the main text), by the following equation:

$$d = \frac{2\pi}{qmax}$$

With q_{max} q value corresponding to the maximum of the correlation peaks reported in the inset of figure 2b (main text).

UV-Vis Spectroscopy

The S.I. mean values for each liposomes/AuNPs mixtures are reported in Table S5, together with the relative standard deviation obtained from five repeated measurements on different samples (see "Preparation of liposomes/AuNPs hybrids" of SI).

	S.I.
DOPC	1.456 ± 0.002
POPC	1.438 ± 0.001
POPC/DPPC	1.377 ± 0.005

DPPC	1.16 ± 0.01
DPPC/DSPC	1.127 ± 0.003
DSPC	1.026 ± 0.006

Table S5 S.I. mean value and standard deviation for each liposomes/AuNPs hybrid.

The fitting parameters describing the sigmoidal best fit (eqn. 1 of the main text) for the S.I. values of liposomes plotted versus the AFM-determined stiffness, reported in Figure 3b of the main text, are the following:

a	**b**	**c**	**d**	**Chi square**
1.4831 ± 0.0485	-0.51151 ± 0.131	0.026043 ± 0.00266	0.0063004 ± 0.00265	0.0015

Table S6 Fitting parameters obtained by fitting the S.I. vs stiffness values of Figure 3c (main text) through the sigmoidal best fit (refer eqn 1 of main text for description of parameters).

The extent of AuNPs aggregation was also evaluated using different optical indexes, both taken from literature and defined in our lab.

In particular, as an alternative to the bending index defined in the main text, which is based on the determination of the area under the absorbance curve associated to AuNP aggregation, we defined another optical parameter (S.I. (2)). This alternative bending index allows evaluating AuNPs aggregation extent by calculating the intensity difference between the free AuNPs primary plasmon band (at 521 nm) and the aggregated AuNPs secondary plasmon peak, whose maximum is located at about 625 nm (see Figure S4). This result is then divided

by the wavelength interval (Δλ) between the two peaks and normalized for the S.I. of neat AuNPs.

$$S.I.(2) = \frac{I_{625} - I_{521}}{\Delta\lambda}$$

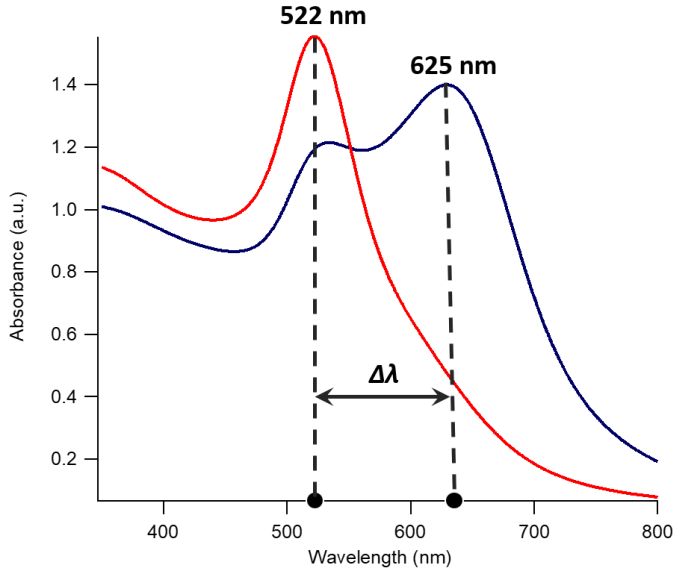

Figure S4 Visual description of the S.I. (2) evaluation.

We also selected another optical index from literature ($A.I._{CONAN}$) [12,13], which is commonly used to describe the aggregation of AuNPs on natural and synthetic vesicles and defined as follows:

$$A.I._{CONAN} = \frac{I_{521}}{I_{650} + I_{800}}$$

with I_{521} , I_{650} and I_{800} UV-Vis absorbances at 521, 650 and 800 nm respectively.

Both the S.I. (2) and the $A.I._{CONAN}$ show a sigmoidal behaviour as a function of membrane stiffness, as reported in Figure S5 and Table S7.

	S.I. (2)	A.I. CONAN
DOPC	-0.1965 ± 0.0004	0.785 ± 0.014
POPC	- 0.14 ± 0.03	0.83 ± 0.17
POPC/DPPC	0.12 ± 0.03	1.02 ± 0.05
DPPC	0.71 ± 0.06	1.99 ± 0.24
DPPC/DSPC	0.76 ± 0.01	2.36 ± 0.05
DSPC	1.04 ± 0.02	3.28 ± 0.24

Table S7 S.I. (2) and A.I. CONAN mean values and standard deviations for each liposomes/AuNPs hybrid.

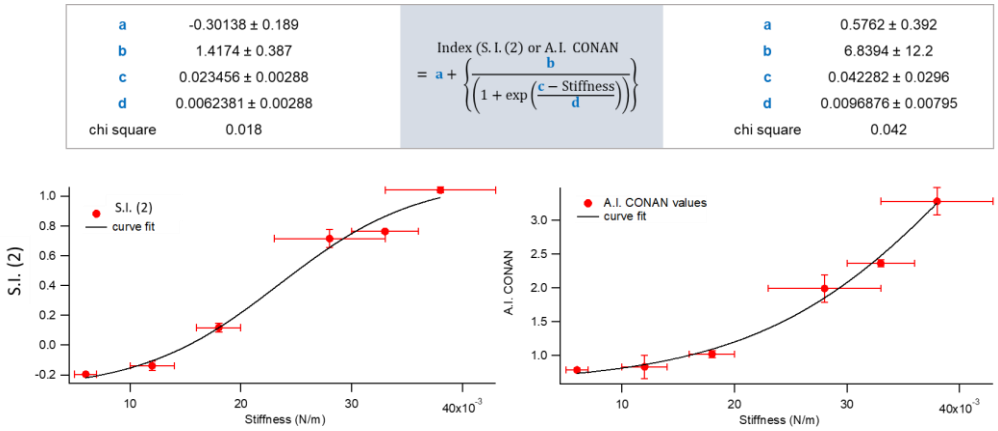

Figure S5 S.I. (2) and A.I. CONAN mean values and as a function of membrane stiffness. The sigmoidal fit curve is shown in black, together with the corresponding equation and fitting parameters (top inset).

Bibliography

1 J. Turkevich, P. C. Stevenson and J. Hillier, *Discuss. Faraday Soc.*, 1951, **11**, 55–75.

2 G. Frens, *Nat. Phys. Sci.*, 1973, **241**, 20–22.

3 S. R. Kline, *J. Appl. Crystallogr.*, 2006, **39**, 895–900.

4 M. Kotlarchyk and S.-H. Chen, *J. Chem. Phys.*, 1983, **79**, 2461.

5 T. Narayanan, M. Sztucki, P. Van Vaerenbergh, J. Gorini, L. Claustre, F. Sever and J. Morse, *J. Appl. Crystallogr.*, 2018, **51**, 1511–1524.

6 A. Ridolfi, M. Brucale, C. Montis, L. Caselli, L. Paolini, A. Borup, A. T. Boysen, F. Loria, M. J. C. Van Herwijnen, M. Kleinjan, P. Nejsum, N. Zarovni, M. H. M. Wauben, D. Berti, P. Bergese and F. Valle, *Anal. Chem.*, 2020, **92**, 10274–10282.

7 D. Nečas and P. Klapetek, *Cent. Eur. J. Phys.*, 2012, **10**, 181–188.

8 W. Haiss, N. T. K. Thanh, J. Aveyard and D. G. Fernig, *Anal. Chem.*, 2007, **79**, 4215–4221.

9 X. Liu, M. Atwater, J. Wang and Q. Huo, *Colloids Surfaces B Biointerfaces*, 2007, **58**, 3–7.

10 D. Vorselen, F. C. Mackintosh, W. H. Roos and G. J. L. Wuite, *ACS Nano*, 2017, **11**, 2628–2636.

11 A. Ridolfi, M. Brucale, C. Montis, L. Caselli, L. Paolini, A. Borup, A. T. Boysen, F. Loria, M. J. C. van Herwijnen, M. Kleinjan, P. Nejsum, N. Zarovni, M. H. M. Wauben, D. Berti, P. Bergese and F. Valle, *Anal. Chem.*, 2020, **92**, 10274–10282.

12 S. Busatto, A. Giacomini, C. Montis, R. Ronca and P. Bergese, *Anal. Chem.*, 2018, **90**, 7855–7861.

13 R. Carney, A. Zendrini, L. Paolini, S. Busatto and A. Radeghieri, *Front. Bioeng. Biotechnol.*, 2020, **7**, 1–10.

Paper IV

Gold nanoparticles interacting with synthetic lipid rafts: an AFM investigation

A. Ridolfi*, L. Caselli*, C. Montis, G. Mangiapia, D. Berti, M. Brucale and F. Valle, *Journal of Microscopy*, 2020, 00, 1–10 (* equally contributed)

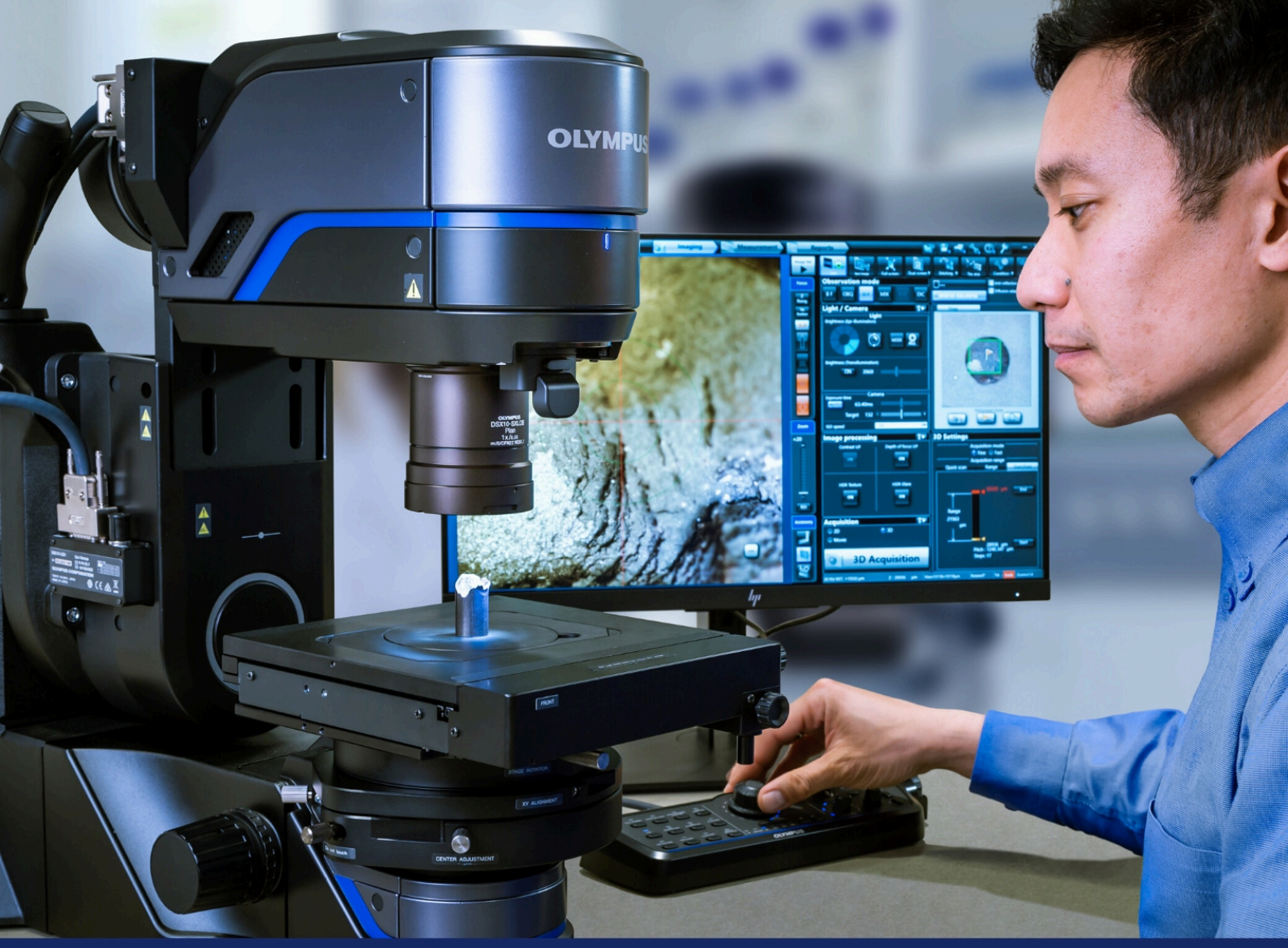

Science Meets Technology with Advanced Optical Metrology

Access in-depth information on methods and applications in the R&D field of optical metrology through free to access article digests of recent peer-reviewed publications and more.

Discover advancedopticalmetrology.com now!

OLYMPUS

WILEY

Journal of Microscopy

Journal of Microscopy, Vol. 00, Issue 0 2020, pp. 1–10 doi: 10.1111/jmi.12910
Received 31 March 2020; accepted 14 May 2020

Gold nanoparticles interacting with synthetic lipid rafts: an AFM investigation

ANDREA RIDOLFI*,†,‡*, LUCREZIA CASELLI‡*, COSTANZA MONTIS*,‡, GAETANO MANGIAPIA§, DEBORA BERTI*,‡, MARCO BRUCALE*,† & FRANCESCO VALLE*,†

*Consorzio Interuniversitario per lo Sviluppo dei Sistemi a Grande Interfase (CSGI), Florence, Italy

†Consiglio Nazionale delle Ricerche, Istituto per lo Studio dei Materiali Nanostrutturati (CNR-ISMN), Bologna, Italy

‡Dipartimento di Chimica 'Ugo Schiff', Università degli Studi di Firenze, Florence, Italy

§GEMS am Heinz Maier-Leibnitz Zentrum (MLZ), Helmholtz-Zentrum Geesthacht GmbH, Garching, Germany

Key words. Atomic force microscopy, gold nanoparticles, lipid rafts, supported lipid bilayers.

Summary

Inorganic nanoparticles (NPs) represent promising examples of engineered nanomaterials, providing interesting biomedical solutions in several fields, like therapeutics and diagnostics. Despite the extensive number of investigations motivated by their remarkable potential for nanomedicinal applications, the interactions of NPs with biological interfaces are still poorly understood. The effect of NPs on living organisms is mediated by biological barriers, such as the cell plasma membrane, whose lateral heterogeneity is thought to play a prominent role in NPs adsorption and uptake pathways. In particular, biological membranes feature the presence of rafts, that is segregated lipid micro and/or nanodomains in the so-called liquid ordered phase (L_o), immiscible with the surrounding liquid disordered phase (L_d). Rafts are involved in various biological functions and act as sites for the selective adsorption of materials on the membrane. Indeed, the thickness mismatch present along their boundaries generates energetically favourable conditions for the adsorption of NPs. Despite its clear implications in NPs internalisation processes and cytotoxicity, a direct proof of the selective adsorption of NPs along the rafts' boundaries is still missing to date. Here we use multicomponent supported lipid bilayers (SLBs) as reliable synthetic models, reproducing the nanometric lateral heterogeneity of cell membranes. After being characterised by atomic force microscopy (AFM) and neutron reflectivity (NR), multidomain SLBs are challenged by prototypical inorganic nanoparticles, that is citrated gold nanoparticles (AuNPs), under simplified and highly controlled conditions. By exploiting AFM, we demonstrate that AuNPs preferentially target lipid phase boundaries as adsorption sites. The herein reported study consolidates and extends the fundamental knowledge on NPs–membrane interactions, which constitute a key aspect to consider when designing NPs-related biomedical applications.

Introduction

Despite the impressive technological advancement in the design of 'smart' inorganic nanoparticles (NPs), their impact on biological systems and related toxicity are still poorly understood (Nel *et al.*, 2009; Henriksen-Lacey *et al.*, 2017), limiting their effective clinical translation. The interaction of engineered nanomaterials, either intentionally or inadvertently released into the environment, with living organisms is mediated by biological barriers, such as cell plasma membranes, which primarily determine NPs biological fate and cytotoxicity (Beddoes *et al.*, 2015). Therefore, the interaction of NPs with biological interfaces is a key research topic, aiming at the safe use of nanotechnology and maximisation of its potential in therapeutics and diagnostics (Mendozza *et al.*, 2019; Zendrini *et al.*, 2020).

In this framework, lipid-based synthetic model membranes are useful platforms to mimic biological interfaces under simplified conditions, allowing for the identification of key determinants regulating nano-bio interactions (Gkeka *et al.*, 2013; Simonelli *et al.*, 2015; Su *et al.*, 2018). Supported lipid bilayers (SLBs) are often used as 2D biomembrane models (Richter *et al.*, 2006; Hardy *et al.*, 2013), enabling to precisely tune their physicochemical properties and avoiding the complications related to the 3D nature of biological membranes. They also represent versatile and promising platforms for the development of biosensors (Nikoleli *et al.*, 2018) and technological assays for biological applications (Worsfold *et al.*, 2006).

In addition, multicomponent SLBs models allow studying the lateral compositional heterogeneity that characterises

* Authors A. Ridolfi and L. Caselli contributed equally to this work.

Correspondence to: A. Ridolfi, Consorzio Interuniversitario per lo Sviluppo dei Sistemi a Grande Interfase (CSGI), via della Lastruccia 3, 50019, Florence, Italy. Tel: +39-051-6398519; e-mail: andrea.ridolfi@ismn.cnr.it

most biological membranes. The existence of discrete lipid domains in natural membranes was questioned for a long time before its direct experimental assessment (Munro, 2003). Recently however, advanced experimental techniques have provided convincing evidence that the self-organisation of lipids and proteins can induce subcompartmentalisation in cell membranes (Lingwood & Simons, 2010), which is thought to have a profound impact on their biological function (Sezgin *et al.*, 2017). A specific case of lateral organisation is represented by lipid rafts, defined as micro and/or nanodomains, enriched in lipids such as cholesterol, sphingomyelin, saturated glycerophospholipids and glycosphingolipids: these lipids segregate in the so-called liquid-ordered phase (L_o), which is immiscible with the surrounding liquid-crystalline (disordered, L_d) phase (Koynova & Tenchov, 2013). This phase heterogeneity induces a thickness mismatch between neighbouring domains and the consequent, ergonically unfavourable, exposure of hydrocarbon regions to water, which results in an energetic cost, due to interfacial energy (Heberle *et al.*, 2013). Rafts are thought to participate in the formation and targeting of nano-sized biogenic lipid vesicles (e.g. extracellular vesicles, EVs) (Busatto *et al.*, 2020). They are also actively involved in multiple membrane processes, for example, they act as structural platforms for organising protein machinery (Lingwood & Simons, 2010), they can preferentially associate with specific membrane proteins (Simons & Ikonen, 1997) and represent centres for the assembly of signalling molecules. From a mechanical point of view, the presence of phase boundaries and, hence, bilayers thickness mismatches, generates deformations and increases membrane permeability (Kuzmin *et al.*, 2005; Rawicz *et al.*, 2008; Sheikh & Jarvis, 2011). All these structural perturbations promote the selective adsorption of materials on the membrane; indeed, as pointed out by Hamada *et al.* (2012), lateral heterogeneity, promoted by the presence of micro-sized lipid rafts, regulates the adsorption of nano/microparticles, with the larger ones preferring the L_d phase-domains and the smaller ones being localised in the L_o phase-domains of cell-sized lipid vesicles. These selective NPs adsorption pathways are also present in the case of nano-sized lipid segregated domains and can be studied exploiting liposomes with tuneable rafts size (Heberle *et al.*, 2013). However, investigating the interaction of NPs with nanometric lipid rafts remains a major challenge, mainly hindered by the small size of the segregated domains, which makes standard optical techniques not suitable for the task. Recent studies demonstrated that gold nanoparticles (AuNPs) adsorb more strongly to phase-separated multicomponent lipid bilayers; in particular, they are believed to preferentially target phase boundaries, due to the intrinsic negative curvature that characterises these regions (Melby *et al.*, 2016; Sheavly *et al.*, 2019).

To the best of our knowledge, this behaviour has only been investigated by computational studies (Sheavly *et al.*, 2019) and experiments involving quartz crystal microbalance (QCM) (Melby *et al.*, 2016), which provide important but indirect evidences. In summary, the preferential adsorption of AuNPs along the boundaries of nano-sized lipid domains has never been directly observed.

To fill this gap, we exploit Atomic Force Microscopy (AFM), to directly visualise the preferential adsorption of AuNPs on the phase boundaries of multicomponent SLBs, presenting both an L_d and an L_o phase-like domains and previously characterised by neutron reflectivity (NR). The L_d domains are mainly composed of 1,2-dioleoyl-sn-glycero-3-phosphocholine (DOPC) with two unsaturated hydrocarbon chains that hinder molecular packing, while the L_o domains are mainly composed of 1,2-dipalmitoyl-sn-glycero-3-phosphocholine (DSPC) lipids; cholesterol molecules occupy the free volume between the lipid acyl chains (Toppozini *et al.*, 2014; Sezgin *et al.*, 2017). The quantitative localisation and morphometry of AuNPs adsorbed on the SLB reveal important information regarding their interaction with the lipid matrix. The study corroborates the already theorised differential NPs-lipid interaction taking place at the phase boundaries of lipid rafts. The presented results could help the development of future NPs-based applications that involve their adsorption on membranes characterised by nanoscale phase segregations.

Materials and methods

Materials

Tetrachloroauric (III) acid (≥99.9%), trisodium citrate dihydrate (≥99.9%), methanol (99.8%), $CHCl_3$ (≥99.9%), NaCl (≥99.5%) and $CaCl_2$ (99.999%) were provided by Sigma-Aldrich (St. Louis, MO, USA). The same for 1,2-dioleoyl-sn-glycero-3-phosphocholine (DOPC) (≥98.0%), cholesterol (≥99.5%) and 1,2-distearoyl-sn-glycero-3-phosphocholine (DSPC) (≥98.0%). All chemicals were used as received. Milli-Q grade water was used in all preparations.

AuNP preparation

Anionic gold nanospheres of 16 nm in size were synthesised according to the Turkevich-Frens method (Turkevich *et al.*, 1951; Frens, 1973). Briefly, 20 mL of a 1 mM $HAuCl_4$ aqueous solution were brought to boiling temperature under constant and vigorous magnetic stirring. Two millilitres of 1% citric acid solution were then added and the solution was further boiled for 20 min, until it acquired a deep red colour. The nanoparticles solution dispersion was then slowly cooled down to room temperature.

Vesicle preparation and SLB formation for neutron reflectivity measurements

Vesicle preparation. The proper amount of a DOPC/DSPC/cholesterol mixture (39/39/22 mol%) was dissolved in

chloroform and a lipid film was obtained by evaporating the solvent under a stream of nitrogen and overnight vacuum drying. The film was then swollen and suspended in warm (50°C) 100 mM NaCl water solution by vigorous vortex mixing, in order to obtain a final 0.5 mg mL^{-1} lipid concentration. The resultant multilamellar vesicles (MLVs) were tip sonicated with a Digital Sonifier Model 450 (Branson, Hampton, NH, USA), provided with a Horn Tip (diameter 25.4 mm), in an intermittent-pulse mode (5 s), with a power of 400 W (amplitude 50%), for 15 min to obtain a homogeneous dispersion of unilamellar vesicles (ULVs).

Surface cleaning procedure. DOPC/DSPC/cholesterol single lipid bilayers were formed on $50 \times 80 \times 15$ mm^3 Silicon mirrors (Andrea Holm GmbH, Tann, Germany; roughness ≤ 5 Å). Substrates were preliminary rinsed in either ultrapure water and ethanol, in order to remove organic residues. After that, they were bath sonicated treated for 30 min in ethanol with a Bandelin DL 102 3L bath sonicator (Bandelin Ultraschall seit 1955, Berlin, Germany), followed by other 30 min in ultrapure water (Millipore Simplicity UV). The surfaces were then cleaned with a Novascan PSD-UV8 UV/ozone plasma (Boone, IA, USA) for 30 min and rinsed in ultrapure water. Finally, they were dried with nitrogen gas and stored in ultrapure water, ready for the deposition.

Vesicle fusion and SLB formation. $CaCl_2$ was added to the vesicle dispersion, reaching a final concentration of 10 mM, just before the injection in the NR measuring cell. This was performed in order to promote their adhesion to the support and their subsequent disruption. Vesicles were left incubating for 30 min; then, the saline buffer was switched to D_2O to promote the vesicle disruption and SLB formation. The use of D_2O instead of ultrapure water ensures a better resolution of the lipid structures for the NR measurements.

Vesicle preparation and SLB formation for AFM measurements

Vesicle preparation. The proper amount of a DOPC/DSPC/cholesterol mixture (39/39/22 mol%) was dissolved in chloroform and a lipid film was obtained by evaporating the solvent under a stream of nitrogen and overnight vacuum drying. The film was then swollen and suspended in warm (50 °C) ultrapure water solution by vigorous vortex mixing, in order to obtain a final 0.5 mg mL^{-1} lipid concentration. The resultant multilamellar vesicles in water were subjected to 10 freeze-thaw cycles and extruded 10 times through two stacked polycarbonate membranes with 100 nm pore size at room temperature, to obtain unilamellar vesicles with narrow and reproducible size distribution. The filtration was performed with the Extruder (Lipex Biomembranes, Vancouver, Canada) through Nuclepore membranes.

Surface cleaning procedure. All reagents were purchased from Sigma-Aldrich Inc (www.sigmaaldrich.com, St. Louis, MO, USA). DOPC/DSPC/Chol supported lipid bilayers were formed on microscopy borosilicate glass coverslips (Menzel Gläser). Glass slides were first immersed in a 3:1 mixture of 96% H_2SO_4 and 50% aqueous H_2O_2 ('oxidising piranha') solution for 2 h in order to remove any organic residue present on their surface. Then, the slides were cleaned in a sonicator bath (Elmasonic Elma S30H, Distrelec, Lainate, MI, Italy) for 30 min in acetone, followed by 30 min in isopropanol and 30 min in ultrapure water (Millipore Simplicity UV). Glass slides were then cleaned with air plasma for 15 min (air plasma cleaner PELCO easiGlow, Ted Pella Inc., Redding, CA, USA) and incubated in ultrapure water for 10 min in order to maximise the number of reactive silanols present on the surface. Finally, they were dried with nitrogen gas and stick to a magnetic disk, ready for the lipid solution deposition.

Vesicle fusion and SLB formation. A 100 μL droplet of buffer solution was first spotted on the SiO_2 slide. The buffer solution consisted of $CaCl_2$ 200 mM diluted 1:10 in KCl 100 mM. A 10 μL droplet containing the lipid mixture was then added to the buffer droplet and left incubating at room temperature for 30 min in order to promote the vesicle adsorption on the surface. After that, the droplet was removed and replaced by a 100 μL droplet of ultrapure water which was then left incubating for other 15 min. AuNPs deposition on the SLB was obtained by adding 5 μL of a 7.8 nM AuNPs dispersion to the ultrapure water droplet and leaving it to incubate for 10 min. After the system equilibrated, the large droplet was gently removed and the slide was inserted in the AFM fluid cell for the measurements.

Neutron reflectivity measurements. NR measurements were conducted at the REFSANS Horizontal TOF reflectometer of the Helmholtz-Zentrum Geesthacht located at the Heinz Maier-Leibnitz Zentrum in Garching, Germany (Kampmann *et al.*, 2006; Moulin & Haese, 2015). Neutrons in the wavelength range 3.0–21.0 Å were used to carry out the measurements. Two incident angles, namely 0.60° and 3.00°, allowed collecting data in the range $0.007 \leq Q/Å^{-1} \leq 0.22$. The arrival times and positions of scattered neutrons were detected on a Denex 2D 500×700 mm^2 multiwire ^3He detector (pixel size 2.1×2.9 mm^2, efficiency 80% at 7 Å, gamma sensitivity $< 10^{-6}$) positioned at 4.5 m from the sample. The detector was installed in a liftable vacuum tube in order to reach exit angles up to 5.2° at the maximum elongation. In order to receive sufficient statistics, a counting time of about 4 h for the measurement was chosen. The software MOTOFIT (Nelson, 2006) was employed for the analysis of the NR curve. Details on data analysis are reported in the SI.

AFM measurements

AFM setup. All AFM experiments were performed at room temperature on a Bruker Multimode 8 (equipped with

Nanoscope V electronics, a sealed fluid cell and a type JV piezoelectric scanner) using Bruker SNL-A probes (triangular cantilever, nominal tip curvature radius 2–12 nm, nominal elastic constant 0.35 N m^{-1}) calibrated with the thermal noise method (Hutter & Bechhoefer, 1993). The AFM fluid cell was filled with a saline buffer solution, consisting of KCl 100 mM, which has the main effect of reducing the Debye length that characterises the electrical double layer (EDL) interaction region between AFM tip and SLB (Müller *et al.*, 1999). In this way, better image resolution can be achieved.

AFM imaging. Imaging was performed in PeakForce mode. In order to minimise deformations or rupture events induced by the scanning probe, the applied force setpoint was kept under 200 pN range. Feedback gain was set on values high enough to obtain optimal image quality but low enough to prevent the introduction of noise signals that would otherwise interfere with the resolution of the different lipid domains, having a height difference of ∼1 nm. The average height value of all bare substrate zones was taken as the baseline zero height reference. Image background subtraction was performed using Gwyddion 2.53.16 (Nečas & Klapetek, 2012). In order to map the edges of lipid rafts and AuNPs, height ranges were manually optimised to define two image masks, the first only containing all Lo domains, the second singling out all NPs. Once both types of objects were correctly selected by appropriately chosen masks, a Gwyddion built-in function was used to automatically detect edges, and the resulting images were exported. Finally, the exported images containing the edges of either Lo domains or NPs, originally present in the same AFM image, were superimposed to reveal all NPs–lipid domains edge overlaps. To estimate the degree of preferential adsorption of NPs along the rafts' edges, we calculated the ratio between the number of NPs adsorbed along the boundaries and the total amount of NPs present in the images.

Results and discussion

Formation of supported lipid bilayers containing lipid rafts

The formation of a continuous planar bilayer [DOPC/DSPC/cholesterol (39/39/22 mol%)], covering the vast majority of the supporting surface, was achieved through vesicle fusion and characterised by NR. Briefly, as described in the Materials and Methods section, liposomes in a saline buffer were mixed with a low amount of $CaCl_2$, injected within the measurement chamber and left adsorbing on the support (a clean Si crystal). The presence of Ca^{2+} ions in solution promotes the crowding of vesicles on the surface by reducing the repulsive interactions between liposomes with surface charge. As reported by Richter *et al.* (2006), when a critical vesicle coverage is reached, the stress on the vesicles becomes sufficient to induce their rupture; in our case the phenomenon was also favoured by the additional osmotic shock, coming from the replacement of the saline buffer with ultrapure water. The edges of the newly-formed SLB are energetically unfavourable and cause the rupture of other surface-bound vesicles. If the density of adsorbed vesicles is sufficiently high, these cascade phenomena can lead to the complete surface coverage.

Given its ability to probe large sample areas (tens of millimetres), neutron reflectivity (NR) was herein applied to probe the effective formation of a homogeneous SLB and its structure along the normal to the SLB plane. Figure 1(A) shows a representative NR profile measured for the SLB in D_2O (green circles), together with the fitting curve (red continuous line). The curve was analysed with MOTOFIT and, consistently with the literature (Montis *et al.*, 2016, 2020; Luchini *et al.*, 2019), it was possible to model the profile of the SLB as a stack of five layers (see scheme in Fig. 1B): the silicon oxide layer, a layer of solvent (D_2O), a layer for the polar headgroups in contact with the support (inner heads), a layer for the lipid chains (chains) and, finally, a layer for the polar headgroups in contact with the solvent (outer heads). Each layer is characterised by a defined contrast (the scattering length density, SLD), thickness (d), roughness (ρ) and hydration (solvent %). The curve fitting results are reported in Table 1. The overall thickness of the bilayer is ∼ 5 nm (given by the sum of the thickness values related to the inner and outer heads, plus the lipid chains). The negligible hydration (0.1%) of the lipid chains layer indicates that the surface was almost completely covered by a homogeneous lipid bilayer. The analysis of the experimental data allowed reconstructing the entire profile of the SLB along the normal to the surface (see Fig. 1B).

While NR provides information on the average structure with respect to the bilayer normal, AFM can be used to resolve in detail the in-plane rafts morphology (Milhiet *et al.*, 2001; Yuan *et al.*, 2002; Mingeot-Leclercq *et al.*, 2008; Cai *et al.*, 2012). The SLB was formed on functionalised borosilicate glass coverslips, by injecting the liposomes (this time suspended in ultrapure water) in the buffer solution where they experienced an osmotic imbalance across the membrane, decreasing their pressurisation (please refer to 'Materials and methods' section for the details). As a result, following the adhesion to the substrate, liposomes will deform adopting more oblate shapes (Ridolfi *et al.*, 2019), increasing the area occupied by each vesicle and favouring the previously described vesicle fusion mechanism. As shown in Figure 1(C), consistently with NR data the surface is almost completely covered by a lipid bilayer, which presents nanometric domains of different heights, with the brighter areas corresponding to thicker membrane regions and the darker ones to thinner SLB portions. Accordingly, the height distribution of Figure 1(D) confirms the presence of two distinct lipid phase-like domains, with height values of $h_d = 3.7$ nm and $h_o = 4.7$ nm, in good agreement with the results obtained by Heberle *et al.* (2013) on the same vesicle preparation. This thickness mismatch can be ascribed to the coexistence of two lipid phases of different composition, dictating variations in the membrane's height

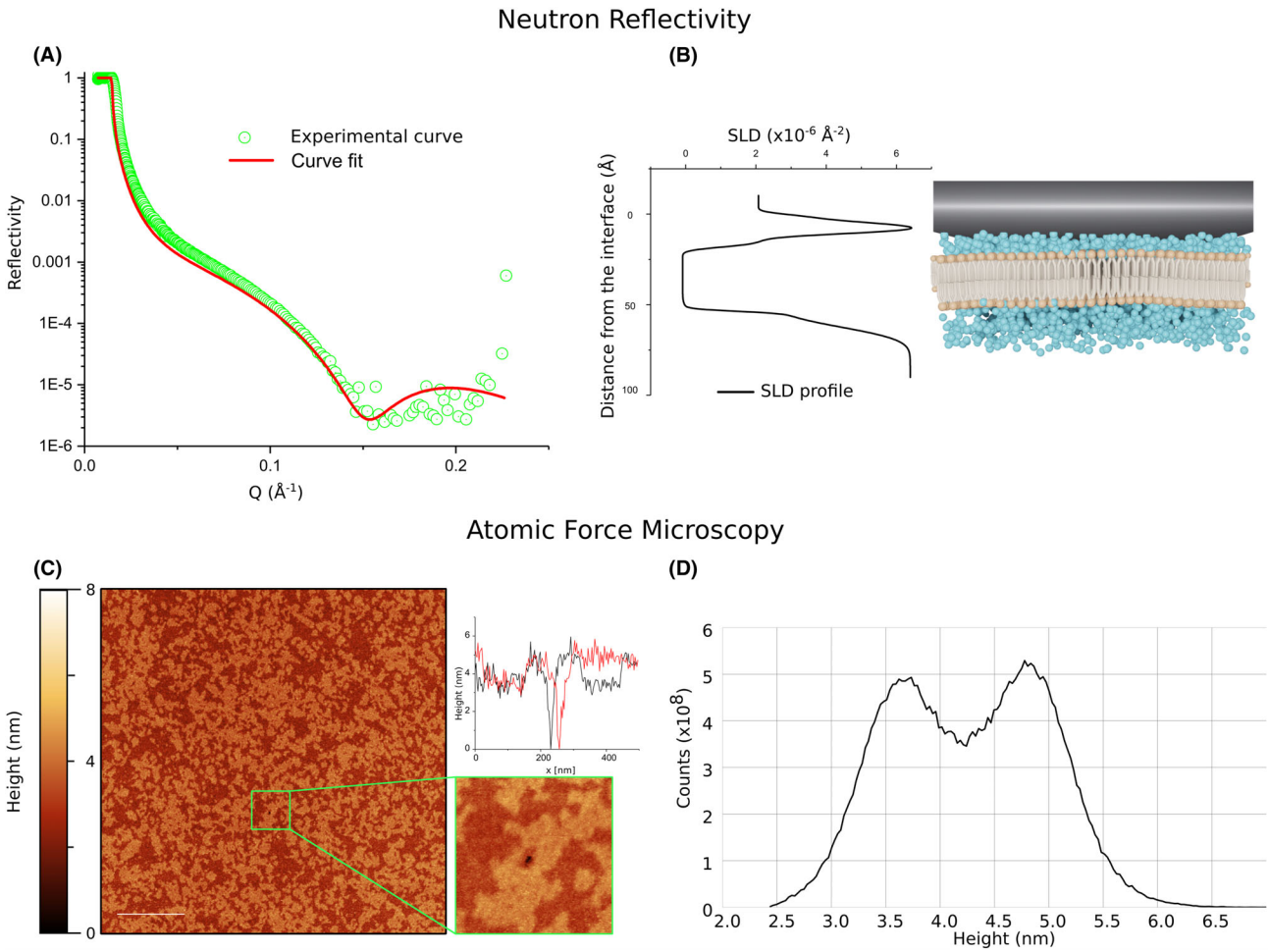

Fig. 1. Characterisation of the multicomponent SLB formed from DOPC/DSPC/cholesterol (39/39/22 mol%) liposomes by vesicle fusion. (A) Neutron Reflectivity profile (green circles) and best fit (continuous red line) corresponding to the SLB in D_2O; from the fitting analysis the average bilayer thickness is $\sim$ 5 nm. (B) Scattering length density (SLD) profile, describing variations of the SLD along the direction perpendicular to the bilayer. (C) Representative AFM topography of the SLB. The bilayer uniformly covers the surface, displaying both the L_o (brighter thicker regions) and L_d phases (darker thinner regions) as segregated domains. The reported scalebar is 1 μm. The 500 × 500 nm micrograph (bottom inset) displays the small hole in the bilayer that allowed flattening the image with respect to the SiO_2 surface. Two perpendicular height profiles were traced, horizontally and vertically, across the whole image (top inset); the profiles confirm the presence of the two distinct lipid phases covering the surface. (D) Height distribution obtained from the AFM image; the two distinct peaks, centred at $h_d = 3.7$ nm and $h_o = 4.7$ nm, describe the different heights that characterise the L_d and L_o phase, respectively.

(Lewis & Engelman, 1983; Petrache *et al.*, 2000; Bleecker *et al.*, 2016): in particular, membrane thickness was found to increase with length or degree of saturation of the lipid tails (Lewis & Engelman, 1983; Petrache *et al.*, 2000). Here the thicker domains can be associated with the L_o phase, which is enriched with cholesterol and DSPC, that is a fully saturated long chain lipid. On the contrary, thinner regions correspond to the L_d lipid phase mainly composed of DOPC, which is characterised by a shorter tail length and two chain unsaturated bonds. After having properly flattened the image, by the application of a mask (see Fig. S4), it is possible to determine the area fractions occupied by each of the two phases. Heberle *et al.* (2013) reported the area fraction corresponding to the L_d phase-like domains for liposomes of the very same composition to be 0.52 (at a temperature of 20°C); our calculations on SLBs at 28°C are in line with those findings, giving a L_d area fraction of 0.50. Results also suggest that the SLB formation did not significantly modify the amount of L_d and L_o lipids, originally present in the unfused vesicles and that the lipid phase behaviour is not affected by the presence of the solid support. The presented results strengthen the essential role of AFM in providing comprehensive morphological details on structure of rafted membranes. In the following paragraph, we extend the existing literature on AFM-based rafts characterisations (Milhiet *et al.*, 2001; Yuan *et al.*, 2002; Mingeot-Leclercq *et al.*, 2008; Cai *et al.*, 2012), by studying the structure of lipid rafts following their interaction with AuNPs.

Table 1. Curve fitting results of NR data obtained with MOTOFIT. The reported fitting parameters are referred to the three layers composing the bilayer [inner heads referred to the layer of polar headgroups in contact with the support, lipid chains referred to the hydrophobic region of the SLB, outer heads referred to the layer of polar headgroups in contact with the solvent (i.e. D_2O)]. For each layer four parameters are reported: d (Å), the thickness of the layer; ρ (Å), roughness of the layer; SLD (10^{-6} Å^{-2}), scattering length density of the layer (calculated from the layer composition); solvent % D_2O penetration in each layer.

Layer name	d (Å)	ρ (Å)	SLD (10^{-6} Å^{-2})	Solvent %
Inner heads	5 ± 2	2 ± 1	1.87	5 ± 1
Lipid chains	38 ± 3	1 ± 1	−0.18	0.1 ± 0.1
Outer heads	6 ± 2	2 ± 1	1.87	16 ± 4

Interaction of AuNPs with lipid rafts: localisation of AuNPs at the boundaries

In order to investigate the interaction of 16 nm citrated AuNPs (please refer to Materials and Methods for AuNP synthesis and to SI for AuNPs characterisation details) with the lipid rafts present in the SLB, 5 µL of the NPs dispersion were injected in the ultrapure water buffer. Different literature reports connect the presence of phase segregation within the lipid bilayer to the selective adsorption of NPs along the domains boundaries (Melby *et al.*, 2016; Sheavly *et al.*, 2019); however, a direct proof of this interaction is still missing to date. AFM represents one of the few techniques that could provide the sufficient resolution to simultaneously resolve the height difference between the two lipid domains ($\sim$ 1 nm) and the morphology of AuNPs. Despite the high resolution provided by AFM, the measurement remains challenging, as the spontaneous attachment of AuNPs to the probe (Fig. S5) can often lead to imaging artefacts. In order to overcome this problem, the AFM fluid cell was filled with the same saline buffer used for SLB formation and the force SetPoint was kept on very low values (lower than $\sim$ 200 pN). The use of the saline buffer as imaging solution should compensate the tip-sample electrical double-layer repulsion (Müller *et al.*, 1999) and limit the attachment of the NPs to the probe. In order to identify the portions of lipid bilayer characterised by the presence of AuNPs, images of 5 × 5 µm regions were initially acquired. Figure 2(A) shows a representative AFM topography of the SLB following the NPs injection. The bigger spherical objects represent vesicles that still have to fuse within the bilayer, while the smaller ones are the AuNPs, which seem to be homogeneously distributed above the SLB.

From a simple AFM topography, small lipid vesicles can be confused with AuNPs or AuNPs clusters; this could introduce statistical noise to the localisation and morphometrical analysis. We recently developed an AFM-based nanomechanical characterisation able to discriminate lipid vesicles from objects with the same morphology but different mechanical behaviour (Ridolfi *et al.*, 2019). This method evaluates the deformation that lipid vesicles undergo once adsorbed on a surface, by calculating their contact angle (α). Through the measurement of α and by assuming that the surface area of the vesicles is preserved upon adsorption, it is also possible to evaluate the diameter that characterises the unperturbed vesicles in solution (called Diameter in solution). As described in Figure 3, lipid vesicles are characterised by a narrow distribution of contact angles over a wide range of sizes (Diameter in solution), while AuNPs present a narrow size distribution and

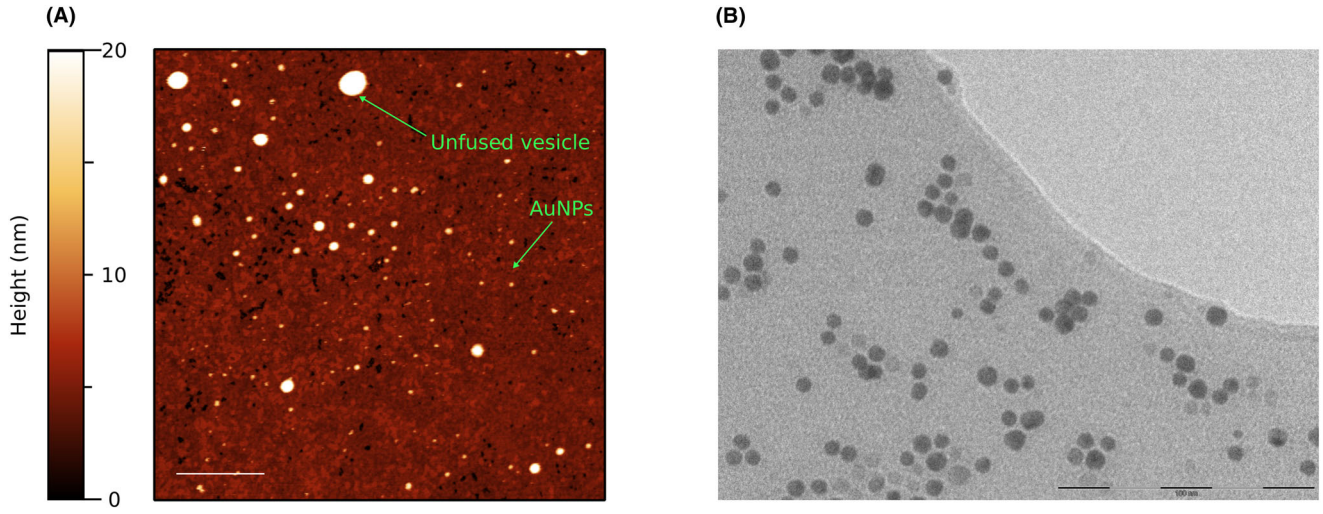

Fig. 2. (A) Representative AFM topography of the SLB following the interaction with AuNPs. Lipid rafts are still visible as differently shaded areas. The larger and heterogeneous spherical objects represent unfused vesicles while the smaller ones are the AuNPs that have been homogeneously adsorbed on the lipid bilayer. Scalebar is 1 µm. (B) Transmission electron microscopy (TEM) image of the AuNPs that were used in the experiments, scalebar is 100 nm (please refer to the SI for details regarding TEM characterisation).

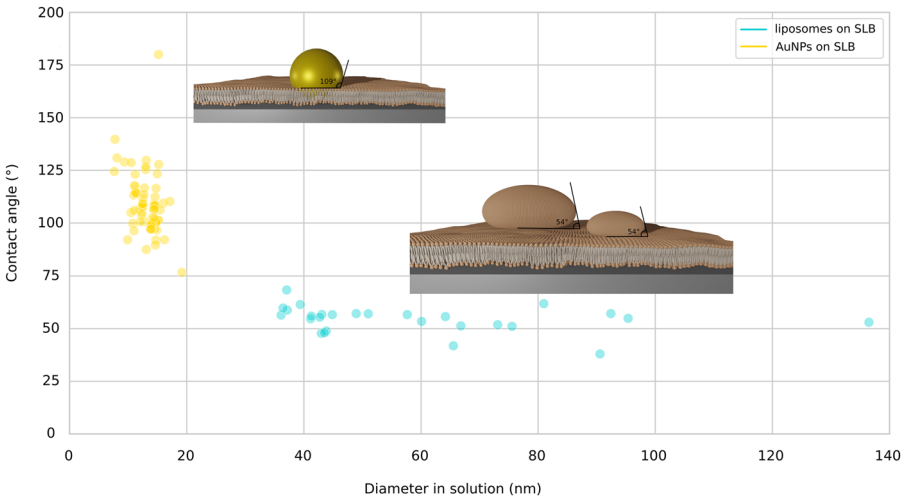

Fig. 3. Plot representing the distributions of contact angle vs solution diameter of either vesicles (blue circles) and AuNPs (yellow circles). Vesicles data have been obtained from the liposomes present in Figure 2(A) while the AuNPs data come from micrographs like the ones reported in Figure 4(A). Even though adsorbed on the SLB, liposomes show their nanomechanical fingerprint: a narrow contact angle distribution over a wide range of sizes. Their average contact angle is $\sim 54°$ hence describing highly deformed shapes, possibly due to the SLB formation procedure. AuNPs display narrow distributions for both their size and contact angle, with average values of 14 nm and 109°, respectively.

higher contact angle values. This enables the easy singling out of the AuNPs and their exclusive inclusion in the next analysis.

In order to precisely determine whether the NPs targeted specific locations on the lipid matrix, the size of the scanned region was further reduced. In Figure 4(A), representative images, with sizes of $\sim 600 \times 600$ nm, illustrating the SLB decorated by AuNPs have been reported. The micrographs of Figure 4(A) constitute the direct proof of the AuNPs selective adsorption along the segregated phase boundaries.

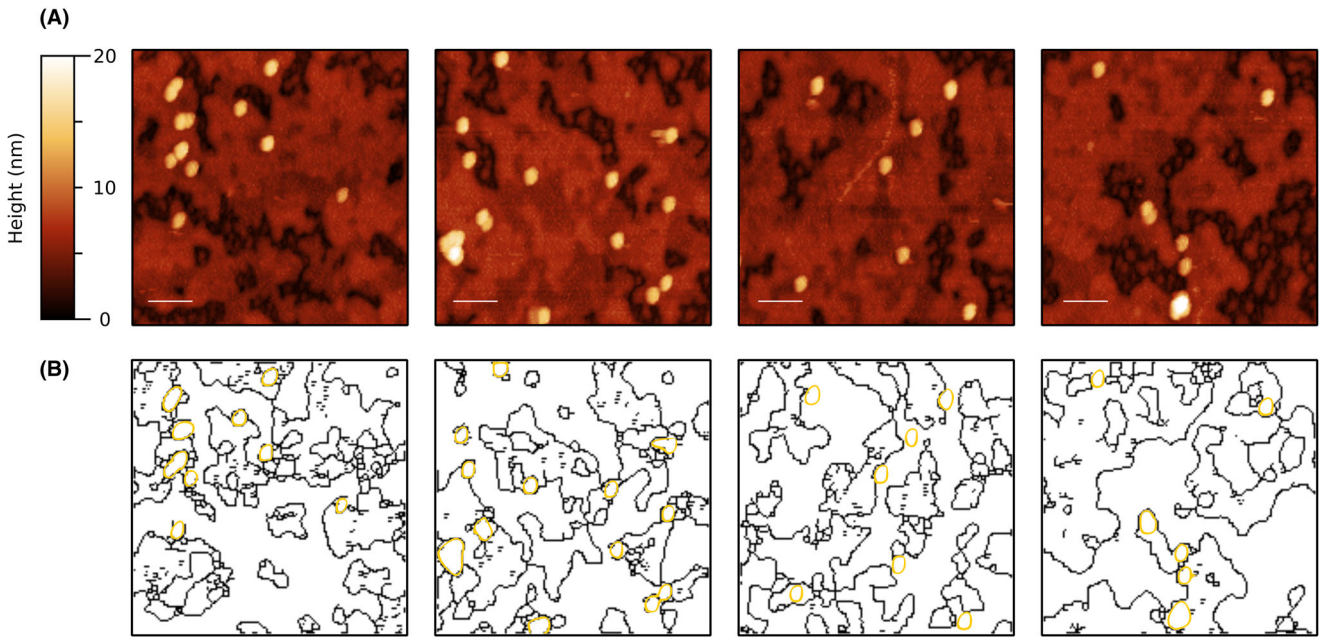

Fig. 4. (A) Representative AFM micrographs that clearly display the selective adsorption of AuNPs along the boundaries of the lipid rafts (brighter regions of the SLB that correspond to the Lo lipid phase). From the images it is also possible to distinguish between isolated and clustered NPs. All scalebars are 100 nm. (B) Contour images obtained from the micrographs. Black lines represent the rafts edges while gold circles define the contours of the AuNPs. The gold NPs edges are always in contact with at least one of the lines describing the lipid segregated phase boundaries.

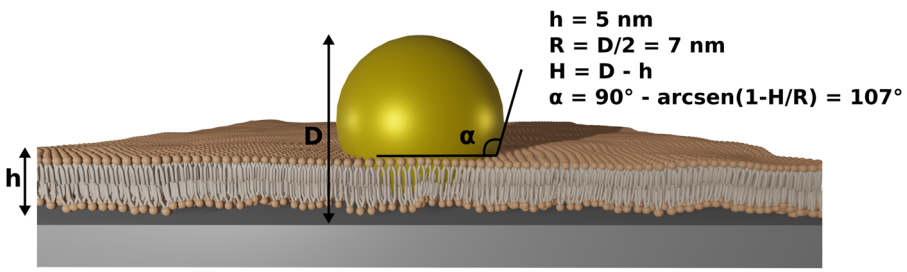

Fig. 5. Schematic representation of the configuration used to evaluate, from a conceptual point of view, the contact angle that would characterise an AuNP with a diameter of 14 nm, adsorbed on a rigid flat surface and surrounded by a ∼ 5 nm lipid bilayer.

In the free image processing software Gwyddion 2.53.16, the sequential application of different masks allowed mapping the edges of either the lipid rafts and NPs shown in Figure 4(A) and, hence, obtaining a clearer indication of their relative positions. In Figure 4(B) the contour images of NPs and rafts have been superimposed with different colours, to highlight that AuNPs preferentially targeted the boundaries of the two lipid phases; indeed, the lines describing their shapes are always in contact with the edges of the lipid rafts. To estimate the degree of preferential adsorption of NPs along the rafts' edges, we calculated the ratio between the number of NPs adsorbed along the boundaries and the total amount of NPs present on the SLB, finding that 91% of the NPs were located along the edges. These results prove the hypothesis that phase boundaries represent energetically favourable niches for lipid–NPs interactions. As previously discussed elsewhere (Sheavly *et al.*, 2019), NPs adsorption induces bilayer bending, which entails an energy penalty that increases the free energy associated with the overall process. This energy penalty is almost completely reduced along the phase boundaries, where the local negative curvature of the membrane, caused by the thickness mismatch between the two lipid phase-like domains minimises the free energy associated with the NPs adsorption (Sheavly *et al.*, 2019).

Inclusion of AuNPs within the lipid bilayer

AuNPs have a diameter of 16 nm (refer to SI for details), which is close to the average height measured with AFM imaging (14 ± 2 nm). This suggests that after adsorbing on the SLB, AuNPs probably penetrate the bilayer and reach the SiO_2 surface. This result further extends the characterisation of NPs–lipid interaction and corroborates our vision of rafts' boundaries as regions of increased permeability (Kuzmin *et al.*, 2005; Rawicz *et al.*, 2008; Sheikh & Jarvis, 2011), where the membrane can easily wrap around the adsorbed NPs. Recent findings (Montis *et al.*, 2020) confirm these results, suggesting that free-standing lipid bilayers can bend around the AuNPs surface, guided by citrate-lipid ligand exchange at the interface. All the above hypotheses are confirmed by the evaluation of the AuNPs contact angle with respect to the SLB. As suggested by Vinelli *et al.* (2008), the contact angle of a perfectly spherical, non-deformable (under the considered forces) object should be 180°, while we measured a substantially lower value. These apparent discrepancies can be rationalised by a careful morphological analysis, as detailed below.

The size of AuNPs is comparable with the tip radius; hence, the effect of tip convolution should be taken into account. This was performed by assuming the NPs as perfectly spherical and non-deformable objects with heights that coincide with their actual diameters. This is a reasonable assumption given that, during an AFM measurement, the error along the vertical direction is negligible compared to the ones in the scanning plane. As a consequence, all the measured radii were then corrected by ∼ 6 nm (corresponding to half the difference between the average NPs height and diameter measured by AFM). The NPs average contact angle, calculated with respect to the SLB and by using the corrected radii, gave a value of 109°, which is in very good agreement with the result that can be obtained from a simple geometrical model (Fig. 5), featuring a 14 nm spherical and undeformable NP immersed in a ∼5 nm lipid bilayer. For that case, α would be equal to 107°; this last result confirms that AuNPs penetrated the lipid bilayer and reached the underlying substrate.

Conclusion

The presence of lipid rafts within the cell membrane has been linked with multiple important biological functions, like the formation and targeting of lipid nanovesicles. The thickness mismatch that originates between the different immiscible segregated domains is thought to generate mechanical stresses that enhance the membrane permeability along these regions. We herein exploited atomic force microscopy to investigate the preferential adsorption of AuNPs along the phase boundaries of SLBs, generated from DOPC/DSPC/cholesterol (39/39/22 mol%) liposomes. Different works in the literature suggested a selective adsorption of AuNPs along the boundaries of lipid segregated domains, but a direct observation of this phenomenon is still missing to date. AFM allowed us to probe the existence of nanometric lipid rafts on the newly

formed SLB and to spot the presence of NPs along their edges, hence providing a direct proof of this preferential adsorption pathway. In addition, we provided useful details about the experimental procedures that could significantly improve the reliability of AFM imaging; indeed, one of the major challenges hindering this type of measurements is the frequent tip contamination, caused by the attachment of the NPs to the AFM probe. We showed that the use of a saline buffer as imaging solution within the AFM fluid cell leads to optimal image quality and strongly reduces tip contamination events. Then, through the application of an AFM-based morphometric nanomechanical characterisation, it was also possible to further investigate the reorganisation of the lipid bilayer, as a consequence of the AuNPs adsorption. We found out that the lipid matrix wrapped around the NPs, allowing them to penetrate within the hydrophobic region until reaching the rigid SiO_2 surface of the slides. The theoretical calculation of the morphological parameters describing this phenomenon is in perfect agreement with the experimental results and further corroborates our interpretation. Further studies will focus on extending this characterisation to membranes with varying compositions and employing NPs of different core and/or size.

Author contributions

The manuscript was written through contributions of all authors. All authors have given approval to the final version of the manuscript. The authors declare no competing financial interests.

Acknowledgements

This work was also supported by the Consorzio Sistemi a Grande Interfase (CSGI) through the evFOUNDRY project, Horizon 2020-Future and emerging technologies (H2020-FETOPEN), ID: 801367. We thank the SPM@ISMN research facility for support in the AFM experiments. Maier-Leibnitz Zentrum is acknowledged for provision of beam-time.

References

Beddoes, C.M., Case, C.P. & Briscoe, W.H. (2015) Understanding nanoparticle cellular entry: a physicochemical perspective. *Adv. Colloid Interface Sci.* **218**, 48–68.

Bleecker, J.V., Cox, P.A., Foster, R.N., Litz, J.P., Blosser, M.C., Castner, D.G. & Keller, S.L. (2016) Thickness mismatch of coexisting liquid phases in noncanonical lipid bilayers. *J. Phys. Chem. B* **120**, 2761–2770.

Busatto, S., Zendrini, A., Radeghieri, A., Paolini, L., Romano, M., Presta, M. & Bergese, P. (2020) The nanostructured secretome. *Biomater. Sci.* **8**, 39–63.

Cai, M., Zhao, W., Shang, X., Jiang, J., Ji, H., Tang, Z. & Wang, H. (2012) Direct evidence of lipid rafts by in situ atomic force microscopy. *Small* **8**, 1243–1250.

Frens, G. (1973) Controlled nucleation for the regulation of the particle size in monodisperse gold suspensions. *Nat. Phys. Sci.* **241**, 20–22.

Gkeka, P., Sarkisov, L. & Angelikopoulos, P. (2013) Homogeneous hydrophobic-hydrophilic surface patterns enhance permeation of nanoparticles through lipid membranes. *J. Phys. Chem. Lett.* **4**, 1907–1912.

Hamada, T., Morita, M., Miyakawa, M., Sugimoto, R., Hatanaka, A., Vestergaard, M.C. & Takagi, M. (2012) Size-dependent partitioning of nano/microparticles mediated by membrane lateral heterogeneity. *J. Am. Chem. Soc.* **134**, 13990–13996.

Hardy, G.J., Nayak, R. & Zauscher, S. (2013) Model cell membranes: techniques to form complex biomimetic supported lipid bilayers via vesicle fusion. *Curr. Opin. Colloid Interface Sci.* **18**, 448–458.

Heberle, F.A., Petruzielo, R.S., Pan, J., Drazba, P., Kučerka, N., Standaert, R.F., Feigenson, G.W. & Katsaras, J. (2013) Bilayer thickness mismatch controls domain size in model membranes. *J. Am. Chem. Soc.* **135**, 6853–6859.

Henriksen-Lacey, M., Carregal-Romero, S. & Liz-Marzán, L.M. (2017) Current challenges toward in vitro cellular validation of inorganic nanoparticles. *Bioconjug. Chem.* **28**, 212–221.

Hutter, J.L. & Bechhoefer, J. (1993) Calibration of atomic-force microscope tips. *Rev. Sci. Instrum.* **64**, 1868–1873.

Kampmann, R., Haese-Seiller, M., Kudryashov, V. *et al.* (2006) Horizontal ToF-neutron reflectometer REFSANS at FRM-II Munich/Germany: first tests and status. *Phys. B Condens. Matter.* **385–386**, 1161–1163.

Koynova, R. & Tenchov, B. (2013) Transitions between lamellar and nonlamellar phases in membrane lipids and their physiological roles. *OA Biochem.* **1**, 9.

Kuzmin, P.I., Akimov, S.A., Chizmadzhev, Y.A., Zimmerberg, J. & Cohen, F.S. (2005) Line tension and interaction energies of membrane rafts calculated from lipid splay and tilt. *Biophys. J.* **88**, 1120–1133.

Lewis, B.A. & Engelman, D.M. (1983) Lipid bilayer thickness varies linearly with acyl chain length in fluid phosphatidylcholine vesicles. *J. Mol. Biol.* **166**, 211–217.

Lingwood, D. & Simons, K. (2010) Lipid rafts as a membrane-organizing principle. *Science (80)* **327**, 46–50.

Luchini, A., Nzulumike, A.N.O., Lind, T.K., Nylander, T., Barker, R., Arleth, L., Mortensen, K. & Cárdenas, M. (2019) Towards biomimics of cell membranes: structural effect of phosphatidylinositol triphosphate (PIP 3) on a lipid bilayer. *Colloids Surf. B Biointerf.* **173**, 202–209.

Melby, E.S., Mensch, A.C., Lohse, S.E., Hu, D., Orr, G., Murphy, C.J., Hamers, R.J. & Pedersen, J.A. (2016) Formation of supported lipid bilayers containing phase-segregated domains and their interaction with gold nanoparticles. *Environ. Sci. Nano.* **3**, 45–55.

Mendozza, M., Caselli, L., Salvatore, A., Montis, C. & Berti, D. (2019) Nanoparticles and organized lipid assemblies: from interaction to design of hybrid soft devices. *Soft Matter.* **15**, 8951–8970.

Milhiet, P.E., Vié, V., Giocondi, M.C. & Le Grimellec, C. (2001) AFM characterization of model rafts in supported bilayers. *Single Mol.* **2**, 109–112.

Mingeot-Leclercq, M.P., Deleu, M., Brasseur, R. & Dufrêne, Y.F. (2008) Atomic force microscopy of supported lipid bilayers. *Nat. Prot.* **3**, 1654–1659.

Montis, C., Caselli, L., Valle, F. *et al.* (2020) Shedding light on membrane-templated clustering of gold nanoparticles. *J. Colloid Interf. Sci.* **573**, 204–214.

Montis, C., Gerelli, Y., Fragneto, G., Nylander, T., Baglioni, P. & Berti, D. (2016) Nucleolipid bilayers: a quartz crystal microbalance and neutron reflectometry study. *Colloids Surf. B Biointerf.* **137**, 203–213.

Montis, C., Salvatore, A., Valle, F., Paolini, L., Carlà, F., Bergese, P. & Berti, D. (2020) Biogenic supported lipid bilayers as a tool to investigate nano-bio interfaces. *J. Colloid Interf. Sci.* **570**, 340–349.

Moulin, J.-F. & Haese, M. (2015) REFSANS: reflectometer and evanescent wave small angle neutron spectrometer. *J. Large-Scale Res. Facil.* **1**, A9.

Müller, D.J., Fotiadis, D., Scheuring, S., Müller, S.A. & Engel, A. (1999) Electrostatically balanced subnanometer imaging of biological specimens by atomic force microscope. *Biophys. J.* **76**, 1101–1111.

Munro, S. (2003) Lipid rafts: elusive or illusive? *Cell* **115**, 377–388.

Nečas, D. & Klapetek, P. (2012) Gwyddion: an open-source software for SPM data analysis. *Cent. Eur. J. Phys.* **10**, 181–188.

Nel, A.E., Mädler, L., Velegol, D. *et al.* (2009) Understanding biophysicochemical interactions at the nano-bio interface. *Nat. Mater.* **8**, 543–557.

Nelson, A. (2006) Co-refinement of multiple-contrast neutron/X-ray reflectivity data using MOTOFIT. *J. Appl. Crystallogr.* **39**, 273–276.

Nikoleli, G.P., Nikolelis, D.P., Siontorou, C.G., Nikolelis, M.T. & Karapetis, S. (2018) The application of lipid membranes in biosensing. *Membranes (Basel)* **8**, 108.

Petrache, H.I., Dodd, S.W. & Brown, M.F. (2000) Area per lipid and acyl length distributions in fluid phosphatidylcholines determined by 2H NMR spectroscopy. *Biophys. J.* **79**, 3172–3192.

Rawicz, W., Smith, B.A., McIntosh, T.J., Simon, S.A. & Evans, E. (2008) Elasticity, strength, and water permeability of bilayers that contain raft microdomain-forming lipids. *Biophys. J.* **94**, 4725–4736.

Richter, R.P., Bérat, R. & Brisson, A.R. (2006) formation of solid-supported lipid bilayers: an integrated view. *Langmuir* **22**, 3497–3505.

Ridolfi, A., Brucale, M., Montis, C. *et al.* (2019) AFM-based high-throughput nanomechanical screening of single extracellular vesicles. *BioRxiv* 854539.

Sezgin, E., Levental, I., Mayor, S. & Eggeling, C. (2017) The mystery of membrane organization: composition, regulation and roles of lipid rafts. *Nat. Rev. Mol. Cell Biol.* **18**, 361–374.

Sheavly, J.K., Pedersen, J.A. & Van Lehn, R.C. (2019) Curvature-driven adsorption of cationic nanoparticles to phase boundaries in multicomponent lipid bilayers. *Nanoscale* **11**, 2767–2778.

Sheikh, K.H. & Jarvis, S.P. (2011) Crystalline hydration structure at the membrane-fluid interface of model lipid rafts indicates a highly reactive boundary region. *J. Am. Chem. Soc.* **133**, 18296–18303.

Simonelli, F., Bochicchio, D., Ferrando, R. & Rossi, G. (2015) Monolayer-protected anionic au nanoparticles walk into lipid membranes step by step. *J. Phys. Chem. Lett.* **6**, 3175–3179.

Simons, K. & Ikonen, E. (1997) Functional rafts in cell membranes. *Nature* **387**, 569–572.

Su, J., Esmaeilzadeh, H., Zhang, F., Yu, Q., Cernigliaro, G., Xu, J. & Sun, H. (2018) An ultrasensitive micropillar-based quartz crystal microbalance device for real-time measurement of protein immobilization and protein-protein interaction. *Biosens. Bioelectron.* **99**, 325–331.

Toppozini, L., Meinhardt, S., Armstrong, C.L., Yamani, Z., Kučerka, N., Schmid, F. & Rheinstädter, M.C. (2014) Structure of cholesterol in lipid rafts. *Phys. Rev. Lett.* **113**(22), 228101.

Turkevich, J., Stevenson, P.C. & Hillier, J. (1951) A study of the nucleation and growth processes in the synthesis of colloidal gold. *Discuss. Faraday Soc.* **11**, 55–75.

Vinelli, A., Primiceri, E., Brucale, M., Zuccheri, G., Rinaldi, R. & Samorì, B. (2008) Sample preparation for the quick sizing of metal nanoparticles by atomic force microscopy. *Microsc. Res. Tech.* **71**, 870–879.

Worsfold, O., Voelcker, N.H. & Nishiya, T. (2006) Biosensing using lipid bilayers suspended on porous silicon. *Langmuir* **22**, 7078–7083.

Yuan, C., Furlong, J., Burgos, P. & Johnston, L.J. (2002) The size of lipid rafts: an atomic force microscopy study of ganglioside GM1 domains in sphingomyelin/DOPC/cholesterol membranes. *Biophys. J.* **82**, 2526–2535.

Zendrini, A., Paolini, L., Busatto, S. *et al.* (2020) Augmented COlorimetric NANoplasmonic (CONAN) method for grading purity and determine concentration of EV microliter volume solutions. *Front. Bioeng. Biotechnol.* **7**, 452.

Supporting Information

Additional supporting information may be found online in the Supporting Information section at the end of the article.

Fig. S1. Experimental SAXS profile (markers) obtained for citrated AuNPs and curve fit (solid black line) according to the Schulz spheres model from the NIST package SANS Utilities.
Fig. S2. UV-Vis absorption spectra of citrated AuNP dispersion (after 1:5 dilution in water).
Fig. S3. AFM topography representing AuNPs either isolated or clustered, adsorbed on a bare mica substrate.
Fig. S4. AFM topography of the SLB obtained from DOPC/DSPC/Chol (39/39/22 %w/w) liposomes.
Fig. S5. AFM topography showing the effects of tip contamination on the imaging of AuNPs adsorbed on the lipid bilayer.
Table. S1. Chemical formula, molecular volumes and corresponding scattering length densities of species relevant to this study

Gold Nanoparticles interacting with Synthetic Lipid Rafts: an AFM investigation

Authors

Andrea Ridolfi* [†,1,2,3], Lucrezia Caselli [†,3], Costanza Montis[1,3], Gaetano Mangiapia[4], Debora Berti[1,3], Marco Brucale[1,2] and Francesco Valle[1,2].

Affiliations

[1] Consorzio Interuniversitario per lo Sviluppo dei Sistemi a Grande Interfase (CSGI), via della Lastruccia 3, 50019 Florence (Italy).

[2] Consiglio Nazionale delle Ricerche, Istituto per lo Studio dei Materiali Nanostrutturati (CNR-ISMN), via Gobetti 101, 40129 Bologna (Italy).

[3] Dipartimento di Chimica "Ugo Schiff", Università degli Studi di Firenze, via della Lastruccia 3, 50019 Florence (Italy).

[4] GEMS am Heinz Maier-Leibnitz Zentrum (MLZ). Helmholtz-Zentrum Geesthacht GmbH, Lichtenbergstr. 1, D-85747 Garching, Germany.

[†] A.R. and L.C. contributed equally to this work.

*Corresponding author. Email: andrea.ridolfi@ismn.cnr.it

SUPPLEMENTARY INFORMATION

AuNPs characterization

1. TRANSMISSION ELECTRON MICROSCOPY

Trasmission electron microscopy (TEM) images were acquired with a STEM CM12 Philips electron microscope equipped with an OLYMPUS Megaview G2 camera, at CeME (CNR Florence Research Area, Via Madonna del Piano, 10 - 50019 Sesto Fiorentino). Drops of citrated AuNP, diluted ten times, were placed on 200 mesh carbon-coated copper grids with a diameter of 3 mm and a thickness of 50 μm (Agar Scientific) and dried at room temperature. Then, samples were analyzed at an accelerating voltage of 100 keV.

2. SMALL ANGLE X-RAY SCATTERING (SAXS)

SAXS measurements were carried out on a S3-MICRO SAXS/WAXS instrument (HECUS GmbH, Graz, Austria) which consists of a GeniX microfocus X-ray sealed Cu Kα source (Xenocs, Grenoble, France) of 50 W power which provides a detector focused X-ray beam with λ = 0.1542 nm Cu Kα line. The instrument is equipped with two one-dimensional (1D) position sensitive detectors (HECUS 1D-PSD-50 M system), each detector is 50 mm long (spatial resolution 54 μm/channel, 1024 channels) and cover the SAXS q-range ($0.003 < q < 0.6\ ^{\circ}Å^{-1}$). The temperature was controlled by means of a Peltier TCCS-3 Hecus. The analysis of SAXS curves was carried out using Igor Pro[1]. SAXS measurements on AuNP aqueous dispersions, was carried out in sealed glass capillaries of 1.5 mm diameter. To analyze AuNPs profiles, we chose a model function with a spherical form factor and a Schulz size distribution[2], which calculates the scattering for a polydisperse population of spheres

with uniform scattering length density. The distribution of radii (Schulz distribution) is given by the following equation:

$$(R) = (z+1)^{z+1} x^z \frac{exp[-(z+1)x]}{R_{avg}\Gamma(z+1)}$$

where R_{avg} is the mean radius, x = R/R_{avg} and z is related to the polydispersity of the dispersion. The form factor is normalized by the average particle volume, using the 3rd moment of R:

$$\langle V \rangle = \frac{4\pi}{3}\langle R^{+3} \rangle = \frac{4\pi}{3}\langle R \rangle^3 \frac{(z+3)(z+2)}{(z+1)^2}$$

The scattering intensity is:

$$I(q) = \left(\frac{4\pi}{3}\right)^2 N_0 \Delta\rho^2 \int_0^\infty f(R) R^6 F^2(qR) dR$$

where N_0 is the total number of particles per unit volume, F(R) is the scattering amplitude for a sphere and $\Delta\rho$ is the difference in the scattering length density between the AuNP and the solvent.

The structural parameters of citrated gold nanoparticles were evaluated from the SAXS profile of Figure S1 according to the above model.

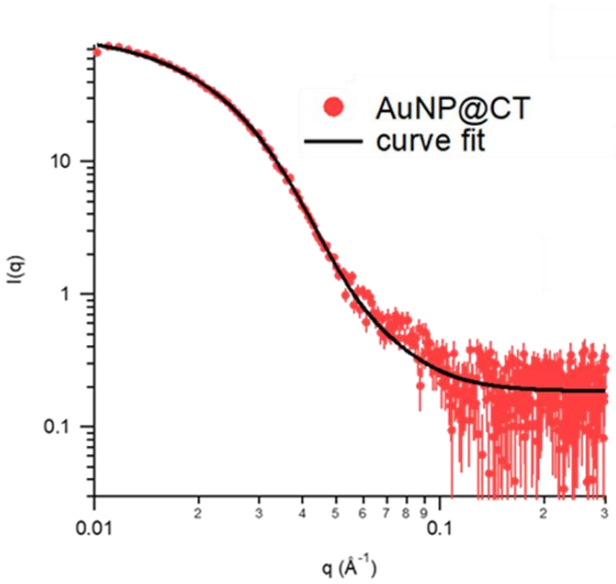

Figure S1 Experimental SAXS profile (markers) obtained for citrated AuNPs and curve fit (solid black line) according to the Schulz spheres model from the NIST package SANS Utilities. The size and polydispersity obtained from the fitting procedure are 13 nm and 0.3, respectively.

3. UV-VIS SPECTROSCOPY

UV-Vis spectra were measured with a JASCO UV-Vis spectrophotometer.

The size of citrate gold nanoparticles was further evaluated from UV-Vis Spectroscopy by the following equation[3]:

$$d = \exp\left(B_1 \frac{A_{spr}}{A_{450}} - B_2\right)$$

with d diameter of gold nanoparticles, A_{spr} absorbance at the surface plasmon resonance peak, A_{450} absorbance at the wavelength of 450 nm and B_1 and B_2 dimensionless parameters, taken as 3 and 2.2, respectively. The obtained diameter value is 16 nm.

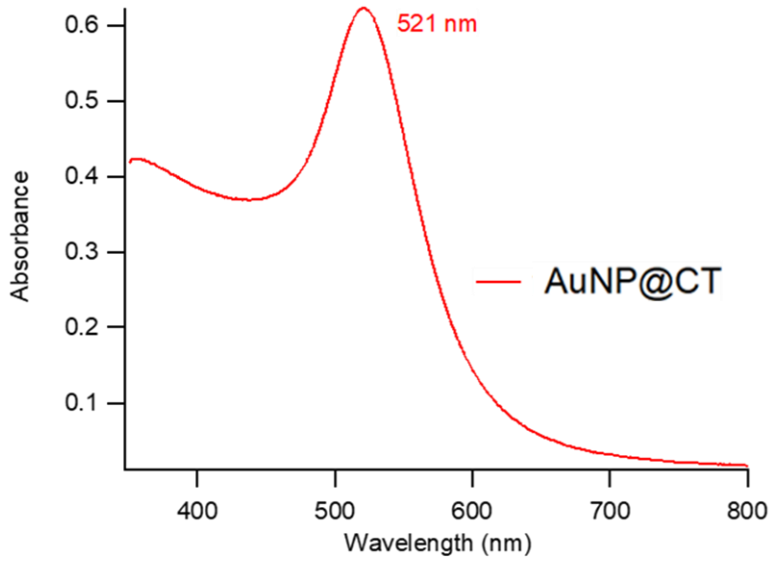

Figure S2 UV-Vis absorption spectra of citrated AuNP dispersion (after 1:5 dilution in water). The plasmon absorption peak is located at 521 nm.

The concentration of citrated gold nanoparticles was determined via UV-Vis spectrometry, using the Lambert-Beer law (E(λ) = ε(λ)lc) and considering the extinction values ε (λ) at the

LSPR maximum, i.e. λ = 521 nm. The extinction coefficient ε(λ) was determined by the following equation[4]:

$$ln\,(\varepsilon) = kln(d) + a$$

with d core diameter of nanoparticles, and k and a dimensionless parameter (k = 3.32111 and a = 10.80505). The arithmetic mean of the size, obtained by both the optical and the scattering analyses, leads to an ε(λ) value of $4.8 \cdot 10^8$ $M^{-1}cm^{-1}$. Consequently, the final concentration of citrated AuNP is ~$7.8 \cdot 10^{-9}$ M.

4. ATOMIC FORCE MICROSCOPY

Preliminary AFM images of AuNPs adsorbed on bare mica substrates were performed in order to test the effect of using a saline buffer as imaging solution, to prevent the attachment of NPs to the AFM tip (please refer to the Materials and Methods section for details regarding the imaging setup and parameters).

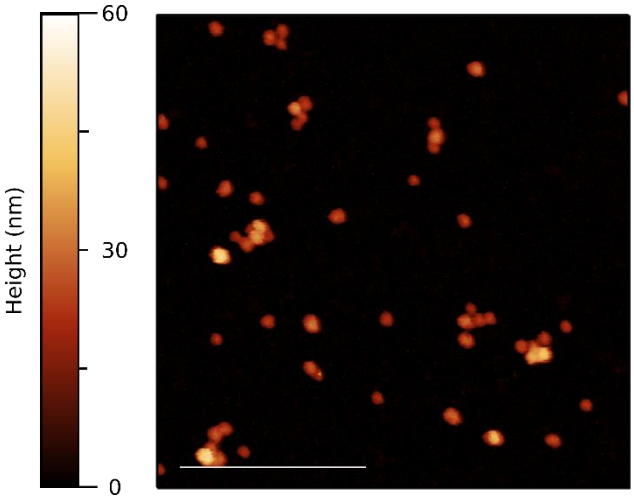

Figure S3 AFM topography representing AuNPs either isolated or clustered, adsorbed on a bare mica substrate. As reported in the Materials and Methods section, AFM imaging was performed using a saline buffer as imaging solution, in order to obtain better image quality and avoid tip contamination due to the attachment of the NPs to the probe. As can be seen from the image, isolated AuNPs get faithfully described by nearly perfect spherical shapes with an average contact angle close to 180°. Scalebar is 400 nm.

Neutron Reflectivity measurements

The software MOTOFIT was employed for the analysis of the NR curves. A five-layer model was employed to analyze the reflectivity profiles of neat SLBs, with scattering length density values calculated for each layer: a bulk subphase of Si (SLD = 2.07 * 10^{-6} $Å^{-2}$), a superficial layer of SiO_2 (SLD = 3.47 * 10^{-6} $Å^{-2}$); a second layer of D_2O (SLD = 6.393 * 10^{-6} $Å^{-2}$); a third layer composed of the polar headgroups of the SLB of the inner leaflet (SLD = 1.87 * 10^{-6} $Å^{-2}$); a fourth layer composed of the bilayer's lipid chains (SLD = -0.18 * 10^{-6} $Å^{-2}$); a fifth layer composed of the polar headgroups of the outer bilayer's leaflet (SLD = 1.87 * 10^{-6} $Å^{-2}$); a bulk superphase of solvent (D_2O, SLD = 6.393 * 10^{-6} $Å^{-2}$). The scattering length density values for the polar headgroups and lipid chains were estimated by taking into account the chemical compositions and the submolecular fragment volumes of phosphatidylcholines as determined by Armen et al. through molecular dynamic simulations[5] (see table S1).

Table S1. Chemical formula, molecular volumes and corresponding scattering length densities of species relevant to this study

Molecule	Chem. Formula	Volume ($Å^3$)	SLD(10^{-6} $Å^{-2}$)
PC headgroups	$C_{10}H_{18}NO_8P$	321.9	1.866
DSPC chains	$C_{34}H_{70}$	1004.6	-0.357
DOPC chains	$C_{34}H_{66}$	982.2	-0.212
cholesterol	$C_{27}H_{46}O$	630	0.210

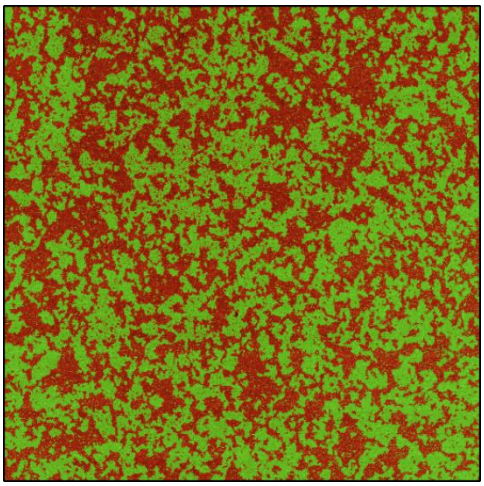

Figure S4 AFM topography of the SLB obtained from DOPC/DSPC/Chol (39/39/22 %w/w) liposomes. Using Gwyddion 2.53.16 it was possible to apply a mask to selectively cover the L_o phase (characterized by higher height values) and estimate the area fraction of each phase. The area fractions of the L_o and L_d phases are approximately 0.50, confirming the results obtained by Heberle et al.[6] on the very same vesicles preparation.

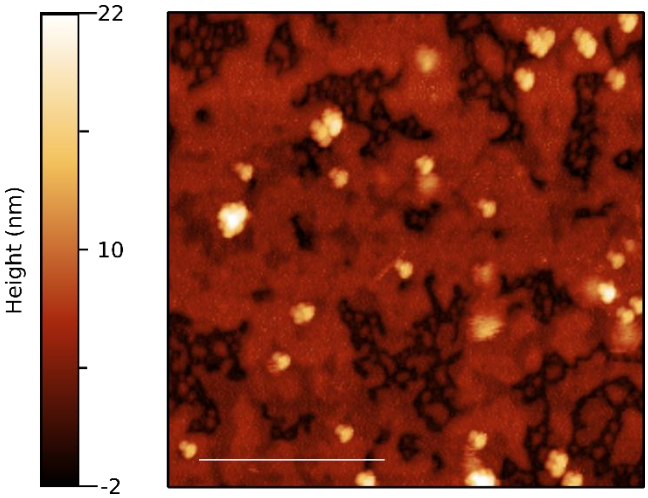

Figure S5 AFM topography showing the effects of tip contamination on the imaging of AuNPs adsorbed on the lipid bilayer. While the SLB gets correctly imaged, all the NPs appear in “clusters” characterized by similar shapes (same protrusions in all the directions). This is a clear indicator that the AFM probe has been contaminated by the attachment of one or multiple NPs which lead to the generation of imaging artifacts. Scalebar is 400 nm.

AUTHOR INFORMATION

Corresponding Author

* E-mail: andrea.ridolfi@ismn.cnr.it

Author Contributions

The manuscript was written through contributions of all authors. All authors have given approval to the final version of the manuscript.

Notes The authors declare no competing financial interests.

ACKNOWLEDGMENTS

This work was also supported by the Consorzio Sistemi a Grande Interfase (CSGI) through the evFOUNDRY project, Horizon 2020-Future and emerging technologies (H2020-FETOPEN), ID: 801367. We thank the SPM@ISMN research facility for support in the AFM experiments. Maier-Leibnitz Zentrum is acknowledged for provision of beam-time.

BIBLIOGRAPHY

1. Kline, S.R. (2006). Reduction and analysis of SANS and USANS data using IGOR Pro. J. Appl. Crystallogr. *39*, 895–900.

2. Kotlarchyk, M., and Chen, S.H. (1983). Analysis of small angle neutron scattering spectra from polydisperse interacting colloids. J. Chem. Phys. *79*, 2461–2469.

3. Haiss, W., Thanh, N.T.K., Aveyard, J., and Fernig, D.G. (2007). Determination of size and concentration of gold nanoparticles from UV-Vis spectra. Anal. Chem. *79*, 4215–4221.

4. Liu, X., Atwater, M., Wang, J., and Huo, Q. (2007). Extinction coefficient of gold nanoparticles with different sizes and different capping ligands. Colloids Surfaces B Biointerfaces *58*, 3–7.

5. Armen, R.S., Uitto, O.D., and Feller, S.E. (1998). Phospholipid component volumes:

Determination and application to bilayer structure calculations. Biophys. J. *75*, 734–744.

6. Heberle, F.A., Petruzielo, R.S., Pan, J., Drazba, P., Kučerka, N., Standaert, R.F., Feigenson, G.W., and Katsaras, J. (2013). Bilayer thickness mismatch controls domain size in model membranes. J. Am. Chem. Soc. *135*, 6853–6859.

Paper V

Interaction of nanoparticles with lipid films: Curvature effects

L. Caselli, A. Ridolfi, G. Mangiapia, E. Gustafsson, N. J. Steinke, C. Montis, T. Nylander and D. Berti, in preparation

Interaction of nanoparticles with lipid films: Curvature effects

Lucrezia Caselli[1], Andrea Ridolfi[1,2], Nina-Juliane Steinke[3], Emil Gustafsson[4], Costanza Montis[1], Tommy Nylander[5] and Debora Berti[1]

[1]University of Florence and CSGI, Department of Chemistry, Via della Lastruccia 3, Sesto Fiorentino 50019, Florence, Italy.

[2] ISMN-CNR and CSGI via Gobetti 101 40129 Bologna (Italy)

[3] Institut Laue-Langevin, DS/LSS, 71 Avenue des Martyrs, CS 20156, F-38042 Grenoble CEDEX 9, (France)

[4] Uppsala University, 752 36 Uppsala, Sweden

[5] Department of Chemistry, Lund University, Naturvetarvägen 14, 223 62, Lund, Sweden

1.Introduction

The interaction of engineered nanostructured materials with biological matter proceeds through an intricate balance of energetic contributions [1–3], which occur at the nano-bio-interface, where nanomaterials, e.g. nanoparticles, meet biological fluids or interfaces. This set of interactions is crucial for the fate of the nanoparticles in living systems or the environment and determines the toxicity or therapeutic efficiency of the nanomaterial itself, depending on if the contact is unwanted or engineered on purpose [4–9]. The curvature of the nanoparticle (i.e. the inverse of its radius for a spherical particle) is one factor that determines the interaction with biological interfaces, regulating, for instance, the endocytic pathway which leads to NPs' internalization in cells [4,10–14].

"Curvature" in a three-dimensional space refers to surfaces [15]: for NPs, this is simply the NPs' surface, while for a lipid membrane, we usually consider the

lipid/water interface (i.e. the region where the lipid polar headgroups are in contact with the aqueous medium) [15,16].

Considering the normal vector in a given point on a surface in 3D, we define two principal curvatures (k_1 and k_2) as the maximum and minimum value of the curvature in the considered point [15,17]. k_1 and k_2 can be combined to give two useful measures of the curvature of a surface, i.e. the Mean (H) and Gaussian (K) curvature [15], defined as follows [15,17]:

$$H = \frac{1}{2}(k_1 + k_2) \quad (1)$$

$$K = k_1 k_2 \quad (2)$$

The 3D shape of a surface can be univocally determined by defining H and K for all its points [15].

Flat surfaces always have zero H and K, since both k_1 and k_2 are zero. Non-flat surfaces can have [15]: i) k_1 and k_2 equal in sign (e.g. the surfaces of spheres), leading to positive H and K for each point of the surface; ii) k_1 and k_2 of opposite sign (e.g. saddle-shaped surfaces), resulting in positive or negative H (depending on the absolute values of k_1 and k_2) and negative K throughout the surface; iii) one (k_1 or k_2) non-zero curvature (e.g. body cylinders), yielding positive or negative H and zero K.

Spherical NPs have constant and uniform H and K; more complex nanomaterials with asymmetric shapes (e.g., nanocubes, -stars, and -rods) will exhibit non-uniform H and K over their surface.

Lipid bilayers, the building blocks of biological membranes, usually assemble in flat lamellae, characterized by zero H and K across their interface. However, biological membranes can also assume non-lamellar configurations, where the bilayer bends in the 3D space: precisely, a “direct” geometry of the membrane corresponds to the outer lipid leaflet (i.e., the one in contact with the external

medium) bending towards the hydrocarbon chain region, while an “inverse” geometry determines an opposite bending [17]. In the first case, H is positive, while K can assume positive (e.g., the membranes of vesicles), negative (e.g., non-lamellar membranes with a direct cubic geometry), or zero (e.g. non-lamellar membranes with a hexagonal geometry) values. At the same time, for inverted assemblies, both H and K are always negative.

The NPs’ curvature, defined by size and shape, strongly affects their reactivity and interaction with lipid membranes. Specifically, it determines the area available for NPs adsorption on lipid surfaces [18], modulating the strength of NP-membrane adhesion forces; moreover, a high surface curvature, either uniformly distributed on the surface of NPs (e.g., small NPs with sizes of a few nm) or localized at the sharp edges of asymmetric NPs (e.g., nanorods), is associated to higher energetic costs in terms of wrapping and internalization by membranes [3,11,13,14]. Finally, curvature plays a significant role in the surface functionalization of NPs (e.g., ligand surface density), affecting their chemical identity [19]. For these reasons, NPs curvature has been intensively investigated as a critical determinant in the interaction with natural and synthetic membranes.

On the contrary, the role of membrane interfacial curvature, connected with membrane geometry, represents a less unexplored research field, which could potentially have a similar impact on interactions at the nano-bio interface. A flat configuration of the lipid bilayer is the most commonly encountered geometry in membranes of healthy cells; however, curved membrane configurations, as cubic bicontinuous arrangements, are known to occur in cells under pathological conditions (e.g., drug detoxification, starving, infection, oxidative stress, and cancer disease) or during certain phases of cell life (e.g. membrane fusion) [20–22]. Up to now, the investigations related to cubic membranes have been limited to a descriptive level, while the biological function of membrane arrangements with non-zero interfacial curvature remains unexplored [21,22]. This is mainly due to the transient nature of non-lamellar biological membranes, which makes their

investigation in natural systems (e.g., through cryo-Transmission Electron Microscopy) very challenging [22].

In this framework, lipid models of synthetic nature, mimicking cubic membranes' structure, can be used to simplify the investigation. Our recent findings [23,24] show that it is possible to obtain solid-supported lipid model surface layers of cubic symmetry, with controlled physicochemical and structural features, enabling the study of NPs-cubic membranes interactions at the nano-bio interface.

Here, we will directly compare the interaction of lamellar and cubic model films of similar composition with hydrophilic gold nanoparticles (AuNPs) of similar size and surface coating, but different shapes, i.e., spheres (AuNSs) vs. rods (AuNSs); this way, we will explore the effect of varying curvature from both the NPs- and the membrane-side.

By combining structural techniques with nanoscale resolution (i.e., Neutron Reflectivity (NR) and Grazing-Incidence Small-Angle Neutron Scattering (GISANS)) with Confocal Laser Scanning Microscopy (CSLM) with a micron-scale resolution, we will characterize the structural modifications induced by NPs on model membranes at two different length scales. In addition, the combination of static with kinetic NR investigation will provide access to NPs-induced restructuring processes of lipid membranes, occurring on different time frames.

Our results represent one of the first attempts to systematically explore curvature's role, modulated by both NPs shape and membrane geometry, in nano-bio interactions.

2.Materials and Methods

2.1 Materials

Tetrachloroauric (III) acid (≥ 99.9%), (11-Mercaptoundecyl)-N,N,N-trimethylammonium bromide (≥ 90%), Cetyl trimethyl ammonium bromide (99%), octanethiol (98.5%), ascorbic acid (98%), AgNO3 (99%), HCl, toluene (99.8%), MeOH (99.8%), EtOH (99.8%), $CHCl_3$ (99%), Tetraoctylammonium bromide (98%), NaBH4 (98%), n-hexane (), 1,2-dioleoyl-sn-glycero-3-phosphocholine (DOPC) were provided by Sigma-Aldrich (St. Louis, MO). Glycerol monooleate (GMO) (99%) was provided by Danisco (Copenhagen, Denmark), while Nile Red (≥ 98%) was supplied by Sigma Aldrich. All chemicals were used as received. Milli-Q grade water was used in all preparations.

2.2 Synthesis of Gold nanospheres (AuNSs)

Gold nanospheres functionalized with the cationic derivative N,N,N-trimethyl(11-mercaptoundecyl)ammonium bromide (TMA) were synthesized as described by McIntosh et al. [25,26]. First, octanethiol-capped spherical gold nanoparticles (NSs) were prepared following the two-phase method developed by Brust et al. [27,28]: an aqueous solution of $HAuCl_4$ (15 ml, 30 mM) was mixed with a solution of tetraoctylammonium bromide (TOAB) in toluene (40 ml, 50 mM). The two-phase mixture was vigorously stirred until all the $HAuCl_4$ was transferred from the aqueous solution into the organic phase; TOAB acts as the phase-transfer reagent. Octanethiol (7.81 µl) was then added to the organic phase. A freshly prepared aqueous solution of sodium borohydride (12.5 ml, 0.4 M) was slowly added with vigorous stirring. On addition of the reducing agent, the organic phase changed color from orange to deep brown within a few seconds. After further stirring for 3 hours, the organic phase was separated, evaporated to 5 ml in a rotary evaporator and mixed with 200 ml ethanol to remove excess thiol.

The mixture was kept for 4 hours at -18°C until a dark brown precipitate was formed, and the supernatant was removed with a pipette; the precipitate was washed with 200 ml of ethanol and put again in the freezer. After 4 hours, the ethanol was removed with a pipette and completely evaporated in a rotary evaporator, obtaining octanethiol-capped gold nanoparticles. NSs capped with TMA were prepared by stirring 100 mg of octanethiol-capped NSs and 150 mg of N,N,N-trimethyl(11- mercaptoundecyl)ammonium bromide in 20 ml of degassed tetrahydrofuran under argon for two days at room temperature. The black precipitate of the gold nanoparticles was purified by repeated suspension, centrifugation, and decantation with dichloromethane. NSs capped with TMA were then dissolved in pure water without the need for pH adjustment**.**

2.3 Synthesis of Gold Nanorods (AuNRs)

Gold NRs were synthesized according to a newly developed seedless growth protocol by El-Seyed [29]. Briefly, $HAuCl_4$ (5.0 mL; 1.0 mM) was added to 5.0 mL of Cetyl trimethyl ammonium bromide (CTAB, 0.2 M) at 27°C, under magnetic stirring. Then, $AgNO_3$ (250 µL; 4.0 mM) was added. Subsequently, HCl (8.0 µL, 37%) was added to obtain a pH of 1-1.15. Then, we added 70 µL ascorbic acid (78.8 mM) under magnetic stirring and waited until the solution was clear. Immediately afterward, Ice-cold $NaBH_4$ (15 µL; 0.01 M) was added and allowed to react overnight. The final dispersion of AuNRs capped with CTAB was characterized by a dark pink colour. The excess of CITAB was removed from the dispersion by 10 cycles of centrifugation, each followed by precipitation of CITAB crystals and removal of the supernatant containing AuNRs.

2.4 Preparation of lamellar and cubic lipid films

We obtained lamellar and cubic lipid films from GMO/DOPC 50/50 % mol/mol and pure GMO, respectively. The lipid solutions in n-hexane (30/70 lipid/hexane % w/w) were spin-coated onto a solid substrate for 10 s at 700 r.p.m and then for 60 s at 2000 r.p.m. Most of the solvent evaporates during this procedure. The lipid-coated substrate was then immediately immersed in excess Milli Q water, leading to lamellar or cubic lipid films by hydration. For the case of lipid films prepared for CLSM analysis, lipid formulations were labelled with hydrophobic Nile Red (0.1 mol% with respect to the total lipid amount), enabling the visualization of lipid layers; 100 µL of the lipid solution in n-hexane were deposited onto a hydrophilic round glass substrate (diameter of 15 mm) prior to spin-coating. Lipid films formed onto the glass substrate were then sealed into a single-well sample holder and hydrated with 2 mL of water before imaging. For the case of NR analysis, samples were formed by depositing 1 mL of n-hexane lipid solution on 50 x 80 x 15 mm^3 Silicon mirrors (Andrea Holm GmbH, Tann, Germany; roughness ≤ 5 Å) to cover almost the whole surface. After spin-coating and hydration, the substrate was sealed into a flow-cell type sample holder. To remove any excess contamination and the remaining n-hexane, an excess of water (at least 25 times the sample cell volume) was flushed through the sample cell. Silicon substrates were preliminary rinsed in either ultrapure water and ethanol, in order to remove organic residues. After that, they were bath sonicated for 30 minutes in ethanol with a Bandelin DL 102 3L bath sonicator, followed by other 30 minutes in ultrapure water (Millipore Simplicity UV). The surfaces were then cleaned with a Novascan PSD-UV8 UV/ozone plasma for 30 min and rinsed in ultrapure water. Finally, they were dried with nitrogen gas and stored in ultrapure water, ready for deposition.

2.5 Neutron Reflectivity (NR)

Static NR measurements (section 3.2) were carried out at the OFFSPEC reflectometer [30] (Isis Neutron and Muon Source, Rutherford Appleton Laboratory, UK).

Neutrons in the wavelength range 1.0–14.5 Å were used to perform the measurements. Two incident angles, 0.50° and 2.00° allowed collecting data in the range $0.008 \leq Q/Å^{-1} \leq 0.3$. The arrival times and positions of scattered neutrons were detected on a ^{3}He 1 x 300 mm linear scintillator detector (1.2 mm pixel size) positioned at 3.5 m from the sample. The set-up allows for a resolution of 2-5% $\Delta Q_z/Q_z$. In order to achieve a good signal-to-noise ratio, a counting time of about 5 hours for the measurement was chosen.

NR kinetics (section 3.3) were performed at the REFSANS Horizontal TOF reflectometer of the Helmholtz-Zentrum Geesthacht, located at the Heinz Maier-Leibnitz Zentrum in Garching, Germany [31]. Neutrons in the wavelength range 3.0–21.0 Å were used to perform the measurements. A horizontally smeared out beam of up to 80 mm width was used to maximise intensity. An incident angle of 3.00° allowed collecting data in the range $0.03 \leq Q/Å^{-1} \leq 0.22$. The arrival times and positions of scattered neutrons were detected on a Denex 2D 500 × 700 mm^2 multiwire ^{3}He detector (pixel size 2.1x2.9 mm^2, efficiency 80% at 7 Å, gamma sensitivity < 10^{-6}) positioned at 4.5 m from the sample. The detector was installed in a liftable vacuum tube in order to reach exit angles up to 5.2° at the maximum elongation. Neutron Reflectivity was acquired at time intervals of 2’30’’, over a time period of 5 h.

2.7 Grazing Incidence Small Angle Neutron Scattering (GISANS)

GISANS measurements were performed at the REFSANS Horizontal TOF reflectometer of the Helmholtz-Zentrum Geesthacht, located at the Heinz Maier-Leibnitz Zentrum in Garching, Germany [31]. Different wavelength of the neutron beam (ranging from 2.7 to 18.1 Å) were selected to perform the measurements, corresponding to different penetration depths within the sample. 13 point beams are impinged on the sample and point focused on the 2D position sensitive detector (Denex 2D 500 × 700 mm^2 multiwire ^3He detector (pixel size 2.1x2.9 mm^2, efficiency 80% at 7 Å, gamma sensitivity < 10^{-6})), placed at a distance of 9 m. For a given wavelength, the two-dimensional intensity data sets describe different (Q_y, Q_z) ranges.

GISANS was employed to investigate films' properties along the directions perpendicular and parallel to the substrate. The in-plane film structure can be studied from the scattering patterns on the (Q_y, Q_z) plane (GISANS). For low angles, α_i and α_f are the angles of incidence and reflection, respectively, of the neutron beam. The associated wavevector in the xz plane is $|k| = 2\pi/\lambda$. The total scattering vector is the difference between the wave vector of the incident beam k_i and the scattered beam k_f:

$$\vec{Q} = \overrightarrow{k_i} - \overrightarrow{k_f}$$

$$\begin{bmatrix} Q_x \\ Q_y \\ Q_z \end{bmatrix} = \begin{bmatrix} \cos\alpha_f \cos 2\theta_f - \cos\alpha_i \\ \cos\alpha_f \sin 2\theta_f \\ \sin\alpha_i + \sin\alpha_f \end{bmatrix}$$

The wavelength is denoted with λ, while $2\theta_f$ indicates the angle in the xy plane, which is relevant to determine lateral correlation lengths. The angle of incidence chosen was just above the critical angle for total reflection (α_c).

2.7 Confocal Laser Scanning Microscopy

A Leica CLSM TCS SP8 confocal microscope, operating in inverted mode, with a 63 x 1.3 numerical aperture water immersion objective, was used to image the lipid-based surface structures in excess water. The fluorescence of Nile Red lipid was excited at 561 nm and the fluorescence was acquired in the 571 nm - 650 nm emission range, with a PMT. Images were taken with a resolution of 512 x 512 pixels using a 400 Hz bidirectional scan with each scanning line averaged four times. Leica software was used to create three-dimensional reconstructions of the z-stacks.

3.Results

3.1 Characterization of gold nanoparticles and lipid films of different curvatures

Figure 1 summarizes the main features of the systems under investigation: AuNPs (Panel A) and lipid films (Panel B) characterized by different curvatures.

Cationic gold nanospheres (AuNSs) and nanorods (AuNRs) were prepared as described in the Materials and Methods section, according to well-known synthetic routes [25–28]. Figure 1, Panel A shows SAXS profiles and TEM images of both AuNSs and AuNRs. The main physicochemical features of AuNPs are summarized in the Table. According to the SAXS results, analyzed with a form factor for spheres with a Schultz polydispersity profile (see SI for details), AuNSs are polydisperse spheres with a metal core of a few nm, in perfect agreement

with TEM analysis. The capping agent mearcaptoundecyl-N,N,N-trimethyl ammonium bromide (TMA) produces an overall positive charge in water, as determined by Z-potential measurements (see SI for details).

The SAXS profile of AuNRs was analysed with a form factor for cylinders with a polydisperse cross section fit model (see SI for details), that yielded 4.5 aspect ratio (length/width) gold nanorods, in line with the TEM analysis; similarly to AuNSs, the presence of Cetyltrimethyl ammonium bromide (CTAB) as capping agent determines a net positive charge of AuNRs in water.

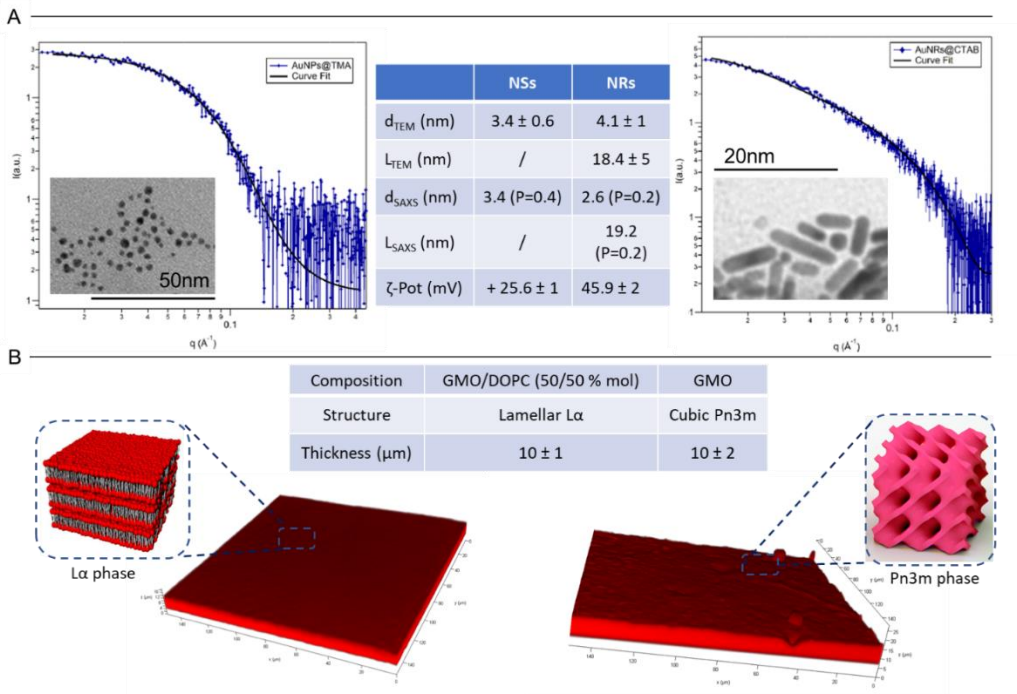

	NSs	NRs
d_{TEM} (nm)	3.4 ± 0.6	4.1 ± 1
L_{TEM} (nm)	/	18.4 ± 5
d_{SAXS} (nm)	3.4 (P=0.4)	2.6 (P=0.2)
L_{SAXS} (nm)	/	19.2 (P=0.2)
ζ-Pot (mV)	+ 25.6 ± 1	45.9 ± 2

Composition	GMO/DOPC (50/50 % mol)	GMO
Structure	Lamellar Lα	Cubic Pn3m
Thickness (μm)	10 ± 1	10 ± 2

Figure 1 Panel A) Physicochemical characterization of NPs. Left: SAXS profile of AuNSs in water (1:3 dilution) and corresponding curve fitting according to the Schultz polydisperse spheres model from the NIST package SANS Utilities. The inset reports a TEM image of AuNSs; middle: diameter values of AuNSs and cross section and length of AuNRs, determined by TEM and SAXS analyses. SAXS results are obtained from the fitting procedures (see SI), providing polydispersity values (i.e., "P" in the Table). Right: SAXS profile of AuNRs in water and curve fitting according to the Cylinder poly radius model from the NIST package SANS Utilities. The inset reports a TEM image of AuNRs; **Panel B) physicochemical characterization of lipid films.** Left part: Three-dimensional reconstruction of a confocal fluorescence z-stack of images of the lamellar film (tilted surface area of 150 x 150 μm). The inset reports the inner Lα structure; middle part: Table reporting

composition, inner structure and average thickness of lipid films; right part: three-dimensional reconstruction of a confocal fluorescence z-stack of images of the cubic film (tilted surface area of 150 x 150 μm). The inset reports the inner cubic Pn3m structure.

Both AuNSs and AuNRs are characterized by a net positive charge, which is known to determine a strong interaction even with zwitterionic lipid membranes, characterized by a slightly negative zeta potential [1,32]. In addition, spherical NPs are characterized by a diameter similar to the rods' cross section, close to the typical thickness of a lipid bilayer; therefore, the main difference between AuNSs and AuNRs is the strong asymmetry of AuNRs, with two curved surfaces (the poles) of similar positive H and K as AuNSs, separated by a cylindrical body, with reduced H (i.e. one half of that of AuNSs) and zero K. We will then investigate how this curvature difference of NPs affects the interaction with lipid interfaces of different interfacial curvature.

Lipid films of different liquid crystalline structure were prepared by spin-coating n-hexane lipid solutions of 1-monoolein (GMO) for the cubic phase and of GMO/DOPC (1,2-Dioleoyl-sn-glycero-3-phosphocholine) (50/50 mol %) for the lamellar phase, on glass coverslips (see Materials and Methods for details on samples' preparation); a fluorescent hydrophobic dye (Nile Red, 0.1 mol % with respect to total lipid amount) was added to allow their visualization in CLSM. The lipid films were then dried in vacuum to completely remove the solvents and hydrated with excess water. Figure 1, Panel B, displays the 3D reconstructions of GMO and GMO/DOPC films. The morphology of the films at the micron-scale appears very similar: a 3D reconstruction highlights a homogeneous thickness at the micron scale with low roughness (see Table in Figure 1B). These lipid mesophases are characterized by a different structural arrangement at a nanometric length scale: for GMO films, lipid molecules arrange in a curved lipid bilayer, folded to form a bicontinuous mesophase (see the scheme of Pn3m phase, sketched in Figure 1B). This assembly is characterized by negative H and K in each point of the lipid/water interface. On the contrary, for GMO/DOPC

films the mesophase is characterized by stacked infinite planar lipid bilayers of zero curvature (see the scheme of Lα phase sketched in Figure 1B). This structural arrangement will be further confirmed in the following section (Neutron Reflectometry data).

3.2 Structural effects of gold nanoparticles on lipid films

We investigated the internal nanostructure of lipid films, with or without AuNSs and AuNRs through NR. GMO and GMO/DOPC films were prepared on silicon blocks as described in the Materials and Methods and hydrated with excess D_2O. Samples were left equilibrating for 12 hours before recording their reflectivity. Subsequently, NPs in D_2O were pumped in the measurement cell, to reach a final Au concentration of 0.12 mg/mL. After 8 hours incubation, the reflectivity of lipid films in the presence of AuNPs was recorded.

The reflectivity profiles of GMO/DOPC (Figure 2a) and GMO (Figure 2b) films without NPs (red curves) are consistent with the formation of highly ordered mesophases, with multiple Bragg reflections.

The reflectivity profile of the GMO-DOPC film (red curve of Figure 2a) evidences a high structural order, with two prominent Bragg peaks located at 0.099 and 0.192 $Å^{-1}$, corresponding to the first two reflexes of the lamellar Lα arrangement (i.e., with *hkl* Miller indices (100) and (200)). As sketched in Figure 2a (left inset), the lamellar structure of the micrometric film consists of a stack of flat lipid bilayers, i.e. characterized by zero interfacial curvature, separated by water layers. The unit cell spacing was calculated using the q-position of the maximum intensity reflex (i.e. *hkl* (100)) through $d = 2\pi(h^2 + k^2 + l^2)^{1/2}/q_{100}$ [33], yielding a value of 6.3 nm, in line with previous results obtained for bulk GMO/DOPC assemblies [34]. Considering a thickness of about 3.4-3.7 nm for the GMO/DOPC bilayer (the literature values are 3.7 nm and 3.4 nm for DOPC and GMO bilayers [35,36], respectively), the water interlayers will have a thickness of 2.6-2.9 nm.

On the other side, the reflectivity profile of the GMO lipid film (red curve in Figure 2b) presents multiple Bragg peaks, indicating also in this case a highly ordered internal structure. The two peaks at 0.093 and 0.115 $Å^{-1}$ identify an inverse cubic diamond phase with crystallographic space group Pn3m and correspond to (110) and (111) Bragg reflexes typical of this arrangement. As sketched in the right inset of Figure 2b, this structure is characterized by a bicontinuous nature, featuring a single lipid bilayer with negative interfacial curvature, which divides the inner space into two sets of interwoven aqueous channels. The lattice spacing d, calculated from the higher intensity reflex (i.e. *hkl* (111)), is 9.7 nm, from which a water channel radius of 2.2 nm was calculated [37].

When AuNSs are added to the GMO/DOPC film, the reflectivity (green curve in Figure 2a) still shows Bragg reflexes typical of the lamellar arrangement, whose positions are unchanged with respect to the case of the neat GMO/DOPC assembly. However, the presence of AuNSs produces a significant reduction in the peaks' intensity (see green curve as compared to red one), connected to a partial disruption of the bilayer arrangement. An alternative interpretation, foreseeing the removal of lipid material as a consequence of the liquid flow through the sample cell, was previously ruled out with a control experiment, aimed to check the stability of model film towards rinsing.

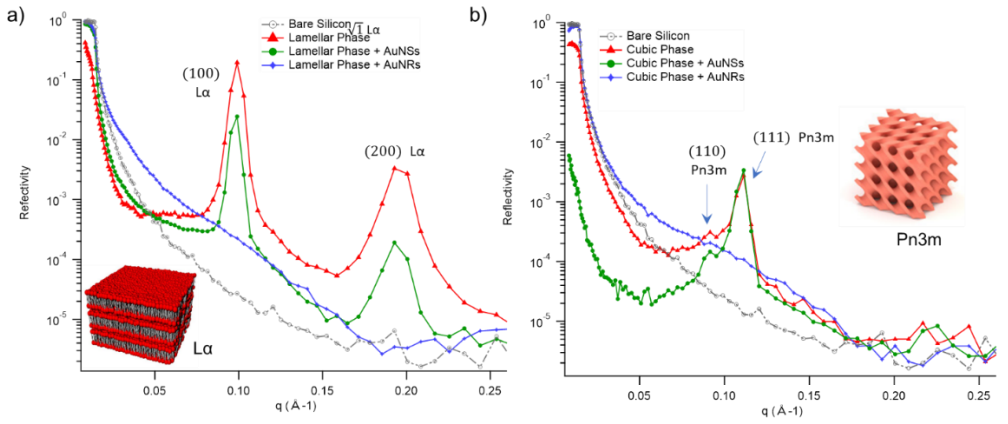

Figure 2 a) Reflectivity profiles of the GMO/DOPC lamellar film in the absence (red curve) and in the presence of AuNSs (green curve) and AuNRs (blue curve). The reflectivity of the bare silica

support is also reported (gray curve). The inset sketches the inner Lα structure of the lipid film; b) Reflectivity of the GMO cubic film in the absence (red curve) and in the presence of AuNSs (green curve) and AuNRs (blue curve). The reflectivity of the bare silica surface is also reported (gray curve). The inset sketches the inner cubic Pn3m structure of the lipid film. Measurements acquired at OFFSPEC [30], ISIS Neutron and Moun Source (United Kingdom).

At variance from what observed for lamellar layers, AuNSs seem to have negligible impact on the cubic lipid film: indeed, the presence of AuNSs does not significantly modify neither the position nor the intensity of the Bragg peaks in Figure 2b (green curve), with respect to the neat GMO film. This suggests that the cubic Pn3m architecture is stable and completely preserved, even after 13 hours of incubation (8 h of incubation + 5 h of measurement) with the AuNSs. This result was further confirmed by NR measurements performed at REFSANS [31] (Heinz Maier-Leibnitz Zentrum in Garching), on the same system and under the same experimental conditions (e.g., incubation time, temperature etc.), highlighting a Pn3m structure which is unmodified by AuNSs (see Fig. S3 of SI for details).

We further investigated the structure of AuNSs/cubic phase hybrid films by means of Grazing Incidence Small Angle Neutron Scattering (GISANS), with the aim of pointing out possible effects of AuNSs on cubic phases, occurring in a longer time frame (8 h of incubation + 24 h of measurement, for a total number of AuNSs-membrane interaction of 32 h). This technique allows also investigating the in-plane lipid arrangement and its alteration due to the AuNPs injection [38]. Consisting of multiple parallel lamellae, lamellar films only have structural order with respect to the film normal, while cubic phases are also characterized by high lateral ordering, whose possible modifications can be easily detected by GISANS.

We performed GISANS on a neat GMO cubic film in D_2O, previously equilibrated for 12 h (Figure 3A). Then, we added AuNSs at the same concentration used for

NR measurements and left incubating for 8 h. The 2D GISANS pattern was subsequently recorded in D_2O (Figure 3B). GISANS patterns were collected at different wavelengths of the neutron source (see Materials and Methods and Figure S1 of SI), corresponding to different penetration depth of the beam within the sample: here, we report representative patterns acquired at intermediate λ (i.e. 3.3 Å).

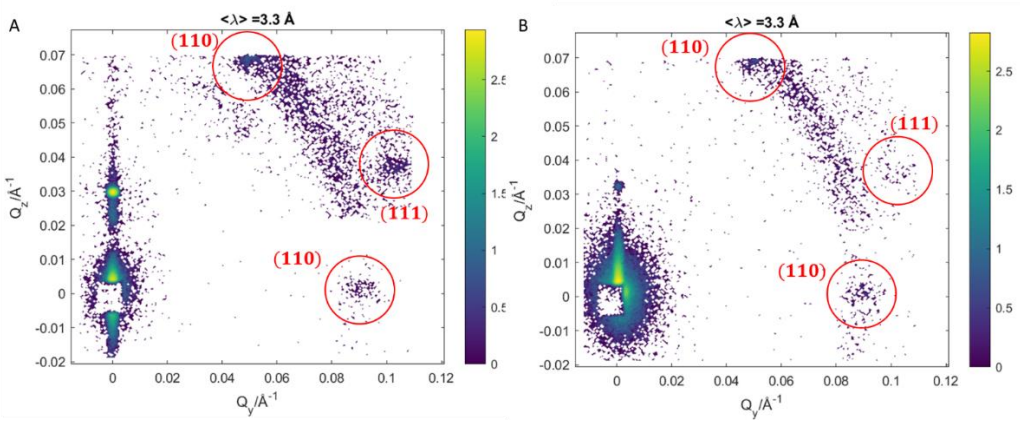

Figure 3 A) GISANS pattern of GMO cubic Pn3m films, in the absence of NPs; B) GISANS pattern of the GMO cubic Pn3m phase in the presence of AuNSs. Measurements acquired at REFSANS, Heinz Maier-Leibnitz Zentrum, Garching, Germany.

The Q_z/Q_x GISANS pattern of the GMO film in the absence of AuNSs shows isolated spots, which represent the (110) and (111) Bragg reflections of the Pn3m arrangement. By averaging the position of these highest intensity points within Q_z/Q_x plots obtained for different neutron wavelengths (see Figure S2 of SI for details), we found that the corresponding q values describe a Pn3m arrangement with a lattice parameter of 100 Å, in perfect agreement with the NR analysis.

Interestingly, the presence of a spot-like pattern, instead of arcs or rings, indicates a highly oriented material [39], i.e. with low mosaicity, and reveals an important difference with respect to bulk GMO assemblies. Bulk cubic phases present multiple, randomly oriented, micron-sized domains of cubic symmetry,

resulting in an isotropic material [40]; instead, these films consist of a cubic arrangement, with spatial orientation along a preferential direction. This phenomenon has already been observed for non-lamellar films of different composition and nano or micron-sized thickness [39,40], formed through spin-coating.

The addition of AuNSs (Figure 3B) produce an almost complete loss of the spot-like pattern, with clusters of higher intensity points barely distinguishable from a continuous ring-shaped background. This effect hints at a significant increase of structural disorder within the mesophase, which can be either due to a partial disruption of the cubic symmetry or to a loss of spatial orientation: indeed, the presence of AuNSs can both partially destroy the cubic arrangement (as already observed for lamellar phases) and/or perturb it, introducing defects within the cubic film, which promote the formation of different randomly oriented domains. Thus, differently from NR, GISANS analysis reveals a non-negligible impact of AuNSs on the cubic structure, when observed on longer time scales. This points out an important role of curvature in the structural stability of model membranes, with cubic membranes preserving their structural stability for longer times than lamellar ones, when exposed to AuNSs.

The impact of AuNRs is dramatically stronger for both lamellar and cubic lipid mesophases (Figure 2a-b). Differently from AuNSs, AuNRs completely destroy both the lamellar (blue curve of Figure 2a) and cubic (blue curve in Figure 2b) arrangements, as evident from the absence of Bragg reflexes in the corresponding reflectivity profiles: this hints to a dramatic effect of NPs shape asymmetry in the interaction with model lipid films.

At a variance with the case of AuNSs, this severe interaction with AuNRs does not allow discriminating between the structural response of lamellar and cubic phases, in the time frame of our experimental observations. To gain insight on this fast disruption process, we performed Neutron Reflectivity kinetics studies,

allowing for monitoring the structural alteration produced by AuNRs on shorter time scales.

3.3 NPs/lipid films Interaction: kinetics of structural modifications

Neutron Reflectivity Kinetics were performed at REFSANS Horizontal TOF reflectometer of the Helmholtz-Zentrum Geesthacht (Heinz Maier-Leibnitz Zentrum in Garching, Germany) [31] and allowed monitoring the progressive disruption of the lamellar and cubic films by AuNRs. To the purpose, we measured the reflectivity of lipid films in H_2O, just before and after the injection of AuNRs within the measuring cell, at time intervals of 2.5 minutes; in order to cover the same measuring time of static NR acquisitions (section 3.2), the NR kinetics were acquired over a time period of 5 hours (see Materials and Methods for further details). In Figure 4, we report the (Q_z,Q_x) representations of NR data, along with the corresponding NR detector screens (right insets), for the lamellar (Panel A) and cubic film (Panel B), before and at different times from the addition of AuNRs.

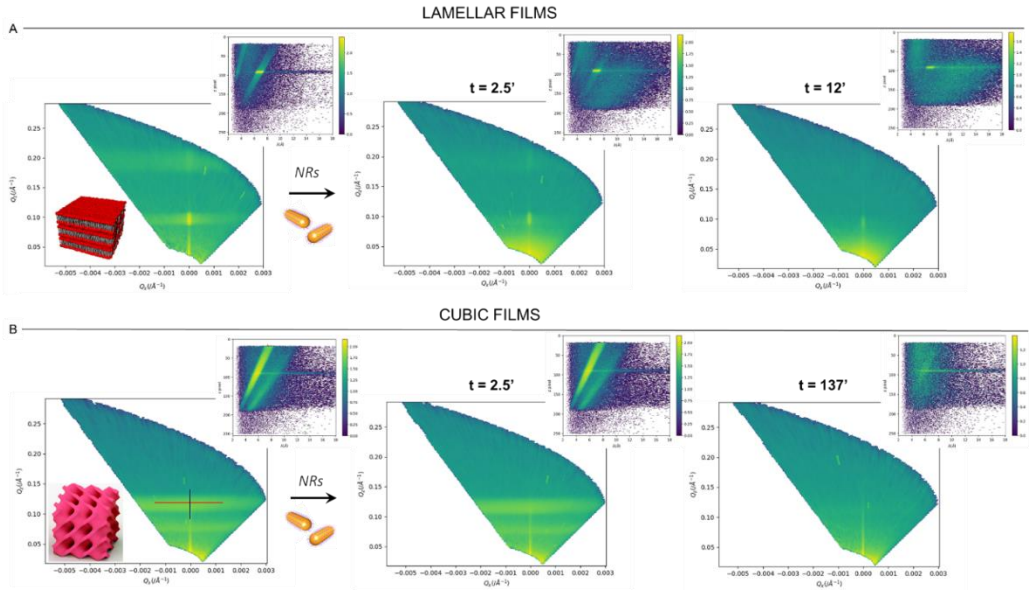

Fig.4 Panel A: (Qz,Qx) representations of the off-specular scattering of a lamellar film in the absence of AuNRs and at different times from the injection of AuNRs. The insets represent the corresponding images of the NR detector; Panel B: (Qz,Qx) representations of the off-specular scattering of a cubic film in the absence of AuNRs and at different times from the injection of AuNRs. The insets represent the corresponding images of the NR detector.

(Q_z,Q_x) representations enable the analysis both of the specular and the off-specular reflectivity of the samples [41]: the integrated intensity along the specular reflectivity line (see blue line in the left (Q_z,Q_x) plot of Panel B) gives the specular reflectivity profile of lamellar and cubic films: these profiles are analogous to the ones of Fig. 2a-b (see Fig. S4 of SI, as an example), except for the lower intensity due to the reduced measuring time and the different medium (i.e., H_2O instead of D_2O).

In addition, the (Q_z,Q_x) maps of both lamellar and cubic films in the absence of NPs show pronounced off-specular patterns, i.e. out of the specular reflectivity line, consisting in marked “Bragg sheets” (see the red line in the left (Q_z,Q_x) plot of Panel B, as an example).

These off-specular features are also visible in the corresponding detector screens, as higher intensity stripes. Bragg sheets are characteristic of highly

ordered samples and provide information on the internal nanostructure: indeed, they are found following the lines $Q_z = (h^2 + k^2 + l^2)^{1/2} 2\pi/d$ [41]. These features coincide with the Bragg peaks from the specular reflectivity, distinguishing the Lα and Pn3m structures of lamellar and cubic films, respectively.

Due to their particularly high intensity, off-specular Bragg sheets allow monitoring the impact of AuNRs on the structure of lipid films over time. Panels A and B highlight a strong effect of AuNRs on both lamellar and cubic arrangements, which can be identified in the smearing out of their characteristic Bragg sheets; this effect advances with time and ultimately leads to the complete loss of the off-specular signal, hinting to the total disruption of the films' architecture. Interestingly, lamellar films completely lose their structural organization significantly faster than cubic ones, with Braggs sheets completely vanishing within 12 minutes. On the contrary, cubic phase off-specular signal is still detectable after more than 2 h of incubation with AuNRs. Thus, cubic phases show an enhanced structural resilience towards the action of rods with respect to lamellar ones, perfectly in line with the previous findings on spherical particles (section 3.2).This hints to a general role of membrane curvature on nano-bio interactions, with highly curved membranes showing an enhanced structural stability towards the interaction with nanomaterials. In addition, the slower disruption process allowed us to appreciate subtler details of the restructuring action of NRs on cubic phases; specifically, specular reflectivity profiles (Figure S4) show that AuNRs produce a non-negligible shrinkage of the cubic phase lattice parameter (i.e., 2 Å), after only 2'30'' of incubation (Figure 4, middle (Q_z, Q_x) plot of Panel B); this shrinking might be the driving process for the subsequent progressive collapse of the mesophase.

In summary, the NR and GISANS analysis allowed characterizing NPs-lipid films interactions at a nanoscale level: giving access to the alterations induced by NPs on the films' nanostructure. The results highlighted that curvature, of either the membrane or NPs, plays a crucial role on nano-bio interactions.

To connect this nanoscale structural information with the global impact of NPs on model membranes, we further characterize NPs-films interaction through real-time direct observation, by means of Confocal Laser Scanning Microscopy (CLSM). This technique enables to follow the morphological modification induced by NPs on lipid films at larger scale (i.e. micron-scale), for a comprehensive view of the phenomenon.

3.4 NPs/lipid films Interaction: real-time morphological effects at the microscale

We performed CLSM, monitoring the effects induced by NPs on the membrane morphology, over the same time frame of Neutron kinetics measurements. To this purpose, fluorescently labelled lamellar and cubic phases (Figure 1, panel B) were imaged before and after the injection of NPs. Figure 5 gathers representative side-view confocal microscopy images of a lamellar film challenged by AuNSs (Figure 4a) and AuNRs (Figure 4b).

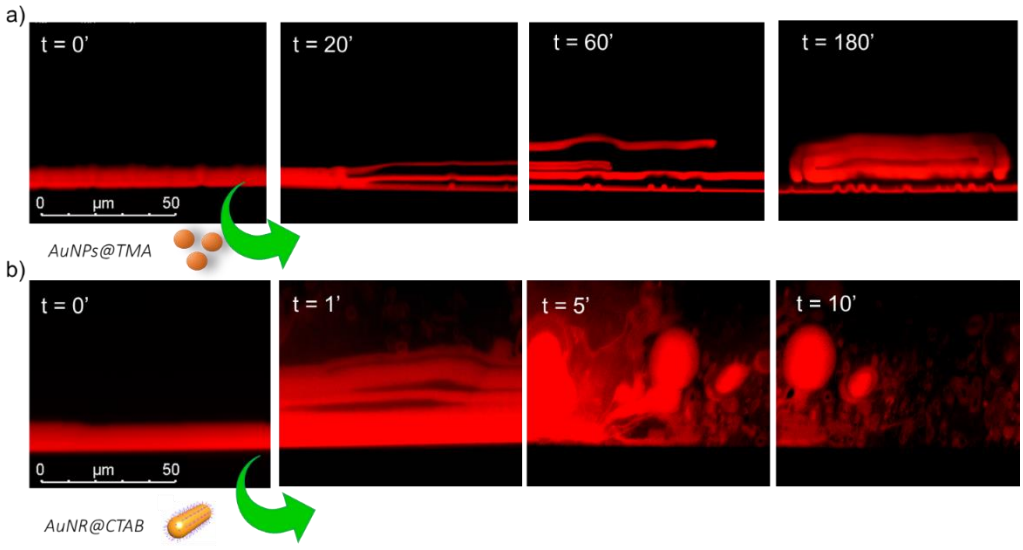

Figure 5 a) Representative confocal microscopy images (side view) of a GMO/DOPC lamellar surface layer interacting with AuNSs. From left to right: lamellar film before (t=0'), after 20', 60',

180’ from the addition of AuNSs. b) Representative confocal microscopy images (side view) of a GMO/DOPC lamellar surface layer interacting with AuNRs. From left to right: lamellar film before (t=0’), after 1’, 5’, 10’ from the addition of AuNRs.

From Figure 5a), the action of spherical AuNSs (added at the same concentration employed in previous analyses) produces an initial swelling of the film (20’), which increases the distance between the different lamellae composing the structure; this process leads to the progressive peeling-off of the lamellar film (60’), with a gradual detachment of the outer surface layers. Once removed from the original matrix, these lipid layers start to bend and fold, ultimately rolling up in closed onion-like vesicular structures (180’), which get partially adsorbed on the film surface. After 180’ of incubation, only a thin layer of the original lamellar film is preserved onto the glass surface, partially covered by micron-sized multilamellar vesicles.

The addition of asymmetrically shaped AuNRs (Figure 5b) has a similar impact on the film morphology, which evolves according to the very same steps previously described for the case of AuNSs. However, the overall process is faster, consisting of an initial massive swelling of the lamellar membrane, which is observed after just 1’ from the AuNRs addition. Moreover, the peeling-off of the film starts already after 5’ and, differently from the case of AuNSs, leads to the complete disruption of the lamellar film within 10’, with only polydisperse vesicular structures remaining adsorbed onto the glass surface.

A completely different behaviour is observed when the same gold nanoparticles challenge cubic surface layers.

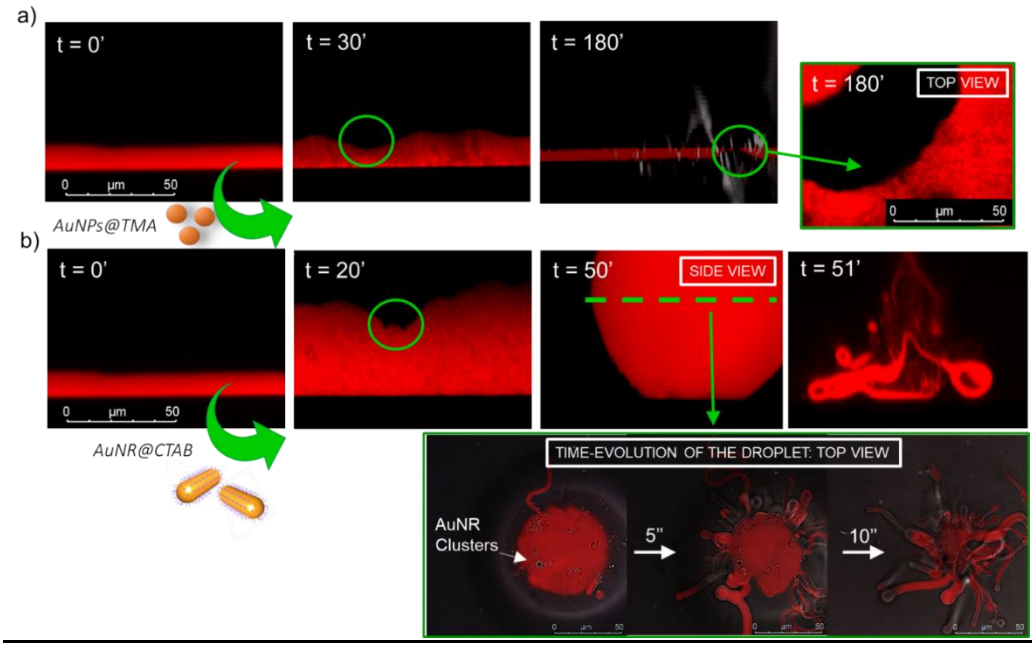

Figure 6 a) Representative confocal microscopy images (side view) of a GMO cubic surface layer interacting with AuNSs. From left to right: lamellar film before (t=0') and after 30', 180' from the addition of NSs. The right inset represents the top view of cubic film after 180' incubation with AuNPs, showing the presence of micron sized holes within the lipid film. b) Representative confocal microscopy images (side view) of a GMO cubic surface layer interacting with AuNRs. From left to right: lamellar film before (t=0') and after 20', 50', 51' from the addition of AuNRs. The bottom right inset collects three top view images of a lipid droplet acquired at 0'', 5'' and 10'' from its formation. The final pictures were obtained from the overlay between the absorption of AuNRs (gryscale) and the fluorescence of Nile Red, labelling the lipid hydrophobic matrix (red color).

Spherical NPs added at the same concentration (Figure 6a) seem to "excavate" the cubic membrane, producing an initial thinning of the film over selected areas (30'). The progressive excavation leads to the formation of cavities, whose depth increases with time, eventually reaching the glass surface. After 180' of incubation, the lipid film, although mostly intact, presents micron-sized holes, which can be visualized from both the side and top view images, reported in Figure 6a.

As previously observed for the case of lamellar membranes, the addition of AuNRs produces faster and more profound morphological modifications (Figure 6b): AuNRs initially increase the film's roughness (20'), with the formation of "hills

and hollows" across the micrometric membrane. Similarly to what previously observed for spherical AuNSs, the lipid film is progressively excavated, showing micron-sized cavities, whose depth increases with time. However, in this case the erosion process is faster and, within few minutes, produces the complete retraction of the cubic film in localized areas of the glass, giving rise to thick lipid droplets, in which the lipid matrix is selectively accumulated (50'). After 50', the lipid film is completely de-wetted, leaving only isolated lipid droplets onto the glass substrate. Then, these lipid droplets get readily destroyed by the action of AuNRs. The disruption process, occurring within few seconds from their formation, can be analysed in detail, following the temporal evolution of an optical (horizontal) section of the droplet. To this purpose, top-view images of a lipid droplet at 0'' and different times from its formation have been acquired in fluorescence and transmission mode, in order to simultaneously capture the fluorescence of Nile Red, labelling the lipid matrix, and gold nanoparticles. Representative images acquired at 0'', 5'' and 10'' from the droplet's formation are reported in Figure 6b (bottom right inset) as the overlay between the transmission (grayscale) and the lipid membrane label fluorescence (red) contributions. At the beginning of the process (left image in the inset), AuNRs, which can be visualized as black spots in the image, are located as micron-sized clusters at the of the lipid droplet's edges, encircling it. Then (central image in the inset), they start to excavate and unroll the lipid droplet by starting from its edges, i.e. their accumulation points, leading to its complete collapse within 10'' (right image in the inset).

Overall, the results gathered lead to two main conclusions: i) in agreement with the NR analysis, the impact of AuNRs on both lamellar and cubic model films is stronger and leads to faster structural and morphological modifications with respect to NSs; ii) NPs interact with lamellar and cubic phases according to two different and well-defined mechanisms, i.e. the peeling-off of the lamellar assembly and the excavation of the cubic one. As these two phenomena has been observed for both spherical and cylindrical NPs, i.e. independently from

their nature, membrane curvature seems to be the main factor determining the NPs/membrane interaction pathway.

4. Discussion:

The ensemble of results gathered contributes to the description of NPs-model membrane interactions at multiple length scales and highlights that this phenomenon is deeply affected by both membrane interfacial curvature (connected to the geometry of the lipid phase) and NPs surface curvature (which defines NPs shape).

4.1 The effect of NPs shape

Both NR and CLSM results point out a major role of NPs asymmetric shape in the interaction with model membranes; in particular, NR measurements show that AuNRs have a profound impact on the structure of both lamellar and cubic films, inducing a complete loss of their structural order in less than 15' and 2 h for Lα and Pn3m phases, respectively. On the contrary, the combination of NR and GISANS analyses highlights that AuNSs act on a completely different time frame: indeed, we only detected a partial disruption of lamellar and cubic structures after 13 h and 32 h of incubation, respectively. These observations are perfectly in line with CLSM findings, highlighting a direct connection between the micron-scale morphological alteration and the nanoscale restructuring of lipid films, induced by NPs. Indeed, CSLM analysis shows that the morphology of lipid films is only partially altered by AuNSs within our experimental time frame (i.e., 3 h), while AuNRs fully destroy lamellar and cubic films within the same time interval.

The impact of NPs surface functionalization, composition and size on lipid membranes have been widely investigated in the last decades and are recognized as key determinants in NPs cytotoxicity [1,5,32,42–45]. On the contrary, much less is known on the effect of NPs shape on both model and natural membranes, with multiple controversial observations, of either theoretical or experimental nature, reported in literature. Asymmetric NPs have higher surface area/volume ratio, which is theoretically predicted to maximize the surface available for their adhesion onto membranes (driven by Van der Waals and possible electrostatic attractive forces [1,18]). This has been often connected to a high reactivity towards lamellar model [32] and natural membranes [46] and to an enhanced uptake by cells [47,48]. On the other side, the high surface curvature at the edges of non-spherical NPs is predicted to increase the energy barrier for NPs wrapping and internalization by lamellar membranes [3]. In line with this observation, recent findings reported lower cellular uptake for asymmetric NPs with respect to spherical ones [13,14]. In addition, to the best of our knowledge, the impact of NPs shape on non-lamellar membranes represents a completely unexplored field to date.

Here, employing spherical and rod-like AuNPs of comparable diameter and surface charge (see section 3.1), we isolated the effect of NPs shape in the interaction with membranes. We found that, when NPs size is similar to the lipid bilayer thickness, shape is a major player, with asymmetric geometries producing more destructive effects. Importantly, this behavior holds for both lamellar and non-lamellar models, highlighting a universal effect of NPs asymmetry on membranes of different curvature.

4.2 The effect of membrane geometry

Beside NPs shape, we found that membrane geometry, connected to its interfacial curvature, represents another key factor at stake in NPs-films interactions: NR and CLSM analyses highlighted that, for a given NP type,

membrane geometry determines both the strength and the pathways of interaction with NPs.

Specifically, our NR results show that, independently from their shape, NPs induce a faster disruption of the nanostructure of lamellar membranes with respect to cubic ones, which results into more rapid morphological modifications at the micron-scale, observed through CSLM.

By combining the NR and CSLM data, we defined two different mechanisms that describe the interaction of NPs with lamellar and cubic phases and are responsible for their different stability towards nanomaterials.

The faster structural modification of Lα films induced by both AuNSs (section 3.2) and AuNRs (section 3.3) is associated with an initial swelling, followed by progressive exfoliation of the multilamellar arrangement (section 3.4), proceeding from the outer lamellar layers. We can hypothesize that, after their injection, NPs start to penetrate the outer part of the lamellar arrangement, i.e. the one exposed to the water external medium. This penetration would primarily occur *via* electrostatic and dipolar interactions between the cationic coating of NPs and the polar headgroup of lipids composing the membrane, directly exposed to the water phase: this interaction would enable the insertion of NPs, together with their hydration shell, within the hydrophilic domains of the phase, i.e. the water layers separating the different lamellae. Then, the mismatch between the thickness of the water layers (around 2-3 nm, see section 3.2 for details) and NPs hydrodynamic size (see Dynamic Light Scattering results in the SI) would be responsible for the initial swelling of the lamellar film, observed through CSLM (Fig. 5). The increasing inter-lamellar distance would reduce the interactions between different lamellae, producing the detachment of the outer lamellar layers, i.e. the first ones to be in contact with NPs. Indeed, lipid bilayers of equal composition are held together only by weak Van Der Waals forces, in equilibrium with repulsive electrostatic and entropic contributions [49]. Thus, inter-bilayer interactions are easily overwhelmed by attractive single bilayer-NPs

forces of electrostatic nature. The thinning of the film favors the penetration of NPs within its deeper part, i.e. the one closer to the solid support, provoking its progressive peeling-off. The loss of the lamellar periodicity as the layers are being detached can be connected with the progressive smearing out of the Lα-structural features, observed through NR (Figure 2 and 4).

On the other side, a different interaction mechanism can be outlined for the case of cubic membranes, connected with their higher structural stability. NR data highlight a progressive disruption of the cubic Pn3m nanostructure by NPs, which starts from the shrinkage of its lattice parameter (section 3.3); this nanoscale phenomenon parallels a progressive excavation of the film observed at the micron-scale (section 3.4), leading to its de-wetting; interestingly, this phenomenon proceeds from NPs clusters, which, acting like micron-sized "diggers", progressively erode and unroll the lipid matrix. We can hypothesize that, in this case, NPs are not able to fully penetrate the internal aqueous region of the film, i.e. the aqueous nanochannels of around 4.4 nm in diameter (see section 3.2 for details), due to its peculiar nanostructure. Indeed, cubic phases represent a 3D highly interconnected network, where a single lipid bilayer folds in the space originating bicontinuous aqueous and lipid domains [21]; this robust 3D architecture would impede a full insertion of NPs within the aqueous channels of smaller size (which would provoke its collapse), preventing a fast unfolding. Instead, the attractive NPs-lipid headgroups forces would result in the absorption of NPs, residing onto the film surface as clusters. As highlighted by NR analysis, their presence induce an immediate shrinking of the phase, leading to local water expulsion and subsequent dehydration of the phase: we can speculate that this phenomenon drives the progressive collapse of the cubic arrangement, which would proceed from the different NPs accumulation points across the membrane, ultimately leading to isolated lipid droplets onto the solid substrate.

The enhanced stability of cubic phases with respect to lamellar ones might have important biological implications. As already introduced, curved membranes of

cubic symmetry are known to occur in cells under pathological conditions (e.g., viral infection, oxidative stress, starving or other diseases). However, cubic membrane-related investigations has been limited at a descriptive level, while the biological function of these arrangements remains unexplored [21]. In particular, it is still unknown whether their formation is solely a result of aberrant processes within diseased cells or represent a functional response to these pathologies.

Engineered NPs share their size range with biologically relevant entities (i.e., DNA, surface proteins, biogenic extracellular vesicles, and viruses), often resulting in similar interaction pathways with cells [1]. Thus, we might connect the higher resilience exhibited by cubic membranes towards NPs with a similar behavior towards natural nano-objects, such as viral pathogens. Within this perspective, our results seem to suggest a possible “protective role” of the cubic architecture, occurring in critical cell conditions to minimize the membrane response towards harmful external perturbations.

To summarize, we found that NPs-lipid membrane interactions depend both on the nanostructure of the membrane and the shape of NPs. These two variables represent two sides of the same coin, as a single parameter, i.e. curvature, can describe their variations. In these terms, we can state that NPs with a non-uniform surface curvature promote a stronger interaction with the lipid matrix. On the other hand, when referring to the lipid membrane interfacial curvature, we observed that flat membranes experience more substantial disruptive effects than curved ones when exposed to NPs. Importantly, we also pointed out that a variation in NPs curvature only affects the strength of interaction with lipid films, but not the interaction pathway; on the contrary, membranes with different curvatures determine completely different interaction mechanisms, responsible for the observed differences in the structural resilience of these systems.

5. Conclusions

Curvature effects are crucial for interactions occurring at the nano-bio-interface. The impact of NPs' curvature on their effects on natural and synthetic lipid membranes has been addressed by several reports, lately. On the other side, the curvature of membranes represents an almost unexplored factor, which could potentially be of similar impact at the nano-bio interface.

In this contribution, we explored the impact of curvature on nano-bio interactions focusing on the NPs or on the membrane. Specifically, we investigated the impact of AuNPs of similar size and surface coating but different shapes (spheres vs. rods) on model lipid films of different geometry (flat lamellar phase vs. curved cubic membranes, encountered in diseased cells). Combining structural techniques with nanoscale resolution, i.e., NR and GISANS, with Confocal Microscopy, which enables the observation of phenomena at the micron-scale, we connected structural and morphological modifications of lipid films induced by NPs, occurring at different length scales. We observed a prominent role of NPs surface curvature in the interaction with both lamellar and non-lamellar films, with sharp-edged AuNRs inducing a prompter disruption of model membranes. On the contrary, -here for the first time- we spotted enhanced structural stability of lipid films towards the action of NPs, promoted by an increase of membrane curvature. We hypothesize that this is due to the different inner structure of lamellar and cubic membranes: indeed, the bilayers composing the lamellar films are only held together by weak Van der Waals interactions and get easily detached the one from the other by the action of NPs. On the other hand, cubic phase films consist of a single 3D architecture which offers a much broader resistance against the NPs disruptive effect. These new findings suggest a possible "protective role" of cubic membranes, which occurs in infected, stressed or starved cells; in this perspective, they would represent biological barriers with enhanced structural resilience, occurring in cells as a "last defence" under extreme conditions.

1 M. Mendozza, L. Caselli, D. Berti and A. Salvatore, *Soft Matter*, 2019, **15**, 8951–8970.

2 R. Michel and M. Gradzielski, *Int. J. Mol. Sci.*, 2012, **13**, 11610–11642.

3 S. Dasgupta, T. Auth and G. Gompper, *J. Phys. Condens. Matter*, 2017, **29**, aa7933.

4 C. M. Beddoes, C. P. Case and W. H. Briscoe, *Adv. Colloid Interface Sci.*, 2015, **218**, 48–68.

5 A. M. Farnoud and S. Nazemidashtarjandi, *Environ. Sci. Nano*, 2019, **6**, 13–40.

6 M. Henriksen-Lacey, S. Carregal-Romero and L. M. Liz-Marzán, *Bioconjug. Chem.*, 2017, **28**, 212–221.

7 E. Blanco, H. Shen and M. Ferrari, *Nat. Biotechnol.*, 2015, **33**, 941–951.

8 P. Falagan-Lotsch, E. M. Grzincic and C. J. Murphy, *Proc. Natl. Acad. Sci. U. S. A.*, 2016, **113**, 13318–13323.

9 C. J. Murphy, A. M. Vartanian, F. M. Geiger, R. J. Hamers, J. Pedersen, Q. Cui, C. L. Haynes, E. E. Carlson, R. Hernandez, R. D. Klaper, G. Orr and Z. Rosenzweig, *ACS Cent. Sci.*, 2015, **1**, 117–123.

10 K. L. Chen and G. D. Bothun, *Environ. Sci. Technol.*, 2014, **48**, 873–880.

11 A. H. Bahrami, *Soft Matter*, 2013, **9**, 8642.

12 S. Dasgupta, T. Auth and G. Gompper, *Soft Matter*, 2013, **9**, 5473–5482.

13 S. Dasgupta, T. Auth and G. Gompper, *Nano Lett.*, 2014, **14**, 687–693.

14 R. Vácha, F. J. Martinez-Veracoechea and D. Frenkel, *Nano Lett.*, 2011, **11**, 5391–5395.

15 S. Hyde, S. Andersson, K. Z. Larsson, T. Blum, S. L. Landh and B. W. Lidin, *The Language of Shape: The Role of Curvature in Condensed Matter: Physics, Chemistry and Biology*, 1997.

16 G. C. Shearman, O. Ces, R. H. Templer and J. M. Seddon, *J. Phys. Condens. Matter*, , DOI:10.1088/0953-8984/18/28/S01.

17 S. J. M. Shearman G C, Ces O, Templer R H, *J. Phys. Condens. Matter*, 2006, **18**, S1105–S1124.

18 Q. Mu, G. Jiang, L. Chen, H. Zhou, D. Fourches, A. Tropsha and B. Yan, *Chem. Rev.*, 2014, **114**, 7740–7781.

19 E. Gonzalez Solveyra and I. Szleifer, *Wiley Interdiscip Rev Nanomed Nanobiotechnol.*, 2016, **8**, 334–354.

20 Z. A. Almsherqi, S. D. Kohlwein and Y. Deng, 2006, **173**, 839–844.

21 Z. A. Almsherqi, T. Landh and S. D. Kohlwein, *Cubic Membranes : The Missing Dimension of Cell Membrane Organization*, Elsevier Inc., 1st edn., 2009, vol. 274.

22 Y. Deng and M. Mieczkowski, 1998, 16–25.

23 D. P. Chang, J. Barauskas, A. P. Dabkowska, M. Wadsäter, F. Tiberg and T. Nylander, *Adv. Colloid Interface Sci.*, 2015, **222**, 135–147.

24 A. P. Dabkowska, M. Valldeperas, C. Hirst, C. Montis, G. K. Pálsson, M. Wang, S. Nöjd, L. Gentile, J. Barauskas, N. J. Steinke, G. E. Schroeder-Turk, S. George, M. W. A. Skoda and T. Nylander, *Interface Focus*, , DOI:10.1098/rsfs.2016.0150.

25 S. Tatur, M. Maccarini, R. Barker, A. Nelson and G. Fragneto, *Langmuir*, 2013, **29**, 6606–6614.

26 C. M. McIntosh, E. A. Esposito, A. K. Boal, J. M. Simard, C. T. Martin and V. M. Rotello, *J. Am. Chem. Soc.*, 2001, **123**, 7626–7629.

27 M. Brust, M. Walker, D. Bethell, D. J. Schiffrin and R. Whyman, *J. Chem. Soc., Chem. Commun.*, 1994, 801–802.

28 S. Tatur and A. Badia, *Langmuir*, 2012, **28**, 628–639.

29 M. R. K. Ali, B. Snyder and M. A. El-Sayed, *Langmuir*, 2012, **28**, 9807–9815.

30 R. M. Dalgliesh, S. Langridge, J. Plomp, V. O. De Haan and A. A. Van Well, *Phys. B Condens. Matter*, 2011, **406**, 2346–2349.

31 R. Kampmann, M. Haese-Seiller, V. Kudryashov, B. Nickel, C. Daniel, W. Fenzl, A. Schreyer, E. Sackmann and J. Rädler, *Phys. B Condens. Matter*, 2006, **385**–**386**, 1161–1163.

32 C. Montis, V. Generini, G. Boccalini, P. Bergese, D. Bani and D. Berti, *J. Colloid Interface Sci.*, 2018, **516**, 284–294.

33 D. E. Sands, *Introduction to Cristallography*, W.A. Benjamin, Inc., New York, NY., 1969.

34 V. Cherezov, J. Clogston, Y. Misquitta, W. Abdel-Gawad and M. Caffrey, *Biophys. J.*, 2002, **83**, 3393–3407.

35 G. Popescu, J. Barauskas, T. Nylander and F. Tiberg, *Langmuir*, 2007, **23**, 496–503.

36 N. Kučerka, S. Tristram-Nagle and J. F. Nagle, *J. Membr. Biol.*, 2006, **208**, 193–202.

37 R. Negrini and R. Mezzenga, *Langmuir*, 2012, **28**, 16455–16462.

38 P. Müller-Buschbaum, *Polym. J.*, 2013, **45**, 34–42.

39 S. J. Richardson, P. A. Staniec, G. E. Newby, N. J. Terrill, J. M. Elliott,

A. M. Squires and W. T. Góźdź, *Langmuir*, 2014, **30**, 13510–13515.

40 M. Rittman, M. Frischherz, F. Burgmann, P. G. Hartley and A. Squires, *Soft Matter*, 2010, **6**, 4058–4061.

41 F. Ott and S. Kozhevnikov, *J. Appl. Crystallogr.*, 2011, **44**, 359–369.

42 P. Vedantam, G. Huang and T. R. J. Tzeng, *J. Nanobiotechnology*, 2013, **4**, 13–20.

43 C. Montis, L. Caselli, F. Valle, A. Zendrini, F. Carlà, R. Schweins, M. Maccarini, P. Bergese and D. Berti, *J. Colloid Interface Sci.*, 2020, **573**, 204–214.

44 T. Pfeiffer, A. De Nicola, C. Montis, F. Carlà, N. F. A. Van Der Vegt, D. Berti and G. Milano, *J. Phys. Chem. Lett.*, 2019, **10**, 129–137.

45 B. Pelaz, G. Charron, C. Pfeiffer, Y. Zhao, J. M. De La Fuente, X. J. Liang, W. J. Parak and P. Del Pino, *Small*, 2013, **9**, 1573–1584.

46 S. Salatin, S. Maleki and A. Y. Khosroushahi, *Cell Biol Int.*, 2015, **39**, 881–890.

47 S. E. A. Gratton, P. A. Ropp, P. D. Pohlhaus, J. C. Luft, V. J. Madden, M. E. Napier and J. M. Desimone, *PNAS*, 2008, **105**, 11613–11618.

48 R. Agarwal, V. Singh, P. Jurney, L. Shi, S. V Sreenivasan and K. Roy, *PNAS*, 2013, **110**, 1–6.

49 J. N. Israelachvili, *Intermolecular and Surface Forces*, 2011, vol. 53.

Supplementary Information for:

Interaction of nanoparticles with lipid films: Curvature effects

Lucrezia Caselli[1], Andrea Ridolfi[1,2], Nina-Juliane Steinke[3], Emil Gustafsson[4], Costanza Montis[1], Tommy Nylander[5] and Debora Berti[1]

[1]University of Florence and CSGI, Department of Chemistry, Via della Lastruccia 3, Sesto Fiorentino 50019, Florence, Italy.

[2] ISMN-CNR and CSGI via Gobetti 101 40129 Bologna (Italy)

[3] Institut Laue-Langevin, DS/LSS, 71 Avenue des Martyrs, CS 20156, F-38042 Grenoble CEDEX 9, (France)

[4] Uppsala University, 752 36 Uppsala, Sweden

[5] Department of Chemistry, Lund University, Naturvetarvägen 14, 223 62, Lund, Sweden

Small Angle X-ray Scattering

SAXS measurements were carried out on a S3-MICRO SAXS/WAXS instrument (HECUS GmbH, Graz, Austria) which consists of a GeniX

microfocus X-ray sealed Cu Kα source (Xenocs, Grenoble, France) of 50 W power which provides a detector focused X-ray beam with λ = 0.1542 nm Cu Kα line. The instrument is equipped with two one-dimensional (1D) position sensitive detectors (HECUS 1D-PSD-50 M system), each detector is 50 mm long (spatial resolution 54 μm/channel, 1024 channels) and cover the SAXS q-range (0.003< q <0.6˚Å −1). The temperature (25°C) was controlled by means of a Peltier TCCS-3 Hecus. The analysis of SAXS curves was carried out using Igor Pro (Kline, 2006). SAXS measurements on AuNPs aqueous dispersions, were carried out in sealed glass capillaries of 1.5 mm diameter. AuNSs dispersion was diluted 1:3 with MilliQ water prior measurement.

To analyze AuNSs scattering profile we chose a model function with a spherical form factor and a Schulz size distribution: (Kotlarchyk and Chen, 1983), it calculates the scattering for a polydisperse population of spheres with uniform scattering length density. The distribution of radii is a Schulz distribution given by the following equation:

$$f(R) = (z+1)^{z+1} x^z \frac{exp[-(z+1)x]}{R_{avg}\Gamma(z+1)}$$

where R_{avg} is the mean radius, $x = R/R_{avg}$ and z is related to the polydispersity. The form factor is normalized by the average particle volume, using the 3rd moment of R:

$$\langle V \rangle = \frac{4\pi}{3}\langle R^{+3} \rangle = \frac{4\pi}{3}\langle R \rangle^{+3} \frac{(z+3)(z+2)}{(z+1)^2}$$

The scattering intensity is:

$$I(q) = \left(\frac{4\pi}{3}\right)^2 N_0 \Delta\rho^2 \int_0^\infty f(R) R^6 F^2(qR) dR$$

where N_0 is the total number of particles per unit volume, *F(R)* is the scattering amplitude for a sphere and $\Delta\rho$ is the difference in scattering length density between the particle and the solvent.

The SAXS profile of AuNRs was fitted by the Cylinder poly radius model from the NIST package SANS Utilities Cylinder-Polydisperse; it calculates the form factor for a polydisperse right circular cylinder with uniform scattering length density and a Schulz polydispersity of the cylinder length is considered. The function calculated is the orientationally averaged cylinder form factor which is then averaged over a Schulz distribution of the cylinder length. The size averaged form factor is thus:

$$P(Q) = \int_0^\infty f(R) d(R) \int_0^{\pi/2} F^2(Q\alpha) \sin\alpha \, d\alpha$$

where f(R) is the normalized Schulz distribution of the length. The limits of the integration are adjusted automatically to cover the full range of length. The scattering amplitude, F, is:

$$F(Q\alpha) = 2V_{cyl}(\rho_{cyl}\rho_{solv}) j_0(QH\cos\alpha) \frac{J_1(QR\sin\alpha)}{(QR\sin\alpha)}$$

Where $J_1(QR\sin\alpha)$ is the first order Bessel function, $V_{cyl} = \pi LR^2$, $j_0(QH\cos\alpha) = \frac{\sin(\mathrm{QHcos}\,\alpha)}{\mathrm{QHcos}\,\alpha}$, with α defined as the angle between the cylinder axis and the scattering vector (Q) and ρ_{cyl} and ρ_{solv} the scattering length density of the nanorod and the solvent respectively. The integral over averages the form factor over all possible orientations of the cylinder with respect to Q.

Transmission Electron Microscopy (TEM)

Trasmission electron microscopy (TEM) images were acquired with a STEM CM12 Philips electron microscope, at CeME (CNR Florence Research Area, Via Madonna del Piano, 10 - 50019 Sesto Fiorentino). The sample was placed on a 200 mesh carbon-coated copper grid.

Dynamic Light Scattering (DLS)

DLS measurements were performed using a Malvern Panalytical Zetasizer Nano ZS90 instrument which does DLS measurements at a fixed scattering angle of 90°. A 4 mW laser of 633 nm wavelength is used as light source, the lag times of the correlator start from 25 ns as shortest and go up to 8000 s, using a maximum number of 4000 channels. After checking monomodality with a CONTIN fit, the ACFs were analyzed through the cumulant fitting stopped to the second order, allowing an estimate of the hydrodynamic diameter and the polydispersity of

AuNSs and AuNRs, which were found equal to: 25.6 ± 0.2 and 37.6 ± 0.1 nm (hydrodynamic diameter) with a 0.3 and 0.21 (PDI), respectively.

Z-Potential

Zeta potential measurements were performed using a Zeta Potential Analyzer (Zeta Plus, Brookhaven Instruments Corporation, Holtsville, NY). Zeta potentials were obtained from the electrophoretic mobility u, according to Helmholtz-Smoluchowski equation: $\zeta = (\eta/\varepsilon) \times u$ with η being the viscosity of the medium, ε the dielectric permittivity of the dispersing medium. The Zeta Potential values are reported as averages from ten measurements.

Inductively Coupled Plasma Atomic Emission Spectroscopy (ICP-AES)

This analysis was kindly done by Dr. Mirco Severi, in order to define the concentration of NPs dispersions, with an ICP-AES Varian 720-ES. For the analysis, 200 μL of NPs dispersion were placed in a vial, then the solvent was evaporated under slight nitrogen flow. The sample, consisting of a dry film of nanoparticles, was diluted to 5 mL with 0.1% super pure nitric acid, obtained by distillation under boiling, then, to the sample, 1 ppm of Ge was added, as internal standard; the sample thus treated was analysed.

The operating conditions for the ICP-AES analysis have been optimized to obtain the maximum signal intensity and are as follows:

Instrument: Varian 720-ES

Power R.F: 1.20 KW

Flow rate of Argon Plasma: 16.5 L min^{-1}

Auxiliary Argon flow rate: 1.50 L min^{-1}

Argon nebulizer flow rate: 0.75 L min^{-1}

Replicated reading time: 5 seconds

Instrument stabilization time: 30 seconds

Sample introduction settings:

Sample uptake: 30 seconds

Flow rate: 1 mL min^{-1}

Rinse time: 70 seconds

Fast Pump (sample delay / rinse): active

Smart rinse: active

Replicates: 3

From the ICP-AES data, it results that the quantity of gold in 200 μL of AuNSs and AuNRs dispersions is equal to 259 μg and 278 μg; as a result, the concentrations of AuNSs and AuNRs are 1.3 mg/mL and 1.4 mg/mL, respectively, evaluated considering the size of AuNPs determined through SAXS.

Grazing-Incidence Small-Angle Neutron Scattering (GISANS)

In order to obtain the lattice parameter of the Pn3m cubic architecture, we selected from the GISANS images shown in Figures S1 and S2 the ones that displayed the spots characteristic of the cubic arrangement. Those selected images were then radially integrated using the software PyMca to produce the radial profiles from which the q-values related to the spots of the Pn3m phase were calculated. The q-value of a spot on the Q_y Q_z plot is identified by the following equation:

$$\boldsymbol{q^2 = q_y^2 + q_z^2}$$

The lattice parameter is evaluated from the q value as described in the main text.

Figure S1 displays all the obtained GISANS Q_y,Q_z plots of the GMO cubic phase film, from which the one in Figure 3a (main text) was selected.

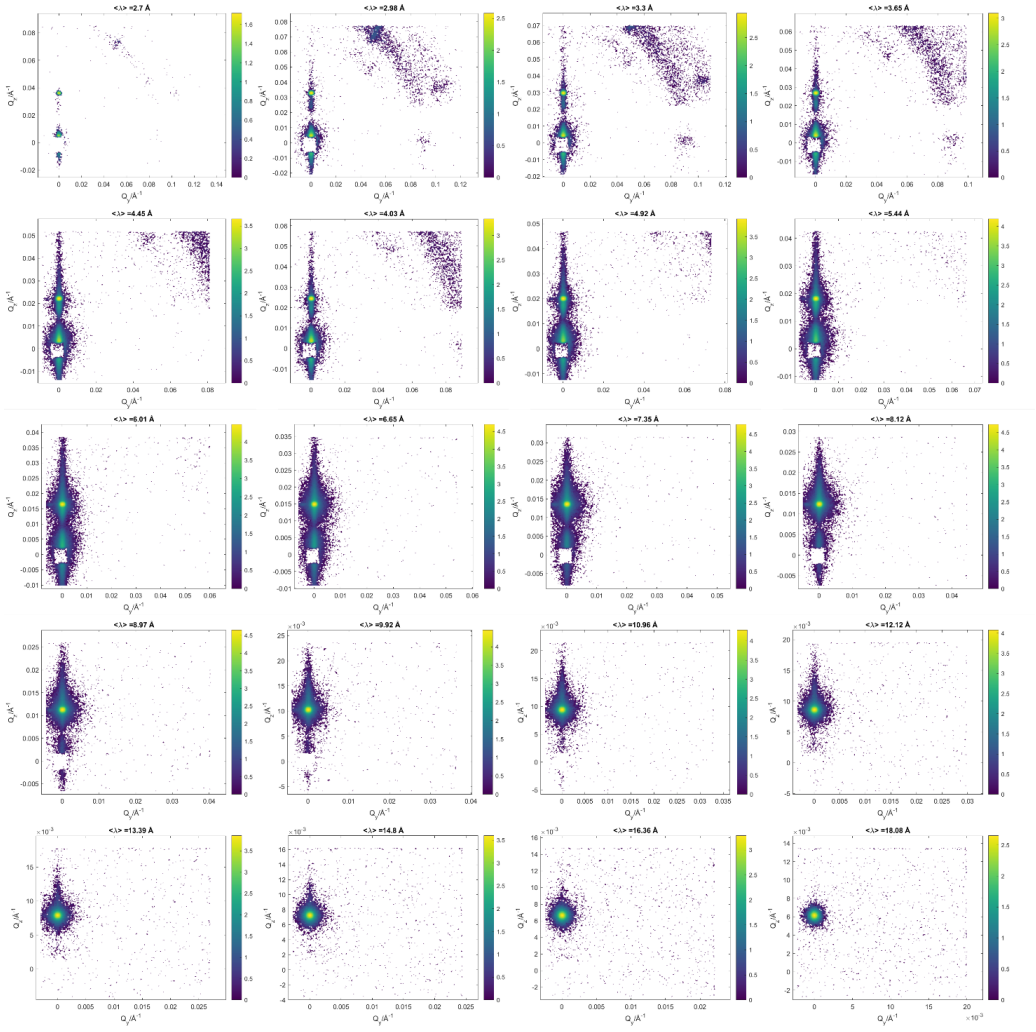

Figure S1: GISANS Q_y Q_z plots obtained for the GMO cubic phase lipid film at different wavelengths. Images obtained with wavelengths of: 2.7 Å, 2.98 Å, 3.3 Å and 3.65 Å were radially integrated to obtain the position of the spots describing the cubic architecture.

Table S1: q positions obtained from the selected GISANS Q_y Q_z plots of Figure S2. The lattice parameters were calculated for each Bragg reflex and then averaged to obtain the one that is representative of the examined Pn3m cubic phase.

	q position ($Å^{-1}$)	
λ	**√2 reflex**	**√3 reflex**
2.7 Å	0.0879	0.1098
2.98 Å	0.0853 0.0929	0.1084
3.3 Å	0.0843 0.0893	0.1101
3.65 Å	0.0866 0.0890	

average q position $Å^{-1}$	**√2 reflex**	**√3 reflex**
	0.0879	0.1094
lattice parameters (Å)	101.0879	99.4403
average lattice parameter (Å)	100.2641	

Figure S2 displays all the obtained GISANS Q_y,Q_z plots of the GMO cubic phase film after AuNSs injection, from which the one in Figure 3b (main text) was selected.

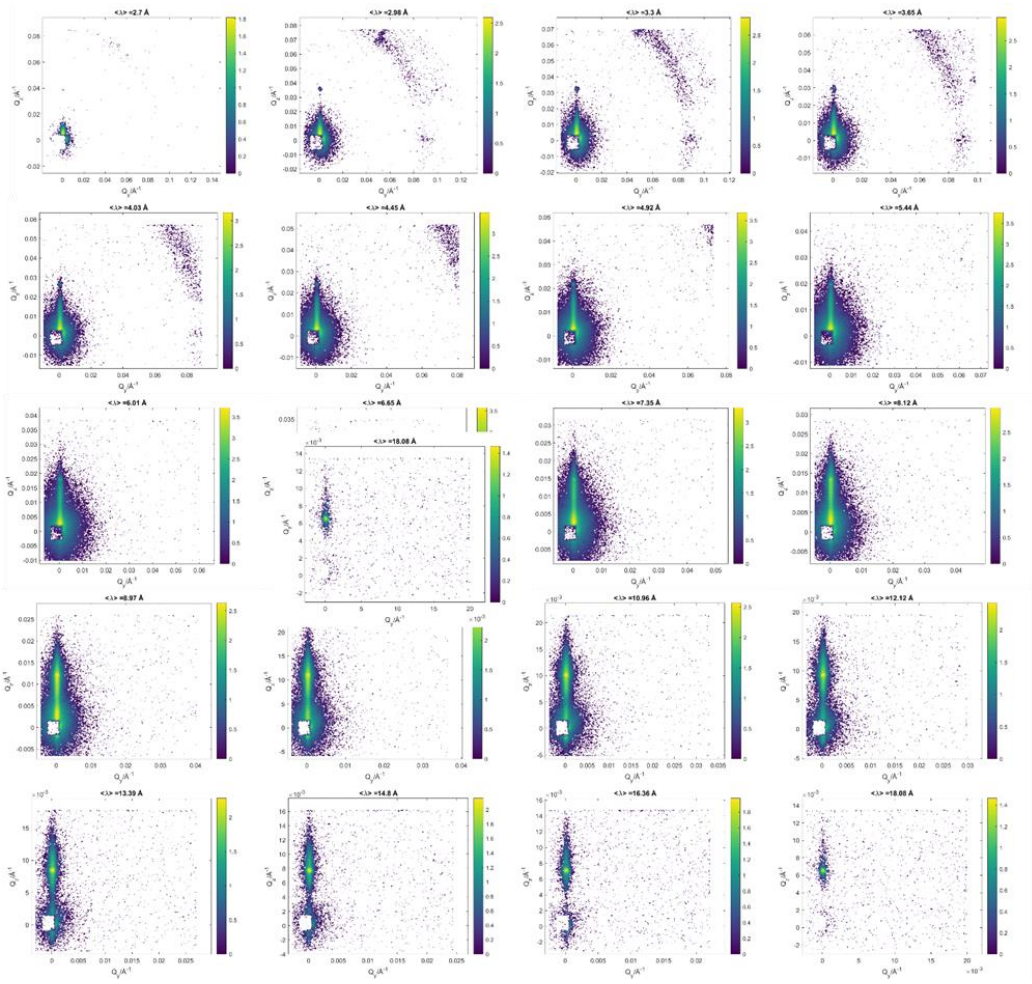

Figure S2: GISANS Q_y Q_z plots obtained for the GMO cubic phase lipid film after AuNSs injection, at different wavelengths. Images obtained with wavelengths of: 2.98 Å, 3.3 Å and 3.65 Å were radially integrated to obtain the position of the spots describing the cubic architecture.

Table S2: q positions obtained from the selected GISANS Q_y Q_z plots of Figure S2. The lattice parameters were calculated for each Bragg reflex and then averaged to obtain the one that is representative of the examined Pn3m cubic phase.

λ	q position (Å^{-1}) √2 reflex	q position (Å^{-1}) √3 reflex
2.98 Å	0.0860	
	0.0919	
3.3 Å	0.0870	
	0.0852	0.1105
3.65 Å	0.0888	
	0.0870	0.1029

	√2 reflex	√3 reflex
average q position Å^{-1}	0.0877	0.1067
lattice parameters (Å)	101.3680	102.0043
average lattice parameter (Å)	101.6861	

Neutron Reflectivity

Figure S3 reports the reflectivity for the cubic film in the absence and in the presence of AuNSs. The (110), (111) and (200) Bragg reflections, which identify the cubic Pn3m phase are highlighted in the graph. Measurements were performed at REFSANS Horizontal TOF reflectometer of the Helmholtz-Zentrum Geesthacht, located at the Heinz Maier-Leibnitz Zentrum in Garching, Germany. The experimental conditions (sample preparation, incubation time, AuNSs concentration, temperature, etc.) and the AuNSs' batch were the same as NR measurement performed at OFFSPEC Reflectometer (see main text for details). The measurement time was 8 h.

The incubation with AuNSs does not modify the intensity of the Pn3m phase, indicating that the structure is not destroyed by nanoparticles. On the other side,

AuNSs produce a high-q shift of the Bragg reflections of the Pn3m phase, which corresponds to a reduction in the lattice parameter of 2 Å (see main text for details on the calculations), in perfect agreement with Neutron Reflectivity Kinetics (see main text and Figure S4).

The reflectivity profile of GMO lipid film, both in the absence and in the presence of AuNSs, shows other peaks, which were ascribed to the (110) and (200) Bragg reflection of the cubic Im3m phase, coexisting with the Pn3m one.

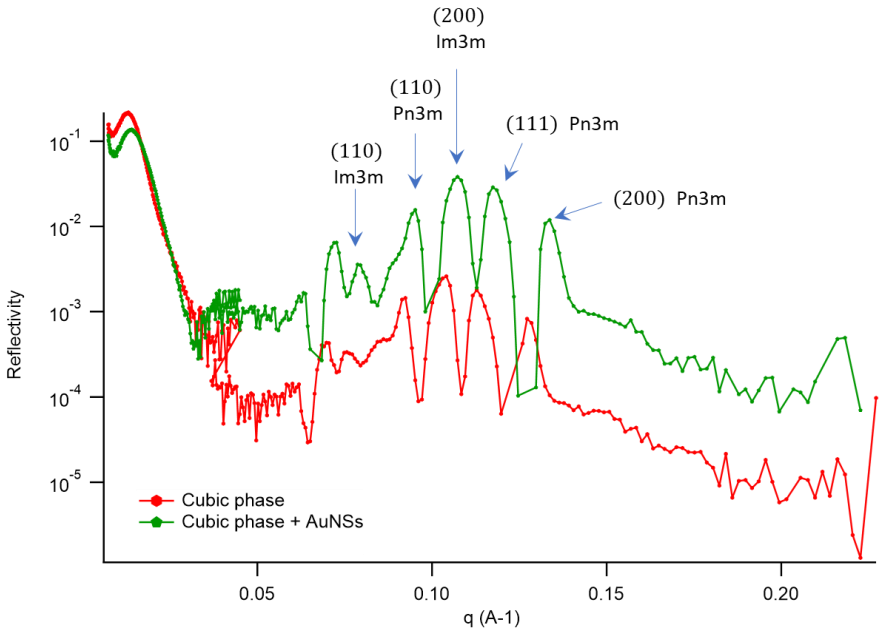

Figure S3 Reflectivity vs q profile of GMO cubic phase film in the absence (red curve) and after 13 h of incubation with AuNSs. The arrows indicate the (110), (111) and (200) Bragg reflexes of the cubic Pn3m phase and the () and () of the Im3m cubic phase. which appear shifted at higher-Q after the addition of AuNRs. Mesurements aquired at REFSANS Horizontal TOF reflectometer of the Helmholtz-Zentrum Geesthacht, located at the Heinz Maier-Leibnitz Zentrum in Garching, Germany.

Figure S4 reports representative specular reflectivities (Panel A), along with the corresponding (Qz,Qx) representations of the off-specular scattering, for the cubic film in the absence and at different times from the addition of AuNRs. The (110) and (111) Bragg reflections, which identify the cubic Pn3m phase and its AuNRs-induced shrinkage, are highlighted in the graph (Panel A).

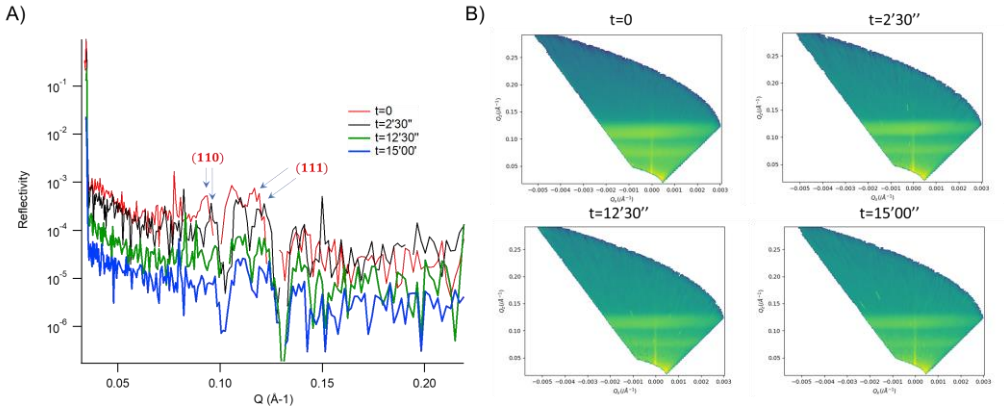

Figure S4 A) Reflectivity vs q profiles of GMO cubic phase film in the absence (red curve) and at different times from the addition of AuNRs. The arrows indicate the (110) and (111) Bragg reflexes of the cubic Pn3m phase, which appear shifted at higher-Q after the addition of AuNRs. B) Corresponding (Qz,Qx) representations of the off-specular scattering of the cubic film in the absence of AuNRs and at different times from the injection of AuNRs. Mesurements aquired at REFSANS Horizontal TOF reflectometer of the Helmholtz-Zentrum Geesthacht, located at the Heinz Maier-Leibnitz Zentrum in Garching, Germany.

Bibliography

Kline, S. R. (2006) 'Reduction and analysis of SANS and USANS data using IGOR Pro', *Journal of Applied Crystallography*, 39(6), pp. 895–900. doi:

10.1107/S0021889806035059.

Kotlarchyk, M. and Chen, S.-H. (1983) ‘Analysis of small angle neutron scattering spectra from polydisperse interacting colloids’, *The Journal of Chemical Physics*, 79(5), p. 2461. doi: 10.1063/1.446055.

Paper VI

Inorganic nanoparticles modify the phase behavior and viscoelastic properties of non-lamellar lipid mesophases

M. Mendozza, L. Caselli, C. Montis, S. Orazzini, E. Carretti, P. Baglioni and D.Berti, *Journal of Colloid and Interface Science*, 2019, 541, 329-338

Journal of Colloid and Interface Science 541 (2019) 329–338

Contents lists available at ScienceDirect

Journal of Colloid and Interface Science

journal homepage: www.elsevier.com/locate/jcis

Regular Article

Inorganic nanoparticles modify the phase behavior and viscoelastic properties of non-lamellar lipid mesophases

Marco Mendozza, Lucrezia Caselli, Costanza Montis, Stefano Orazzini, Emiliano Carretti, Piero Baglioni, Debora Berti *

Department of Chemistry Ugo Schiff, University of Florence and CSGI, Via della Lastruccia 3, 50019 Florence, Italy

GRAPHICAL ABSTRACT

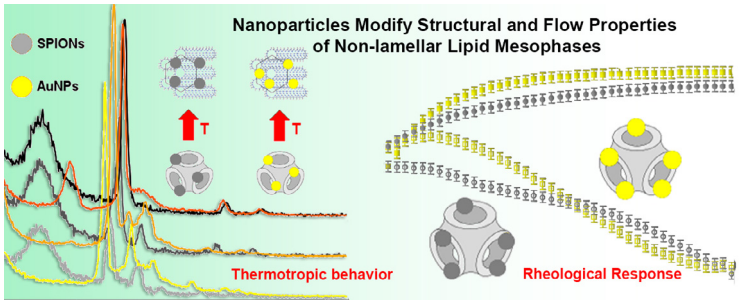

ARTICLE INFO

Article history:
Received 3 December 2018
Revised 21 January 2019
Accepted 22 January 2019
Available online 23 January 2019

Keywords:
Liquid crystalline mesophases
AuNPs
SPIONs
Phytantriol
Cubic lipid phases

ABSTRACT

The inclusion of inorganic nanoparticles (NPs) within organized lipid assemblies combines the rich polymorphism of lipid phases with advanced functional properties provided by the NPs, expanding the applicative spectrum of these materials. In spite of the relevance of these hybrid systems, fundamental knowledge on the effects of NPs on the structure and physicochemical properties of lipid mesophases is still limited. This contribution combines Small-Angle X-ray Scattering (SAXS) and Rheology to connect the structural properties with the viscoelastic behavior of liquid crystalline mesophases of Phytantriol (Phyt) containing two kinds of hydrophobic NPs of similar size, i.e., gold NPs (AuNPs) and Superparamagnetic Iron Oxide NPs (SPIONs). Both types of NPs spontaneously embed in the hydrophobic domains of the liquid crystalline mesophase, deeply affecting its phase behavior, as SAXS results disclose. We propose a general model to interpret and predict the structure of cubic mesophases doped with hydrophobic NPs, where the effects on lipid phase behavior depend only on NPs' size and volume fraction but not on chemical identity. The rheological measurements reveal that NPs increase the solid-like behavior of the hybrid and, surprisingly, this effect depends on the chemical nature of the NPs. We interpret these results by suggesting that the long-range dipolar interactions of SPIONs affect the viscoelastic response of the material and provide an additional control parameter on mechanical properties. Overall, this study discloses new fundamental insights into hybrid liquid crystalline mesophases doped with hydrophobic NPs, highly relevant for future applications, e.g. in the biomedical field as smart materials for drug delivery.

1. Introduction

The inclusion of inorganic nanoparticles into organized lipid assemblies has the potential to combine the properties of the two components to produce smart materials and nanodevices for

Abbreviations: LLCs, lyotropic liquid crystals; DDS, drug-delivery systems; Phyt, phytantriol; SPIONs, superparamagnetic iron oxide nanoparticles; AuNPs, gold nanoparticles.

* Corresponding author.
E-mail address: debora.berti@unifi.it (D. Berti).

https://doi.org/10.1016/j.jcis.2019.01.091
0021-9797/

a variety of diverse applications in the biomedical field. For instance, gold nanorods have been embedded in lipid vesicles for applications in hyperthermia [1,2]; quantum dots-loaded liposomes have been proposed for diagnostic purposes [3–6]; superparamagnetic iron oxide nanoparticles (SPIONs) have been included in liposomes, to form magnetoliposomes, applied both for MRI [7,8] and as drug delivery systems that can release their payload in a space- and time-controlled manner, thanks to responsivity to static and alternating magnetic fields [9–11]. The most explored amphiphilic scaffolds are lipid vesicles, but more recently some studies have addressed the insertion of inorganic NPs [12,13] into non-lamellar lipid assemblies formed through self-assembly of polymorphic lipids. While some applicative examples have been reported, a fundamental understanding of the impact of NPs on lipid phase behavior, necessary to design these materials for a specific biomedical application is, to date, very limited.

It is well known that lipid self-assembly in water gives rise to a rich phase diagram, with a complex variety of architectures and morphologies, as in the case of glyceryl-monooleate (GMO) and Phytantriol (Phyt). For these latter systems, the phase diagrams have been thoroughly investigated over the years [14]. Depending on the water content, lamellar structures (Lc and Lα) and bicontinuous cubic mesophases (gyroid Ia3d and diamond Pn3m) are observed at room temperature, while hexagonal structures and inverted micelles are formed at higher temperatures. The presence of additives modifies and controls the geometry of these lipid architectures. This is the case for fatty acids [15,16], photo-switchable molecules [17–19], and proteins [20] that can be even crystallized within the lyotropic phase [21,22]. Recently, Briscoe et al. [23,24] investigated the effects of hydrophobic silica NPs on dioleoyl-phosphatidylethanolamine mesophases, highlighting a temperature and pressure-dependent lamellar to hexagonal phase transition. Mezzenga and coauthors studied the inclusion of hydrophilic SPIONs in monolinolein assemblies, observing the structural responsiveness of the lipid-SPION hybrids to static magnetic fields [25,26]. In a previous work, we showed that the addition of hydrophobic SPIONs to a GMO Pn3m cubic phase induces a transition to hexagonal phase, which can be understood as a balance between the free energies of membrane elastic curvature and lipid frustration packing [27]. Additionally, we highlighted that the same phase transition occurs by applying a low frequency alternating magnetic field (AMF), due to the local heating produced by the magnetic relaxation of NPs [27,28].

The central purpose of this study is the separation of thermodynamic effects, due to insertion of hydrophobic hard spheres with a given curvature into locally bilayered structures, from functional effects, specifically originating from the chemical nature of the NPs. To this aim, we leverage our previous studies on hybrid lipid cubic mesophases [27,28] to investigate two kinds of hydrophobic NPs and map the phase and flow behavior with SAXS and Rheology. Phytantriol (Phyt), endowed with lyotropic and thermotropic polymorphism, was doped with NPs characterized by the same size and similar hydrophobic coating, but different core, i.e., AuNPs and SPIONs.

The ensemble of results here gathered, besides providing fundamental knowledge on the phase behavior of such hybrid systems, discloses new insights on the interaction between nanomaterials and non-lamellar biomimetic interfaces at the molecular level, fostering the applicative potentials of these smart materials in the biomedical field [29–32].

2. Materials and methods

2.1. Materials

Fe(III)-acetylacetonate (97%), 1,2-hexadecanediol (90%), oleylamine (70%), oleic acid (90%), diphenylether (99%), denatured ethanol and hexane mixture of isomers employed for the synthesis of hydrophobic SPIONs, were purchased from Sigma Aldrich (St. Louis MO), the same for Gold-(III) tetrachloride (99.995%) and tetraoctylammonium bromide (TOAB 98%). Phytantriol (Phyt) was a gift of Royal DSM. The synthesis of AuNPs and SPIONs is reported in the SI.

2.2. Preparation of bulk cubic mesophases

Bulk cubic phases with or without SPIONs and AuNPs were prepared according to the following procedure: 30 mg of Phyt were weighted in 2 mL glass vessels in the absence (for neat Phyt mesophases) or in the presence (for NPs-loaded Phyt mesophases) of appropriate volumes of SPIONs and AuNPs dispersions in hexane. About 1 mL of hexane was used to solubilize the mixtures, then the solvent was removed under a gentle nitrogen flux. The dry films were left under vacuum overnight, then hydrated with 50 μL Milli-Q water and centrifuged ten times, 5 min each time, at 9000 rpm, alternating a run with the cap facing upward with another with the cap facing downward.

2.3. Small-Angle X-ray Scattering (SAXS)

SAXS measurements were performed on a S3-MICRO SAXS/WAXS instrument (HECUS GmbH, Graz, Austria) which consists of a GeniX microfocus X-ray Sealed Cu Kα source (Xenocs, Grenoble, France) with power 50 W. The source provides a focused X-ray beam with $\lambda = 0.1542$ nm Cu Kα line [33,34]. The instrument is equipped with two one-dimensional (1D) position sensitive detectors, (HECUS 1D-PSD-50M system) each detector is 50 mm long (spatial resolution 54 μm/channel, 1024 channels) and covers a q-range of $0.003 < q < 0.6$ Å^{-1} (SAXS) and $1.2 < q < 1.9$ Å^{-1}, (WAXS). The temperature was controlled by means of a Peltier TCCS-3 Hecus. SAXS curves of bulk cubic phases were recorded at 25, 35 and 50 °C in a solid sample-holder. The hexane dispersions of SPIONs and AuNPs were inserted in a glass capillary to record SAXS profiles. NPs dry films were prepared as follows: the NPs dispersion in hexane was placed in a glass capillary and dried under vacuum overnight to remove the solvent.; SAXS profiles were then recorded. SAXS data analysis is detailed in the SI.

2.4. Rheology

All rheology tests were performed using a Physica-Paar UDS 200 rheometer, equipped with a plate-plate geometry measuring system (diameter of the upper plate 20 mm, measuring gap: 200 μm). The temperature was controlled with a Peltier device. All the oscillatory measurements were performed within the linear viscoelastic range (1 Hz about the amplitude sweep curves). For all the measurements, once the samples were deposited on the surface of the measuring plate, a delay time of 10 min was set in order to ensure the complete equilibration of the sample; in that way no loading effect was observed for all the investigated samples. In order to minimize the evaporation of water, silicone oil was applied to the rim of the samples when temperature was varied in 25–50 °C. The instrumental setups for the rheology tests are the following:

i. Frequency sweep test: frequency range 100–0.001 Hz; amplitude 0.1% strain;
ii. Amplitude sweep test: strain % from 0.001% to 10%; frequency 1 Hz.

3. Results and discussion

3.1. Structure of Phyt mesophases doped with hydrophobic NPs

Fig. 1 summarizes the physicochemical characterization of the NPs (AuNPs and SPIONs) employed in the study. Briefly, AuNPs with a dodecanethiol coating in hexane were synthesized according to Brust et al. [35] (see SI for details), leading to slightly polydisperse nanospheres, as visible from the TEM images (Fig. 1d). The analysis of the NPs' SAXS profile yielded an average core diameter of 3.0 nm and a polydispersity index of 0.28, as estimated through a Schultz distribution [36] (see Fig. 1c): a similar value was obtained from TEM (average diameter 2.8 nm, see SI for details). Hydrophobic SPIONs were synthesized according to Wang et al. [37], leading to a stable hexane dispersion of magnetite nanospheres coated with oleic acid/oleylamine, with slightly larger size than AuNPs, as visible from TEM images (Fig. 1b) and from SAXS (Fig. 1a) curve fitting results: core diameter of 3.6 nm (3.8 nm by TEM) and polydispersity 0.30. The two different NPs' samples are therefore characterized by a hydrophobic coating, which is expected to drive their inclusion in the hydrophobic domains of the mesophase, and by relatively small core size, which is a necessary prerequisite to determine a minimum local perturbation to the bilayered arrangement of Phyt, of 2.8 nm thickness [38].

The effects of increasing amounts of hydrophobic NPs (SPIONs and AuNPs) on the structure of the liquid crystalline mesophases of Phyt in water excess at 25 °C were monitored with SAXS (Fig. 2b, 2c).

It is well known that the binary system Phyt/H_2O with excess water at room temperature is a Pn3m cubic mesophase, with the amphiphilic Phyt molecules assembled as bilayers folded in a tridimensional cubic structure [39]. Accordingly, the Bragg peaks of the cubic phase are clearly recognizable in the corresponding SAXS profile (Fig. 2b, Fig. 2c, blue dashed lines).

Before discussing the phase behavior of hybrid NPs/Phyt systems, some consideration should be made about the Phyt bilayer thickness as compared with NPs' size. While the former is 2.8 nm [39], the overall sizes of magnetic and gold nanoparticles, considering their shell composed by oleic acid (chain length 2 nm [40]) and dodecanethiol (1.4 nm [41]), are 7.6 nm and 5.8 nm respectively. In the hypothesis of interdigitation between Phyt and the coating alkyl chains, it is mainly the hindrance of NPs' cores to determine a local perturbation in the bilayer (see the sketch in Fig. 2d). Dodecanethiol is covalently bound to the surface of AuNPs (the excess is removed during the synthesis work-up, see SI for details), while oleic acid and oleylamine are in excess in SPIONs dispersion. Therefore, to better compare Phyt/SPIONs and Phyt/AuNPs data without coating effects, Phyt/AuNPs samples were prepared adding the same quantity of SPIONs stabilizing agent (see sections S-4 and S-5 in SI for details).

The addition of increasing amounts of both SPIONs and AuNPs results in a clear modification of the mesostructure. Even small amounts of NPs (1×10^{-5} NPs/Phyt) causes the appearance of an additional peak, broad and centered at 0.18 $Å^{-1}$ for AuNPs and more intense and centered at 0.06 $Å^{-1}$ for SPIONs. These peaks are present for all Phyt/NPs SAXS profiles (see Fig. 2b, 2c), without any significant shift of the maximum, irrespectively of the amounts of NPs. To gain more insight on this effect, we recorded SAXS profiles of dry NPs films (see Section 2 for details on samples preparation). The dry AuNPs film (Fig. 2b, red curve) exhibits a broad peak, centered at 0.18 $Å^{-1}$, which perfectly matches the q-value of the extra-peak in the mixed mesophase (see Fig. 2b). The SAXS profile

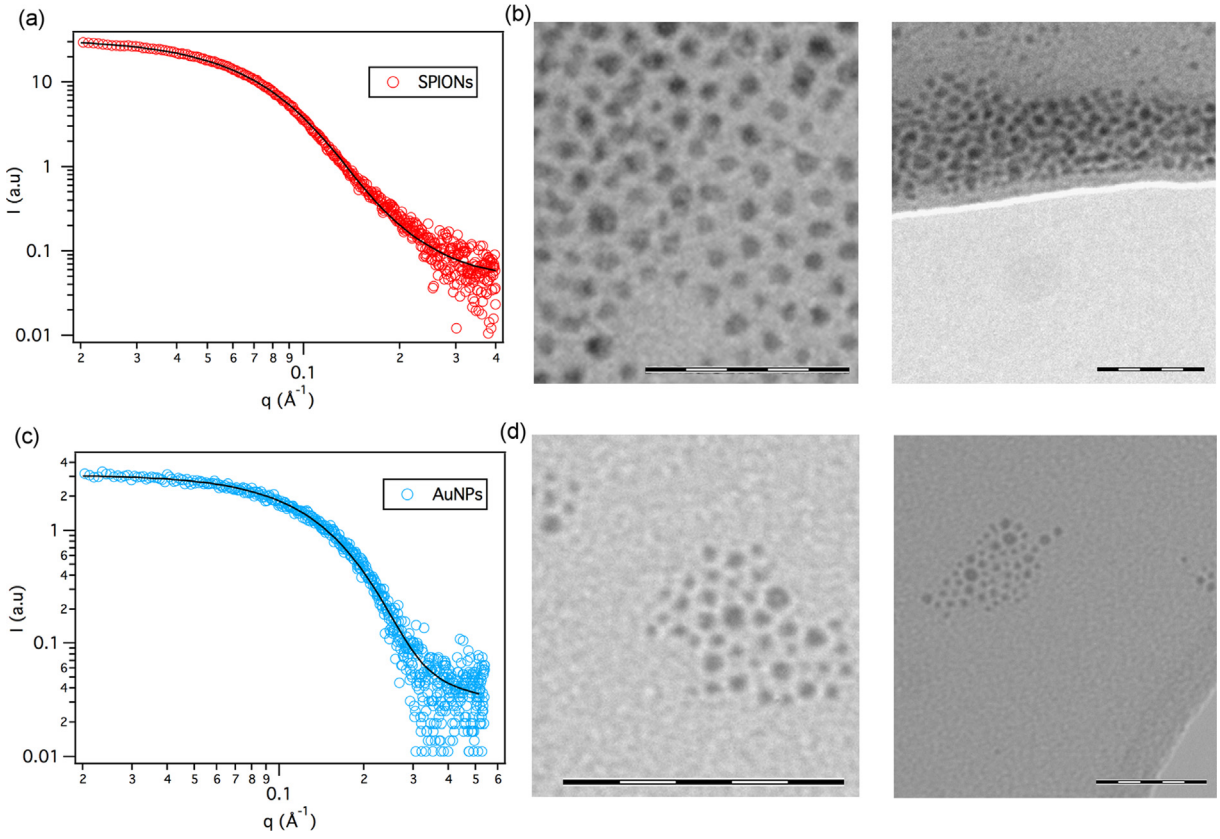

Fig. 1. Structural characterization of hydrophobic AuNPs and SPIONs: (a, c) Small-Angle X-ray Scattering profiles of SPIONs (a) and AuNPs (c) in hexane: the continuous lines represent the best fitting curves according to a Schultz polydisperse spheres distribution; (b, d) representative TEM images of (b) SPIONs and (d) AuNPs. The scale bar in TEM images is 50 nm.

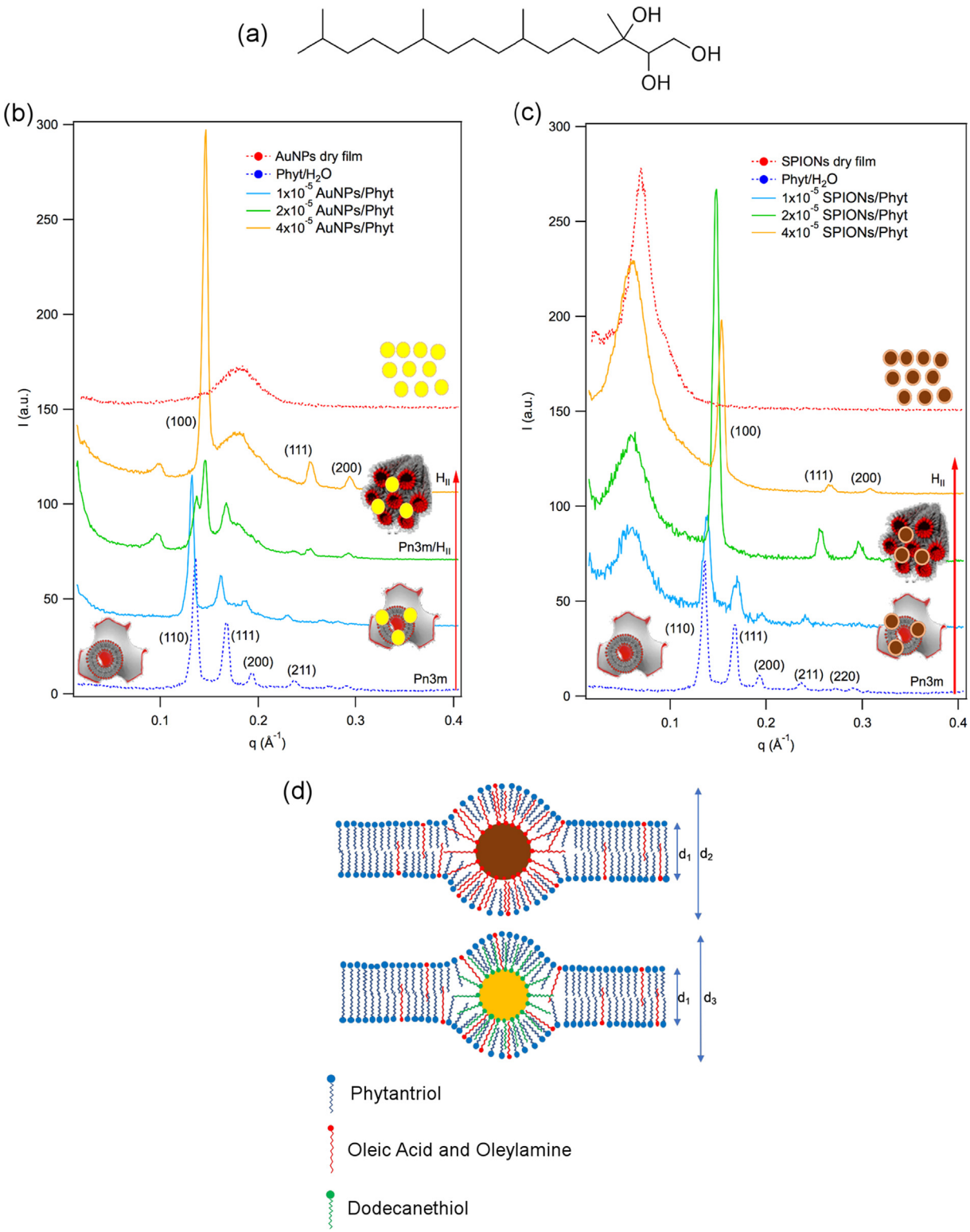

Fig. 2. (a) Chemical structure of Phyt; (b, c) SAXS of Phyt/H_2O mesophases as the concentration (1×10^{-5}, 2×10^{-5}, 4×10^{-5} per Phyt molecule) of (b) AuNPs and (c) SPIONs increases, compared to the SAXS profile of Phyt/H_2O in the absence of NPs (blue dashed line) and with the spectra measured for a dry film of (b) AuNPs and (c) SPIONs (dashed red lines); the Miller indexes assignments (*hkl*) of the Pn3m and hexagonal phase are reported in the graphs. In (d) is reported the nanoscale visualization of NPs encapsulated in the bilayer. (For interpretation of the references to colours in this figure legend, the reader is referred to the web version of this article.)

of dry SPIONs (Fig. 2c, red curve) is characterized by an intense peak (centered at 0.07 $Å^{-1}$), which is slightly shifted at higher scattering vectors with respect to the extra-peak in the corresponding mixed mesophase. We attribute the peaks observed for the dry films as arising from interparticle correlations, thereby ascribing the extra-peaks in the hybrid samples to a partial clusterization of NPs along the grain boundaries of the polycrystalline mesophases, as previously shown for similar systems in other studies

[13,42,43]. The difference in the correlation length of SPIONs and AuNPs in the dry film might be both related to the core differences or to the slightly different hydrophobic coating of NPs, which might lead to a different arrangement of the alkyl chains between-neighboring NPs. The shift of the correlation peak from 0.07 $Å^{-1}$ (dry film) to 0.06 $Å^{-1}$ (NPs inside Phyt) observed for SPIONs, which corresponds to a variation in the NP-NP correlation distance from 8.90 to 10.5 nm, hints at the coexistence of SPIONs at the grain boundaries with particles effectively embedded in the mesophase. The same effect is clearer for AuNPs, where an additional correlation peak at 0.097 $Å^{-1}$ is detected, which can unambiguously attributed the appearance of the peak to AuNPs embedded inside the lipid architecture. Interestingly, the estimated correlation distance (6.5 nm) closely matches the nanometric organization of the mesophase.

Upon increasing the NPs amount, a phase transition from cubic (Pn3m) to hexagonal (H_{II}) phase is detected. In particular, at the lowest NPs amount (light blue lines, Fig. 2b, c), both mixed mesophases retain the Pn3m cubic structure; the intermediate amount of SPIONs (2×10^{-5} NPs/Phyt, Fig. 2b, green curve) is sufficient to induce the phase transition, while the same number of AuNPs induces a partial transition to the hexagonal phase, highlighted by the coexistence of the typical Bragg reflections of both phases (Fig. 2c, green curve); finally, at the highest amount of NPs (4×10^{-5} NPs/Phyt) (Fig. 2b, c, yellow curve), both mesophases are H_{II}. In a recent study we reported the same Pn3m-H_{II} phase transition induced by hydrophobic SPIONs on GMO mesophases, ascribing it to the balance between free energies of elastic curvature and frustration packing [27]. The results here gathered extend our previous findings to a different lipid (Phyt vs GMO), additionally showing that the effect of the hydrophobic nature of SPIONs and AuNPs is similar; it has to be pointed out that even if NPs' number is the same, their different size results in a difference in volume fractions (see SI for details). This value, higher for SPIONs, fully justifies the less pronounced phase transition of Phyt/AuNPs with respect to the SPIONs mesophase with lower and intermediate amount of NPs. We can conclude that the structural arrangement of the hybrid lipid/hydrophobic NPs mesophases is dependent on: (i) the equilibrium structure of the lipid binary phase; (ii) the hydrophobic nature of the coating of the NPs, leading to their preferential partition in the hydrophobic domains of the lipid scaffold; (iii) the size of NPs, which determines the degree of perturbation of the bilayer curvature at the NPs inclusions, thereby affecting the frustration packing energy of the lipid scaffold [27]. The relevance of this latter parameter is also suggested by the slight variation between SPIONs and AuNPs amounts required to completely trigger the phase transition, fully in line with the slight size and polydispersity difference between the two NPs types.

We then fixed the NPs/Phyt ratio to 1×10^{-5} and varied the temperature from 25 °C to 50 °C, to explore the thermotropic phase behavior of the hybrid mesophases (Fig. 3).

Fig. 3a displays the profiles of the binary Phyt/H_2O system in excess water, which shows the characteristic Pn3m-H_{II} transition at 50 °C, in full agreement with the literature [39].

Upon loading with the same number of SPIONs and AuNPs, (Fig. 3b and 3c, respectively) the Pn3m phase persists at room temperature (blue curves); a temperature increase to 35 °C partially promotes the phase transition to the hexagonal phase, both for SPIONs (more pronounced) and for AuNPs (Fig. 3b, c green curves). Therefore, the Pn3m-H_{II} transition can be induced both by increasing the amounts of NPs and, at a fixed amount of NPs, by raising the temperature up to a value which is considerably lower than the transition temperature of the binary phase. The correlation peak, observed for higher NPs concentrations (see Fig. 2), also appears increasing the temperature for the sample with the lower amount of nanoparticles (Fig. 3c) and the sharp signal is preserved after 24 h of the thermal cycle (see SI for details). This effect might be related to a reorganization of the NPs which, at higher temperature, are characterized by a higher mobility inside the mesophase. Nevertheless, the present results further prove that this behavior is not specifically related to a defined lipid molecule or NP kind but can be considered as a general phenomenon. In addition, in this description, the nature of the NPs core does not show major impact.

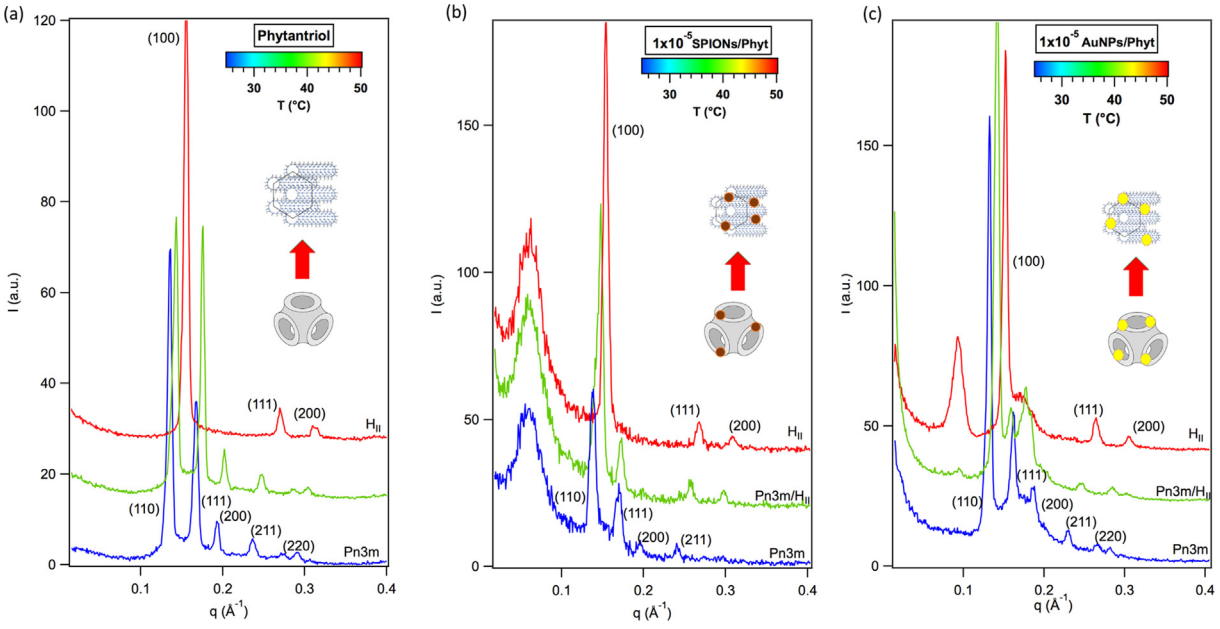

Fig. 3. SAXS profiles of Phyt/H_2O mesophases in the absence (a) and in the presence of (b, c) 1×10^{-5} NPs ((b) SPIONs and (c) AuNPs) per Phyt molecule at 25 °C (blue), 35 °C (green curves) and 50 °C (red curves); the Miller indexes assignments (*hkl*) of the Pn3m and hexagonal phase are also reported. (For interpretation of the references to colours in this figure legend, the reader is referred to the web version of this article.)

3.2. Rheological behavior of Phyt mesophases doped with hydrophobic NPs

In order to understand the effect of NPs on the viscoelastic properties of Phyt/NPs systems, rheological experiments were performed on the same hybrid mesophases.

Amplitude sweep measurements at a fixed frequency of 1 Hz and at T = 25 °C are shown in Fig. 4, where the storage modulus G′ (the elastic component of the complex modulus G*) and the loss modulus G″ (the dissipative component of G*) of the different liquid crystalline mesophases are displayed as a function of the applied strain. The curves measured for the hybrid Pn3m mesophases doped with 1×10^{-5} NPs per Phyt molecule (red markers, SPIONs in Fig. 4a, AuNPs in Fig. 4c) are compared to those measured for Phyt/H_2O in the absence of NPs (blue markers). Fig. 4b, d show the profiles measured for hybrid H_{II} mesophases doped with increasing amounts (light blue markers 2×10^{-5} NPs per Phyt molecule, green markers 4×10^{-5} NPs per Phyt molecule) of NPs (SPIONs in Fig. 4b, AuNPs in Fig. 4d).

It is known that different structural arrangements of liquid crystalline mesophases are characterized by markedly diverse rheological responses [42,44]. Accordingly, the inclusion of NPs (both SPIONs and AuNPs) in the Phyt/H_2O cubic mesophase, which induces a cubic-to-hexagonal phase transition, is associated with a striking variation in the rheological behavior: as a matter of fact, for Phyt/H_2O system and for low NPs loading, the amplitude sweep curves (Fig. 4a, c) are characterized by the typical behavior of a 3D isotropic network, with no preferential directionality, e.g., similarly to Xantan Gum [45] and PVA [46]-based gels. In particular, G″ shows a non-monotonic behavior: after an initial increase for low strain values, it reaches a maximum, above which a strain increase causes the disruption of the network, resulting in the decrease of both G′ and G″, previously interpreted by McLeish and coworkers with a "slip-plane" model, where the local cubic order is disrupted along the direction of applied shear, while the bulk connectivity of the 3D network is preserved [47,48].

As discussed in the previous section, NPs promote the Pn3m to H_{II} phase transition (see Fig. 2). The 1D-directional nature of the hexagonal phase, whose domains are able to align along the shear direction [49], determines a very different behavior, with monotonic decrease of both *moduli* with increasing strain (Fig. 4b, d).

In summary, the arrangement of the lipid scaffold appears as the main factor affecting the rheological behavior, as inferred from amplitude sweep measurements. Within the same structural arrangement (Pn3m or H_{II}), increasing the NPs number density does not have major effects. This evidence also suggests an overall structural integrity of the mesophase, where lipid assembly persists in the presence of NPs embedded in the hydrophobic domains.

To gather additional insight into the flow behavior, we investigated the dependence of the storage and loss moduli of the material on the frequency of the applied shear perturbation, by performing frequency sweep measurements in the linear viscoelastic regime (strain 0.1%, see Materials and Methods for details). The main results are reported in Fig. 5.

In line with the amplitude sweep profiles, the results highlight a different dependence of both G′ and G″ on the frequency of the applied strain for Pn3m (Fig. 5a, c) and H_{II} (Fig. 5b, d) mesophases.

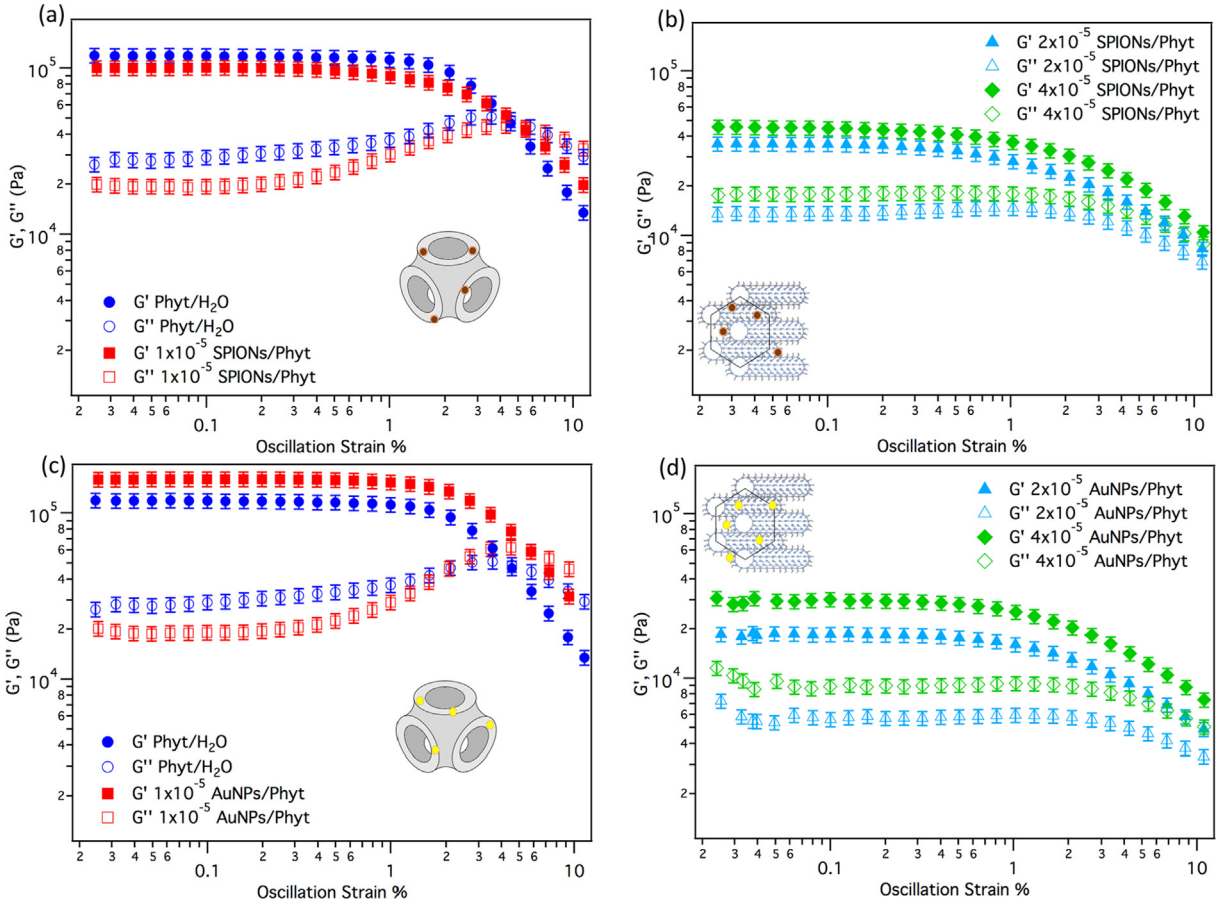

Fig. 4. Amplitude sweep analysis performed at 1 Hz and 25 °C for: (a, c) Phyt/H_2O Pn3m mesophase in the absence (blue markers) and in the presence (red markers) of 1×10^{-5} SPIONs (a) and AuNPs (c) per Phyt molecule; (b, d) Phyt/H_2O H_{II} mesophase in the presence of 2×10^{-5} (light blue markers) and 4×10^{-5} (green markers) SPIONs (b) and AuNPs (d) per Phyt molecule. (For interpretation of the references to colours in this figure legend, the reader is referred to the web version of this article.)

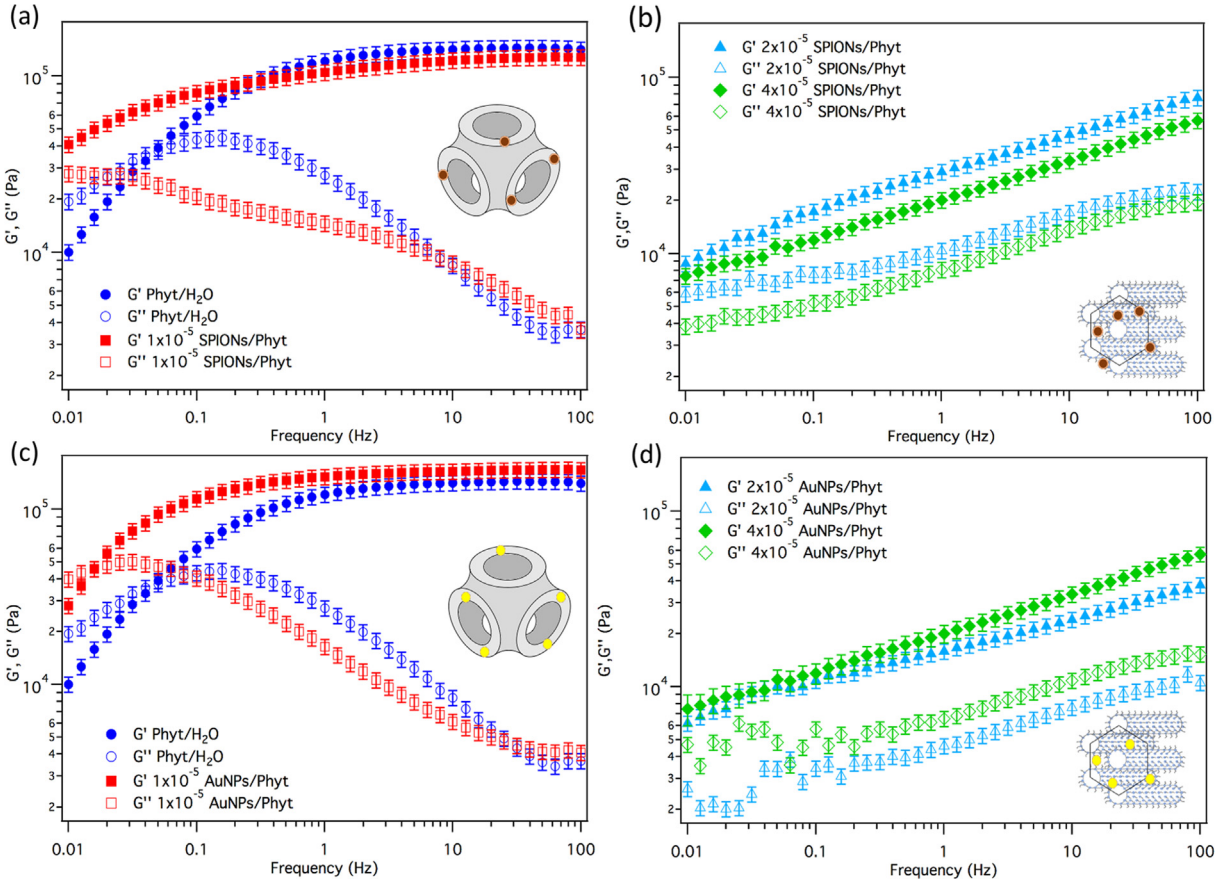

Fig. 5. Frequency sweep curves measured at 25 °C for: (a, c) Phyt/H_2O Pn3m mesophase in the absence (blue markers) and in the presence (red markers) of 1×10^{-5} SPIONs (a) and AuNPs (c) per Phyt molecule; (b, d) Phyt/H_2O H_{II} mesophase in the presence of 2×10^{-5} (light blue markers) and 4×10^{-5} (green markers) SPIONs (b) and AuNPs (d) per Phyt molecule. (For interpretation of the references to colours in this figure legend, the reader is referred to the web version of this article.)

As a first observation, the transition from Pn3m to H_{II} induces a decrease of G′, highlighting the lower rigidity of the hexagonal phase [50,51], which can be again attributed to the transition from a 3D-to-1D geometry, as confirmed by the trend of tanδ (tanδ = G″/G′) reported in the SI.

The Pn3m mesophases (Fig. 5a, c) behave as a viscoelastic fluid: for $\omega > \omega_c$ (with ω_c crossover frequency between G′ and G″ curves), G′ is higher than G″, which indicates a predominantly elastic behavior, while the viscous character is dominant for $\omega < \omega_c$. Concerning the H_{II} mesophase (Fig. 5b, d), the material is characterized by a solid-like behavior, with G′ higher than G″ in the whole range of investigated frequencies. In this region of the phase diagram, increasing the number density of NPs does not significantly affect the viscoelastic properties, probably due to the alignment of nanoparticles along the hexagonal domains.

Conversely, the inclusion of nanoparticles in a Pn3m mesophase, significantly modifies its rheological behavior. In particular, although the same general trend described for the binary phase is preserved for the cubic phases doped with SPIONs (Fig. 5a, red markers) and AuNPs (Fig. 5c, red markers), the crossover frequency between G′ and G″ is shifted to lower ω values. This effect is particularly marked for SPIONs, with the crossover frequency located outside the accessible frequency range of our rheometer.

The crossover frequency marks the transition from the rubbery plateau to the viscous regime and corresponds to the longest relaxation time ($\tau_{max} = 1/\omega_c$) of the system, i.e. the longest characteristic time required to relax back to the equilibrium configuration. According to the model proposed by Mezzenga et al. [44,52], the physical meaning of this relaxation time $\tau_{max} = 1/\omega_c$ can be attributed to the diffusion time of the lipid molecules at the water-lipid interface; this value provides therefore a characteristic order of magnitude for the diffusion processes occurring at the interface and can be used as an indication for the release kinetics of the active molecules through the hydrophobic/hydrophilic interface [52]. The τ_{max} value markedly increases in the presence of 1×10^{-5} NPs/Phyt, passing from 3.1 s to 10 s for AuNPs and to >10 s for SPIONs, accounting for a slower response of the material to the applied stress, which is a clear signature of an enhanced solid-like behavior.

To rule out that this effect is caused by the partition of the SPIONs coating agents in the bilayer (added also to Phyt/AuNPs, to better compare the two systems, see SI for details), we performed a control experiment where the same amount of oleic acid and oleylamine was directly added to Phyt without NPs (see SI for details). This results in a negligible shift in the crossover frequency with respect to the neat binary phase. Therefore, the possible compositional change of the lipid scaffold determined by these hydrophobic molecular additives, does not substantially affect the lipid/water interface relaxation time.

Moreover, as discussed in the SAXS section, NPs affect the lattice parameter of the mesostructure, shrinking the water channels. Since it has been reported [51] that the swelling of the cubic phase has a major impact on the crossover frequency values, as a further control experiment we performed rheological experiments on Phyt/oleic acid/oleylamine Pn3m mesophases, tuning the composition to match the lattice parameter of NPs/Phyt (see SI). The

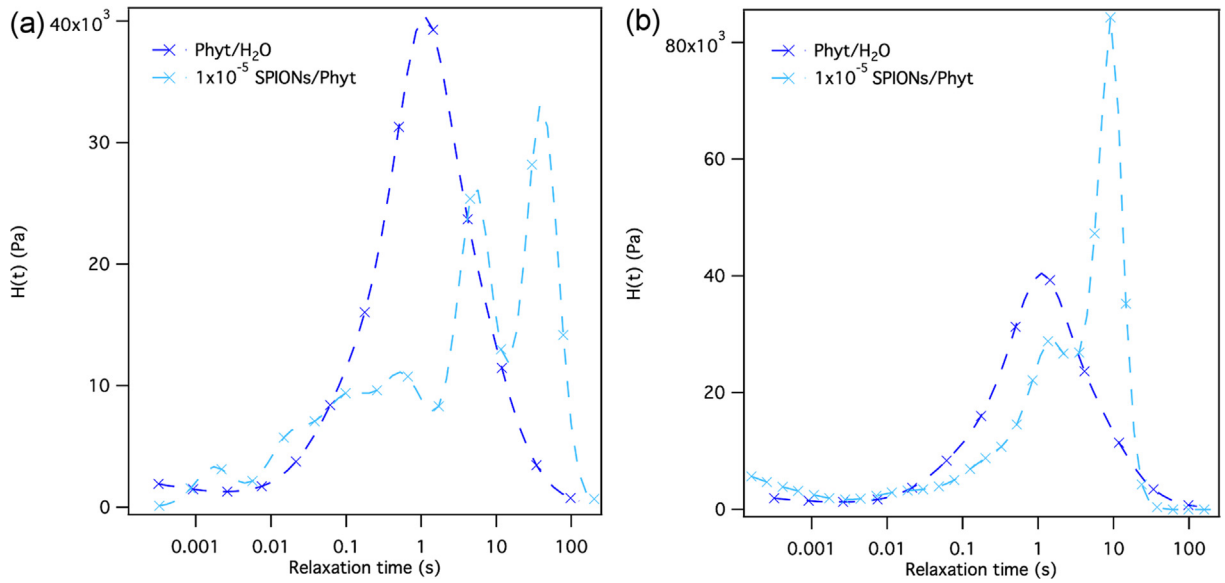

Fig. 6. Viscoelastic relaxation spectra of Pn3m mesophases: Phyt/H_2O (blue markers and line in both plots), Phyt/SPIONs (cyan markers and line in (a)), and Phyt/AuNPs (cyan markers and line in (b)). (For interpretation of the references to colours in this figure legend, the reader is referred to the web version of this article.)

variation of the frequency sweep profile is indeed negligible and therefore possible effects due to a different degree of swelling of the cubic phase can be safely ruled out.

In summary, the presence of NPs is the main factor that tunes the viscoelastic relaxation of the cubic mesophase. To better appreciate this point, the frequency sweep curves were transformed in continuum relaxation spectra [44,51] (Fig. 6, see SI for the different inversion methods tested). The behavior of Pn3m cubic mesophases can be described with a monomodal distribution of relaxation times: the main term is identified with the characteristic diffusion time of lipids at the water-lipid interface, i.e. τ_{max}.

With NPs, the relaxation mode distribution broadens and the spectrum complexity increases, indicating a higher polydispersity [51]. For both kinds of NPs, the main relaxation mode splits into a multimodal distribution, suggesting a non-trivial effect on the rheological properties of lipid bilayer. This feature can be interpreted in terms of the coexistence of lipids freely diffusing at the lipid/water interface, with a slower relaxation time, i.e. τ_{max}, ascribable to a hampered lipid diffusion at the NPs' surface. Interestingly, this is a similar effect highlighted through Fluorescence Correlation Spectroscopy [53,54], for hydrophilic AuNPs interacting with free-standing lipid membrane. Moreover, although the NPs' diameter is comparable, the concentration identical and the effects on phase behavior similar (as highlighted from SAXS measurements), the addition of SPIONs is related to a significantly higher τ_{max} value with respect to AuNPs (9.1 s vs 37.9 s), as the comparison between Fig. 6a and b, highlights. Therefore, the chemical nature of NPs might be critical for the rheological response of the material. This significant effect is, we believe, well beyond what can be expected considering the slight difference in NPs sizes, therefore hinting to a "core" effect in the viscoelastic response. A working hypothesis is that the long-range dipolar interactions between the SPIONs, which are absent in the AuNPs-doped systems, act as a structuring factor on the material, increasing the elastic over viscous response of the material upon the applied stress. This stiffening effect likely originates at the nanoscale level, where dipolar interactions between SPIONs inside the bilayer may additionally hamper the free diffusion of lipids. Indeed, while AuNPs do not significantly influence the diffusion times of lipid molecules at the lipid/water interface, corresponding to the higher-τ peak in the relaxation spectrum (Fig. 6b, light blue dashed line), SPIONs cause a substantial shift in the "free-diffusion" time of lipids, suggesting an alteration of molecular mobility in the whole bilayer.

4. Conclusions

In this contribution we explored the structural and rheological effects of the insertion of hydrophobic SPIONs and AuNPs of similar size in liquid crystalline mesophases of Phytantriol at maximum water swelling. SAXS results highlighted that both types of NPs are embedded in the liquid crystalline mesophase and that their presence promotes a cubic to hexagonal phase transition, with no noteworthy dependence on the type of NPs, but only on their number density, in line with previous data on glycerol-monooleate/SPIONs hybrid mesophases [27]. These results are consistent with the fact that simple thermodynamic considerations, related to the mesophase geometry, the coating and size of NP, can describe in general terms the phase behavior.

The rheological response of such architectures, addressed here for the first time, reveals that the presence of NPs enhances the solid-like behavior of the material. Interestingly, this effect is significantly more pronounced for SPIONs, evidencing possible long-range dipolar interactions between SPIONs that may constitute an additional structuring factor for the material, decreasing its deformability upon stress deformation.

Overall, the comparison of structural and rheological results highlights that different features of the NPs are relevant in affecting the properties of the mesophase: NPs surface (i.e., hydrophobic nature of the coating, driving localization in the lipid scaffold) and size, modulate the local perturbation of the lipid assemblies and affect the phase behavior at rest, while the core composition (AuNPs vs SPIONs) seems to become relevant for the rheological response and for the relaxation to mechanical perturbation.

These results shed light on the structural and physicochemical properties of lipid/NPs mixed liquid crystalline mesophases, disclosing new fundamental knowledge for future biomedical applications.

Acknowledgment

Mirko Severi is gratefully acknowledged for ICP-AES analysis; CSGI is acknowledged by all the authors for partial funding.

Appendix A. Supplementary material

Supplementary data to this article can be found online at https://doi.org/10.1016/j.jcis.2019.01.091.

References

[1] W.K. Fong, T.L. Hanley, B. Thierry, A. Tilley, N. Kirby, L.J. Waddington, B.J. Boyd, Understanding the photothermal heating effect in non-lamellar liquid crystalline systems, and the design of new mixed lipid systems for photothermal on-demand drug delivery, Phys. Chem. Chem. Phys. 16 (2014) 24936–24953, https://doi.org/10.1039/c4cp03635b.

[2] W.K. Fong, T.L. Hanley, B. Thierry, N. Kirby, B.J. Boyd, Plasmonic nanorods provide reversible control over nanostructure of self-assembled drug delivery materials, Langmuir 26 (2010) 6136–6139, https://doi.org/10.1021/la100644s.

[3] I.L. Medintz, H.T. Uyeda, E.R. Goldman, H. Mattoussi, Quantum dot bioconjugates for imaging, labelling and sensing, Nat. Mater. 4 (2005) 435–446, https://doi.org/10.1038/nmat1390.

[4] J.A. Kloepfer, N. Cohen, J.L. Nadeau, FRET between CdSe quantum dots in lipid vesicles and water- And lipid-soluble dyes, J. Phys. Chem. B 108 (2004) 17042–17049, https://doi.org/10.1021/jp048094c.

[5] G. Gopalakrishnan, C. Danelon, P. Izewska, M. Prummer, P.Y. Bolinger, I. Geissbühler, D. Demurtas, J. Dubochet, H. Vogel, Multifunctional lipid/quantum dot hybrid nanocontainers for controlled targeting of live cells, Angew. Chemie – Int. Ed. 45 (2006) 5478–5483, https://doi.org/10.1002/anie.200600545.

[6] W.T. Al-jamal, K.T. Al-jamal, B. Tian, L. Lacerda, P.H. Bomans, P.M. Frederik, K. Kostarelos, Lipid quantum dot bilayer vesicles, ACS Nano 2 (2008).

[7] K. Yang, Y. Liu, Y. Liu, Q. Zhang, C. Kong, C. Yi, Z. Zhou, Z. Wang, G. Zhang, Y. Zhang, N.M. Khashab, X. Chen, Z. Nie, Cooperative assembly of magneto-nanovesicles with tunable wall thickness and permeability for MRI-guided, Drug Deliv. (2018), https://doi.org/10.1021/jacs.8b00884.

[8] M.S. Martina, J.P. Fortin, C. Ménager, O. Clément, G. Barratt, C. Grabielle-Madelmont, F. Gazeau, V. Cabuil, S. Lesieur, Generation of superparamagnetic liposomes revealed as highly efficient MRI contrast agents for in vivo imaging, J. Am. Chem. Soc. 127 (2005) 10676–10685, https://doi.org/10.1021/ja0516460.

[9] E. Amstad, J. Kohlbrecher, E. Müller, T. Schweizer, M. Textor, E. Reimhult, Triggered release from liposomes through magnetic actuation of iron oxide nanoparticle containing membranes, Nano Lett. 11 (2011) 1664–1670, https://doi.org/10.1021/nl2001499.

[10] A. Salvatore, C. Montis, D. Berti, P. Baglioni, Multifunctional magnetoliposomes for sequential controlled release, ACS Nano 10 (2016) 7749–7760, https://doi.org/10.1021/acsnano.6b03194.

[11] C.C. Piccinetti, C. Montis, M. Bonini, R. Laurà, M.C. Guerrera, G. Radaelli, F. Vianello, V. Santinelli, F. Maradonna, V. Nozzi, A. Miccoli, I. Olivotto, Transfer of silica-coated magnetic (Fe_3O_4) nanoparticles through food: a molecular and morphological study in Zebrafish, Zebrafish 11 (2014) 567–579, https://doi.org/10.1089/zeb.2014.1037.

[12] M. Szlezak, D. Nieciecka, A. Joniec, M. Pękała, E. Gorecka, M. Emo, M.J. Stébé, P. Krysiński, R. Bilewicz, Monoolein cubic phase gels and cubosomes doped with magnetic nanoparticles-hybrid materials for controlled drug release, ACS Appl. Mater. Interfaces acsami.6b12889 (2017), https://doi.org/10.1021/acsami.6b12889.

[13] E. Venugopal, S.K. Bhat, J.J. Vallooran, R. Mezzenga, Phase behavior of lipid-based lyotropic liquid crystals in presence of colloidal nanoparticles, Langmuir 27 (2011) 9792–9800, https://doi.org/10.1021/la201767p.

[14] C. Fong, T. Le, C.J. Drummond, Lyotropic liquid crystal engineering–ordered nanostructured small molecule amphiphile self-assembly materials by design, Chem. Soc. Rev. 41 (2012) 1297, https://doi.org/10.1039/c1cs15148g.

[15] N. Tran, A.M. Hawley, J. Zhai, B.W. Muir, C. Fong, C.J. Drummond, X. Mulet, High-throughput screening of saturated fatty acid influence on nanostructure of lyotropic liquid crystalline lipid nanoparticles, Langmuir 32 (2016) 4509–4520, https://doi.org/10.1021/acs.langmuir.5b03769.

[16] N. Tran, X. Mulet, A.M. Hawley, C. Fong, J. Zhai, T.C. Le, J. Ratcliffe, C.J. Drummond, Manipulating the ordered nanostructure of self-assembled monoolein and phytantriol nanoparticles with unsaturated fatty acids, Langmuir 34 (2018) 2764–2773, https://doi.org/10.1021/acs.langmuir.7b03541.

[17] S. Aleandri, C. Speziale, R. Mezzenga, E.M. Landau, Design of light-triggered lyotropic liquid crystal mesophases and their application as molecular switches in 'On Demand' release, Langmuir 31 (2015) 6981–6987, https://doi.org/10.1021/acs.langmuir.5b01945.

[18] K.J. Tangso, W.K. Fong, T. Darwish, N. Kirby, B.J. Boyd, T.L. Hanley, Novel spiropyran amphiphiles and their application as light-responsive liquid crystalline components, J. Phys. Chem. B 117 (2013) 10203–10210, https://doi.org/10.1021/jp403840m.

[19] S. Jia, J.D. Du, A. Hawley, W.K. Fong, B. Graham, B.J. Boyd, Investigation of donor-acceptor stenhouse adducts as new visible wavelength-responsive switching elements for lipid-based liquid crystalline systems, Langmuir 33 (2017) 2215–2221, https://doi.org/10.1021/acs.langmuir.6b03726.

[20] Q. Liu, Y. Da Dong, B.J. Boyd, Selective sequence for the peptide-triggered phase transition of lyotropic liquid-crystalline structures, Langmuir 32 (2016) 5155–5161, https://doi.org/10.1021/acs.langmuir.6b00547.

[21] L. Van'T Hag, L. De Campo, C.J. Garvey, G.C. Feast, A.E. Leung, N.R. Yepuri, R. Knott, T.L. Greaves, N. Tran, S.L. Gras, C.J. Drummond, C.E. Conn, Using SANS with contrast-matched lipid bicontinuous cubic phases to determine the location of encapsulated peptides, proteins, and other biomolecules, J. Phys. Chem. Lett. 7 (2016) 2862–2866, https://doi.org/10.1021/acs.jpclett.6b01173.

[22] L. van 't Hag, A. Anandan, S.A. Seabrook, S.L. Gras, C.J. Drummond, A. Vrielink, C.E. Conn, Direct demonstration of lipid phosphorylation in the lipid bilayer of the biomimetic bicontinuous cubic phase using the confined enzyme lipid A phosphoethanolamine transferase, Soft Matter. 13 (2017) 1493–1504, https://doi.org/10.1039/C6SM02487D.

[23] J.M. Bulpett, T. Snow, B. Quignon, C.M. Beddoes, T.-Y.D. Tang, S. Mann, O. Shebanova, C.L. Pizzey, N.J. Terrill, S.A. Davis, W.H. Briscoe, Hydrophobic nanoparticles promote lamellar to inverted hexagonal transition in phospholipid mesophases, Soft Matter. 11 (2015) 8789–8800, https://doi.org/10.1039/c5sm01705j.

[24] C.M. Beddoes, J. Berge, J.E. Bartenstein, K. Lange, A.J. Smith, R.K. Heenan, W.H. Briscoe, Hydrophilic nanoparticles stabilising mesophase curvature at low concentration but disrupting mesophase order at higher concentrations, Soft Matter. 12 (2016) 6049–6057, https://doi.org/10.1039/C6SM00393A.

[25] J.J. Vallooran, R. Negrini, R. Mezzenga, Controlling anisotropic drug diffusion in lipid-Fe_3O_4 nanoparticle hybrid mesophases by magnetic alignment, Langmuir 29 (2013) 999–1004, https://doi.org/10.1021/la304563r.

[26] J.J. Vallooran, S. Bolisetty, R. Mezzenga, Macroscopic alignment of lyotropic liquid crystals using magnetic nanoparticles, Adv. Mater. 23 (2011) 3932–3937, https://doi.org/10.1002/adma.201101760.

[27] M. Mendozza, C. Montis, L. Caselli, M. Wolf, P. Baglioni, D. Berti, On the thermotropic and magnetotropic phase behavior of lipid liquid crystals containing magnetic nanoparticles, Nanoscale 10 (2018) 3480–3488, https://doi.org/10.1039/c7nr08478a.

[28] C. Montis, B. Castroflorio, M. Mendozza, A. Salvatore, D. Berti, P. Baglioni, Magnetocubosomes for the delivery and controlled release of therapeutics, J. Colloid Interface Sci. 449 (2015) 317–326, https://doi.org/10.1016/j.jcis.2014.11.056.

[29] L. Boge, A. Västberg, A. Umerska, H. Bysell, J. Eriksson, K. Edwards, A. Millqvist-Fureby, M. Andersson, Freeze-dried and re-hydrated liquid crystalline nanoparticles stabilized with disaccharides for drug-delivery of the plectasin derivative AP114 antimicrobial peptide, J. Colloid Interface Sci. 522 (2018) 126–135, https://doi.org/10.1016/j.jcis.2018.03.062.

[30] U. Bazylińska, J. Kulbacka, J. Schmidt, Y. Talmon, S. Murgia, Polymer-free cubosomes for simultaneous bioimaging and photodynamic action of photosensitizers in melanoma skin cancer cells, J. Colloid Interface Sci. 522 (2018) 163–173, https://doi.org/10.1016/j.jcis.2018.03.063.

[31] N. Tran, M. Hocquet, B. Eon, P. Sangwan, J. Ratcliffe, T.M. Hinton, J. White, B. Ozcelik, N.P. Reynolds, B.W. Muir, Non-lamellar lyotropic liquid crystalline nanoparticles enhance the antibacterial effects of rifampicin against Staphylococcus aureus, J. Colloid Interface Sci. 519 (2018) 107–118, https://doi.org/10.1016/j.jcis.2018.02.048.

[32] Q. Liu, J. Hu, M.R. Whittaker, T.P. Davis, B.J. Boyd, Nitric oxide-sensing actuators for modulating structure in lipid-based liquid crystalline drug delivery systems, J. Colloid Interface Sci. 508 (2017) 517–524, https://doi.org/10.1016/j.jcis.2017.08.079.

[33] M. Raudino, G. Selvolini, C. Montis, M. Baglioni, M. Bonini, D. Berti, P. Baglioni, Polymer films removed from solid surfaces by nanostructured fluids: microscopic mechanism and implications for the conservation of cultural heritage, ACS Appl. Mater. Interfaces 7 (2015), https://doi.org/10.1021/acsami.5b00534.

[34] M. Mamusa, L. Sitia, F. Barbero, A. Ruyra, T.D. Calvo, C. Montis, A. Gonzalez-Paredes, G.N. Wheeler, C.J. Morris, M. McArthur, D. Berti, Cationic liposomal vectors incorporating a bolaamphiphile for oligonucleotide antimicrobials, Biochim. Biophys. Acta – Biomembr. 1859 (2017), https://doi.org/10.1016/j.bbamem.2017.06.006.

[35] M. Brust, M. Walker, D. Bethell, D.J. Schiffrin, R. Whyman, Synthesis of thiol-derivatised gold nanoparticles in a two-phase liquid-liquid system, J. Chem. Soc. Chem. Commun. (1994) 801–802, https://doi.org/10.1039/C39940000801.

[36] M. Kotlarchyk, S.-H. Chen, Analysis of small angle neutron scattering spectra from polydisperse interacting colloids, J. Chem. Phys. 79 (1983) 2461, https://doi.org/10.1063/1.446055.

[37] L. Wang, J. Luo, Q. Fan, M. Suzuki, I.S. Suzuki, M.H. Engelhard, Y. Lin, N. Kim, J.Q. Wang, C.J. Zhong, Monodispersed core-shell Fe_3O_4@Au nanoparticles, J. Phys. Chem. B 109 (2005) 21593–21601, https://doi.org/10.1021/jp0543429.

[38] H. Sub Wi, K. Lee, H. Kyu Pak, Interfacial energy consideration in the organization of a quantum dot–lipid mixed system, J. Phys. Condens. Matter. 20 (2008) 494211, https://doi.org/10.1088/0953-8984/20/49/494211.

[39] J. Barauskas, T. Landh, Phase behavior of the phytantriol/water system, Langmuir 19 (2003) 9562–9565, https://doi.org/10.1021/la0350812.

[40] J. Xie, C. Xu, N. Kohler, Y. Hou, S. Sun, Controlled PEGylation of monodisperse Fe_3O_4 nanoparticles for reduced non-specific uptake by macrophage cells, Adv. Mater. 19 (2007) 3163–3166, https://doi.org/10.1002/adma.200701975.

[41] J. Chen, M.A. Reed, C.L. Asplund, A.M. Cassell, M.L. Myrick, A.M. Rawlett, J.M. Tour, P.G. Van Patten, Placement of conjugated oligomers in an alkanethiol matrix by scanned probe microscope lithography, Appl. Phys. Lett. 75 (1999) 624–626, https://doi.org/10.1063/1.124461.

[42] J.B. Marlow, M.J. Pottage, T.M. McCoy, L. De Campo, A. Sokolova, T.D.M. Bell, R. F. Tabor, Structural and rheological changes of lamellar liquid crystals as a result of compositional changes and added silica nanoparticles, Phys. Chem. Chem. Phys. 20 (2018) 16592–16603, https://doi.org/10.1039/C8CP02101E.

[43] J.J. Vallooran, S. Handschin, S. Bolisetty, R. Mezzenga, Twofold light and magnetic responsive behavior in nanoparticle-lyotropic liquid crystal systems, Langmuir 28 (2012) 5589–5595, https://doi.org/10.1021/la300449q.
[44] R. Mezzenga, C. Meyer, C. Servais, A.I. Romoscanu, L. Sagalowicz, R.C. Hayward, Shear rheology of lyotropic liquid crystals: a case study, Langmuir 21 (2005) 3322–3333, https://doi.org/10.1021/la046964b.
[45] K. Hyun, M. Wilhelm, C.O. Klein, K.S. Cho, J.G. Nam, K.H. Ahn, S.J. Lee, R.H. Ewoldt, G.H. McKinley, A review of nonlinear oscillatory shear tests: analysis and application of large amplitude oscillatory shear (LAOS), Prog. Polym. Sci. 36 (2011) 1697–1753, https://doi.org/10.1016/j.progpolymsci.2011.02.002.
[46] K. Hyun, S.H. Kim, K.H. Ahn, S.J. Lee, Large amplitude oscillatory shear as a way to classify the complex fluids, J. Nonnewton. Fluid Mech. 107 (2002) 51–65. Pii S0377-0257(02)00141-6\rDoi 10.1016/S0377-0257(02)00141-6.
[47] S. Radiman, C. Toprakcioglu, T. McLeish, Rheological Study of ternary cubic phases, Langmuir 10 (1994) 61–67, https://doi.org/10.1021/la00013a009.
[48] J.L. Jones, T.C.B. McLeish, Rheological response of surfactant cubic phases, Langmuir 11 (1995) 785–792, https://doi.org/10.1021/la00003a020.
[49] G. Schmidt, P. Lindner, I. Laue-langevin, Small-angle neutron scattering from a hexagonal phase under shear, Colloid Polym. Sci. 88 (1996) 85–88, https://doi.org/10.1007/BF00658914.
[50] M. Pouzot, R. Mezzenga, M. Leser, L. Sagalowicz, S. Guillote, O. Glatter, Structural and rheological investigation of Fd3m inverse micellar cubic phases, Langmuir 23 (2007) 9618–9628, https://doi.org/10.1021/la701206a.
[51] C. Speziale, R. Ghanbari, Rheology of Ultraswollen Bicontinuous Lipidic Cubic Phases, 2018. http://doi.org/10.1021/acs.langmuir.8b00737.
[52] L. Sagalowicz, R. Mezzenga, M.E. Leser, Investigating Reversed Liquid Crystalline Mesophases, 11 (2006) 224–229. http://doi.org/10.1016/j.cocis.2006.07.002.
[53] C. Montis, A. Zendrini, F. Valle, S. Busatto, L. Paolini, A. Radeghieri, A. Salvatore, D. Berti, P. Bergese, Size distribution of extracellular vesicles by optical correlation techniques, Colloids Surfaces B Biointerfaces. 158 (2017), https://doi.org/10.1016/j.colsurfb.2017.06.047.
[54] C. Montis, D. Maiolo, I. Alessandri, P. Bergese, D. Berti, Interaction of nanoparticles with lipid membranes: a multiscale perspective, Nanoscale 6 (2014) 6452–6457, https://doi.org/10.1039/C4NR00838C.

Inorganic Nanoparticles Modify the Phase Behavior and Viscoelastic Properties of Non-lamellar Lipid Mesophases

*Marco Mendozza, Lucrezia Caselli, Costanza Montis, Stefano Orazzini, Emiliano Carretti, Piero Baglioni, Debora Berti**

[1]Department of chemistry "Ugo Schiff" and CSGI, University of Florence, Via della Lastruccia 3, 50019-Sesto Fiorentino, Florence, Italy.

Materials and Methods

S.1- Synthesis of SPIONs

Iron oxide nanoparticles were synthesized according to the protocol reported by Wang et al.[1]. Briefly, 0.71 g $Fe(acac)_3$ (2 mmol) were dissolved in 20 mL of phenyl ether with 2 mL of oleic acid (6 mmol) and 2 mL of oleylamine (4 mmol) under nitrogen atmosphere and vigorous stirring. 1,2-hexadecanediol (2.58g, 10 mmol) was added into the solution. The solution was heated to 210 °C, refluxed for 2 h and then cooled to RT. Ethanol was added to the solution and the precipitate collected, washed with ethanol and redispersed in 20 mL of hexane in the presence of 75 mM each of oleic acid and oleylamine. A stable dispersion of the magnetic SPIONs with a hydrophobic coating of oleic acid and oleylamine in hexane was obtained.

S.2- Synthesis of AuNPs

Hydrophobic gold nanoparticles are synthesized according to the protocol reported by Brust et al.[2] Briefly, an aqueous solution of $HAuCl_4$ (30 ml, 30 mM) was mixed with a solution of tetraoctylammonium bromide (TOAB) in toluene (80 ml, 50 mM). The two-phase mixture was vigorously stirred until all the Gold-(III) compound was transferred into

the organic layer. Then, dodecanethiol (l70 mg) was added to the organic phase. A freshly prepared aqueous solution of sodium borohydride (25 ml, 0.4 M) was slowly added with vigorous stirring. After 3 h stirring the organic phase was separated, evaporated to 10 ml in a rotavapor and mixed with 400 ml ethanol to remove excess thiol. The mixture was kept for 24 h at -18°C and the dark brown precipitate was filtered off and washed with ethanol. The crude product was dissolved in 10 ml toluene and again precipitated with 400 ml ethanol. Then, the twice washed precipitated was dispersed in 20 mL hexane.

S.3- SAXS data analysis

Equation (1) was used to calculate lattice parameter (d) of cubic and hexagonal phase:

$$q = \left(\frac{2\pi}{d}\right)\sqrt{h^2 + k^2 + l^2} \qquad (1)$$

where (hkl) are Miller index related to the considered structures. In a Pn3m structure are (110), (111), (200), (211), (220)… while in H_{II} mesophases are (100), (111), (200)… Eq. (2)[3] was used to calculate water channel radii r_w in Pn3m cubic phase while Eq. (3)[3] was used to calculate volume water fraction φ_w:

$$r_w = \sqrt{(-A_0/2\pi\chi)}d - l_c \qquad (2)$$

$$\varphi_w = 1 - 2A_0\left(\frac{l_c}{d}\right) - \frac{4}{3}\pi\chi\left(\frac{l_c}{d}\right)^3 \qquad (3)$$

where A_0 and χ are topological parameters respectively the ratio of the area of the minimal surface in a unit cell to (unit cell volume)$^{2/3}$ and the Euler−Poincaire characteristic, that for the diamond cubic mesophase (Pn3m), are A_0=1.919 and χ=-2. Equation (4)[4] and (5)[5] describe water channel radii (r_w) of hexagonal phase H_{II} and water volume fraction (φ_w) respectively:

$$r_w = \frac{0.5256d - l_c}{0.994} \qquad (4)$$

$$\varphi_w = \frac{2\pi r_w^2}{\sqrt{3}d^2} \qquad (5)$$

We assumed that chain length l_c into the range of 25-50 °C, is constant and assume value of about 9 Å calculated by the data reported in literature through Eq.(2-3) [6]. Moreover, we assumed that %w/w of Fe_3O_4 and Au was negligible to evaluate water fraction both for cubic and hexagonal phase.

To Fit SAXS curves of both dispersed gold and iron oxide nanoparticles, we used Sphere-Schulz Model by NIST[7,8]. This model calculates the scattering for a polydisperse population of sphere with uniform Scattering Length Density (SLD). The distribution of radii is a Schulz distribution as in Eq. (6):

$$f(R) = (z+1)^{z+1} x^z \frac{\exp[-(z+1)x]}{R_{avg}\Gamma(z+1)} \qquad (6)$$

Where R_{avg} is the mean radius, $x=R/R_{avg}$, z is related to the polydispersity, $p=\sigma/R_{avg}$, by $z=1/p^2-1$. σ^2 is the variance of distribution. The scattering intensity is modeled as reported in Eq. (7):

$$I(q) = \left(\frac{4\pi}{3}\right)^2 N_0 \Delta\rho^2 \int_0^\infty f(R) R^6 F^2(qR) dR \qquad (7)$$

where N_0 is the total number of particles per unit volume, and $\Delta\rho$ is the difference in scattering length density, F(qR) the scattering amplitude for a sphere reported in Eq. (8):

$$F(x) = \frac{3[\sin(x) - x\cos(x)]}{x^3} \qquad (8)$$

No interparticle interference effects are included in this calculation.

Supplementary Figures

S.4- ICP-AES analysis of SPIONs, AuNPs and TEM image analysis

The ICP-AES analyses were performed to determine the weight concentration of both types of NPs and the results are 2.19 mg/mL and 3.78 mg/mL for SPIONs and AuNPs respectively. Thus, considering the density of Fe_3O_4 and Au, which are 5.17 g/cm^3 and 19.31 g/cm^3 respectively, the amounts of NPs added in the Phyt mesophase in order to have the same number of AuNPs or SPIONs in each samples are reported in table S1:

Table S1: Percentage in weight of nanoparticles with respect to lipid, mg of oleic acid and oleylamine, number of nanoparticles and volume fraction of SPIONs and AuNPs

N° nanoparticles	**N° nanoparticles/lipid molecule**	mg of oleic acid and oleylamine	SPIONs Volume fraction #	AuNPs Volume fraction #
5.57×10^{14}	**1×10^{-5}**	1*	4.2×10^{-4}	1.9×10^{-4}
1.13×10^{15}	**2×10^{-5}**	3*	8.5×10^{-4}	3.9×10^{-4}
2.26×10^{15}	**4×10^{-5}**	6*	1.7×10^{-3}	7.9×10^{-4}

***** dispersed as stabilizer agent in SPIONs or added to lipids with the appropriate amount of AuNPs dispersion

calculated as ratio of the NPs and phytantriol volumes, taking into account that 30 mg of phytantriol (density 0.935 g/cm^3) were used to prepare each sample

In order to further prove that NPs are included in the hydrophobic regions of the mesophase, the following control experiment was performed: 100 mg of a Phyt mesophase was prepared as described in the experimental section with the addition 0.234 mg of SPIONs and 0.15 mL MilliQ water. The sample was kept at 50 °C for 1 h to promote the cubic to hexagonal phase transition with shrinkage of the lattice parameter and water release from the aqueous domains. The released water was analyzed with ICP-AES to determine iron content (SPIONs released from the mesophase). The magnetite concentration was found equal to 1.29×10^{-4} mg/mL in 0.15 mL of analyzed water, corresponding to 8.35×10^{-3}% released SPIONs of the initial 0.234 mg amount.

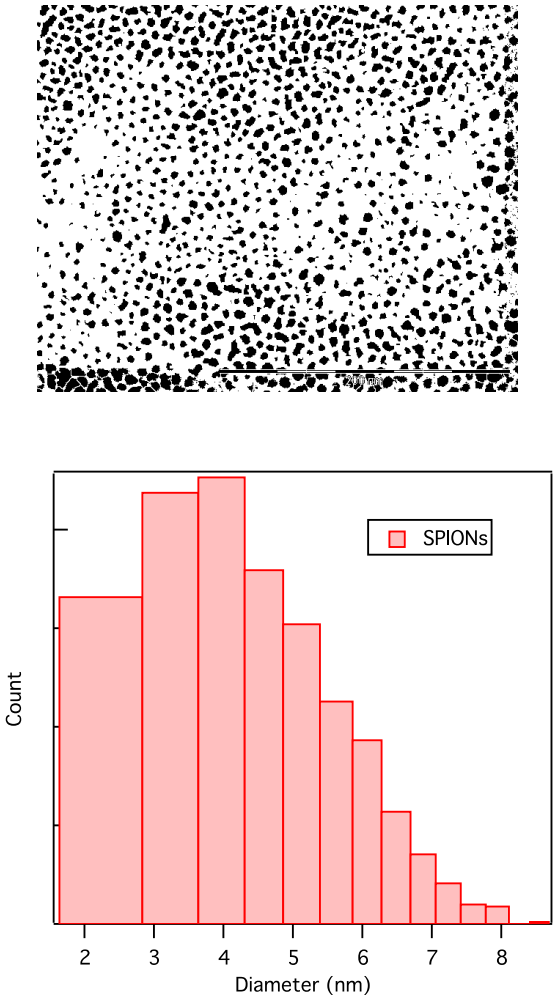

Figure S1: Size distribution of SPIONs estimated from three different TEM images through Image J.

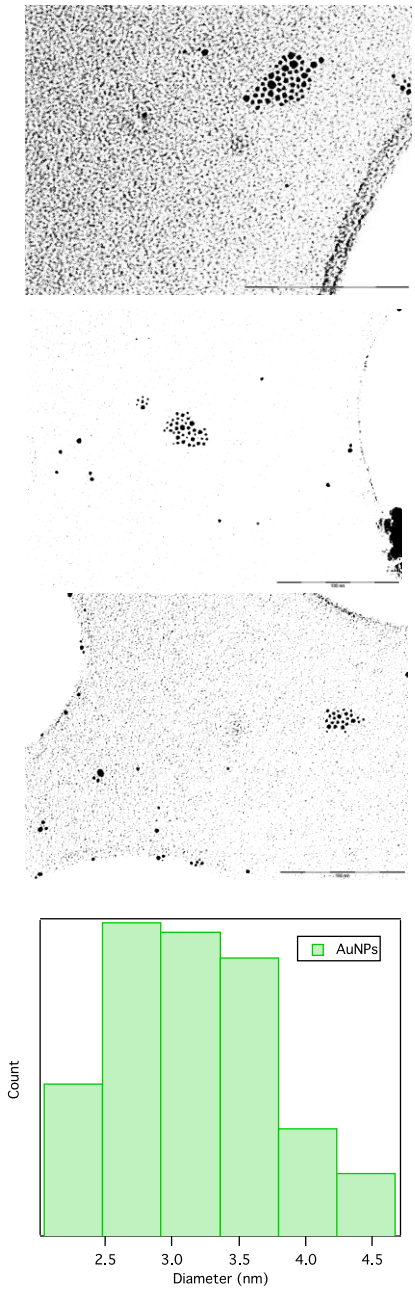

Figure S2: Size distribution of AuNPs estimated from three different TEM images through Image J.

S.5- SAXS of Phytantriol mesophases loaded with Oleic Acid/Oleylamine

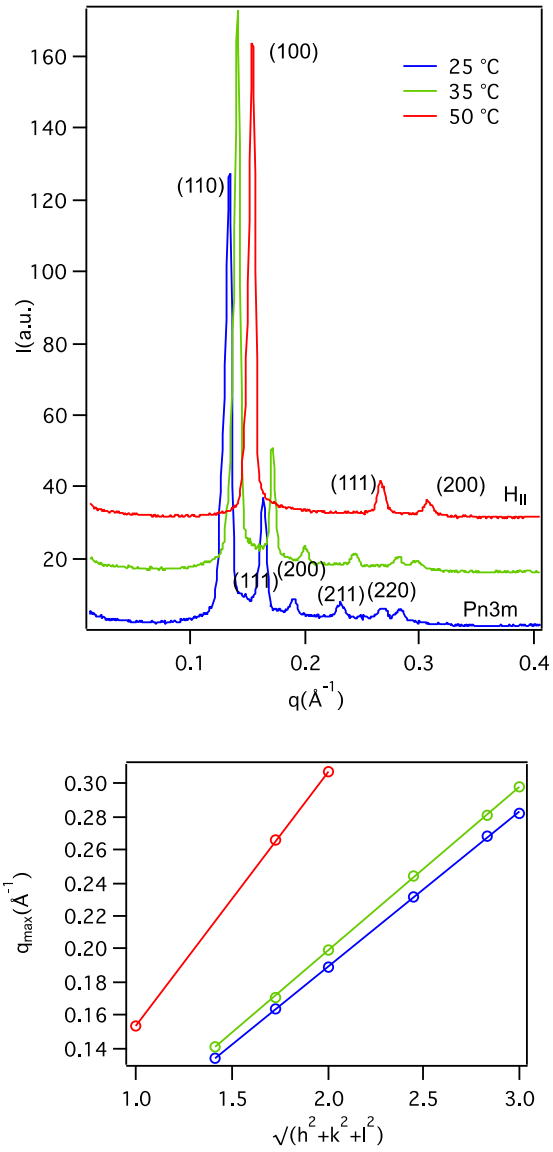

Figure S3: SAXS curves of phytantriol assembled with 1 mg of a mixture Oleic Acid/Oleylamine at 25-35-50 °C (respectively blue, cyan, green, and red) and Miller index on q_{max} to determine variation of lattice parameter with temperature.

Table S2. Lattice parameters, water channel radii and water volume fraction of phytantriol assembled with 1 mg of a mixture 50:50 of oleic acid and oleylamine

T (°C)	Lattice parameter (Å)	Water channel radii (Å)	Water volume fraction
25	67	17	0.505
35	63	16	0.476
50	41	13	0.347

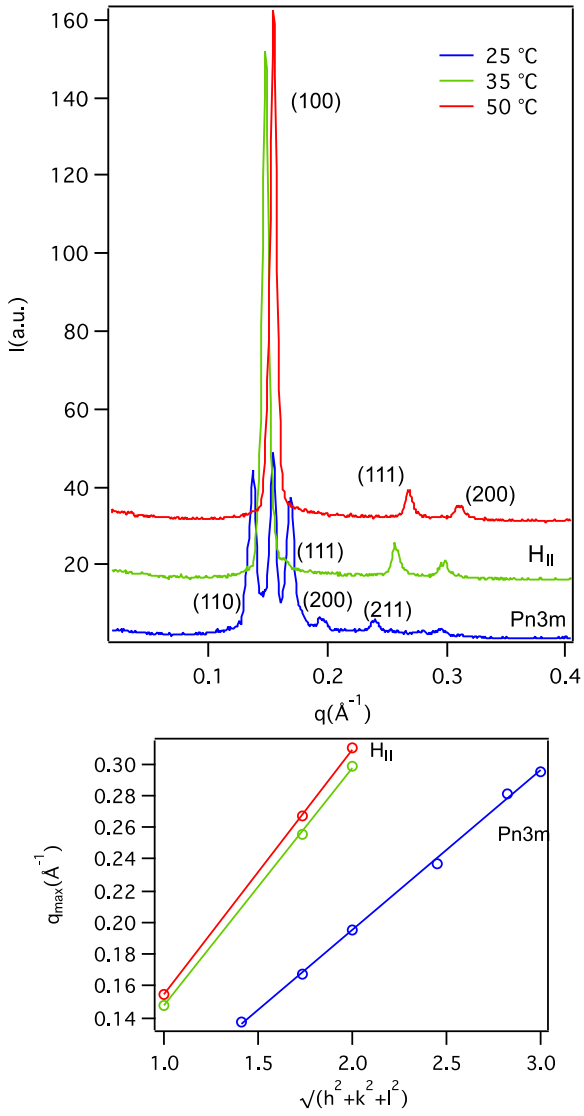

Figure S4: SAXS curves of phytantriol assembled with 3 mg of a mixture Oleic Acid/Oleylamine and Miller index on q_{max} to determine variation of lattice parameter both for cubic (blue) and hexagonal phase (cyan, green, red) with temperature into the range from 25-50 °C.

Table S3. Lattice parameters, water channel radii and waer volume fraction of phytantriol assembled with 3 mg of a mixture 50:50 of Oleic acid and oleylamine.

T (°C)	Lattice parameter (Å)	Water channel radii (Å)	Water volume fraction
25	62	15	0.468
35	42	13	0.347
50	40	12	0.326

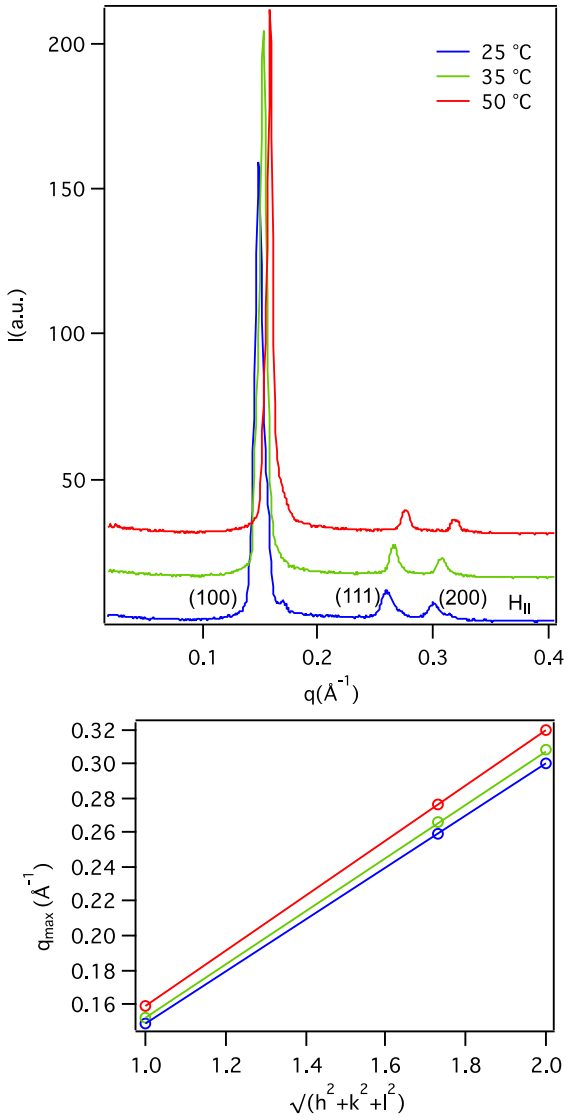

Figure S5: SAXS curves of phytantriol assembled with 6 mg of a mixture Oleic Acid/Oleylamine and Miller index on q_{max} to determine variation of lattice parameter of hexagonal phase with temperature into the range from 25-50 °C.

Table S4. Lattice parameters, water channel radii and water volume fraction of phytantriol assembled with 6 mg of a mixture 50:50 of oleic acid and oleylamine.

T (°C)	Lattice parameter (Å)	Water channel radii (Å)	Water volume fraction
25	42	13	0.347
35	40	12	0.326
50	39	12	0.326

S.6- SAXS: Thermal reversibility of phytantriol with SPIONs and AuNPs

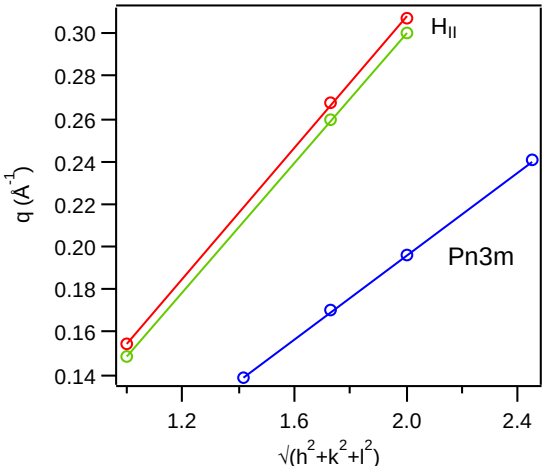

Figure S6. Lattice parameter of phytantriol assembled with $1x10^{-5}$ SPIONs/Phyt of Pn3m mesophase at 25 °C (blue curve) and hexagonal phase at 35-50 °C. SAXS profiles are showed in main text.

Table S5. Lattice parameters, water channel radii and water volume fraction of phytantriol assembled with $1x10^{-5}$ SPIONs/Phyt (data showed in main text)

T (°C)	Lattice parameter (Å)	Water channel radii (Å)	Water volume fraction
25	64	16	0.484
35	42	13	0.347
50	41	12	0.326

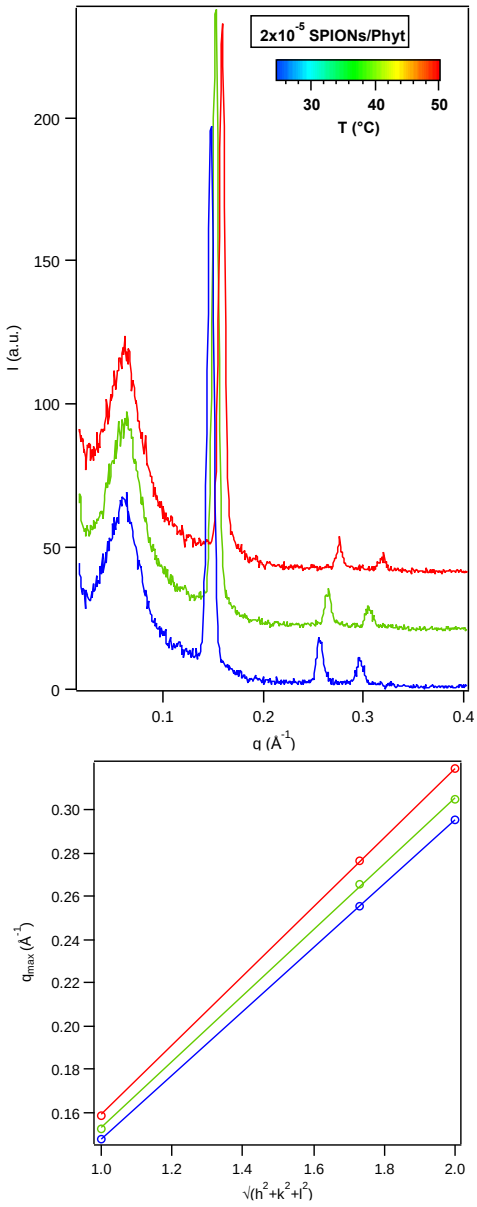

Figure S7. SAXS curves of phytantriol assembled with $2x10^{-5}$ SPIONs/Phyt and Miller index on q_{max} to determine variation of lattice parameter of hexagonal phase with temperature into the range from 25-50 °C.

Table S6. Lattice parameters, water channel radii and water volume fraction of phytantriol assembled with $2x10^{-5}$ SPIONs/Phyt

T (°C)	Lattice parameter (Å)	Water channel radii (Å)	Water volume fraction
25	43 (H_{II})	14	0.384
35	41 (H_{II})	13	0.347
50	39 (H_{II})	12	0.326

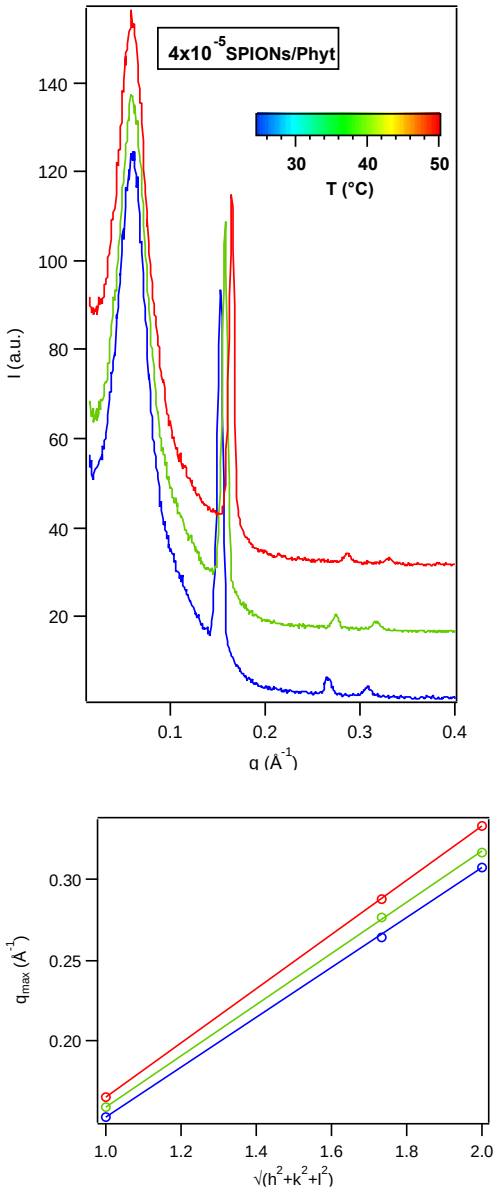

Figure S8. SAXS curves of phytantriol assembled with $4x10^{-5}$ SPIONs/Phyt and Miller index on q_{max} to determine variation of lattice parameter of hexagonal phase with temperature into the range from 25-50 °C.

Table S7. Lattice parameters, water channel radii and water volume fraction of phytantriol assembled with $4x10^{-5}$ SPIONs/Phyt

T (°C)	Lattice parameter (Å)	Water channel radii (Å)	Water volume fraction
25	41 (H_{II})	13	0.347
35	39 (H_{II})	12	0.326
50	38 (H_{II})	11	0.324

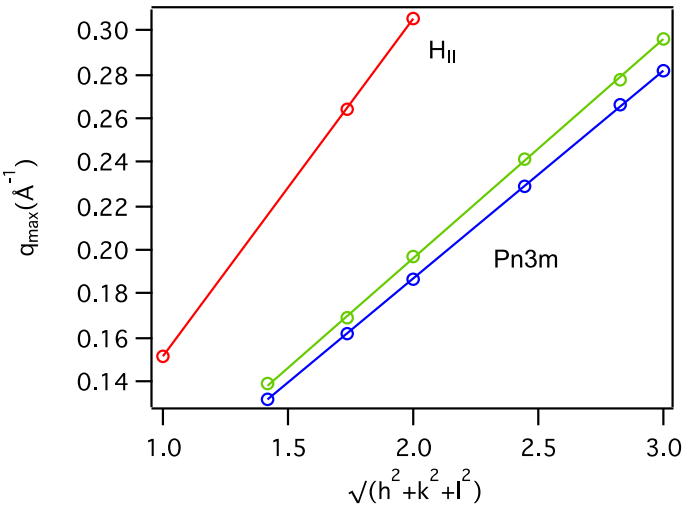

Figure S9. Q_{max} as function of Miller Index to calculate lattice parameter of phytantriol mesophases assembled with $1x10^{-5}$ AuNPs/Phyt

Table S8. Lattice parameters, water channel radii and water volume fraction of phytantriol assembled with $1x10^{-5}$ AuNPs/Phyt (data showed in main text)

T (°C)	Lattice parameter (Å)	Water channel radii (Å)	Water volume fraction
25	66	17	0.505
35	63	16	0.476
50	41	13	0.347

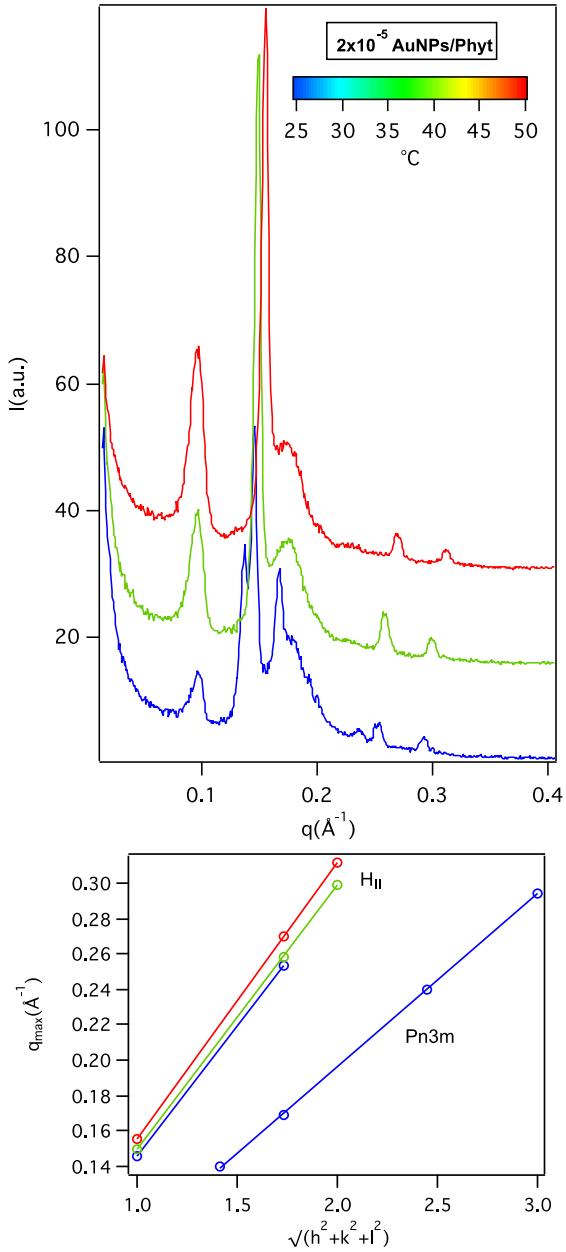

Figure S10: Lattice parameter of phytantriol mesophases assembled with $2x10^{-5}$ AuNPs/Phyt and lattice parameter into the range 25-50 °C.

Table S9. Lattice parameters, water channel radii and water volume fraction of phytantriol assembled with $2x10^{-5}$ AuNPs/Phyt varying the temperature.

T (°C)	Lattice parameter (Å)	Water channel radii (Å)	Water volume fraction
25	64 (Pn3m)	16	0.484
	43 (H_{II})	14	0.384
35	42	13	0.347
50	40	12	0.326

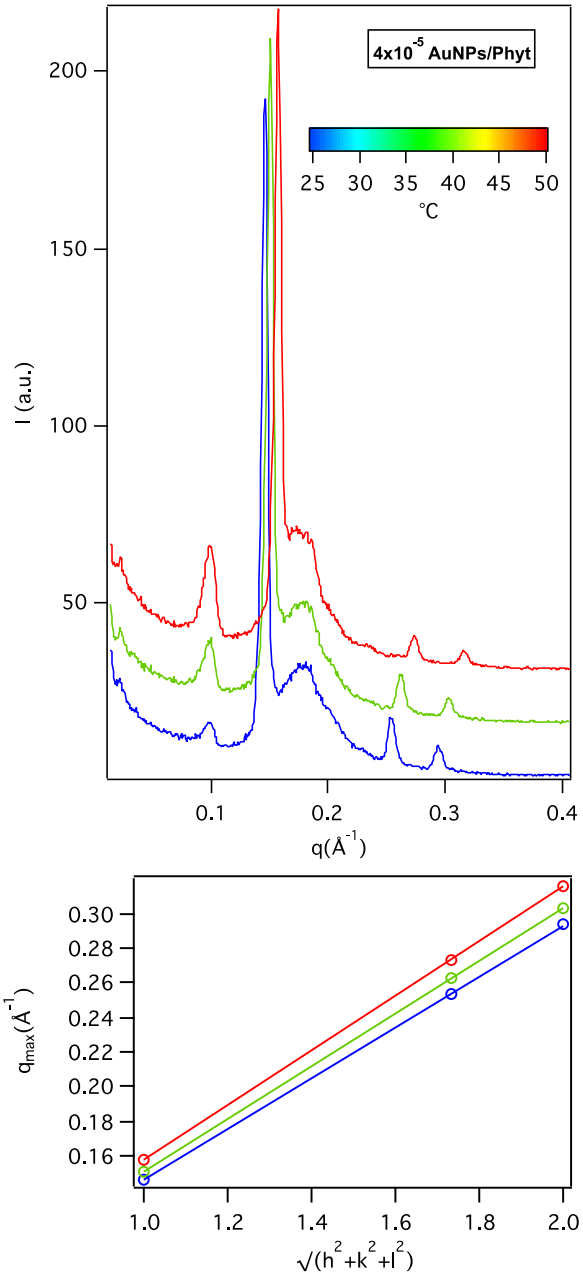

Figure S11: Lattice parameter of phytantriol mesophases assembled with $4x10^{-5}$ AuNPs/Phyt and lattice parameter into the range 25-50 °C.

Table S10. Lattice parameters, water channel radii and waer volume fraction of phytantriol assembled with $4x10^{-5}$ AuNPs/Phyt varying the temperature.

T (°C)	Lattice parameter (Å)	Water channel radii (Å)	Water volume fraction
25	43	14	0.384
35	41	13	0.347
50	40	12	0.326

S.7 SAXS: Thermal reversibility of phytantriol with SPIONs and AuNPs

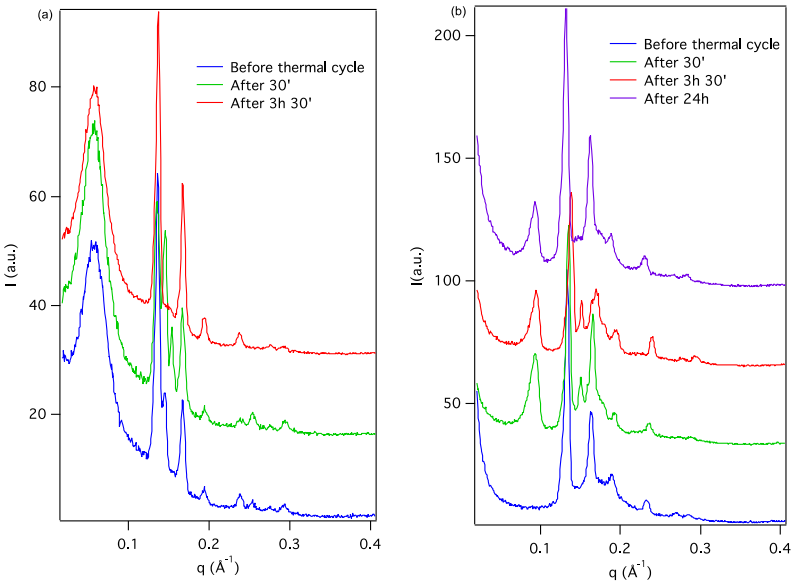

Figure S12. SAXS profiles of Phytantriol assembled with $1x10^{-5}$ (a) SPIONs/Phyt and (b) AuNPs/Phyt before and after the thermal cycle of 50 °C to detect the recovery of the lipid structures. Phyt/SPIONs assemblies shows a recovery of Bragg reflex after 3h and 30 minutes, while Phyt/AuNPs shows the recovery only after 24 h.

S.8-Supplementary Amplitude Sweep curves

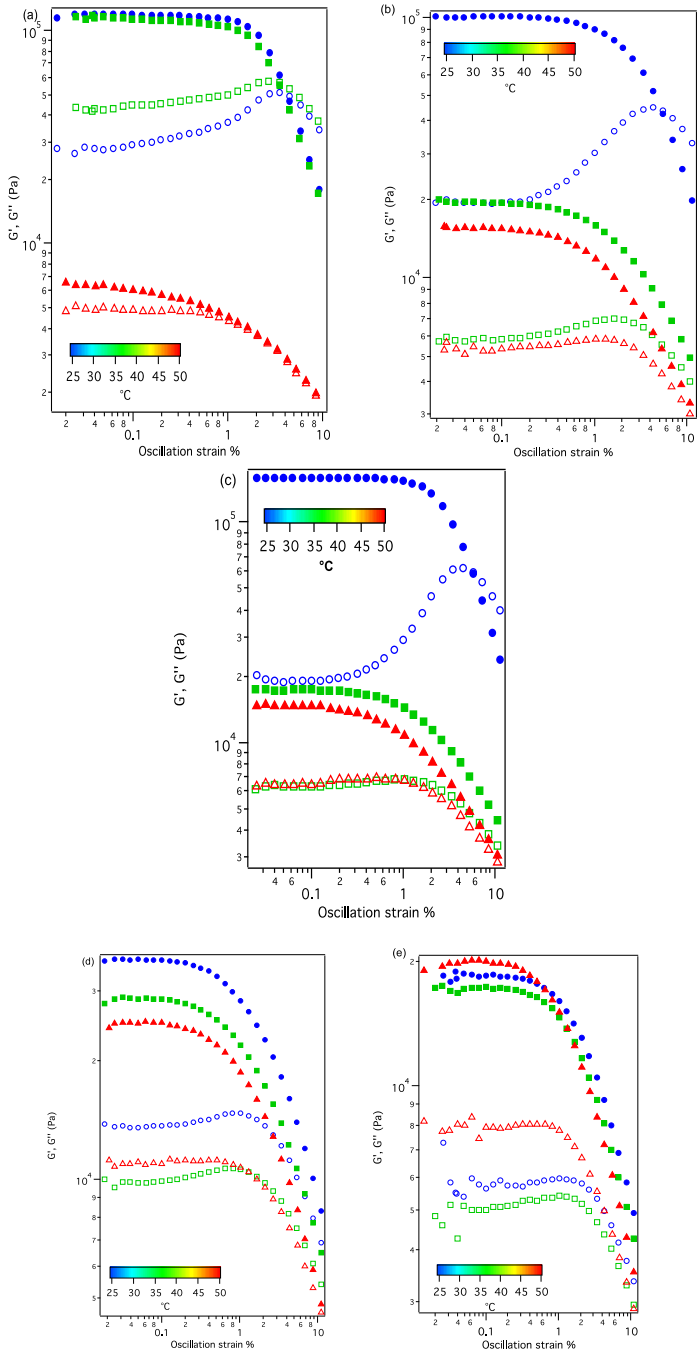

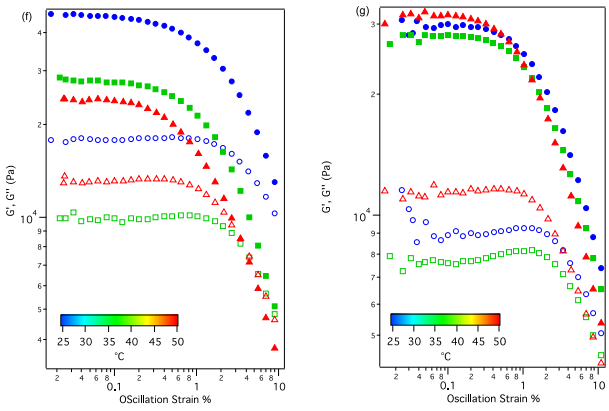

Figure S13. Amplitude sweep curves at 25 °C (blue), 35 °C (green) and 50 °C (red) for (a) phytantriol binary matrix, (b) $1x10^{-5}$ SPIONs/Phyt, (c) $1x10^{-5}$ AuNPs/Phyt, (d) $2x10^{-5}$ SPIONs/Phyt, (e) $2x10^{-5}$ AuNPs/Phyt, (f) $4x10^{-5}$ SPIONs/Phyt and (g) $4x10^{-5}$ AuNPs/Phyt.

S.9- Supplementary Frequency Sweep curves and data analysis

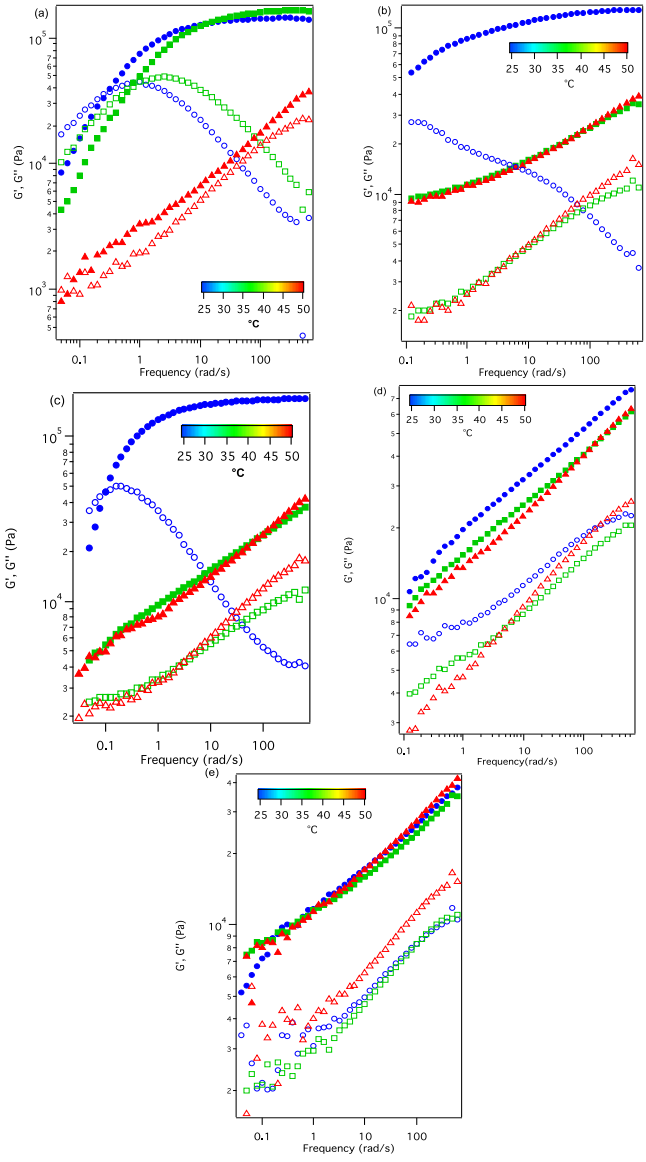

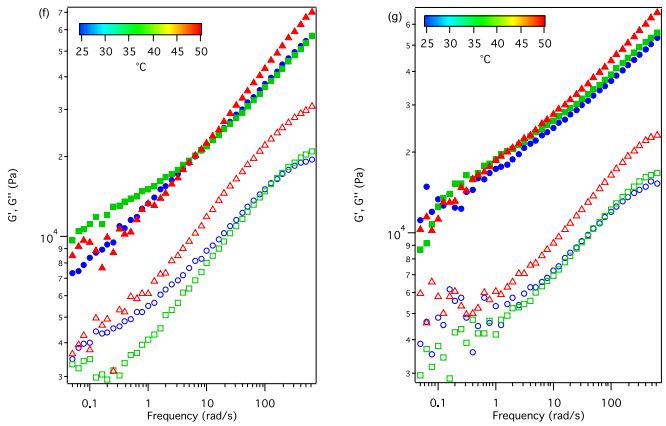

Figure S14. Frequency sweep curves at 25 °C (blue), 35 °C (green) and 50 °C (red) for (a) phytantriol binary matrix, (b) $1x10^{-5}$ SPIONs/Phyt, (c) $1x10^{-5}$ AuNPs/Phyt, (d) $2x10^{-5}$ SPIONs/Phyt, (e) $2x10^{-5}$ AuNPs/Phyt, (f) $4x10^{-5}$ SPIONs/Phyt and (g) $4x10^{-5}$ AuNPs/Phyt.

Frequency Sweep curves were fitted with three terms Maxwell Model, which are describe by Eq. (9-10):

$$G'(\omega) = \sum_{i=1}^{3} \frac{\omega^2 \tau_i^2}{1 + \omega^2 \tau_i^2} G_i^0 \qquad (9)$$

$$G''(\omega) = \sum_{i=1}^{3} \frac{\omega^2 \tau_i}{1 + \omega^2 \tau_i^2} G_i^0 \qquad (10)$$

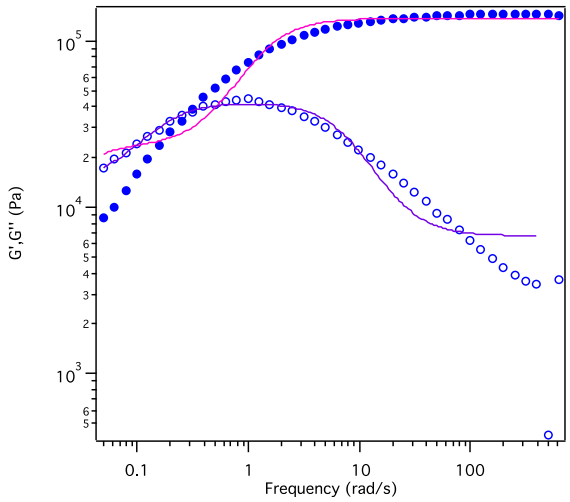

Figure S15. Three terms Maxwell model fitting of storage and loss modulus of Phyt/H_2O at 25°C.

The curve fitting of Phyt/H_2O rheological profiles with this model are displayed in Figure S13. Clearly, the adopted model does not fully describe the system, that is likely to be characterized by a high polydispersity. A suitable approach to describe polydisperse systems the continuum spectrum H(t) of relaxation times, which depends from G' and G'' through the following equations (11-12):

$$G'(\omega) = G_0 + \int_0^\infty H(\tau) \frac{(\omega\tau)^2}{1+(\omega\tau)^2} \frac{d\tau}{\tau} \qquad (11)$$

$$G''(\omega) = G_0 + \int_0^\infty H(\tau) \frac{\omega\tau}{1+(\omega\tau)^2} \frac{d\tau}{\tau} \qquad (12)$$

H(t) can be extracted according to different algorithms for the inversion of the equation (11-12) [9]. In the following section the continuum relaxation spectra of the experimental frequency sweep curves are displayed.

S.10-Continuum time relaxation spectra:

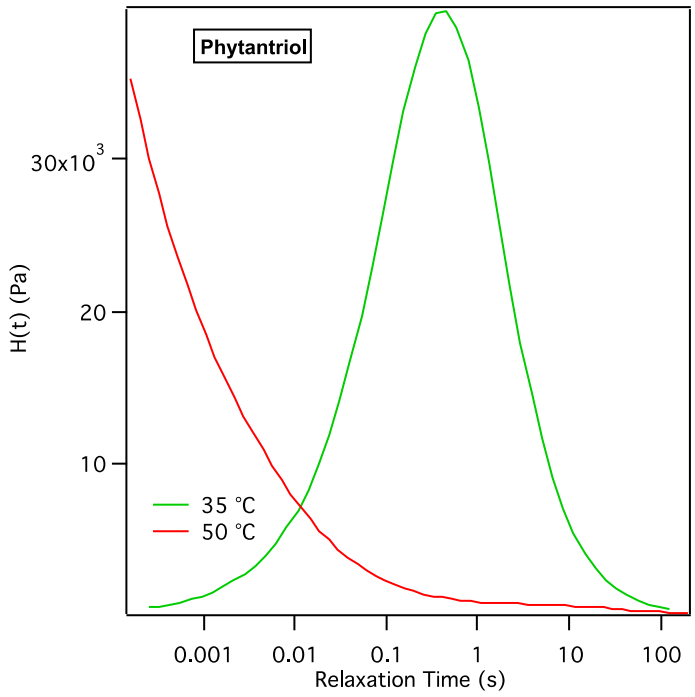

Figure S16: Continuum time relaxation spectra of Phyt/H_2O assemblies without nanoparticles at 35 °C (green curve) and 50 °C (red curve)

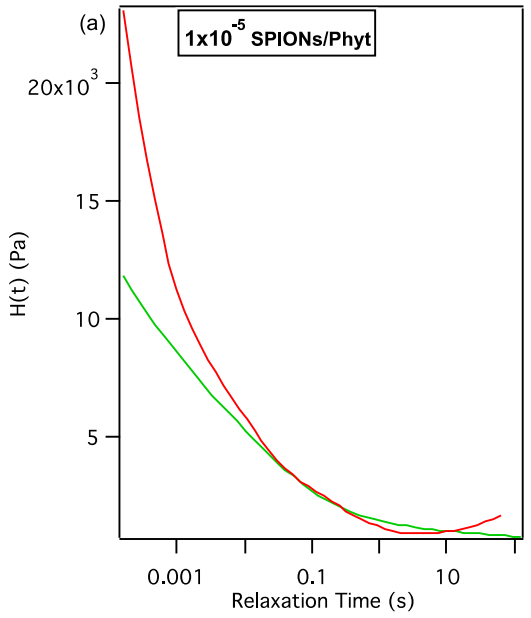
(a)
1x10-5 SPIONs/Phyt
20x10^3
15
10
5
H(t) (Pa)
0.001
0.1
10
Relaxation Time (s)

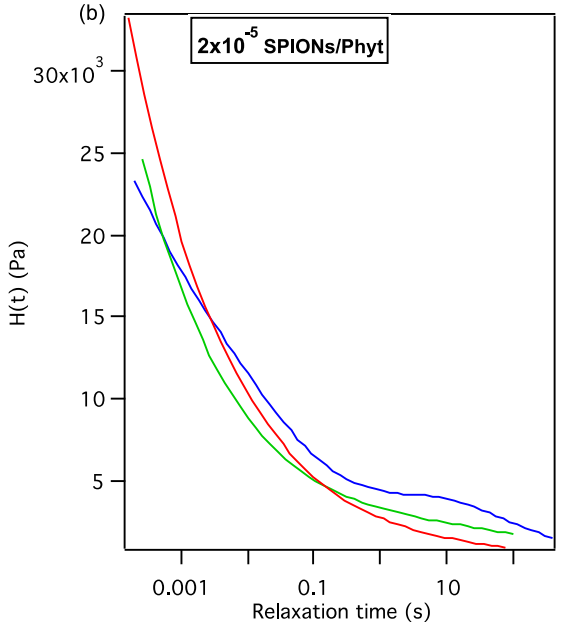
(b)
2x10-5 SPIONs/Phyt
30x10^3
25
20
15
10
5
H(t) (Pa)
0.001
0.1
10
Relaxation time (s)

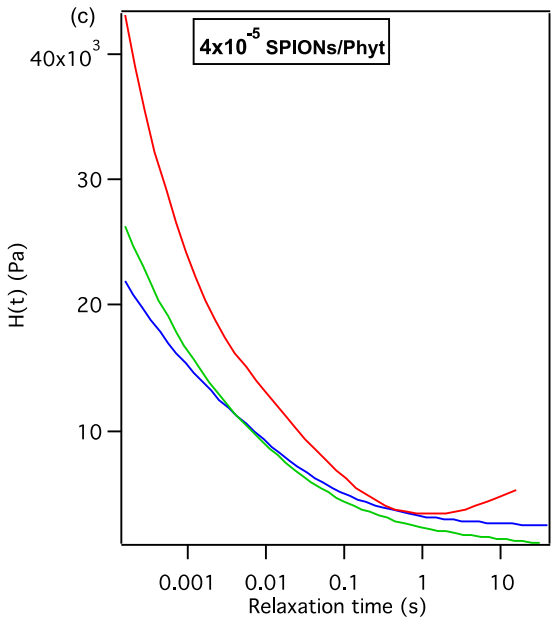

Figure S17. Continuum time relaxation spectra of phytantriol mesophases assembled with $1x10^{-5}$ SPIONs/Phyt (a), $2x10^{-5}$ SPIONs/Phyt (b) and $4x10^{-5}$ SPIONs/Phyt (c) at 25 (blue curves), 35 (green curves) and 50 °C (red curves). The curve of cubic mesophase at 25 °C doped with $1x10^{-5}$ SPIONs/Phyt is shown in main text.

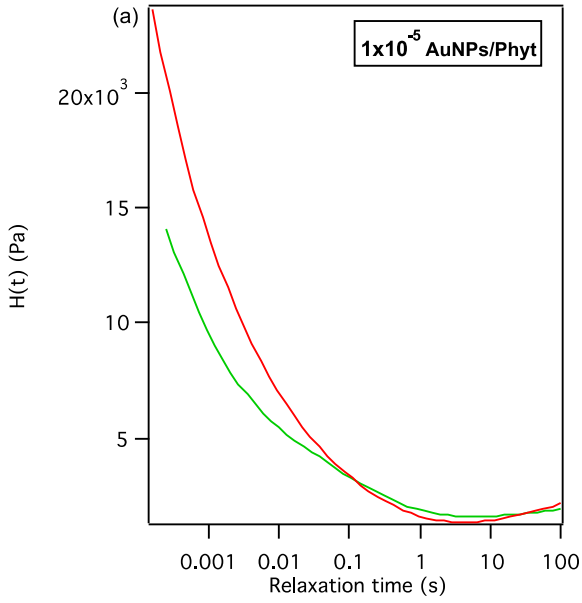
(a)
1x10-5 AuNPs/Phyt
20x10^3
15
10
5
H(t) (Pa)
0.001
0.01
0.1
1
10
100
Relaxation time (s)

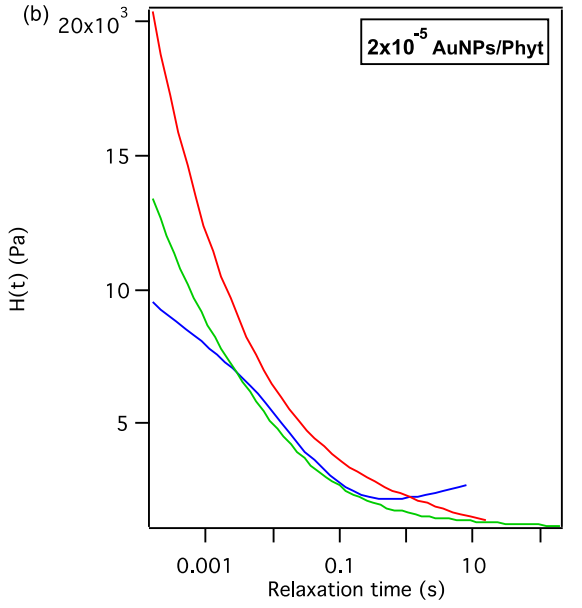
(b)
20x10^3
2x10-5 AuNPs/Phyt
15
10
5
H(t) (Pa)
0.001
0.1
10
Relaxation time (s)

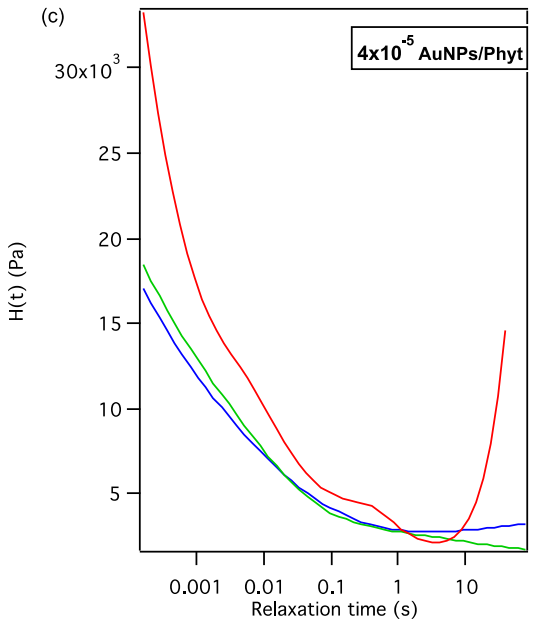

Figure S18. Continuum time relaxation spectra of phytantriol mesophases assembled with $1x10^{-5}$ AuNPs/Phyt (a), $2x10^{-5}$ AuNPs/Phyt (b) and $4x10^{-5}$ AuNPs/Phyt (c) at 25 (blue curves), 35 (green curves) and 50 °C (red curves). The curve of cubic mesophase at 25 °C doped with $1x10^{-5}$ AuNPs/Phyt is shown in main text.

S11- Plot of tanδ vs frequency

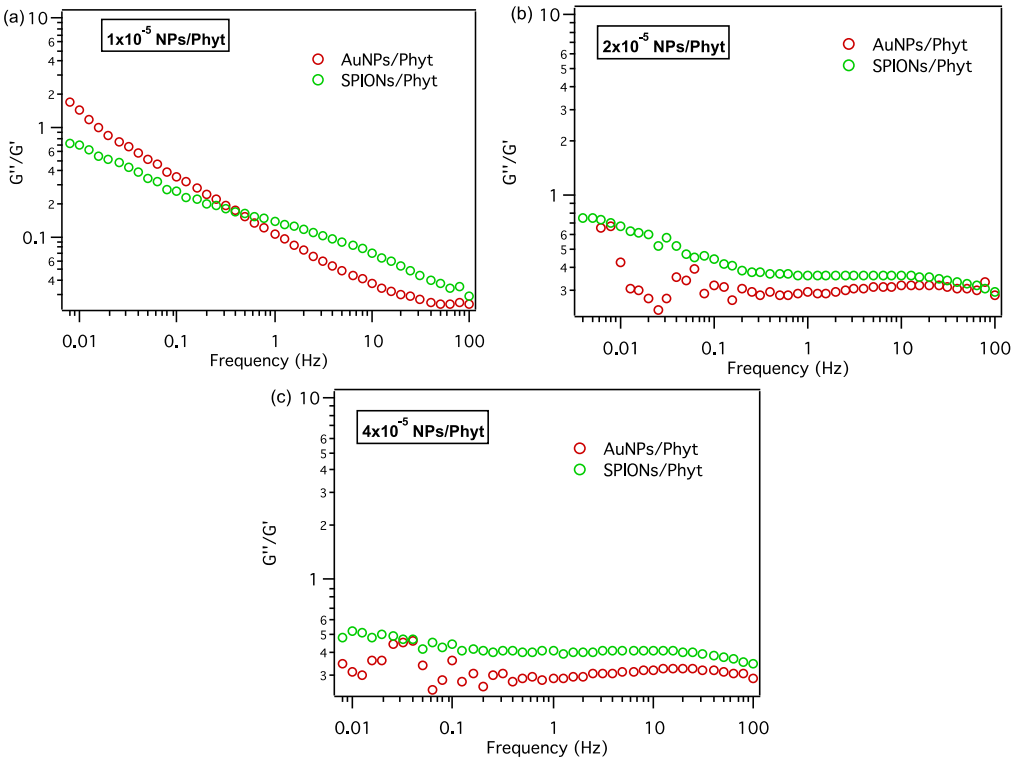

Figure S19: Loss and storage modulus ratio as function of frequency at 25 °C relative to mesophases doped with different amount of both nanoparticles; (a) shows tanδ curves of Phyt/NPs cubic mesophases to the lower amount of nanoparticles $1x10^{-5}$ NPs/Phyt, (b) shows tanδ curves of Phyt assembled with $2x10^{-5}$ NPs/Phyt and (c) Phyt hexagonal mesophases with $4x10^{-5}$ NPs/Phyt.

S.12 Frequency Sweep curves and relaxation spectra of Phytantriol assembled with oleic acid-oleylamine

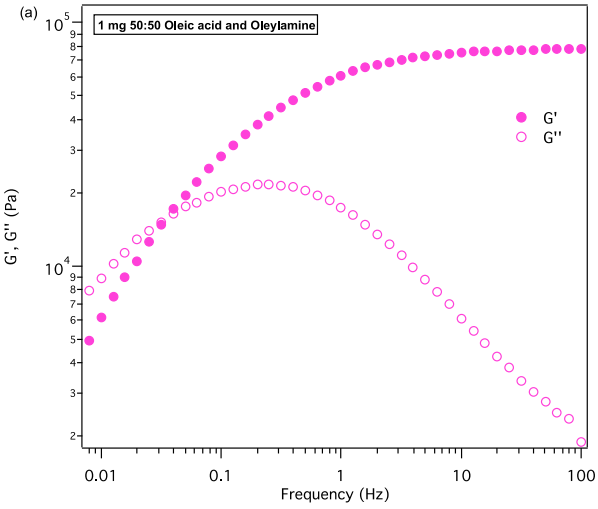

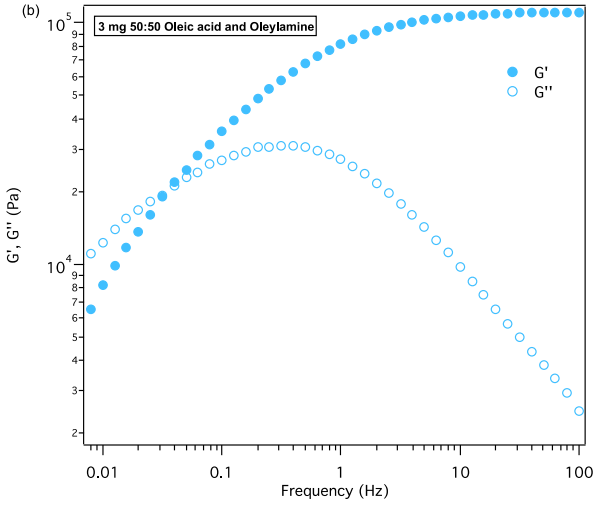

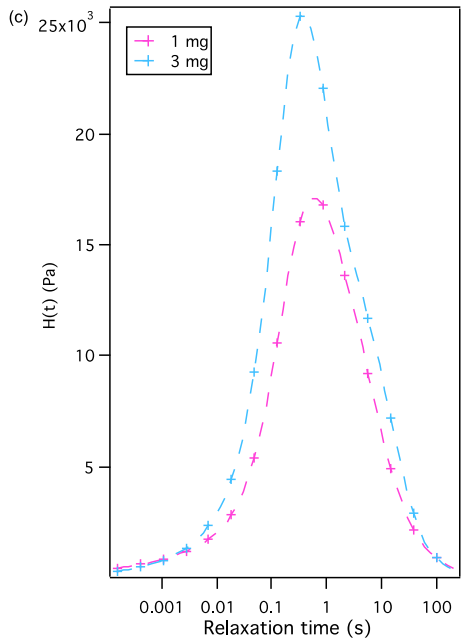

Figure S20: Storage (G') and Loss (G'') moduli of phytantriol assembled with different amount of stabilizer agents (oleic acid and oleylamine 50:50 ratio). (a) G' (purple full markers) and G'' (purple empty markers) of Phyt/1 mg of the mixture; (b) G' (cyan full markers) and G'' (cyan empty markers) of Phyt/3 mg of the mixture; (c) both relaxation spectra extracted by frequency sweep curves of (a) Phyt/1 mg and (b) Phyt/3 mg.

REFERENCES

[1] S.H. Sun, H. Zeng, Size-controlled synthesis of magnetite nanoparticles, J. Am. Chem. Soc. 124 (2002) 8204–8205. doi:10.1021/ja026501x.

[2] M. Brust, M. Walker, D. Bethell, D.J. Schiffrin, R. Whyman, Synthesis of thiol-derivatised gold nanoparticles in a two-phase liquid-liquid system, J. Chem. Soc. Chem. Commun. (1994) 801–802. doi:10.1039/C39940000801.

[3] R. Negrini, R. Mezzenga, Diffusion, molecular separation, and drug delivery from lipid mesophases with tunable water channels, Langmuir. 28 (2012) 16455–16462. doi:10.1021/la303833s.

[4] C.W. Reese, Z.I. Strango, Z.R. Dell, S. Tristram-Nagle, P.E. Harper, Structural insights into the cubic-hexagonal phase transition kinetics of monoolein modulated by sucrose solutions., Phys. Chem. Chem. Phys. 17 (2015) 9194–204. doi:10.1039/c5cp00175g.

[5] D. Marsh, Handbook of lipid bilayers, 2013. doi:10.1201/b11712.

[6] Y. Da Dong, I. Larson, T. Hanley, B.J. Boyd, Bulk and dispersed aqueous phase behavior of phytantriol: Effect of vitamin E acetate and F127 polymer on liquid crystal nanostructure, Langmuir. 22 (2006) 9512–9518. doi:10.1021/la061706v.

[7] M. Kotlarchyk, S. Chen, Analysis of small angle neutron scattering spectra from polydisperse interacting colloids, J. Chem. Phys. 79 (1983) 2461. doi:10.1063/1.446055.

[8] D. Begriff, A. Hand, D. Zerlegung, D. Fraktionierung, A. Grund, D. Fraktionierbarkeit, S. Kurven, S.- Dinger, I. Authenticated, D. Date, Die Verteilungsfunktionen polymolekularer Stoffe und ihre Ermittelung durch Zerlegung in Fraktionen ., 70 (1940) 155–193.

[9] J. Honerkamp, J. Weese, A nonlinear regularization method for the calculation of relaxation spectra, Rheol. Acta. 32 (1993) 65–73. doi:10.1007/BF00396678.

Paper VII

On the thermotropic and magnetotropic phase behavior of lipid liquid crystals containing magnetic nanoparticles

M. Mendozza, C. Montis, L. Caselli, M. Wolf, P. Baglioni and D.Berti, *Nanoscale*, 2018, 10 (7), 3480-3488

Nanoscale

PAPER

View Article Online
View Journal | View Issue

Cite this: *Nanoscale*, 2018, **10**, 3480

On the thermotropic and magnetotropic phase behavior of lipid liquid crystals containing magnetic nanoparticles†

Marco Mendozza, [a] Costanza Montis, [a] Lucrezia Caselli, [a] Marcell Wolf,[b] Piero Baglioni[a] and Debora Berti *[a]

Received 14th November 2017,
Accepted 26th January 2018

DOI: 10.1039/c7nr08478a

rsc.li/nanoscale

The inclusion of superparamagnetic iron oxide nanoparticles (SPIONs) in lipid mesophases is a promising strategy for drug-delivery applications, combining the innate biocompatibility of lipid architectures with SPIONs' response to external magnetic fields. Moreover, the organization of SPIONs within the lipid scaffold can lead to locally enhanced SPIONs concentration and improved magnetic response, which is key to overcome the current limitations of hyperthermic treatments. Here we present a Small-Angle X-ray Scattering (SAXS) structural investigation of the thermotropic and magnetotropic behavior of glyceryl monooleate (GMO)/water mesophases, loaded with hydrophobic SPIONs. We prove that even very low amounts of SPIONs deeply alter the phase behavior and thermotropic properties of the mesophases, promoting a cubic to hexagonal phase transition, which is similarly induced upon application of an Alternating Magnetic Field (AMF). Moreover, in the hexagonal phase SPIONs spontaneously self-assemble within the lipid scaffold into a linear supraparticle. This phase behavior is interpreted in the framework of the Helfrich's theory, which shows that SPIONs affect the mesophase both from a viscoelastic and from a structural standpoint. Finally, the dispersion of these cubic phases into stable magnetic colloidal particles, which retain their liquid crystalline internal structure, is addressed as a promising route towards magneto-responsive drug-delivery systems (DDS).

Introduction

Lipid self-assembly into lamellar and non-lamellar architectures is ubiquitous in natural systems,[1] the most prominent example being the lamellar structural unit of cell membranes. Synthetic lipid assemblies have been used to model and understand membrane-related processes in simplified architectures[2,3] and to engineer compartmentalized systems that can have numerous applications, especially in the biomedical field. Based on their molecular architecture and on experimental conditions, lipids show a rich polymorphism, with structures where both hydrophobic and hydrophilic domains occur. The volume fractions and the morphology of these domains depend on the phase structure and phase transitions can be promoted by tuning control parameters, such as temperature, pressure and water content.

Several features of lipid assemblies lend themselves to the development of nanostructured vehicles for the encapsulation and release of drugs[4–6] or nucleic acids.[7,8] Structural change in lipid mesophase is caused by some external stimuli like temperature, pH[9] and magnetic field[10,11] or, in other case, adding additives that modify lipid assembly.[12,13]

Glyceryl monooleate (GMO) has been extensively studied for its biocompatibility, biodegradability and variegate phase structure, which depends on water content and temperature. At room temperature, the GMO/H_2O mixture displays a lamellar phase L_c for low water amounts and a bicontinuous cubic phase gyroid (*Ia3d*) and diamond (*Pn3m*) at relatively higher water contents. These mesophases have a high degree of symmetry and periodical water nanochannels,[14] whose geometry can be described using infinite periodical minimal surfaces (IPMS) or, in other words, a triply periodically surface with zero mean curvature. The three possible IPMSs described by Schoen and Schwartz are the gyroid (G), diamond (D) and primitive (P), with spatial groups *Ia3d*, *Pn3m* and *Im3m*, respectively, all of them observed for GMO cubic phases, depending on the experimental conditions. While the phase

[a]*Department of chemistry and CSGI, University of Florence, Via della Lastruccia 3, Sesto Fiorentino, 50019 Florence, Italy. E-mail: debora.berti@unifi.it*
[b]*Institute of Inorganic Chemistry, Graz University of Technology, Stremayrgasse 9/IV, 8010 Graz, Austria*

†Electronic supplementary information (ESI) available: Detailed Materials and methods section, additional SAXS data, derivation of principal equation and DLS analysis. See DOI: 10.1039/c7nr08478a

diagram of GMO/H_2O binary system is well-established, the structural effects of additives on GMO-based systems have been the subject of more recent studies addressing the relevant phenomena connected with the topological variations of GMO mesophases designed for drug delivery, *e.g.*, in drug loading-release processes[15] or protein crystallization.[16,17]

Concerning this topic, the inclusion of magnetic nanoparticles (SPIONs) in lipid mesophases is of particular interest, giving the possibility to endow the lipid matrix with responsiveness to magnetic fields. Recently, it has been shown that hydrophilic SPIONs embedded in monolinolein liquid crystals control the structural organization of the lipid mesophase when exposed to an external static magnetic field.[18–20]

A prominent relevance, particularly for biomedical applications, is SPIONs responsiveness to alternating magnetic fields (AMF). In this respect, the inclusion of SPIONs into lipid scaffolds is interesting from at least two different standpoints. First, as a possible way to overcome the necessity of high SPIONs concentration in tissues, to abide by the so-called Brezovich criterion, *i.e.*, the exposure safety limit to magnetic fields for the application of SPIONs in hyperthermia-based medical treatments.[21–23] Secondly, as a promising strategy for the development of biocompatible smart lipid-based drug delivery systems (DDS) responsive to static and alternating magnetic fields.

The responsivity of SPIONs to alternating magnetic fields (AMF) has been extensively addressed for applications in hyperthermia-based therapies. SPIONs concentrated into tumor tissues, *e.g.* thanks to a DDS or to simple enhanced permeability and retention (EPR) effect, act as local heaters, if subjected to AMF, due to Brownian and Néel relaxations, eventually causing the ablation of cells or tissues that need to be removed. To reach a sustainable efficiency, the local concentration of SPIONs in the target tissues should reach a level which is virtually unachieaveble.[21] This limitation has been tackled either by modifying the morphology of NPs[22] or by employing clusters of NPs,[24] rather than separated NPs. The spontaneous organization of SPIONs in lipid scaffolds of different architectures represents a strategy to achieve a locally enhanced SPIONs' concentration, maintaining a fine control on the particle arrangement and, thus, on their overall magnetic response.

The inclusion of SPIONs in lipid assemblies, particularly liposomes to form magnetoliposomes,[25–27] has been reported in the literature. When embedded in DPPC (dipalmitoyl-phosphatidylcholine) liposomes, SPIONs act as local heaters upon application of a low-frequency alternating magnetic field (LF-AMF) and induce a gel-to-liquid-crystalline transition of the bilayer, with enhanced permeability and consequent release of molecules entrapped in the lumen.

In a previous work,[10] whose findings were also confirmed by Szlezak *et al.*,[4] we demonstrated that a GMO cubic phase doped with hydrophobic SPIONs displays a similar AMF-responsivity, showing burst release of a model hydrophilic drug contained in the water channels of the mesophase when exposed to a LF-AMF. At variance from the gel to liquid crystalline phase transition occurring in DPPC magnetoliposomes, the structural variations on the cubic lipid scaffold implied in the controlled release of hydrophilic drugs from water channels are not yet clear.

A fundamental comprehension of the effect of SPIONs on phase behavior of lipid mesophases is key to fully explore the potential of these hybrid devices, both for hyperthermia and for controlled release applications.

In this contribution, we investigate the structural effects of the inclusion of hydrophobic SPIONs towards the polymorphic behavior of GMO assemblies in water excess. The phase behavior of GMO/H_2O/SPIONs is investigated as a function of the SPIONs percentage with respect to GMO and as a function of temperature. The arrangement of the SPIONs in lipid scaffolds of different geometries is investigated as well. The structure of GMO/H_2O/SPIONs hybrid architectures in different conditions (SPIONs amount and temperature) is interpreted according to simple thermodynamic considerations in the framework of Helfrich's theory, to understand the effect of SPIONs on the structural and viscoelastic features of the lipid assemblies and devise a simple predictive model for SPIONs–lipids interaction. Finally, to explore the applicative potential of these hybrid architectures, we investigate the thermotropic behavior of dispersed GMO/water/SPIONs assemblies (magnetocubosomes), and we perform an on-line investigation on the structural responsiveness of bulk GMO/water/SPIONs assemblies to LF-AMF, monitoring the magnetotropic response of the system.

Results and discussion

SPIONs inclusion in GMO mesophases

Hydrophobic Fe_3O_4 magnetic nanoparticles (SPIONs) passivated with oleic acid and oleylamine were synthesized according to a well-established protocol[28,29] (see ESI for details†). The SAXS curves of the as-prepared dispersions (2.19 mg mL^{-1} Fe_3O_4 from ICP-AES) were diluted 1 : 3 in hexane and measured to infer the nanoparticle size with two different approaches, a model-free Guiner fit (radius 18 ± 3 Å[30]) and a Schulz polydisperse spheres form factor fit (radius 20 ± 2 Å, see ESI†). Generally, lipid bilayers have thicknesses around 40 Å; some theoretical reports identify a threshold of 60 Å for nanoparticles' diameter not to destroy the lipid architecture,[31] even if the final effect is strictly dependent on hydrophobic/hydrophilic nature of NPs.[32] The synthesized SPIONs have therefore an ideal size to be embedded in a lipid membrane without disrupting the bilayer.

GMO cubic phases (50% w/w lipid–water fraction) were prepared, as described in the Experimental section (see ESI†), with different amounts of SPIONs, ranging from 0.23% w/w to 1.1% w/w with respect to GMO quantity. If expressed as number of nanoparticles per lipid unit surface, or as number of lipid molecules per nanoparticle (considering for the cubic phase a specific area of 400 m^2 g^{-1} (ref. 33), see Table 1) these

Table 1 GMO/H_2O/SPIONs samples composition: SPIONs weight percentage with respect to GMO amount (w/w% SPIONs); number of SPIONs per GMO/H_2O cubic phase area unit (N_{SPIONs}/A_{GMO}) and volume unit (N_{SPIONs}/V_{GMO}); number of GMO molecules per SPION (N_{GMO}/N_{SPIONs})

w/w% SPIONs	N_{SPIONs}/A_{GMO} (μm^{-2})	N_{SPIONs}/V_{GMO} (μm^{-3})	N_{GMO}/N_{SPIONs}
0.23	~46	~17 312	~91 743
0.47	~93	~35 000	~45 248
0.94	~188	~70 313	~22 522
1.1	~217	~81 250	~19 493

quantities result in relatively low NP concentrations, for all the investigated samples.

Fig. 1 shows the SAXS profiles of the mesophases in water at 25 °C in the absence and in the presence of increasing amounts of SPIONs. GMO 50% w/w is a *Pn3m* coexisting with water excess and represents the maximum swelling of this lipid at room temperature. When SPIONs are inserted in the liquid crystalline (LC) phase at 0.23–0.47% w/w SPIONs/GMO, the scattering peaks that describe the spatial correlation of the diamond cubic structure are preserved, but shifted to higher scattering vectors with respect to the binary system, indicating a shrinking of the liquid crystalline phase. At 0.94% w/w Fe_3O_4, the scattering profile shows the coexistence of the diamond cubic and another phase, whose nature, inverted hexagonal (H_{II}), becomes clear for higher amounts of magnetic nanoparticles. It has been reported that a *Pn3m*-H_{II} phase transition might occur upon perturbation of the lipid arrangement due to addition of alkanes or alkenes,[12] or inclusion of peptides.[34–36] To rule out that this transition is due to the partitioning of the NPs' coating agents (oleic acid and oleylamine) into the GMO bilayer, we performed a control experiment where the maximum amount of oleic acid and oleylamine was directly added to GMO without NP at 25 °C, yielding the profile of the diamond phase (see ESI† for details). No other components are present in GMO-SPIONs samples, since the SPIONs dispersions are separated from precursors (see Materials and methods section, ESI†) and milliQ water is employed for sample preparation.

Therefore, the structural transition observed for GMO is due to the insertion of SPIONs in the lipid scaffold; this NP-promoted transition could be relevant in the framework of a better understanding of nano-bio interfaces and possible toxic effects caused by SPIONs.[37] This finding is also consistent with recent works of Briscoe and coworkers,[38] who demonstrated a noteworthy effect of silica nanoparticles in shifting the phase boundaries between hexagonal H_{II} and lamellar L_α phases in phospholipids assemblies.

As clearly shown in Fig. 1, the SAXS curves in the presence of SPIONs display an additional peak at low q, attributable to spatial correlations of the SPIONs in the lipid matrix,[10] whose intensity increases as the amount of nanoparticles increases. The existence of a correlation distance, of about 110–120 Å if calculated as $2\pi/q_{max}$, implies that SPIONs exhibit a quasi-ordered arrangement within the lipid scaffold. The relatively large correlation distance can be justified taking into

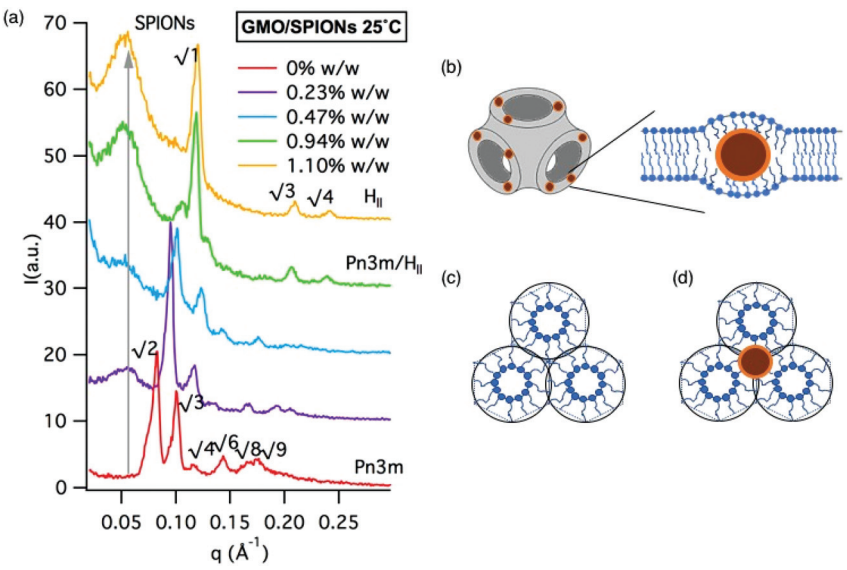

Fig. 1 (a) SAXS profiles of GMO 50% w/w water liquid crystalline phases in the presence of different SPIONs amounts: from bottom to top SAXS curves of the samples with increasing SPIONs percentages (0; 0.32; 0.47; 0.94; 1.1% w/w with respect to GMO amount) are displayed with suitable offsets; (b) (c) (d) schemes representing the effect of the SPIONs on the packing frustration energy: (b) when inserted in a lipid bilayer, the SPIONs increase the packing frustration and bring an energy penalty caused by the stretch of lipid chains to fill the voids along the equatorial position of nanoparticles, (c) in the hexagonal phase the chain ends would fall on the circles. As a result, the major packing frustration is localized in the void spaces of the cylindrical structure, (d) hexagonal phase with SPIONs: the previous frustration packing is released, with the hydrophobic nanoparticles localized in the void spaces.

account a contribution due to the spatial organization imposed by the lipid phase geometry and, probably, an additional contribution due to magnetic dipolar and van der Waals interactions between the SPIONs, similarly to what observed for concentrated dispersions of magnetic nanoparticles upon solvent evaporation.[39] GMO/H_2O/SPIONs systems are peculiar both in terms of the polymorphic behavior of the GMO lipid matrix induced by the presence of SPIONs and in terms of SPIONs ordered arrangement within the lipid scaffold imposed by GMO phase geometry in water excess.

In order to rationalize the *Pn3m*-H_{II} phase transition induced by the NPs from a thermodynamic point of view, we can write the total free energy of a lipid bilayer g_T as composed of three terms:[33] g_C free energy of elastic curvature, g_P frustration packing free energy and g_{inter} interaction energy term, that is generally negligible.

$$g_T = g_C + g_P + g_{inter} \quad (1)$$

Considering the energy difference between the hexagonal (final) and cubic (initial) phase, the variation of the total free energy of the bilayer, connected with the cubic to hexagonal phase transition Δg_T is:

$$\Delta g_T = g_{H_{II}} - g_{Pn3m} = \Delta g_C + \Delta g_P \quad (2)$$

It is known that the hexagonal phase[40] is characterized by a higher frustration packing energy than the bicontinuous cubic phase ($\Delta g_P > 0$), and by a lower energy of elastic curvature ($\Delta g_C < 0$).[41] Taking into account that, in the absence of SPIONs, the cubic to hexagonal phase transition is already favored according to the elastic contribution (g_C), we can hypothesize that a major effect of the SPIONs on the free energy of the bilayer in the hexagonal phase is a decrease in the frustration packing energy. In fact, above a relatively low NP concentration threshold, we observe only a hexagonal phase. In a simplistic approach, g_P can be described with a harmonic oscillator-like equation:[40] its contribution arises from lipid chains that are stretched or compressed with respect to their relaxed state. In the presence of NPs embedded in a *Pn3m* structure, the lipids close to a NP experience a packing frustration due to the fact that their hydrocarbon chains stretch to fill the hydrophobic cavities (Fig. 1b). The increase of frustration packing contribution is thus a possible driving force to the cubic to hexagonal phase transition: NPs can fill the voids of cylindrical structure (Fig. 1d), without any stretching penalty for the lipid hydrocarbon chains (Fig. 1c). It has been shown that larger hydrophilic nanoparticles dramatically impact the organization of lipid mesophases, eventually driving completely different structural effects.[42] Clearly, in the above-described behaviour, the hydrophobicity of the SPIONs and their size matching with the lipid bilayer thickness, have a major role.

Thermotropic behavior of GMO-SPIONs assemblies

Fig. 2a reports the well-known phase diagram of GMO as temperature and water percentage are varied (readapted with permission from ref. 33) compared to the phase behavior of GMO/SPIONs/water 50% w/w (Fig. 2b), as temperature and SPIONs content are varied. In the absence of SPIONs, the *Pn3m* to H_{II} transition occur at 90 °C; in the presence of SPIONs, the transition temperature, Fig. 2b, decreases proportionally to the amount of NPs, down to 25 °C, for the highest Fe_3O_4% w/w.

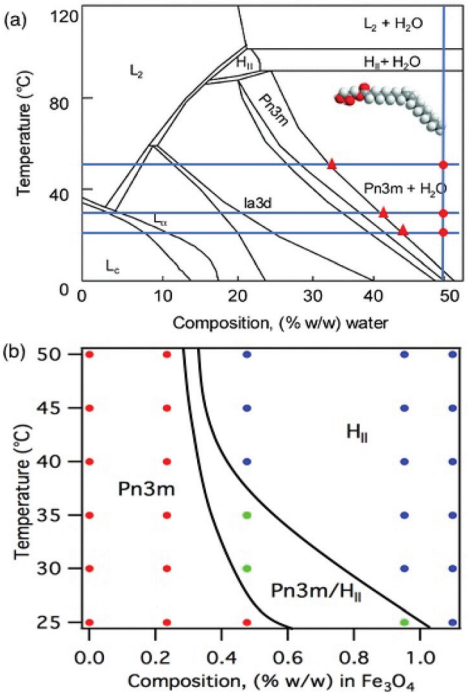

Fig. 2 (a) Phase diagram of GMO (readapted with permission from ref. 33). (b) Phase diagram of GMO/SPIONs at 50% w/w water content: structural dependence on temperature (°C) and on SPIONs content (% w/w with respect to GMO amount).

To interpret this behavior, we first focus on the binary system. In the range 25 °C–50 °C, GMO 50% w/w H_2O system keeps a bicontinuous diamond cubic phase structure, with the characteristic peaks progressively shifted to higher scattering vectors, with lattice parameters of 104 ± 2 Å, (25 °C), 96 ± 2 Å (35 °C), 84 ± 1 Å (50 °C), which fully match the literature results[43] (see ESI† for details). If we adopt the previously described thermodynamic approach (eqn (2)), in this case Δg_T represents the variation of the free energy of GMO cubic phase between 50 °C (final state) and 25 °C (initial state). In the absence of a phase transition, Δg_P dependence on temperature is minor.[41] Thus, Δg_T can be considered in first approximation as only dependent on the variation of the free energy of elastic curvature Δg_C. The Helfrich's free energy of elastic curvature g_C [44] adapted for a lipid bilayer can be expressed as:

$$g_C = 2\kappa_B(H - H_0{}^B)^2 + \kappa_G^B K \quad (3)$$

with $H_0{}^B$ and H mean spontaneous and mean curvatures respectively, in this case equal to zero,[45] κ_B and κ_G^B bending and Gaussian elastic moduli and K Gaussian curvature. g_C can be thus considered dependent on K and κ_G^B, which are related

to the viscoelastic properties of the lipid membrane. The Gaussian curvature K can be related to the experimentally observed lattice parameters d of the *Pn3m* cubic phase through the Gauss–Bonnet theorem[1] $\langle K\rangle_0 = 2\pi\chi/\sigma d^2$, where K_0 is the mean Gaussian curvature to the mid-plane of lipid bilayer, χ is the Euler–Poincare parameter ($\chi_{Pn3m} = -2$) and σ is a topological constant ($\sigma_{Pn3m} = 1.919$).[1] In the absence of SPIONs, a linear decrease of the GMO *Pn3m* lattice parameter d with temperature increase, with slope −0.8 Å °C^{-1} (see ESI† for details) is observed, which, taking into account eqn (3) in combination with the Gauss–Bonnet theorem, is with a concomitant decrease in free energy of elastic curvature g_C. Thus, in the absence of any constraint due to SPIONs, as temperature increases the hydrophobic chains splay out from each other[45,46] and adopt a new curvature, due to a higher flexibility of the membrane, that leads to a decrease of lattice parameters.

If we consider the ternary sample containing the lowest amount of SPIONs (0.23% w/w), in the range 25 °C–50 °C the *Pn3m* lipid structure is preserved (see Fig. 2). The same thermodynamic considerations discussed are thus applied. Interestingly, in this case a milder dependence of the lattice parameter on temperature is observed, with a slope of −0.25 Å °C^{-1} (see ESI† for details). The lower sensitivity of the lattice parameters to temperature means that, in the presence of SPIONs, the decrease of the free energy of elastic curvature g_C is lower. Clearly, the SPIONs do not have effect only on the frustration packing free energy, as discussed in the previous paragraph, but affect also the viscoelastic properties of the membrane, through g_C. The effect of nanoparticles on the elastic properties of lipid mono-bilayer has been recently addressed, highlighting either softening or stiffening effects on the lipid phases depending on physico-chemical properties of NPs, generally considered with a hydrophilic coating.[47] In this case the modifications of the viscoelastic properties of the membrane are provoked by hydrophobic SPIONs embedded in the membrane.

Finally, we focused our attention on the sample whose phase transition is in the range 30–40 °C, close to physiological temperature, 0.47% w/w of SPIONs.

In Fig. 3 the SAXS profiles of 50% w/w GMO (25–35–50 °C Fig. 3a) and this latter sample (at 25–30–35–40–45–50 °C, Fig. 3b) are displayed. For GMO/SPIONs 0.47% w/w, the diamond cubic phase, which is the only present at 25 °C, is preserved at 30 and 35 °C, with a minor sensitivity of the lattice parameter on the temperature and the appearance of some extra peaks. Due to the coexistence with an inverse hexagonal phase H_{II}, these extra peaks are not ascribable to the *Pn3m* structure. The cubic phase signature completely disappears in the range 35–40 °C and since 40 °C only the H_{II} phase can be observed. With the same thermodynamic considerations, the total free energy of lipid bilayer Δg_T can be written in terms of Δg_P and Δg_C contributions, which can be separately considered. As already pointed out, in the absence of phase transition g_P exhibits a minor temperature dependence.[41]

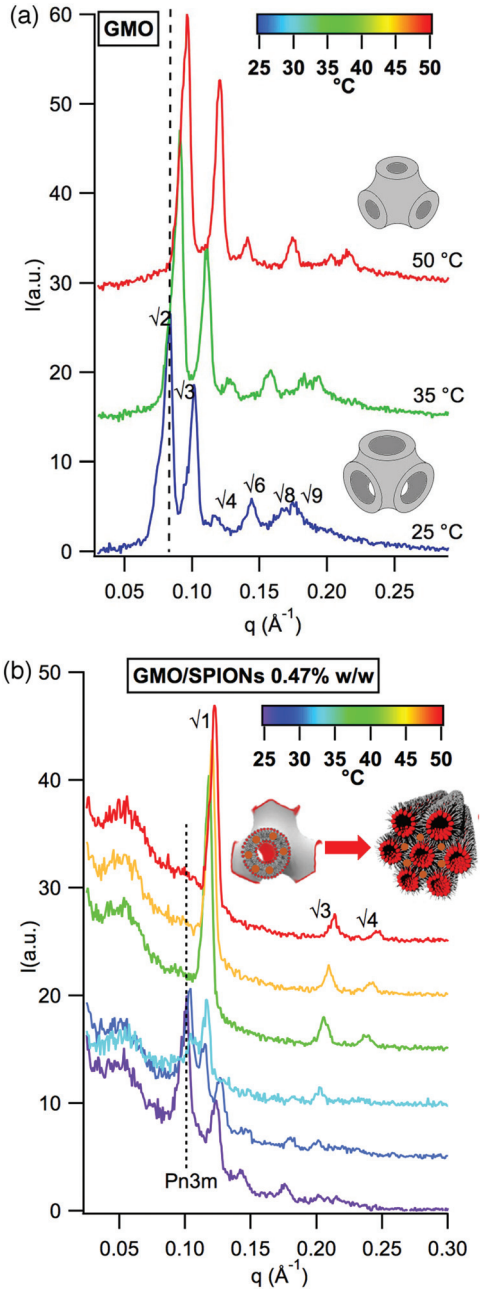

Fig. 3 (a) SAXS curves of bulk cubic phase of GMO assembled in water at 25–35–50 °C with 50% w/w water. Water channel shrink enhancing temperature. (b) SAXS curves of GMO cubic phase assembled with 0.47% w/w SPIONs and 50% w/w water at 25–30–35–40–45–50 °C Phase transition from cubic to hexagonal phase was observed above 35 °C.

Thus, Δg_P (H_{II}-*Pn3m*) can be considered as a temperature independent, positive value. Concerning Δg_C, the difference in the free energy of elastic curvature between the hexagonal (final) and the cubic (initial) phase,[48] can be expressed through a relatively simple equation (eqn (4), whose extended derivation is reported in the ESI†), being the elastic moduli of the monolayers κ and κ_G related to the corresponding parameters of symmetric bilayers[40] through $\kappa_B = 2\kappa$ and $\kappa_G^B = 2(\kappa_G - 2H_0\kappa l_c)$, and

taking into account that $K = 0$ for H_{II} while $H = 0$ for *Pn3m* at the bilayer mid-plane.

$$\Delta g_C = 4\kappa {H_{H_{II}}}^2 - 2K_{Pn3m}(\kappa_G - 2H_0\kappa l_c). \quad (4)$$

Due to the previous considerations, Δg_C for a *Pn3m* to H_{II} transition is always negative. Thus, being the Δg_P term positive and practically invariant in the 25–50 °C temperature range,[41] the occurrence of *Pn3m*-H_{II} phase transition can only be ascribed to the free energy of elastic curvature compensating and overcoming the frustration packing free energy at a defined temperature (eqn (5)):

$$|\Delta g_P| < |\Delta g_C(T)| \quad (5)$$

By combining eqn (4) and (5) we can write (eqn (6)):

$$\frac{\Delta g_P}{\kappa} + 4H_{H_{II}}^2 < 2K_{Pn3m}\left(\frac{\kappa_G}{\kappa} - 2H_0 l_c\right) \quad (6)$$

κ, κ_G, H_0 decrease if temperature increase. κ and κ_G are related to the membrane elasticity while H_0 depends on the molecular geometry. Ultimately, the prevalence of a H_{II} or a *Pn3m* phase depends on the balance between these two contributions, H_0 and κ_G/κ. In the GMO cubic phase without NPs, the phase transition to the hexagonal phase is promoted at 90 °C. In the presence of SPIONs, as already discussed, an overall increase of the spontaneous curvature occurs, also at room temperature, determining an overall decrease of Δg_P, which, thus, decreases the minimum value of free energy of elastic curvature necessary to observe the phase transition (see eqn (5)). Thus, the presence of the SPIONs acts in the thermotropic behavior of the GMO liquid crystalline phase having influence both on the free energy of elastic curvature and on the free energy of packing frustration.

Overall, these energetic considerations are useful to highlight the potential of GMO/NPs systems; the thermotropism can be finely tuned through SPIONs content in lipid structure considering that magnetic nanoparticles affect both frustration packing and elastic curvature free energies.

Thermotropic behavior of GMO-SPIONs nanoparticles

The hybrid bulk cubic phase of GMO/SPIONs with 0.47% w/w SPIONs was dispersed with Pluronic F127 as stabilizer as described in the Experimental section, to give cubosomes with a hydrodynamic radius in the range 2000–2500 Å (ref. 49) (see ESI† for details). The structure and thermotropic behavior of the cubosomes dispersion was investigated with SAXS within a temperature range of 25–49 °C. For GMO cubosomes, the structure is a primitive cubic phase *Im3m*[50,51] (Fig. 4a), *i.e.*, a more hydrated phase than Pn3 m, characterized by larger water channels, which size, as in the *Pn3m*, decreases with temperature (from 26 Å at 25 °C to 20 Å at 49 °C in the *Im3m* and from 24 Å at 25 °C and 16 Å at 50 °C in the *Pn3m*). In the same temperature range the lattice parameter d decreases by 2 nm (see ESI†), following a sigmoidal-like trend with inflection point at 36 °C, close to physiological temperature, making cubosomes interesting for drug delivery of both hydrophobic and hydrophilic therapeutics.

The SAXS profiles of magnetocubosomes, in the same temperature range (Fig. 4b) are consistent with a less hydrated diamond cubic phase with respect to bare cubosomes, coexisting with a H_{II} even at 25 °C. The cubic phase signature disappears above 35 °C and the hexagonal phase is the only one at 37 °C. The larger stability range of H_{II} phases for GMO-SPIONs hybrid systems is consistent with what was observed for the bulk cubic phase and is indeed very interest-

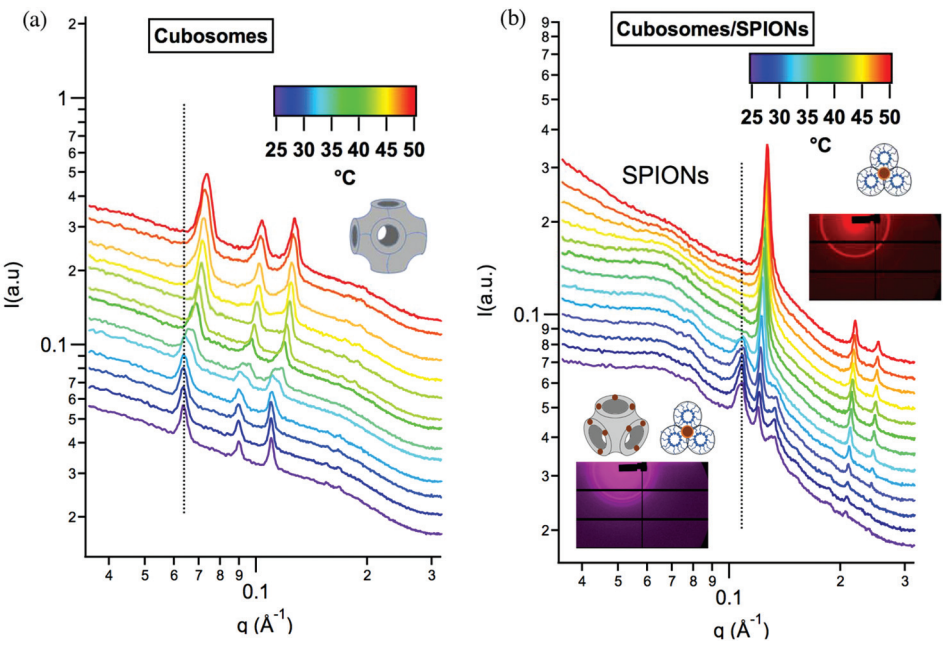

Fig. 4 SAXS curves of (a) cubosomes and (b) magnetocubosomes monitored in the 25 °C–49 °C temperature range with 2 °C temperature steps.

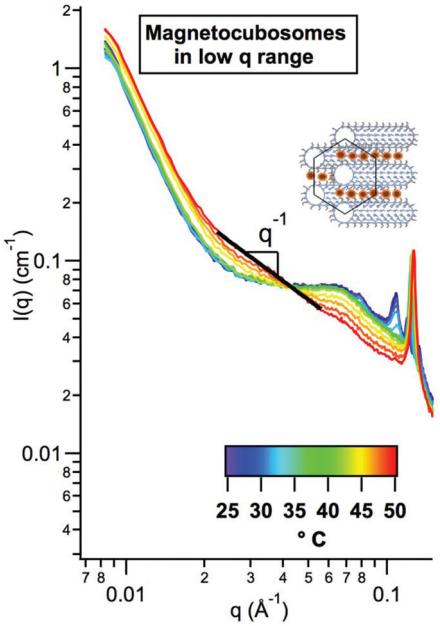

Fig. 5 Detail on low-q range of SAXS curves of magnetocubosomes acquired in the 25–49 °C temperature range (see Fig. 4b). Variation of scattering intensity for magnetic nanoparticles was detected during the increase of temperature. At 49 °C self-organization of SPIONs into the lipid architecture shows a pearl-necklace like structure (q^{-1}).

ing in order to design temperature responsive drug delivery systems: in fact, the transition to hexagonal phase implies a shrinking of the lipid nanoparticles, with water expulsion. This structural modification implies therefore a huge release of the aqueous content of the aqueous channels with possible release of the confined active principles.

A very interesting feature emerges in the low-q region of the SAXS spectra of magnetocubosomes (see Fig. 4b compared to Fig. 4a and 5): at 25 °C, the main feature of low-q region is the structure factor corresponding to a correlation length of the nanoparticles embedded in the lipid architecture, observed in the same position as in the bulk cubic phase. This structure factor peak is preserved up to 40 °C. From 42 °C on, this peak disappears and a different structural feature occurs, consisting on a reorganization of the NPs. We can hypothesize that a decrease in viscosity of the lipid phase allows particle diffusion into the hydrophobic domain and the magnetic dipolar interaction drives a pearl-necklace organization.[39] In Fig. 5 the low-q SAXS range is highlighted, showing at 49 °C a distinct and relatively extended q^{-1} scalar law beyond Guiner region. We can infer the radius of the pearls (18 Å), corresponding to the NPs radius and the length of the necklace (281 Å); from these values, we can hypothesize that 5–6 nanoparticles align in the lipid structure. Recently, modulation of nanoparticles shape or their aggregates have been proposed to overcome the so-called Brezovich effect. NPs controlled aggregation might enhance the heating power of SPIONs,[52] and/or modulate their magnetic properties.[53] With our results, we demonstrate that a fine control on the SPIONs arrangement can be achieved exploiting the polymorphic behavior of a lipid scaffold. The spontaneous controlled arrangement in linear structure can profoundly modify magnetic properties, as predicted in some computational studies[54,55] and finally alter magnetic properties.

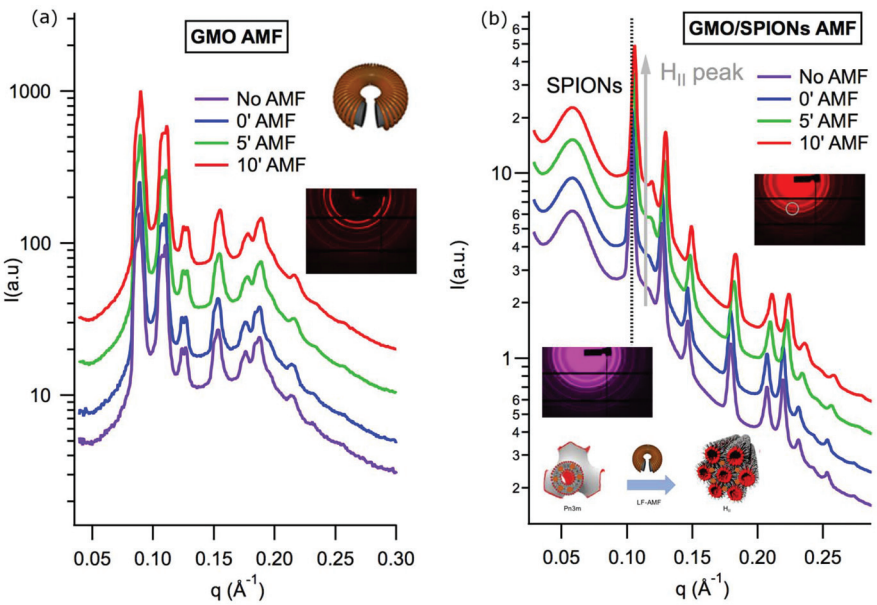

Fig. 6 SAXS curves of (a) GMO bulk cubic phase and (b) GMO bulk cubic phase with 0.47% SPIONs monitored during 10 minutes LF-AMF application at r.t. (a) A very mild shift of cubic phase Bragg peaks in present upon 10 minutes AMF application, corresponding to an temperature increase of 0.6 °C; (b) the appearance of an extra-peak at low q occur attributable to a H_{II} phase proves the occurrence of a $Pn3m/H_{II}$ phase transition.

Magnetotropic behavior of GMO-SPIONs assemblies

It is well known that SPIONs are responsive to an alternating magnetic field: their magnetic relaxation causes local heating. This effect is used in drug delivery systems to trigger the release from vehicles as liposomes[11,26,27] or magnetocubosomes[4,10] of model drug confined in the hydrophilic domains. For the first time, we report the structural effects of the AMF monitored "live", *i.e.* during the AMF application, on the structure of a GMO cubic bulk phase self-assembled in the presence or in the absence of SPIONs (Fig. 6). With a dedicated experimental setup, we monitored through SAXS the structural changes in the bulk cubic phase during the application of an alternating magnetic field. As we can see from Fig. 6a, the AMF applied to GMO cubic phase (without SPIONs) does not induce structural changes, apart from a mild Joule Effect of the coil, which causes an overall minor shift ($\sim 4.4 \times 10^{-4}$ Å^{-1}) of the profile, consistent with a temperature increase of 0.6 °C.

Conversely, when SPIONs-loaded *Pn3m* GMO mesophases are subjected to AMF, Fig. 6b, the appearance of an extra peak is highlighted, which position is identical to the first reflection of the H_{II} phase (see Fig. 2b). During 10 minutes application, the intensity of the peak increases, though the transition is not complete. However, complete absence of phase transition and negligible temperature increase when NPs are not present and the perfect correspondence of this peak with the hexagonal phase allows us attributing it unambiguously to the local heating effect of the SPIONs that, probably due to the very localized effect, provoke a locally confined phase transition of the lipid scaffold.

Conclusions

Hydrophobic magnetic nanoparticles endow GMO cubic mesophases with responsiveness to alternating magnetic fields,[10] allowing spatio-temporal control of the release of small molecules confined in their lipid bilayers or in the water channels. The mechanistic aspects of this process, of particular relevance in the field of controlled drug-delivery, were not yet elucidated.

In this contribution, we have explored and interpreted the structural effects of SPIONs on the thermotropic and lyotropic phase behaviour of bulk and dispersed cubic lipid phases. As the concentration of SPIONs in the lipid scaffold increases, a *Pn3m*-H_{II} phase transition is promoted. For Pn3 m GMO/SPIONs/water systems, the transition temperature to an H_{II} phase is lowered with respect to GMO/water (90 °C). The thermotropic properties of magnetocubosomes were also investigated, and the same structural effects were detected. We explain this phase behaviour in terms of changes of frustration packing and elastic features of the lipid bilayer. The same transition was induced applying an alternating magnetic field, due to local heating operated by the NPs. The structural change causes a shrinking of the mesophase, responsible for the release of hydrophilic molecules, initially confined in the water channels. Additionally, we detected in the hexagonal phase a spontaneous re-organization of the NPs into a pearl-necklace supraparticle. This result is fully in line with our hypothesis on the NPs-induced frustration packing of the mesophase as the driving force of the transition.

These data and their interpretation open new perspectives both from fundamental and applicative standpoints. Concerning the first aspect, the results here presented contribute to the elucidation of NPs' interactions with synthetic or natural lipid membranes, demonstrating that NPs affect the viscoelastic properties of lipid bilayers, shifting the mesophases' phase boundaries. This effect can be harnessed to tune the mesophase response to AMF and drive the release of host molecules, with numerous applications in the field of drug delivery. In addition, lipid mesophases steer the organization of single NPs into magnetic supraparticles with preserved colloidal stability. This approach opens the way to control the spontaneous supraorganization of SPIONs in a lipid scaffold, possibly overcoming the Brezovich limit, which nowadays hampers clinical applicability of magnetic hyperthermia.[53]

Conflicts of interest

There are no conflicts to declare.

Acknowledgements

Annalisa Salvatore and Giacomo Becheri are acknowledged by all the authors for taking part to SAXS experiments and Annalisa Salvatore also for contribution on SPIONs synthesis. We gratefully acknowledge the allocation of beamtime at Elettra, Trieste, Italy.

References

1 R. H. Templer, *Curr. Opin. Colloid Interface Sci.*, 1998, **3**, 255–263.
2 A. Marín-Menéndez, C. Montis, T. Díaz-Calvo, D. Carta, K. Hatzixanthis, C. J. Morris, M. McArthur and D. Berti, *Sci. Rep.*, 2017, **7**, 41242.
3 S. Smeazzetto, F. Tadini-Buoninsegni, G. Thiel, D. Berti and C. Montis, *Phys. Chem. Chem. Phys.*, 2016, **18**, 1629–1636.
4 M. Szlezak, D. Nieciecka, A. Joniec, M. Pękała, E. Gorecka, M. Emo, M. J. Stébé, P. Krysiński and R. Bilewicz, *ACS Appl. Mater. Interfaces*, 2017, **9**(3), 2796–2805.
5 R. Negrini and R. Mezzenga, *Langmuir*, 2012, **28**, 16455–16462.
6 W. Sun, J. J. Vallooran, A. Zabara and R. Mezzenga, *Nanoscale*, 2014, **6**, 6853–6859.
7 S. Murgia, S. Lampis, P. Zucca, E. Sanjust and M. Monduzzi, *J. Am. Chem. Soc.*, 2010, **132**, 16176–16184.
8 P. Huang, J. Zhao, C. Wei, X. Hou, P. Chen, Y. Tan, C.-Y. He, Z. Wang and Z.-Y. Chen, *Biomater. Sci.*, 2017, **5**, 120–127.

9 R. Negrini and R. Mezzenga, *Langmuir*, 2011, **27**, 5296–5303.
10 C. Montis, B. Castroflorio, M. Mendozza, A. Salvatore, D. Berti and P. Baglioni, *J. Colloid Interface Sci.*, 2015, **449**, 317–326.
11 M. Bonini, D. Berti and P. Baglioni, *Curr. Opin. Colloid Interface Sci.*, 2013, **18**, 459–467.
12 H. Vacklin, B. J. Khoo, K. H. Madan, J. M. Seddon and R. H. Templer, *Langmuir*, 2000, **16**, 4741–4748.
13 N. Tran, A. M. Hawley, J. Zhai, B. W. Muir, C. Fong, C. J. Drummond and X. Mulet, *Langmuir*, 2016, **32**, 4509–4520.
14 S. J. Marrink and D. P. Tieleman, *J. Am. Chem. Soc.*, 2001, **123**, 12383–12391.
15 T. G. Meikle, S. Yao, A. Zabara, C. E. Conn, C. J. Drummond and F. Separovic, *Nanoscale*, 2017, **9**, 2471–2478.
16 L. van 't Hag, A. Anandan, S. A. Seabrook, S. L. Gras, C. J. Drummond, A. Vrielink and C. E. Conn, *Soft Matter*, 2017, **13**, 1493–1504.
17 A. Zabara, T. G. Meikle, J. Newman, T. S. Peat, C. E. Conn and C. J. Drummond, *Nanoscale*, 2017, **9**, 754–763.
18 J. J. Vallooran, S. Bolisetty and R. Mezzenga, *Adv. Mater.*, 2011, **23**, 3932–3937.
19 J. J. Vallooran, S. Handschin, S. Bolisetty and R. Mezzenga, *Langmuir*, 2012, **28**, 5589–5595.
20 J. J. Vallooran, R. Negrini and R. Mezzenga, *Langmuir*, 2013, **29**, 999–1004.
21 R. Di Corato, A. Espinosa, L. Lartigue, M. Tharaud, S. Chat, T. Pellegrino, C. Ménager, F. Gazeau and C. Wilhelm, *Biomaterials*, 2014, **35**, 6400–6411.
22 L. Lartigue, P. Hugounenq, D. Alloyeau, S. P. Clarke, M. Lévy, J.-C. Bacri, R. Bazzi, D. F. Brougham, C. Wilhelm and F. Gazeau, *ACS Nano*, 2012, **6**, 10935–10949.
23 A. Hervault, A. E. Dunn, M. Lim, C. Boyer, D. Mott, S. Maenosono and N. T. K. Thanh, *Nanoscale*, 2016, **8**, 12152–12161.
24 D. Maiolo, C. Pigliacelli, P. Sánchez Moreno, M. B. Violatto, L. Talamini, I. Tirotta, R. Piccirillo, M. Zucchetti, L. Morosi, R. Frapolli, G. Candiani, P. Bigini, P. Metrangolo and F. Baldelli Bombelli, *ACS Nano*, 2017, **11**, 9413–9423.
25 A. Salvatore, C. Montis, D. Berti and P. Baglioni, *ACS Nano*, 2016, **10**, 7749–7760.
26 Y. Chen, A. Bose and G. D. Bothun, *ACS Nano*, 2010, **4**, 3215–3221.
27 M. S. Martina, J. P. Fortin, C. Ménager, O. Clément, G. Barratt, C. Grabielle-Madelmont, F. Gazeau, V. Cabuil and S. Lesieur, *J. Am. Chem. Soc.*, 2005, **127**, 10676–10685.
28 S. Sun, H. Zeng, D. B. Robinson, S. Raoux, P. M. Rice, S. X. Wang and G. Li, *J. Am. Chem. Soc.*, 2004, **126**, 273–279.
29 L. Wang, J. Luo, Q. Fan, M. Suzuki, I. S. Suzuki, M. H. Engelhard, Y. Lin, N. Kim, J. Q. Wang and C. J. Zhong, *J. Phys. Chem. B*, 2005, **109**, 21593–21601.
30 G. Capuzzi, F. Pini, C. M. C. Gambi, M. Monduzzi, P. Baglioni and J. Teixeira, *Langmuir*, 1997, **53**, 6927–6930.
31 H. Sub Wi, K. Lee and H. Kyu Pak, *J. Phys.: Condens. Matter*, 2008, **20**, 494211.
32 C. M. Beddoes, J. Berge, J. E. Bartenstein, K. Lange, A. J. Smith, R. K. Heenan and W. H. Briscoe, *Soft Matter*, 2016, **12**, 6049–6057.
33 C. Fong, T. Le and C. J. Drummond, *Chem. Soc. Rev.*, 2012, **41**, 1297.
34 M. Fuhrmans, V. Knecht and S. J. Marrink, *J. Am. Chem. Soc.*, 2009, **131**, 9166–9167.
35 A. Yaghmur, P. Laggner, S. Zhang and M. Rappolt, *PLoS One*, 2007, **2**(5), e479.
36 N. Johner, S. Mondal, G. Morra, M. Caffrey, H. Weinstein and G. Khelashvili, *J. Am. Chem. Soc.*, 2014, **136**, 3271–3284.
37 C. C. Piccinetti, C. Montis, M. Bonini, R. Laurà, M. C. Guerrera, G. Radaelli, F. Vianello, V. Santinelli, F. Maradonna, V. Nozzi, A. Miccoli and I. Olivotto, *Zebrafish*, 2014, **11**, 567–579.
38 J. M. Bulpett, T. Snow, B. Quignon, C. M. Beddoes, T.-Y. D. Tang, S. Mann, O. Shebanova, C. L. Pizzey, N. J. Terrill, S. A. Davis and W. H. Briscoe, *Soft Matter*, 2015, **11**, 8789–8800.
39 Y. Lalatonne, J. Richardi and M. P. Pileni, *Nat. Mater.*, 2004, **3**, 121–125.
40 G. C. Shearman, O. Ces, R. H. Templer and J. M. Seddon, *J. Phys.: Condens. Matter*, 2006, **18**, S1105–S1124.
41 R. H. Templer, J. M. Seddon, P. M. Duesing, R. Winter and J. Erbes, *J. Phys. Chem. B*, 1998, **102**, 7262–7271.
42 E. Venugopal, S. K. Bhat, J. J. Vallooran and R. Mezzenga, *Langmuir*, 2011, **27**, 9792–9800.
43 B. Angelov, A. Angelova, V. M. Garamus, G. Lebas, S. Lesieur, M. Ollivon, S. S. Funari, R. Willumeit and P. Couvreur, *J. Am. Chem. Soc.*, 2007, **129**, 13474–13479.
44 W. Helfrich, *Z. Naturforsch.*, 1973, **28**, 693–703.
45 S. T. Hyde, *J. Phys. Chem.*, 1989, **93**, 1458–1464.
46 S. T. Hyde, *Curr. Opin. Solid State Mater. Sci.*, 1996, **1**, 653–662.
47 I. Hoffmann, R. Michel, M. Sharp, O. Holderer, M.-S. Appavou, F. Polzer, B. Farago and M. Gradzielski, *Nanoscale*, 2014, **6**, 6945–6952.
48 D. P. Siegel and M. M. Kozlov, *Biophys. J.*, 2004, **87**, 366–374.
49 C. Neto, D. Berti, G. D. Aloisi, P. Baglioni and K. Larsson, *Prog. Colloid Polym. Sci.*, 2000, **115**, 295–299.
50 J. Y. T. Chong, X. Mulet, L. J. Waddington, B. J. Boyd and C. J. Drummond, *Soft Matter*, 2011, **7**, 4768.
51 B. Angelov, A. Angelova, B. Papahadjopoulos-Sternberg, S. Lesieur, J. F. Sadoc, M. Ollivon and P. Couvreur, *J. Am. Chem. Soc.*, 2006, **128**, 5813–5817.
52 P. Guardia, R. Di Corato, L. Lartigue, C. Wilhelm, A. Espinosa, M. Garcia-Hernandez, F. Gazeau, L. Manna and T. Pellegrino, *ACS Nano*, 2012, **6**, 3080–3091.
53 D. Maity, P. Chandrasekharan, P. Pradhan, K.-H. Chuang, J.-M. Xue, S.-S. Feng and J. Ding, *J. Mater. Chem.*, 2011, **21**, 14717.
54 P. V. Melenev, V. V. Rusakov and Y. L. Raikher, *Tech. Phys. Lett.*, 2008, **34**, 248–250.
55 V. Schaller, G. Wahnström, A. Sanz-Velasco, S. Gustafsson, E. Olsson, P. Enoksson and C. Johansson, *Phys. Rev. B: Condens. Matter Mater. Phys.*, 2009, **80**, 1–4.

Electronic Supplementary Material (ESI) for Nanoscale.

On the thermotropic and magnetotropic phase behavior of lipid liquid crystals containing magnetic nanoparticles

*Marco Mendozza[1], Costanza Montis[1], Lucrezia Caselli[1], Marcell Wolf[2], Piero Baglioni[1] and Debora Berti[1]**

[1]Department of chemistry and CSGI, University of Florence, Via della Lastruccia 3, 50019-Sesto Fiorentino, Florence, Italy.

[2]Institue of Inorganic Chemistry, Graz University of Technology, Stremayrgasse 9/IV, 8010 Graz, Austria

Materials and Methods

S.1- Materials

Fe(III)acetylacetonate, 1,2-hexadecanediol, oleylamine, oleic acid, diphenylether, ethanol and mixture of hexane employed for the synthesis of SPIONs, were purchased from Sigma Aldrich (St. Louis MO), the same for Glyceryl Monooleate (GMO) and Pluronic F-127.

S.2- Synthesis of magnetic nanoparticles

Iron oxide nanoparticles were synthesized according to the protocol reported by Wang et al.[1]. Briefly, 0.71 g $Fe(acac)_3$ (2 mmol) were dissolved in 20 mL of phenyl ether with 2 mL of oleic acid (6 mmol) and 2 mL of oleylamine (4 mmol) under nitrogen atmosphere and vigorous stirring. 1,2-hexadecanediol (2.58g, 10 mmol) was then added. The solution was heated at 210 °C, refluxed for 2 h and then cooled down to RT. Ethanol was added to the dispersion and the precipitate collected, washed with ethanol to remove residual precursors and side products from the synthesis and redispersed in 20 mL hexane in the presence of 75 mM of both oleic acid and oleylamine. A stable dispersion of the SPIONs with a hydrophobic coating of oleic acid and oleylamine in hexane was obtained.

S.3- Preparation of bulk and disperse cubic phase

The preparation of bulk cubic phase with or without SPIONs was carried out according to the following procedure. First, 30 mg of GMO were weighted in a 2mL glass vial. For GMO/SPIONs systems, the appropriate volume of SPIONs dispersion was then added. About 1 mL hexane was used to solubilize the mixture and then the solvent was removed with a gentle

nitrogen flux. GMO or GMO/SPIONs systems were left under vacuum overnight sheltered from light. The dry film was then hydrated with 30 μL Milli-Q water and the sample was then centrifuged at least 5 times altering a cycle with cap facing upward with another with cap facing downward.

For the preparation of cubosomes, first GMO or GMO-SPIONs film was obtained, as previously described. 8 mg of Pluronic F-127 were then added to the dry film and the mixture was heated in a water bath at 70 °C for 5' to melt the Pluronic F-127 and then vortexed for 5'. Five cycles of heating-vortexing were carried out and then 500 μL of preheated H_2O at 70 °C were added. The dispersion was then sonicated in a bath-sonicator at 59 kHz and 100% power for 6 h, to homogenize the system.

S.4- Small-Angle X-ray Scattering (SAXS) Hecus

SAXS measurements were carried out on a S3-MICRO SAXS/WAXS instrument (HECUS GmbH, Graz, Austria) which consists of a GeniX microfocus X-ray Sealed Cu Ka source (Xenocs, Grenoble, France) power 50 W which provides a detector focused X-ray beam with k = 0.1542 nm Cu Ka line. The instrument is equipped with two one-dimensional (1D) position sensitive detectors, (HECUS 1D-PSD-50 M system) each detector is 50 mm long (spatial resolution 54 lm/channel, 1024 channels) and cover the SAXS q-range ($0.003 < q < 0.6$ Å^{-1}) and the WAXS q-range ($1.2 < q < 1.9$ Å^{-1}). The temperature was controlled by means of a Peltier TCCS-3 Hecus. SAXS curves of bulk cubic phase were recorded at 25-30-35-40-45-50 °C in a solid sample-holder. Dispersion of SPIONs were recorded in a glass capillary.

S.5- Small-Angle X-ray Scattering (SAXS) Elettra Synchrotron

Analysis of cubosomes and magnetocubosomes were carried out at SAXS beamline of synchrotron radiation Elettra, Trieste, Italy operated at 2 GeV and 300 mA ring current. The experiments were carried with $\lambda = 1.5a$ Å and SAXS signal was detected with Pilatus 3 1M detector in q-range from 0.008 $Å^{-1}$ to 0.45 $Å^{-1}$. Thermic behavior of colloidal dispersion of cubosomes and magnetocubosomes were carried out through thermostat from 25 °C to 49 °C increasing the temperature of 2 °C each step. Equilibration time at each temperature was 5 minutes. SAXS curves were recorded in a glass capillary for cubosomes and magnetocubosomes dispersions and in a solid sample-holder for the cubic phases.

S.6- SAXS analysis

Equation (1) was used to calculate lattice parameter of cubic and hexagonal phase:

$$q = \left(\frac{2\pi}{d}\right)\sqrt{h^2 + k^2 + l^2} \qquad (S1)$$

Eq. (2) was used to calculate water channel radii r_w in cubic phase while eq (3) was used to calculate volume water fraction:

$$r_w = \sqrt{(-\sigma/2\pi\chi)}d - l_c \qquad (S2)$$

$$\varphi_w = 1 - 2A_0\left(\frac{l_c}{d}\right) - \frac{4}{3}\pi\chi\left(\frac{l_c}{d}\right)^3 \qquad (S3)$$

Equation (4)[2] and (5)[3] describe water channel radii of hexagonal phase and water volume fraction respectively:

$$r_w = \frac{0.5256d - l_c}{0.994} \qquad (S4)$$

$$\varphi_w = \frac{2\pi r_w^2}{\sqrt{3}d^2} \qquad (S5)$$

We assumed that l_c into the range of 25-50 °C, is constant and assume value of about 17 Å. Moreover, to evaluate water fraction both for cubic and hexagonal phase we assumed that %w/w of Fe_3O_4 negligible.

S.7- LF-AMF specifications

A sinusoidal magnetic field was generated in the gap of a broken toroidal magnet carrying a solenoid through which an alternating electric current (AC) from a tone generator was led as described elsewhere[4]. The samples to be treated with LF-AMF were placed in the middle of the gap. Due to the design of the experimental apparatus, the magnetic field inside the cell is not isotropic. During the experiments, the field frequency was set at 6.22 kHz. Magnetic field values of magnet range from 100-330 mT with 10 V and 8 A.

Supplementary Figures

S.8- SAXS characterization of magnetic nanoparticles

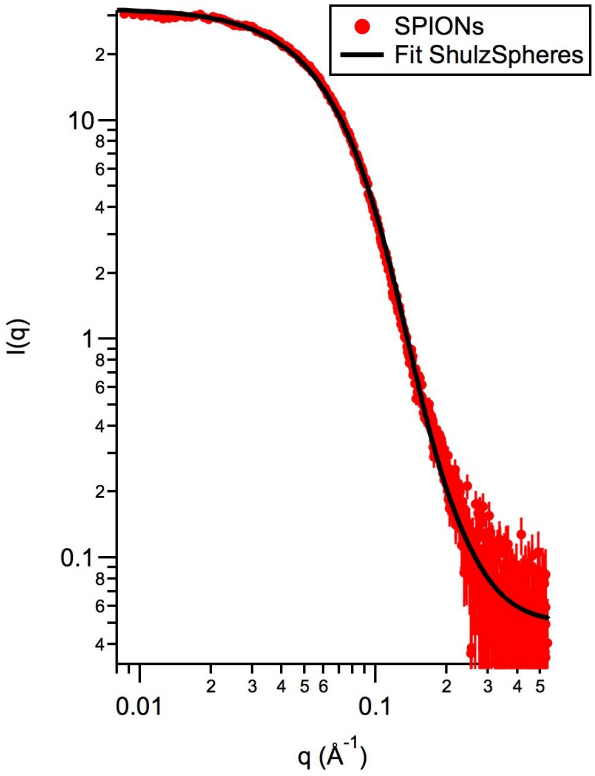

Figure S1: SAXS curve of magnetic nanoparticles disperse in hexane diluted 1:3 (red) fitted by polidisperse Shultz Sphere model (black line).

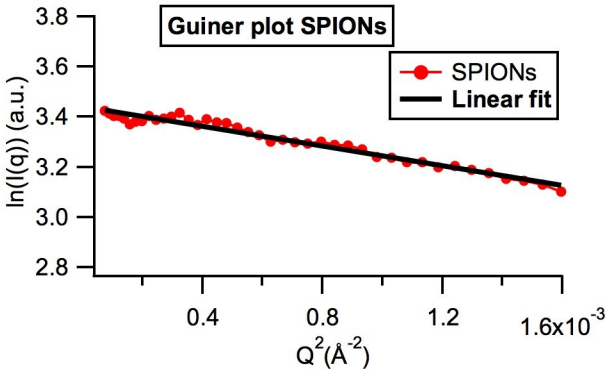

Figure S2: SAXS curves of magnetic nanoparticles with linear fit in Guiner region.

To investigate the dimension of magnetic nanoparticles synthesized as reported in S.2 section, we diluted 1:3 in hexane magnetic nanoparticles. We employed "SphereSchultz Model" by NIST to estimate the radius and polidispersity of SPIONs, which were found equal to 20±3 Å and 0.35 respectively. Moreover, the SAXS curve was analyzed with the Guiner limit law finding a gyration radius of 24 Å. In the hypothesis of spherical and monodisperse nanoparticles, the average radius of the SPIONs derived from Guinier plot is R= 31 Å. This result, corrected for the polidispersity of the colloidal dispersion[5], is about 18 Å, and this is fully consistent with the radius obtained from the "SphereSchultz Model" analysis.

S.9- Lattice parameters of GMO/H_2O systems and SAXS curves of GMO/H_2O/oleic acid-oleylamine

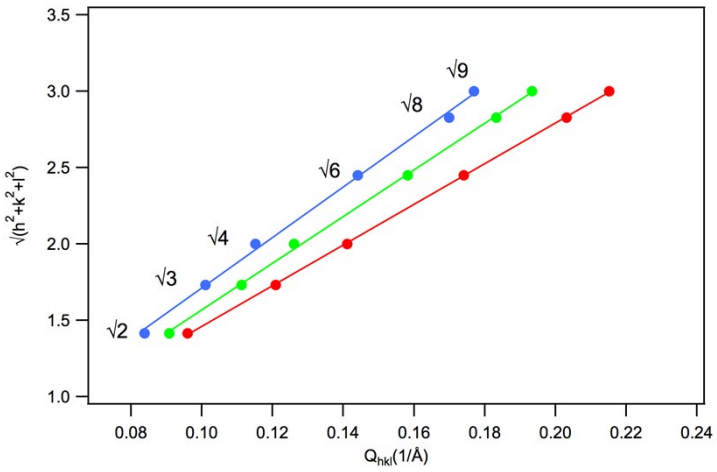

Figure S3: SAXS analysis of GMO/H_2O mesophases at 25 °C (blue line and markers), 35 °C (green line and markers) and 50 °C (red line and markers): square root of the sum of the h,k,l Miller indexes of each peak vs q-peak position (blue, green, red circles); linear fit of the experimental data to calculate lattice parameters the different mesophases (blue, green, red line).

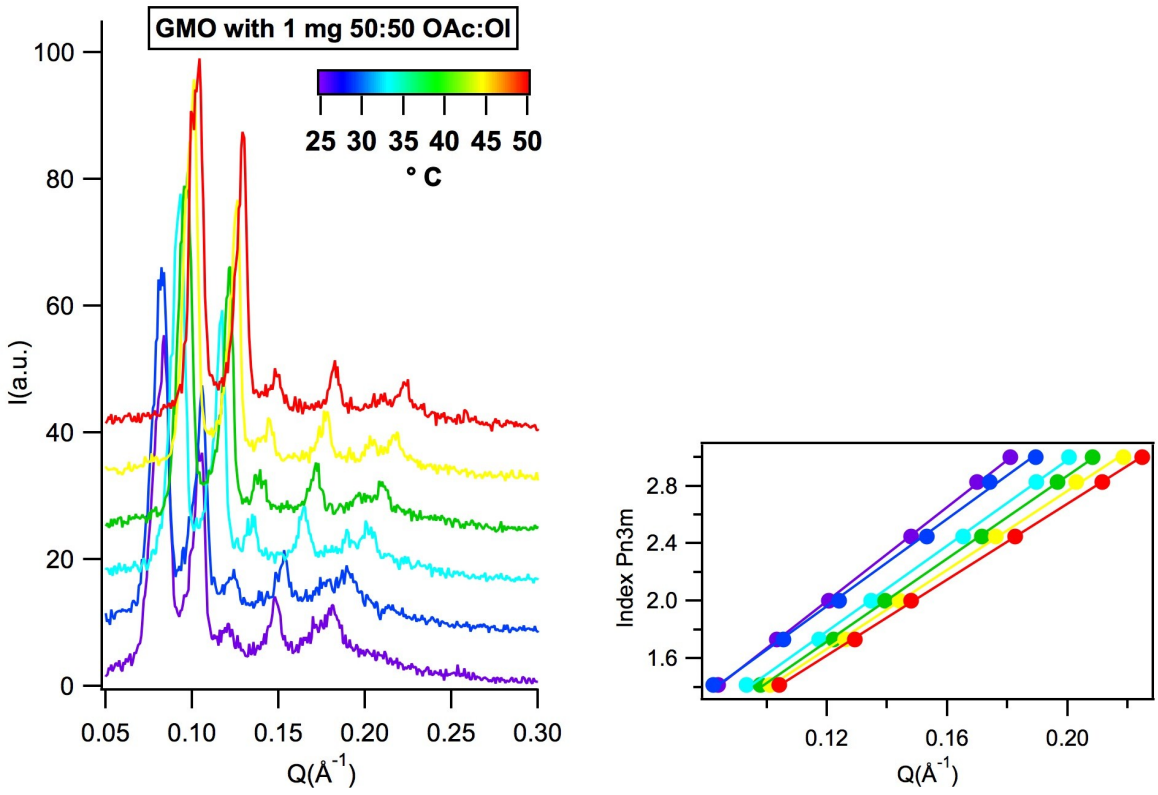

Figure S4: SAXS curves of GMO assembled with 1 mg of a mixture Oleic Acid/Oleylamine at 25-30-35-40-45-50 °C (respectively violet, blue, cyan, green, yellow and red) and Miller index on Q_{max} to determine the trend of Pn3m lattice parameter with temperature. No phase transition was observed in this system.

Table S1. Lattice parameters, water channel radii and water volume fraction of GMO assembled with 1 mg of a mixture 50:50 of Oleic acid and oleylamine

T (°C)	Lattice parameter (Å)	Water channel radii (Å)	Water volume fraction
25	103	23	0.40
30	95	20	0.36
35	94	20	0.36
40	91	19	0.34
45	86	17	0.31
50	83	15	0.29

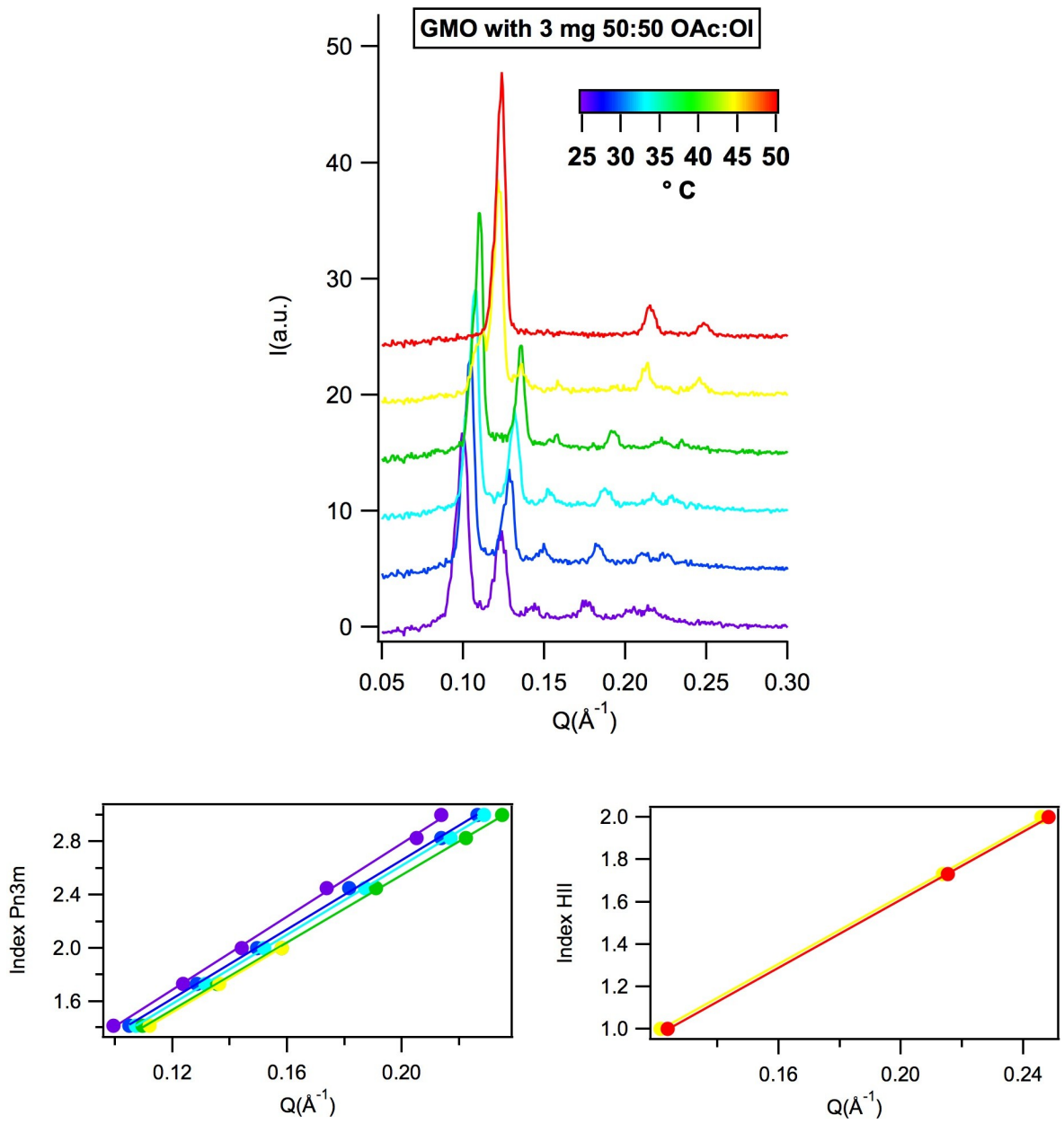

Figure S5: SAXS curves of GMO assembled with 3 mg of a mixture Oleic Acid/Oleylamine and Miller index on Q_{max} to determine the trend of the lattice parameter both for cubic (violet, blue, cyan, green and yellow) and hexagonal phase (yellow and red line) with temperature in the 25-50 °C temperature range. At 45°C the coexistence of cubic and hexagonal phases was detected. Only at 50 °C a pure inverse hexagonal phase was detected.

Table S2. Lattice parameters, water channel radii and waer volume fraction of GMO assembled with 3 mg of a mixture 50:50 of Oleic acid and oleylamine.

T (°C)	Lattice parameter (Å)	Water channel radii (Å)	Water volume fraction
25	86	17	0.31
30	82	15	0.28
35	82	15	0.28
40	80	14	0.26
45	80 (Pn3m)	14	0.26
	50 (H_{II})	9	0.13
50	50	9	0.13

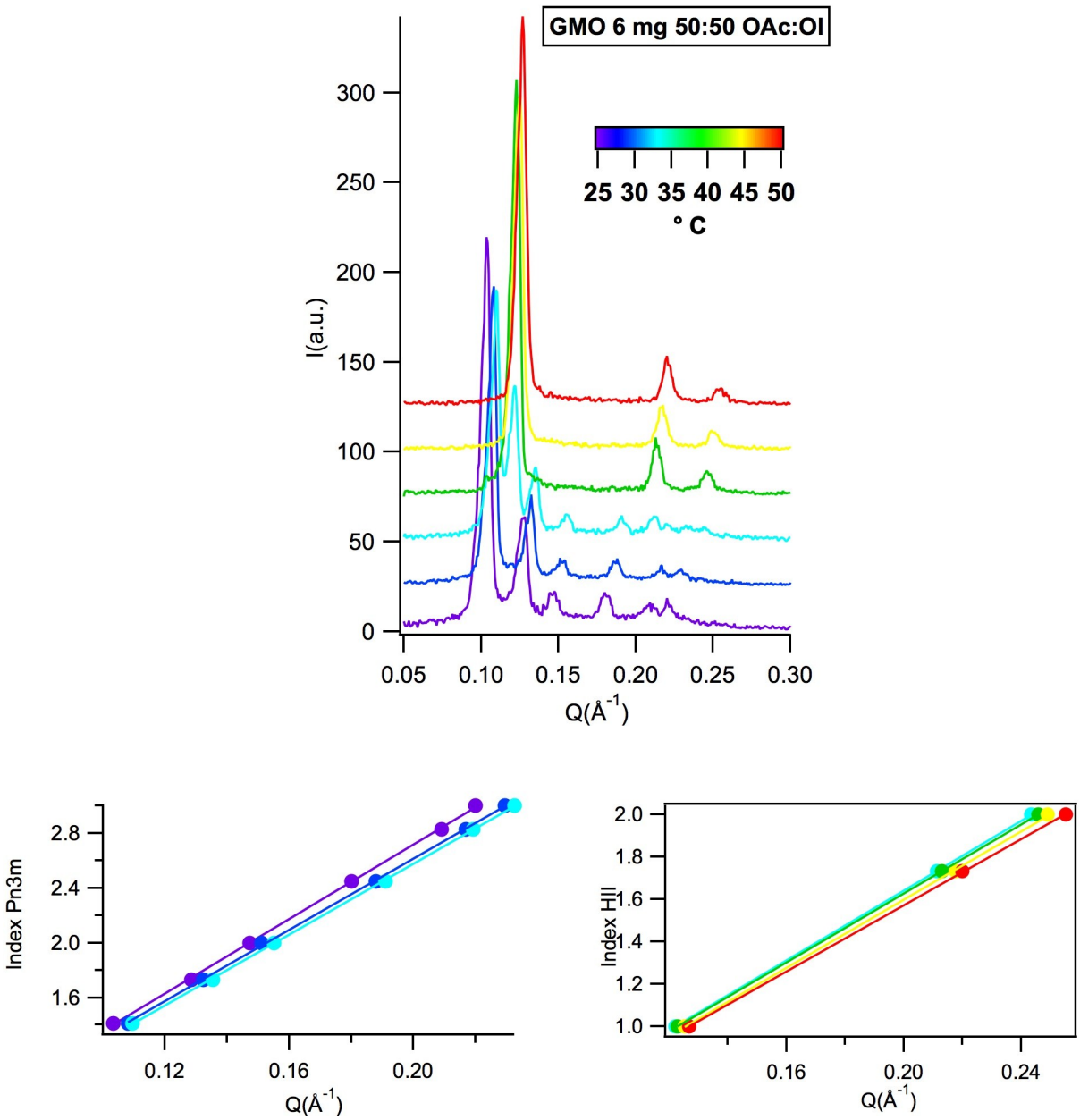

Figure S6: SAXS curves of GMO assembled with 6 mg of a mixture Oleic Acid/Oleylamine and Miller index on Q_{max} to determine the trend of the lattice parameter both for cubic (violet, blue and cyan) and hexagonal phase (cyan, green and yellow and red line) with temperature in the 25-50 °C temperature range. At 35°C the coexistence of cubic and hexagonal phases was detected. From 40 °C a pure inverse hexagonal phase was detected.

Table S3. Lattice parameters, water channel radii and waer volume fraction of GMO assembled with 6 mg of a mixture 50:50 of oleic acid and oleylamine.

T (°C)	Lattice parameter (Å)	Water channel radii (Å)	Water volume fraction
25	85	16	0.3
30	82	15	0.28
35	81 (Pn3m)	15	0.27
	52(H_{II})	10.4	0.14
40	51	9.8	0.14
45	51	9.8	0.14
50	49	8.8	0.12

S.10- SAXS curves of GMO/H_2O/SPIONs

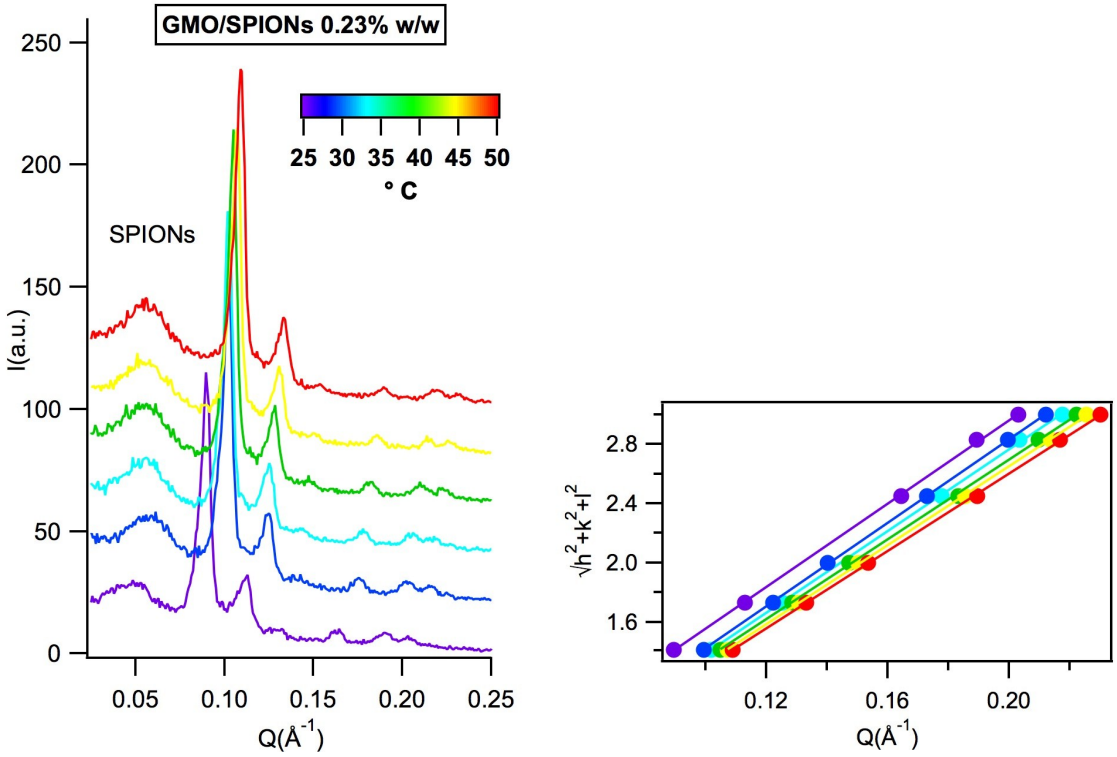

Figure S7: SAXS curves of GMO assembled with 0.23% w/w Fe_3O_4 (mixture of OAc/Ol is 1.33 mg) and Miller index on Q_{max} to determine the variation of the lattice parameter for cubic phase with temperature in the 25-50 °C temperature range. No phase transition with this amount of SPIONs was detected.

Table S4. Lattice parameters, water channel radii and waer volume fraction of GMO assembled with 0.23% SPIONs at increasing temperatures.

T (°C)	Lattice parameter (Å)	Water channel radii (Å)	Water volume fraction
25	88	17	0.32
30	88	17	0.32
35	86	16.6	0.31
40	84	15.8	0.29
45	84	15.8	0.29
50	82	15	0.28

Table S5. Lattice parameters, water channel radii and waer volume fraction of GMO assembled with 0.47% SPIONs at increasing temperatures.

T (°C)	Lattice parameter (Å)	Water channel radii (Å)	Water volume fraction
25	87 (Pn3m)	17	0.31
30	86 (Pn3m)	16.6	0.31
	55 (H_{II})	12	0.17
35	85 (Pn3m)	16	0.3
	54 (H_{II})	11	0.16
40	53 (H_{II})	11	0.15
45	52 (H_{II})	10	0.14
50	51 (H_{II})	9.8	0.14

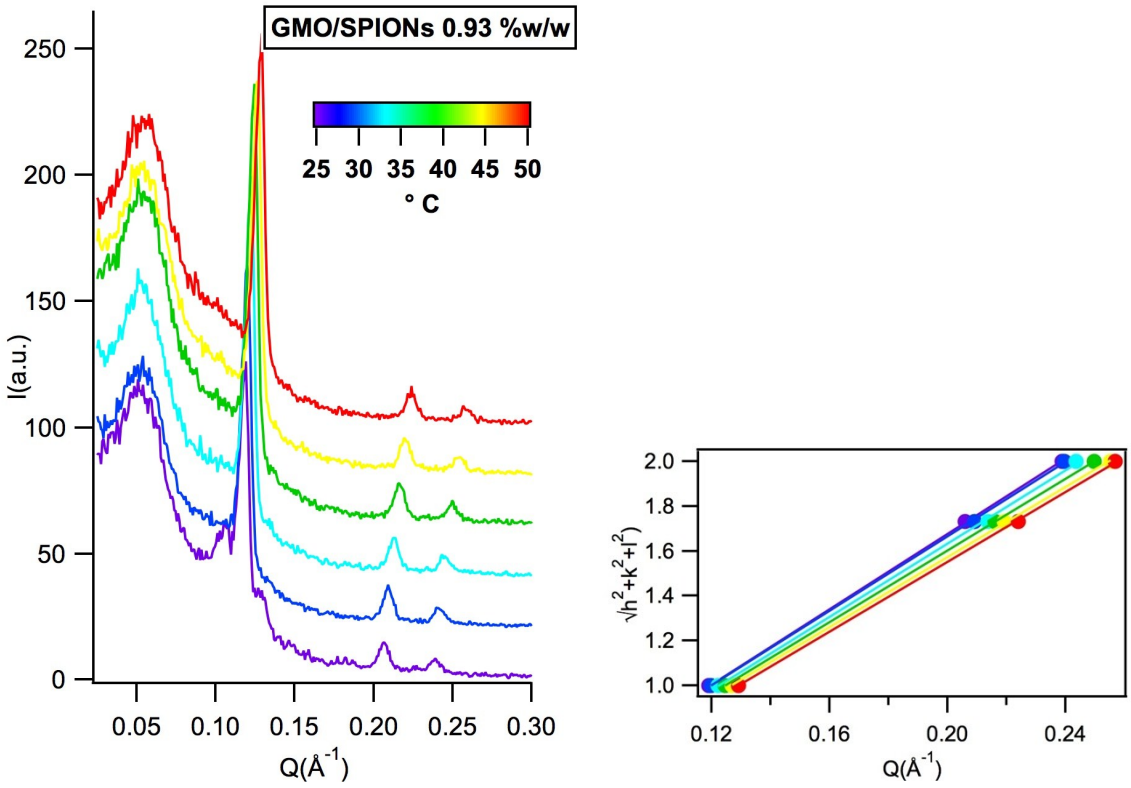

Figure S8: SAXS curves of GMO assembled with 0.93% w/w Fe_3O_4 (5.33 mg of a mixture OAc/Ol) and Miller index on Q_{max} to determine the trend of the lattice parameter for the inverse hexagonal phase with temperature in the 25-50 °C temperature range.

Table S6. Lattice parameters, water channel radii and water volume fraction of GMO assembled with 0.93% SPIONs at increasing temperatures.

T (°C)	Lattice parameter (Å)	Water channel radii (Å)	Water volume fraction
25	53	11	0.15
30	52	10	0.14
35	51	9.8	0.13
40	50	9.3	0.13
45	49	8.8	0.12
50	49	8.8	0.12

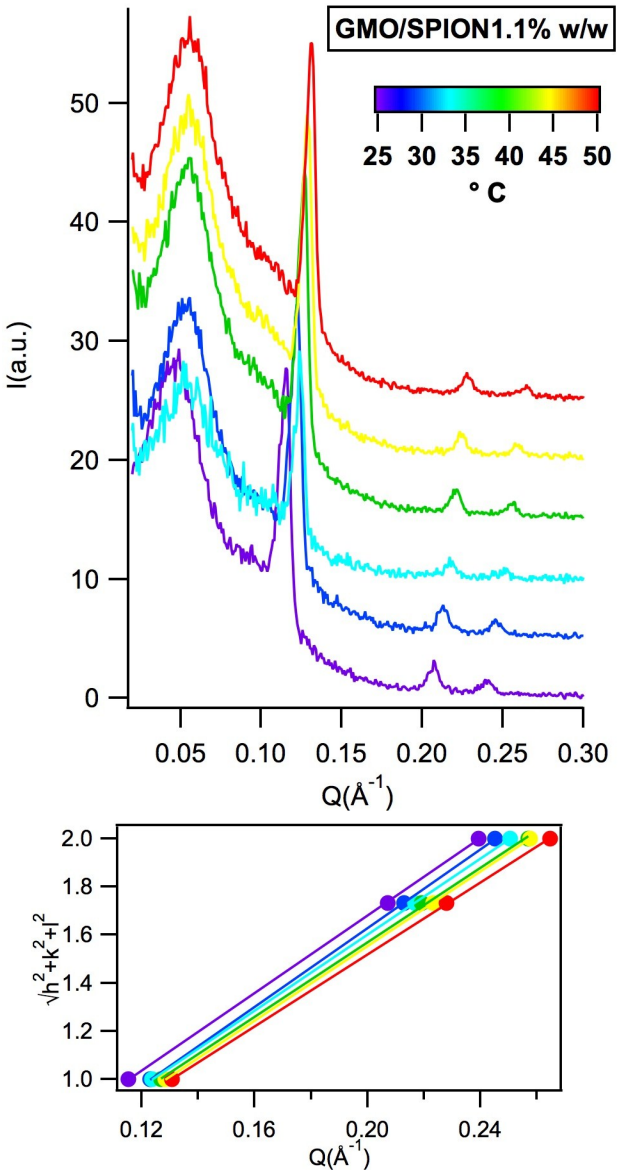

Figure S9: SAXS curves of GMO assembled with 1.1% w/w Fe_3O_4 (6.13 mg of a mixture OAc/Ol) and Miller index on Q_{max} to determine the trend of the lattice parameter for the inverse hexagonal phase with temperature in the 25-50 °C temperature rang.

Table S7. Lattice parameters, water channel radii and water volume fraction of GMO assembled with 1.1% SPIONs at increasing temperatures.

T (°C)	Lattice parameter (Å)	Water channel radii (Å)	Water volume fraction
25	50	9.3	0.13

30	51	9.8	0.14
35	49	8.8	0.12
40	49	8.8	0.12
45	49	8.8	0.12
50	47	7.7	0.1

S.11- Temperature dependence of GMO/H_2O/SPIONs lattice parameters

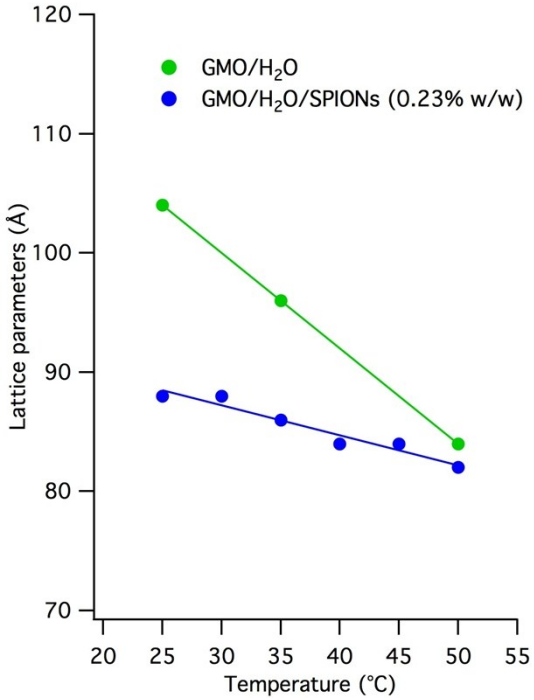

Figure S10: Linear fit of lattice parameters in GMO/H_2O system (green line) and GMO/H_2O/SPIONs (0.23% w/w) (blue line) on temperature. Both the systems have the same cubic structure (Pn3m).

S.12- DLS analysis of cubosomes and magnetocubosomes

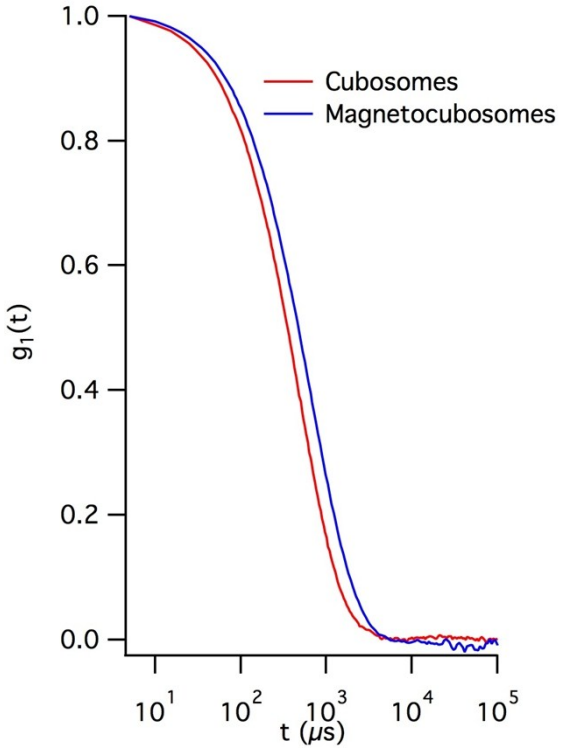

Figure S11: Dynamic Light Scattering (DLS) curves of cubosomes and magnetocubosomes water dispersion diluted 1:500 before the measurement.

Table S8. Hydrodynamic diameter and polydispersity of cubosomes and magnetocubosomes. DLS curves analyzed through a cumulant analysis stopped to the second order.

T (°C)	Hydrodynamic diameter (nm)	Polydispersity
Cubosomes	240	0.19
Magnetocubosomes	260	0.12

S.13- Temperature dependence of cubosomes and magnetocubosomes lattice parameters

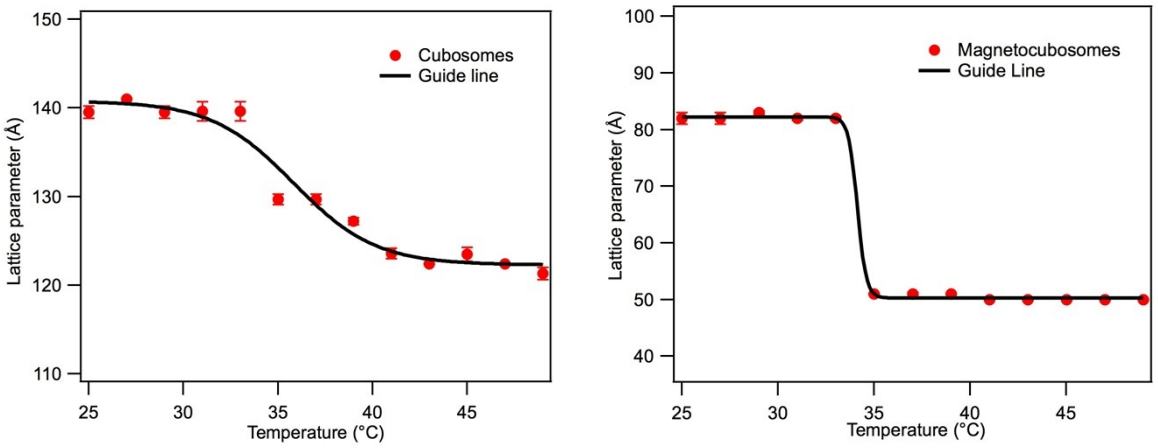

Figure S12: Trend of lattice parameters of cubosomes and magnetocubosomes with temperature in the 25-50°C temperature range, estimated from SAXS data. The lattice parameter *d* decreases following a sigmoidal-like trend. The overall lattice parameter decrease is of about 2 nm for cubosomes and 3 nm for magnetocubosomes in the 25°C-50°C temperature range. Magnetocubosomes present a phase transition Pn3m-H_{II} very close to the physiological temperature.

S.14- Derivation of Equation 4 of the main text

In the framework of Helfrich theory, the free energy of elastic curvature of a lipid bilayer g_C can be expressed as:

$$g_C = 2\kappa^B(H - H_0^B)^2 + \kappa_G^B K \quad (S6)$$

where κ^B and κ_G^B are the bending and Gaussian elastic moduli respectively, H and K are the mean and Gaussian curvatures and H_0^B is the spontaneous curvature of the bilayer. Considering that for a symmetric lipid bilayer $H_0^B = 0$, the H_{II} phase is characterized by a Gaussian curvature K=0 and that the mean curvature for a Pn3m at the mid-plane H=0, we can write equation (6) for the hexagonal and cubic phases as follows:

$$g_c(H_{II}) = 2\kappa_B H^2 \quad (S7)$$

$$g_C(Pn3m) = \kappa_G^B K \quad (S8)$$

If we express the bending and Gaussian elastic moduli for a bilayer in terms of the corresponding terms for a monolayer, we obtain:

$$\kappa_B = 2\kappa \quad (S9)$$

$$\kappa_G^B = 2(\kappa_G - 2H_0\kappa l_c) \quad (S10)$$

and can rewrite (7) and (8) as follows:

$$g_c(H_{II}) = 4\kappa H^2 \quad (S11)$$

$$g_C(Pn3m) = 2(\kappa_G - 2H_0\kappa l_c)K \quad (S12)$$

Considering a cubic-to-hexagonal phase transition, we can write the variation of elastic curvature as:

$$\Delta g_C = 4\kappa H_{H_{II}}^2 - 2K_{Pn3m}(\kappa_G - 2H_0\kappa l_c) \quad (S13)$$

REFERENCES

(1) Wang, L.; Luo, J.; Fan, Q.; Suzuki, M.; Suzuki, I. S.; Engelhard, M. H.; Lin, Y.; Kim, N.; Wang, J. Q.; Zhong, C. J. *J. Phys. Chem. B* **2005**, *109* (46), 21593.

(2) Reese, C. W.; Strango, Z. I.; Dell, Z. R.; Tristram-Nagle, S.; Harper, P. E. *Phys. Chem. Chem. Phys.* **2015**, *17* (14), 9194.

(3) Marsh, D. *Handbook of lipid bilayers*; 2013.

(4) Salvatore, A.; Montis, C.; Berti, D.; Baglioni, P. *ACS Nano* **2016**, *10* (8), 7749.

(5) Kotlarchyk, M.; Chen, S.-H. *J. Chem. Phys.* **1983**, *79* (5), 2461.